# ADVANCES IN POLARIMETRY AND ELLIPSOMETRY: FUNDAMENTALS AND APPLICATIONS

EDITED BY: Haofeng Hu, Jingping Zhu, Hao Jiang and Ji Qi
PUBLISHED IN: Frontiers in Physics

frontiers Research Topics

# frontiers



ISSN 1664-8714
ISBN 978-2-83250-261-7
DOI 10.3389/978-2-83250-261-7

## About Frontiers

Frontiers is more than just an open-access publisher of scholarly articles: it is a pioneering approach to the world of academia, radically improving the way scholarly research is managed. The grand vision of Frontiers is a world where all people have an equal opportunity to seek, share and generate knowledge. Frontiers provides immediate and permanent online open access to all its publications, but this alone is not enough to realize our grand goals.

## Frontiers Journal Series

The Frontiers Journal Series is a multi-tier and interdisciplinary set of open-access, online journals, promising a paradigm shift from the current review, selection and dissemination processes in academic publishing. All Frontiers journals are driven by researchers for researchers; therefore, they constitute a service to the scholarly community. At the same time, the Frontiers Journal Series operates on a revolutionary invention, the tiered publishing system, initially addressing specific communities of scholars, and gradually climbing up to broader public understanding, thus serving the interests of the lay society, too.

## Dedication to Quality

Each Frontiers article is a landmark of the highest quality, thanks to genuinely collaborative interactions between authors and review editors, who include some of the world's best academicians. Research must be certified by peers before entering a stream of knowledge that may eventually reach the public - and shape society; therefore, Frontiers only applies the most rigorous and unbiased reviews.
Frontiers revolutionizes research publishing by freely delivering the most outstanding research, evaluated with no bias from both the academic and social point of view. By applying the most advanced information technologies, Frontiers is catapulting scholarly publishing into a new generation.

## What are Frontiers Research Topics?

Frontiers Research Topics are very popular trademarks of the Frontiers Journals Series: they are collections of at least ten articles, all centered on a particular subject. With their unique mix of varied contributions from Original Research to Review Articles, Frontiers Research Topics unify the most influential researchers, the latest key findings and historical advances in a hot research area! Find out more on how to host your own Frontiers Research Topic or contribute to one as an author by contacting the Frontiers Editorial Office: frontiersin.org/about/contact

# ADVANCES IN POLARIMETRY AND ELLIPSOMETRY: FUNDAMENTALS AND APPLICATIONS

Topic Editors:
**Haofeng Hu,** Tianjin University, China
**Jingping Zhu,** Xi'an Jiaotong University, China
**Hao Jiang,** Huazhong University of Science and Technology, China
**Ji Qi,** Imperial College London, United Kingdom

**Citation:** Hu, H., Zhu, J., Jiang, H., Qi, J., eds. (2022). Advances in Polarimetry and Ellipsometry: Fundamentals and Applications. Lausanne: Frontiers Media SA.
doi: 10.3389/978-2-83250-261-7

# Table of Contents

frontiers | Frontiers in Physics

EDITORIAL
published: 20 June 2022
doi: 10.3389/fphy.2022.916571

# Editorial: Advances in Polarimetry and Ellipsometry: Fundamentals and Applications

*Haofeng Hu*[1]*, *Hao Jiang*[2], *Qi Ji*[3] and *Jingping Zhu*[4]

[1]School of Marine Science and Technology, Tianjin University, Tianjin, China, [2]State Key Laboratory of Digital Manufacturing Equipment and Technology, Huazhong University of Science and Technology, Wuhan, China, [3]Department of Surgery and Cancer, Imperial College London, London, United Kingdom, [4]School of Electronic Science and Engineering, Xi'an Jiaotong University, Xi'an, China

**Keywords: polarimetry, polarimetric imaging, ellipsometry, polarization, Mueller matrix, Stokes vector**

## Editorial on the Research Topic

### Advances in Polarimetry and Ellipsometry: Fundamentals and Applications

Polarization is a fundamental property of light waves. Originating from polarization, there are two categories of techniques: polarimetry and ellipsometry. Polarimetry is the technique for measuring and interpreting polarization information, and ellipsometry usually refers to the polarimetry that characterizes thin films and surfaces using polarization changes. In the past decades, polarimetry and ellipsometry have shown promising applications in various fields, including target detection, biomedical imaging, characterization of surfaces and thin films, etc., while the theory, instrument, and polarization information interpretation for polarimetry and ellipsometry are constantly developing at the same time. We are glad to see that this special issue collects 13 articles, which report both the latest technological advances and the applications of polarimetry and ellipsometry.

In the field of polarimetry, remarkable works on polarimetric imaging in scattering media and polarimetry for biomedical applications have been covered in the current Research Topic. Shi et al. proposed a method to remove haze by using a self-supervised neural network that combines scene polarization information, which does not require any haze-free image as the constraint for neural network training. Song et al. proposed a method of polarization-imaging recovery in complex underwater environment based on investigating the scattering characteristics of underwater suspension particles and bubble by using the theory of radiation transfer. Wang et al. investigated the propagation of linear and circular polarized light in the scattering medium. They found that both the linear and circular polarimetric imaging had an ability to reduce the image degradation caused by smoke, and the propagation of the polarized light, especially the circular polarized light, is determined by medium conditions. Hu et al. review the recent advances of polarimetric imaging through scattering media from the perspectives of the principle, basic model, imaging configuration and applications, and they provide a brief summary and comparison across various methods in this Topic. Ivanov et al. measured the Mueller matrices of multiple formalin-fixed human colon samples including healthy and malignant regions, and investigated several unsupervised and supervised machine learning algorithms for histopathological classification based on polarimetric data. Wan et al. proposed a new angular-based Mueller matrix polarimetry parameter, and demonstrated that the proposed parameter can differentiate subwavelength pore sizes well. Xu et al. proposed a high-throughput method for online identification of bioaerosols based on multi-angle polarization index system, and showed that bioaerosols like pollen can be distinguished from other types of aerosols with this method.



***Edited and reviewed by:***
*Lorenzo Pavesi,*
*University of Trento, Italy*

***Correspondence:**
*Haofeng Hu*
*haofeng_hu@tju.edu.cn*

***Specialty section:***
*This article was submitted to Optics and Photonics, a section of the journal Frontiers in Physics*

***Received:*** *09 April 2022*
***Accepted:*** *31 May 2022*
***Published:*** *20 June 2022*

***Citation:***
*Hu H, Jiang H, Ji Q and Zhu J (2022) Editorial: Advances in Polarimetry and Ellipsometry: Fundamentals and Applications. Front. Phys. 10:916571. doi: 10.3389/fphy.2022.916571*

In the field of ellipsometry, remarkable works on instrumentation, methodology and applications have been covered in the current Research Topic. To achieve enhanced repeatability of the instrument in the applications in Integrated Circuit (IC) industry, Jiang et al. proposed a general optimal instrument matrix to minimize the estimation variance for both Gaussian additive noise and Poisson shot noise as well as a peak matching algorithm to compress the repeatability errors due to the bias of the trigger signal and the limited sampling frequency. Hansen et al. reported an improved calibration method for Mueller ellipsometry to detect the geometrical anisotropy of the structure, and further combined it with multiple instruments as a hybrid metrology to improve the measurement accuracy on three-dimensional periodic structures. Käseberg et al. reported their in-house Mueller matrix microscope based on an imaging system and a dual-rotating compensator configuration for the ellipsometric system, and further carried out the comparison of the results on a specific designed sample containing geometrical nanostructures with lateral dimensions ranging from 50 to 5000 nm to traceable atomic force microscopy measurements. Yao et al. proposed the quasi-Brewster angle technique (qBAT) based on ellipsometry to inspect the quality of polished $Lu_2O_3$ single crystal, to achieve fast, nondestructive, and high-sensitive surface/subsurface damage assessment. Li et al. utilized the Mueller Matrix Spectroscopic Ellipsometry on the nanoscale subsurface damage detection of 4H-SiC wafers induced by grinding and polishing, which could be expected to benefit process optimization in the whole wafer manufacturing. Dong et al. introduced their analysis model based on the rigorous coupled-wave analysis (RCWA) method to retract the correlation between the incidental and azimuthal angles and the reflectivity of different diffraction orders, with the objective to show the potential of the Morpho butterfly scales-based biosensor.

In summary, we hope that the collection presented in this Research Topic, "Advances in Polarimetry and Ellipsometry: Fundamentals and Applications", will contribute to the progress of research and development activities in the field.

## AUTHOR CONTRIBUTIONS

All authors listed have made a substantial, direct, and intellectual contribution to the work and approved it for publication.

**Conflict of Interest:** The authors declare that the research was conducted in the absence of any commercial or financial relationships that could be construed as a potential conflict of interest.

**Publisher's Note:** All claims expressed in this article are solely those of the authors and do not necessarily represent those of their affiliated organizations, or those of the publisher, the editors and the reviewers. Any product that may be evaluated in this article, or claim that may be made by its manufacturer, is not guaranteed or endorsed by the publisher.

frontiers in Physics

ORIGINAL RESEARCH
published: 20 December 2021
doi: 10.3389/fphy.2021.795639

# Surface and Subsurface Quality Assessment of Polished $Lu_2O_3$ Single Crystal Using Quasi-Brewster Angle Technique

*Chengyuan Yao*[1], *Wanfu Shen*[1,2], *Xiaodong Hu*[1] *and Chunguang Hu*[1]*

[1]State Key Laboratory of Precision Measuring Technology and Instruments, Tianjin University, Tianjin, China, [2]Nanchang Institute for Microtechnology, Tianjin University, Tianjin, China

The sesquioxide $Lu_2O_3$ single crystal has attracted tremendous attention as potential host material for high-power solid-state lasers. As polishing is the terminal process of conventional ultra-precision machining, the quality of polished crystal directly impacts the crucial performance indicators of optics. The high melting point of $Lu_2O_3$ single crystal makes crystal preparation difficult. Therefore, investigations on the surface/subsurface quality inspection of polished $Lu_2O_3$ single crystal are scarce. In this paper, we utilize the quasi-Brewster angle technique (qBAT) based on ellipsometry to inspect the quality of polished $Lu_2O_3$ single crystal, achieving fast, non-destructive, and high-sensitive surface/subsurface damage assessment. A systematic crystal processing scheme is designed and polished $Lu_2O_3$ crystal samples are obtained. To verify the results of qBAT, the surface and subsurface quality are tested using optical profilometer and transmission electron microscope, respectively. The consistency of the test results demonstrates the feasibility, high sensitivity, and accuracy of the qBAT. To our knowledge, this is the first time that the qBAT is applied to investigate the polished surface/subsurface quality of $Lu_2O_3$ single crystal. In conclusion, this method provides a powerful approach to the high-precision characterization of the surface/subsurface quality of $Lu_2O_3$ single crystal, and has significant potential for material property study and process optimization during ultra-precision machining.

**Keywords: $Lu_2O_3$ single crystal, polishing, surface damage, subsurface damage, quasi-Brewster angle technique, ellipsometry**

OPEN ACCESS

***Edited by:***
*Hao Jiang,*
*Huazhong University of Science and Technology, China*

***Reviewed by:***
*Haozhe Wang,*
*Massachusetts Institute of Technology, United States*
*Alexandra Pena Revellez,*
*UPR2940 Institut Neel (NEEL), France*

***Correspondence:**
*Chunguang Hu*
*cghu@tju.edu.cn*

***Specialty section:***
*This article was submitted to Optics and Photonics, a section of the journal Frontiers in Physics*

***Received:*** *15 October 2021*
***Accepted:*** *16 November 2021*
***Published:*** *20 December 2021*

***Citation:***
*Yao C, Shen W, Hu X and Hu C (2021) Surface and Subsurface Quality Assessment of Polished $Lu_2O_3$ Single Crystal Using Quasi-Brewster Angle Technique. Front. Phys. 9:795639. doi: 10.3389/fphy.2021.795639*

## INTRODUCTION

$Lu_2O_3$ single crystal as sesquioxide has proven to be prospective for high-power solid-state lasers, high-energy radiation detection, and semiconductors due to its high thermal conductivity, low phonon energy, high-density scintillators, high absorption efficiency, wide band gap, and robust thermal stability [1–7]. Polishing, as the terminal process of traditional ultra-precision machining, can achieve high surface flatness and roughness, but inevitably produces surface and subsurface damage. Typical surface and subsurface damage include pits, scratches, subsurface cracks, residual stresses, dislocations, etc. [8, 9]. Surface/subsurface damage directly diminishes the strength, lifetime, coating quality, imaging quality, and laser damage threshold of optics. However, investigations on the surface/subsurface quality of polished $Lu_2O_3$ single crystals are scarce, which severely limits the

design, fabrication, and application of related devices. The prerequisite for effective suppression and removal of surface and subsurface damage is high precision inspection. Therefore, the assessment of surface/subsurface damage on polished $Lu_2O_3$ has momentous theoretical research significance and practical value.

Conventional surface inspection methods, such as optical profilometer, atomic force microscope (AFM), and scanning tunneling microscope (STM), are sufficient for surface quality testing needs [10–13]. Since subsurface damage is overlapped by the sample surface, high precision assessment of subsurface damage is challenging. In addition, as ultra-precision machining moves toward atomic and close-to-atomic scale manufacturing (ACSM), subsurface damage scales approach the nano/sub-nano level and are coupled, further increasing the difficulty of detection [14]. Subsurface damage detection methods are categorized into destructive and non-destructive methods according to its destructiveness to the sample. Destructive detection methods normally employ physical or chemical approaches to remove the portion covering the subsurface damage, thereby exposing the subsurface damage directly, and then using conventional methods for defect detection. Destructive methods include transmission electron microscopy (TEM), magnetorheological finishing (MRF) polishing, chemical etching, etc. [15–18]. Although the accuracy is relatively high, they will cause irreversible and permanent damage to the sample, making it extremely restrictive in many fields. Non-destructive methods are mainly optical methods, depending on the interaction between light and matter. They have advantages such as contact free and high speed, and they include optical coherence tomography (OCT), laser scattering, X-ray diffraction (XRD), quasi-Brewster angle technique (qBAT), etc. [19–22]. Non-destructive methods have relatively low measurement accuracy and can usually only measure samples with low damage. In addition, they are susceptible to environmental interference.

Quasi-Brewster angle technique (qBAT) based on ellipsometry achieves simultaneous detection of surface and subsurface damage by measuring the phase difference curves of the sample in the vicinity of the Brewster angle. Specifically, the slope at the quasi-Brewster angle reflects the surface roughness, and the quasi-Brewster angle shift (*qBAS*) represents the subsurface damage. The qBAT has been utilized to investigate the surface/subsurface quality of fused silica, quartz crystal, $CaF_2$ crystal [22, 23]. In our previous work, surface/subsurface damage of gadolinium gallium garnet (GGG) crystals at the rough and fine polishing processes was investigated using the qBAT [24]. By establishing appropriate optical models for various polishing processes, the applicability of qBAT is extended to rough polishing. Moreover, the trend of *Slope* falling and then rising during polishing was observed first, which was verified by the surface morphology measurement results. In summary, related studies have amply demonstrated that qBAT is a promising method for polished surface/subsurface quality assessment.

In this paper, the surface/subsurface quality of $Lu_2O_3$ single crystal at the fine polishing and chemical mechanical polishing (CMP) processes was assessed using qBAT. By designing systematic crystal processing scheme, $Lu_2O_3$ single crystals with different surface/subsurface qualities were obtained at the fine polished and CMP processes, respectively. The phase difference curves of different samples were measured near the Brewster angle employing variable angle ellipsometer. The measurement data were analyzed based on the principle of qBAT to obtain the surface/subsurface quality of the different samples. To verify the measurement results of qBAT, the surface and subsurface damage were measured using optical profilometer and TEM, respectively. The consistency of the results illustrates the validity and high sensitivity of qBAT. In conclusion, this study provides a powerful approach for polished surface/subsurface quality assessment of hard and brittle materials such as $Lu_2O_3$ single crystal and explores the potential applications of qBAT.

# MATERIALS AND METHODS

## Polishing Process

$Lu_2O_3$ single crystal samples were prepared by the edge-defined film-fed growth (EFG) method, and the details of the crystal preparation are given in [25]. The sample diameter is about 12 mm and the thickness is 1 mm. To obtain fine polished and CMP samples with different surface/subsurface damage, we designed a processing scheme as shown in **Table 1**. The processing scheme consists of two processes, lapping and polishing. Lapping is divided into rough lapping and fine lapping, and polishing is classified into rough polishing, fine polishing, and CMP. This study focuses on the fine polishing and CMP, and a total of nine samples were obtained. Five fine polished samples were polished for 20–100 min, with one piece removed from the polishing equipment at a 20-min interval. Four CMP samples were polished for 20–80 min with a 20-min interval. Note that the processing scheme is progressive from lapping to polishing. This is considered from the machining efficiency, as the material removal rate of polishing is far lower compared with lapping. Thus, the scheme guarantees a relatively fast removal of crystal defects caused by the preceding processes such as wire cutting and grinding. In addition, as ellipsometry measurements in the oblique incidence configuration are susceptible to interference from backside reflections, the samples are polished on one side and roughened on the other.

## Quasi-Brewster Angle Technique (qBAT)

The prerequisite for qBAT is to build a reasonable optical model for the damage of samples. **Figure 1A**, **Figure 1B**, and **Figure 1C** show the schematic diagrams of the optical models corresponding to the ideal crystal (Ideal), only surface roughness (SR), and simultaneous existence of surface roughness and subsurface damage (SSD), respectively. In this paper, it is assumed that the ideal crystal is $Lu_2O_3$ single crystal without any surface roughness and subsurface damage. The model is the reference to evaluate the effect of surface roughness and subsurface damage on the phase difference curve, which is not available in the actual fabrication. Crystal processing normally results in both surface roughness and subsurface damage. The surface quality is relatively high in the fine polishing and CMP, and the surface

**TABLE 1 |** $Lu_2O_3$ single crystal processing scheme

| No | Process | Consumables | Parameters |
|---|---|---|---|
| 1 | Rough lapping | Cast iron plate<br>W40 emery | Lapping disc speed 50 r/min<br>Lapping load 107 g/cm$^2$<br>Lapping time 20 min |
| 2 | Fine lapping | Cast iron plate<br>W20 emery | Lapping disc speed 60 r/min<br>Lapping load 127 g/cm$^2$<br>Lapping time 60 min |
| 3 | Rough polishing | Asphalt polishing pad<br>W2.5 $Al_2O_3$ | Polishing pad speed 70 r/min<br>Polishing load 127 g/cm$^2$<br>Polishing time 100 min |
| **4** | **Fine polishing** | IC1000 polishing pad<br>W0.1 diamond power | Polishing pad speed 70 r/min<br>Polishing load 127 g/cm$^2$<br>Polishing time 20–100 min<br>Take out one piece every 20 min |
| **5** | **Chemical mechanical polishing** | Flannel polishing pad<br>$SiO_2$ polishing solution | Polishing pad speed 70 r/min<br>Polishing load 107 g/cm$^2$<br>Polishing time 20–80 min<br>Take out one piece every 20 min |

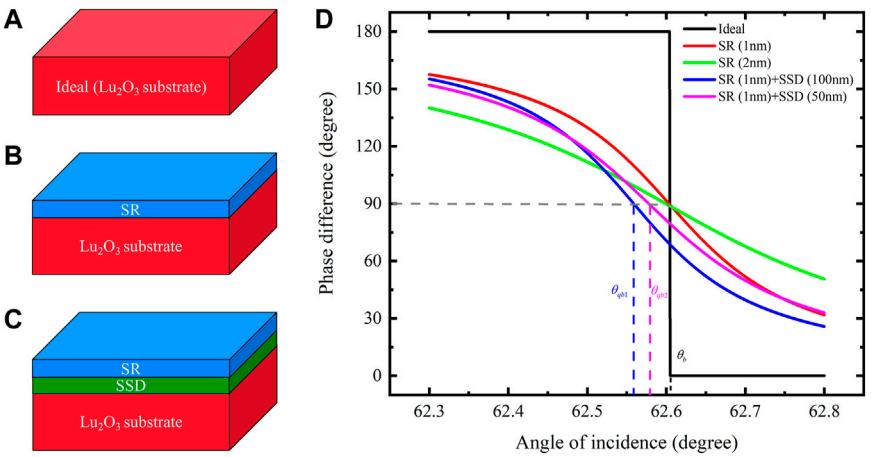


**FIGURE 1 | (A–C)** are the corresponding optical models for ideal crystal (Ideal), only surface roughness (SR), and both surface roughness and subsurface damage (SSD), respectively; **(D)** is the corresponding simulation result.

roughness is generally in the nanometer scale. The sample surface contains pits, scratches, and height undulations, and the subsurface damage is more complex and diverse and coupled with each other. To simplify the model, they are equated as surface roughness (SR) layer and subsurface damage (SSD) layer, respectively. In addition, there is no strict boundary between surface roughness and subsurface damage, and the boundaries in **Figure 1B** and **Figure 1C** are schematic lines. The surface roughness layer and subsurface damage layer are characterized using the effective medium approximation (EMA) model [26], as shown in

$$f_1\frac{\varepsilon_1-\varepsilon}{\varepsilon_1-2\varepsilon}+(1-f_1)\frac{\varepsilon_2-\varepsilon}{\varepsilon_2-2\varepsilon}=0 \tag{1}$$

where $\varepsilon_1$, $\varepsilon_2$ are the corresponding dielectric constants of medium 1 and medium 2, here are air and $Lu_2O_3$ single crystal, respectively. $\varepsilon$ is the calculated effective dielectric constant. $f_1$ and $(1-f_1)$ are the corresponding porosities of medium 1 and medium 2, accordingly. It should be noted that the porosities of the surface roughness layer and the subsurface damaged layer are different.

Based on qBAT, surface roughness is evaluated by analyzing the slope of the phase difference curve at the quasi-Brewster angle ($\theta_{qb}$); subsurface damage is assessed by the shift between $\theta_{qb}$ and the Brewster angle ($\theta_b$). The $\theta_{qb}$ is defined as the angle of incidence corresponding to the phase difference equals to 90° in the optical model shown in **Figure 1C**. The expressions for *Slope* and the quasi-Brewster angle shift (*qBAS*) are shown in **Eqs 2**, **3**:

$$Slope = f'(\theta,\Delta)\big|_{\theta=\theta_{qb}} \tag{2}$$

$$qBAS = \theta_{qb}-\theta_b \tag{3}$$

where $\theta$ and $\Delta$ are the incident angle and phase difference, respectively. $f'$ $(\theta, \Delta)$ is the first-order derivative equation of the corresponding fitted curve of the phase difference

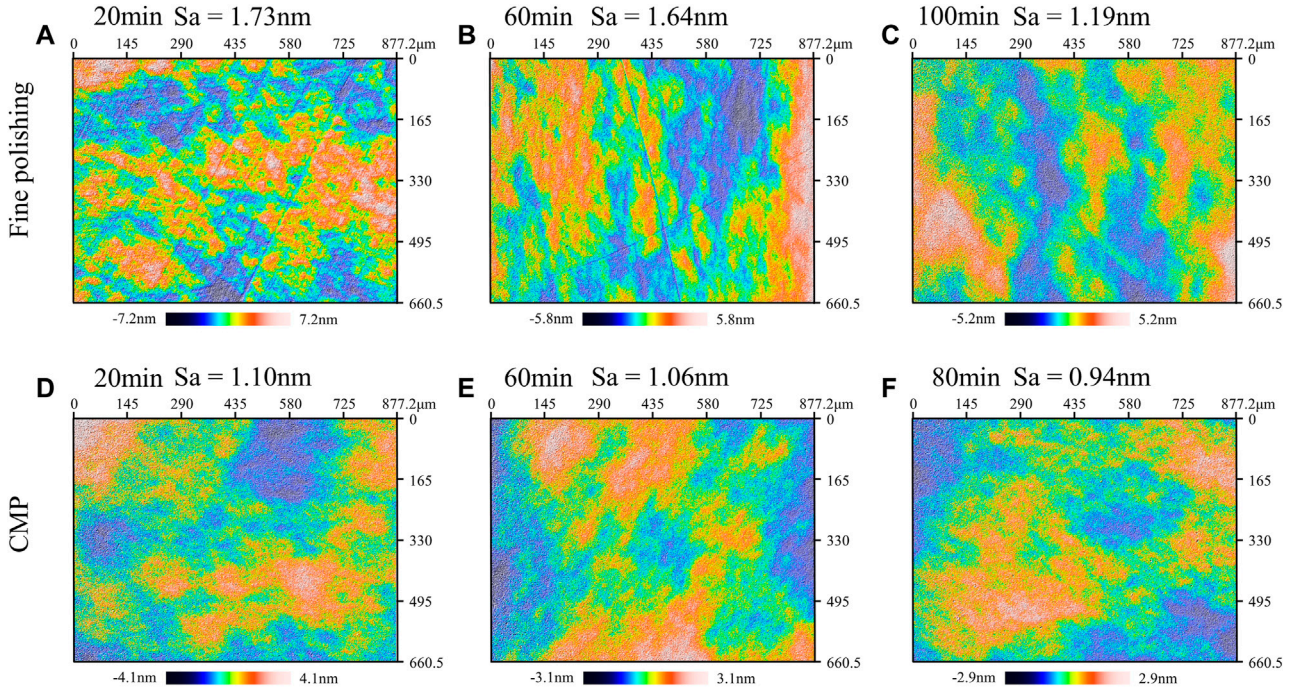


**FIGURE 2 | (A–C)** are typical measurements of optical profilometer for 20, 60, and 100 min samples of fine polishing, respectively; **(D–F)** are typical measurements of optical profilometer for 20, 60, and 80 min samples of CMP, respectively.

curve. Details of the derivation of $\theta_b$, $\theta_{qb}$, and $\Delta$ are given in [24].

Figure 1D shows the simulation results of the phase difference curves near Brewster angle for the corresponding optical models in **Figure 1A**, **Figure 1B**, and **Figure 1C**. The wavelength is 640 nm, and the corresponding refractive indices for air and $Lu_2O_3$ single crystal are 1 and 1.9296, respectively [27]. The incident angle ranges from 62.3 to 62.8° in steps of 0.001°. The corresponding EMA models for both the surface roughness layer and the subsurface damage layer are mixtures of air and $Lu_2O_3$ single crystal with porosities of 0.5 and 0.002, respectively. The simulation experiments were done in MATLAB software. The phase difference curve corresponding to ideal crystal changes abruptly by 180° when the incident angle is $\theta_b$, as shown by the black line in **Figure 1D**. When only surface roughness exists, the slope of the phase difference curve at Brewster angle decreases and is no longer an abrupt change. However, the Brewster angle hardly shifts, as shown in the red and green lines in **Figure 1D**. It is worth noting that the *Slope* of the green curve in **Figure 1D** is smaller than the *Slope* of the red curve in **Figure 1D**. It indicates that *Slope* represents the surface roughness, and the thicker the surface roughness layer, the smaller the *Slope*. When the surface roughness layer and subsurface damage layer coexist, the *Slope* changes and the $\theta_{qb}$ shifts, indicating that the *qBAS* reflects the subsurface damage, as shown by the blue and magenta lines in **Figure 1D**. In addition, the absolute value of the *qBAS* corresponding to 100 nm subsurface damage layer thickness ($|\theta_{qb2}-\theta_b|$) is larger than that of 50 nm ($|\theta_{qb1}-\theta_b|$), indicating that the more severe the subsurface damage, the larger the absolute value of *qBAS*. The thickness of the surface damage layer is fixed at 1 nm when varying the thickness of the subsurface damage. This is rational because the surface quality in fine polishing and CMP is high, with roughness basically in the nanometer scale. The results of related studies and the measurements of the optical profilometer in *Results and Discussion* verify this conclusion [28, 29]. In summary, qBAT can achieve rapid and synchronous inspection of surface roughness and subsurface damage.

## RESULTS AND DISCUSSION

### Surface/Subsurface Quality Measurement Based on Optical Profilometer and TEM

To obtain surface morphology and surface roughness (Sa), all samples were measured using optical profilometer (Sneox, Sensofar). Typical measurements selected from fine polishing and CMP are shown in **Figure 2**. The measurement area is 877.2 × 660.5 μm using ×20 objective and PSI algorithm. Many scratches exist at the start of fine polishing, and as polishing proceeds the scratches gradually decrease until they disappear, as shown in **Figure 2A–C**. The surface of the CMP samples is smoother and free from obvious defects such as scratches, as shown in **Figure 2D–F**. The surface roughness (Sa) shows decreasing trend with respect to the fine polished samples. Each sample was measured at three randomly selected locations in the center area, and the average of the three measurements was used as the final surface roughness (Sa).

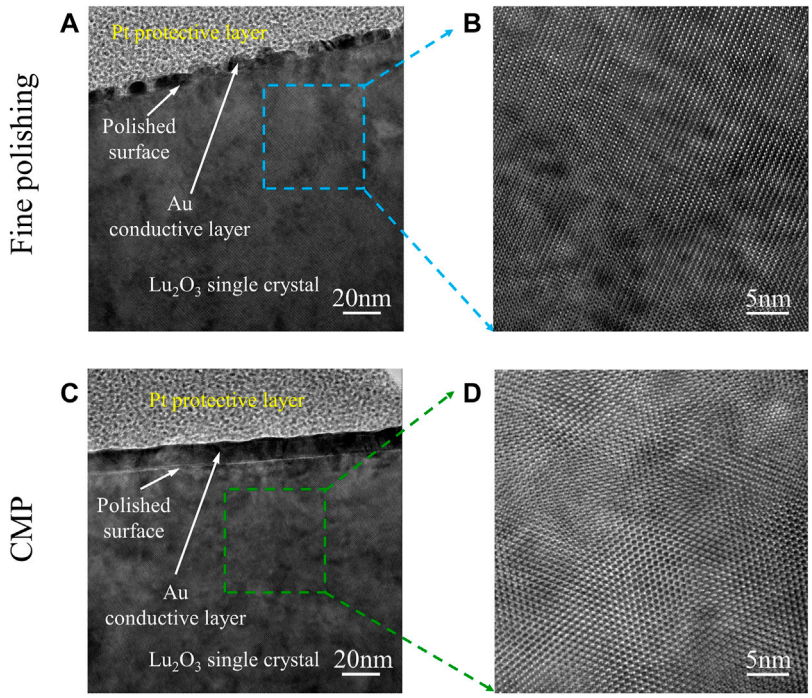


**FIGURE 3 | (A)** and **(C)** are the cross-sectional TEM images of the 60 min fine polished and 60 min CMP samples, respectively; **(B)** and **(D)** are the high magnification images of the positions in the dashed boxes in **(A)** and **(C)**, respectively.

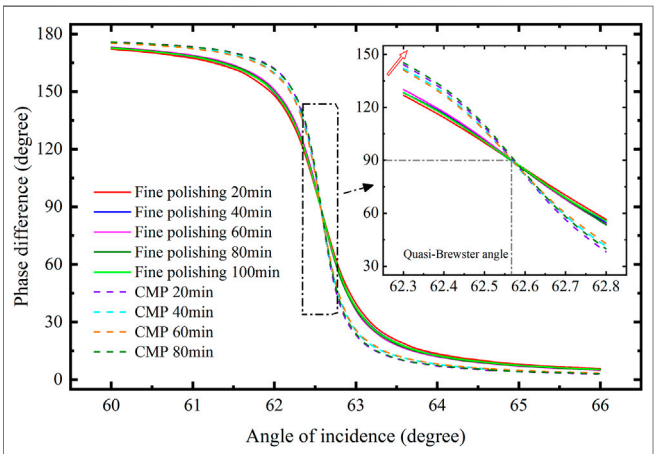


**FIGURE 4 |** Phase difference curve measurement results for all samples.

The final measured results of Sa of all samples are shown in **Figure 5B**. The overall Sa tends to decrease as polishing progresses, and the surface roughness of all CMP samples is lower than that of the fine polished samples. In addition, the error bar is relatively large, which is attributed to the surface that is already smooth and the surface roughness (Sa) is around 1 nm, when a slight sub-nanometer undulation of the surface will lead to significant deviation. The measurement area (877.2 × 660.5 μm) is a tiny fraction of the sample surface size (about 12 mm in diameter), so multiple measurements at different locations are bound to vary slightly.

Transmission electron microscopy (FEI, Talos F200X, operating at 200kV) is utilized to analyze subsurface damage of samples. Owing to the weak conductivity of $Lu_2O_3$ single crystal, Au conductive layer needs to be pre-deposited on the sample surface to facilitate the TEM specimen preparation. The Pt protective layer was deposited again to prevent additional subsurface damage caused by focused ion beam (FIB) during the TEM specimen thinning process. Two typical samples with 60 min of fine polishing and 60 min of CMP were selected for cross-sectional TEM measurement, as shown in **Figure 3A** and **Figure 3C**. No apparent subsurface damages, such as subsurface cracks, deformation layers, and residual stresses, are observed in both the fine polished and the CMP samples. To further investigate the minute subsurface damage of both, high magnification TEM tests were performed on the areas in the dashed boxes in **Figure 3A, C**, respectively, as shown in **Figure 3B, D**. It can be seen that the lattice distribution is regular and uniform, and there are almost no dislocations, twins, and amorphous and other defects. In conclusion, the TEM measurement results demonstrate that there is virtually no subsurface damage in either of the two typical samples. It should be emphasized that since the TEM specimen preparation will damage the sample, the actual measurement procedure is optical non-destructive tests, including optical profilometer and ellipsometer measurements, followed by TEM.

## qBAT Measurement Results

The phase difference of all polished samples near Brewster angle was measured using variable angle ellipsometer (J.A. Woollam,

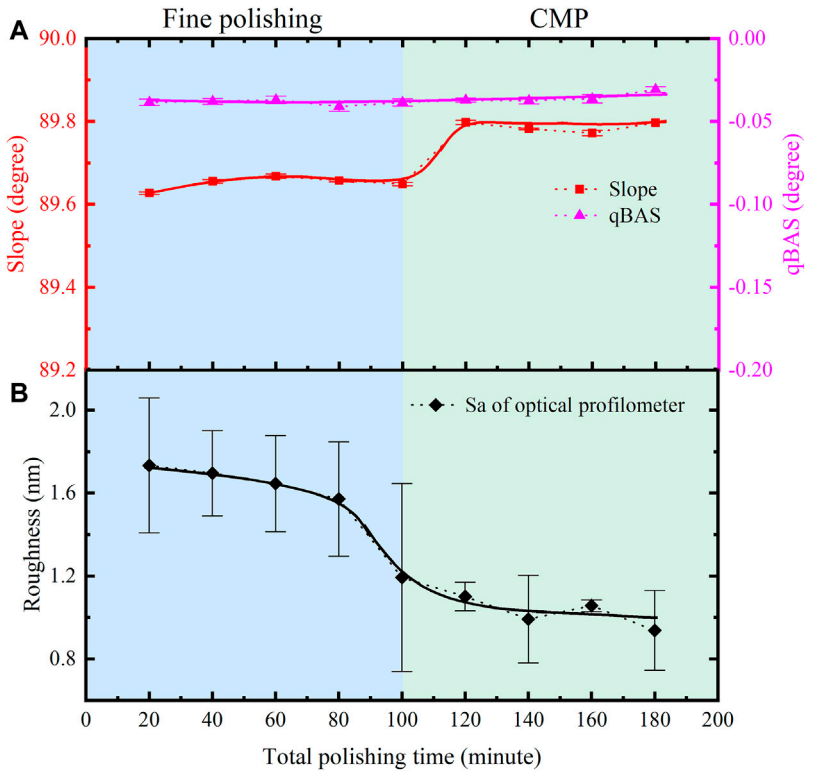


**FIGURE 5 | (A)** *Slope* and *qBAS* measurement results for all samples. **(B)** Surface roughness Sa measurement results for all samples.

RC2), and all phase difference curves are shown in **Figure 4**. The incident angle range is 60–66°, 0.1° as increment, and the long axis and short axis of elliptical measurement spot are about 6 and 4 mm, respectively. The phase difference measured data corresponding to the wavelength of 640 nm are selected. As with the optical profilometer test, we selected three locations in the central area of the sample for measurement, and the average of the three measurements was adopted as the final result. The solid and dotted lines are the phase difference curves of the five fine polished samples and the four CMP samples, respectively. All the phase difference curves are steep and the *Slope* is close to 90°, indicating that the surface roughness is small, which is in agreement with the measurement results of the optical profilometer. To observe the details in the vicinity of Brewster angle, the data in the range of 62.3–62.8° incidence angle were magnified, as shown in the inset of **Figure 4**. The *Slope* of the CMP samples is significantly larger than that of the fine polished samples, which shows that the surface roughness of the CMP samples is lower than that of the fine polished ones. Also, the preliminary judgment is that the *Slope* shows a rising trend with the increase of polishing time. Note that the $\theta_{qb}$ for all the fine polished and CMP samples is rarely shifted, indicating that the subsurface damage is basically unchanged.

**Figure 5A** shows the Slope and qBAS measured results for all samples, which are calculated by fitting the phase difference curves in **Figure 4**. The horizontal axis is the total polishing time, and the CMP polishing time is to be added to the 100 min of fine polishing. The corresponding 3D optical profilometer surface roughness (Sa) measurement results are shown in **Figure 5B**. *Slope* tends to rise as polishing proceeds and basically remains stable at CMP process, indicating that the surface roughness tends to decrease and eventually stabilize. The results match with the optical profilometer measurements, as shown in **Figures 2**, **5B**, and demonstrate the feasibility of qBAT to inspect the polished surface roughness. During the whole polishing process, the change of Sa is basically within 1 nm, and the trend of *Slope* variation can coincide with it, revealing the sub-nanometer level sensitivity of the qBAT to surface roughness. In addition, the *Slope* trend does not correspond precisely to the Sa measurement due to the larger measurement area of the ellipsometer, which is about 33 times larger than that of the optical profilometer. *Slope* measurements are more representative of surface roughness for large-size crystal and not susceptible to local surface undulations. The relatively large roughness error bar of the 100 min fine polished sample indicates that the uniformity of the surface roughness is poor. The magenta line in **Figure 5A** is the *qBAS* measured result, which remains basically stable around −0.03°, approaching the ideal value of 0°. It implies that the subsurface damage of all samples is virtually identical and subsurface damage is rare, which is consistent with the TEM measurement results, as shown in **Figure 3**. The feasibility of qBAT to evaluate subsurface damage is verified. When no subsurface damage exists, the theoretical value of *qBAS* is 0, but the actual measurement is about −0.03°. This is attributed to that *qBAS* is directly influenced by the refractive index of the selected $Lu_2O_3$ single crystal. The refractive index in the reference literature is inevitably

deviated from the actual refractive index, which leads to shifts between the *qBAS* measurements and the theoretical values.

## CONCLUSION

In this study, the surface and subsurface damage of fine polished and CMP $Lu_2O_3$ single crystal was investigated using the qBAT. To obtain samples with various surface/subsurface damage, a crystal processing scheme was designed. To verify the measurement results of the qBAT, the surface and subsurface quality were characterized by commercial 3D optical profilometer and TEM, respectively. The consistency of the measured results demonstrates the feasibility and high sensitivity of qBAT for evaluating surface and subsurface damage on polished $Lu_2O_3$ single crystal. Consequently, the qBAT enables fast, non-destructive, and facile inspection of polished surfaces and subsurface damage. It overcomes the intrinsic drawbacks of conventional inspection methods, which are complicated, time consuming, and costly. Rapid and simultaneous analysis of surface and subsurface damage based on *Slope* and *qBAS* measurement results provides critical guidance for the optimization of polishing processes during machining. In conclusion, this study provides an efficient approach for polished $Lu_2O_3$ surface/subsurface damage assessment and further broadens the application of qBAT.

## DATA AVAILABILITY STATEMENT

The raw data supporting the conclusions of this article will be made available by the authors, without undue reservation.

## AUTHOR CONTRIBUTIONS

All authors listed have made a substantial, direct, and intellectual contribution to the work and approved it for publication.

## FUNDING

The project is supported by National Key Research and Development Program (grant no. 2019YFB2005601), the General Program of NSFC (52075383), and Major scientific research instrument development project of NSFC (61927808).

## REFERENCES

1. Liu J, Yang X, Chen R, Feng B, Zhu H, Luan C, et al. Vertical Nanoporous GaN Substrates for Photonic Engineering: Lu2O3:Eu Single crystal Thin Films as an Example. *J Alloys Comp* (2021) 892:162069. doi:10.1016/j.jallcom.2021.162069
2. Guzik M, Pejchal J, Yoshikawa A, Ito A, Goto T, Siczek M, et al. Structural Investigations of Lu2O3 as Single Crystal and Polycrystalline Transparent Ceramic. *Cryst Growth Des* (2014) 14:3327–34. doi:10.1021/cg500225v
3. Hou W, Zhao H, Li N, Xue Y, Shi J, Xu X, et al. Spectroscopic Properties of Er: Lu2O3 crystal in Mid-infrared Emission. *Opt Mater* (2019) 98:109508. doi:10.1016/j.optmat.2019.109508
4. Hu J, Guo H, Du W, Yang F, Yang Q, Feng H. Luminescent Properties and X-ray Imaging Result of Lu2O3:Eu Structured Scintillation Film on YSZ Single crystal Substrate by LCVD Method. *Ceramics Int* (2021) 47:28505–10. doi:10.1016/j.ceramint.2021.07.007
5. Zhang D, Lin W, Lin Z, Jia L, Zheng W, Huang F. Lu2O3: A Promising Ultrawide Bandgap Semiconductor for Deep UV Photodetector. *Appl Phys Lett* (2021) 118:211906. doi:10.1063/5.0048752
6. Zhang N, Zhou H, Yin Y, Wang T, Zhang J, Ye L, et al. Exploring Promising Up-Conversion Luminescence Single crystal Fiber in Sesquioxide Family for High Temperature Optical Thermometry Application. *J Alloys Comp* (2022) 889:161348.
7. Zhang S, Guo X, Jin Z, Kang R, Guo D. Material Removal Characteristics of Precorroded Lu2O3 Laser Crystals and Elastic Deformation Model during Nanoscratch Process. *Tribology Int* (2020) 143:106027. doi:10.1016/j.triboint.2019.106027
8. Aida H, Takeda H, Doi T. Analysis of Mechanically Induced Subsurface Damage and its Removal by Chemical Mechanical Polishing for Gallium Nitride Substrate. *Precision Eng* (2021) 67:350–8. doi:10.1016/j.precisioneng.2020.10.007
9. Li M, Karpuschewski B, Ohmori H, Riemer O, Wang Y, Dong T. Adaptive Shearing-Gradient Thickening Polishing (AS-GTP) and Subsurface Damage Inhibition. *Int J Machine Tools Manufacture* (2021) 160:103651. doi:10.1016/j.ijmachtools.2020.103651
10. Michaels JA, Janavicius L, Wu X, Chan C, Huang HC, Namiki S, et al. Producing Silicon Carbide Micro and Nanostructures by Plasma-Free Metal-Assisted Chemical Etching. *Adv Funct Mater* (2021) 31:2103298. doi:10.1002/adfm.202103298
11. Sagbas B, Gümüş BE, Kahraman Y, Dowling DP. Impact of Print Bed Build Location on the Dimensional Accuracy and Surface Quality of Parts Printed by Multi Jet Fusion. *J Manufacturing Process* (2021) 70:290–9. doi:10.1016/j.jmapro.2021.08.036
12. Erinosho MF, Akinlabi ET, Johnson OT. Characterization of Surface Roughness of Laser Deposited Titanium alloy and Copper Using AFM. *Appl Surf Sci* (2018) 435:393–7. doi:10.1016/j.apsusc.2017.11.131
13. Luo Y, Jelic V, Chen G, Nguyen PH, Liu Y-JR, Calzada JAM, et al. Nanoscale Terahertz STM Imaging of a Metal Surface. *Phys Rev B* (2020) 102:205417. doi:10.1103/physrevb.102.205417
14. Mathew PT, Rodriguez BJ, Fang F. Atomic and Close-To-Atomic Scale Manufacturing: A Review on Atomic Layer Removal Methods Using Atomic Force Microscopy. *Nanomanuf Metrol* (2020) 3:167–86. doi:10.1007/s41871-020-00067-2
15. Sun X, Zhu W, Wu D, Li C, Wang J, Zhu Y, et al. Surface-reaction Induced Structural Oscillations in the Subsurface. *Nat Commun* (2020) 11:305. doi:10.1038/s41467-019-14167-1
16. Zhang Q, Chu C, Zhang Z, Zhu Y. Nanosecond UV Laser Induced Subsurface Damage Mechanics of Cemented Tungsten Carbide. *Ceramics Int* (2021) 47:32927–37. doi:10.1016/j.ceramint.2021.08.191
17. Shafrir SN, Lambropoulos JC, Jacobs SD. Subsurface Damage and Microstructure Development in Precision Microground Hard Ceramics Using Magnetorheological Finishing Spots. *Appl Opt* (2007) 46:5500–15. doi:10.1364/ao.46.005500
18. Neauport J, Ambard C, Cormont P, Darbois N, Destribats J, Luitot C, et al. Subsurface Damage Measurement of Ground Fused Silica Parts by HF Etching Techniques. *Opt Express* (2009) 17:20448–56. doi:10.1364/oe.17.020448
19. Hou F, Zhang M, Zheng Y, Ding L, Tang X, Liang Y. Detection of Laser-Induced Bulk Damage in Optical Crystals by Swept-Source Optical Coherence Tomography. *Opt Express* (2019) 27:3698–709. doi:10.1364/oe.27.003698
20. Trost M, Herffurth T, Schmitz D, Schröder S, Duparré A, Tünnermann A. Evaluation of Subsurface Damage by Light Scattering Techniques. *Appl Opt* (2013) 52:6579–88. doi:10.1364/ao.52.006579
21. Frangulyan TS, Vasil'ev IP, Ghyngazov SA. Effect of Grinding and Subsequent thermal Annealing on Phase Composition of Subsurface Layers of Zirconia Ceramics. *Ceramics Int* (2018) 44:2501–3. doi:10.1016/j.ceramint.2017.10.234

22. Wang J, Maier RL. Surface Assessment of CaF_2 Deep-Ultraviolet and Vacuum-Ultraviolet Optical Components by the Quasi-Brewster Angle Technique. *Appl Opt* (2006) 45:5621–8. doi:10.1364/ao.45.005621
23. Ma B, Shen Z, He P, Ji Y, Sang T, Jiao H, et al. Subsurface Quality of Polished SiO2 Surface Evaluated by Quasi-Brewster Angle Technique. *Optik* (2011) 122: 1418–22. doi:10.1016/j.ijleo.2010.09.019
24. Yao C, Huo S, Shen W, Sun Z, Hu X, Hu X, et al. Assessing the Quality of Polished Brittle Optical crystal Using Quasi-Brewster Angle Technique. *Precision Eng* (2021) 72:184–91. doi:10.1016/j.precisioneng.2021.04.019
25. Yin Y, Wang G, Jia Z, Mu W, Fu X, Zhang J, et al. Controllable and Directional Growth of Er:Lu2O3 Single Crystals by the Edge-Defined Film-Fed Technique. *CrystEngComm* (2020) 22:6569–73. doi:10.1039/d0ce00855a
26. Fung TH, Veeken T, Payne D, Veettil B, Polman A, Abbott M. Application and Validity of the Effective Medium Approximation to the Optical Properties of Nano-Textured Silicon Coated with a Dielectric Layer. *Opt Express* (2019) 27: 38645–60. doi:10.1364/oe.27.038645
27. Medenbach O, Dettmar D, Shannon RD, Fischer RX, Yen WM. Refractive index and Optical Dispersion of Rare Earth Oxides Using a Small-Prism Technique. *J Opt A: Pure Appl Opt* (2001) 3:174–7. doi:10.1088/1464-4258/3/3/303
28. Lu A, Jin T, Liu Q, Guo Z, Qu M, Luo H, et al. Modeling and Prediction of Surface Topography and Surface Roughness in Dual-axis Wheel Polishing of Optical Glass. *Int J Machine Tools Manufacture* (2019) 137:13–29. doi:10.1016/j.ijmachtools.2018.10.001
29. Suratwala T, Steele W, Feit M, Shen N, Dylla-Spears R, Wong L, et al. Mechanism and Simulation of Removal Rate and Surface Roughness during Optical Polishing of Glasses. *J Am Ceram Soc* (2016) 99:1974–84. doi:10.1111/jace.14220

**Conflict of Interest:** The authors declare that the research was conducted in the absence of any commercial or financial relationships that could be construed as a potential conflict of interest.

**Publisher's Note:** All claims expressed in this article are solely those of the authors and do not necessarily represent those of their affiliated organizations, or those of the publisher, the editors, and the reviewers. Any product that may be evaluated in this article, or claim that may be made by its manufacturer, is not guaranteed or endorsed by the publisher.

frontiers in Physics

ORIGINAL RESEARCH
published: 03 January 2022
doi: 10.3389/fphy.2021.789232

# Polarization-Based Haze Removal Using Self-Supervised Network

*Yingjie Shi*[1,2], *Enlai Guo*[1,2]*, *Lianfa Bai*[1,2] *and Jing Han*[1,2]*

[1]*Jiangsu Key Laboratory of Spectral Imaging and Intelligent Sense, Nanjing University of Science and Technology, Nanjing, China,*
[2]*School of Electronic and Optical Engineering, Nanjing University of Science and Technology, Nanjing, China*

Atmospheric scattering caused by suspended particles in the air severely degrades the scene radiance. This paper proposes a method to remove haze by using a neural network that combines scene polarization information. The neural network is self-supervised and online globally optimization can be achieved by using the atmospheric transmission model and gradient descent. Therefore, the proposed method does not require any haze-free image as the constraint for neural network training. The proposed approach is far superior to supervised algorithms in the performance of dehazing and is highly robust to the scene. It is proved that this method can significantly improve the contrast of the original image, and the detailed information of the scene can be effectively enhanced.

**Keywords: polarization, dehazing, neural network, selfsupervised, haze remove method**

OPEN ACCESS

***Edited by:***
*Haofeng Hu,*
*Tianjin University, China*

***Reviewed by:***
*Jinge Guan,*
*North University of China, China*
*Abhishek K. Singh,*
*The Ohio State University,*
*United States*

***Correspondence:**
*Enlai Guo*
*njustgel@njust.edu.cn*
*Jing Han*
*eohj@njust.edu.cn*

***Specialty section:***
*This article was submitted to Optics and Photonics, a section of the journal Frontiers in Physics*

***Received:*** *04 October 2021*
***Accepted:*** *22 November 2021*
***Published:*** *03 January 2022*

***Citation:***
*Shi Y, Guo E, Bai L and Han J (2022) Polarization-Based Haze Removal Using Self-Supervised Network. Front. Phys. 9:789232. doi: 10.3389/fphy.2021.789232*

## 1 INTRODUCTION

The existence of haze, due to the tiny water droplets or solid particles suspended in the air, brings many inconveniences to daily life. The air can no longer be regarded as an isotropic medium which leads to scattering of the transmitted light. The scene image received by the camera or human eyes has a severe degradation. As the distance from the target increases or the concentration of suspended particles increases, the scattering becomes more and more serious. Therefore, the details of the distant target are more severely lost, and the contrast of the captured image is also reduced more. Eliminating the influence of haze on the collected image is often required which can make it easier for the observer to identify the target.

The current methods for dehazing mainly include the data-driven method [1–3], the method based on prior knowledge [4–6], and the method based on physical models [7–10]. The first two types of methods hardly contain physical models, therefore, the problem these methods solved is essentially ill-posed. Data-driven methods often need to obtain a large number of hazy-clean pairs in advance for training and use deep learning or image feature extraction methods to achieve haze removal. The method based on prior knowledge mainly combines some statistical characteristics in the image contained haze. Appropriate parameters need to be selected and combined with the prior model to remove haze in the acquired image. Most of these methods can achieve dehazing through one image, but the limited information contained in the single image cannot provide the unique characters of the scene. Changes of the scene or objects with special colors in the scene may cause the failure of dehazing [4, 11, 12]. As another type of approach, methods based on physical models can solve the shortcomings of the above two types of methods to a certain extent. Physical-model-based methods often use the depth map or analyze the changes in the polarization state of the scene. These methods often need to take multiple images, through the depth map of the scene or the polarization intensity difference, to obtain the transmission map during the scattering process. Both of these methods can construct a unique model based on the characteristics of the scene itself, so the haze can

be removed more accurately. But sometimes methods based on physical models also require empirical knowledge to select appropriate filtering parameters [13–15].

Many data-driven or prior knowledge-based methods have emerged in the field of computer vision to achieve haze removal. Cai et al. realized dehazing through a single frame image by an end-to-end structure Convolutional Neural Network (CNN) [1]. A total of 100,000 sets of data are used for the model training during the experiment; such a huge amount of data consumes a lot of time in the collection and calculation process. Akshay et al. used the Generative Adversarial Networks (GAN) to achieve dehazing with a single frame image. The simulation data is used in the training process, and this strategy causes the trained model to not be well applied to actual scenarios [16]. He et al. analyzed the color distribution in the haze image and proposed a Dark Channel Prior (DCP) method for dehazing. But this method may be invalid when the target color in the scene is inherently similar or close to the background airtight (such as a white wall, snowy ground, etc.) [4].

The earliest dehazing process often uses polarization information to build a physical model. Schechner et al. used the polarization state difference of the scene due to scattering to achieve haze removal. However, it is necessary to manually select the window in the picture to determine the airlight intensity, which will introduce a lot of errors [7]. In recent years, polarization-based methods have been continuously developed. Shen et al. proposed a dehazing method by using the polarization state information to iteratively find the transmission map [17]. Liu et al. used polarization to separate the high-frequency and low-frequency information of the scene to achieve dehazing [13]. Shen et al. used the fusion of polarization intensity, hue, and saturation to achieve dehazing [18]. Because scene information such as depth can be extracted from the polarization difference of the two frames scene image, these methods can be used in most scenes without a priori. These methods may need to adjust the angle of the polarizer to obtain the two images with the largest polarization difference, so the data collection process is cumbersome.

This paper proposes a Polarization-based Self-supervised Dehazing Network named PSDNet that combines the difference of polarization information with deep learning to eliminate the influence of haze on the image. The feature map of the neural network is activated through the transmission map calculated by the scene polarization state. Then the transmission map with more accurate depth information is estimated and has richer detail. The transmission map, haze-free image, and airlight can be calculated by the network and a self-supervised closed loop is formed to optimize the network. Because the physical model is used as a constraint, huge amounts of data are no longer needed to optimize the weight of the network. PSDNet only needs two frames of orthogonal polarization state images of the scene as input to remove scene haze based on online training. The global optimization of the neural network also solves the problem of inaccurate selection of airlight and makes it dehaze more accurately. Compared with similar methods, the proposed method can more effectively improve the visibility of target details and is highly robust to the scene.

# 2 METHOD AND MODEL DESIGN

## 2.1 Basics of Polarization-Based Dehazing

When imaging through the atmosphere containing haze, the particles in the atmosphere will cause scattering of the scene radiance which leads to degrading the target image. As shown in **Figure 1**, the scattered scene radiance and the scattered light from the illumination are received by the camera. The intensity of airlight increases as the distance increases, which can be expressed as

$$A = A_{\infty}(1 - t(x)), \tag{1}$$

where $A_{\infty}$ is the intensity of atmospheric light at infinity, and $t(x)$ represents the rate of transmission at position $x$, describing the scattering and absorption of radiance in the atmosphere, $t(x)$ is given by

$$t(x) = exp\left(-\int_0^x \beta(x')\,dx'\right), \tag{2}$$

where $\beta(x')$ is the extinction coefficient caused by scattering or absorption. When the extinction coefficient in the atmosphere does not change with distance, $\beta(x') = \beta$, **Eq. 2** can be written as

$$t(x) = exp(-\beta x). \tag{3}$$

The process of removing the haze from the image is to restore the radiation intensity and color information of the original scene, which is usually modeled as

$$I(x) = L(x)t(x) + A_{\infty}(1 - t(x)), \tag{4}$$

where $L(x)$ is the radiance of the scene at position $x$ when there are no scattering particles in the atmosphere, and it is also the "clear image." $L(x)$ can be expressed as

$$L(x) = \frac{I(x) - A_{\infty}(1 - t(x))}{t(x)}, \tag{5}$$

where $I(x)$ denotes the degraded version of $L(x)$ by atmospheric scattering. The effects of scattering on the polarization characteristics have been extensively studied. Generally, in the process of imaging through the atmosphere containing scattering particles, the degree of polarization of the original scene is almost negligible. The polarization is more related to the scattering process in the transmission of optical signals and is sensitive to the scattering distance [7]. Therefore, the transmission map can be calculated according to the difference in the polarization state in the captured image. A plane can be defined according to the light ray from the source to the scatterer and the line of sight from the camera. The airlight can be divided into two polarization components that are parallel and perpendicular to this plane, named $A^{\parallel}$ and $A^{\perp}$ respectively. The degree of polarization of airlight can be calculated by

$$p = \frac{A^{\perp} - A^{\parallel}}{A}, \tag{6}$$

where

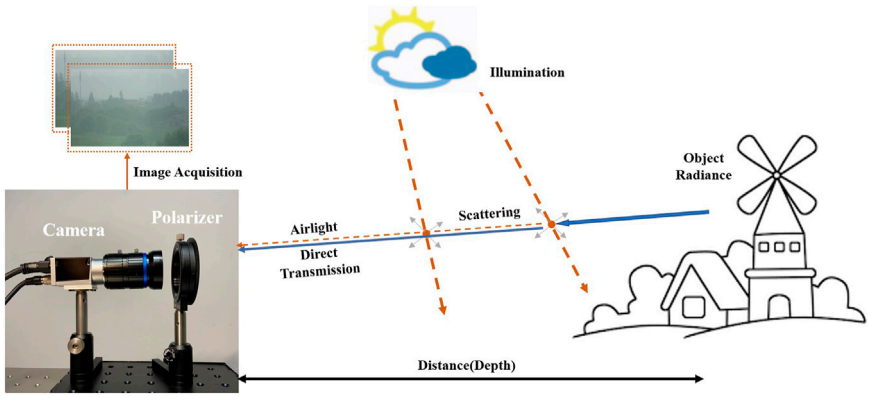


**FIGURE 1 |** Schematic diagram of scattering model and data collection process. The illumination light (such as the sunlight) is scattered by atmospheric particles as airlight. The intensity of airlight increases as the distance increases and the object radiance is scattered and attenuated along the optical path. Two scenes with orthogonal polarization states are collected by rotating the front polarizer of the camera.

$$A = A^{\perp} + A^{\parallel}, \tag{7}$$

is the total radiance due to airlight, and $A$ also equal to $A_{\infty}(1 - t(x))$. The intensity of $A^{\parallel}$ and $A^{\perp}$ is related to the size of the scattering particles in the scene. In some published dehazing methods by using polarization, the parallel component is associated with the minimum measured radiance at a pixel and the perpendicular component is associated with the maximum radiance. This limitation requires rotating the polarizer during data collection to ensure that the two components have the largest difference, which increases the time for data collection. PSDNet only needs two images that have a polarization difference and has no limitation to the degree of polarization difference, so only two frames of orthogonal polarization scene images at any angle are needed. To avoid confusion in the calculation, stipulate that $A^{\perp} > A^{\parallel}$. The airlight at any point in the captured picture can be estimated by

$$A^{scene} = \frac{I^{\perp} - I^{\parallel}}{p} \tag{8}$$

where $I^{\perp}$ and $I^{\parallel}$ are the scene images taken when the polarization direction is the same as $A^{\perp}$ and $A^{\parallel}$. The transmission map t is calculated by

$$t = 1 - \frac{A^{scene}}{A_{\infty}} = 1 - \frac{(I^{\perp} - I^{\parallel})}{pA_{\infty}} = 1 - \frac{(I^{\perp} - I^{\parallel})A}{(A^{\perp} - A^{\parallel})A_{\infty}} \tag{9}$$

therefore, the airlight intensity at infinity $A_{\infty}$ only needs to be estimated to recover the radiance of the scene without haze. The brightest point in the image is often considered ted as $A_{\infty}$. Although those strategies have good performance in most scenes, the brightest light intensity cannot accurately express $A_{\infty}$ when white objects appear in the scene. The accuracy of manually selecting the $A_{\infty}$ will also affect the final dehazing result. In addition, the reliability of the transmission map also determines the quality of the haze removed image, and the accuracy of the atmospheric degree of polarization also affects the accuracy of the transmission map. Airlight is generally considered as partially linearly polarized light. With the rotation of the polarization axis of the polarizer, the rise and fall of the light intensity can be observed. The maximum and minimum light intensity are needed in the degree of polarization calculation, and if the polarization axis orientation of the polarizer cannot correspond to the direction of the airlight polarization, the degree of polarization is calculated inaccurately, which will cause the calculation error of the transmission map. Given the limitations of these methods, PSDNet is designed in which all calculations are in the same optimization process, so the transmission map and the airlight can be estimated simultaneously and accurately.

## 2.2 Model Design

To remove haze and get clear images, it is essential to obtain the transmission map and airlight, so PSDNet consists of three subnetworks, as shown in **Figure 7**. PSDNet-L, PSDNet-T, and PSDNet-A are used to calculate the target radiation $L^{object}$, transmission map, and the scene airlight $A^{scene}$ respectively. Both PSDNet-L and PSDNet-T consist of convolution layers and pooling layers, and the structure of the network does not have a downsampling process which can reduce the loss of more detail. The last layer of all sub-networks uses the sigmoid function to normalize the output. Since the attributes of airlight are not related to the original scene distribution, PSDNet-A is composed of an encoder and a decoder, which are down-sampled and up-sampled respectively to extract global features and estimate the airlight [19].

The subnetwork PSDNet-T consists of two segments: PSDNet-$T^1$ and PSDNet-$T^2$. PSDNet-$T^1$ can extract the features of the scene from the haze image, then the transmission map estimated by the network is obtained. Meanwhile, the transmission map by using the conventional approach also can be calculated, and this calculation process uses the airlight estimated by PSDNet-A and the original image. When the scene polarization difference is minor as shown in **Figure 2B**, the calculated transmission map can respond to any

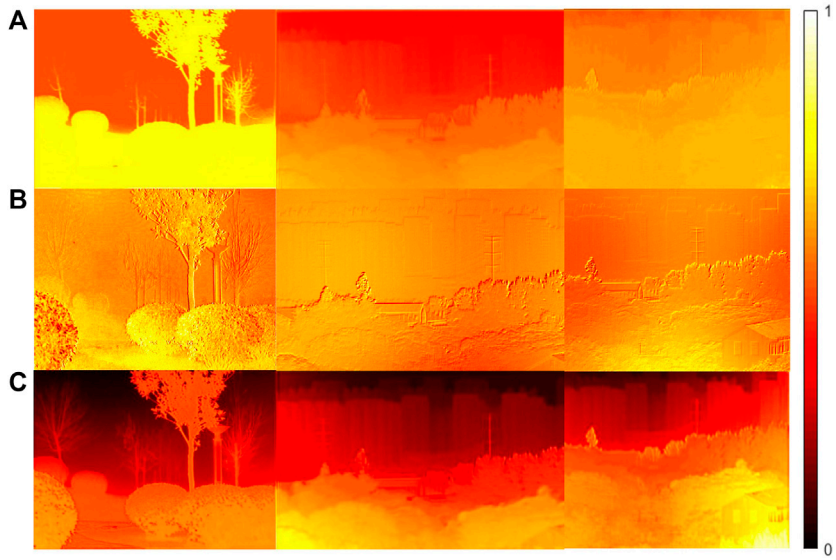


**FIGURE 2 |** Comparison of the transmission map. **(A)** Transmission map estimated by PSDNet-T[1]. **(B)** Transmission map calculated by scene polarization state. **(C)** Transmission map for the final use dehazing after fusion by PSDNet-T[2].

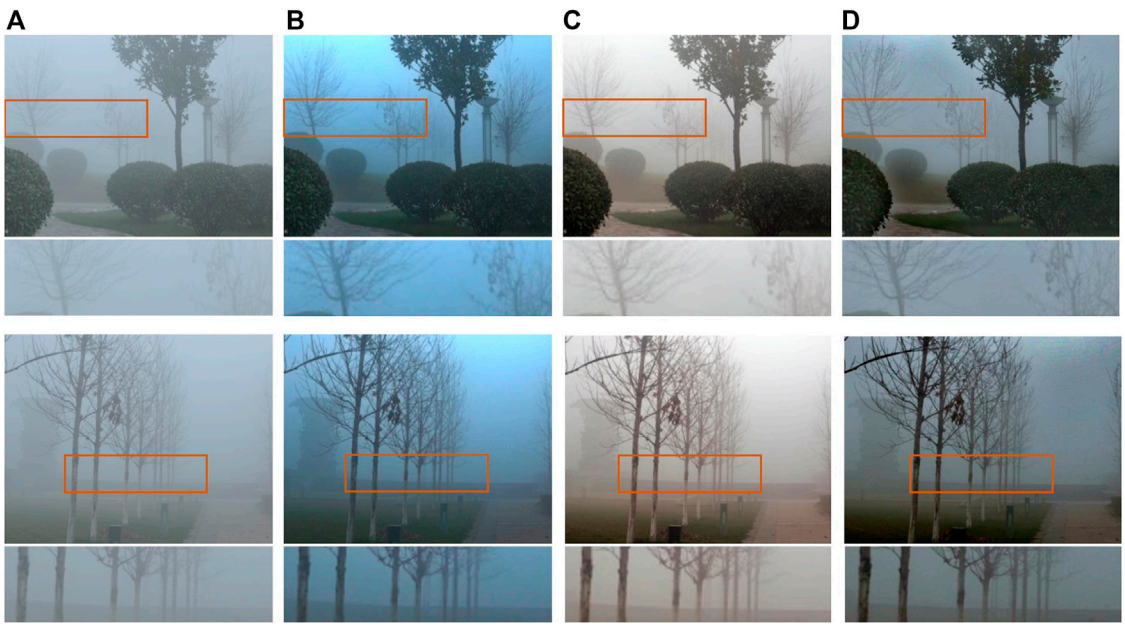


**FIGURE 3 |** The performance of different methods in the open-source dataset. **(A)** Original haze image. **(B–D)** Result of the DCP method, IIDWP method, and the proposed method respectively.

part of the scene but is often discontinuous. To be able to carry out effective dehazing, those transmission maps need to be properly filtered. The neural network can extract continuous feature maps as shown in **Figure 2A**, but details may be lost due to the lack of label constraints. Therefore, the PSDNet-T[2] is designed to fuse the feature maps and the transmission map calculated by polarization, and the transmission map involved in dehazing is obtained finally. In the fusion results as shown in **Figure 2C**, the inaccurate rate of transmission is corrected, and the transmission map has a higher contrast which will enhance the final dehazing effect.

Finally, the clean image, transmission image, and atmospheric light estimated by the neural network are synthesized according to **Eq. 4**. The Mean Square Error (MSE) is used as a loss function to calculate the difference between the synthesized haze image and the real image. The MSE is formulated as:

$$MSE = \frac{1}{H*W}\sum_{i=1}^{H}\sum_{j=1}^{W}[I'(i,j) - I(i,j)]^2, \quad (10)$$

where $I'$ is the synthesized haze image and the $I$ is the image collected in the real scene. $H$ and $W$ are the height and width of those images, respectively. Different from the supervised algorithm, the self-supervised constraint strategy makes PSDNet not need a lot of haze-free images as the Ground Truth (GT) to constrain the optimization of the neural network. The results of dehazing depend on the quality of the transmission map and airlight. The effective use of polarization information makes it easy to estimate the transmission map more correctly, and the structure of the network combined with the physical model allows airlight to be estimated more accurately, then the original irradiance of the scene can be restored more effectively.

# 3 EXPERIMENT

## 3.1 Experimental Comparison on the Open-Source Dataset

An iterative image dehazing method with polarization (IIDWP) is proposed by Linghao Shen et al. [17]. Both the IIDWP method and the method proposed in this paper use the iterative optimization approach and scene polarization for dehazing. However, the IIDWP method only performs the iterative operation in the transmission map calculations process, and the final haze-free image quality may still be affected by airlight estimation or parameter selection. The method proposed in this paper is based on global learning optimization. And there is no need to set algorithm parameters; the airlight estimation and transmission map calculation are in the same iterative process, which makes it easier to optimize to the globally optimal result. Shen et al. provide an open-source dataset that contains haze images with orthogonal polarization states [17]. And this open-source dataset is utilized to compare dehazing performance among different methods firstly. A classic method using a single-frame for dehazing, the method based on the Dark Channel Prior (DCP) [4], is also selected as a comparison. The provided original image resolution is 942*609 pixels, and all images are resized as 960*576 pixels to facilitate convolution calculation in neural networks. In the comparison experiment, the dehaze results exposed by the author who provided the original data are used directly.

Two scenes with severe pattern degradation are selected for comparison, as shown in **Figure 3**. In these two selected scenes, detailed information such as the ends of branches is severely lost due to the high density of haze. In terms of increasing image contrast, all three dehazing methods work admirably; however, the results by using methods based on DCP or IIDWP have substantial color aberrations in the sky. Thanks to the global optimization strategy of the PSDNet, the optimal airlight and the corresponding transmission map can be estimated more accurately. Therefore, the proposed method not only can better enhance the scene details but also preserve the color information of the original image.

## 3.2 Comparison With Similar Approach on the Captured Dataset by Ourselves

Although the proposed method is learning-based, it can perform self-supervision based on the polarization prior and physical model. So the PSDNet does not require GT as a constraint of the neural network compared with supervised networks. It is worth noting that Li et al. designed an end-to-end neural network named AOD-Net, which also incorporates the atmospheric transmission model [12]. As a representative of learning-based supervised algorithms for dehazing, the performance of AODNet is used as a comparison. In addition, the result of a method based on DCP is also used to compare the performance of the different approaches.

The nature of the supervised algorithm determines that AODNet requires a lot of data to build the association between haze images and haze-free images. It is difficult to collect massive hazy-clean pairs in the real scene, but the depth information of the picture is easier to obtain, so the dataset required for network training can be generated based on **Eq. 4, 1**. Haze image provided by NYU-Depth V2 [20] is simulated based on the depth images, which is the public dataset of New York University. Both the simulated haze dataset and the real outdoor dataset RESIDE-beta collected in Beijing [21] are used as the training dataset. A total of 50,000 hazy-clean pairs are used to train AOD-Net, and the other 10,000 pairs are used to verify the effectiveness of the trained model.

The data used for comparison was taken on a hazy morning, and the scenes are filmed from a distance of between 1 and 4 km. The system for pictures collection consists of a rotatable polarizer ($\phi$ = 50.8 mm, extinction ratio = 1,000:1) and a color industrial camera (Basler, acA1920-40gc), and a telephoto industrial camera lens (f = 100 mm, 8 megapixels) is mounted on the camera. All original images have a raw resolution of 1920*1,200 pixels, and the center area with a size of 1920*1,156 pixels is cropped and rescaled to 960*576 pixels.

The final saved model is used to compare the dehazing effect of the method. The reference training epoch of AODNet is 40. To further improve the accuracy of the trained model, the final training epoch is increased to 50 and more than 36 h are used for training. In contrast, the proposed approach does not need to be trained in advance with the data mentioned above, only the haze image is needed as input and perform online learning. Therefore, the online training epoch of PSDNet is 800 but the consumed time is less than 5 min. And all the training environment is PyTorch 1.2.0 with RTX TITAN with I7-9700 CPU under ubuntu 16.04.

The scene image used to compare the effectiveness of different methods is captured in severe haze weather. The original scene image is shown in **Figure 4A**, and buildings in the distance need to be carefully discerned to see the outline, and the details are almost indistinguishable. **Figure 4B** shows the result of dehazing by the supervised algorithm AOD-Net. Although this method can effectively remove haze in the close-up of the scene, specifics about the distant scene are almost no enhancement. The main reason is that although huge amounts of data are used to train the network, these data cannot contain all scenarios in practice.

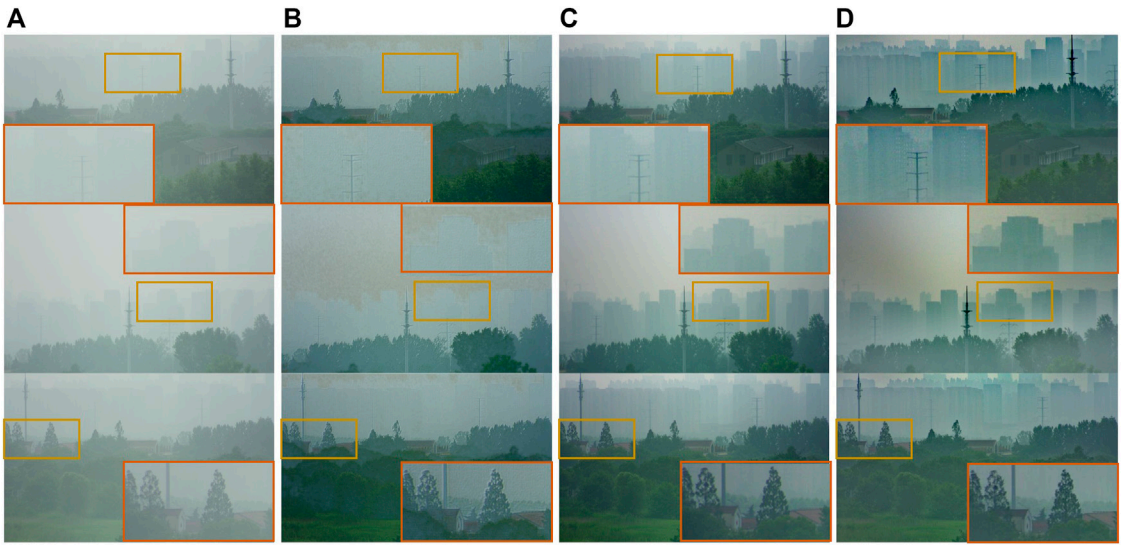


**FIGURE 4 |** The performance of different methods in real haze images collected by ourselves. **(A)** Original scene image. **(B–D)** Result of the AOD-Net, DCP method, and the proposed method respectively.

Ultimately, the trained models cannot be well applied to the widely varying real scenarios. **Figure 4C** shows the result of using the DCP to recover the original scene. The contour information in the long-distance can be distinguished after multiple parameter selection and tuning, but some details still cannot be recovered effectively. **Figure 4D** shows the dehazing result by using the proposed method, and haze removal can be more successful whether the scene is a close-distance or a long-distance. In the first scene, the windows on the buildings can be distinguished after dehazing by the proposed method, but it is completely sightless in the original image. And the tower crane in the zoomed-in area achieves visibility in the second scene, which is sightless too in the original.

The above comparison is almost intuitive; in terms of objective criteria, the result of image edge extraction can reflect the contrast level of the image. The edge extraction results of a high contrast image are more complete, and the target in the image is easier to distinguish. In the event of an image with low contrast, the opposite outcome is produced. Therefore, the dehazing results of different methods are subjected to edge detection to compare the image cleanliness from a more objective point of view. The Prewitt operator is a discrete differential operator which is often used in edge detection algorithms. At each point in the image, the result by using the Prewitt operator is either the corresponding gradient vector or the norm of the vector. The Prewitt operator is used to extract the edges of the dehazing results. Because the gradient approximation has a certain smoothing effect on the noise, edges cannot be extracted in low-contrast images, which is more conducive to contrast. The haze concentration in the far-field is much greater, and it is less visible in the original image without dehazing, so the detail and completeness of the edges extracted can reflect the quality of the dehazing result.

As shown in **Figure 5**, the original haze image and the dehazing result by AOD-Net can barely extract the edge contours of the distant buildings. Although the dehazing result by the DCP method can be detected to a certain extent, some distant building outlines are incomplete. The most complete edge of the distant contours can be extracted in the PSDNet dehazing results. The superior dehazing ability of PSDNet compared with other methods is shown, and the results of the comparison are also consistent with the visualization effect.

Since the proposed method does not require clean images as GT constrains neural networks, there are no haze-clean pairs used to assess haze removal quality. Therefore, the image quality assessment method that requires reference data cannot be used. But in order to analyze the ability of different methods to remove haze more objectively, contrast, saturation, and ENIQA [22] are selected as evaluation indexes to analyze the results of haze removal corresponding to different methods. Haze significantly reduces the contrast and saturation of the captured image, so for dehazing results, the higher the two indicators, the better the resolution of the target details. ENIQA is a high-performance general-purpose no-reference (NR) image quality assessment (IQA) method based on image entropy. The image features are extracted from two domains. In the spatial domain, the mutual information between the color channels and the two-dimensional entropy is calculated. In the frequency domain, the two-dimensional entropy and the mutual information of the filtered sub-band images are computed as the feature set of the input color image. Then the support vector machine is used to classify and give the indicator, and the final output score is between 0 and 1; the lower the score, the higher the image quality. In addition, different methods have great different dehazing abilities of different distance scene images, so the image is divided into two parts that is distant scene and the nearby scene in the objective indicators calculation process.

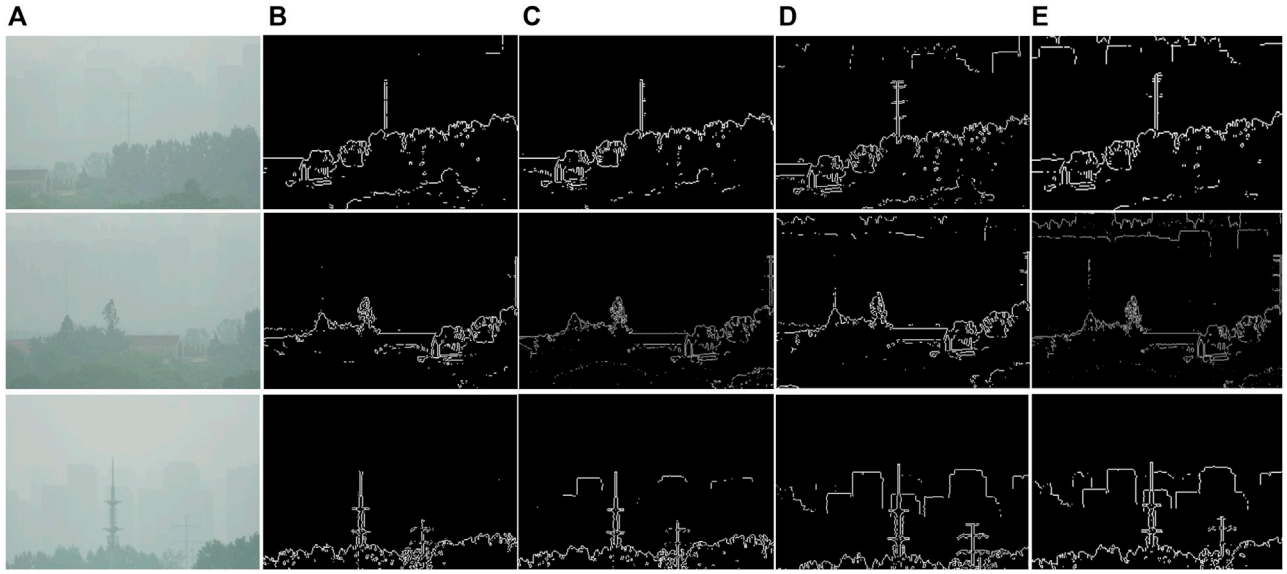


**FIGURE 5 |** The result of edge detection by using the Prewitt operator after dehazing. **(A)** Original scene image. **(B–E)** The edge extraction result of the original image, the AOD-Net dehazing result, the DCP dehazing result, and the dehazing result of our method respectively.

**TABLE 1 |** Indicator for the part of the image that contains a distant scene.

| | Original | AODNet | DCP | Ours | IIDWP |
|---|---|---|---|---|---|
| Contrast | 0.047 | 0.070 | 0.133 | **0.158** | 0.135 |
| Saturation | 0.074 | 0.083 | 0.093 | **0.106** | 0.089 |
| ENIQA | 0.392 | 0.381 | 0.391 | **0.274** | 0.280 |

*Bold values indicate the best values.*

**TABLE 2 |** Indicator for the part of the image that contains a nearby scene.

| | Original | AODNet | DCP | Ours | IIDWP |
|---|---|---|---|---|---|
| Contrast | 0.116 | **0.278** | 0.235 | 0.128 | 0.240 |
| Saturation | 0.076 | **0.224** | 0.179 | 0.138 | 0.163 |
| ENIQA | 0.392 | 0.190 | 0.285 | **0.137** | 0.239 |

*Bold values indicate the best values.*

The average haze removal indicator for the part of the picture that contains a distant scene is shown in **Table 1**, and the indicator for the part that contains a nearby scene is shown in **Table 2**. From the point of view of picture contrast and saturation index, the proposed method can be more effectively dehazing in the distant scene, and AODNet can be more effectively dehazing in the nearby scene; the conclusion is also consistent with subjective evaluation. This is mainly because AODNet conducts point-to-point optimization through haze-clean pairs in the training process, and the dehazing ability is limited to the scenes in the training set. And this approach cannot adapt to images with large differences in haze distribution compares to the training dataset. The proposed method utilizes the property of polarization changing of light during transmission in an atmosphere containing haze; therefore, a distant scene where the light travels further can be used to estimate the transmission map more accurately, and the clearer details can be recovered. Besides, as the distance increases the effect of haze on image quality becomes more severe, the enhancement of detail in the image containing distant scenes is more useful. In addition, when ENIQA is used as evaluate indicator, the proposed method can improve the image quality in both scenes.

## 3.3 Robust and Efficiency of PSDNet

To demonstrate the robust of PSDNet, experiments, in which trained models of different scenes are used to remove the haze on one against another, are designed. Two types of scenes are selected in the training process, as shown in **Figure 6**; *scene 1* has similar distribution with *scene 3*, and *scene 2* has major differences with *scene 3*. Compared with *scene 3*, *scene 1* is collected on the same day and has the same haze distribution. In both scenes with trees in the near and buildings in the far distance, it should be noted that they are collected at different angles and the target distribution is not the same. *Scene 2* is the hazy polarization data disclosed by Shen et al. [17]. The two scenes of weather, target distribution, and illumination are different, moreover, *scene 2* is composed of plants and without buildings at a distance.

As shown in **Figure 6E**, when the model trained with *scene 1* is used as the pre-loaded model, the dehazing result of *scene 3* by direct inference in the detail improvement surpasses the result by using the method based on DCP. During this dehazing process, only the pre-loaded model is used, and PSDNet without any online training. Performance in the final comparison also reflects that the PSDNet combined with the physical model has good robustness to the different scenes. When the model trained with *scene 2* is used to remove the haze of *scene 2*, the result is shown in **Figure 6F**; only 25 iterations of online learning are required to get

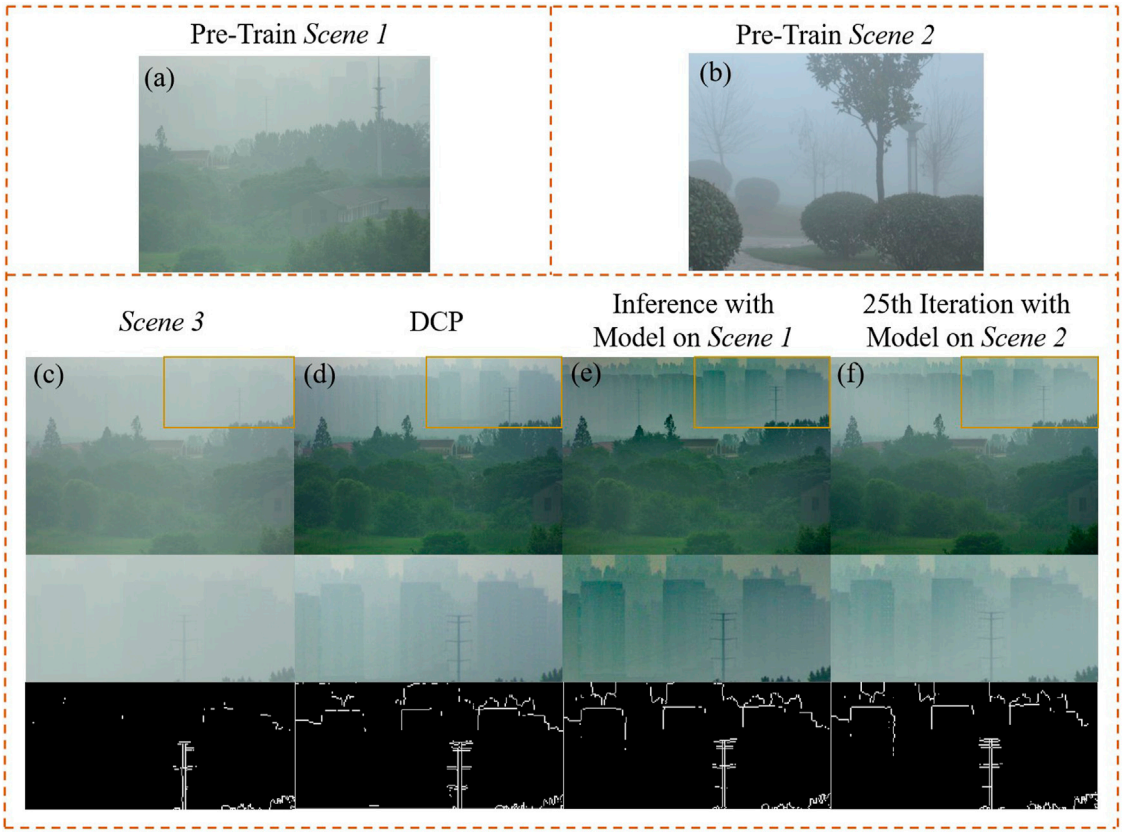


**FIGURE 6 |** Cross-scene dehazing capability comparison. **(A)** Pre-training *scene 1*. **(B)** Pre-training *scene 2*. **(C)** *Scene 3* to be dehazed. **(D)** Dehazing results by using the DCP-based method. **(E)** *Scene 3* dehazing results by using the *scene 1* training model for direct inference. **(F)** haze removal results using the training model of *scene 2* as a pre-training model and 25 gradients are back-propagation for updates. The distant scenes with severe image degradation are locally zoomed in and edge extraction is performed to compare the dehazing ability of different methods.

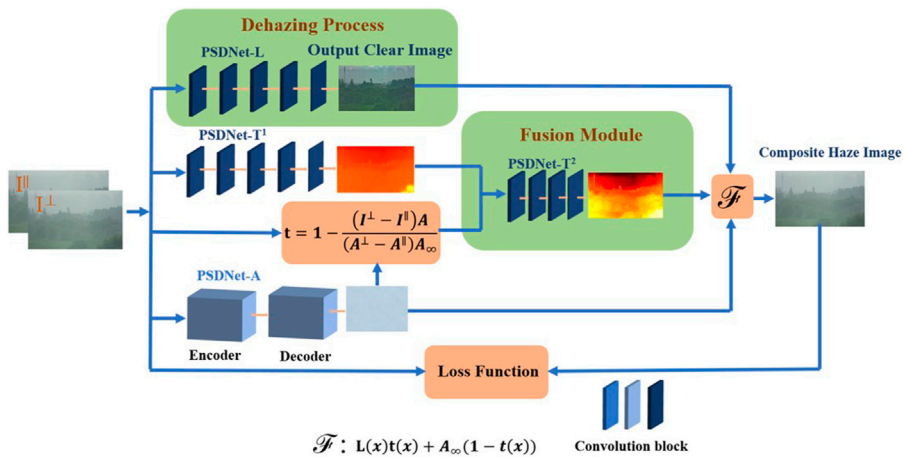


**FIGURE 7 |** Schematic diagram of PSDNet.

**TABLE 3 |** Comparison of calculating time using different methods.

| Method | Computing platform | Preparation time(s) | Single inference/calculation time(s) |
|---|---|---|---|
| DCP | I7-9700 | None | 2.18 |
| AODNet | I7-9700 and RTX titan | 11.09 | 0.53 |
| Ours | I7-9700 and RTX titan | 13.53 | **0.34** |

*Bold value indicate the best values.*

superior dehazing outcomes than those obtained using the DCP method. In addition, when the pre-trained model is loaded, only the computational process of the *Dehazing Process* in **Figure 7** is required, so the running efficiency of the network can be greatly improved.

As mentioned above, supervised algorithms need a big quantity of data for training; aside from the collection of haze-free pairs that take a lot of time, the model training procedure takes a significant amount of computer resources and time. AODNet, for example, takes more than 36 h to train 50 epochs, but PSDNet takes less than 5 min to train 800 epochs in the same computational environment, and less than 10 s is needed to complete 25 epoch of training when the pre-trained model is loaded. PSDNet is unquestionably quicker than supervised algorithms.

As shown in **Table 3**, the time required by different algorithms for haze removal is compared. There is a preparation time since AODNet and PSDNet need to load the model to the GPU, but the model only has to be loaded once, and then the network can remove the haze of numerous pictures. In terms of time comparison, the single frame dehazing time of PSDNet only takes 0.34 s. The dehazing speed of PSDNet, which is significantly faster than AODNet and DCP-based methods, makes it possible to achieve quasi-real-time dehazing.

## 4 DISCUSSION

According to the experimental results, we have the following discussions.

1) PSDNet combined with the physical model can efficiently utilize the scene polarization information for accurate estimation of the transmission map and form a self-supervised closed loop. Therefore, haze-free images are not required as GT for constraint during all training processes, which reduces the dependence on data. Compared with the dehazing results of traditional methods using polarization and the dehazing results of supervised networks, PSDNet has better performance in enhancing scene details and color retention, and can almost achieve the enhancement from unseen to visible target in some scenes.
2) PSDNet is robust for different scenarios. Because the physical models included in the neural network are built based on actual haze scenes, PSDNet is effective at most scenes. And the network structure incorporated physical priors can help the models trained with different scenes to migrate or online learning. The training times can be reduced to 1/32 of the original by loading the pre-trained model (from 800 epochs to 25 epochs, result as shown in **Figure 6F**). For similar scenes, the pre-trained model can be directly used to remove haze without retraining (result as shown in **Figure 6E**).
3) Because PSDNet does not require a large amount of data for training, this advantage not only drastically reduces the data acquisition time but also saves the time for model training. Compared to the supervised algorithm AODNet, which takes 36 h to train 50 epochs, PSDNet takes less than 5 min for 800 iterations, and the training time can be compressed to less than 10 s when loading the pre-trained model. When performing model inference for dehazing, PSDNet is three times faster than traditional methods based on DCP, and also faster than similar supervised class algorithms.

## 5 CONCLUSION

This paper proposes a method that combines the polarization difference of the scene with the neural network to achieve dehazing. Since the polarization prior can effectively guide and activate the extracted feature maps of neural networks, the proposed network does not need haze-free pairs as GT to constrain the training process. Only two frames of scene images with orthogonal polarization at any angle are required as input, then the self-supervision and global online optimization learning approach are used for haze removal. The airlight can be better estimated by the self-supervised closed-loop optimization process. Therefore, the proposed method has good results in preserving the color of the original image and enhancing the details compared to similar algorithms based on polarization or supervised learning-based. In actual dense haze scenes, almost invisible details of distant targets can be identified by using the proposed approach for dehazing. The training time and dehazing efficiency of the network have obvious advantages in the comparison of similar methods, and it is expected to achieve real-time haze removal. The proposal of this method promotes the development of the combination of deep learning and physical models in the field of anti-scattering.

## DATA AVAILABILITY STATEMENT

The raw data supporting the conclusions of this article will be made available by the authors, without undue reservation.

## AUTHOR CONTRIBUTIONS

YS performed the numerical calculation and wrote the manuscript. EG and JH performed the data analysis and provided constructive discussions. EG, LB, and JH are the main supervisors, and they provided supervision and feedback and reviewed the research.

## FUNDING

This research is supported by the National Natural Science Foundation of China (62031018, 61971227, 62101255); Jiangsu Provincial Key Research and Development Program (BE2018126).

## REFERENCES

1. Cai B, Xu X, Jia K, Qing C, Tao D. Dehazenet: An End-To-End System for Single Image Haze Removal. *IEEE Trans Image Process* (2016) 25:5187–98. doi:10.1109/tip.2016.2598681
2. Zhang X, Dong H, Pan J, Zhu C, Tai Y, Wang C, et al. Learning to Restore Hazy Video: A New Real-World Dataset and a New Method. In: Proceedings of the IEEE/CVF Conference on Computer Vision and Pattern Recognition; 2021 Jun 19–25 (2021). p. 9239–48. doi:10.1109/cvpr46437.2021.00912
3. Dong H, Pan J, Xiang L, Hu Z, Zhang X, Wang F, et al. Multi-scale Boosted Dehazing Network with Dense Feature Fusion. In: Proceedings of the IEEE/CVF Conference on Computer Vision and Pattern Recognition; 2020 Jun 19–25 (2020). p. 2157–67. doi:10.1109/cvpr42600.2020.00223
4. He K, Sun J, Tang X. Single Image Haze Removal Using Dark Channel Prior. *IEEE Trans Pattern Anal Mach Intell* (2010) 33:2341–53. doi:10.1109/TPAMI.2010.168
5. Bahat Y, Irani M. Blind Dehazing Using Internal Patch Recurrence. In: 2016 IEEE International Conference on Computational Photography (ICCP); 2016 May 13–15; Evanston, IL. IEEE (2016). p. 1–9. doi:10.1109/iccphot.2016.7492870
6. Berman D, Treibitz T, Avidan S. Non-local Image Dehazing. In: Proceedings of the IEEE Conference on Computer Vision And Pattern Recognition; 2016 Jun 26–Jul 1; Las Vegas, NV (2016). p. 1674–82. doi:10.1109/cvpr.2016.185
7. Schechner YY, Narasimhan SG, Nayar SK. Polarization-based Vision through Haze. *Appl Opt* (2003) 42:511–25. doi:10.1364/ao.42.000511
8. Liang J, Ren L, Ju H, Zhang W, Qu E. Polarimetric Dehazing Method for Dense Haze Removal Based on Distribution Analysis of Angle of Polarization. *Opt Express* (2015) 23:26146–57. doi:10.1364/oe.23.026146
9. Qu Y, Zou Z. Non-sky Polarization-Based Dehazing Algorithm for Non-specular Objects Using Polarization Difference and Global Scene Feature. *Opt Express* (2017) 25:25004–22. doi:10.1364/oe.25.025004
10. Pang Y, Nie J, Xie J, Han J, Li X. Bidnet: Binocular Image Dehazing without Explicit Disparity Estimation. In: Proceedings of the IEEE/CVF Conference on Computer Vision and Pattern Recognition; 2020 Jun 19–25 (2020). p. 5931–40. doi:10.1109/cvpr42600.2020.00597
11. Yang X, Xu Z, Luo J. Towards Perceptual Image Dehazing by Physics-Based Disentanglement and Adversarial Training. In: Proceedings of the AAAI Conference on Artificial Intelligence; 2018 Feb 2–7; New Orleans, LA, 32 (2018).
12. Li B, Peng X, Wang Z, Xu J, Feng D. Aod-net: All-In-One Dehazing Network. In: Proceedings of the IEEE International Conference on Computer Vision; 2017 Oct 22–29; Venice (2017). p. 4770–8. doi:10.1109/iccv.2017.511
13. Liu F, Cao L, Shao X, Han P, Bin X. Polarimetric Dehazing Utilizing Spatial Frequency Segregation of Images. *Appl Opt* (2015) 54:8116–22. doi:10.1364/ao.54.008116
14. Fang S, Xia X, Huo X, Chen C. Image Dehazing Using Polarization Effects of Objects and Airlight. *Opt Express* (2014) 22:19523–37. doi:10.1364/oe.22.019523
15. Van der Laan JD, Scrymgeour DA, Kemme SA, Dereniak EL. Detection Range Enhancement Using Circularly Polarized Light in Scattering Environments for Infrared Wavelengths. *Appl Opt* (2015) 54:2266–74. doi:10.1364/ao.54.002266
16. Dudhane A, Singh Aulakh H, Murala S. Ri-gan: An End-To-End Network for Single Image Haze Removal. In: Proceedings of the IEEE/CVF Conference on Computer Vision and Pattern Recognition Workshops; 2019 Jun 16–20; Long Beach, CA (2019). doi:10.1109/cvprw.2019.00253
17. Shen L, Zhao Y, Peng Q, Chan JCW, Kong SG. An Iterative Image Dehazing Method with Polarization. *IEEE Trans Multimedia* (2018) 21:1093–107. doi:10.1109/TMM.2018.2871955
18. Shen L, Reda M, Zhao Y. Image-matching Enhancement Using a Polarized Intensity-Hue-Saturation Fusion Method. *Appl Opt* (2021) 60:3699–715. doi:10.1364/ao.419726
19. Ren W, Liu S, Zhang H, Pan J, Cao X, Yang MH. Single Image Dehazing via Multi-Scale Convolutional Neural Networks. In: European Conference on Computer Vision; 2016 Jun 26–Jul 1; Las Vegas, NV. Springer (2016). p. 154–69. doi:10.1007/978-3-319-46475-6_10
20. Nathan Silberman PK, Hoiem D, Fergus R. Indoor Segmentation and Support Inference from Rgbd Images. In: European Conference on Computer Vision; 2012 Oct 7–13; Firenze (2012). doi:10.1007/978-3-642-33715-4_54
21. Li B, Ren W, Fu D, Tao D, Feng D, Zeng W, et al..Benchmarking Single Image Dehazing and beyond. *IEEE Trans Image Process* (2018) 28:492–505. doi:10.1109/TIP.2018.2867951
22. Chen L, Zhao J, Lin M, Yang G, He C. No-reference Perceptual Quality Assessment of Stereoscopic Images Based on Binocular Visual Characteristics. *Signal Processing: Image Commun* (2019) 76:1–10. doi:10.1016/j.image.2019.03.011

**Conflict of Interest:** The authors declare that the research was conducted in the absence of any commercial or financial relationships that could be construed as a potential conflict of interest.

**Publisher's Note:** All claims expressed in this article are solely those of the authors and do not necessarily represent those of their affiliated organizations, or those of the publisher, the editors, and the reviewers. Any product that may be evaluated in this article, or claim that may be made by its manufacturer, is not guaranteed or endorsed by the publisher.

frontiers in Physics

ORIGINAL RESEARCH
published: 05 January 2022
doi: 10.3389/fphy.2021.806904

# Effects of Measurement Configurations on the Sensitivity of *Morpho* Butterfly Scales Based Chemical Biosensor

*Zhengqiong Dong*[1,2†], *Hang Zhao*[2†], *Lei Nie*[2*], *Shaokang Tang*[2], *Chenyang Li*[2] *and Xuanze Wang*[1,2]

[1]Hubei Key Laboratory of Manufacture Quality Engineering, Wuhan, China, [2]School of Mechanical Engineering, Hubei University of Technology, Wuhan, China

The *Morpho* butterfly wing with tree-shaped alternating multilayer is an effective chemical biosensor to distinguish between ambient medium, and its detection sensitivity is inextricably linked to the measurement configuration including incident angle, azimuthal angle, and so on. In order to reveal the effects and the selection of measurement configuration. In this work, the model of the *Morpho* butterfly wing is built using the rigorous coupled-wave analysis method by considering its profile is a rectangular-groove grating. On basis of the above model, the reflectivity of different diffraction orders at a different incident angle and azimuthal angle is calculated, and the influence of incident angle and azimuthal angle on performance of *Morpho* butterfly scales-based biosensor is analyzed. The optimal incident angle at each azimuthal angle is given according to the proposed choice rule, then the azimuthal angle and the corresponding incident angle can be selected further.

**Keywords: chemical biosensor, morpho butterfly, measurement configuration, sensitivity, rigorous coupled-wave analysis**

OPEN ACCESS

***Edited by:***
*Haofeng Hu,*
*Tianjin University, China*

***Reviewed by:***
*Chunguang Hu,*
*Tianjin University, China*
*Tielin Shi,*
*Huazhong University of Science and Technology, China*

***Correspondence:**
*Lei Nie*
*leinie@hbut.edu.cn*

[†]*These authors have contributed equally to this work and share first authorship*

***Specialty section:***
*This article was submitted to Optics and Photonics, a section of the journal Frontiers in Physics*

***Received:*** *01 November 2021*
***Accepted:*** *08 December 2021*
***Published:*** *05 January 2022*

***Citation:***
*Dong Z, Zhao H, Nie L, Tang S, Li C and Wang X (2022) Effects of Measurement Configurations on the Sensitivity of* Morpho *Butterfly Scales Based Chemical Biosensor. Front. Phys. 9:806904. doi: 10.3389/fphy.2021.806904*

## INTRODUCTION

In recent years, the *Morpho* butterfly wings are widely studied for their selective absorption and reflection of electromagnetic waves with different wavelengths [1–6]. The structural color—*Morpho* blue is the main color of the *Morpho* butterfly wing in connection with various optical phenomena such as scattering, interference, and diffraction [7, 8]. Several optical modeling methods such as finite-difference time-domain (FDTD) [7, 9, 10] and rigorous coupled-wave analysis (RCWA) [11–13] have been introduced to analyze the optical properties of the *Morpho* blue. The analysis has shown that the tree-like microstructure existed in the wing scales is the major cause of *Morpho* blue formation [11]. According to their conclusion, many applications of the tree-like microstructure have been proposed, including the establishment of color selection ability by fabricating the tree-like structure [10, 14–16], distinguishing between different vapors [2, 17, 18] and different ambient liquids [13, 19, 20] with butterfly wing.

In a famous application proposed by Potyrailo [18] which is using the butterfly wing as a biosensor to distinguish vapors, they showed that the iridescent scales of the *Morpho* sulkowskyi butterfly have different optical responses when it acts on different individual vapors, and this optical response dramatically outperforms the existing nano-engineered photonic sensors. By further expanding the application range of butterfly wing-based biosensors, Yang et al. [13] also found that the color and the

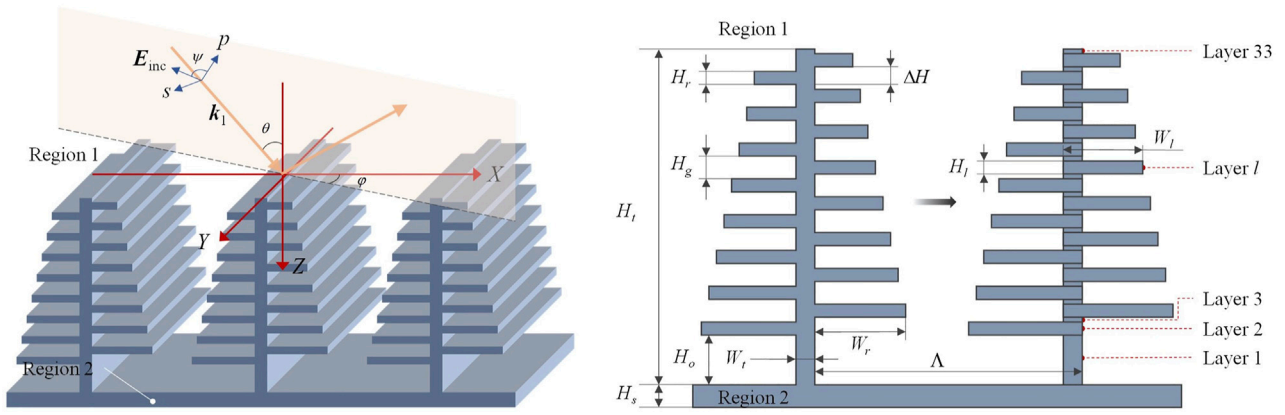


**FIGURE 1 | (A)** Geometry of the *Morpho* butterfly wing scale; **(B)** layers division for inverse modeling based on RCWA.

brightness of the butterfly wings change significantly when the surrounding medium of the butterfly wing was altered. Namely, they demonstrated that the reflectance peak shift (RPS) is proportionate to the refractive index of the ambient medium. However, the simulations and experiments were inclined to conduct at normal incidence with an azimuthal angle of 0° under TM mode. This leads us to consider several questions:

1) Does the measurement configuration which is the combination of normal incidence and zero-degree azimuthal angle is the only one that can ensure the RPS is proportional to the refractive index of ambient medium?
2) Does the law that the RPS is proportional to the refractive index of the ambient medium still fulfilled if the measurement configuration varies?
3) Can we select an optimal measurement configuration to maximize the RPS for an ambient medium?

To answer these questions, we simulated the reflectance for the tree-like structure under different ambient media at different incident angles and azimuthal angles.

## MODELING BASED ON RCWA METHODS

One essential feature in the *Morpho* butterfly wing scale which is widely studied is the tree-shaped alternating multilayer as shown in **Figure 1A**. According to the previous work [7], the multilayer interference phenomenon and grating diffraction phenomenon are the two main reasons that cause the structural colours of the *Morpho* butterfly wing. This sliced structure is suitable for calculating in RCWA, here we choose to emphasize the grating diffraction phenomenon using RCWA. The complex refractive indexes of region 1 and region 2 are $n_1$ and $n_2$ respectively. In the rectangular coordinate system, incident angle and azimuthal angle are respectively $\theta$ and $\varphi$, the intersection angle between incident electric vector $\boldsymbol{E}_{\text{inc}}$ and incident wave vector $\boldsymbol{k}_1$ is polarizing angle $\psi$. The tree-shaped alternating multilayer model is an ordered array of ridges with lamellae running nearly parallel to the substrate of the scale and periodically staggered on both sides of each ridge, which can be characterized by the following parameters: the thickness of the lamellae $H_r$; the thickness of the air gap $H_g$; the offset ΔH between the left lamellae and the corresponding right lamellae along the Z-axis; the width of the bottom lamellae $W_r$; the width of the trunk $W_t$; the height between the top surface of the substrate and the bottom surface of the longest lamellae $H_o$; the thickness of the substrate $H_s$; the height of the trunk $H_t$; and the period $\Lambda$. As shown on the right-hand side of **Figure 1B**, the tree-shaped structure is easy to be sliced into 33 layers, and layer $l$ can be regarded as a rectangular grating with width and height of $W_l$ and $H_l$ respectively. For the sliced structure, it is obvious that it's a typical multiple overlay model.

In the grating region, the periodic relative permittivity of layer $l$ is expandable in the forms of Fourier series [21, 22]:

$$\varepsilon_l(x) = \sum_n \varepsilon_{l,n} \exp\left(\mathrm{j}\frac{2\pi n}{\Lambda}\right) \tag{2-1}$$

where $\varepsilon_{l,n}$ is the $n$th component of the Fourier series of layer $l$.

The electrical component of the incident plane wave defined as an incident normalized electrical field is given by:

$$\boldsymbol{E}_{\text{inc}} = \boldsymbol{u}\exp\left(-\mathrm{j}\boldsymbol{k}_1 \cdot \boldsymbol{r}\right) \tag{2-2}$$

Where $\boldsymbol{u}$ is the normalized electrical component, $\boldsymbol{r}$ is the position vector of an arbitrary point on the wave plane.

According to the Rayleigh expansion, the normalized solutions in region 1 (Z < 0) and region 2 (Z > $H_t$) are expressed as [23, 24]:

$$\boldsymbol{E}_1 = \boldsymbol{E}_{\text{inc}} + \sum_i \boldsymbol{R}_i \exp\left[-\mathrm{j}\left(k_{xi}x + k_y y - k_{1,zi}z\right)\right] \tag{2-3}$$

$$\boldsymbol{E}_2 = \sum_i \boldsymbol{T}_i \exp\left\{-\mathrm{j}\left[k_{xi}x + k_y y + k_{2,zi}(z-d)\right]\right\} \tag{2-4}$$

Where $\boldsymbol{R}_i$ and $\boldsymbol{T}_i$ are amplitude vectors of $i$th incident wave and reflected wave. $k_{xi}$, $k_y$, and $k_{m,zi}$ ($m$ = 1,2) are the X, Y, and Z components of the $i$th diffraction wave vector, respectively. The mathematic expressions of $k_{xi}$, $k_y$ and $k_{m,zi}$ are given by:

$$k_{xi} = k_0\left(n_1 \sin\theta\cos\varphi - i\lambda/\Lambda\right) \tag{2-5}$$

$$k_y = k_0 n_1 \sin\theta \sin\varphi \tag{2-6}$$

$$k_{m,zi} = \begin{cases} +\sqrt{(k_0 n_m)^2 - k_{xi}^2 - k_y^2},\ (k_0 n_m)^2 \geq k_{xi}^2 + k_y^2 \\ -\mathrm{j}\sqrt{k_{xi}^2 + k_y^2 - (k_0 n_m)^2},\ (k_0 n_m)^2 < k_{xi}^2 + k_y^2 \end{cases}, m = 1, 2 \tag{2-7}$$

In the grating region ($0 < Z < D$), the electrical field and magnetic field of layer $l$ can be expressed by the Fourier expansion of the harmonic waves in space as follows [22]:

$$\boldsymbol{E}_{l,g} = \sum_i \left[S_{l,xi}(z)\hat{\boldsymbol{x}} + S_{l,yi}(z)\hat{\boldsymbol{y}} + S_{l,zi}(z)\hat{\boldsymbol{z}}\right] \exp\left[-\mathrm{j}\left(k_{xi}x + k_y y\right)\right] \tag{2-8}$$

$$\boldsymbol{H}_{l,g} = -\mathrm{j}\sqrt{\frac{\varepsilon_0}{\mu_0}} \sum_i \left[U_{l,xi}(z)\hat{\boldsymbol{x}} + U_{l,yi}(z)\hat{\boldsymbol{y}} + U_{l,zi}(z)\hat{\boldsymbol{z}}\right] \exp\left[-\mathrm{j}\left(k_{xi}x + k_y y\right)\right] \tag{2-9}$$

where $\boldsymbol{S}_{l,i}(z) = S_{l,xi}(z)\hat{\boldsymbol{x}} + S_{l,yi}(z)\hat{\boldsymbol{y}} + S_{l,zi}(z)\hat{\boldsymbol{z}}$ and $\boldsymbol{U}_{l,i}(z) = U_{l,xi}(z)\hat{\boldsymbol{x}} + U_{l,yi}(z)\hat{\boldsymbol{y}} + U_{l,zi}(z)\hat{\boldsymbol{z}}$ related to $W_l$ and $H_l$ are the electrical and magnetic components of the $i$th space harmonic vector in layer $l$, respectively. And $\boldsymbol{E}_{l,g}$ and $\boldsymbol{H}_{l,g}$ satisfy Maxwell's equation in the grating region:

$$\nabla \times \boldsymbol{E}_{l,g} = -\mathrm{j}\omega\mu_0 \boldsymbol{H}_{l,g} \tag{2-10}$$

$$\nabla \times \boldsymbol{H}_{l,g} = \mathrm{j}\omega\varepsilon_0\varepsilon_l(x, y)\boldsymbol{E}_{l,g} \tag{2-11}$$

Where $\varepsilon_0$ and $\mu_0$ are permittivity and permeability in free space.

By substituting **(2-8)**, **(2-9)** into **(2-10)**, **(2-11)** and eliminating $\boldsymbol{E}_{l,gz}$ and $\boldsymbol{H}_{l,gz}$ (the Z components of $\boldsymbol{E}_{l,g}$ and $\boldsymbol{H}_{l,g}$), and applying the inverse rule [25], the coupled-wave equations under TE mode can be obtained:

$$\left[\partial^2 \mathbf{S}_{l,y} \Big/ \partial\left(z'\right)^2\right] = \left[\mathbf{A}_l\right]\left[\mathbf{S}_{l,y}\right] \tag{2-12}$$

Where, $\boldsymbol{S}_{l,y}$ is the Y component of $\sum \boldsymbol{S}_{l,i}(z)$, $\boldsymbol{A}_l = \boldsymbol{K}_x - \boldsymbol{E}_l$ and $\boldsymbol{K}_x$ is an $N$-dimensional diagonal matrix ($N$ is the number of Fourier series) whose diagonal elements are defined by $k_{xi}/k_0$, $\boldsymbol{E}_l$ is an $N$-dimensional Toeplitz matrix composed of $\varepsilon_{l,g}$, whose element of the $p$th row and the $q$th column is $\varepsilon_{l,p-q}$.

Likewise, the coupled-wave equations under TM mode can be obtained:

$$\left[\partial^2 \mathbf{U}_{l,y} \Big/ \partial\left(z'\right)^2\right] = \left[\mathbf{F}_l\right]^{-1}\left[\mathbf{B}_l\right]\left[\mathbf{U}_{l,y}\right] \tag{2-13}$$

Where, $\boldsymbol{U}_{l,y}$ is the Y component of $\sum \boldsymbol{S}_{l,i}(z)$, $\boldsymbol{F}_l$ is an $N$-dimensional Toeplitz matrix composed of $(\frac{1}{\varepsilon})_{l,g}$, whose element of the $p$th row and the $q$th column is $(\frac{1}{\varepsilon})_{l,p-q}$.$\mathbf{B}l$ is expressed by $\boldsymbol{B}_l = \boldsymbol{K}_x \boldsymbol{E}_l^{-1} \boldsymbol{K}_x - \boldsymbol{I}$.

Then the $\boldsymbol{S}_{l,i}(z)$ and $\boldsymbol{U}_{l,i}(z)$ can be obtained by solving the coupled-wave equations (**2-12**) and (**2-13**).

Finally, to get the electric field component $R_s$ under TE mode ($\psi = 90°$) and magnetic field component $R_p$ under TM mode ($\psi = 0°$) of the reflected wave, the continuous conditions should be considered on the boundaries of every layer and at interfaces of the adjacent region.

**TABLE 1 |** The values of structural parameters.

| | $H_r$ | $H_g$ | $\Delta H$ | $W_r$ | $W_t$ | $H_o$ | $H_s$ | $H_t$ |
|---|---|---|---|---|---|---|---|---|
| Value (nm) | 80 | 120 | 120 | 270 | 100 | 400 | 600 | 2000 |

## SIMULATIONS AND DISCUSSIONS

In simulations, the tree-shaped structure has the same complex refractive index 1.56 + 0.06i [26] as the substrate, and the complex refractive index is constant in the wavelength range [27], which is from 193 to 1,000 nm with a wavelength step of 5 nm. The difference between adjacent lamellae on both sides of the trunk is a constant of 20 nm. The tree-shaped alternating multilayer is periodic along the X-axis with a pitch $\Lambda$ of 700 nm. The values of other structural parameters shown in **Figure 1** are set in **Table 1**. The modeling and parameters solution is carried out with the program we have written in MATLAB.

Before studying the impact of measurement configurations on the sensitivity of *Morpho* butterfly scales-based chemical biosensor, we take account of a special condition in Zhu's study [7]. In which case a diffraction grating consists of alternating multilayers was illuminated by a beam at normal incidence with a specified wavelength under TM polarization. Then the reflectivity under different diffraction orders was calculated. The results showed that only the first-order diffraction is mainly responsible for the reflectivity peak that causes the structural colour with waveband of visible light. Likewise, we simulated the reflectivity at normal incidence under zeroth and first-order diffraction for the structure in **Figure 1** with visible light. Since an arbitrarily polarized light can be transformed into a linear combination of TE and TM polarized light, we focus on the simulations for TE and TM polarization. In the simulations, the surrounding mediums of the structure are air, carbinol, and ethanol, respectively.

The results shown in **Figure 2** indicate that the reflectivity under first-order diffraction is indeed mainly responsible for the peak of total reflectivity in the three cases, while the reflectivity under zeroth-order diffraction is suppressed owing to the destructive interference of the multilayer in the visible waves. However, the effects of reflectivity caused by different incident angles and azimuthal angles are rarely considered. For a diffraction grating, different measurement configurations differ in their sensitivity grades [28–30]. Once the optimal measurement configuration is obtained, the optimal measurement does become available.

For the *Morpho* butterfly scales-based chemical biosensor, the refractive index of ambient gas or liquid is characterized through the colour of the *Morpho* butterfly's wing. Therefore, to find the optimal measurement configuration and enhance the colour change more markedly. We simulated the reflectivity of the structure in **Figure 1** at different incident angles and azimuthal angles (the range of the incident angle was set from 0 to 89° with an increment of 0.05°, and the range of the azimuthal angle was set from 0 to 170° with an increment of 10°) using visible light under the TE mode. Since the difference

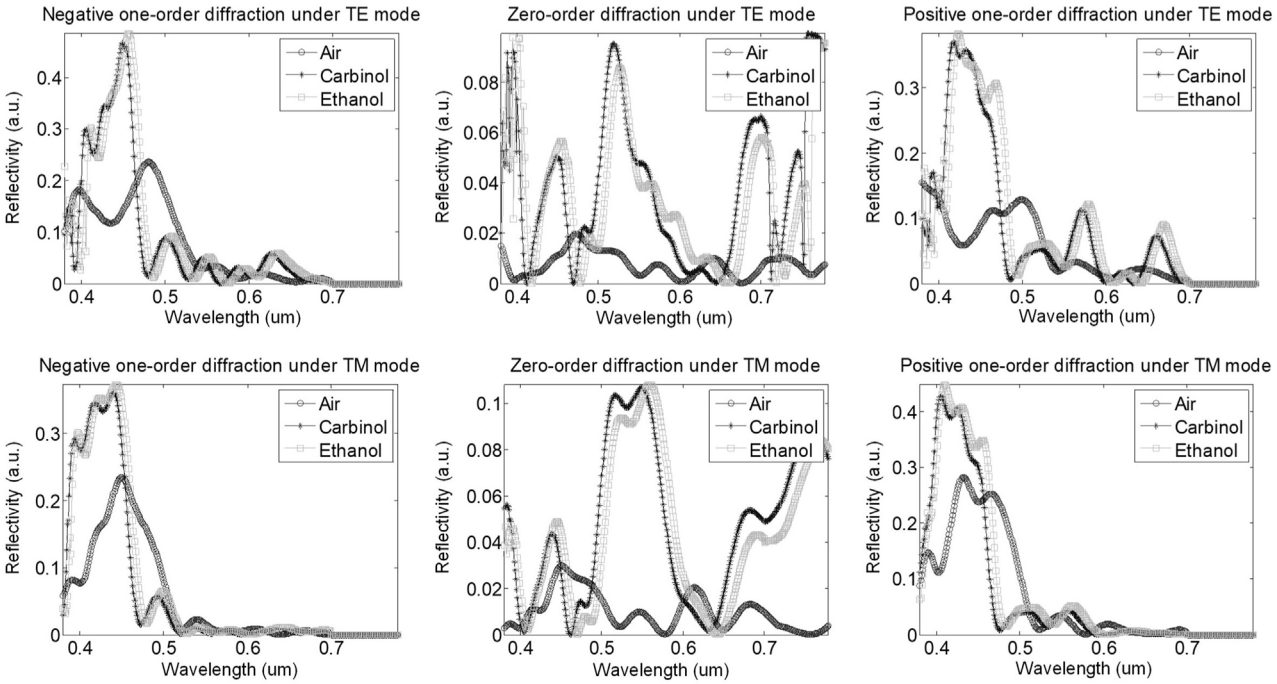


**FIGURE 2 |** Simulated results of the reflectivity of zeroth and first-order diffraction under TE and TM mode.

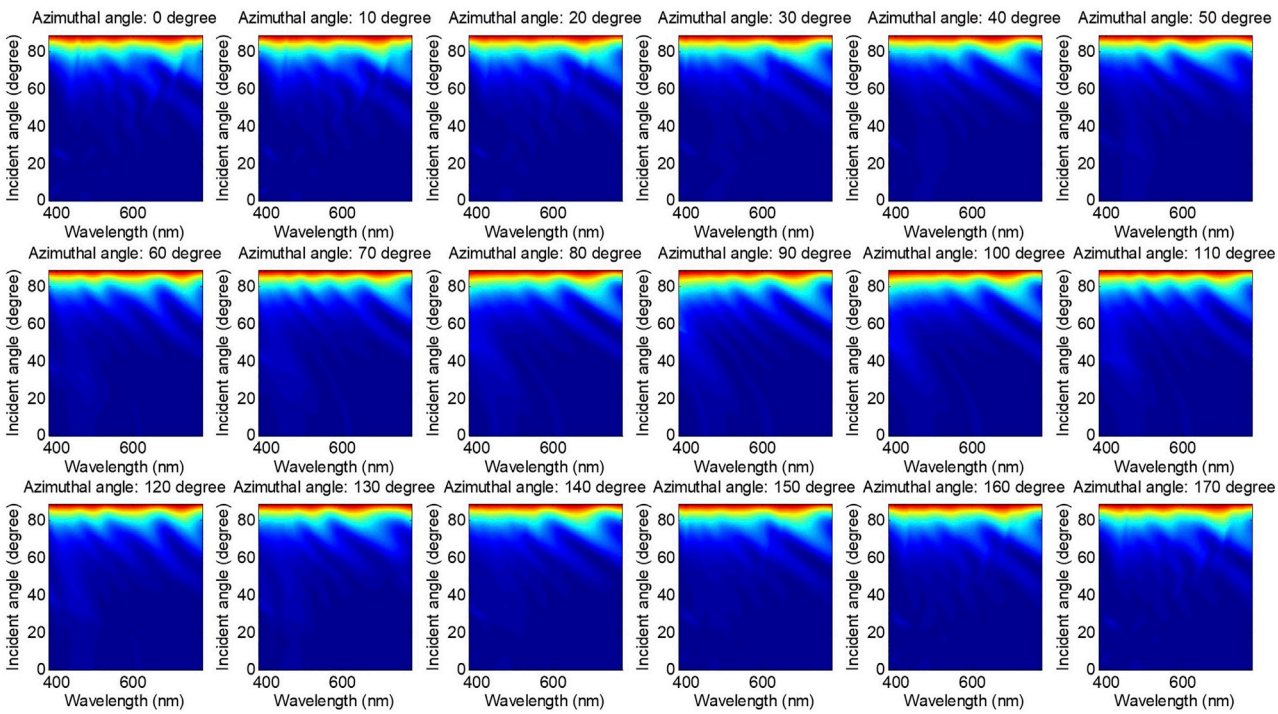


**FIGURE 3 |** Simulated results of zeroth-order diffraction reflectivity of air under TE mode.

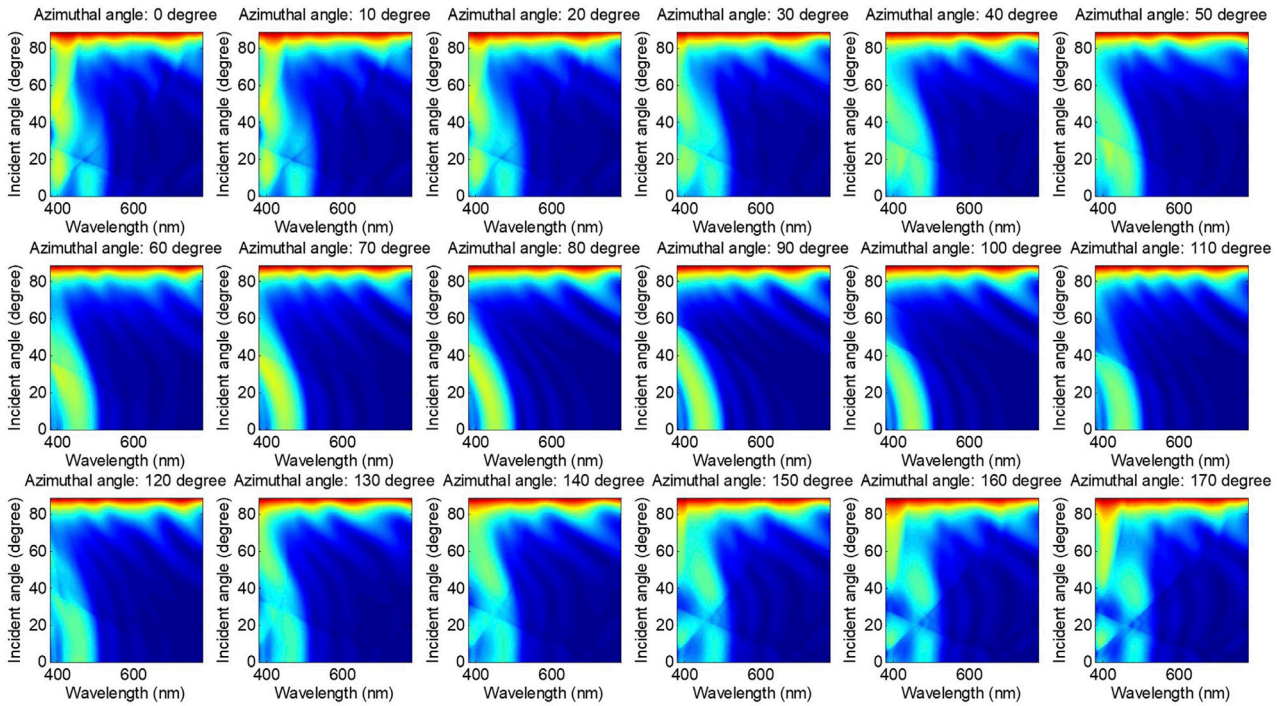


**FIGURE 4 |** Simulated results of total diffraction orders reflectivity of air under TE mode.

between carbinol and ethanol is only the refractive index, we do not simulate both. In the following simulations which are from **Figures 3 to 6**, the ambient materials are air (refractive index equals 1) and ethanol (refractive index equals 1.36), respectively.

In **Figure 4**, the reflectivity of the total diffraction orders was simulated for the *Morpho* butterfly's wing with the ambient air. When compared to **Figure 3** apples-to-apples, we find that the sum of the reflectivity aside from zeroth-order diffraction is mainly responsible for the left part of each subfigure. Namely, it is the chief cause of structural colour. And the left part of each subfigure varies with the azimuthal angle, which means the sum of the reflectivity of the diffraction orders other than the zeroth order is sensitive to the azimuthal angle. These phenomena show that if we want to characterize the structural parameters or the optical parameters of the butterfly wing using the Optical Critical Dimension (OCD) liked method, the zeroth-order should not be used. In addition, visually, we can find that the structural colour of the *Morpho* butterfly is not always blue under some specified incident angle and azimuthal angle—The simulation is carried out under the condition of 110° azimuthal angle for example. The total reflectivity of the butterfly wing is low in the incident angle region which is from 42 to 70 under the 110° azimuthal angle, in which case the colour of the *Morpho* butterfly will look a lit bit like black to the naked eye. Then we have carried out other simulations for the butterfly wing which is surrounded by the liquid of ethanol, the simulations are shown in **Figures 5**, **6**.

When doing the apples-to-apples comparison with **Figures 3**, **5** shows the same characteristic, the reflectivity of zeroth-order diffraction is insensitivity to the azimuthal angle, and there is an upper threshold of incident angle below which the reflectivity is quite low under all the wavelengths. The direct difference between **Figures 3**, **5** is that the reflectivity obtained above the incident angle of 80° is more regular in **Figure 3**. In contrast, there are many peaks and valleys on the top of each subfigure in **Figures (4–6)** share similar characteristics that result from the sum of the total diffraction orders except for the zeroth-order. Also, the sum of the non-zeroth diffraction orders is sensitive to the azimuthal angle when the butterfly wing is surrounded by the liquid of ethanol.

In Yang's study [13], they showed that the reflectance peak migrates from 475 to 565nm and 570 nm when the surrounding medium change from air to carbinol and ethanol, respectively. Moreover, the law that the wavelength of the reflectivity peak of total orders increases with the refractive index of ambient medium can be discovered. It must be stressed that the simulation and experiment were conducted in the conditions of normal incidence and the azimuthal angle of 0°. But when we adjust the incident angle and azimuthal angle in the simulation, the law introduced above no longer obtain in some cases. The simulation results are shown as follows:

We can detect that the two curves which denote the RPS of carbinol and ethanol under total diffraction orders have some intersections. These appearances show that the RPS of the carbinol is bigger than that of ethanol under some specified incident angles and azimuthal angles. Take the case of the

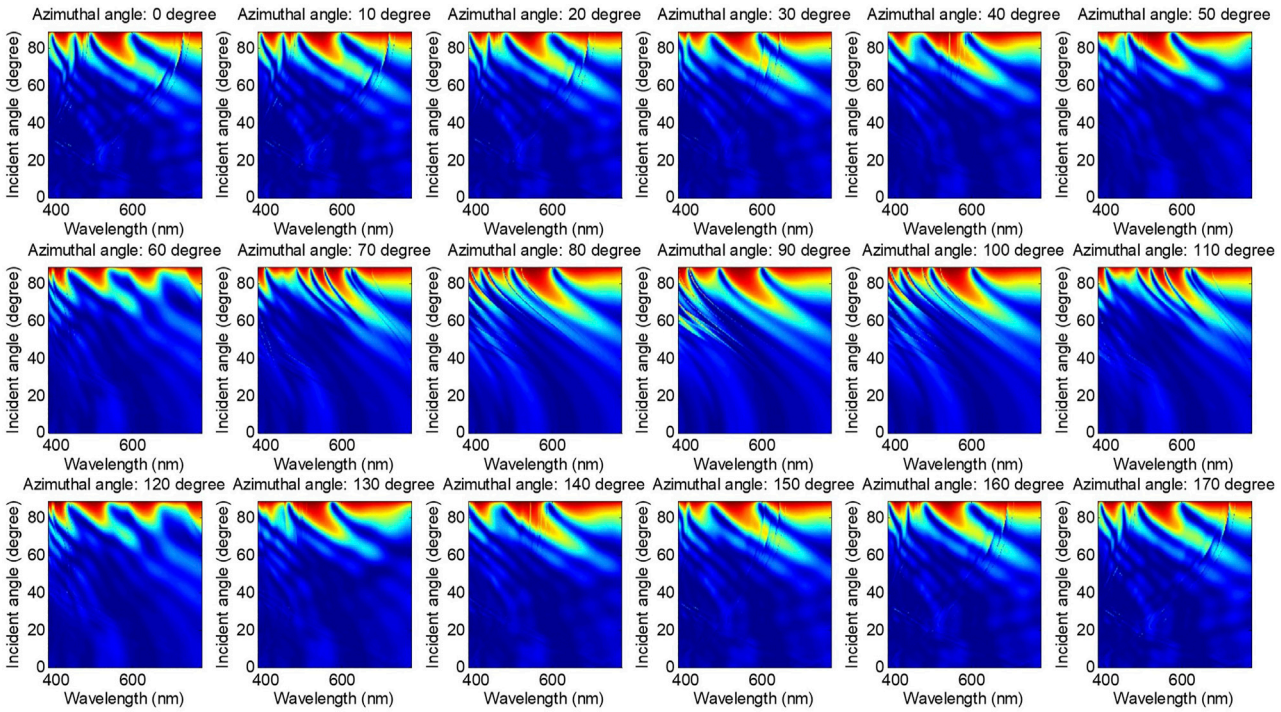


**FIGURE 5 |** Simulated results of zeroth-order diffraction reflectivity of alcohol under TE mode.

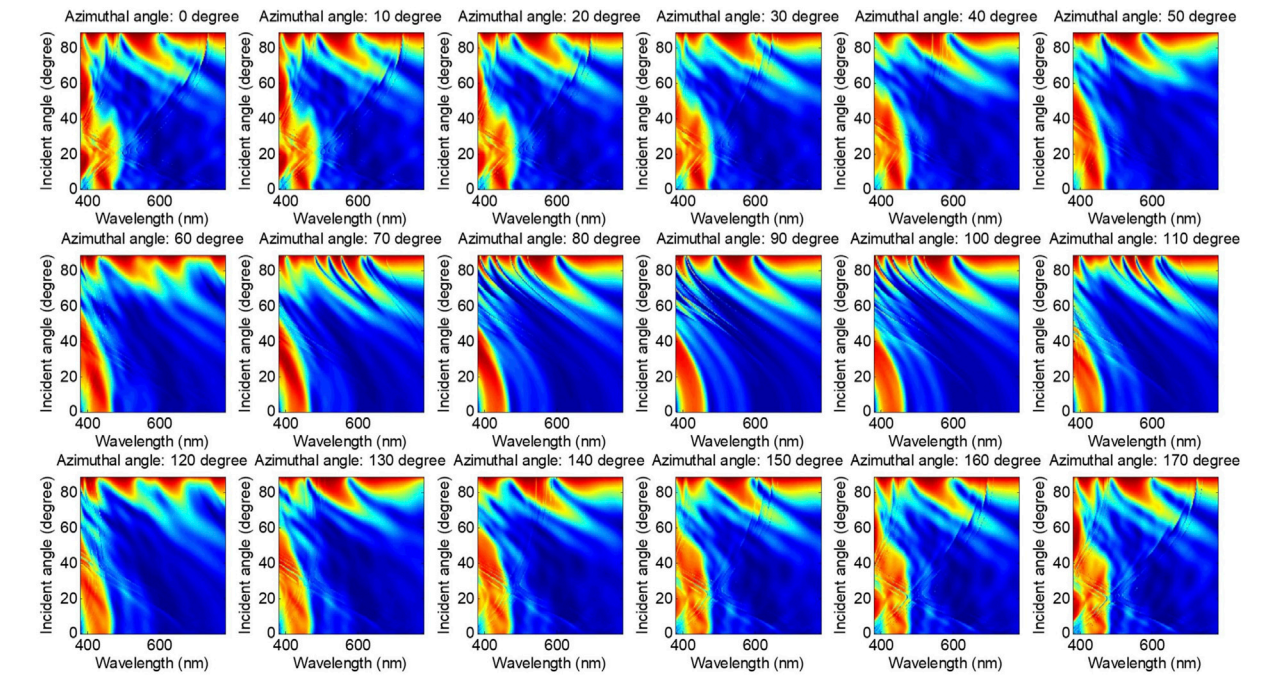


**FIGURE 6 |** Simulated results of total diffraction orders reflectivity of alcohol under TE mode.

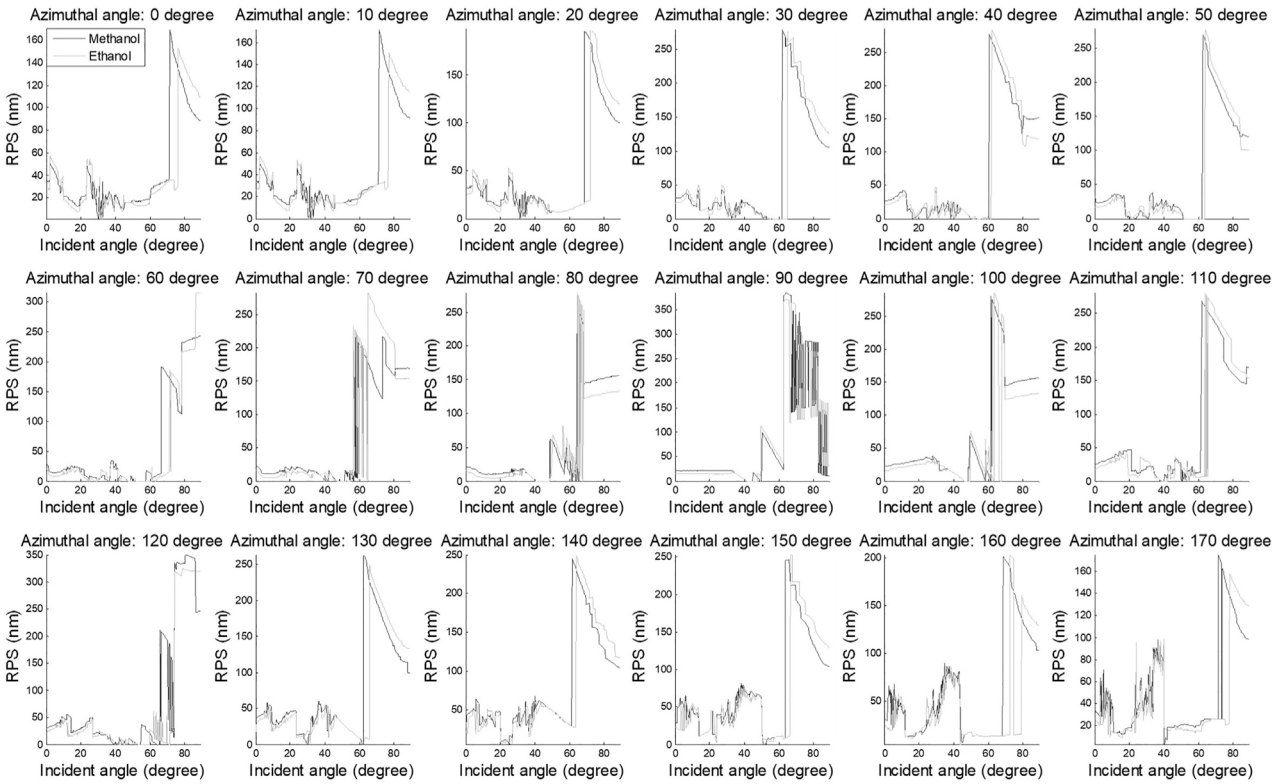


**FIGURE 7 |** Simulated results of RPS of total diffraction orders.

sub-figure in the top-left corner of **Figure 7**, we can see that the RPS of the carbinol is smaller than that of the ethanol with incident angle range of 60–75°, it quite coheres with the conclusion in Yang's paper [13]. However, the RPS of the carbinol is bigger than that of the ethanol between the incident angle of 75 and 85°. Thus, if the RPS should be used for distinguishing between ambient media of the butterfly wing scale-based biosensor, the measurement configuration must be selected carefully to ensure that the RPS is proportional or inversely proportional to the refractive index of ambient medium.

In most researches of nano/micro-structures, zeroth-order diffraction is the highest priority. Hence, we also simulate the RPS under zeroth-order diffraction for the ambient medium of carbinol and ethanol, respectively. The simulation result is shown in **Figure 8**.

It is obvious that the curves in **Figure 8** show more volatility compared with the curves in **Figure 7**, and we can hardly determine whether one is higher between two curves. In other words, the zeroth-order diffraction is not a very appropriate observation parameter to distinguish two ambient media with similar refractive index. Even so, we can find that when the azimuthal angle is set as 80, 90, and 100°, the number of oscillations is much less than the other sub-figures, and the curve has longer smooth parts.

Since the RPS is used to represent and characterize different ambient media in the *Morpho* butterfly wing-based biosensor, the difference between the RPSs should be maximized for ambient medium with a similar refractive index. Furthermore, not all measurement configurations can guarantee that the RPS is proportional to the refractive index of ambient medium in the simulations discussed above, and given the uncertainty (including random noise, system noise, the uncertainty of tool's incident angle, and azimuthal angle, etc.) in the practical measurement, those continuously increased incident angles under a specified azimuthal angle should be select to guarantee a trend that the relative bigger refractive index corresponds to a bigger RPS. Hence, the measurement configuration such as the incident angle and azimuthal angle should be set prudentially. We have extracted those measurement configurations that can satisfy the relationship of direct proportion between the RPS and refractive index for both zeroth-order diffraction and total diffraction orders beforehand. The statistical result is shown in **Figure 9** (the range of incident angle in the above simulations is from 0 to 89° with an increment of 0.25°, which means the number of incident angles is 357):

In **Figure 9**, the "excellent" incident angles mean that if the measurement is conducted under these incident angles, the RPS is proportional to the refractive index of ambient medium. From the two sub-figures, we can observe that the number of "excellent" incident angles under zeroth-order diffraction is bigger than that of the total diffraction orders for most of the azimuthal angles. One issue is that the difference of RPS for ambient medium should be maximized to ensure good sensitivity of the biosensor.

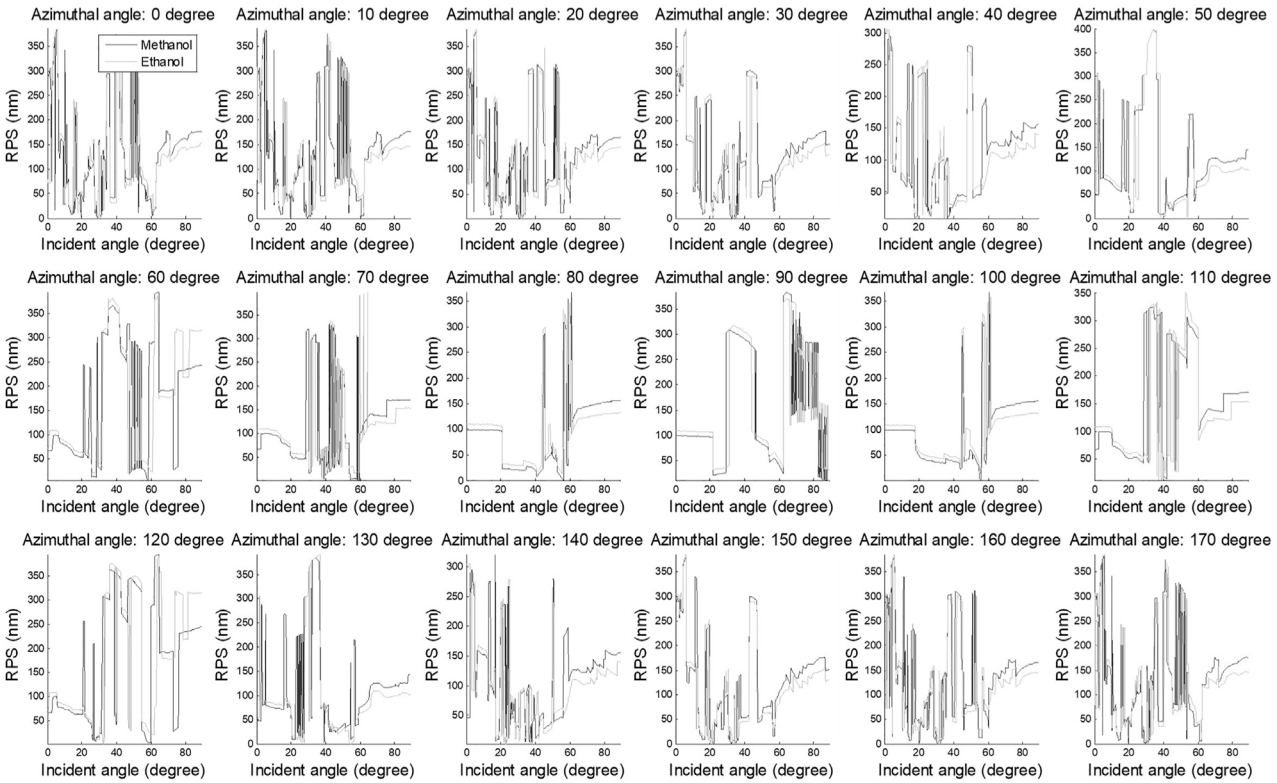


**FIGURE 8 |** Simulated results of RPS of zeroth-order diffraction.

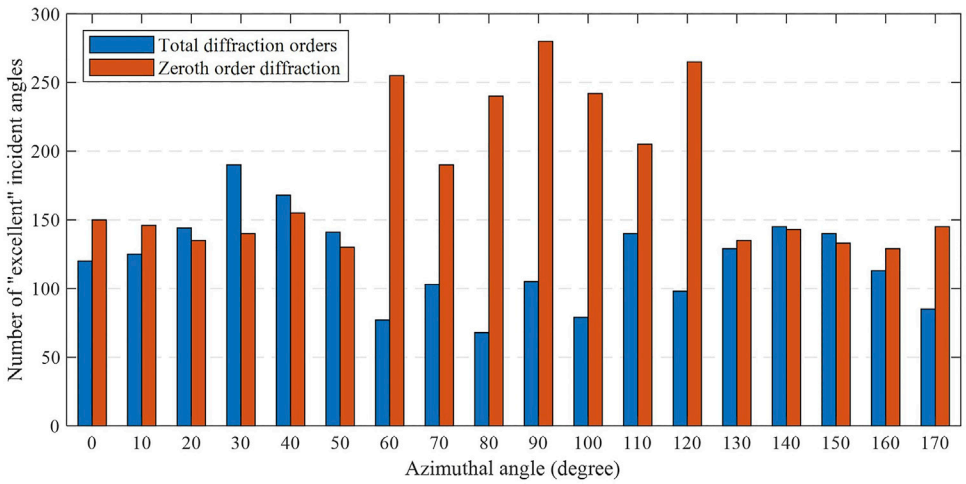


**FIGURE 9 |** The number of "excellent" incident angles of total diffraction orders and zero-order diffraction.

Hence, the incident angle that can maximize the difference should be picked up from those "excellent" incident angles under a specified azimuthal angle. The other issue is that the continuous sub-range of incident angle that contains our picks should strive to be longer, because of the uncertainty of tool's incident angle, etc. in the practical measurement. Based on this strategy, the well-chosen incident angles which we called optimal incident angles are shown in **Figure 10B**.

In **Figure 10A**, the maximal difference of RPS between ambient carbinol and ethanol under total diffraction orders is

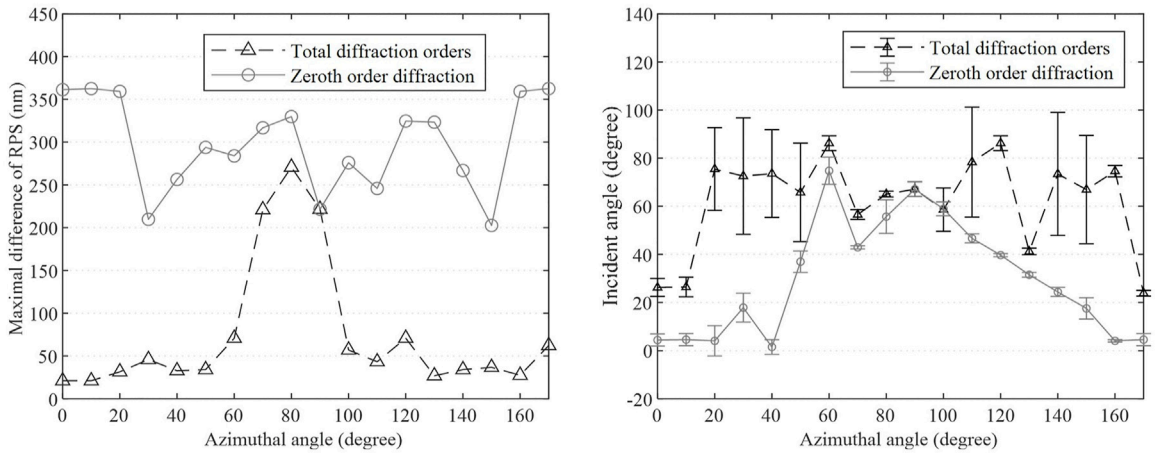


**FIGURE 10 | (A)** The maximal RPS difference and **(B)** continuous incident angle range of total diffraction orders and zeroth-order diffraction at each azimuthal angle.

275 nm at the azimuthal angle of 80°, and the corresponding optimal incident angle is 68°. However, for the zeroth-order diffraction, the RPS is over 200 nm under all the azimuthal angles. In **Figure 10B**, the continuous ranges not only contain the optimal incident angle but also ensure the RPS is proportional to the refractive index of the ambient medium. For the azimuthal angle of 80°, the continuous range of corresponding incident angle is too short, it will lead to the criterion of direct proportion may not be valid at larger uncertainty in practical measurement. Compared with the total diffraction orders, the zeroth-order diffraction can provide a bigger difference of RPS between the carbinol and ethanol under a few incident angles and azimuthal angles. However, the continuous ranges of incident angles have shorter lengths for most of the azimuthal angles. Thus, if we want to distinguish two different ambient media accurately, a perfect tradeoff should be gained among the RPS and the continuous range before measuring.

## CONCLUSION

In this paper, the impact of incident angle and azimuthal angle on *Morpho* butterfly scales-based biosensors has been investigated. According to the simulation result of reflectivity under zeroth-order diffraction and non-zeroth order diffraction, we can conclude that the reflectivity of zeroth-order diffraction is less sensitive to the azimuthal angle than of non-zeroth order diffraction, and the non-zeroth order diffraction is a major contributor to structural color for most incident angles. Thus, we suggest that zeroth-order diffraction should not be used to characterize the structural parameters or the optical parameters of the butterfly wing by the method parallel to OCD. Furthermore, we have calculated the RPS of carbinol and ethanol relative to the air, the law obtained at normal incidence and zero-degree azimuthal angle is no longer active in some cases. The appropriate incident angle and azimuthal angle must be reconsidered. On the one hand, we hope the RPS is proportional to refractive index, and have obvious difference among ambient media with similar reflectivity index. On the other hand, we also expect the incident angle that satisfies previous point to have a wider contiguous range. Therefore, a compromise between above two points can be made, according to the maximal RPS difference and the continuous range of optimal incident angles at each azimuthal angle we have given. Theoretically, the selected configuration can provide better robustness and accuracy especially if exist in larger uncertainty of measurement. In the future work, we will carry out experiments for further verification of this beneficial effect.

## DATA AVAILABILITY STATEMENT

The raw data supporting the conclusion of this article will be made available by the authors, without undue reservation.

## AUTHOR CONTRIBUTIONS

HZ, ST, and CL performed the simulations under the guidance of ZD and LN, ZD, HZ, and XW wrote the manuscript with contributions from all.

## FUNDING

National Natural Science Foundation of China (Grant No. 51975191).

## REFERENCES


1. Li Q, Zeng Q, Shi L, Zhang X, Zhang KQ. Bio-Inspired Sensors Based on Photonic Structures of Morpho Butterfly Wings: A Review. *J Mater Chem C* (2016) 4(9):1752–63. doi:10.1039/C5TC04029A
2. He J., Villa NS., Luo Z., An S., Shen Q., Tao P., et al. Integrating Plasmonic Nanostructures with Natural Photonic Architectures in Pd-Modified Morpho Butterfly Wings for Sensitive Hydrogen Gas Sensing. *RSC Adv* (2018) 8(57): 32395–400. doi:10.1039/C8RA05046E
3. De Bellis I, Ni B, Martella D, Parmeggiani C, Keller P, Wiersma DS., et al. Color Modulation in Morpho Butterfly Wings Using Liquid Crystalline Elastomers. *Adv Intell Syst* (2020) 2(9):2000035. doi:10.1002/aisy.202000035
4. Luo Z., Weng Z., Shen Q., An S., He J., Fu B., et al. Vapor Detection through Dynamic Process of Molecule Desorption from Butterfly Wings. *Pure Appl Chem* (2020) 92(2):223–32. doi:10.1515/pac-2019-0118
5. Yamashita K, Kunitsu K, Hattori T, Kuwahara Y, Saito A. Demonstration of a Diffraction-Based Optical Diffuser Inspired by the Morpho Butterfly. *Opt Express* (2021) 29(19):30927–36. doi:10.1364/OE.436193
6. Song B, Johansen VE, Sigmund O, Shin JH. Reproducing the Hierarchy of Disorder for Morpho-Inspired, Broad-Angle Color Reflection. *Sci Rep* (2017) 7(1):1–8. doi:10.1038/srep46023
7. Zhu D, Kinoshita S, Cai D, Cole JB. Investigation of Structural Colors inMorphobutterflies Using the Nonstandard-Finite-Difference Time-Domain Method: Effects of Alternately Stacked Shelves and ridge Density. *Phys Rev E* (2009) 80(5):051924. doi:10.1103/PhysRevE.80.051924
8. Giraldo MA, Stavenga DG. Brilliant Iridescence of Morpho Butterfly wing Scales Is Due to Both a Thin Film Lower Lamina and a Multilayered Upper Lamina. *J Comp Physiol A* (2016) 202(5):381–8. doi:10.1007/s00359-016-1084-1
9. Zhang S, Chen Y. Nanofabrication and Coloration Study of Artificial Morpho Butterfly Wings with Aligned Lamellae Layers. *Sci Rep* (2015) 5(1):1–10. doi:10.1038/srep16637
10. Rodríguez RE., Agarwal SP., An S., Kazyak E., Das D., Shang W., et al. Biotemplated Morpho Butterfly Wings for Tunable Structurally Colored Photocatalysts. *ACS Appl Mater Inter* (2018) 10(5):4614–21. doi:10.1021/acsami.7b14383
11. Butt H, Yetisen AK, Mistry D, Khan SA, Hassan MU, Yun SH. MorphoButterfly-Inspired Nanostructures. *Adv Opt Mater* (2016) 4(4): 497–504. doi:10.1002/adom.201500658
12. Kim HM, Kim SH, Lee GJ, Kim K, Song YM. Parametric Studies on ArtificialMorphoButterfly Wing Scales for Optical Device Applications. *J Nanomater* (2015) 16(1):1–7. doi:10.1155/2015/451834
13. Yang X, Peng Z, Zuo H, Shi T, Liao G. Using Hierarchy Architecture of Morpho Butterfly Scales for Chemical Sensing: Experiment and Modeling. *Sensors Actuators A: Phys* (2011) 167(2):367–73. doi:10.1016/j.sna.2011.03.035
14. Zhang S, Chen Y, Lu B, Liu J, Shao J, Xu C. Lithographically-generated 3D Lamella Layers and Their Structural Color. *Nanoscale* (2016) 8(17):9118–27. doi:10.1039/C6NR00936K
15. Watanabe K, Hoshino T, Kanda K, Haruyama Y, Kaito T, Matsui S. Optical Measurement and Fabrication from a Morpho-Butterfly-Scale Quasistructure by Focused Ion Beam Chemical Vapor Deposition. *J Vac Sci Technol B* (2005) 23(2):570–4. doi:10.1116/1.1868697
16. Kang SH, Tai TY, Fang TH. Replication of Butterfly wing Microstructures Using Molding Lithography. *Curr Appl Phys* (2010) 10(2):625–30. doi:10.1016/j.cap.2009.08.007
17. Poncelet O., Tallier G., Mouchet SR., Crahay A., Rasson J., Kotipalli R., et al. Vapour Sensitivity of an ALD Hierarchical Photonic Structure Inspired by Morpho. *Bioinspir Biomim* (2016) 11(3):036011. doi:10.1088/1748-3190/11/3/036011
18. Potyrailo RA, Ghiradella H, Vertiatchikh A, Dovidenko K, Cournoyer JR, Olson E. Morpho Butterfly wing Scales Demonstrate Highly Selective Vapour Response. *Nat Photon* (2007) 1(2):123–8. doi:10.1038/nphoton.2007.2
19. Han Z., Yang M., Li B., Mu Z., Niu S., Zhang J., et al. Excellent Color Sensitivity of Butterfly wing Scales to Liquid Mediums. *J Bionic Eng* (2016) 13(3):355–63. doi:10.1016/S1672-6529(16)60308-6
20. Xue H., Liu D., Chi D., Xu C., Niu S., Han Z., et al. Toward the Burgeoning Optical Sensors with Ultra-Precision Hierarchical Structures Inspired by Butterflies. *Adv Mater Inter* (2021) 8(15):2100142. doi:10.1002/admi.202100142
21. Moharam MG, Gaylord TK, Pommet DA, Grann EB. Stable Implementation of the Rigorous Coupled-Wave Analysis for Surface-Relief Gratings: Enhanced Transmittance Matrix Approach. *J Opt Soc Am A* (1995) 12(5):1077–86. doi:10.1364/JOSAA.12.001077
22. Moharam MG, Gaylord TK, Grann EB, Pommet DA. Formulation for Stable and Efficient Implementation of the Rigorous Coupled-Wave Analysis of Binary Gratings. *J Opt Soc Am A* (1995) 12(5):1068–76. doi:10.1364/JOSAA.12.001068
23. Moharam MG, Gaylord TK. Coupled-Wave Analysis of Reflection Gratings. *Appl Opt* (1981) 20(2):240–4. doi:10.1364/AO.20.000240
24. Gaylord TK, Moharam MG. Analysis and Applications of Optical Diffraction by Gratings. *Proc IEEE* (1985) 73(5):894–937. doi:10.1109/PROC.1985.13220
25. Li L. Use of Fourier Series in the Analysis of Discontinuous Periodic Structures. *J Opt Soc Am A* (1996) 13(9):1870–6. doi:10.1364/JOSAA.13.001870
26. Vukusic P, Sambles JR, Lawrence CR, Wootton RJ. Quantified Interference and Diffraction in Single Morpho Butterfly Scales. *Proc R Soc Lond B* (1999) 266(1427):1403–11. doi:10.1098/rspb.1999.0794
27. Wu W, Liao G, Shi T, Malik R, Zeng C. The Relationship of Selective Surrounding Response and the Nanophotonic Structures of Morpho Butterfly Scales. *Microelectronic Eng* (2012) 95:42–8. doi:10.1016/j.mee.2011.12.017
28. Foldyna M., De Martino A., Garcia-Caurel E., Ossikovski R., Licitra C., Bertin F., et al. Critical Dimension of Biperiodic Gratings Determined by Spectral Ellipsometry and Mueller Matrix Polarimetry. *Eur Phys J Appl Phys* (2008) 42(3):351–9. doi:10.1051/epjap:2008089
29. Novikova T, De Martino A, Hatit SB, Drévillon B. Application of Mueller Polarimetry in Conical Diffraction for Critical Dimension Measurements in Microelectronics. *Appl Opt* (2006) 45(16):3688–97. doi:10.1364/AO.45.003688
30. Vagos P, Hu J, Liu Z, Rabello S. Uncertainty and Sensitivity Analysis and its Applications in OCD Measurements. Metrology, Inspection, and Process Control for Microlithography XXIII. *Int Soc Opt Photon* (2009) 7272: 543–551. doi:10.1117/12.814363


**Conflict of Interest:** The authors declare that the research was conducted in the absence of any commercial or financial relationships that could be construed as a potential conflict of interest.

frontiers in Physics

ORIGINAL RESEARCH
published: 11 January 2022
doi: 10.3389/fphy.2021.815360

# Polarimetric Imaging in the Environment Containing Medium and Object

*Daqian Wang*, Xin Wang, Peifeng Pan and Jun Gao*

*School of Computer and Information, Hefei University of Technology, Hefei, China*

Polarimetric imaging has been studied and applied to the problem of visibility restoration in various scenarios such as haze, mist and underwater. Although studies have shown that under certain conditions, circular polarimetric imaging has certain advantages over linear polarimetric imaging, however, for a complex environment containing both scattering medium and object, the performance of linear and circular polarimetric imaging is affected by many factors. In this paper, the propagation of linear and circular polarized light in the scattering medium is theoretically analyzed, then the simulation experiments under different experimental conditions are carried out and the conclusions are summarized. In order to validate the simulation results, the measurement experiments are carried out in dynamic smoke scenarios with different smoke concentrations. The results show that, the propagation of the polarized light, especially the circular polarized light, is determined by medium conditions. Generally, both the linear and circular polarimetric imaging had an ability to reduce the image degradation caused by smoke, however, under some certain environment conditions, unlike the linear polarized channels, the difference between the orthogonal circular polarized channels may be approached or even reversed, which may limit the circular polarization-based difference imaging and visibility restoration performance.

**Keywords: polarimetric imaging, propagation of polarized light, mixed medium, linear polarization, circular polarization**

OPEN ACCESS

***Edited by:***
*Ji Qi,*
*Imperial College London, United Kingdom*

***Reviewed by:***
*Fei Liu,*
*Xidian University, China*
*Ran Liao,*
*Tsinghua University, China*

****Correspondence:***
*Daqian Wang*
*d.wang19@imperial.ac.uk*

***Specialty section:***
*This article was submitted to Optics and Photonics, a section of the journal Frontiers in Physics*

***Received:*** *15 November 2021*
***Accepted:*** *13 December 2021*
***Published:*** *11 January 2022*

***Citation:***
*Wang D, Wang X, Pan P and Gao J (2022) Polarimetric Imaging in the Environment Containing Medium and Object. Front. Phys. 9:815360. doi: 10.3389/fphy.2021.815360*

## 1 INTRODUCTION

When the polarized light propagates in the scattering medium, it undergoes multiple scattering with particles, leading to randomization of its direction, phase, and polarization state [1]. Due to the differences of material, structure and shape between the object and the background, their polarization properties are significantly different. Polarimetric imaging can enhance the difference between the object area and the background medium and highlight the details of the object by measuring and processing the polarization information. Nowadays, Polarimetric imaging has been applied in fields like object detection [2–4], biomedical imaging [5, 6].

Existing studies have shown that polarization gating can eliminate the contribution of scattered photons that lose the original polarization information caused by multiple scattering, and retain the photons that experience few scattering times that maintain the original polarization state component, so as to improve the image contrast [7, 8]. In addition, the circular polarimetric imaging is implemented in some scenarios, due to its advantages over the linear polarization [9–11]. However, due to the polarization memory effect, the helicity of circular polarized light can be

reversed in some cases [12, 13]. Therefore, the law of the propagation of circular polarized light in the medium is more complex than that of linear polarized light and the influence of polarization memory effect should be fully considered in application.

We study the propagation of polarized light in a mixed environment including medium and object. Thus, we should model the polarimetric scattering in the medium and the polarimetric reflection by object surface. Linear polarimetric imaging is widely used in research and application, but due to some advantages of circular polarimetric imaging, however, we are still interested in the performance of linear and circular polarimetric imaging under different experimental conditions. This paper first studies the propagation of linear and circular polarized light in scattering medium. On this basis, simulation experiments are implemented based on Monte Carlo simulation program and the variation of the intensity of orthogonal polarization channels affected by different factors are analyzed. In addition, in order to validate the simulation results, a polarization setup is built for measurement experiments and a series of experimental data of different polarization channels are collected and the results are analyzed. The results show that, the propagation of the polarized light, especially the circular polarized light, can be affected by the medium factors such as concentration, wavelength and distance. Generally, both the linear and circular polarimetric imaging had an ability to reduce the image degradation caused by smoke, however, under some certain environment conditions, unlike the linear polarized channels, the difference between the orthogonal circular polarized channels may be approached or even reversed, which may limit the circular polarization-based difference imaging and visibility restoration performance.

# 2 SIMULATION OF THE PROPAGATION OF POLARIZED LIGHT IN MIXED MEDIUM

In order to fully understand the propagation of polarized light in mixed media, we developed a Monte Carlo based simulation program [14, 15], and studied the process of polarized light propagating in medium through a series of simulation experiments. The significance of carrying out the simulation experiments is that, the propagation of polarized light in real scenarios is affected by many factors, such as the wavelength, the particle size, the concentration, the refractive index and the thickness of medium. However, it is difficult to evaluate the impact of each factor and include all the factors in measurement experiments. Therefore, the simulation experiments can help us better understand the propagation of linear and circular polarized light in different medium conditions.

## 2.1 Theoretical Basis of Propagation of Polarized Light

For linear polarimetric imaging, numerous polarization-maintaining photons can be detected at the upper layer of the scattering medium [1, 7]. As the photons penetrate into the deeper layer, due to the multiple scattering, the photons lose their initial polarization state and become randomized [1]. Therefore, the polarization difference imaging is to eliminate multiple scattered photons, so as to highlight the details and contrast of the object area. In addition, for circular polarimetric imaging, after photons scattered at large angles or reflected by the object surface, their helicity will be reversed compared with the initial helicity, while photons scatter forward at small angles will maintain the helicity [16, 17]. Some studies also pointed out that the helicity reversal is related to the relative size of photon's wavelength and medium particle size [12, 18]. However, in the environment containing both medium and target, the situation will become more complicated when the polarimetric scattering and reflection have to be considered simultaneously.

## 2.2 Structure of the Program

The scenario can be simplified as a mixture of the smoke medium in the upper layer and the object in the lower layer. Monte Carlo based simulation program can track the photon's movement in the medium and update the photon's polarization state. By counting the energy of backscattered photons on the receiving plane, the radiance of orthogonal polarization channels can be obtained.

The flow chart of the simulation program is shown in **Figure 1**, which mainly includes three main modules:

1) The scattering medium module can process the scattering of photons in the medium, and update the photon's position, direction and polarization parameters after each movement;
2) The surface geometric modeling module can carry out geometric modeling on the object surface [19, 20], and update the photons' reflection direction from the object surface;
3) The material modeling module can convert the object surface material into the corresponding optical parameters, generate the corresponding Mueller matrix [21, 22] and update the photons' polarization state after reflection.

## 2.3 Simulation Experiments Under Different Experimental Conditions

The simulation experiments were carried out and the experimental conditions were set to match the measurement scenarios. The simulations focused on the radiance of orthogonal polarization channels in the environment containing medium and object. Because the particle size of the medium has a huge impact on the interaction between polarized photons and particles. Our simulation experiments chose two particle diameters, small-sized (0.2 μm) and large-sized (8.0 μm), and study the factors of concentration, wavelength and detection distance.

### 2.3.1 Effect of Concentration on the Propagation of Polarized Light

In the measurement experiment, the concentration of smoke is an important factor, affecting the polarimetric imaging performance. Theoretically, with the increase of smoke

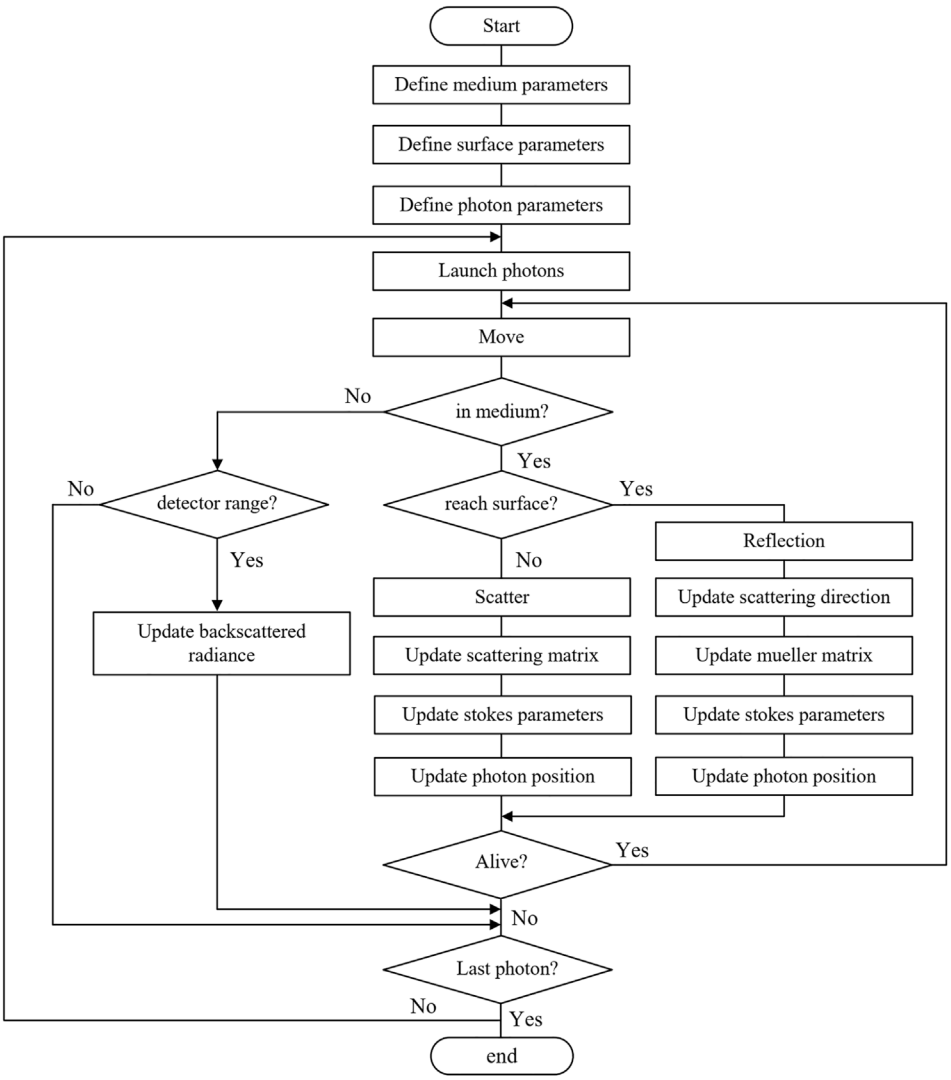


**FIGURE 1 |** The flow chart of simulation program.

concentration, the number of particles per unit volume of the medium increases, the scattering coefficient of particles increases [23], the step size of photons generally decreases, the penetration depth of photons decreases, and the diffusion radius of photons increases. However, the propagation of polarized light with different initial polarization states is different. We simulated the backscattered intensity of linear and circular polarization with concentrations in the medium of small-sized and large-sized particles. The receiving plane was placed 10 cm above the object [24]. The smoke as the scattering medium was filled between the object and the receiving plane. The pencil beam light source was vertically incident into the environment at 10 cm above the object, and the refractive index of smoke particles at 0.630 μm was 1.57 + 0.4277i [25]. The refractive index of the object surface was set to 1.5, which corresponded to the material of the standard color chart (Spydercheckr) [26]. We set the medium concentration to a reasonable value to ensure that the calculated scattering coefficient was within the normal range in the actual scenarios [27]. The absorption coefficient was usually set to a small value [28]. The detailed simulation parameters were shown in **Table 1**.

The 3D distributions of backscattered intensity of polarization channels in the medium with small-sized particles were shown in **Figure 2**. The backscattered intensity at the centre of the plane was high because of the reflection, while the radiance at the periphery was low. The backscattered intensity at the centre of each distribution was marked in each subgraph. As shown in **Figure 2A**, for the horizontally linear polarized illumination, the horizontal linear polarized (co-polarized) light dominated the backscattered intensity, while for the right circular polarized illumination, an obvious helicity reversal phenomenon happened, that is, the left circular polarized light dominated the backscattered intensity, as shown in **Figure 2B**. Therefore, for the medium with small-sized (0.2 μm) particles, with the

**TABLE 1 |** Simulation parameters of medium with different concentrations.

| Parameters | 0.2 μm | 8.0 μm |
|---|---|---|
| Illumination | Linear Polarized, Circular Polarized | Linear Polarized, Circular Polarized |
| Wavelength | 0.630 μm | 0.630 μm |
| Anisotropy $g$ | 0.2052 | 0.7646 |
| Density | $4 \times 10^{-4}$, $12 \times 10^{-4}$, $20 \times 10^{-4}$, $28 \times 10^{-4}$ particles/μm$^3$ | $2 \times 10^{-7}$, $4 \times 10^{-7}$, $6 \times 10^{-7}$, $8 \times 10^{-7}$ particles/μm$^3$ |
| Scattering coefficient $\mu_s$ [27] | 0.0348, 0.1042, 0.1737, 0.2432 cm$^{-1}$ | 0.2059, 0.4118, 0.6177, 0.8236 cm$^{-1}$ |
| Absorption coefficient $\mu_a$ [28] | 0.0100 cm$^{-1}$ | 0.0100 cm$^{-1}$ |
| Refractive index (Smoke particle) [24] | 1.57 + 0.4277i | 1.57 + 0.4277i |
| Refractive index (Object) [26] | 1.50 | 1.50 |
| Number of photons | 50,000 | 50,000 |

gradual increase of medium concentration, the intensity of co-polarized light and left circular polarized light decreased significantly, while that of cross-polarized light and right circular polarized light maintained at a very low level.

The 3D distributions of backscattered intensity of polarization channels in the medium with large-sized particles (8.0 μm) were shown in **Figure 3**. With the gradual increase of the concentration, the intensity of co-polarized and left circular polarization channel first decreased and then increased, while the intensity of cross-polarized and right circular polarization components increased significantly. Especially, the intensity of right-handed circular polarization component exceeded the left-handed polarization component when the concentration reached a certain degree. This was because when the medium concentration was low, the collision probability between photons and particles was low, backscattered photons were mostly reflected from the surface, or scattered at a large angle, so the helicity was mainly reversed. With the increase of medium concentration, the scattering coefficient of particles increased, the collision probability between photons and particles increased, and the multiple scattering of photons could be decomposed into multiple small angle scattering, therefore, the number of photons that maintained the original helicity increased as a whole. Therefore, for a particle polydisperse medium with different concentrations, the difference between the orthogonal linear polarized channels is maintained, while the difference between the orthogonal circular channels may be approached or even reversed.

### 2.3.2 Effect of Wavelength on the Propagation of Polarized Light

In the measurement experiment, the wavelength also has an important impact on the results of polarimetric imaging. We carried out simulation experiments under different wavelengths and most of the simulation parameter settings were the same as the previous. As shown in **Table 2**, the concentration was set as a constant. The wavelength was selected in the range of visible light wavelength: 0.43, 0.48, 0.53, 0.58, 0.63 μm. The 3D distributions of backscattered intensity of polarization channels were shown in **Figures 4**, **5**, respectively. For the medium with small-sized particles, the scattering coefficient of particles decreased gradually with the increase of initial wavelength, then the step size of photons generally increased, photons were easier to reach and reflect from the object surface, therefore for the co-polarized light and left circular channel, the intensity of the received backscattered light increased gradually, while the cross-polarized and right circular channel were insensitive to the variation of the wavelength, as shown in **Figure 4**. In addition, for the medium with large-sized particles, the scattering coefficient did not change significantly with the increase of wavelength, because the effective cross-section of the particle (proportional to scattering coefficient) [23] is large enough relative to the wavelength. Therefore, the intensity of all the polarization channels varied slightly, as shown in **Figure 5**, and the intensity of right circular component was higher than that of left circular component at all wavelengths. This was because in the medium with large-sized particles, the scattering coefficient of particles was high, the collision probability between photons and particles was large, and the multiple scattering of photons could be decomposed into multiple small angle scattering, so the number of photons that maintained the original helicity increased as a whole, and the number of photons reflected by the target surface decreased. Therefore, the difference between orthogonal linear polarized channels was more obvious compared with circular polarized channels.

### 2.3.3 Effect of Detection Distance on the Propagation of Polarized Light

In the measurement experiment, in the medium with uniform distribution, the distance between the detector and the object determines the thickness of the scattering medium. When the moving distance of photon in the medium exceeds its transport mean free path (MFP), the scattering direction will become randomized, which affecting the intensity of backscattered polarized channels [24]. Therefore, when studying the influence of detection distance on the propagation of polarized light, the photon's transport MFP in the medium should be fully considered. For the medium with small-sized particles, the transport MFP was about 12.1 cm, while for the medium with large-sized particles, the transport MFP was about 6.9 cm. Therefore, for different medium environments, we set different detection distances for the simulations. The simulation parameters were listed in **Table 3**.

For the medium with small-sized particles, with the increase of the detection distance, the backscattered intensity of co-polarized and left circular polarized channel decreased significantly, while the intensity of cross-polarized and right circular polarized channel decreased slightly, as shown in **Figure 6**; while for the

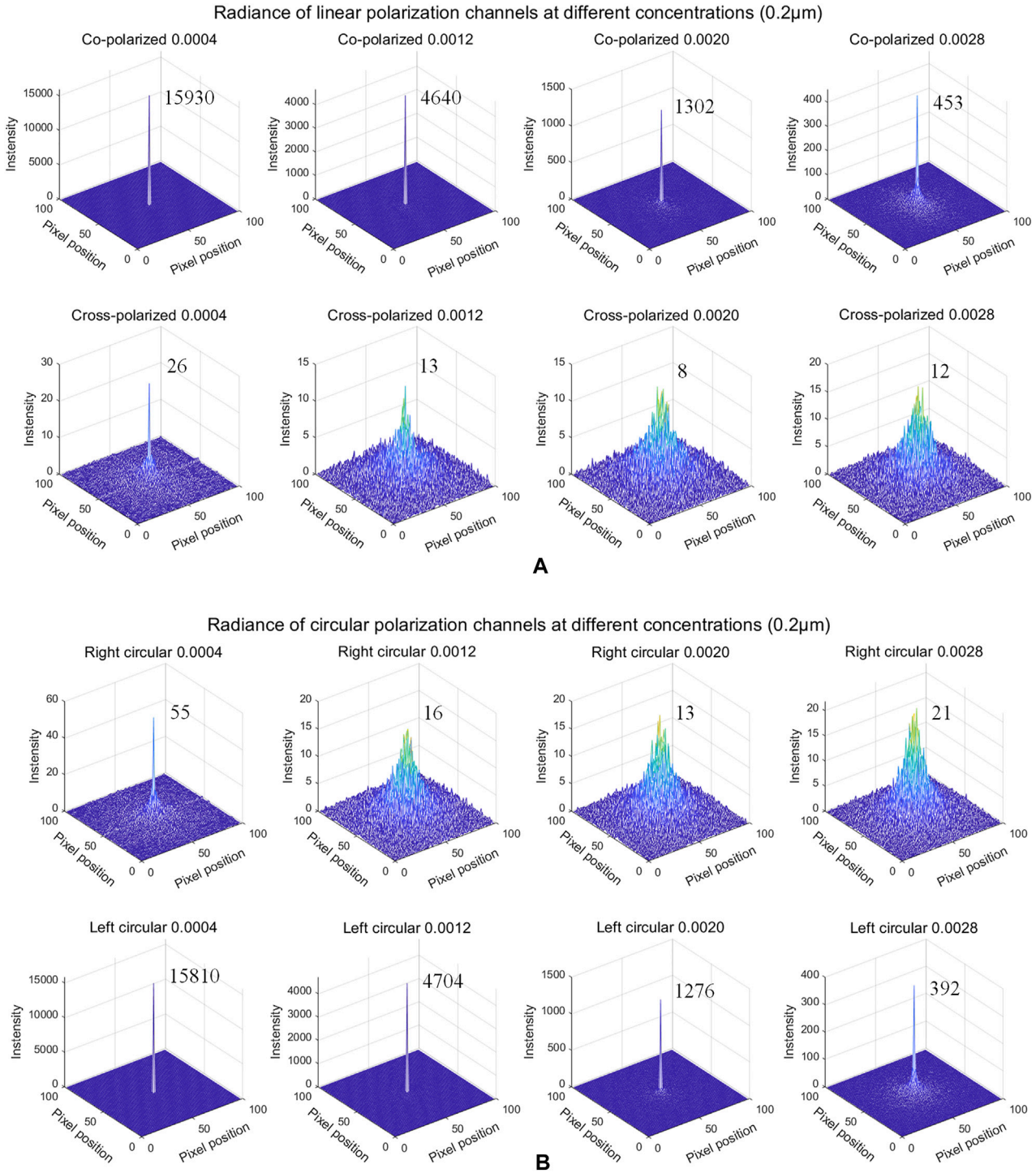


**FIGURE 2 |** Radiance of polarization channels at different concentrations in the medium with small-sized particles (0.2 μm). **(A)** co-polarized and cross-polarized radiance, **(B)** right circular and left circular polarized radiance.

medium with large-sized particles, the backscattered intensity of all channels first decreased rapidly and the decrease amplitude of co-polarized and left circular polarized channels was much higher than that of cross-polarized and right circular polarized channels. With the gradual increase of detection distance and reaching the photon's transport MFP, the right circular component exceeded the left circular component, as shown in **Figure 7**. This was because the receiving plate was gradually away from

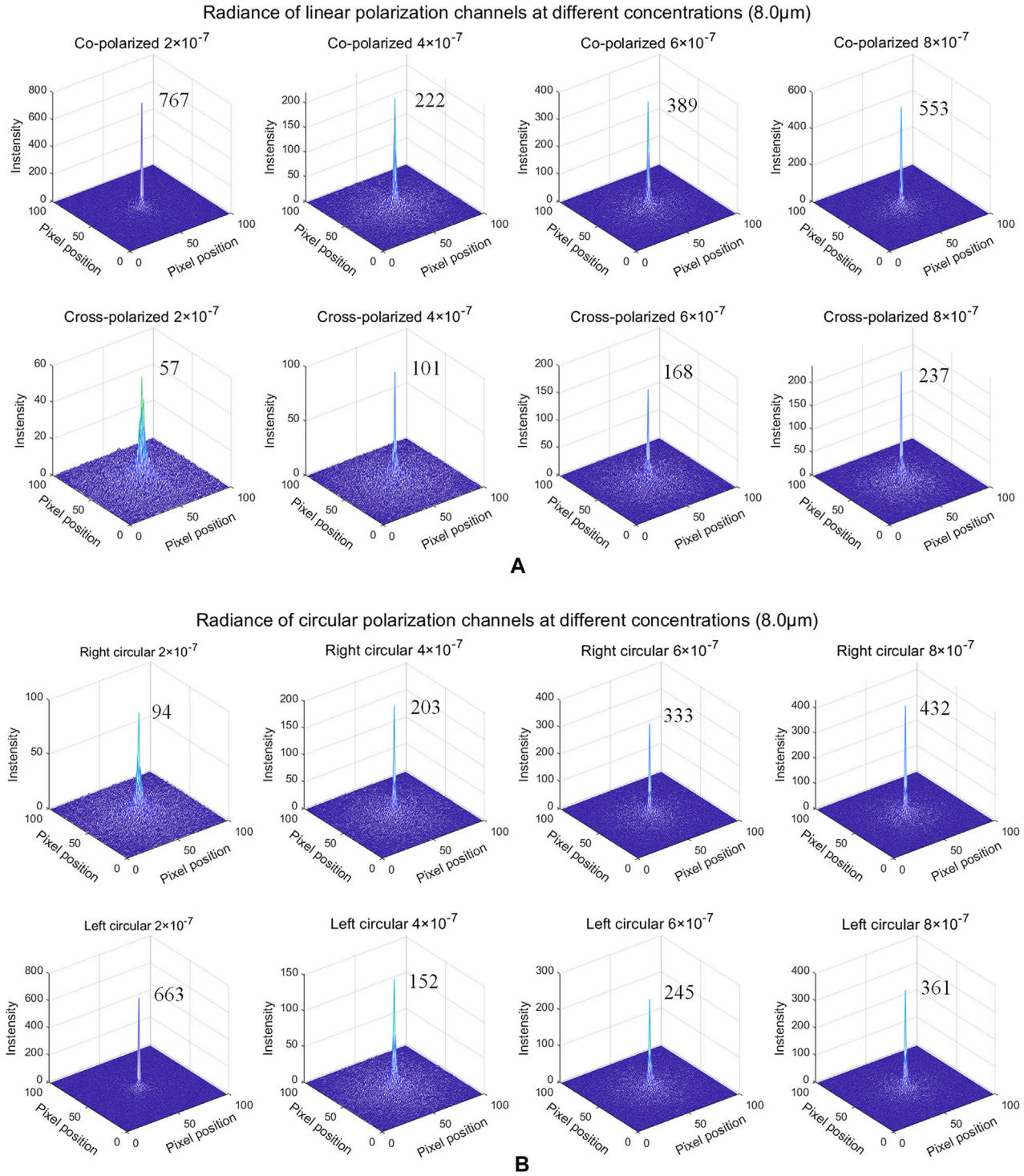


**FIGURE 3 |** Radiance of polarization channels at different concentrations in the medium with large-sized particles (8.0 μm). **(A)** co-polarized and cross-polarized radiance, **(B)** right circular and left circular polarized radiance.

the target, the number of received helicity reversal photons due to object surface reflection was greatly reduced. As the distance continued to increase, the intensity of all channels remained nearly stable and did not change significantly with the increase of distance.

## 3 POLARIZATION BASED VISIBILITY RESTORATION METHOD

In order to compare the performance of linear and circular polarization imaging on visibility recovery, we described the

**TABLE 2 |** Simulation parameters of medium with different wavelengths.

| Parameters | 0.2 μm | 8.0 μm |
|---|---|---|
| Illumination | Linear Polarized, Circular Polarized | Linear Polarized, Circular Polarized |
| Wavelength | 0.430, 0.480, 0.530, 0.580, 0.630 μm | 0.430, 0.480, 0.530, 0.580, 0.630 μm |
| Anisotropy $g$ | 0.2052 | 0.7646 |
| Density | $12 \times 10^{-4}$ particles/μm$^3$ | $6 \times 10^{-7}$ particles/μm$^3$ |
| Scattering coefficient $\mu_s$ | 0.3151, 0.2290, 0.1884, 0.1405, 0.1042 cm$^{-1}$ | 0.6290, 0.6277, 0.6785, 0.6737, 0.6177 cm$^{-1}$ |
| Absorption coefficient $\mu_a$ | 0.0100 cm$^{-1}$ | 0.0100 cm$^{-1}$ |
| Refractive index (Smoke particle) | 1.57 + 0.4277i | 1.57 + 0.4277i |
| Refractive index (Tissue) | 1.50 | 1.50 |
| Number of photons | 50,000 | 50,000 |

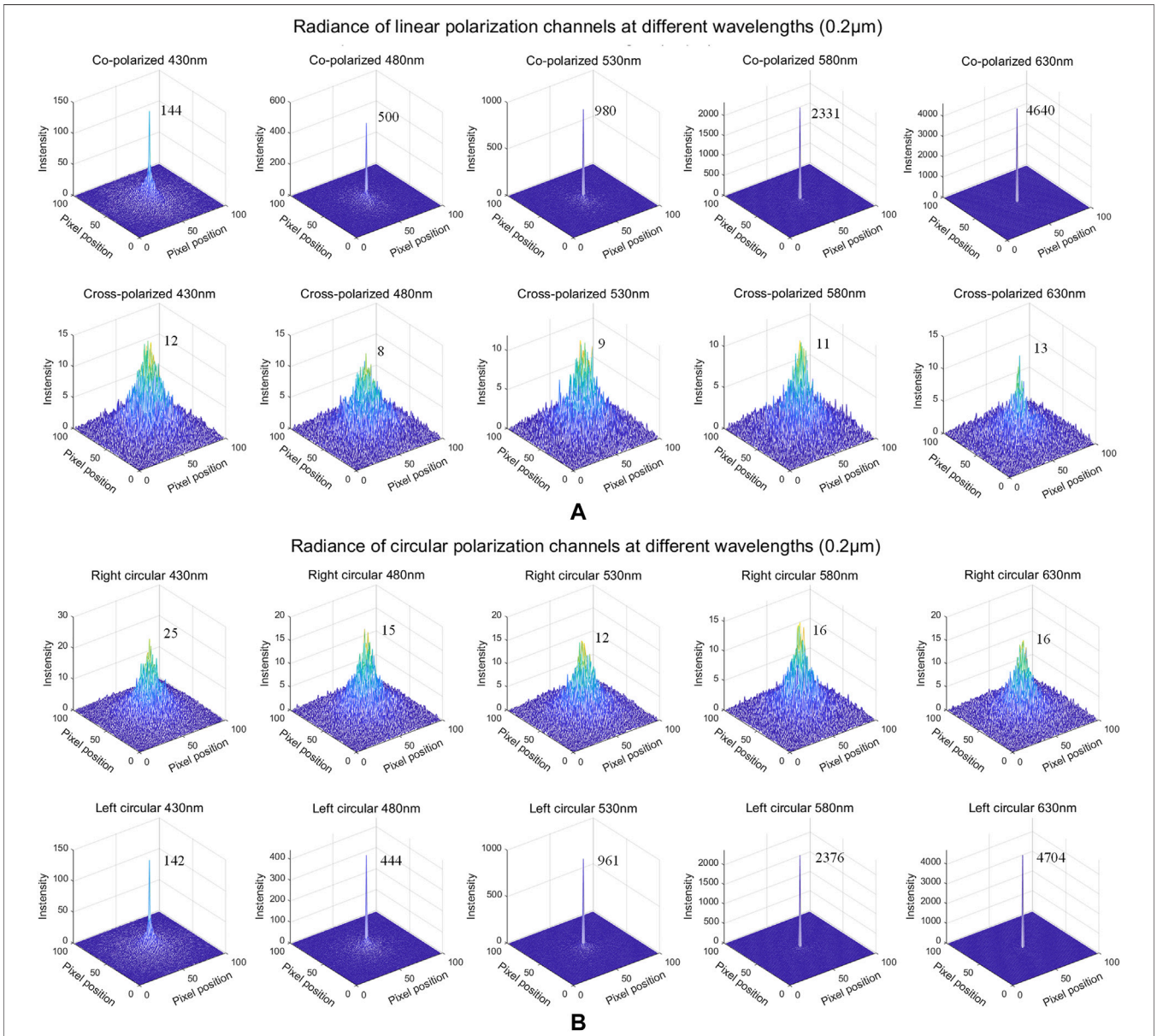


**FIGURE 4 |** Radiance of polarization channels at different wavelengths in the medium with small-sized particles (0.2 μm). **(A)** co-polarized and cross-polarized radiance, **(B)** right circular and left circular polarized radiance.

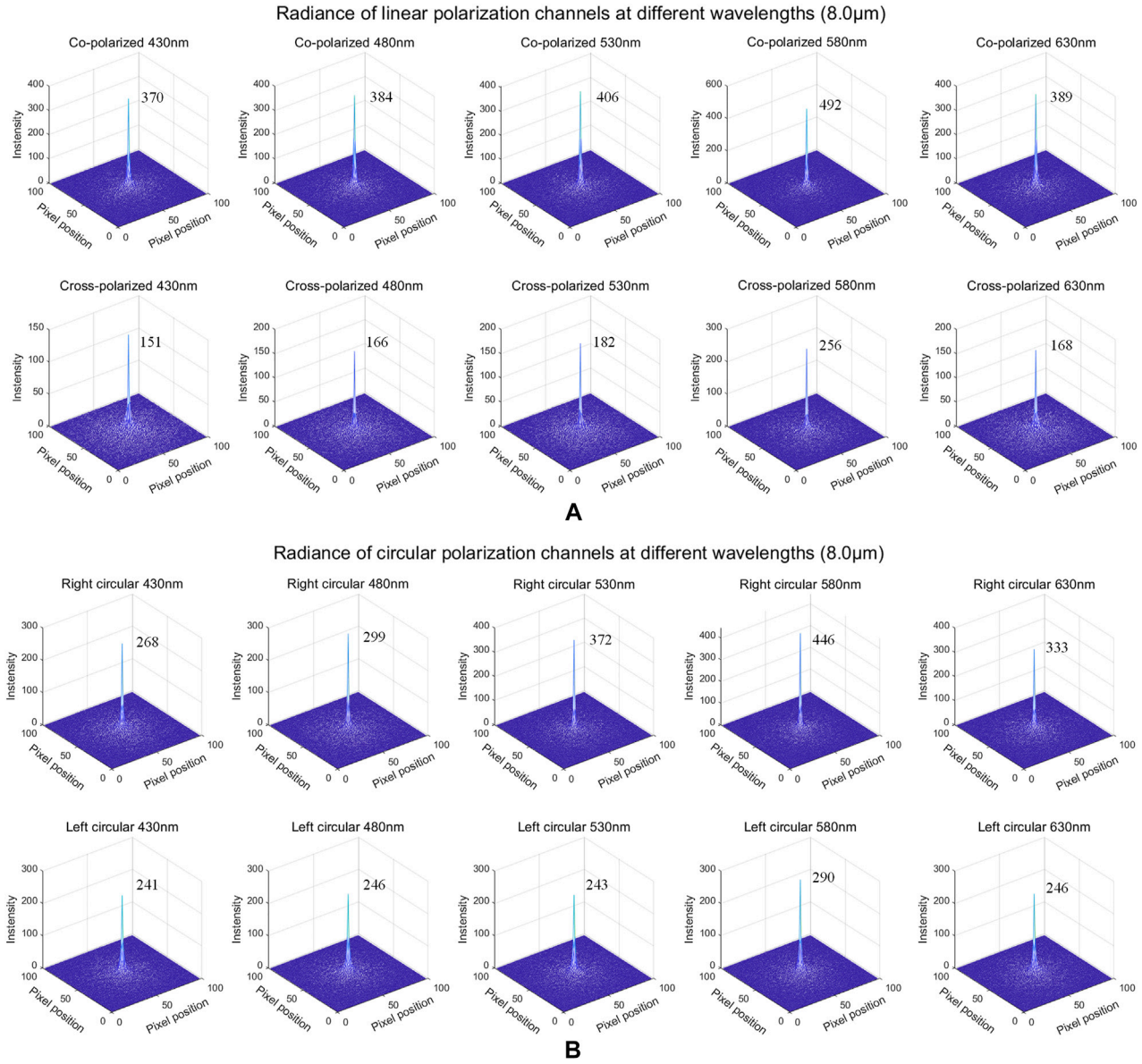


**FIGURE 5 |** Radiance of polarization channels at different wavelengths in the medium with large-sized particles (8.0 μm). **(A)** co-polarized and cross-polarized radiance, **(B)** right circular and left circular polarized radiance.

**TABLE 3 |** Simulation parameters of medium with different distances.

| **Parameters** | **0.2 μm** | **8.0 μm** |
|---|---|---|
| Illumination | Linear Polarized, Circular Polarized | Linear Polarized, Circular Polarized |
| Wavelength | 0.630 μm | 0.630 μm |
| Anisotropy $g$ | 0.2052 | 0.7646 |
| Density | $12 \times 10^{-4}$ particles/μm$^3$ | $6 \times 10^{-7}$ particles/μm$^3$ |
| Scattering coefficient $\mu_s$ | 0.1042 cm$^{-1}$ | 0.6177 cm$^{-1}$ |
| Absorption coefficient $\mu_a$ | 0.0100 cm$^{-1}$ | 0.0100 cm$^{-1}$ |
| Refractive index (Smoke particle) | 1.57 + 0.4277i | 1.57 + 0.4277i |
| Refractive index (Tissue) | 1.50 | 1.50 |
| Number of photons | 50,000 | 50,000 |
| Distance | 5 cm, 10 cm, 15 cm, 20 cm | 2.5 cm, 5 cm, 7.5 cm, 10 cm |

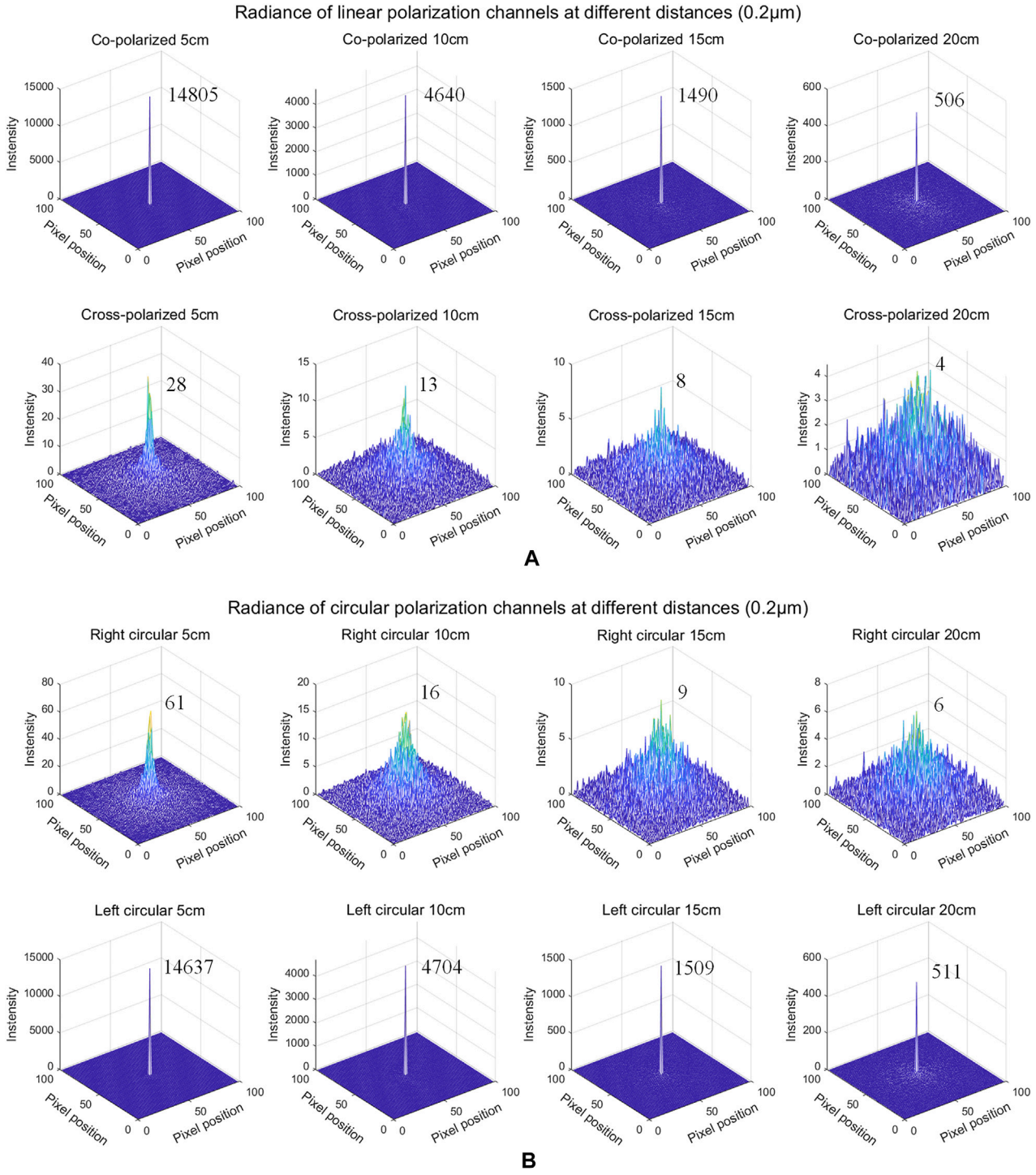


**FIGURE 6 |** Radiance of polarization channels at different distances in the medium with small-sized particles (0.2 μm) **(A)** co-polarized and cross-polarized radiance, **(B)** right circular and left circular polarized radiance at 5 cm, 10 cm, 15 cm, 20 cm, respectively.

polarization-based visibility restoration method. The polarization-based image degradation model for orthogonal polarization state was written as:

$$\begin{cases} I_{\parallel} = J_{\parallel}t + A_{\parallel}(\infty)(1-t) \\ I_{\perp} = J_{\perp}t + A_{\perp}(\infty)(1-t) \end{cases} \quad (1)$$

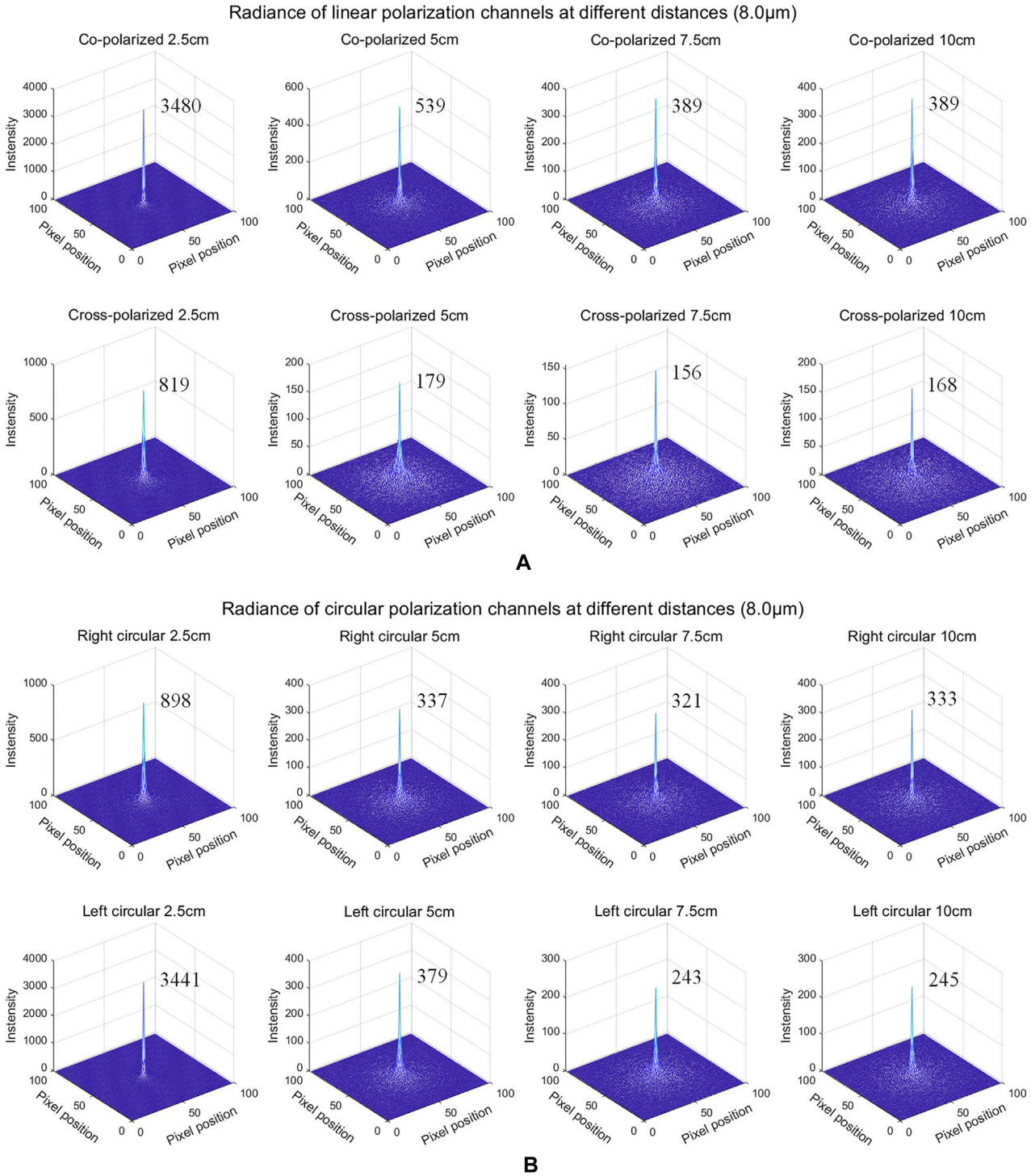


**FIGURE 7 |** Radiance of polarization channels at different distances in the medium with large-sized particles (8.0 μm) **(A)** co-polarized and cross-polarized radiance, **(B)** right circular and left circular polarized radiance at 2.5 cm, 5 cm, 7.5 cm, 10 cm, respectively.

where I and J represent the results of polarimetric imaging with and without a scattering medium, respectively, A is the intensity of environment light with infinite optical depth, meaning that the object radiance is completely obscured by the scattering medium, $t$ is the transmission parameter which describes the proportion of the sample's signal attenuated in the scattering medium, the subscript $\parallel$ and $\perp$ indicate that the polarization state of the variable is parallel or orthogonal to the incident polarization state.

The polarization difference calculation was implemented to estimate the parameters of the model. When the incident light penetrates the scattering medium and reaches the object layer, the polarization state of the photons will become randomized due to multiple scattering. We can assume that the polarization components $J_{\parallel}$ and $J_{\perp}$ after passing through the transparent medium and reflected by the target are nearly equal in intensity [18]. Therefore, the polarization component reflected from the object can be ignored and the polarization difference calculation could be written as:

$$\left|I_{\parallel} - I_{\perp}\right| = A_{\parallel}(\infty)(1 - t) \tag{2}$$

The reason for adding the absolute value calculation here is because for the circular polarization imaging, the helicity of the backscattered circular polarization state may be reversed. Then the transmission parameter of the degradation model could be estimated as:

$$t = 1 - \frac{\left|I_{\parallel} - I_{\perp}\right|}{A_{\parallel}(\infty)} \tag{3}$$

The parameter A can be estimated by the proposed algorithm in [29].

In summary, the visibility restoration result could be estimated as:

$$J = J_{\parallel} + J_{\perp} = \frac{I_{\parallel} + I_{\perp} - A_{\parallel}(\infty) - A_{\perp}(\infty)}{t} + A_{\parallel}(\infty) + A_{\perp}(\infty) \tag{4}$$

## 4 MEASUREMENT EXPERIMENTS

In order to validate the conclusion from simulation results, we carried out the polarimetric imaging experiment in the measurement scenario. We built a polarization imaging setup which can realize linear polarization and circular polarimetric imaging with nearly consistent conditions. A series of experimental data of different polarization channels were collected and the results were analyzed.

The experimental setup was shown in the **Figure 8**. The polarization state generator (PSG) was composed of an LED white illuminant GI-060411 (440–670 nm), a calibrated 45° linear polarizer and a calibrated quarter wave plate. The polarization state analyzer (PSA) was composed of a LUCID-TRI050S polarization camera and a quarter calibrated plate. Retaining or removing the quarter wave plate from the PSG can realize the switching between circular polarization and linear polarimetric imaging device. All the equipment was placed in a container with a black foam cover, and a fogger could generate smoke through heating the fog fluid and could inject into the container through a pipe. The SpyderCheckr was selected as the object, and two pairs of orthogonal backscattered polarization channels were collected. According to the parameters of the fogger and observation of the sedimentation velocities of particles [30], the smoke particle size was mainly in the range of 1–5 μm.

For circular polarization imaging, the axis direction of linear polarizer was at an angle of 45° with the fast axis or slow axis

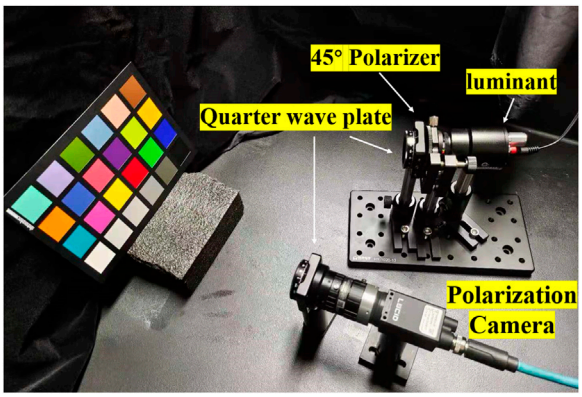


**FIGURE 8 |** The polarization setup.

direction of the quarter wave plate, which could generate right or left circular polarized incident light, respectively. The fast axis of the quarter wave plate of PSA was placed along the vertical direction, and the intensities of left and right circular polarization were presented on the 45° and 135° channels of polarization camera, respectively. For linear polarization imaging, in order to minimize the variation of experimental conditions, the quarter wave plate of PSA was retained while that of PSG was removed. At this time, the incident light was 45° linear polarized light, and the intensities of linear co-polarized and cross-polarized were presented on 135° and 45° channels, respectively.

## 5 RESULT AND DISCUSSION

In the measurement experiment, the horizontal linear and right circular polarized light were used as the illumination. We filled the smoke into the container until the object signal was completely obscured by the scattering medium. With the settlement of smoke particles, the smoke concentration gradually decreased. We continuously captured the backscattered images of orthogonal polarization channels at different concentrations. We selected the intensity of orthogonal linear and circular polarization channels at four different concentrations, as shown in **Figures 9**, **10** respectively.

By comparing **Figures 9A, F** and **Figures 10A, F**, in the smoke free scenario, as the linear polarized incident light was reflected by the object, the co-polarized component was still dominant in the backscattered intensity, while for the circular polarized illumination, the helicity of the reflected circular polarized light was reversed, the intensity of left circular component was higher than that of right circular component.

In order to quantitatively analyzed the impact of the increase of smoke concentration on the intensity of each channel, we selected eight color blocks from the SpyderCheckr and quantitatively study their intensity varies with the smoke concentration, as shown in **Figure 11**. For the linear polarimetric imaging, as the smoke concentration increased, the intensity of color blocks with high RGB value (Primary Yellow, Apple Green) gradually decreased, because the signal is gradually obscured by the

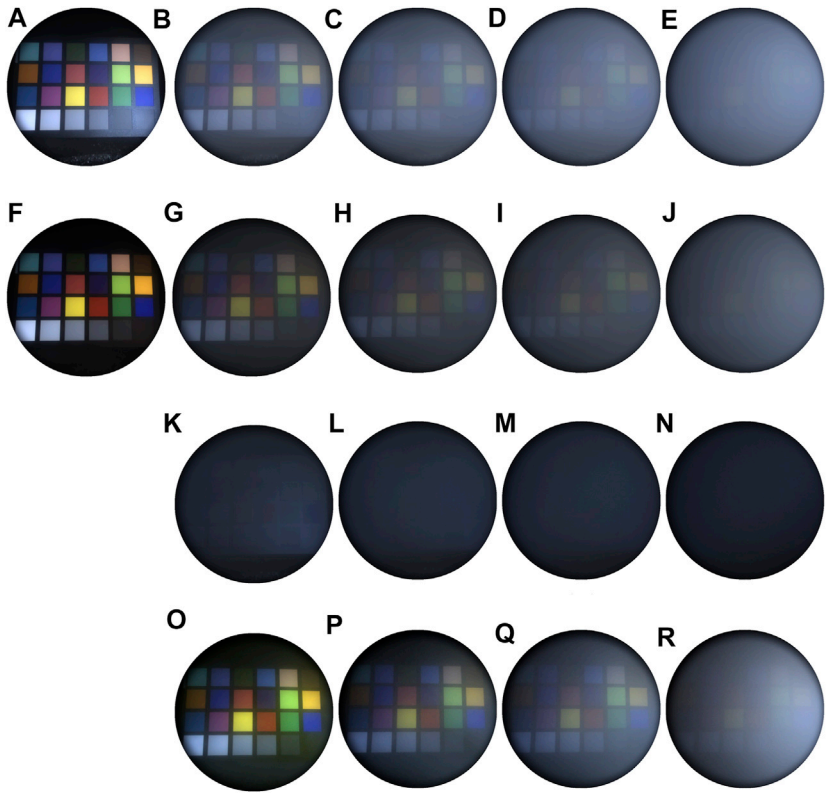


**FIGURE 9 |** The results of linear polarimetric imaging: the intensity of co-polarized **(A)** and cross-polarized **(F)** in smoke-free scenario, the intensity of co-polarized **(B–E)** and cross-polarized **(G–J)** channels at four different concentrations, the corresponding polarization difference results **(K–N)** and visibility restoration results **(O–R)**.

smoke, but the intensity of color blocks with low RGB value (Blueprint, Violet) gradually increased, because the smoke has a color of gray and it will lead to the increase of the intensity. A significant difference between orthogonal linear polarized channels could be observed, that was the co-polarized component was higher than that of cross-polarized component at all concentrations. However, for the circular polarimetric imaging, as the smoke concentration increased, the left circular component gradually decreased at all concentrations, because as the scattering coefficient increased, the photons were harder to reach the object, which then influence the intensity of left circular component generated by surface reflection. While for the right circular component, the trend was similar to that of linear polarized component, the photons relatively maintained their polarization state in a series of small angle scattering, and when the concentration reached a certain degree, the intensity exceeded the left circular component. The conclusions drawn by measurement experiments are consistent with those obtained from the simulations.

In addition, the visibility of the smoke images was restored based on the proposed method. The polarization difference results were shown in **Figure 9** and **Figures 10K–N**, and the visibility restoration results under different concentrations were shown in **Figure 9** and **Figures 10O–R**. Combining the qualitative and quantitative comparisons, it can be concluded that, under these concentration conditions, both the linear and circular polarimetric imaging had an ability to reduce the image degradation caused by smoke. For linear polarimetric imaging, the difference between co-polarized and cross-polarized component is maintained at different concentrations. However, as the smoke concentration increased, the left circular component gradually decreased while the right circular gradually increased, the polarization difference may be invalidated under certain medium scenarios and lead to failure of visibility restoration.

The main reasons for the differences between the simulations and the measurement experiments are as follows:

1) According to Malus' law, the linear polarizer is not ideal and can be partially passed by the light with other polarization state, therefore, in the smoke free scenario, the difference between co-polarized and cross-polarized channel, right circular and left circular was not obvious as the simulation results.
2) The experimental scenario was a particle polydisperse medium, in addition, a white luminant with wide

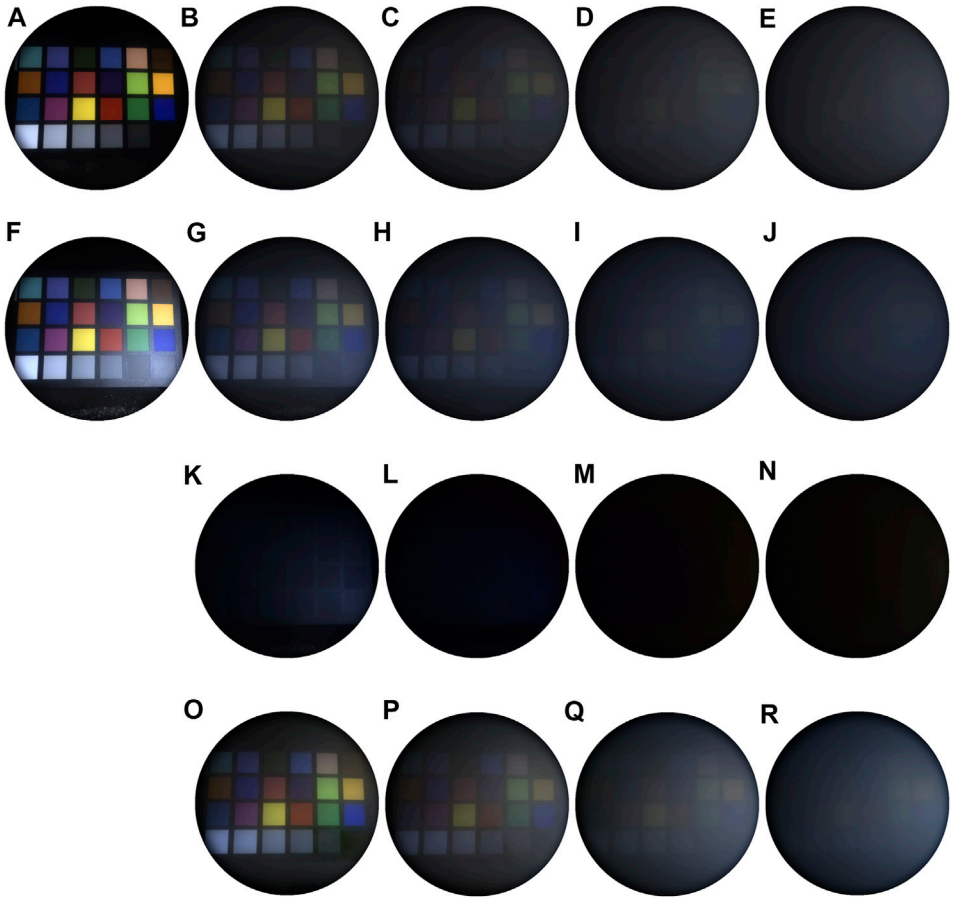


**FIGURE 10 |** The results of circular polarimetric imaging: the intensity of right circular polarized **(A)** and left circular polarized **(F)** in smoke-free scenario, the intensity of right circular polarized **(B–E)** and left circular polarized **(G–J)** channels at four different concentrations, the corresponding polarization difference results **(K–N)** and visibility restoration results **(O–R)**.

wavelength range was used in the measurement but usually a single wavelength for the simulation, which will lead to the difference between the simulation and measured results.

3) Since the removal of the quarter-wave plate led to the variation of the intensity of incident light, and the two imaging experiments were carried out successively, so it was not possible to ensure that the smoke concentration was at the same level. Therefore, we couldn't directly compare the intensity of linear and circular polarization channels at different concentrations as in simulation experiments, and we also couldn't directly compare the visibility restoration performance of linear and circular polarimetric imaging.

## 6 CONCLUSION

For polarimetric imaging in scattering medium, the selection of appropriate experimental conditions has an important impact on the polarimetric imaging. In order to study the propagation of linear and circular polarized light in the environment containing medium and object, based on the Monte Carlo simulation program, simulation experiments were carried out and the influence of factors such as concentration, wavelength and detection distance on the propagation of linear and circular polarized light were studied. In addition, the polarization setup was built to collect the intensity of linear and circular polarization channels under different medium concentrations. The variation of the intensity of color blocks with the concentration and the visibility restoration performance was studied and analyzed. The results show that in the scattering medium containing the object, factors such as concentration, wavelength and distance will change the number of scattering times of polarized light in the medium, thereby affecting the propagation of the polarized light. Generally, both the linear and circular polarimetric imaging had an ability to reduce the image degradation caused by smoke. For linear illumination, as the number of scattering increases, the backscattered intensity of the co-polarized component decreases, and the intensity of the cross-polarized component gradually increases, but the difference between orthogonal linear polarization channels is maintained

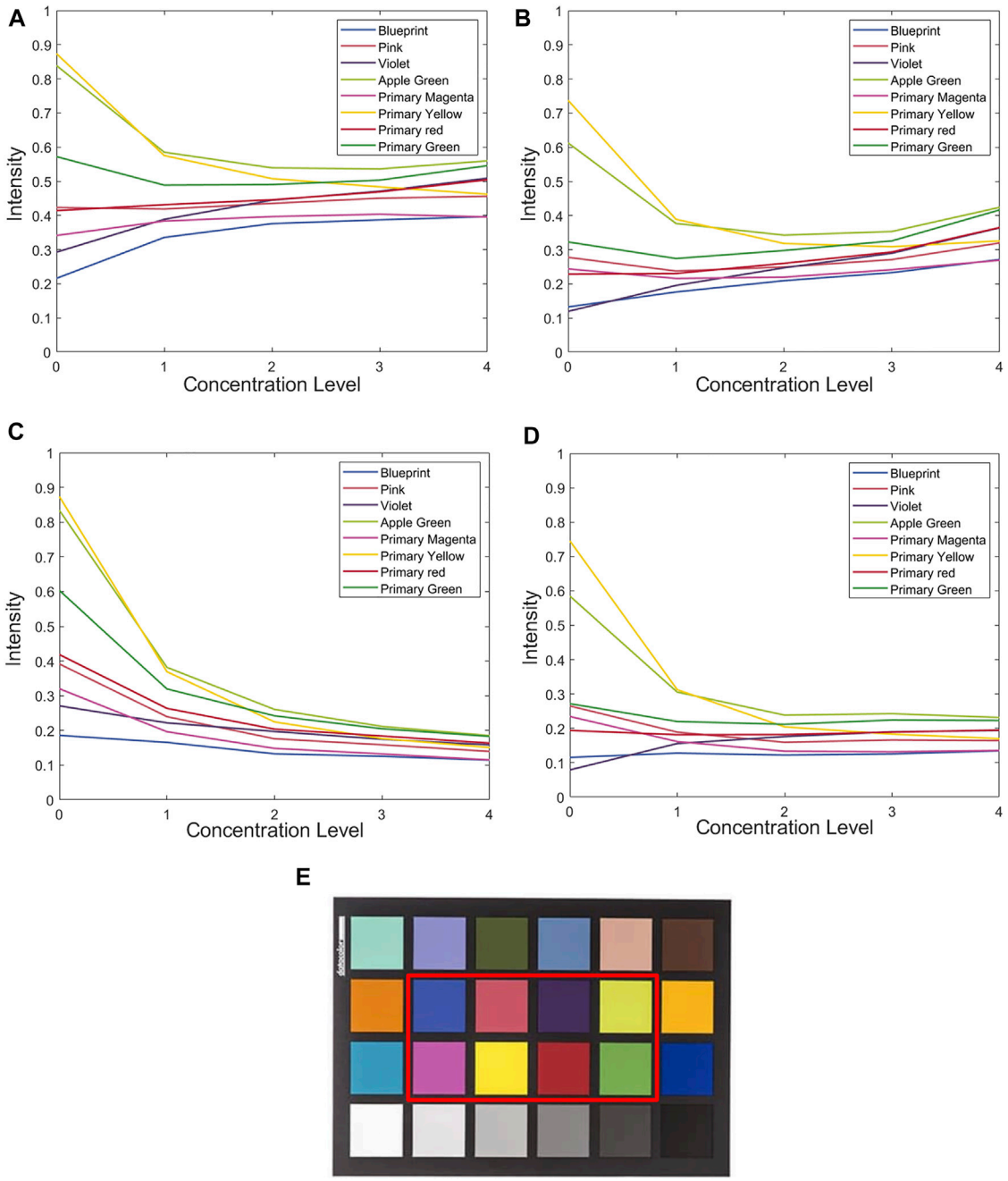


**FIGURE 11 |** The intensity of orthogonal polarization channels at with different concentrations **(A)** co-polarized channel, **(B)** cross-polarized channel, **(C)** left circular polarized channel, **(D)** right circular polarized channel, **(E)** the selected eight color blocks in SpyderCheckr. The ordinate indicates the normalized backscattered intensity. The abscissa indicates the concentration level of scattering medium, (level) 0 represents a smoke-free scenario, and (level) 1–4 represents a gradual increase of the smoke concentration.

but the difference will gradually decrease. For right circular illumination, in a medium with a small number of scattering times, the helicity of the reflected light from the object is reversed so that left circular polarized component will dominate the backscattered light. As the number of scattering times increases, the left circular component continues to decrease while that of the right circular polarization gradually increases. However, under some certain conditions, right circular component may approach or exceed the left circular component, which may limit the circular polarization-based difference imaging and visibility restoration performance.

## DATA AVAILABILITY STATEMENT

The original contributions presented in the study are included in the article/supplementary material, further inquiries can be directed to the corresponding author.

## AUTHOR CONTRIBUTIONS

DW was responsible for writing the manuscript and completing experiments. XW was responsible for assisting in relevant experiments and analyzing the results. PP was responsible for assisting in the simulation experiments. JG was responsible for the research content and theoretical guidance.

## ACKNOWLEDGMENTS

Support is acknowledged from China Scholarship Council (No. 201906690041), National Natural Science Foundation of China (61971177, 62171178).

## REFERENCES

1. Gnanatheepam E, Kanniyappan U, Dornadula K, Prakasarao A, Singaravelu G. Polarization Gating Technique Extracts Depth Resolved Fluorescence Redox Ratio in Oral Cancer Diagnostics. *Photodiagnosis Photodyn Ther* (2020) 30: 101757. doi:10.1016/j.pdpdt.2020.101757
2. Schechner YY, Narasimhan SG, Nayar SK. Polarization-Based Vision Through Haze. *Appl Opt* (2003) 42(3):511–25. doi:10.1364/AO.42.000511
3. Treibitz T, Schechner YY. Active Polarization Descattering. *IEEE Trans Pattern Anal Mach Intell* (2009) 31(3):385–99. doi:10.1109/TPAMI.2008.85
4. Schechner YY, Karpel N. Recovery of Underwater Visibility and Structure by Polarization Analysis. *IEEE J Oceanic Eng* (2005) 30(3):570–87. doi:10.1109/JOE.2005.850871
5. Qi J, Elson DS. Mueller Polarimetric Imaging for Surgical and Diagnostic Applications: a Review. *J Biophotonics* (2017) 10(8):950–82. doi:10.1002/jbio.201600152
6. Qi J, Elson DS. A High Definition Mueller Polarimetric Endoscope for Tissue Characterisation. *Sci Rep* (2016) 6(1):1–11. doi:10.1038/srep25953
7. Sridhar S, Da Silva A. Enhanced Contrast and Depth Resolution in Polarization Imaging Using Elliptically Polarized Light. *J Biomed Opt* (2016) 21(7):071107. doi:10.1117/1.JBO.21.7.071107
8. Lizana A, Van Eeckhout A, Adamczyk K, Rodríguez C, Escalera JC, Garcia-Caurel E, et al. Polarization Gating Based on Mueller Matrices. *J Biomed Opt* (2017) 22(5):1. doi:10.1117/1.JBO.22.5.056004
9. Ni X, Alfano RR. Time-resolved Backscattering of Circularly and Linearly Polarized Light in a Turbid Medium. *Opt Lett* (2004) 29(23):2773–5. doi:10.1364/OL.29.002773
10. Kartazayeva SA, Ni X, Alfano RR. Backscattering Target Detection in a Turbid Medium by Use of Circularly and Linearly Polarized Light. *Opt Lett* (2005) 30(10):1168–70. doi:10.1364/OL.30.001168
11. Nothdurft R, Yao G. Applying the Polarization Memory Effect in Polarization-Gated Subsurface Imaging. *Opt Express* (2006) 14(11):4656–61. doi:10.1364/OE.14.004656
12. Kuzmin V, Meglinski I. Helicity Flip of the Backscattered Circular Polarized Light. In: *Biomedical Applications of Light Scattering IV*. San Francisco, CA: International Society for Optics and Photonics (2010). p. 75730Z. doi:10.1117/12.841193
13. Kim AD, Moscoso M. Backscattering of Circularly Polarized Pulses. *Opt Lett* (2002) 27(18):1589–91. doi:10.1364/OL.27.001589
14. Ramella-Roman JC, Prahl SA, Jacques SL. Three Monte Carlo Programs of Polarized Light Transport into Scattering media: Part I. *Opt Express* (2005) 13(12):4420–38. doi:10.1364/OPEX.13.004420
15. Ramella-Roman JC, Prahl SA, Jacques SL. Three Monte Carlo Programs of Polarized Light Transport into Scattering media: Part II. *Opt Express* (2005) 13(25):10392–405. doi:10.1364/OPEX.13.010392
16. van der Laan JD, Wright JB, Scrymgeour DA, Kemme SA, Dereniak EL. Evolution of Circular and Linear Polarization in Scattering Environments. *Opt Express* (2015) 23(25):31874–88. doi:10.1364/OE.23.031874
17. Doronin A, Macdonald C, Meglinski I. Propagation of Coherent Polarized Light in Turbid Highly Scattering Medium. *J Biomed Opt* (2014) 19(2):025005. doi:10.1117/1.JBO.19.2.025005
18. Shukla P, Sumathi R, Gupta S, Pradhan A. Influence of Size Parameter and Refractive index of the Scatterer on Polarization-Gated Optical Imaging Through Turbid media. *J Opt Soc Am A* (2007) 24(6):1704–13. doi:10.1364/JOSAA.24.001704
19. Walter B, Marschner SR, Li H, Torrance KE. Microfacet Models for Refraction through Rough Surfaces. In: EGSR'07: Proceedings of the 18th Eurographics Conference on Rendering Techniques, Grenoble, France, June 25–27, 2007 (2007).
20. Heitz E. Understanding the Masking-Shadowing Function in Microfacet-Based BRDFs. *J Comput Graph Tech* (2014) 3(2):32–91.
21. Germer TA. Angular Dependence and Polarization of Out-of-Plane Optical Scattering from Particulate Contamination, Subsurface Defects, and Surface Microroughness. *Appl Opt* (1997) 36(33):8798–805. doi:10.1364/AO.36.008798
22. Germer TA. *SCATMECH: Polarized Light Scattering C++ Class Library*. (2021). Available from: https://www.nist.gov/publications/scatmech-polarized-light-scattering-c-class-library?pub_id=841413 (Accessed November 10, 2021).
23. OMLC. *Definition and Units of Scattering Coefficient*. (2021). Available from: https://omlc.org/classroom/ece532/class3/musdefinition.html (Accessed December 1, 2021).
24. Novikova T, Bénière A, Goudail F, De Martino A. Sources of Possible Artefacts in the Contrast Evaluation for the Backscattering Polarimetric Images of Different Targets in Turbid Medium. *Opt Express* (2009) 17(26):23851–60. doi:10.1364/OE.17.023851
25. Li S, Cheng X, Mei P, Lu S, Yang H, Zhang H. Multiple Scattering of Light Transmission in a Smoke Layer. *Optik* (2014) 125(9):2185–90. doi:10.1016/j.ijleo.2013.10.040
26. Wikipedia. *List of Refractive Indices*. (2021). Available from: https://en.m.wikipedia.org/wiki/List_of_refractive_indices (Accessed November 10, 2021).
27. Dieselnet. *Smoke Density*. (2021). Available from: https://dieselnet.com/calculator/smoke1.html (Accessed September 15, 2021).
28. Biophotonics. *Cloud Based Monte Carlo Tool for Photon Transport*. (2021). Available from: http://www.biophotonics.fi/ (Accessed November 8, 2021).
29. Berman D, Treibitz T, Avidan S. Air-light Estimation Using Haze-Lines. In: 2017 IEEE International Conference on Computational Photography (ICCP), Cluj-Napoca, Romania, June 29–July 1, 2017 (2017). p. 1–9. doi:10.1109/ICCPHOT.2017.7951489
30. Smokemachines. *Particle Size & Settling Velocities*. (2021). Available from: http://www.smokemachines.com/settling-velocities-particle-size.aspx (Accessed November 12, 2021).

**Conflict of Interest:** The authors declare that the research was conducted in the absence of any commercial or financial relationships that could be construed as a potential conflict of interest.

The handling editor declared a past collaboration with one of the authors DW.

**Publisher's Note:** All claims expressed in this article are solely those of the authors and do not necessarily represent those of their affiliated organizations, or those of the publisher, the editors and the reviewers. Any product that may be evaluated in this article, or claim that may be made by its manufacturer, is not guaranteed or endorsed by the publisher.

frontiers in Physics

ORIGINAL RESEARCH
published: 12 January 2022
doi: 10.3389/fphy.2021.820552

# Error Analysis for Repeatability Enhancement of a Dual-Rotation Mueller Matrix Ellipsometer

*Zhou Jiang*[1], *Song Zhang*[1], *Jiaming Liu*[1], *Qi Li*[2]*, *Hao Jiang*[1]* and *Shiyuan Liu*[1]

[1]State Key Laboratory of Digital Manufacturing Equipment and Technology, Huazhong University of Science and Technology, Wuhan, China, [2]National Institute of Metrology, Beijing, China

Since the Mueller matrix ellipsometer has been used as a highly accurate tool for thin film measurement, the error analysis and repeatability enhancement of such a tool are of great importance. The existence of the Poisson–Gaussian mixed noise and the random bias of the trigger signal in the optical measurement system may reduce the repeatability and accuracy of a measurement. Utilizing the probabilistic analysis, the random errors in the Mueller matrix measurements are quantified. A quantitative analysis on the instrument matrix has been carried out to assess the individual effects for different error sources. We proposed a general optimal instrument matrix which is capable of minimizing the estimation variance for both Gaussian additive noise and Poisson shot noise. Besides, a peak-matching algorithm is proposed to compress the repeatability errors due to the bias of the trigger signal and the limited sampling frequency. The effectiveness of the proposed methods is shown using both virtual simulations and experiments carried out on our self-developed instrument, which potentially paves a way to reduce the requirements on motor performance, acquisition card resolution, and trigger accuracy, which are critical to cost reduction.

**Keywords: Mueller matrix ellipsometer, thin film measurement, noise, error, repeatability**

OPEN ACCESS

***Edited by:***
*Xiaoyong Hu,*
*Peking University, China*

***Reviewed by:***
*Chao He,*
*University of Oxford, United Kingdom*
*Honghui He,*
*Tsinghua University, China*
*Tingkui Mu,*
*Xi'an Jiaotong University, China*
*Sofyan Taya,*
*Islamic University of Gaza, Palestine*
*Changcai Cui,*
*Huaqiao University, China*

***Correspondence:**
*Qi Li*
*liqi@nim.ac.cn*
*Hao Jiang*
*hjiang@hust.edu.cn*

***Specialty section:***
*This article was submitted to Optics and Photonics, a section of the journal Frontiers in Physics*

***Received:*** *23 November 2021*
***Accepted:*** *16 December 2021*
***Published:*** *12 January 2022*

***Citation:***
*Jiang Z, Zhang S, Liu J, Li Q, Jiang H and Liu S (2022) Error Analysis for Repeatability Enhancement of a Dual-Rotation Mueller Matrix Ellipsometer. Front. Phys. 9:820552. doi: 10.3389/fphy.2021.820552*

## 1 INTRODUCTION

Benefiting from the characteristics such as high-precision, fast, non-contact, easy-to-integrate, ellipsometer has been used as a practical standard tool in the semiconductor industry [1, 2], for optical properties measurements of thin films [3–5] and the thickness measurement of ultrathin oxide films [6]. Besides, there exists an increasing trend in the modern ellipsometry to deal with increasingly complex media such as biomedical specimens [7]. To achieve ultrahigh accuracy in a measurement, various systematic errors as well as random errors [8–12] have to be seriously considered.

Although an ellipsometer can provide ultrahigh measurement precision, it is always disturbed by detector noise (such as signal-independent Gaussian additive noise and signal-dependent Poisson shot noise) [13–16] and the bias of the trigger signal, which induce the random fluctuations and offsets of the intensity signals. In ellipsometric experiments, the major sources of the random errors are the inevitable thermally generated noise in light sources, detectors, and electronic circuits [17]. Usually, random noise can be reduced by signal averaging and can be measured by performing multiple identical runs and by calculating the mean and standard deviation [18].

Reducing the estimation variance is a feasible way to improve the measurement precision [14, 16, 19–23]. Up to now, many researchers have explored reducing the estimation variance of Mueller

matrix elements as well as the ellipsometric parameters to improve the repeatability accuracy [13–16, 19–29], among which optimizing the instrument matrices is an effective way [15, 20, 22, 26]. The objective of these optimization methods may focus on minimizing the total variance of all the 16 Mueller matrix elements as well as the elements in the diagonal boxes for most of the applications such as the isotropic film thickness metrology. Since the elements on the off-diagonal blocks of such samples are zeros, the measurement precision only depends on the eight elements related to the ellipsometric parameters. Therefore, the optimal instrument matrix for all the 16 Mueller matrix elements could no longer be the best option for the accuracy enhancement [15].

In the instrumentation of the ellipsometer, trigger signals are usually used to start intensity acquisition. In addition to the random error sources mentioned previously that from the detector, there is another random error source that arises from the random bias of the trigger signals, which exhibits as the random offset of the initial azimuth of the wave plates. Such a random error due to the hardware constraints is mainly caused by unstable trigger signals and the resolution limitation of the acquisition board. Averaging the multiple measurements is a commonly used and effective method to reduce the timing repeatability error and various random errors in the existing ellipsometer data processing [30]. However, such method may distort the voltage data within the cycle when a random offset of the intensity signal exists and then degrades the accuracy of the measurement. Therefore, it is necessary to eliminate the random offset of the acquired signal.

In this article, first, we measured the Gaussian additive noise, the Poisson shot noise, and the signal drift caused by the random bias of the trigger signal, and then the three kinds of random errors are quantified using probabilistic analysis where the associated error model can be used for the simulation experiment. Second, a generalized random error propagation model is proposed to describe the transitive relation between the system parameters and the Mueller matrix elements, when the Gaussian additive noise, the Poisson shot noise, and the bias of the trigger signal exist in the instrument system. Then, the system matrices of the instrument are evaluated which make the estimation variance of the Mueller matrix elements minimum. At the same time, the random error caused by the bias of the trigger signal in the ellipsometer has rarely been studied seriously. So, an offset elimination method based on the peak-matching algorithm is proposed, with which the offset can be reduced by 4 times. Then, the random error model is fed into the proposed general error propagation model for verification. The results show that the estimated variance can be effectively reduced by the proposed method. Last, we use practical experiments to show the effectiveness of the proposed methods. The results show that the variance of the measured thickness of the standard silica is significantly reduced with the proposed methods applied.

Such a significant enhancement indicates that the requirements on motor performance, acquisition card resolution, and trigger accuracy can be reduced with the help of the proposed method, which may be highly valuable for the cost reduction of instrumentation.

## 2 INSTRUMENT AND PRINCIPLE

**Figure 1** illustrates a system layout of a single wavelength ellipsometer (SWE), which consists of three parts: a CW He–Ne laser (HRS015B 100-240VAC, Thorlabs, United States), a polarization state generator (PSG), and a polarization state analyzer (PSA). The light source is installed on an adjustment frame to precisely control the laser light path. The laser light transmits through an optical isolator (IO-2D-633-VLP, Thorlabs, United States) which prevents the interference of reflected light and is divided into two beams with an intensity ratio of 1:9 by a beam splitter (BS025, Thorlabs, United States). One of the beams enters a detector 1 (PDA36A2, Thorlabs, United States) directly for the elimination of the intensity fluctuations of the light source and the other enters the main optical path. After passing through a bandpass filter (FLH633-5, Thorlabs, United States) and being reflected on a mirror (64-013, Edmund, United States), the light incidents on a sample through the PSG at an angle of 65°. Then, the reflected light from the sample was modulated by the PSA and collected by the detector 2 (PDA36A2, Thorlabs, United States).

With the aforementioned configuration, the instrument can acquire the full Mueller matrix of the sample. The light path is controlled by six diaphragms with an adjustable aperture size. In order to fulfill the requirements of high-precision real-time measurement, a high-precision data acquisition card (USB6281, NI, United States) is required. In addition, our self-developed SWE is equipped with a micro-spot component for the measurement in specific situations.

It should be emphasized that in order to improve the measurement accuracy and stability of the instrument as much as possible, the azimuth angle of each optical component in the instrument and the gain coefficients of the photodetector can be optimized.

**Figure 2** shows the SWE that we built it in the laboratory. Since we have adopted sophisticated mechanical design and manufacturing, the self-built SWE has high accuracy. Due to the unique optical path design, a series of factors such as light source fluctuation error, ambient light interference, incident angle tilt error, and improper installation error of the polarizer and wave plate, can be eliminated. In order to minimize the beam-wandering effect, we adopt the specific mechanical design. The pitching of the laser can be adjusted accurately by the adjusting device I. A dual-aperture III and dual-reflecting-mirror II design is introduced to ensure the accurate alignment of the laser in PSG. By adjusting the attitude of the reflecting mirrors to guide the laser pass through the small apertures, the accuracy of the alignment can be evaluated by observing the shape of the laser spot. In the PSA part, another pair of apertures V and a dual-axis moving stage IV are used. A camera is used to analyze the spot shape when the stage is moving. When the optical path is perfectly aligned, the small round spot will be achieved. In this way, the beam-wandering effect could be significantly compressed.

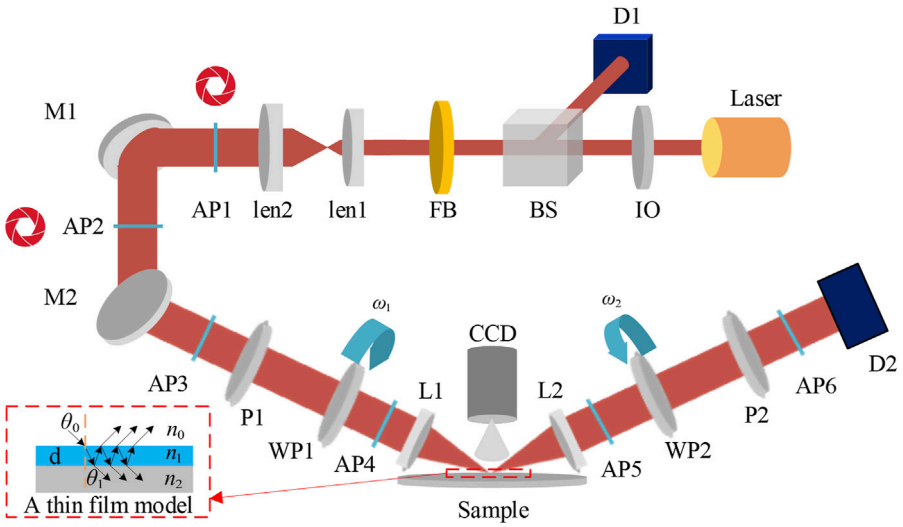


**FIGURE 1 |** Critical components and beam path of the SWE. The ellipsometer is composed of a He–Ne laser light source (He–Ne laser), an optical isolator (IO), a beam splitter (BS), two detectors (D1 and D2), a narrowband filter (FB), a beam expander (BE)(GBE-03A, Thorlabs, United States), six apertures (AP1-AP6)(SM1D12CZ, Thorlabs, United States), two mirrors (M1 and M2), two polarizers (P1 and P2)(LPVISC100-MP2, Thorlabs, United States), two continuously rotating wave plates (WP1 and WP2)(WPQ10M-633, Thorlabs, United States), two focus lenses (L1 and L2), and a CCD camera (Mer-503-20 GM-P, DAHENG, China). Incident and reflected beams are denoted in red.

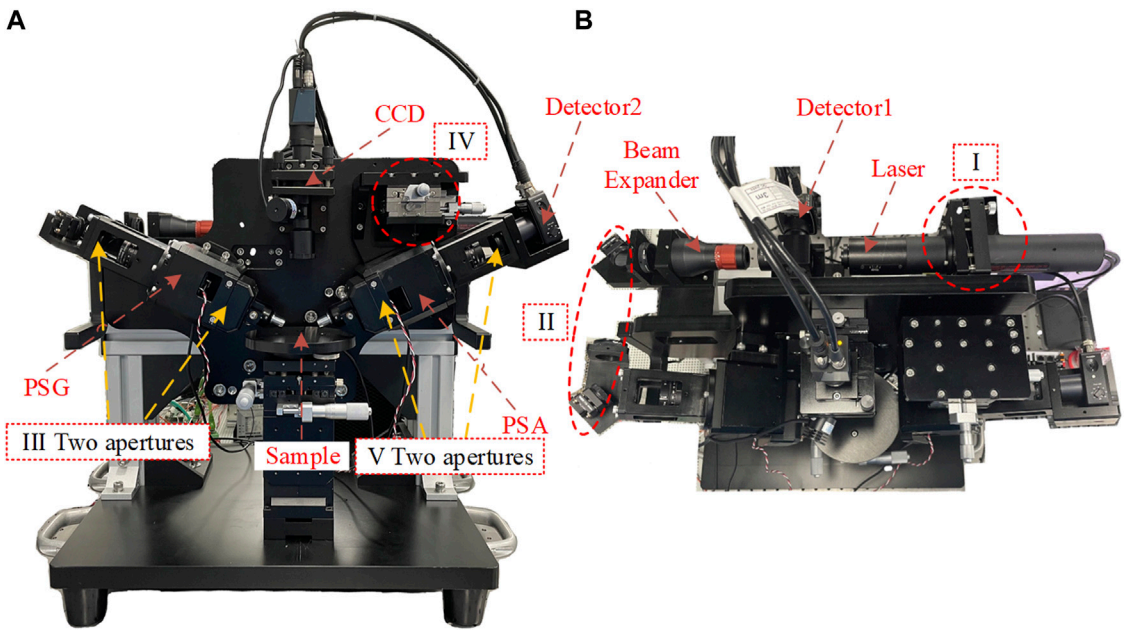


**FIGURE 2 |** Instrumentation of SWE **(A)** front view and **(B)** top view.

When a thin film is measured, the light intensity matrix $\boldsymbol{I}_{\mathrm{dec}}$ received by the photodetector can be expressed by multiplying the matrix $\boldsymbol{G}$ of the PSG, the Mueller matrix $\boldsymbol{M}_{\mathrm{S}}$ of the sample, and the matrix $\boldsymbol{A}$ of the PSA.

$$\boldsymbol{I}_{\mathrm{dec}} = \boldsymbol{A} \cdot \boldsymbol{M}_{\mathrm{S}} \cdot \boldsymbol{G}, \tag{1}$$

The Stokes vector of the incident beam after passing through the PSG and the reflective beam after passing through the PSA are described as **Eqs 2** and **3**, respectively [31].

$$\boldsymbol{S}_{\mathrm{PSG}}^{k} = \left\{\boldsymbol{R}\left[-C_1^k\right] \cdot \boldsymbol{M}_{\mathrm{C1}}(\delta_1) \cdot \boldsymbol{R}\left[-C_1^k\right]\right\} \cdot \{\boldsymbol{R}[-P] \cdot \boldsymbol{M}_{\mathrm{P}} \cdot \boldsymbol{R}[P]\} \cdot \boldsymbol{S}_{\mathrm{in}}, \tag{2}$$

$$\boldsymbol{H}_{\mathrm{PSA}}^{k} = \{\boldsymbol{R}[-A]\cdot\boldsymbol{M}_{\mathrm{A}}\cdot\boldsymbol{R}[A]\}\cdot\left\{\boldsymbol{R}\left[-C_2^k\right]\cdot\boldsymbol{M}_{\mathrm{C2}}(\delta_2)\cdot\boldsymbol{R}\left[-C_2^k\right]\right\}, \tag{3}$$

where the $\theta$ ($\theta = P, A$) is the azimuth angle of the corresponding component in the PSG and PSA, and $\delta_y$ (y = 1, 2) is the retardation due to the weak linear birefringence of the polarizer material. The first and second compensators are driven by two servo hollow motors (AgilityRH, Applimotion, United States), and their fast axis azimuths are changing according to the relations: ${C_1}^k = \omega_1 t_k + C_{\mathrm{S1}}$ and ${C_2}^k = \omega_2 t_k + C_{\mathrm{S2}}$, where $C_{\mathrm{S1}}$ and $C_{\mathrm{S2}}$ are the initial azimuths of the compensators.

In a single measurement cycle, the matrix $\boldsymbol{G}$ and $\boldsymbol{A}$ consisted of the Stokes vector ${\boldsymbol{S}_{\mathrm{PSG}}}^k$ and ${\boldsymbol{H}_{\mathrm{PSA}}}^k$ that outputs polarized light from the PSG and PSA can be expressed as:

$$\boldsymbol{G} = \left[\boldsymbol{S}_{\mathrm{PSG}}^1\ \boldsymbol{S}_{\mathrm{PSG}}^2\ \boldsymbol{S}_{\mathrm{PSG}}^3\cdots\boldsymbol{S}_{\mathrm{PSG}}^K\right], \tag{4}$$

$$\boldsymbol{A} = \left[\boldsymbol{H}_{\mathrm{PSA}}^1\ \boldsymbol{H}_{\mathrm{PSA}}^2\ \boldsymbol{H}_{\mathrm{PSA}}^3\cdots\boldsymbol{H}_{\mathrm{PSA}}^K\right], \tag{5}$$

We use nonlinear regression intensity fitting algorithm (the Levenberg–Marquardt algorithm) to quickly and accurately extract the sample's Mueller matrix and optical parameters from the measured periodic signal. To achieve high performance of the instrument, the system needs to be carefully calibrated [32]. The instrument was calibrated by carrying out the measurements on the standard silica film samples. Since the theoretical Mueller matrices of the sample could be calculated from the refractive indices ($n$, $k$), thicknesses $d$, and incidence angles $\theta$ of the measurements, the instrument can provide the measured Mueller matrices. Utilizing the intensity fitting method [33], the parameters of the system $\boldsymbol{p} = (d, \theta, P, A, \delta_1, \delta_2, C_1, C_2)$ could be accurately determined. Since in the present work we mainly focus on the issues induced by Gaussian additive noise, Poisson shot noise, and the bias of the trigger signal, the details of the calibration could refer to [34]. Besides, we have developed a broadband MME and proposed a series of general methods on system calibration [34], wave plate alignment, and calibration [35–39] as well as depolarization correction [40] to ensure the performance of the developed instrument. The system parameter $\boldsymbol{p}$ can be obtained from the following equation:

$$\boldsymbol{p} = \underset{\boldsymbol{p}\in\boldsymbol{\Omega}_{\mathrm{p}}}{\operatorname{argmin}}\left[\boldsymbol{I}^{\mathrm{meas}} - \boldsymbol{I}^{\mathrm{calc}}(\boldsymbol{p})\right]^{\mathrm{T}}\boldsymbol{\Gamma}_{\boldsymbol{I}^{\mathrm{meas}}}^{+}\left[\boldsymbol{I}^{\mathrm{meas}} - \boldsymbol{I}^{\mathrm{calc}}(\boldsymbol{p})\right], \tag{6}$$

where $\boldsymbol{I}^{\mathrm{meas}}$ is the actual measurement intensity matrix, and $\boldsymbol{I}^{\mathrm{calc}}$ is the theoretical intensity matrix. $\boldsymbol{\Omega_p}$ indicates the value range of the system parameter. Then, the system parameter $\boldsymbol{M}_{\mathrm{S}}$ can be obtained from the following equation:

$$\boldsymbol{M}_{\mathrm{S}} = \underset{\boldsymbol{M}_{\mathrm{S}}\in\boldsymbol{\Omega}_{\mathrm{M}}}{\operatorname{argmin}}\left[\boldsymbol{I}^{\mathrm{meas}} - \boldsymbol{I}^{\mathrm{calc}}(\boldsymbol{p}, \boldsymbol{M}_{\mathrm{S}})\right]^{\mathrm{T}}\boldsymbol{\Gamma}_{\boldsymbol{I}^{\mathrm{meas}}}^{+}\left[\boldsymbol{I}^{\mathrm{meas}} - \boldsymbol{I}^{\mathrm{calc}}(\boldsymbol{p}, \boldsymbol{M}_{\mathrm{S}})\right], \tag{7}$$

where $\boldsymbol{\Omega}_{\mathrm{M}}$ indicates the value range of the system Mueller matrix, $\Gamma + \boldsymbol{I}^{meas}$ is the Moore–Penrose pseudo-inverse of the covariance matrix of the measured intensity matrix, and $\Gamma + \boldsymbol{I}^{meas} = (\Gamma + \boldsymbol{I}^{meas} \cdot \Gamma\, \boldsymbol{I}^{meas})^{-1} \cdot \Gamma\, T\, \boldsymbol{I}^{meas}$. Then, the thickness $d$ can be obtained from the following equation:

$$\boldsymbol{d} = \underset{d\in\boldsymbol{\Omega}_d}{\operatorname{argmin}}\left[\boldsymbol{M}^{\mathrm{meas}} - \boldsymbol{M}^{\mathrm{calc}}(\boldsymbol{a}^*, d)\right]^{\mathrm{T}}\boldsymbol{\Gamma}_{\boldsymbol{M}^{\mathrm{meas}}}^{+}\left[\boldsymbol{M}^{\mathrm{meas}} - \boldsymbol{M}^{\mathrm{calc}}(\boldsymbol{a}^*, d)\right], \tag{8}$$

where $\boldsymbol{\Omega}_d$ indicates the value range of the thickness, $\boldsymbol{a}^\star$ denotes the priori value of reconstruction and $\boldsymbol{M}^{\mathrm{meas}}$ is the measurement Mueller matrix and $\boldsymbol{M}^{\mathrm{calc}}$ is the theoretical Mueller matrix and $\Gamma + \boldsymbol{M}^{meas}$ is the Moore–Penrose pseudo-inverse of the covariance matrix of the measured Mueller matrix and $\Gamma + \boldsymbol{M}^{meas} = (\Gamma + \boldsymbol{M}^{meas} \cdot \Gamma\, \boldsymbol{M}^{meas})^{-1} \cdot \Gamma\, T\, \boldsymbol{M}^{meas}$.

## 3 SOURCES OF ERRORS AND CALIBRATION

In this article, Gaussian additive noise, Poisson shot noise, and the random bias of the trigger signal have become three of the most important factors affecting the repeatability accuracy. The variances of the final measurement results of the Mueller matrix element and thickness are influenced by these three factors seriously. The distribution of the three kinds of random errors must be calibrated respectively.

First of all, we measured the thermal noise and dark noise of the detectors at different gain levels which are typical Gaussian additive noise. **Figure 3** shows the probability density function histogram of the Gaussian additive noise such as dark noise and thermal noise of the two detectors at 632.8 nm. The dark noise obeyed Gaussian distribution as expected. Then, the mean and variance can be obtained from the detected data through the Gaussian fitting. The generic signal independent noise (Gaussian additive noise) model can be described by

$$\mathrm{P}(x) = \frac{1}{\sqrt{2\pi}\delta}e^{-(x-\mu)/2\delta^2}, \tag{9}$$

where P($x$) is probability density function, $x$ is the value of the dark noise, $\mu$ is the mean of $x$, $\delta$ is the standard deviation of $x$, and $\delta^2$ is the variance of $x$.

As shown in **Figure 3**, the bars represent the probability density function from the measurements, and the red line shows the Gaussian fit. The dark noise's mean value of detector 1 is 0.0184 V when we take different gain levels. The variances of 10 dB, 20 dB, and 30 dB are 3.2e-05, 4.3e-05, and 7.8e-05, respectively. The dark noise's mean values of detector 2 are 0.0140 V, 0.0141, and 0.0143 V for the gain levels 10 dB, 20 dB, and 30 dB, respectively. The variances of 10 dB, 20 dB, and 30 dB are 6.0e-05, 6.5e-05, and 9.2e-05, respectively.

The gain 30 dB is usually selected in the actual measurement. The variance and the mean values of the dark noise of the detector 2 are 9.2e-05 and 0.0143 V, respectively. The generic signal independent noise model is given by **Eq. 6**. We generate the intensity measurements in the simulation, and each measurement is corrupted by the noise-obeying Gaussian distribution model in the following section.

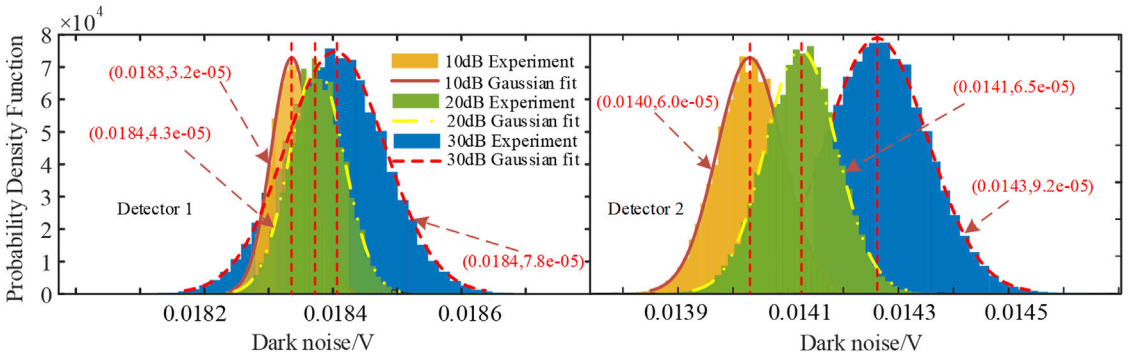


**FIGURE 3 |** Calibration results of Gaussian additive noise of detector 1 and detector 2.

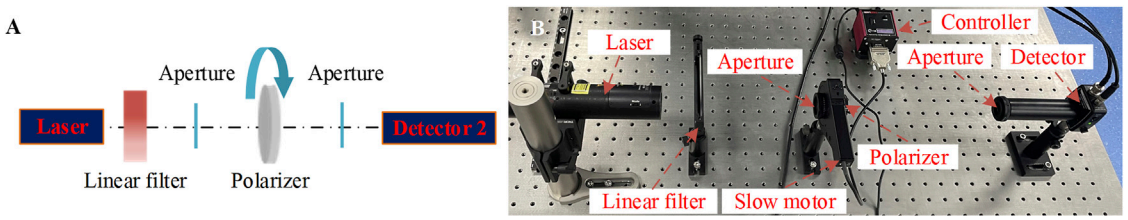


**FIGURE 4 |** Solution for Poisson shot noise calibration of the detector **(A)** schematic diagram and **(B)** experiment setup.

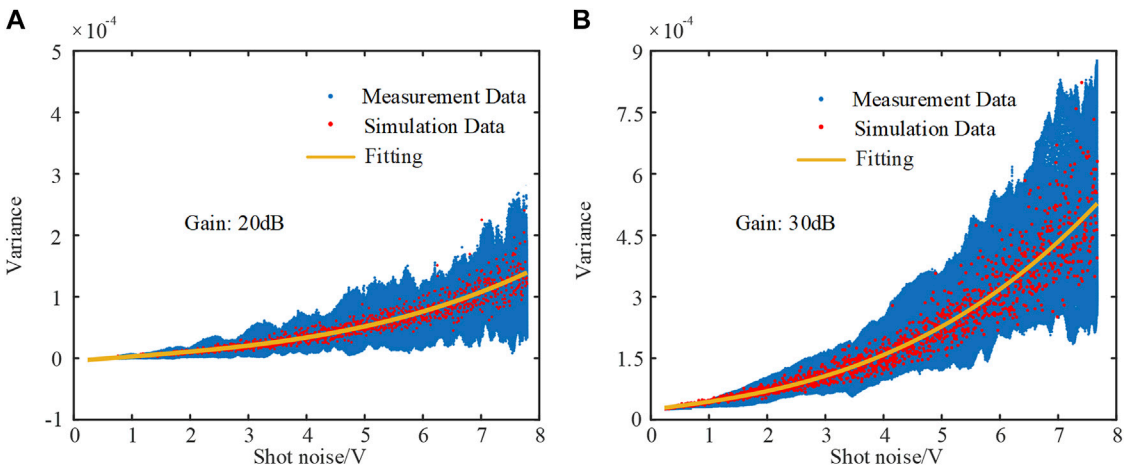


**FIGURE 5 |** Calibration results of Poisson shot noise of detector 2 at **(A)** 20 dB and **(B)** 30 dB at 632.8 nm.

Second, the Poisson shot noise of detector 2 was calibrated separately as shown in **Figure 4.** A silicon photoelectric detector captures a periodic intensity produced by a rotating polarizer. The mean and variance of the Poisson shot noise are calculated after multiple measurements. Poisson shot noise will be modeled from the measured raw data.

As shown in **Figure 5**, the variance of the Poisson shot noise and the mean of the intensity conform the cubic nonlinear relation. A general analytical model is deduced to describe the Poisson shot noise as

$$\mathrm{P}(x) = a \cdot \mathrm{P}_{\mathrm{Poisson}}(x) + b \cdot \mathrm{P}^2_{\mathrm{Poisson}}(x) + c \cdot \mathrm{P}^3_{\mathrm{Poisson}}(x), \quad (10)$$

$$\mathrm{P}_{\mathrm{Poisson}}(x) = \frac{\lambda^x e^{-\lambda}}{x!}, \quad (11)$$

where $\mathrm{P}(x)$ is the probability density function, $\mathrm{P}_{\mathrm{Poisson}}(x)$ is the probability density function of Poisson distribution, $a$, $b$, and $c$ are

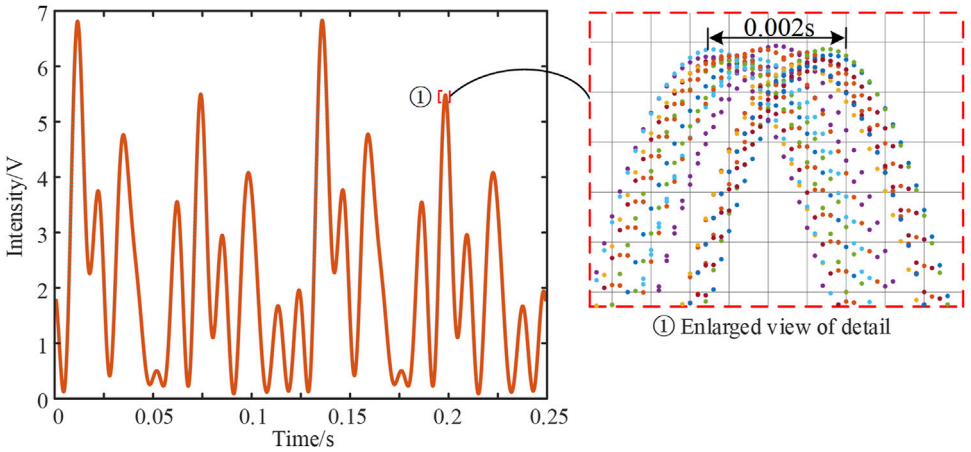


**FIGURE 6 |** Time repeatability error due to the synchronization error of the external trigger and the limited sampling frequency of data acquisition.

the adjustment parameters, and λ is equal to the expected value of $x$ when that is also equal to its variance. The maximum variances of intensity measurements are $3 \times 10^{-4}$ and $9 \times 10^{-4}$ for gain levels 20 dB and 30 dB, respectively.

We use the proposed analytical model to generate the simulated shot noise and get its mean and variance respectively. Measured noise and normalized noise calculated by the general analytical model are shown in **Figure 5**, and the data match well. We generate the intensity measurements in the simulation, and each measurement is corrupted by the noise-obeying Poisson distribution model in the following section.

Last, usually due to the delay or advancement of the external trigger and the limited sampling frequency of the acquisition board, the initial point of each measurement will be offset, which causes the timing repeatability error. It can be observed that the period shift intensifies with the increase of measurement time. Such error is shown as the initial angle deviation of the two wave plates associated to the motor speed and sampling frequency.

The intensity data are collected in the same cycle each time after the acquisition board is triggered, and we take the measurement 30 times. **Figure 6** shows that the 30 measurements result with 5,000 points in a cycle are superimposed together when the sampling frequency is 20 kHz. It can be observed that there is a staggered situation between cycles which is completely random due to the triggers start randomly and inaccurately. The period is staggered by about 2 ms (0.002 s), which causes the distortion of the data when these periodic data are taken on an average. Therefore, it is necessary to reduce the timing repeatability error through hardware or algorithm. The motors rotate the wave plate with the speed of 1,440°/s and 7,200°/s, so that the period shift will cause the offset of the initial azimuth of the wave plates. The relationship between the range of the initial azimuth deviation should be the same as the relationship between the motor speed because the range of the initial azimuth deviation is calculated by multiplying the motor speed and the offset time 2 ms. The random initial azimuth bias ranges of first and second wave plates are $C_{S1}$±1.44° and $C_{S2}$±7.2°, respectively.

# 4 ERROR PROPAGATION SIMULATION AND OPTIMIZATION METHOD

The errors caused by Gaussian additive noise and Poisson shot noise are random errors that affect the repeatability accuracy of the system. Besides, the timing repeatability error caused by the limited sampling frequency and random trigger is a random error as well.

According to the system model and error propagation model, the variance caused by the random error can be calculated. First, we inject the instrument random error into the SWE system, and then we can calculate the variance of the Mueller matrix and the thickness of the film. In order to evaluate the effect of the random error on the measurement accuracy, we address the noise properties of MME by theoretical analysis and simulations and further determine the correlation between the random errors and the estimate variance of the measurement system for the optimization.

## 4.1 Error Propagation

In this article, the data analysis for MME is the nonlinear regression iteration. Standard ellipsometry measures the ellipsometric parameters of the samples. We can estimate the ellipsometric parameters by measuring the Mueller matrix $\boldsymbol{M}_S$. Let us denote [15].

$$\boldsymbol{M}_S = \begin{bmatrix} m_{11} & m_{12} & m_{13} & m_{14} \\ m_{21} & m_{22} & m_{23} & m_{24} \\ m_{31} & m_{32} & m_{33} & m_{34} \\ m_{41} & m_{42} & m_{43} & m_{44} \end{bmatrix}, \tag{12}$$

the 4 × 4 Mueller matrix of the sample. The ellipsometric parameters can be measured by an MME, which consists of a light source, a PSG with an instrument matrix $\boldsymbol{G}$, and a PSA with an instrument matrix $\boldsymbol{A}$. **Equation 1** can be expressed in the form of vector as [14–16, 19]:

$$Vec(I_k) = Vec(\boldsymbol{A}_k \cdot \boldsymbol{M}_S \cdot \boldsymbol{G}_k) = (\boldsymbol{G}_K^T \otimes \boldsymbol{A}_k) Vec(\boldsymbol{M}_S) (k \in [1, K]), \tag{13}$$

where $k$ represents the $t_k$-measured flux, and $K$ is the number of sampling point.

$$I_k = S_0 \cdot \left(\boldsymbol{G}_K^{\mathrm{T}} \otimes \boldsymbol{A}_k\right) \cdot Vec\left(\boldsymbol{M}_{\mathrm{S}}\right), \tag{14}$$

where $Vec\ (\boldsymbol{M}_{\mathrm{S}})$ is a 16-dimensional vector obtained by reading the Mueller Matrix $\boldsymbol{M}_{\mathrm{S}}$ in a lexicographic order and ⊗ denotes the Kronecker product. $\boldsymbol{G}_k$ and $\boldsymbol{A}_k$ are vectors, and they can be derived by **Eqs. 2** and **3**, respectively. $S_0$ is the intensity of the light source, as

$$\boldsymbol{G}_k\left(C_1^k, P, \delta_1\right) = \begin{bmatrix} 1 \\ \cos^2\left(2C_1^k\right)\cos\left(2P\right) + \sin\left(2C_1^k\right)\cos\left(2C_1^k\right)\cos\left(2P\right) + \cdots \\ \sin^2\left(2C_1^k\right)\cos\left(2P\right)\cos\delta_1 - \sin\left(2C_1^k\right)\cos\left(2C_1^k\right)\sin\left(2P\right)\cos\delta_1 \\ \sin^2\left(2C_1^k\right)\sin\left(2P\right) + \sin\left(2C_1^k\right)\cos\left(2C_1^k\right)\cos\left(2P\right) - \cdots \\ \sin\left(2C_1^k\right)\cos\left(2C_1^k\right)\cos\left(2P\right)\cos\delta_1 + \cos^2\left(2C_1^k\right)\cos\left(2P\right)\cos\delta_1 \\ -\sin\left(2C_1^k\right)\cos\left(2P\right)\sin\delta_1 + \cos^2\left(2C_1^k\right)\sin\left(2P\right)\sin\delta_1 \end{bmatrix}; \tag{15}$$

$$\boldsymbol{A}_k\left(C_2^k, A, \delta_2\right) = \begin{bmatrix} 1 \\ \cos^2\left(2C_2^k\right)\cos\left(2A\right) + \sin\left(2C_2^k\right)\cos\left(2C_2^k\right)\sin\left(2A\right) + \cdots \\ \sin^2\left(2C_2^k\right)\cos\left(2A\right)\cos\delta_2 - \sin\left(2C_2^k\right)\cos\left(2C_2^k\right)\sin\left(2A\right)\cos\delta_2 \\ \sin^2\left(2C_2^k\right)\sin\left(2A\right) + \sin\left(2C_2^k\right)\cos\left(2C_2^k\right)\cos\left(2A\right) - \cdots \\ \sin\left(2C_2^k\right)\cos\left(2C_2^k\right)\cos\left(2A\right)\cos\delta_2 + \cos^2\left(2C_2^k\right)\sin\left(2A\right)\cos\delta_2 \\ \sin\left(2C_2^k\right)\cos\left(2A\right)\sin\delta_2 - \cos^2\left(2C_2^k\right)\sin\left(2A\right)\sin\delta_2 \end{bmatrix}. \tag{16}$$

Since the initial fast axes of the retarders are $C_1^{\mathrm{initial}}$ and $C_2^{\mathrm{initial}}$ and $K$ flux measurements are performed during the fundamental optical period $\pi/\omega$ with a rotating frequency ratio [41, 42] of $5\omega$: $N\omega$, the fast-axes azimuth combinations of ($C_1^k$, $C_2^k$) can be determined as [13, 36].

$$\begin{gathered} \left(C_1^k, C_2^k\right) = \left\{\frac{5\left(k-1\right)}{K-1}\pi + C_1^{\mathrm{initial}}, \frac{N\left(k-1\right)}{K-1}\pi + C_2^{\mathrm{initial}}\right\} \\ k \in [1, K]; \\ N \in [1, 2, 3, 4, 6, 7, 8, 9, 11, 12, 13, 14, 16, 17, 18, 19, 21, 22, 23, 24, 25] \end{gathered}, \tag{17}$$

We can denote the instrument matrix as

$$Vec\left(\boldsymbol{I}\right) = \begin{bmatrix} \boldsymbol{G}_1^{\mathrm{T}} \otimes \boldsymbol{A}_1 \\ \boldsymbol{G}_2^{\mathrm{T}} \otimes \boldsymbol{A}_2 \\ \cdots \\ \boldsymbol{G}_k^{\mathrm{T}} \otimes \boldsymbol{A}_k \end{bmatrix} \cdot Vec\left(\boldsymbol{M}_{\mathrm{S}}\right) = \boldsymbol{T} \cdot Vec\left(\boldsymbol{M}_{\mathrm{S}}\right), \tag{18}$$

where the $Vec(\boldsymbol{I})$ is the $K$-element vector of intensity measured by the detector 2, and $\boldsymbol{T}$ is the $K \times 16$ instrument matrix of the Mueller matrix ellipsometer.

When the measurements are disturbed by Gaussian additive noise, the estimation variance of each element of the measured Mueller matrix $Vec\ (\boldsymbol{M}_{\mathrm{S}})$ can be denoted as [14].

$$\sigma_i^2\left(C_1^k, P, \delta_1, C_2^k, A, \delta_2, N\right) = \sigma_{\mathrm{Gaussian}}^2\left[\left(\boldsymbol{T}^{\mathrm{T}}\boldsymbol{T}\right)^{-1}\right]_{ii}, \forall i \in [1, 16], \tag{19}$$

where the variance is the function of ($C_1^k$, $P$, $\delta_1$, $C_2^k$, $A$, $\delta_2$, $N$) and $\sigma_{\mathrm{Gaussian}}^2$, and we can observe the relationship between the variance and the variates from the equation.

When the measurements are disturbed by Poisson shot noise, the estimation variance of each element of the measured Mueller matrix $Vec\ (\boldsymbol{M}_{\mathrm{S}})$ can be denoted as [14].

$$\begin{aligned} &\sigma_i^2\left(C_1^k, P, \delta_1, C_2^k, A, \delta_2, N, Vec\left(\boldsymbol{M}_{\mathrm{S}}\right)\right) \\ &\quad = \left[\left(\boldsymbol{T}^{\mathrm{T}}\boldsymbol{T}\right)^{-1}\left(\boldsymbol{T}^{\mathrm{T}}\boldsymbol{\Gamma}_{\boldsymbol{I}}\boldsymbol{T}\right)\left(\boldsymbol{T}^{\mathrm{T}}\boldsymbol{T}\right)^{-1}\right]_{ii}, \forall i \in [1, 16], \end{aligned} \tag{20}$$

where

$$\boldsymbol{\Gamma}_{\boldsymbol{I}} = \begin{bmatrix} \left(\boldsymbol{G}_1^{\mathrm{T}} \otimes \boldsymbol{A}_1\right) \cdot Vec\left(\boldsymbol{M}_{\mathrm{S}}\right) & 0 & \cdots & 0 \\ 0 & \left(\boldsymbol{G}_2^{\mathrm{T}} \otimes \boldsymbol{A}_2\right) \cdot Vec\left(\boldsymbol{M}_{\mathrm{S}}\right) & \cdots & 0 \\ \cdots & \cdots & \cdots & \cdots \\ 0 & 0 & \cdots & \left(\boldsymbol{G}_K^{\mathrm{T}} \otimes \boldsymbol{A}_K\right) \cdot Vec\left(\boldsymbol{M}_{\mathrm{S}}\right) \end{bmatrix}, \tag{21}$$

where the variance is the function of ($C_1^k$, $P$, $\delta_1$, $C_2^k$, $A$, $\delta_2$, $Vec$ ($\boldsymbol{M}_{\mathrm{S}}$)), and we can observe the relationship between the variance and the variates from the equation. Contrary to the case of Gaussian additive noise, we found that the estimation variance of Poisson shot noise is dependent on the Mueller matrix of the sample.

Besides, when the measurements are disturbed by the random bias of the trigger signal, the relationship between the sample matrices is obtained by the experimental measurement, and the actual Mueller matrix can be expressed as:

$$\boldsymbol{M}_{\mathrm{S}} = \boldsymbol{M}_0 + \Delta\boldsymbol{M} = \boldsymbol{M}_0 + \boldsymbol{\mu}_{\mathrm{M}} + \boldsymbol{\varepsilon}_{\mathrm{M}}, \tag{22}$$

where the $\boldsymbol{M}_{\mathrm{S}}$ is the experimentally measured sample Mueller matrix, $\boldsymbol{M}_0$ is the true value of the sample Mueller matrix, $\Delta\boldsymbol{M}$ is the overall measurement error of the sample Mueller matrix, $\boldsymbol{\mu}_{\mathrm{M}}$ is the Mueller matrix systematic error, and $\boldsymbol{\varepsilon}_{\mathrm{M}}$ is the Mueller matrix random error.

The random bias of the trigger signal will cause the offset of the initial azimuth of the wave plate within an approximate angle. Then, we can think of the random error as a random combination of many system errors which is the deviation of the azimuth. The Mueller matrix systematic error can be denoted as

$$\boldsymbol{\mu}_{\mathrm{M}} = \boldsymbol{Q}\left(\boldsymbol{p}^*\right)\left(\Delta\boldsymbol{D} + \boldsymbol{r}_{\boldsymbol{D}}\right)\boldsymbol{M}_0 \approx \boldsymbol{Q}\left(\boldsymbol{p}^*\right)\Delta D\boldsymbol{M}_0 = \boldsymbol{Q}\left(\boldsymbol{p}^*\right)\boldsymbol{J}_{\boldsymbol{D_p}|\boldsymbol{p}=\boldsymbol{p}^*}\Delta\boldsymbol{p}\boldsymbol{M}_0, \tag{23}$$

where the $\boldsymbol{Q}\ (\boldsymbol{p}^*)$ is the calibrated system matrix, $\boldsymbol{\Delta D}$ is the system matrix error caused by system parameter deviation, $\boldsymbol{r}_D$ is the system matrix error caused by the optical component characterization model, $\boldsymbol{M}_0$ is the true value of the sample Mueller matrix, $\boldsymbol{J}_{\boldsymbol{Dp}|\boldsymbol{p}=\boldsymbol{p}^*}$ is the Jacobian matrix of the system matrix $\boldsymbol{D}$ to the partial differential coefficient of the system parameter $\boldsymbol{p}$ at $\boldsymbol{p}=\boldsymbol{p}^*$, and $\Delta\boldsymbol{p}$ is the system parameter deviation. We will quantitatively analyze the variance (Var [$\boldsymbol{M}_0$+$\boldsymbol{\mu}_{\mathrm{M}}$]) caused by the errors on the measurement results by simulations.

## 4.2 Optimization Method

In view of the aforementioned three kinds of random errors, optimization methods can be proposed to improve the repeatability accuracy of the instrument according to the error propagation equation. For the Gaussian additive noise and Poisson shot noise, the instrument matrix can be optimized to improve measurement results. For the bias of the trigger signal error, a method based on timing signal peak matching is proposed to reduce the offset of the wave plate's azimuth.

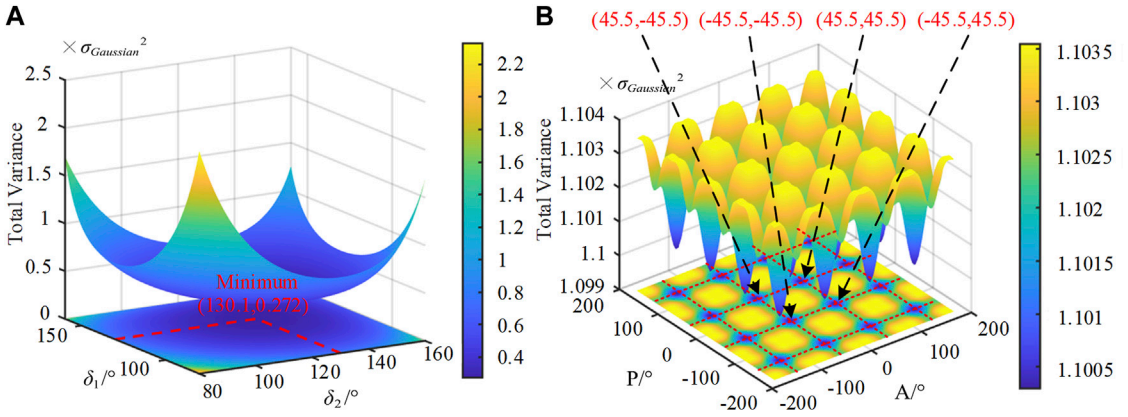


**FIGURE 7 |** Calculated total estimation variances for Gaussian noise when **(A)** retardance $\delta_1 \neq \delta_2$ ($\delta_1$, $\delta_2$)∈[-180°,180°], $P = A = 0°$ and **(B)** retardance $\delta_1 = \delta_2 =$ 130.1°, $P \neq A$ ($P$, $A$)∈[-180°,180°].

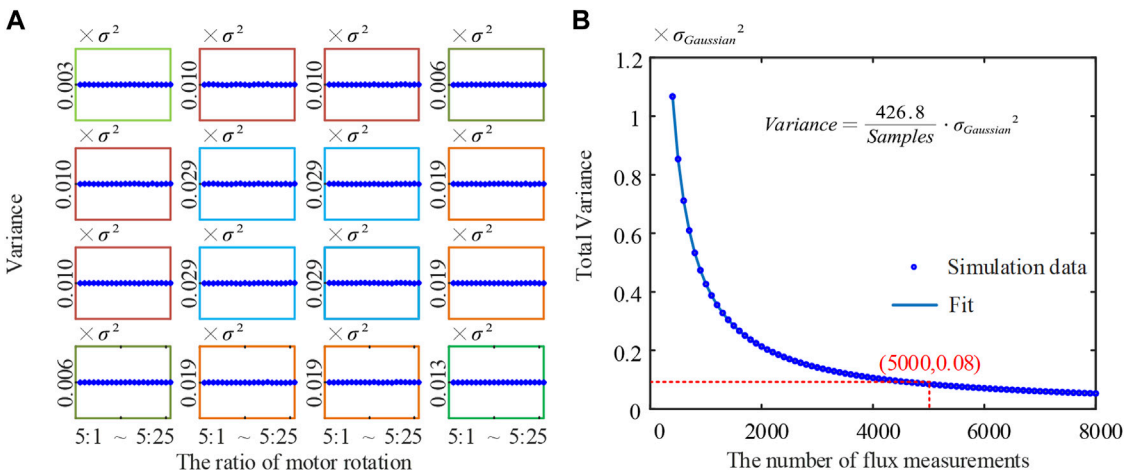


**FIGURE 8 |** Theoretical analysis for Gaussian noise **(A)** estimation variances of Mueller matrix elements when the ratio of motors' rotation speed is 5$\omega$:$N\omega$ and **(B)** total estimation variances dependency on the number of sampling points.

### 4.2.1 Gaussian Additive Noise

From **Eq. 15**, we know that the estimation variance varies with ($C_1^k$, $P$, $\delta_1$, $C_2^k$, $A$, $\delta_2$, $N$) and $\sigma^2_{\text{Gaussian}}$. Then, the impact of the different dependent variables can be observed. First, $P$ and $A$ are assumed to be 0°, and the relationship between the estimation variance and ($\delta_1$, $\delta_2$) is shown in **Figure 7A**. It can be observed that the total estimation variance reaches the minimum when the $\delta_1 = \delta_2 = 130.1°$. Second, $\delta_1$ and $\delta_2$ are assumed to be 130.1°, and the relationship between the estimation variance and ($P$, $A$) is shown in **Figure 7B**. It can be observed that the total estimation variance is minimized when $P$ is around 45.5°/−45.5° and $A$ is around −45.5°/45.5°. The dark blue area in **Figure 7B** represents the values of $P$ and $A$, which minimize the total variance estimation.

As shown in **Figure 8A**, the estimated variances are independent to the rotating frequency ratio of MME when the Gaussian additive noise is dominant. Then, we cannot reduce the variances by changing the rotation ratio of the motors. The estimated variance is also inversely proportional to the number of sampling $K$. As shown in **Figure 8B**, in the actual instrument configuration, we can find the function of variance and the number of flux measurements is $variance = (426.8/K)\cdot\sigma^2_{\text{Gaussian}}$ . With the number of $K$ increasing, the variance reduces rapidly until $K$ is 5,000.

### 4.2.2 Poisson Shot Noise

From **Eq. 16**, we know that the estimated variance varies with the parameters ($C_1^k$, $P$, $\delta_1$, $C_2^k$, $A$, $\delta_2$, $N$) and the Mueller Matrix of samples $Vec$ ($\boldsymbol{M}_S$). When the Poisson shot noise is dominant, the estimated variance is strongly correlated with the sample. Here, we use the standard silica films with different thicknesses as simulation samples to study the impact of instrument matrix parameters. As shown in **Figure 9A**, the 16 Mueller matrix elements vary with the thicknesses of the samples, and we can

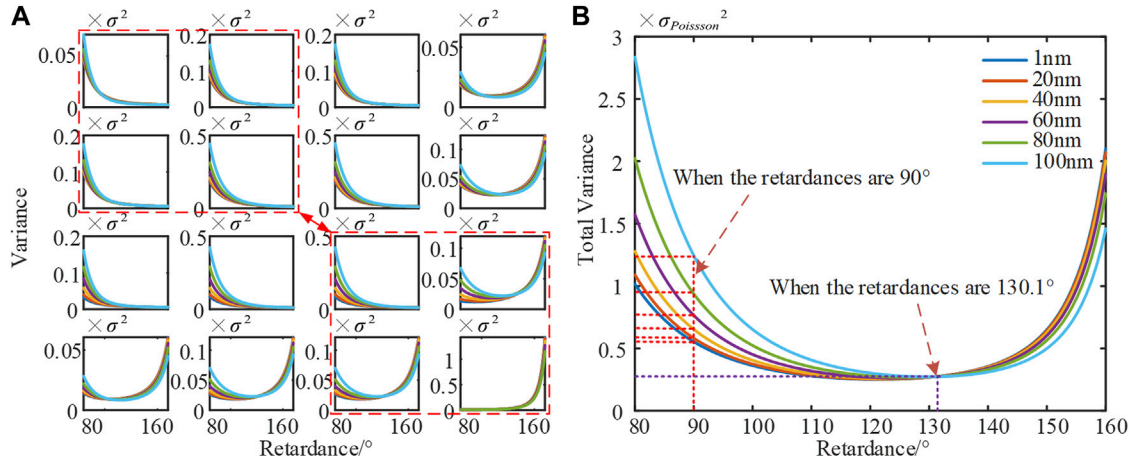


**FIGURE 9 |** Theoretical analysis for Poisson shot noise **(A)** Mueller matrix elements estimation variances dependency on retardance for samples with different thicknesses and **(B)** total estimation variances dependency on retardance for samples with different thicknesses.

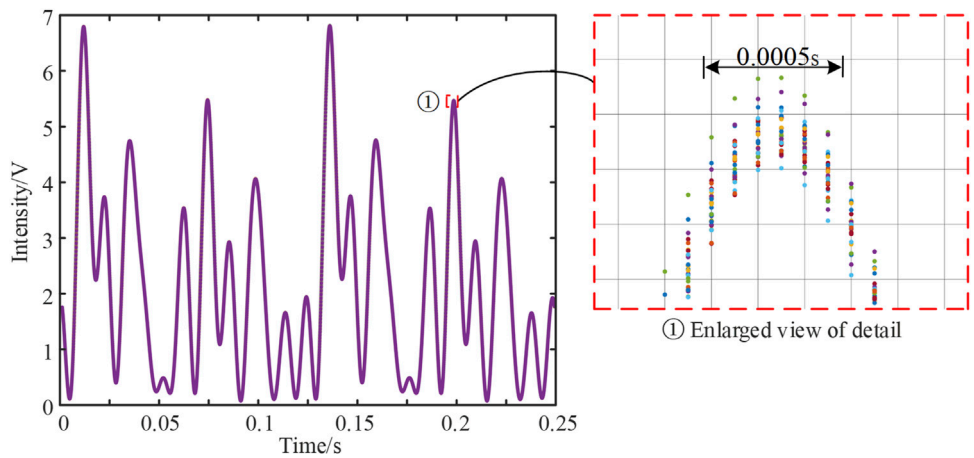


**FIGURE 10 |** Signal waveform after using peak-matching algorithm.

observe that the different Mueller matrix elements have different tendencies when the retardances of wave plates change. As shown in **Figure 9B**, we can observe that the total variance becomes larger as the thickness increases when the retarders are 90° (a quarter-wave plate). However, the thickness parameter of different standard silica samples is out of action when $\delta_1 = \delta_2 = 130.1°$, and the minimum of total variance can be obtained.

### 4.2.3 The Bias of the Trigger Signal and Peak-Matching Algorithm

The random bias of the trigger signal will cause the random offset of the retarder's azimuth. In order to eliminate the effect of the timing repeatability error, a peak-matching algorithm is proposed to relieve the strict requirements of initial angle compensatory and synchronicity of triggers in the instrument. When several periods of the intensity are collected, the signals are processed by a low-pass filter first to remove the high-frequency noise. Then, the peaks of the sampled periods will be picked out to record their sequence number. To avoid the data distortion, the peak should be included in one optical cycle. The reset of points for further process could be determined by taking the points before and after the peak sequence number continuously. Specifically, if we sampled $M$ points in one optical cycle, we need to select $M$ data including the peak. Without losing generality, suppose the peak sequence number is $j$, we can define an optical cycle is from the sampling points with sequence number of ($j$-$i$, $M + j$-$i$), where $i$ could be an arbitrary number. By applying the same process on the data collected in each cycle, the peak in each cycle will be guaranteed with the same sequence, so that the distortion of the data could be eliminated.

**Figure 10** shows a signal waveform after applying peak-matching algorithm. Comparing with the previous

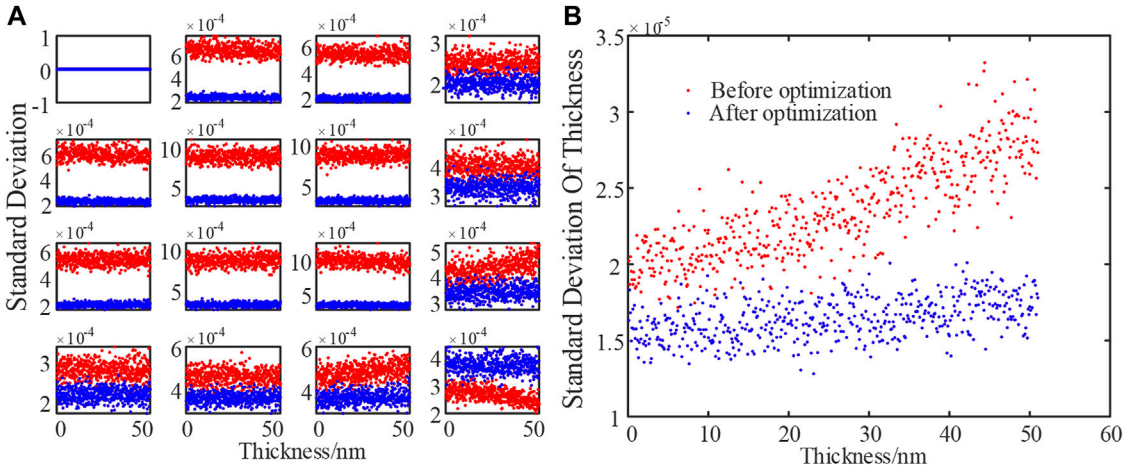


**FIGURE 11 |** Simulation results for Gaussian noise **(A)** estimated standard deviation of Mueller matrix elements for the samples with different thicknesses and **(B)** thickness-dependent standard deviation of the measured thickness.

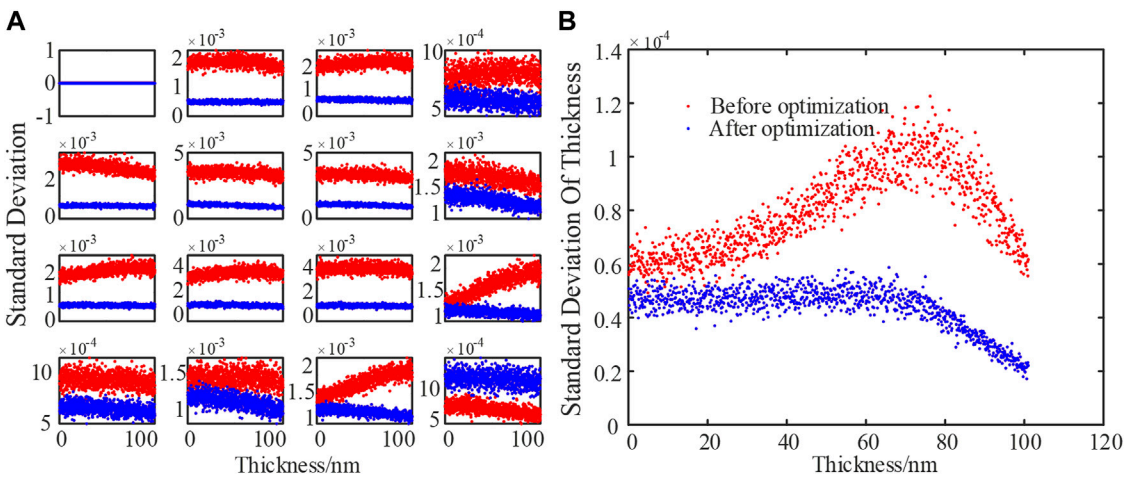


**FIGURE 12 |** Simulation results for Poisson shot noise **(A)** estimated standard deviation of Mueller matrix elements for the samples with different thicknesses and **(B)** thickness-dependent standard deviation of the measured thickness.

measurement result shown in **Figure 6**, the reduction of the timing repeatability error (staggers of the periods) can be clearly observed. As reported in **Figure 10**, the offset is reduced from 0.002 to 0.0005 s. After multiplying the motor speed by the offset time, we can calculate that the corresponding random initial azimuth bias ranges of the two wave plates are reduced from ±1.44° and ±7.2° to ±0.36° and ±1.8°, respectively.

## 5 NUMERICAL SIMULATION

First, the Gaussian additive noise attribution measured by the experiment in the previous work is added to the system. The influence on the standard deviations of Mueller matrix elements and thickness can be observed. As shown in **Figure 11**, the standard deviations of Mueller matrix elements and the thickness are obviously reduced when the instrument matrix is optimized, and the level of standard deviation fluctuation is about $10^{-5}$. The impact of Gaussian additive noise on the Mueller matrix elements is independent to the sample, and this phenomenon conforms to the theoretical expectation. However, the standard deviation of the calculated thickness increases slightly with the increase of the sample thickness.

Second, the Poisson shot noise attribution measured by the experiment is added to the numerical system. The improvements of the repeatability in the Mueller matrix and the thickness measurements are shown in **Figure 12**. When the instrument matrix is optimized, the level of standard deviation

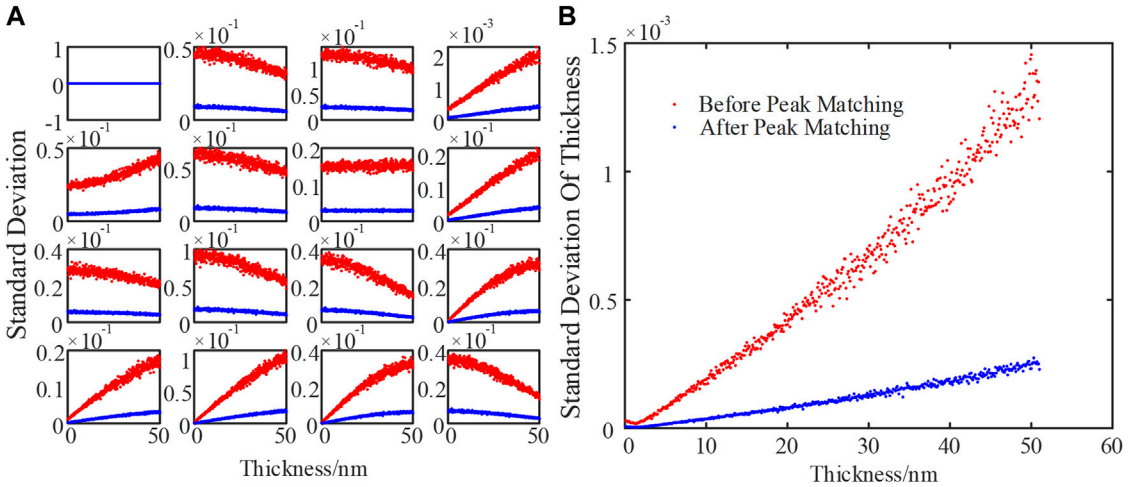


**FIGURE 13 |** Simulation results for the random bias of the trigger signal (**A**) estimated standard deviation of Mueller matrix elements for the samples with different thicknesses and **(B)** thickness-dependent standard deviation of the measured thickness.

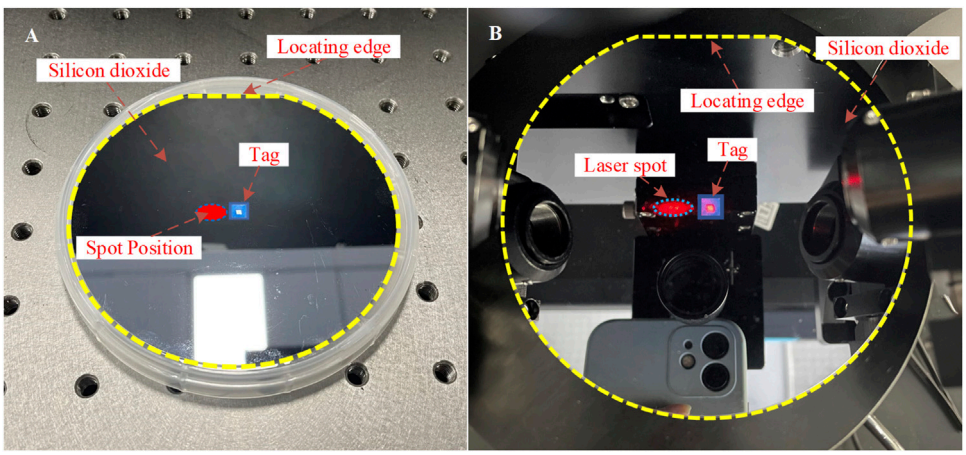


**FIGURE 14 |** Diagram of the point positioning **(A)** silicon wafer and **(B)** *in situ* measurement.

fluctuation of the optimized simulation result is below $0.5 \times 10^{-4}$. The standard deviation of the calculated thickness results increases slightly first and then falls with the increase of sample thickness.

Last, we set the sampling frequency as 20 Khz, then the rotation speed of the PSG motor and PSA motor are 1,440°/s and 7,200°/s, respectively. Moreover, the timing repeatability errors of the PSG motor and the PSA motor are randomly varying within the range of ±1.44° and ±7.2°, respectively. The standard deviation of the thickness fluctuates within the level of about $10^{-3}$. The statistical results are shown red in **Figure 13**. Compared to the red dot which stands for the standard deviations before optimization, the blue dots shown in **Figure 13** show the clear error compression on the Mueller matrix and the thickness measurements when the proposed peak-matching algorithm was introduced. We can also observe that the error increases as the film thickness increases.

As can be seen from **Figure 13B**, after optimizing the instrument matrix and taking the method of peak-matching algorithm, the repeatability accuracy can be increased by an order of magnitude.

## 6 EXPERIMENT RESULT AND DISCUSSION

To verify the validity of the proposed method, thin film measurement experiments on standard silicon dioxide film samples have been carried out. At first, a tag is attached to the center of the sample surface, whose edge is parallel to the locating edge of the sample. The measurements are carried out 30 times on

**TABLE 1 |** Results of film thickness measurements.

| Sample | | Before applying proposed methods | | After applying proposed methods | | Reduction |
|---|---|---|---|---|---|---|
| $SiO_2$ | | Mean thickness (nm) | Std | Mean thickness (nm) | Std | Std |
| Sample 1 | Marked point 1 | 2.0544 | 1.9211e-03 | 2.0607 | 4.0757e-04 | 78.785% |
| Sample 2 | Marked point 2 | 14.3861 | 1.6651e-03 | 14.2759 | 7.3632e-04 | 55.779% |
| Sample 3 | Marked point 3 | 61.3980 | 3.9619e-03 | 61.4302 | 8.0106e-04 | 79.781% |

the point next to the left edge of the tag. During the measurement, the sample is held by a vac-sorb pump installed on the sample stage to ensure no movement is introduced during the test. After changing the system configuration, the tag and the locating edge will be used to limit the spatial variance of the testing area. Then, the measurement will be carried out another 30 times. The standard deviation of the thicknesses will be calculated, and the result of the two tests will be compared to evaluate the effectiveness of the proposed method.

Three different thickness silicon dioxide films are prepared first, whose nominal thicknesses are about 2, 15, 55 nm (Standard Silicon Dioxide, Eoptics, China). Each standard silicon dioxide film is measured 30 times with our self-developed SWE. The Mueller matrix elements as well as the standard deviation of 30 measurements for each element can be obtained. The standard deviations of 16 measured Mueller matrix elements can be reduced to $1 \times 10^{-4}$ when the proposed methods are applied. Besides, the thicknesses of each film are calculated with the algorithm represented by **Eq. 8**. It can be observed from **Table 1** that the standard deviation of the thickness has been drastically reduced. For example, the measurement standard deviations for the measuring point of Sample 1, Sample 2, and Sample 3 have been reduced by 78.785, 55.779, and 79.781%, respectively.

## 7 CONCLUSION

In this work, an instrument matrix optimization method and a peak-matching algorithm have been proposed to improve the repeatability accuracy for ellipsometry. The analysis on the correlation between the random errors and the system configurations is carried out to search the optimal instrument matrix for film measurements. The estimation variances on individual Mueller matrix elements are derived analytically for Gaussian noise, Poisson noise, and the bias of the trigger signal. Numerical simulations show that the proposed method is robust and can dramatically improve the measurement repeatability accuracy. The experimental results show that the proposed method can significantly compress the standard deviation of the measured Mueller matrix elements and thickness. The results show that the proposed method can reduce the standard deviations of measurement results by more than 50% on silicon dioxide films of different thickness measurements. The proposed methods pave a potential way to reduce the requirements on motor performance, acquisition card resolution, and trigger accuracy, which are critical to cost reduction.

## DATA AVAILABILITY STATEMENT

The original contributions presented in the study are included in the article/supplementary material, further inquiries can be directed to the corresponding authors.

## AUTHOR CONTRIBUTIONS

ZJ performed the instrumentation, simulation, experimental demonstration, and manuscript drafting; SZ performed the instrumentation, formulation, and manuscript editing; JL contributed to data processing and manuscript editing; QL contributed to result discussion and funding acquisition; HJ contributed to conceptualization, result discussion, manuscript review and editing, and funding acquisition; and SL contributed to result discussion, manuscript editing, and project administration.

## FUNDING

This work was funded by the National Natural Science Foundation of China (51975232) and the National Key Research and Development Plan (Grant No. 2017YFF0204705).

## REFERENCES

1. Collins RW, Koh J, Fujiwara H, Rovira PI, Ferlauto AS, Zapien JA, et al. Recent Progress in Thin Film Growth Analysis by Multichannel Spectroscopic Ellipsometry. *Appl Surf Sci* (2000) 154-155:217–28. doi:10.1016/S0169-4332(99)00482-1
2. Fan Z, Tang Y, Wei K, Zhang Y. Calibration of Focusing Lens Artifacts in a Dual Rotating-Compensator Mueller Matrix Ellipsometer. *Appl Opt* (2018) 57: 4145. doi:10.1364/AO.57.004145
3. Lee J, Rovira PI, An I, Collins RW. Rotating-Compensator Multichannel Ellipsometry: Applications for Real Time Stokes Vector Spectroscopy of Thin Film Growth. *Rev Scientific Instr* (1998) 69:1800–10. doi:10.1063/1.1148844
4. Aspnes DE, Studna AA. High Precision Scanning Ellipsometer. *Appl Opt* (1975) 14:220. doi:10.1364/AO.14.000220
5. Nguyen NV, Pudliner BS, An I, Collins RW. Error Correction for Calibration and Data Reduction in Rotating-Polarizer Ellipsometry: Applications to a Novel Multichannel Ellipsometer. *J Opt Soc Am A* (1991) 8:919. doi:10.1364/JOSAA.8.000919

6. Kim KJ. Review on the Thickness Measurement of Ultrathin Oxide Films by Mutual Calibration Method. *Surf Interf Anal* (2021) 7040. doi:10.1002/sia.7040
7. He C, He H, Chang J, Chen B, Ma H, Booth MJ. Polarisation Optics for Biomedical and Clinical Applications: a Review. *Light Sci Appl* (2021) 10:194. doi:10.1038/s41377-021-00639-x
8. Dong H, Tang M, Gong Y. Measurement Errors Induced by Deformation of Optical Axes of Achromatic Waveplate Retarders in RRFP Stokes Polarimeters. *Opt Express* (2012) 20:26649. doi:10.1364/OE.20.026649
9. Dai H, Yan C. Measurement Errors Resulted from Misalignment Errors of the Retarder in a Rotating-Retarder Complete Stokes Polarimeter. *Opt Express* (2014) 22:11869. doi:10.1364/OE.22.011869
10. West EA, Smith MH. Polarization Errors Associated with Birefringent Waveplates. *Opt Eng* (1995) 34(6):1574–80. doi:10.1117/12.202079
11. Boulbry B, Bousquet B, Jeune BL, Guern Y, Lotrian J. Polarization Errors Associated with Zero-Order Achromatic Quarter-Wave Plates in the Whole Visible Spectral Range. *Opt Express* (2001) 9:225. doi:10.1364/OE.9.000225
12. Miao Z, Tang Y, Wei K, Zhang Y. Random Error Analysis of Normalized Fourier Coefficient in Dual-Rotating Compensator Mueller Matrix Ellipsometer. *Meas Sci Technol* (2021) 32:125602. doi:10.1088/1361-6501/ac1a80
13. Jiang B, Meng K, Youcef-Toumi K. Quantification and Reduction of Poisson-Gaussian Mixed Noise Induced Errors in Ellipsometry. *Opt Express* (2021) 29:27057. doi:10.1364/OE.432793
14. Quan N, Zhang C, Mu T, Li S, You C. Estimation Variance of Dual-Rotating-Retarder Mueller Matrix Polarimeter in the Presence of Gaussian thermal Noise and Poisson Shot Noise. *J Opt* (2020) 22:025701. doi:10.1088/2040-8986/ab613c
15. Li X, Hu H, Wu L, Liu T. Optimization of Instrument Matrix for Mueller Matrix Ellipsometry Based on Partial Elements Analysis of the Mueller Matrix. *Opt Express* (2017) 25:18872. doi:10.1364/OE.25.018872
16. Twietmeyer KM, Chipman RA. Optimization of Mueller Matrix Polarimeters in the Presence of Error Sources. *Opt Express* (2008) 16:11589. doi:10.1364/OE.16.011589
17. El-Agez TM, El Tayyan AA, Taya SA. Rotating Polarizer-Analyzer Scanning Ellipsometer. *Thin Solid Films* (2010) 518:5610–4. doi:10.1016/j.tsf.2010.04.067
18. El-Agez TM, Taya SA. An Extensive Theoretical Analysis of the 1 : 2 Ratio Rotating Polarizer-Analyzer Fourier Ellipsometer. *Phys Scr* (2011) 83:025701. doi:10.1088/0031-8949/83/02/025701
19. Smith MH. Optimization of a Dual-Rotating-Retarder Mueller Matrix Polarimeter. *Appl Opt* (2002) 41:2488. doi:10.1364/AO.41.002488
20. Sabatke DS, Descour MR, Dereniak EL, Sweatt WC, Kemme SA, Phipps GS. Optimization of Retardance for a Complete Stokes Polarimeter. *Opt Lett* (2000) 25:802. doi:10.1364/OL.25.000802
21. Duan QY, Gupta VK, Sorooshian S. Shuffled Complex Evolution Approach for Effective and Efficient Global Minimization. *J Optim Theor Appl* (1993) 76:501–21. doi:10.1007/BF00939380
22. Goudail F. Noise Minimization and Equalization for Stokes Polarimeters in the Presence of Signal-dependent Poisson Shot Noise. *Opt Lett* (2009) 34:647. doi:10.1364/OL.34.000647
23. Lee S, Lee M, Kang M. Poisson-Gaussian Noise Analysis and Estimation for Low-Dose X-ray Images in the NSCT Domain. *Sensors* (2018) 18:1019. doi:10.3390/s18041019
24. Dinu M, Quochi F. Amplitude Sensitivity Limits of Optical Sampling for Optical Performance Monitoring. *J Opt Networking* (2002) 1:237–48.
25. Dai J, Goudail F, Boffety M, Gao J. Estimation Precision of Full Polarimetric Parameters in the Presence of Additive and Poisson Noise. *Opt Express* (2018) 26:34081. doi:10.1364/OE.26.034081
26. Li X, Liu T, Huang B, Song Z, Hu H. Optimal Distribution of Integration Time for Intensity Measurements in Stokes Polarimetry. *Opt Express* (2015) 23:27690. doi:10.1364/OE.23.027690
27. Anna G, Goudail F. Optimal Mueller Matrix Estimation in the Presence of Poisson Shot Noise. *Opt Express* (2012) 20:21331. doi:10.1364/OE.20.021331
28. Goudail F, Bénière A. Estimation Precision of the Degree of Linear Polarization and of the Angle of Polarization in the Presence of Different Sources of Noise. *Appl Opt* (2010) 49:683. doi:10.1364/AO.49.000683
29. Takakura Y, Ahmad JE. Noise Distribution of Mueller Matrices Retrieved with Active Rotating Polarimeters. *Appl Opt* (2007) 46:7354. doi:10.1364/AO.46.007354
30. Modine FA, Jellison GE, Gruzalski GR. Errors in Ellipsometry Measurements Made with a Photoelastic Modulator. *J Opt Soc Am* (1983) 73:892. doi:10.1364/JOSA.73.000892
31. Taya SA, El-Agez TM, Alkanoo AA. A Spectroscopic Ellipsometer Using Rotating Polarizer and Analyzer at a Speed Ratio 1:1 and a Compensator. *Opt Quant Electron* (2014) 46:883–95. doi:10.1007/s11082-013-9799-5
32. El-Agez TM, Taya SA. Development and Construction of Rotating Polarizer Analyzer Ellipsometer. *Opt Lasers Eng* (2011) 49:507–13. doi:10.1016/j.optlaseng.2011.01.005
33. Zhang S, Jiang H, Gu H, Chen X, Liu S. High-speed Mueller Matrix Ellipsometer with Microsecond Temporal Resolution. *Opt Express* (2020) 28:10873. doi:10.1364/OE.389825
34. Liu S, Chen X, Zhang C. Development of a Broadband Mueller Matrix Ellipsometer as a Powerful Tool for Nanostructure Metrology. *Thin Solid Films* (2015) 584:176–85. doi:10.1016/j.tsf.2015.02.006
35. Gu H, Chen X, Shi Y, Jiang H, Zhang C, Gong P, et al. Comprehensive Characterization of a General Composite Waveplate by Spectroscopic Mueller Matrix Polarimetry. *Opt Express* (2018) 26:25408. doi:10.1364/OE.26.025408
36. Gu H, Chen X, Zhang C, Jiang H, Liu S. Study of the Retardance of a Birefringent Waveplate at Tilt Incidence by Mueller Matrix Ellipsometer. *J Opt* (2018) 20:015401. doi:10.1088/2040-8986/aa9b05
37. Gu H, Chen X, Jiang H, Zhang C, Li W, Liu S. Accurate Alignment of Optical Axes of a Biplate Using a Spectroscopic Mueller Matrix Ellipsometer. *Appl Opt* (2016) 55:3935. doi:10.1364/AO.55.003935
38. Gu H, Chen X, Jiang H, Zhang C, Liu S. Optimal Broadband Mueller Matrix Ellipsometer Using Multi-Waveplates with Flexibly Oriented Axes. *J Opt* (2016) 18:025702. doi:10.1088/2040-8978/18/2/025702
39. Gu H, Liu S, Chen X, Zhang C. Calibration of Misalignment Errors in Composite Waveplates Using Mueller Matrix Ellipsometry. *Appl Opt* (2015) 54:684. doi:10.1364/AO.54.000684
40. Li W, Zhang C, Jiang H, Chen X, Liu S. Depolarization Artifacts in Dual Rotating-Compensator Mueller Matrix Ellipsometry. *J Opt* (2016) 18:055701. doi:10.1088/2040-8978/18/5/055701
41. Taya SA, El-Agez TM, Alkanoo AA. Rotating Polarizer, Compensator, and Analyzer Ellipsometry. *Chin Phys. B* (2013) 22:120703. doi:10.1088/1674-1056/22/12/120703
42. Taya SA, El-Agez TM, Alkanoo AA. Ellipsometric Configurations Using a Phase Retarder and a Rotating Polarizer and Analyzer at Any Speed Ratio. *Chin Phys. B* (2012) 21:110701. doi:10.1088/1674-1056/21/11/110701


**Conflict of Interest:** The authors declare that the research was conducted in the absence of any commercial or financial relationships that could be construed as a potential conflict of interest.

frontiers in Physics

ORIGINAL RESEARCH
published: 19 January 2022
doi: 10.3389/fphy.2021.791459

# Enhanced Measurement Accuracy for Nanostructures Using Hybrid Metrology

*Poul-Erik Hansen*, Sabrina Rostgaard Johannsen, Søren Alkærsig Jensen and Jonas Skovlund Møller Madsen*

*Danish Fundamental Metrology A/S, Hørsholm, Denmark*

Light-matter interplay is widely used for analyzing the topology of surfaces on small scales for use in areas such as nanotechnology, nanoelectronics, photonics, and advanced materials. Conventional optical microscope imaging methods are limited in resolution to a value comparable to the wavelength, the so-called Abbe limit, and cannot be used to measure nano-sized structures. Scatterometry and Mueller ellipsometry are spectroscopic optical methods that can measure structures smaller than the wavelength. However, the relative uncertainties of the structure dimensions measured with scatterometry increase with decreasing structure size, and the industry is therefore replacing simple intensity based scatterometry with Mueller ellipsometry for the most demanding measurements. The accuracy of Mueller ellipsometry and scatterometry are closely related to the ability of the employed regression and regularization algorithms to extract the structural dimension. In this work, we demonstrate how the measurement accuracy on three-dimensional periodic structures may be increased by measuring the same periodic structure with multiple techniques and applying a $\chi^2$-regression method that finds the best solution based on the input from all the instruments. We furthermore report on a new and improved calibration method for Mueller ellipsometry and demonstrate how the Mueller matrix may be used to find the geometrical anisotropy of the structure.

**Keywords: metrology, Mueller ellipsometry, inverse modelling, scatterometry, nanostructures**

OPEN ACCESS

***Edited by:***
*Ji Qi,*
*Imperial College London,*
*United Kingdom*

***Reviewed by:***
*Sébastien Robert Mouchet,*
*University of Exeter, United Kingdom*
*Alpan Bek,*
*Middle East Technical University,*
*Turkey*

****Correspondence:***
*Poul-Erik Hansen*
*peh@dfm.dk*

***Specialty section:***
*This article was submitted to Optics and Photonics, a section of the journal Frontiers in Physics*

***Received:*** *08 October 2021*
***Accepted:*** *29 November 2021*
***Published:*** *19 January 2022*

***Citation:***
*Hansen P-E, Johannsen SR, Jensen SA and Madsen JSM (2022) Enhanced Measurement Accuracy for Nanostructures Using Hybrid Metrology. Front. Phys. 9:791459. doi: 10.3389/fphy.2021.791459*

## 1 INTRODUCTION

Nanostructures have a wide array of applications in optics, diagnostics, food science, sensing, and process inspection monitoring. Some of these applications include enhancing waveguide coupling, improving linear encoders, making hyperspectral cameras and printing color images [1–4]. Imaging technologies like Optical Microscopy (OM), Atomic Force Microscopy (AFM) and Scanning Electron Microscopy (SEM) are the dominating quality assesment technologies in low volume, high-cost nanoscale manufacturing, whereas scatterometry and Mueller ellipsometry are the preferred technologies for high volume manufacturing. However, the measurement accuracy for all of the above-mentioned technologies is decreasing with the ever decreasing nanostructure sizes. OM cannot measure the shape of objects with lateral sizes less than 1 μm; AFM cannot accurately measure shape but can measure the nanostructure height if the separation width is longer than the tip width; lateral and vertical dimensions from SEM pictures are hard to obtain if the width of the borderline produced by the secondary electron becomes a significant part of the dimension to be measured [5]. Scatterometry and Mueller ellipsometry can measure the shape of periodic

nanostructures [6–8]; however, the accuracy of the shape dimensions decrease with decreasing nanostructure sizes and increasing complexity. We proposed to use hybrid metrology that combines scatterometry, Mueller ellipsometry, and AFM for shape reconstruction of nanostructures. Scatterometry can be defined as the measurement and analysis of light diffracted by structures using fixed polarization settings.

The scattered (or diffracted) light is a signature or "fingerprint" which reflects the details of the structure itself. For a periodic device, such as a series of lines and spaces in silicon, the scattered light consists of distinct diffraction orders at angular locations specified by the well-known grating equation. The fraction of the incident power diffracted into any order is sensitive to the shape and dimensional parameters of the diffracting structure and may therefore be used to characterize the structure itself [9]. This is done using a mathematical model of the structure based on a priori information and a rigorous simulation of the light-structure interaction. Rigorous Coupled Wave Analysis (RCWA) [10] is the common workhorse for scatterometry modelling due to its speed, convergence and relatively simple implementation. In RCWA, the nanostructure is approximated by rectangular slabs, and Maxwell's equations are solved by coupling the boundary conditions between the slabs. The dimensional parameters are obtained using a best-fit procedure between experimental data and calculated values [11].

Ellipsometry measures the polarization-dependent optical response from a sample [9]. In the conventional configuration, an amplitude and a phase parameter, describing the change in polarization in an isotropic sample, are measured. Mueller ellipsometry is a more advanced method, which may be further divided into two groups: Non-normalized Mueller ellipsometers that measure all 16 Mueller matrix elements, and normalized Mueller ellipsometers in which the 16 Mueller matrix elements are normalized with the first Mueller matrix element $m_{11}$. The sensitivity of Mueller ellipsometry comes from the measurement of both the magnitude and phase of the Fresnel response/reflection from the sample, and as a rule of thumb, the sensitivity increases with asymmetries and increased density of the structure. Furthermore, it is possible to use the same mathematical modelling method as in scatterometry. Several strategies exist for precision Mueller ellipsometry measurement and have been investigated by a number of authors [12–16]. A necessary prerequisite for high precision Mueller ellipsometry measurements is accurate calibration of the Mueller ellipsometer. We have developed a new calibration method consisting of a fast method for monitoring the most important experimental settings on a daily basis and a more comprehensive method for monitoring of the entire instrument. The method, explained in section 2.1, makes it possible to correct for fluctuation in the dominating experimental parameters on a much shorter timescale and easily monitor the linearity of the instrument response.

In this paper, we report on the progress of accurate determination of the dimensional parameters of three-dimensional periodic nanostructures by measuring the same periodic structure with multiple technologies and applying a $\chi^2$-regression method with regularization that finds the best solution based on the input from all the instruments. We have measured a square patterned periodic grating with truncated cone shapes with a 200 nm period in the $x$ and $y$ direction, see **Figure 1**, using scatterometry, Mueller ellipsometry, and AFM. The $\chi^2$-regression method contains two parts, the first part includes the scatterometry and Mueller ellipsometry contribution, while the second part is a Tikhonov regularization part used for including the AFM height measurement. We demonstrate that the hybrid metrology approach improves the accuracy of the obtained dimension. In particular, we observe an improvement for strongly correlated parameters. The paper is organized in the following way: In **Section 2**, we describe the experimental scatterometry and Mueller ellipsometry setups together with the newly developed method for calibration of the Mueller ellipsometer. In **section 3**, the forward model used for simulating the light-matter interaction is presented. In **section 4**, we explain the applied inverse method, showing how it is used to find the dimensional parameters and calculate the corresponding uncertainties. **Section 5** is devoted to the discussion of the obtained results, and **section 6** summarizes the results obtained.

## 2 MATERIALS AND METHODS

The experimental system is a combined goniometric and spectroscopic setup. In this work, we use only the

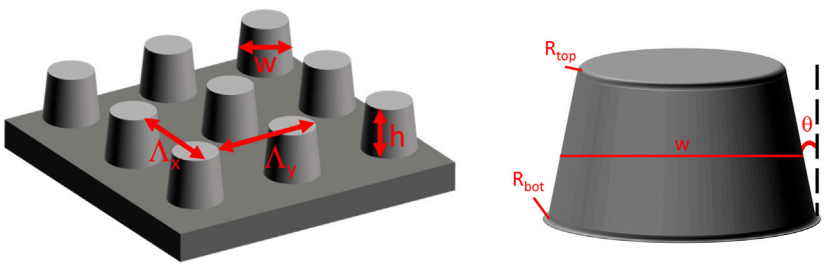


**FIGURE 1 |** Illustration of the truncated cone model and the parameterization used to describe the physical sample. The parameters (periods, $\Lambda_x$ and $\Lambda_y$, height, $h$, and width, $w$) specified by the manufacturer are shown on the left, while the additional parameters used (sidewall angles, $\theta$, and corner rounding radii, $R_{top}$ and $R_{bot}$) are shown on the right. The width is defined as the full-width-half-max of the cone.

spectroscopic scatterometry and Mueller ellipsometry measurement modes. A sketch of the setup can be seen in **Figure 2**. As radiation source, we use a Laser-Driven Light Source (LDLS) (Energetiq, EQ-99X). The LDLS lamp covers a wavelength range from 170 to 2,200 nm. The light is focused onto a 150 μm pinhole using parabolic mirrors and secondly collimated by an UV-to-NIR corrected triplet lens (Edmund Optics, 180 mm). The collimated light passes through a polarization state generator (PSG) made from an $\alpha$ - BBO polarizer (Edmund Optics, 68–827) followed by a photo elastics modulator (PEM, Hinds Instrument, I/FS50). At this point the beam diameter is roughly 1.5 mm. The angle of incidence on the sample may be varied between +/- 90° via a rotation stage (Thorlabs, NR360S) equipped with angular encoder (Heidenhain, ERA 4200C). The detector arm can be scanned over nearly the complete diffraction plane, +/- 175°, and is equipped with a polarization state analyzer (PSA), made from a photo elastic modulator (Hinds Instrument, I/FS60) and an $\alpha$ - BBO polarizer (Edmund Optics, 68–827), followed by a spatial mirror (Thorlabs, RC08APC-P01) that focuses the light into a fiber coupled monochromator (Spectral products, DK242). The monochromator is equiped with two gratings, a UV-optimized grating for wavelengths below 400 nm and another for the wavelengths above. The output from the monochromator is focused on a PMT detector (Hamamatsu, R928P). The detected signal is split into a DC and an AC signal using an analog filter (SIM 965, Stanford Research System) with a low-pass frequency cut at 30 Hz. The DC signal is fed into an analog PID controller (SIM 960, Stanford Research System) that together with a custom build PMT amplifier, controls the high voltage power supply (PS 310, Stanford Research System) of the PMT such that the recorded signal is always taken at the same DC value ((1.35 ± 0.005) V in the presented work). A digitizer (Agilent L4534A) is used for simultaneous sampling of the recorded signal together with the PSG and PSA waveforms. The waveforms are long-pass filtered at 1 MHz and voltage limited to +/- 8 V in the digitizer prior to data analysis. By rotating these PEMS to different angles (labeled $\theta_{m_0}$ and $\theta_{m_1}$), one can probe different elements of the Mueller Matrix. The PEM waveforms and the signal are analyzed by fast Fourier transformation. **Eq. 4** in the **Supplementary Material** of ref. [17] shows that the recorded Mueller ellipsometer signal may be written as a Fourier expansion of frequencies in the following way:

$$\begin{aligned} I = I_{DC} &+ I_{f_0}\cos\left(\omega_0 t + \phi_0 - \frac{\pi}{2}\right) + I_{f_1}\cos\left(\omega_1 t + \phi_1 - \frac{\pi}{2}\right) \\ &+ I_{2f_0}\cos\left(2\omega_0 t + 2\phi_0\right) + I_{2f_1}\cos\left(2\omega_1 t + 2\phi_1\right) \\ &+ I_{f_0+f_1}\cos\left((\omega_0+\omega_1)t + \phi_0 + \phi_1\right) \\ &+ I_{2f_0+f_1}\cos\left((2\omega_0+\omega_1)t + 2\phi_0 + \phi_1 - \frac{\pi}{2}\right) \\ &+ I_{f_0+2f_1}\cos\left((\omega_0+2\omega_1)t + \phi_0 + 2\phi_1 - \frac{\pi}{2}\right) \\ &+ I_{2f_0+2f_1}\cos\left((2\omega_0+2\omega_1)t + 2\phi_0 + 2\phi_1\right) + \ldots \end{aligned} \quad (1)$$

Where $\omega_i = 2\pi f_i$, $i = 0, 1$ and $\phi_0$, $\phi_1$ are the angular frequencies and phases of the photo elastic modulators. $I_{f_i}$ are the amplitudes and $I_{DC}$ is the DC value that is kept constant for all measurements. The measurands obtained from Fourier transformation of the signal are:

$$\begin{aligned} I_{DC} \quad \text{and} \quad I_{f_i}, f_i \in \{&f_0,\ f_1,\ 2f_0,\ 2f_1,\ f_0+f_1,\ 2f_0 \\ &+f_1,\ f_0+2f_1,\ 2f_0+2f_1\} \end{aligned} \quad (2)$$

It is demonstrated in [17] that the nine measurands in **(2)** give a complete description of the signal, $I$, in **Eq. 1**. The normalized intensities $A_{f_i} = I_{f_i}/I_{DC}$ can be directly related to the Mueller matrix elements as explained in **section 2.1**, and the 15 normalized Mueller matrix elements may be obtained by measuring $A_{f_i}$ for different angular positions of the PSG ($\theta_{m_0}$) and PSA ($\theta_{m_1}$). The Muller ellipsometry data obtained are normalized with the $m_{11}$ Mueller matrix element. The Mueller matrix element, $m_{11}$, can be measured using scatterometry. During the scatterometry measurements, the PEMs were not oscillating and the outgoing light was connected via fiber to a UV to NIR spectrometer (Ocean optics, FLAME-S-XR1-ES) instead of the monochromator.

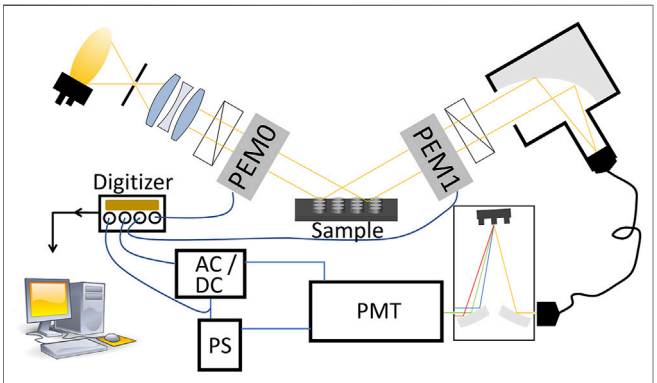


**FIGURE 2 |** Schematic illustration of the experimental setup. The main components are the light source, the two photo elastic modulators (PEM0 and PEM1), a monochromator and a detection system based on a photomultiplier tube (PMT), a high voltage power supply (PS) and electronics measuring the AC and DC components of the signal (AC/DC).

## 2.1 Data Acquisition and Calibration Method for Mueller Ellipsometry

The details of the data acquisition are explained in the **Supplementary Material**. Here we continue by showing how precision calibration of the setup can be made prior to measurement. The main results of this section are **Eqs 4**, **6**. **Eq. 4** presents new expressions for improving the measured Bessel amplitudes, and **Eq. 6** is a high precision formulation of the standard formulas in [15]. The notation used in the derivations are similar to the one used in [15]. The prior-to-measurement calibration is by far the most important calibration since PEMs are very stable devices. However, regular system calibration is needed to monitor the performance of the entire system, and a simple method for this is described in the **Supplementary Material**.

The quantities measured with the Mueller ellipsometry setup are the eight normalized intensities $A_{f_i} = I_{f_i}/I_{DC}$, see (2). In this section we show that the normalized intensities $A_{f_i}$ are well defined functions of the Mueller matrix elements ($m_{ij}$), the Bessel amplitudes ($A_0$, $A_1$) and the static strain ($\delta_0$, $\delta_1$) of the PEM phase retardation, the two polarizer angles ($\theta_{p_0}$, $\theta_{p_1}$), the two PEM angles ($\theta_{m_0}$, $\theta_{m_1}$) used to select the Mueller matrix elements of interest, and the Bessel functions of the first kind $J_n$. With a suitable choice of polarizer and PEM angles, a normalized intensity $A_{f_i}$ is dominated by a single Mueller matrix element as indicated in **Eq. 6**. However, the influences of other Mueller matrix elements are only eliminated if all the Bessel amplitudes $A_0$, $A_1$ have been adjusted so that $J_0(A_0) = J_0(A_1) = 0$ (e.g. $A_0 = A_1 = 2.404\,8$), if the static strains $\delta_0$, $\delta_1$ are zero, and if all polarizers and PEM angles are perfectly set. This optimal situation can hardly be obtained in practice, so precise calibrations are needed. We perform a system calibration in which all of the system is calibrated, and a prior-to-measurement calibration of the Bessel amplitudes and the static strain. During calibration, we find the optimal voltages for each PEM in order to make sure that the value of $A_0$ and $A_1$ are within the range from 2.28 to 2.38 for all the measured wavelengths. This range ensures that we are within the linear range of the Bessel functions and safely away from the point where $J_0$ changes sign. In practice, this is done by making a calibration function (polynomial of second degree) for each combination of PEM and monochromator grating, resulting in four wavelength-voltage calibration functions. The measurement of the Bessel amplitudes is obtained from transmission calibration measurements without sample in the Mueller ellipsometer, using $\theta_{p_0} \approx \theta_{p_1} \approx -45^\circ$ and $\theta_{m_0} \approx \theta_{m_1} \approx 0^\circ$ and assuming $J_0(A_0) \approx J_0(A_1) \approx 0$, so that we can expand the Bessel function as

$$\begin{aligned} J_0(A_0) &\approx C\left(A_p - A_0\right) \\ J_0(A_1) &\approx C\left(A_p - A_1\right) \end{aligned} \tag{3}$$

where $C = 0.519\,6$ and $A_p = 2.4048$. After derivation, see **Supplementary Material**, we find the following very useful expressions for $A_0$ and $A_1$

$$\begin{aligned} A_0 &= A_p - \frac{A_{2f_1}}{2CD\left(J_2\left(A_p\right) + \left(J_1\left(A_p\right) - J_3\left(A_p\right)\right)\dfrac{A_{2f_0}}{4CDJ_2\left(A_p\right)}\right)} \\ A_1 &= A_p - \frac{A_{2f_0}}{2CD\left(J_2\left(A_p\right) + \left(J_1\left(A_p\right) - J_3\left(A_p\right)\right)\dfrac{A_{2f_1}}{4CDJ_2\left(A_p\right)}\right)} \end{aligned} \tag{4}$$

where $D = \cos(2(\theta_{m_1} - \theta_{m_0})) \approx \pm 1$ is a measure of the relative angular position of the PEMs. **Eq. 4** is very important for high precision measurements since the normalized intensities $A_{f_i}$ are strongly dependent on the correct values for the Bessel amplitudes. The static strain measurement is performed in order to see if the assumption $\delta_0$, $\delta_1 \approx 0$ holds for all wavelengths, the measurements are performed by setting $\theta_{p_0} \approx -45^\circ$, $\theta_{p_1} \approx 0$, $\theta_{m_0} \approx 0$, $\theta_{m_1} \approx -45^\circ$ and measuring $A_{2f_0+f_1}$, $A_{f_0+2f_1}$,

$$\begin{aligned} \delta_0 &= \frac{A_{2f_0+f_1}\left(1 + C_{b_0}C_{b_1}C_{m_0}C_{m_1} + C_{b_0}S_{m_0} + C_{b_0}C_{b_1}S_{m_0}S_{m_1}\right)}{-2J_2(A_0)J_1(A_1)} \\ \delta_1 &= \frac{A_{2f_1+f_0}\left(1 + C_{b_0}C_{b_1}C_{m_0}C_{m_1} + C_{b_0}S_{m_0} + C_{b_0}C_{b_1}S_{m_0}S_{m_1}\right)}{-2J_2(A_1)J_1(A_1)} \end{aligned} \tag{5}$$

where $C_{b_0} = \cos(2(\theta_{m_0} - \theta_{p_0}))$, $C_{b_0} = \cos(2(\theta_{m_1} - \theta_{p_1}))$, $C_{m_0} = \cos(2\theta_{m_0})$, $C_{m_1} = \cos(2\theta_{m_1})$, $S_{b_0} = \sin(2(\theta_{m_0} - \theta_{p_0}))$, $S_{b_0} = \sin(2(\theta_{m_1} - \theta_{p_1}))$, $S_{m_0} = \sin(2\theta_{m_0})$ and $S_{m_1} = \sin(2\theta_{m_1})$. **Figure 3** shows typical Bessel amplitude and static strain values for the measurement system. Assuming that $\delta_0$, $\delta_1 \approx 0$, $S_{b_0} = \pm 1_{b_0}$, $S_{b_1} = \pm 1_{b_1}$, $C_{b_0} = 0$ and $C_{b_1} = 0$, like in most setups, we can write the expressions that relate the normalized intensity $A_{f_i} = \frac{I_{f_i}}{I_{DC}}$ and the Mueller matrix elements, $m_{ij}$

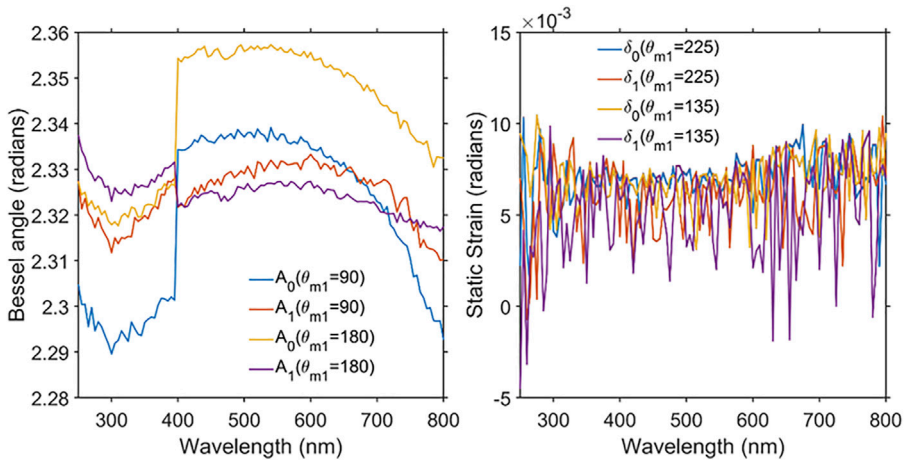


**FIGURE 3 |** Typical Bessel amplitudes $A_0$, $A_1$ and static strains $\delta_0$, $\delta_1$ as a function of wavelength. We note that the Bessel amplitudes are in the desired range from 2.28 to 2.38. A jump is seen around the wavelength of 400 nm, where the monochromator grating and PEM calibration function is changed.

$$
\begin{aligned}
A_{f_0} &\approx 2J_1(A_0)m_{14}(\pm 1_{b_0})\frac{I_{DC}}{I_{DC_0}}\\
A_{f_1} &\approx 2J_1(A_1)(-m_{41}(\pm 1_{b_1}))\frac{I_{DC}}{I_{DC_0}}\\
A_{2f_0} &\approx 2J_2(A_0)(-m_{13}C_{m_0}(\pm 1_{b_0}) + m_{12}(\pm 1_{b0})S_{m_0})\frac{I_{DC}}{I_{DC_0}}\\
A_{2f_1} &\approx 2J_2(A_1)(-m_{31}C_{m_1}(\pm 1_{b_1}) + m_{21}(\pm 1_{b_1})S_{m_1})\frac{I_{DC}}{I_{DC_0}}\\
A_{f_0+f_1} &\approx -2J_1(A_0)J_1(A_1)(-m_{44}(\pm 1_{b0})(\pm 1_{b1}))\frac{I_{DC}}{I_{DC_0}}\\
A_{2f_0+f_1} &\approx 2J_1(A_1)J_2(A_0)(-m_{42}S_{m_0}(\pm 1_{b_0})(\pm 1_{b_1})\\
&\quad +m_{43}C_{m_0}(\pm 1_{b_0})(\pm 1_{b_1}))\frac{I_{DC}}{I_{DC_0}}\\
A_{f_0+2f_1} &\approx 2J_1(A_0)J_2(A_1)(m_{24}(\pm 1_{b_0})(\pm 1_{b_1})S_{m_1}\\
&\quad -m_{34}C_{m_1}(\pm 1_{b_0})(\pm 1_{b_1}))\frac{I_{DC}}{I_{DC_0}}\\
A_{2f_0+2f_1} &\approx 2J_2(A_0)J_2(A_1)(-m_{32}C_{m_1}(\pm 1_{b_0})(\pm 1_{b_1})S_{m_0}\\
&\quad + m_{33}C_{m_0}C_{m_1}(\pm 1_{b_0})(\pm 1_{b_1})+\\
&\quad m_{22}(\pm 1_{b_0})(\pm 1_{b_1})S_{m_0}S_{m_1} - m_{23}C_{m_0}(\pm 1_{b_0})(\pm 1_{b_1}))S_{m_1}\frac{I_{DC}}{I_{DC_0}}
\end{aligned}
\tag{6}
$$

where the ratio between the correct DC value and the measured DC value $\left(\frac{I_{DC_0}}{I_{DC}}\right)$ is given by,

$$
\begin{aligned}
\frac{I_{DC_0}}{I_{DC}} &\approx 1 - \frac{C\left((A_p - A_0)(-m_{13}C_{m_0}(\pm 1_{b_0}) + m_{12}(\pm 1_{b0})S_{m_0}) + (A_p - A_1)(-m_{31}C_{m_1}(\pm 1_{b_1}) + m_{21}(\pm 1_{b_1})S_{m_1})\right)}{I_{DC}}\\
&\approx 1 - \frac{C\left((A_p - A_0)\frac{A_{2f_0}}{2J_2(A_0)} + (A_p - A_1)\frac{A_{2f_1}}{2J_2(A_1)}\right)}{I_{DC}}.
\end{aligned}
\tag{7}
$$

**Eq. 7** demonstrates that the correction term vanishes for perfect Bessel amplitudes and that it gets less important with higher $I_{DC}$ values. A high value and low variation are thus optimal. In this paper, we have used a value of (1.350 ± 0.005) V. The calibration Mueller matrix is the Mueller matrix of air, which is a non-depolarizing Mueller matrix. However, the measured calibration Mueller matrix may be influenced by small depolarization $(0.98 < \beta(\lambda) < 1)$ from the components in the setup, for $\lambda > 300$ nm. This depolarization may be found from the following formula [18–20]:

$$
\frac{1}{\beta^2(\lambda)}\sum_{i,j=1}^{4} m_{ij}^2(\lambda) = 4m_{11}^2(\lambda). \tag{8}
$$

The measured Mueller matrix, with the sample in place, is renormalized with the instrument depolarization in order to exclude the influence of the system components in the data fitting. The beta values are shown in **Figure 4**. For the sample, we see a large dip for wavelenghts below 300 nm. This is attributed to our signal quality in this spectral region. We have increased the measurement uncertainty in this region to lower the effect on the final measurement.

## 2.2 Sample and Measurements

A periodic patterned silicon structure $\Gamma_x = \Gamma_y = 200$ nm was purchased from Eulitha AG.

The Mueller ellipsometry measurements were performed at 70° angle of incidence, and 15 Mueller matrix elements have been measured by performing measurements at PSG angles, $\theta_{m_0} = [180, 135, 135, 180]^\circ$ and PSA angles $\theta_{m_1} = [135, 135, 180, 90]^\circ$. The Mueller matrix elements were calculated from the measured intensities in **(2)** following the procedure described in section 2.1 and in the **Supplementary Material**. Scatterometry measurements $I(\lambda)$ were also performed at a 70° angle of incidence together with a reference measurement $I_{ref}(\lambda)$ taken on a flat piece of Si100, and a dark measurement $I_{dark}(\lambda)$ obtained by blocking the light source. The light was polarized perpendicular to the incidence plane during all measurements. The diffraction efficiencies, $\eta(\lambda)$, are calculated from the three scatterometry measurements in the following way:

$$
\eta(\lambda) = R(\lambda)\frac{I(\lambda) - I_{dark}(\lambda)}{I_{ref}(\lambda) - I_{dark}(\lambda)} \tag{9}
$$

where $R(\lambda)$ is the wavelength-dependent reflection coefficient of the material used for the reference measurement.

For the AFM measurements of the heights of the gratings, we used a metrology AFM (Park Systems, NX20, Suwon, South Korea) in tapping mode, equipped with Point Probe Plus tips (Nanosensors), with a specified apex radius < 10 nm. The AFM has an xy-stage equipped with optical distance sensors and a z-flexure stage equipped with strain gauge distance sensors. The microscope was calibrated in the *z*-direction using a step height standard as described in [21]. The area measured by the AFM was well within the area covered by the beam spot in the optical measurements. The images were analyzed using the step height module in Scanning Probe Image Processor (SPIP) (ver. 6.7.3, Image Metrology) and following the ISO 5436 standard for measuring step heights. We stress that only the height is measured by the AFM. Following this standard, we eliminate the effect of sample-tip convolution on the measured height.

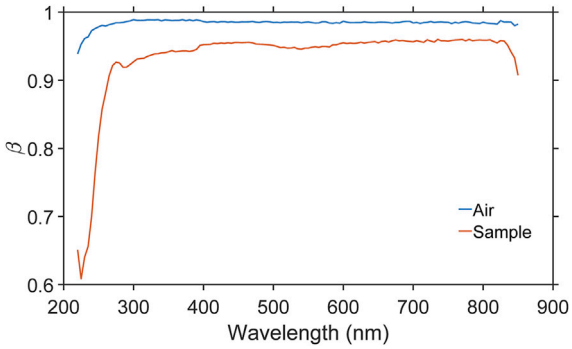


**FIGURE 4 |** Measured values of the depolarization $\beta$ with and without a sample (Air). For wavelengths below 300 nm, we see a steep drop for the sample measurements, which is not present in the air measurement. This demonstrates sample depolarization for lower wavelengths. The depolarization measured without the sample is referred to as the instrument depolarization.

## 2.3 RCWA for Nanostructure Characterization

Light scattering from the periodic patterened nanostructure is modeled by rigorously solving Maxwell's equations in the

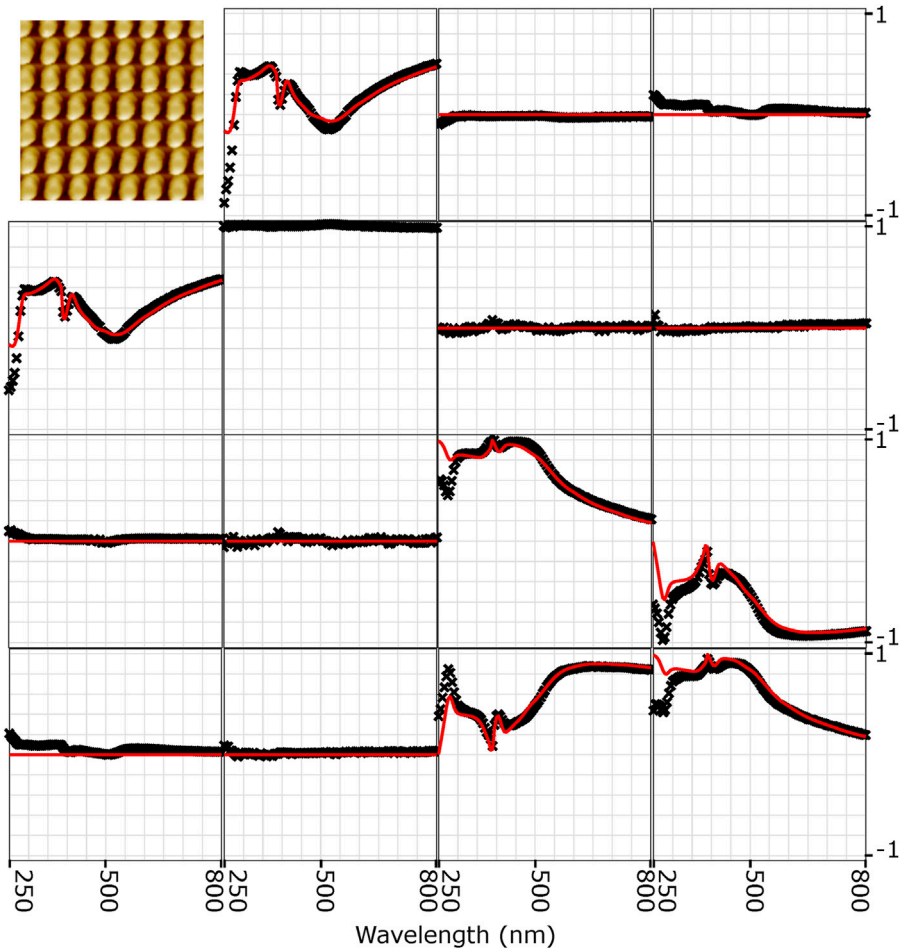


**FIGURE 5 |** Experimental Mueller ellipsometry measurements (black crosses) and fitted Mueller ellipsometry results (red lines). The upper left corner shows an AFM picture of the structure. A strong agreement between model and fit are found within all Mueller matrix elements for wavelengths > 300 nm. All the anisotropic Mueller matrix elements: $m_{13}$, $m_{14}$, $m_{23}$, $m_{24}$, $m_{31}$, $m_{32}$, $m_{41}$ and $m_{42}$ have been set to zero in the model.

relevant frequency domain. The rigorous coupled-wave (RCWA) software described in [11] has been extended to handle arbitrary repeated profiles with complex material distributions. The profile is approximated by division into multiple slabs. Each slab consists of $N_q$ building blocks that all have the same height $h_q$. Each building block within a slab is furthermore labeled with an index $i$. Each building block $b(q, i)$ is then characterized by its widths $w_x(q, i)$, $w_y(q, i)$ and offsets $x(q, i)$, $y(q, i)$ in the x- and $y$ direction, respectively. Furthermore, each block is characterized by its permittivity $\epsilon(q, i)$ and permeability $\mu(q, i)$. The lateral periodicities of the slabs are given by the periodicity of the microstructure.

The new software runs within the Matlab environment and is used for forward calculations of the diffracted fields and efficiencies. The model structure used in the forward calculation is based on a priori information from the sample manufacturer, together with scanning electron microscope images of similar structures. These investigations showed that the nanostructure could be represented by the truncated cone geometry shown in **Figure 1**. The periodic truncated cone geometry may be characterized by a set of geometrical quantities $\mathbf{a}_0$ (e.g. period $\Gamma_x$, $\Gamma_y$ height $h$, width $w$, sidewall angle $\theta$, an oxide layer of thickness $d$, and corner radii $R_1$ and $R_2$). The Fresnel reflection coefficients $r_{pp}$, $r_{sp}$, $r_{ps}$, $r_{ss}$ are calculated using RCWA as function of wavelength $\lambda$, angle of incidence $\theta$, azimuth angle $\phi$ of the nanostructure relative to the scattering plane, refractive index $n + ik$ of the material, and for a specified set of geometrical sample quantities $\mathbf{a}_0$. The Fresnel coefficients from the RCWA simulations are related to the Mueller matrix by

$$M = \begin{pmatrix} 1 & 0 & 0 & 1 \\ 1 & 0 & 0 & -1 \\ 0 & 1 & 1 & 0 \\ 0 & -i & i & 0 \end{pmatrix} \left( \begin{pmatrix} r_{pp} & r_{ps} \\ r_{sp} & r_{ss} \end{pmatrix} \otimes \begin{pmatrix} r_{pp}^{*} & r_{ps}^{*} \\ r_{sp}^{*} & r_{ss}^{*} \end{pmatrix} \right) \begin{pmatrix} 1 & 0 & 0 & 1 \\ 1 & 0 & 0 & -1 \\ 0 & 1 & 1 & 0 \\ 0 & -i & i & 0 \end{pmatrix}^{-1} \tag{10}$$

where ⊗ denotes the Kronecker product and * denotes complex conjugation. The full polarization properties of a sample are contained in the 4 × 4 Mueller matrix ($M$), which for oblique incidence relates the Stokes vectors of the incident ($S_i$) and reflected ($S_r$) directions.

$$S_r = MS_i \tag{11}$$

In this work, we use normalized elements and $m_{11} \equiv 1$. The Stokes vector has the components

$$S_r = \begin{pmatrix} I \\ Q \\ U \\ V \end{pmatrix} = \begin{pmatrix} I_p + I_s \\ I_p - I_s \\ I_{+45} - I_{-45} \\ I_R - I_L \end{pmatrix} \tag{12}$$

where $I_p$, $I_s$, $I_{+45}$, and $I_{-45}$ are, respectively, the irradiances of polarized light components parallel ($p$), perpendicular ($s$), at +45° and at -45° relative to the plane of incidence; $I_R$ and $I_L$ are the intensities of right- and left-handed circularly polarized light.

## 2.4 Inverse Modelling Method

Generally speaking, the inverse problem we consider is the task of calculating from a set of measurements the dimensional parameters that produced those results. Several techniques can be applied to solve inverse problems [10, 11]. The approach used here is based on setting up a regression problem in the following sense: Given a vector of measurement data $y \in R^n$, an RCWA model function, $f_{\mathrm{RCWA}}$, that maps the parameter, $p \in R^m$, describing the truncated cone geometry that we want to determine to the measurement space $f_{\mathrm{RCWA}}$: $R^m \rightarrow R^n$. The mapping function maps the parameter $p$ into calculated scatterometry diffraction efficiencies ($\eta^c$) and calculated Mueller ellipsometry parameters ($m_{ij}^c$), resulting in an approximation of the measurement data. If one has additional knowledge about the measurement errors, e.g. if one knows the variances $\sigma_i^2$ of each of the measured values $y_i$, one can use this knowledge to weight the different measurements accordingly, hence limiting the influence of observations that are expected to have a large error. If more knowledge of the parameters $p$ exists from other experiments, this knowledge may be incorporated into the $\chi^2$-function as a penalty term. The most common penalty terms are Bayesian and Tikhonov regularization. Tikhonov regularization can be used to incorporate measurands of one or more parameters included in $p$ from other instruments in a direct and appealing way. The $\chi^2$-regularization method used in this work contains two parts, the scatterometry and Mueller ellipsometry contribution and the AFM height measurement. The latter is incorporated as a Tikhonov regularization used to penalize the model from fitting a height, $h_c$, different than the height, $h$, measured by AFM.

$$\begin{aligned}\chi^2(p) \;=\; & \frac{1}{2}\left(\frac{(h-h^c)^2}{\sigma_{AFM}^2} + \frac{1}{7N}\sum_{i=1}^{N}\left[\frac{\left(m_{12}(\lambda_i) - m_{12}^c(\lambda_i,p)\right)^2}{\sigma_{m_{12}}(\lambda_i)^2}\right.\right. \\ & + \frac{\left(m_{21}(\lambda_i) - m_{21}^c(\lambda_i,p)\right)^2}{\sigma_{m_{21}}(\lambda_i)^2} + \frac{\left(m_{33}(\lambda_i) - m_{33}^c(\lambda_i,p)\right)^2}{\sigma_{m_{33}}(\lambda_i)^2} \\ & + \frac{\left(m_{44}(\lambda_i) - m_{44}^c(\lambda_i,p)\right)^2}{\sigma_{m_{44}}(\lambda_i)^2} + \frac{\left(m_{34}(\lambda_i) - m_{34}^c(\lambda_i,p)\right)^2}{\sigma_{m_{34}}(\lambda_i)^2} \\ & \left.\left. + \frac{\left(m_{43}(\lambda_i) - m_{43}^c(\lambda_i,p)\right)^2}{\sigma_{m_{43}}(\lambda_i)^2} + \frac{\left(\eta(\lambda_i) - \eta^c(\lambda_i,p)\right)^2}{\sigma_{\eta}(\lambda_i)^2}\right]\right)\end{aligned} \tag{13}$$

where the superscript $c$ indicates calculated values, and $N$ is the number of wavelengths. The above equation can be minimized by applying a combination of global and local optimization algorithms, in our case we use differential evolution as a global optimization method [22] and the Levenberg-Marquardt method for local optimization. Once we have determined the best fit, we can also estimate the uncertainties, $u(p)$, from the diagonal elements of the covariance matrix ($\Sigma$) using

$$\Sigma = \left(\boldsymbol{J}^T U^{-1} \boldsymbol{J}\right)^{-1} \tag{14}$$

where $U$ is a matrix containing all the squared measurement uncertainties in the diagonal while all other entries are zero, and $\boldsymbol{J}$ is the Jacobian of the elements $m_{ij}^c$, $\eta^c$ and $h^c$ in **Eq. 13** with respect to the truncated cone parameters; height ($h$), width ($w$), and sidewall angle ($\theta$). $\boldsymbol{J}$ be expressed as

$$\boldsymbol{J} = \begin{bmatrix} \frac{\partial m_{ij}^c(\lambda_1)}{\partial h} & \frac{\partial m_{ij}^c(\lambda_1)}{\partial w} & \frac{\partial m_{ij}^c(\lambda_1)}{\partial \theta} \\ \vdots & \vdots & \vdots \\ \frac{\partial m_{ij}^c(\lambda_N)}{\partial h} & \frac{\partial m_{ij}^c(\lambda_N)}{\partial w} & \frac{\partial m_{ij}^c(\lambda_N)}{\partial \theta} \\ \frac{\partial \eta^c(\lambda_1)}{\partial h} & \frac{\partial \eta^c(\lambda_1)}{\partial w} & \frac{\partial \eta^c(\lambda_1)}{\partial \theta} \\ \vdots & \vdots & \vdots \\ \frac{\partial \eta^c(\lambda_N)}{\partial h} & \frac{\partial \eta^c(\lambda_N)}{\partial w} & \frac{\partial \eta^c(\lambda_N)}{\partial \theta} \\ \frac{\partial h^c}{\partial h} & \frac{\partial h^c(\lambda_n)}{\partial w} & \frac{\partial h^c}{\partial \theta} \end{bmatrix} \tag{15}$$

# 3 RESULTS AND DISCUSSION

The fitting of the Mueller ellipsometer and scatterometry signal for the silicon structures was performed as described in the previous sections and the results are shown in **Figure 5** and **Figure 6**.

The nonzero values of the elements in the off-diagonal blocks of the Mueller-matrix in **Figure 5** allow for an investigation of their interrelationships. A careful inspection provides the following relationships for all wavelengths: $m_{12} = m_{21}$, $m_{13} = m_{31}$, $m_{14} = m_{41}$, $m_{23} = m_{32}$, $m_{24} = m_{42}$, $m_{34} = -m_{43}$, $m_{33} = m_{44}$ leading to 8 unique elements that are reduced to 7 independent elements by **Eq. 8**. Of particular interest is when the sample is illuminated with unpolarized light $S_i = [1,0,0,0]^T$ (T denotes transpose). In this case according to **Eq. 11**, the Stokes vector of the reflected beam is determined from the elements in the first column of the Mueller-matrix $S_r = [1, m_{21}, m_{31}, m_{41}]^T$, the so-called polarizance of the sample. It can be noticed that $m_{31} = 0$, $m_{21} \neq 0$, and $m_{41} > 0$, indicating that the incident light is reflected with right-handed polarization, and that the most positive values of $m_{41}$ are found at low wavelengths. This conversion is possible if the sample has periodic structural anisotropy such that TE and TM waves experience different refractive indices (form birefringence

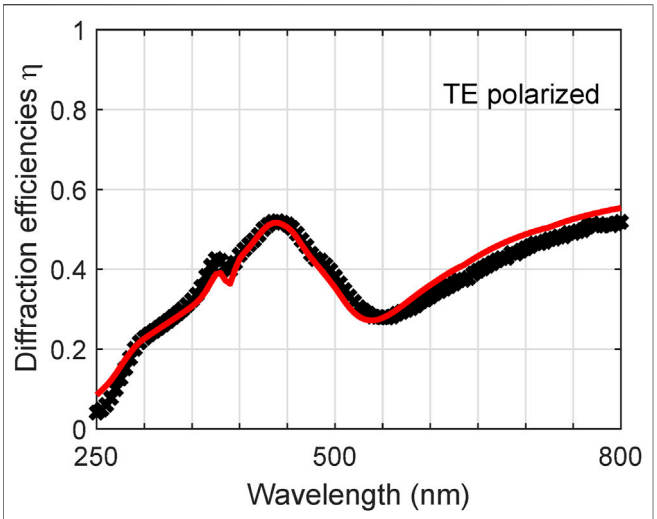


**FIGURE 6 |** Experimental scatterometry data (black crosses) and the corresponding optimal $\eta^c$ found by minimizing the expression in **Eq. 13** (red line).

[23]. The state of polarization of light can be visualized with the polarization ellipse and explained by two parameters: the ellipticity $e$ and the azimuth angle $\phi$. We will also use the ellipticity angle $\varepsilon = \arctan(e)$. The parameters $\varepsilon$ and $\phi$ are related to the Stokes vector $S$ in **Eq. 11**, which for the special case of incident unpolarized light can be expressed as [24].

$$\varepsilon = \frac{1}{2}\arcsin\left(\frac{m_{41}}{\sqrt{m_{21}^2 + m_{31}^2 + m_{41}^2}}\right)$$
$$\phi = \arctan\left(\frac{m_{21}}{m_{31}}\right). \tag{16}$$

**Eq. 16** yields $e \approx 0.1$ and $\phi \approx \frac{\pi}{2}$. We are thus lead to the conclusion that the truncated cone in **Figure 1** is not completely symmetric, but has shape anisotropy in the $y$-direction. We believe that it is this anisotropy that gives rise to the generally observed disagreement between experimental data and fit at lower wavelengths in **Figure 5**.

**Figure 7** shows the results obtained using only one of the methods (AFM, scatterometry and Mueller ellipsometry) and the results obtained by combining more than one method. We observe that all individual methods give a fair estimate of the measurand(s), with Mueller ellipsometry having the lowest uncertainties. The combination of the three technologies is expected to improve the results obtained from **Eqs 13–15** since the three technologies measure the dimensions by probing different physical measurands. AFM measures the physical height directly through contact forces between tip and sample, scatterometry optically assesses part of the Mueller matrix element $m_{11}$, and normalized Mueller ellipsometry measures the rest of the Mueller matrix elements, divided by $m_{11}$. The direct AFM height measurement constrains the height search to a more narrow region set by the Tikhonov penalty term

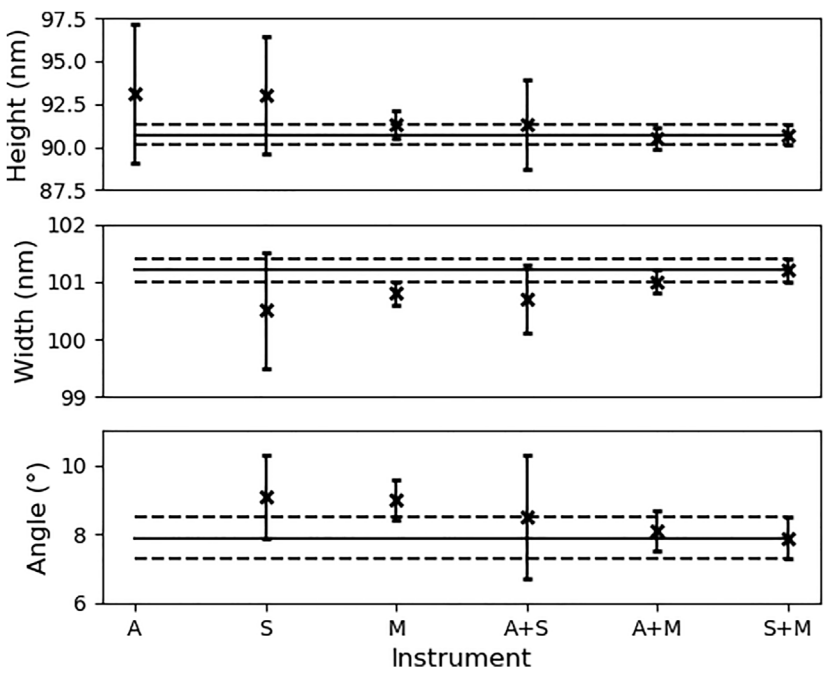


**FIGURE 7 |** Measurement results for the patterned silicon structure, $\Gamma_x = \Gamma_y = 200$ nm, with uncertainties. The fully drawn line corresponds to the result found by combining all instruments, and the dashed lines denote the upper and lower boundary defined by the uncertainties. The uncertainties shown are the $2\sigma$ taken at 95% confidence level. We use the abbreviations A for AFM, S for scatterometry, and M for Mueller ellipsometry in the figure. The corner roundings and the oxide layer has been locked to $R_{top} = R_{bot} = 5$ nm and $d = 2$ nm. AFM was only used for height measurement of the structures. The shown values are tabulated in **Supplementary Table S1**.

and is thus expected to influence the results if a strong correlation between grating parameters $p$ exist in the optical measurements. We furthermore observe that the results obtained by the combination of data from more than one method show a reduced sidewall angle, whereas smaller relative variations are observed in height and width. The results obtained from combining all methods are assumed to give the most robust results, and is therefore considered to be the best estimate of the correct results. **Figure 7** shows that the combination of AFM measurement with one of the optical methods moves the sidewall angle towards the best estimate, and that the combination of AFM and Mueller ellipsometry nearly gives the best estimate. It is also evident from the figure that the combination of the two optical methods reproduces the results obtained by combining all the methods. This shows that AFM measurement with the given uncertainty does not improve the result of combined Mueller ellipsometry and scatterometry, demonstrating that the combination of the two technologies reduces the correlation between the grating parameters $p$.

Precise measurement of sidewall angle has become increasingly important in the semiconductor industry for high precision measurement of the full width half maximum gate linewidth [5]; with decreasing gate line-width dimension. The most common source of sidewall angle variation is photoresist exposure due to focus variation. The sidewall angle is not well monitored by top-down CD-SEMs, which is typically employed to measure the top gate line-width [6]. Inverse modeling techniques like Mueller ellipsometry and scatterometry has an advantage by enabling complete sample profile control that allows simultaneous monitoring of height, width and sidewall angle. This work suggests that non-normalized Mueller ellipsometry in the form of combined Mueller ellipsometry and scatterometry is the optimal solution since it gives the same results as data fusion between AFM, Mueller ellipsometry and scatterometry. In our case, this is fortunate since scatterometry can be performed in the Mueller ellipsometry setup without moving the sample and at nearly no additional time cost. This work furthermore emphasizes the need for the development and calibration of an automated non-normalized Mueller ellipsometer for precision metrology inspection of nanostructures.

## 4 CONCLUSION

In the current work, the importance of hybrid metrology was discussed as a method for precision measurements of two dimensional periodic structures. We have presented and demonstrated the use of new and improved formulas for high precision Mueller ellipsometry. The analysis was carried out by setting up a regression problem that minimizes a $\chi^2$ loss function. The input to the loss function could be data from a single instrument or data from multiple instruments. The analysis demonstrates that data fusion from multiple instruments can be used to reduce the correlation between the dimensional parameters measured by the optical methods. The results for non-normalized Mueller ellipsometry, combination of scatterometry and normalized Mueller ellipsometry, is particularly interesting since it gives more accurate results than the other methods and the same accuracy as applying all hybrid methods. This demonstrates that non-normalized Mueller ellipsometry is a versatile method for periodic nanostructure reconstruction. The results also demonstrated that parameters such as sidewall angle, that were highly correlated for only one instrument, became less correlated if data for more instruments were analyzed together, making it possible to determine these parameters with higher accuracy. This study also suggests that at a certain point you do not get any improvement by adding input from more instruments if you already have found the best possible parameter set. The results of this work demonstrate that the developed method is capable of meeting the demands of height and width uncertainties less than 1 nm. This paper has also put great emphasis on instrument calibration, since it is very important for precision measurements. Finally, it has been demonstrated that the polarization ellipsoid obtained from Mueller ellipsometry can be used to determine the anisotropic shape of the geometrical structure, giving a better understanding of the data than if only scatterometry data is available.

## DATA AVAILABILITY STATEMENT

The raw data supporting the conclusions of this article will be made available by the authors, without undue reservation.

## AUTHOR CONTRIBUTIONS

PEH: RCWA theory and code writing. Calibration theory and code writing, inverse modelling theory, Mueller ellipsometer measurements, writing the paper. SRJ Discussing results and performing AFM measurements. SAJ Discussing results and writing the paper. JSMM: Mueller ellipsometer measurements, scatterometry measurements, inverse modelling coding and optimization, writing the paper.

## FUNDING

This project has received funding from the Danish Agency for Institutions and Educational Grants and the EMPIR project 15SIB09 3DNano. The EMPIR program is co-financed by the Participating States and from the European Union's Horizon 2020 research and innovation program. PEH and SAJ were supported by the Danish Agency for Institutions and the EMPIR projects 17FUN01 BeCOMe and 20FUN02 POLight, both cofinanced by the Participating States and from the European Union's Horizon 2020 research and innovation programme.

## SUPPLEMENTARY MATERIAL

The Supplementary Material for this article can be found online at: https://www.frontiersin.org/articles/10.3389/fphy.2021.791459/full#supplementary-material

## REFERENCES


1. Pan C, Liu Z, Pang Y, Zheng X, Cai H, Zhang Y, et al. (2018). Design of a High-Performance In-Coupling Grating Using Differential Evolution Algorithm for Waveguide Display. *Opt Express* 26, 26646–62. doi:10.1364/OE.26.026646
2. Lee W, Park S-J (2014). Porous Anodic Aluminum Oxide: Anodization and Templated Synthesis of Functional Nanostructures. *Chem Rev* 114, 7487–556. doi:10.1021/cr500002z
3. Bernd MGS, Bragança SR, Heck N, Filho LCd. S. Synthesis of Carbon Nanostructures by the Pyrolysis of wood Sawdust in a Tubular Reactor. *J Mater Res Technol* (2017) 6:171–7. doi:10.1016/j.jmrt.2016.11.003
4. VK Tewary, editor. *Modeling, Characterization, and Production of Nanomaterials*. Amsterdam: No. Number 73 in Woohead Publishing series in electronic and optical materialsElsevier (2015).
5. Bingham PR, Price JR, Tobin KW, Karnowski TP, Bennett MH, Bogardus EH, et al. Sidewall Structure Estimation from CD-SEM for Lithographic Process Control. In: KWT Jr. I Emami, editors. *Process and Materials Characterization and Diagnostics in IC Manufacturing*, 5041. Santa Clara, CA: International Society for Optics and Photonics (SPIE Event: Advanced Microelectronic Manufacturing) (2003). p. 115–26. doi:10.1117/12.485229
6. Lee H, Ranjan A, Prager D, Bandy KA, Meyette E, Sundararajan R, et al. *Advanced Profile Control and the Impact of Sidewall Angle at Gate Etch for Critical Nodes*. California, USA): San Jose (2008). p. 69220T. doi:10.1117/12.774962
7. Wurm M, Endres J, Probst J, Schoengen M, Diener A, Bodermann B. Metrology of Nanoscale Grating Structures by UV Scatterometry. *Opt Express* (2017) 25:2460. doi:10.1364/OE.25.002460
8. Chen X, Liu S, Zhang C, Jiang H, Ma Z, Sun T, et al. Accurate Characterization of Nanoimprinted Resist Patterns Using Mueller Matrix Ellipsometry. *Opt Express* (2014) 22:15165. doi:10.1364/OE.22.015165
9. Raymond C. Overview of Scatterometry Applications in High Volume Silicon Manufacturing. In: AIP Conference Proceedings, 788 (2005). p. 394–402. doi:10.1063/1.2062993
10. Moharam MG, Gaylord TK. Rigorous Coupled-Wave Analysis of Planar-Grating Diffraction. *J Opt Soc America* (1981) 71:811–8. doi:10.1364/JOSA.71.000811
11. Madsen MH, Hansen P-E. Scatterometry—fast and Robust Measurements of Nano-Textured Surfaces. *Surf Topography: Metrology Properties* (2016) 4: 023003–28. doi:10.1088/2051-672X/4/2/023003
12. Garcia-Caurel E, De Martino A, Gaston J-P, Yan L. Application of Spectroscopic Ellipsometry and Mueller Ellipsometry to Optical Characterization. *Appl Spectrosc* (2013) 67:1–21. doi:10.1366/12-06883
13. Compain E, Poirier S, Drevillon B. General and Self-Consistent Method for the Calibration of Polarization Modulators, Polarimeters, and Mueller-Matrix Ellipsometers. *Appl Opt* (1999) 38:3490. doi:10.1364/AO.38.003490
14. Jellison GE, Modine FA. Two-modulator Generalized Ellipsometry: experiment and Calibration. *Appl Opt* (1997) 36:8184. doi:10.1364/AO.36.008184
15. Tompkins HG, Irene EA. *Handbook of Ellipsometry*. Norwich: William Andrew Publishing (2005).
16. Arteaga O, Freudenthal J, Wang B, Kahr B. Mueller Matrix Polarimetry with Four Photoelastic Modulators: Theory and Calibration. *Appl Opt* (2012) 51: 6805–17. doi:10.1364/AO.51.006805
17. Hansen P-E, Madsen MH, Lehtolahti J, Nielsen L. Traceable Mueller Polarimetry and Scatterometry for Shape Reconstruction of Grating Structures. *Appl Surf Sci* (2017) 421:471–9. doi:10.1016/j.apsusc.2017.02.091
18. Fry ES, Kattawar GW. Relationships between Elements of the Stokes Matrix. *Appl Opt* (1981) 20:2811. doi:10.1364/AO.20.002811
19. Gil JJ, Bernabeu E. A Depolarization Criterion in Mueller Matrices. *Optica Acta Int J Opt* (1985) 32:259–61. doi:10.1080/713821732
20. Goldstein DH. *Polarized Light*. 3rd edn. Boca Raton: CRC Press (2011). p. 3.
21. Garnaes J, Kofod N, Kühle A, Nielsen C, Dirscherl K, Blunt L. Calibration of Step Heights and Roughness Measurements with Atomic Force Microscopes. *Precision Eng* (2003) 27:91–8. doi:10.1016/S0141-6359(02)00184-8
22. Hansen P-E, Nielsen L. Combined Optimization and Hybrid Scalar–Vector Diffraction Method for Grating Topography Parameters Determination. *Mater Sci Eng B* (2009) 165:165–8. doi:10.1016/j.mseb.2009.09.006
23. Richter I, Sun P-C, Xu F, Fainman Y. Design Considerations of Form Birefringent Microstructures. *Appl Opt* (1995) 34:2421. doi:10.1364/AO.34.002421
24. Arwin H, Magnusson R, Landin J, Järrendahl K. Chirality-induced Polarization Effects in the Cuticle of Scarab Beetles: 100 Years after Michelson. *Philos Mag* (2012) 92:1583–99. doi:10.1080/14786435.2011.648228
25. Hansen P-E, Madsen JS. Thickness and Refractive index Analysis of Ellipsometry Data of Ultra-thin Semi-transparent Films. In: *Imaging and Applied Optics 2018*, 24. JM4A: Optical Society of America (2018).


**Conflict of Interest:** The authors declare that the research was conducted in the absence of any commercial or financial relationships that could be construed as a potential conflict of interest.

frontiers in Physics

ORIGINAL RESEARCH
published: 21 January 2022
doi: 10.3389/fphy.2021.814559

# Mueller Matrix Ellipsometric Approach on the Imaging of Sub-Wavelength Nanostructures

*Tim Käseberg*[1]*, *Jana Grundmann*[1], *Thomas Siefke*[2], *Petr Klapetek*[3,4], *Miroslav Valtr*[3,4], *Stefanie Kroker*[1,5,6] *and Bernd Bodermann*[1]

[1]*Physikalisch-Technische Bundesanstalt, Braunschweig, Germany,* [2]*Institute of Applied Physics, Friedrich-Schiller-Universität, Jena, Germany,* [3]*Department of Primary Nanometrology and Technical Length, Czech Metrology Institute, Brno, Czechia,* [4]*CEITEC, University of Technology, Brno, Czechia,* [5]*Institut für Halbleitertechnik, Technische Universität, Braunschweig, Germany,* [6]*Laboratory for Emerging Nanometrology, Technische Universität, Braunschweig, Germany*

Conventional spectroscopic ellipsometry is a powerful tool in optical metrology. However, when it comes to the characterization of non-periodic nanostructures or structured fields that are much smaller than the illumination spot size, it is not well suited as it integrates the results over the whole illuminated area. Instead, imaging ellipsometry can be applied. Especially imaging Mueller matrix ellipsometry is highly useful in nanostructure characterization and defect inspection, as it is capable to measure the complete Mueller matrix for each pixel in a microscope image of the sample. It has been shown that these so-called Mueller matrix images can help to distinguish geometrical features of nanostructures in the sub-wavelength regime due to visible differences in off-diagonal matrix elements. To further investigate the sensitivity of imaging Mueller matrix ellipsometry for sub-wavelength sized features, we designed and fabricated a sample containing geometrical nanostructures with lateral dimensions ranging from 50 to 5,000 nm. The structures consist of square and circular shapes with varying sizes and corner rounding. For the characterization of their Mueller matrix images, we constructed an in-house Mueller matrix microscope capable of measuring the full Mueller matrix for each pixel of a CCD camera, using an imaging system and a dual-rotating compensator configuration for the ellipsometric system. The samples are illuminated at 455 nm wavelength and the measurements can be performed in both transmission and reflection. Using this setup, we systematically examine the sensitivity of Mueller matrix images to small features of the designed nanostructures. Within this contribution, the results are compared with traceable atomic force microscopy measurements and the suitability of this measurement technique in optical nanometrology is discussed. AFM measurements confirm that the fabricated samples closely match their design and are suitable for nanometrological test measurements. Mueller matrix images of the structures show close resemblance to numerical simulations and significant influence of sub-wavelength features to off-diagonal matrix elements.

**Keywords: metrology, nanometrology, ellipsometry, mueller ellipsometry, imaging ellipsometry, nanostructures, mueller matrix ellipsometry**

OPEN ACCESS

***Edited by:***
*Hao Jiang,*
*Huazhong University of Science and Technology, China*

***Reviewed by:***
*Alpan Bek,*
*Middle East Technical University, Turkey*
*Xiuguo Chen,*
*Huazhong University of Science and Technology, China*

***Correspondence:**
*Tim Käseberg*
*tim.kaeseberg@ptb.de*

***Specialty section:***
*This article was submitted to Optics and Photonics, a section of the journal Frontiers in Physics*

***Received:*** *13 November 2021*
***Accepted:*** *16 December 2021*
***Published:*** *21 January 2022*

***Citation:***
*Käseberg T, Grundmann J, Siefke T, Klapetek P, Valtr M, Kroker S and Bodermann B (2022) Mueller Matrix Ellipsometric Approach on the Imaging of Sub-Wavelength Nanostructures. Front. Phys. 9:814559. doi: 10.3389/fphy.2021.814559*

# 1 INTRODUCTION

When it comes to nanostructure characterization via optical metrology, spectroscopic ellipsometry is one of the most powerful and versatile tools available today [1–7]. Especially Mueller matrix ellipsometry, which measures all polarizing properties of the sample under investigation and summarizes them in a 4 by 4 Mueller matrix, is a useful method in layer composition characterization or the retrieval of geometrical parameters of periodic nanostructures [8–10]. As an optical technique, its advantages compared to other methods like atomic force microscopy (AFM) or scanning electron microscopy (SEM) lie in its non-invasive nature, speed, and low setup complexity. However, conventional spectroscopic ellipsometry meets its limits regarding measurements of structured fields smaller than the illumination spot. The measurement signal is usually integrated over the whole illuminated area on the sample. Thus, when the structured fields are inherently smaller than the illumination spot, unwanted signals from the surrounding disturb the measurement signal and lead to distorted results. An additional example where conventional ellipsometry is not well-suited is the measurement of structures that are non-periodic. The integrated Mueller matrix of an individual, non-periodic nanostructure can barely be distinguished from one measured on the substrate alone.

In the cases where conventional ellipsometry does not provide reliable measurement results due to the geometry of the sample, imaging ellipsometry can be used instead. In imaging Mueller matrix ellipsometry, an imaging system is integrated into the analyzing arm of the ellipsometer. This way, the influence of the sample on the polarization is examined spatially and a Mueller matrix for each pixel in an image of the sample is the result. Using such a setup, we can examine the polarizing properties of the sample locally, not limited by the illumination spot size. It is also possible to distinguish different regions of interest in the same measurement that possibly feature different structure characteristics, which makes it also a promising tool for defect inspection measurements [11–20].

The evaluation of Mueller matrix images is usually carried out using the same techniques as in conventional ellipsometry. Measurement results are averaged over homogeneous areas in the images and structural or material parameters are then determined with approximative models by solving the inverse problem [14, 19, 20]. In this paper however, we treat Mueller matrix images with rigorous three-dimensional models of single individual structures instead, by solving the inverse problem from numerically simulating the Mueller matrix images to find relations between nanostructure geometries and measurable effects in off-diagonal elements of the Mueller matrix. For this purpose, we realized an imaging Mueller matrix ellipsometry setup for reflection and transmission measurements at visible wavelengths, which for the first time also features a mode that enables reflection measurements under normal incidence. Thus, the setup combines an imaging Mueller matrix ellipsometer with a Mueller matrix microscope and allows fluid transitions between measurements from angles of incidence ranging between 0° and 90° without laborious reconstructions. Besides our setup, we show and discuss AFM and Mueller matrix measurements on a sample specially designed to test and demonstrate the sensitivity of Mueller matrix images to the form (ranging from circular to square) of individual nanoscale structures. The comparison of measurements and numerical simulations shows clear connections between the shape of nanostructures and their local influence on the Mueller matrix, which can help to reconstruct the non-periodic nanostructures from optical measurements alone. As a potential application for this serves the characterization of the resolution-induced corner rounding present in nanolithographically manufactured structures like semiconductor contact holes with symmetries comparable to the structures examined in this contribution. This paper is organized as follows: In **Section 2**, a thorough description of our imaging Mueller matrix ellipsometry setup as well as of the samples is given. **Section 3** presents the results of the measurements on the samples, followed by a discussion of the results in **Section 4**. In the end, **Section 5** summarizes our results.

# 2 MATERIALS AND METHODS

## 2.1 Imaging Mueller Matrix Ellipsometry

Our setup is schematically depicted in **Figure 1**. The general layout of the setup follows the dual-rotating compensator ellipsometry configuration [21], but with the arms moving in the horizontal plane as can be seen in the photography in **Figure 2**. A large aperture rotation stage forms the basis of this setup. It is used to rotate the analyzing arm of the ellipsometric system around the sample. The sample is mounted in the middle of the aperture of the large rotation stage on top of a smaller rotation stage and linear adjustment stages. This way, the sample can be rotated independently from the analyzing arm, which allows for measurements at arbitrary sets of incidence and reflection angles.

The illuminating arm (left side of **Figure 2**) begins with a light source, which is a blue LED with a center wavelength of 455 nm. The advantage of using monochromatic light with a short wavelength is that a higher resolution in the imaging system can be reached while keeping chromatic aberrations low. For applications at different wavelengths, the LED can be replaced by a white light LED and several filters. The light from the LED is then collected by a large lens, focused onto an aperture and then collimated. The lens system around the aperture serves as a telescope to guide the light through the following optics as well as to emulate a point source for easier collimation. Afterwards, a 90:10 beam splitter plate guides a portion of the light to a powermeter as an intensity reference before it hits the sample. The remaining light then passes a linear Glan-Thompson polarizer (PGT 2.10 from Bernhard Halle Nachfl. GmbH) as well as a superachromatic quarter-wave plate (RSU 1.4.10 from Bernhard Halle Nachfl. GmbH), which together form the polarization state generator. For the measurements shown here, the polarizer is fixed to a horizontal position while the quarter-wave plate is rotated to generate different states of polarization. After passing a 50:50 beam splitter cube (which

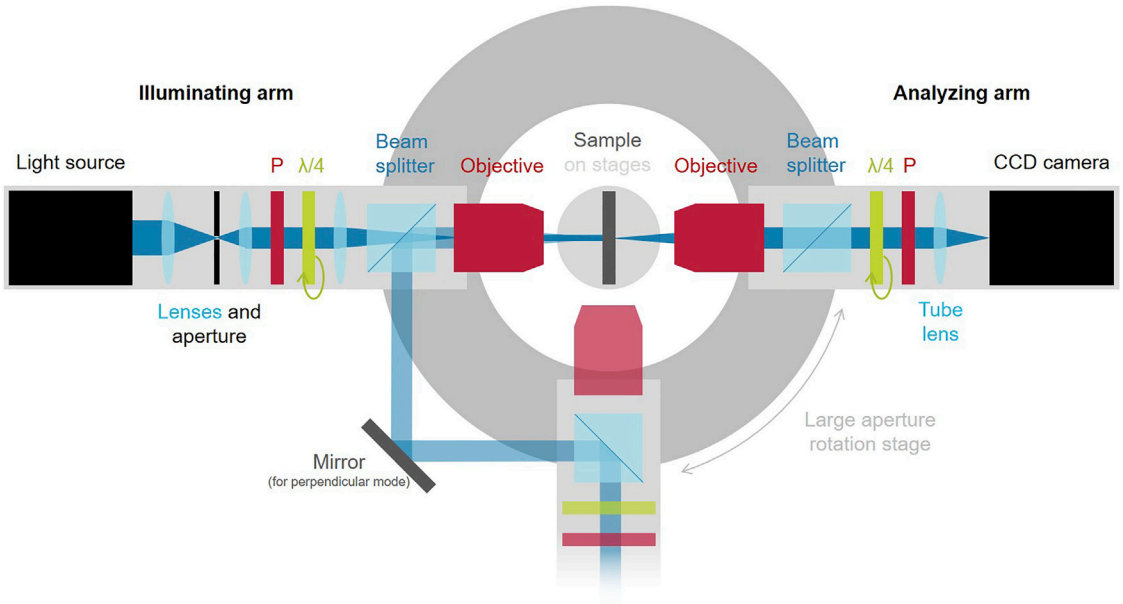


**FIGURE 1 |** Imaging Mueller matrix ellipsometry setup, top view sketch. P: polarizer, λ/4: quarter-wave plate.

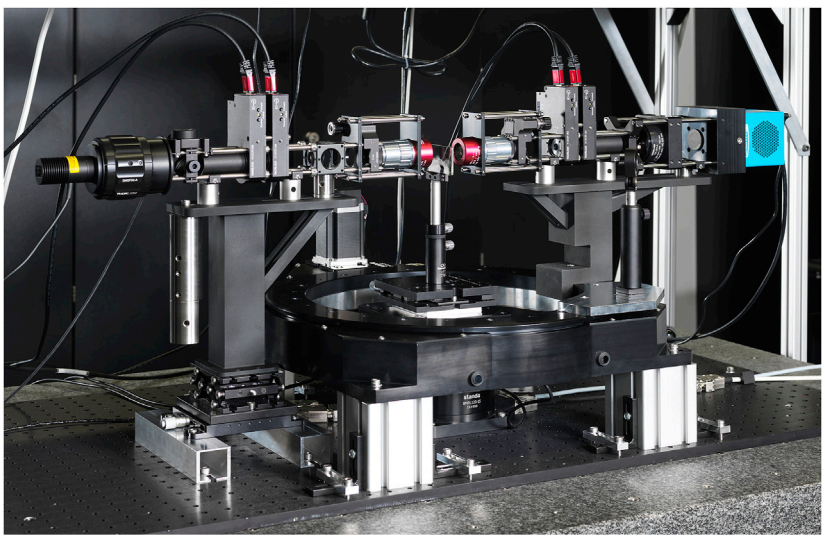

**FIGURE 2 |** Imaging Mueller matrix ellipsometry setup.

is used for perpendicular incidence measurements described below), the polarized light is then focused onto the back focal plane of an objective (M Plan Apo NIR B 50x from Mitutoyo). Due to the collimated light being focused on the objective's entry pupil, the light hitting the sample is mostly collimated again, leading to a homogeneous illumination of the sample in the imaging system. In optical microscopy, this configuration is referred to as Koehler illumination [22, 23]. Contrary to conventional, non-imaging ellipsometry, it is more important to generate a homogeneously illuminated image in this setup than to produce a small focal spot, because the results will be later evaluated for each individual pixel in the image instead of being integrated over the illuminated area.

The analyzing arm mostly mirrors the illuminating arm. It starts with another objective (M Plan Apo NIR B 50x from Mitutoyo) with a working distance of 25.5 mm, a numerical aperture of 0.42 and a ×50 magnification. The long working distance of the objectives allows for the measurement of samples with a diameter of up to 5 cm without restricting the movement of the arms around the sample. This enables a fluent transition

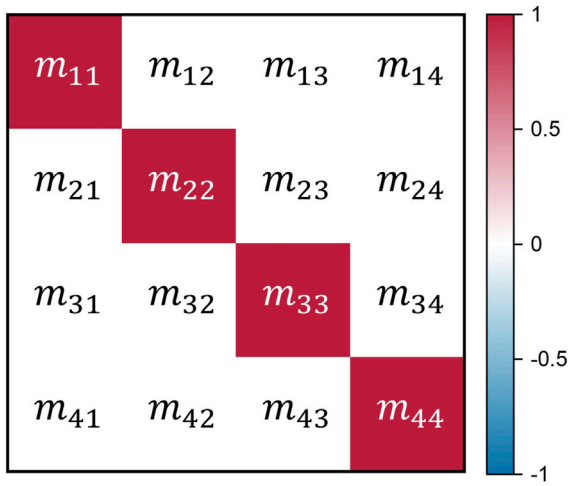


**FIGURE 3 |** Mueller matrix example for a transmission measurement without sample.

between reflection and transmission measurements. In reflection, angles of incidence between 90° and 37.5° can be reached, limited only by the size of the objectives. The polarization state of the light is then analyzed by another set of quarter-wave plate and linear polarizer, which both can again be rotated around the optical axis. Afterwards, a tube lens focuses the light onto the chip of a CCD camera. The camera chip features 2,688 by 2,200 pixels with a size of 4.54 µm by 4.54 µm [24].

Measurement results are presented as 4 by 4 Mueller matrices where each element contains one image with the values of this particular matrix element for each pixel in the image. To show a simple example for how measurements are presented in this contribution, an idealized transmission measurement without sample is shown in **Figure 3**. The values of the dimensionless matrix elements are color-coded, where red stands for a positive sign and blue represents a negative sign. The Mueller matrix of the free space is just the identity matrix, so all matrix elements in **Figure 3** are zero except for those on the main diagonal where they are 1. **Figure 3** also contains the common naming for the individual matrix elements, which are usually numbered in the following way:

$$\underline{M} = \begin{pmatrix} m_{11} & m_{12} & m_{13} & m_{14} \\ m_{21} & m_{22} & m_{23} & m_{24} \\ m_{31} & m_{32} & m_{33} & m_{34} \\ m_{41} & m_{42} & m_{43} & m_{44} \end{pmatrix}.$$

### 2.1.1 Microscopy Mode

For measurements at normal incidence, our setup features a special microscopy mode. In this mode, the analyzing arm is moved to a position in a 90° angle to the illuminating arm and a mirror is placed between the objective and the polarization state analyzer. The setup now resembles the layout of a conventional optical microscope with perpendicular incidence. This is also illustrated in **Figure 1** as the transparent beam path. The light reflected from the sample back into the objective of the illuminating arm is then guided by the beam splitter over the mirror and another beam splitter into the analyzing arm. This way, reflection measurements at normal incidence can be carried out without major reconstructions of the system. Additionally, the sample can still be rotated independently for angle corrections or potentially for minor scatterometric applications.

### 2.1.2 Measurement Procedure

The setup is operated with a standard dual-rotating compensator configuration [21]. During the measurement, the polarizers are fixed to parallel positions for high intensity throughput. The first polarizer imprints a linear polarization on the illumination from the light source while the second polarizer analyzes the state of polarization after interaction with the sample. Meanwhile, the first quarter-wave plate rotates in steps of 5°, and the second quarter-wave plate rotates in steps of 25°, which is a way to create a harmonic modulation of the states of polarization. The modulated intensity measured at each pixel of the CCD camera depends not only on the polarizing optics in the system, but also on the influence of the Mueller matrix of the sample, and can be described as:

$$I = c \cdot \sum_{i,j=1}^{4} a_i p_j m_{ij}, \tag{1}$$

where $p$ and $a$ represent the elements of the Stokes vectors resulting from the influence of the optical components in the illuminating and the analyzing arm, respectively, starting from an unpolarized light source. The elements of the Mueller matrix of the sample are described by $m_{ij}$ (compare **Figure 3**), while $c$ is a constant factor for the camera sensitivity [21]. This modulated intensity can be evaluated by a Fourier analysis in each individual pixel of the CCD camera to obtain the Mueller matrix elements $m_{ij}$ for each pixel and thus Mueller matrix images [25].

The stepwise movement of the compensators allows for a better control of the measurement as well as a better quality of the measured images in the CCD camera. At each step, several images can be recorded and averaged for a reduction of image noise. This method leads to measurement times of about 7 minutes for a full rotation of the first compensator. Alternatively, a continuous rotation mode where the movement of the retarders is synchronized with the frame rate of the camera is possible to speed up the measurement at the expense of image quality. The evalutation of the Mueller matrix images is performed using a custom built Python program.

## 2.2 Nanoform Sample

For systematic tests on the influence of the form and symmetry of nanostructures on off-diagonal Mueller matrix elements, we designed and fabricated a sample consisting of individual structures written into a 100 nm thick layer of polymethylmethacrylat (PMMA) on a 100 mm diameter silicon wafer using electron beam lithography. The structures are placed in the middle of 5 mm by 5 mm sized fields on the sample to prevent interactions between different structures and to leave enough room for the illumination spot of the measurement

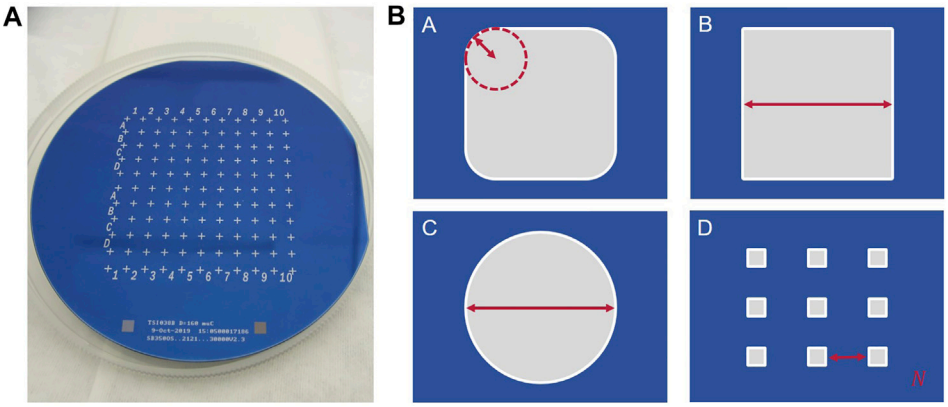


**FIGURE 4 |** Overview of the sample with nanoform structures. **(A)** Wafer with columns and rows. Structure parameters are varied over the columns. **(B)** Sketches of the structures in the different rows. Red arrows highlight which parameters are varied. **(i)**: Corner rounding of fixed size squares. **(ii)**: Size of squares. **(iii)**: Size of circles. **(iv)**: Pitch and number (*N*) of structures in a small array.

**TABLE 1 |** Sample design feature parameter overview.

| Row | A | B | C | D |
|---|---|---|---|---|
| **Feature** | **Corner radius** | **Width** | **Diameter** | **Number, pitch** |
| **Column** | — | — | — | — |
| 1 | 100 nm | 50 nm | 50 nm | 1 × 1, 10 µm |
| 2 | 150 nm | 75 nm | 75 nm | 2 × 2, 10 µm |
| 3 | 200 nm | 100 nm | 100 nm | 3 × 3, 10 µm |
| 4 | 300 nm | 200 nm | 200 nm | 4 × 4, 10 µm |
| 5 | 400 nm | 250 nm | 250 nm | [empty] |
| 6 | 500 nm | 500 nm | 500 nm | 1 × 1, 20 µm |
| 7 | 750 nm | 750 nm | 750 nm | 2 × 2, 20 µm |
| 8 | 1,000 nm | 1,000 nm | 1,000 nm | 3 × 3, 20 µm |
| 9 | 1,500 nm | 1,500 nm | 1,500 nm | 4 × 4, 20 µm |
| 10 | 2,000 nm | 2,000 nm | 2,000 nm | [empty] |
| **Fixed** | Width = 5 µm | — | — | Width = 1 µm |

system to only illuminate one structure at a time. An overview of the sample is depicted in **Figure 4**. The fields are organized in rows, labeled from A to D, for different structure types and in columns, labeled from 1 to 10, for different feature sizes. Row A contains square structures with 5 µm width and height and varying corner radii between 100 nm and 2 µm, resulting in a transition from nearly perfect square to nearly perfect circle. Rows B and C contain square and circular structures, respectively, ranging in diameter from 50 nm to 2 µm. Row D contains small arrays of 1 µm sized squares with 10 and 20 µm pitch and up to 4 by 4 squares per array. For a more detailed list of the sample parameters, **Table 1**. Previously, a test wafer has been produced and characterized concerning the feature size fabrication accuracy using SEM [26].

## 2.3 Simulations

For an elaborated evaluation of ellipsometric measurements, the solution of the inverse problem is usually needed. In this course, a model of the examined structures is built and then fitted to the measurement results to retrieve information like layer thicknesses, structure geometries, or material parameters. However, in the case of imaging ellipsometry on non-periodic structures, their simulation is inherently more complex than for simple layer structures, periodic structures, or in non-imaging ellipsometry. The reason for this is the need for three-dimensional models of the structure itself which take significantly higher computational costs compared to the periodic two-dimensional models in conventional ellipsometry or the layer-stack models usually used in imaging ellipsometry [4, 27]. Only by modelling the nanostructures in three dimensions, the local influence of the geometric parameters of non-periodic nanostructures on the Mueller matrix can correctly be accounted for. Additionally, for a correct reconstruction of the Mueller matrix images measured with an imaging system, the simulation of microscope images with a defined illumination would be needed. This includes the superposition of many simulations at different pupil points inside the numerical aperture of the light illuminating the sample. In doing so, a high number of pupil points is as important as their distribution inside the numerical aperture, and both affect the computational costs of solving the inverse problem as a whole [28, 29].

For this reason, we modelled the structures on the sample using the finite element method (FEM) Maxwell solver JCMsuite [30] based only on the target values for a qualitative comparison. The illumination was simulated using only one pupil point, which corresponds to a plane wave illumination, at 455 nm wavelength under perpendicular incidence. Using mesh sizes of up to 500 nm and finite element degrees up to 5, computational costs for the simulation of one structure included about 350 GB RAM and about 2 h of computation time.

# 3 RESULTS

## 3.1 Imaging Mueller Matrix Measurements

The structures in row A on the sample feature 5 µm by 5 µm sized square structures with different corner radii. We measured the Mueller matrix images of these structures at our setup, using the perpendicular incidence microscopy mode. As an example, **Figure 5A**) shows the results for structures A1, A5, and A10.

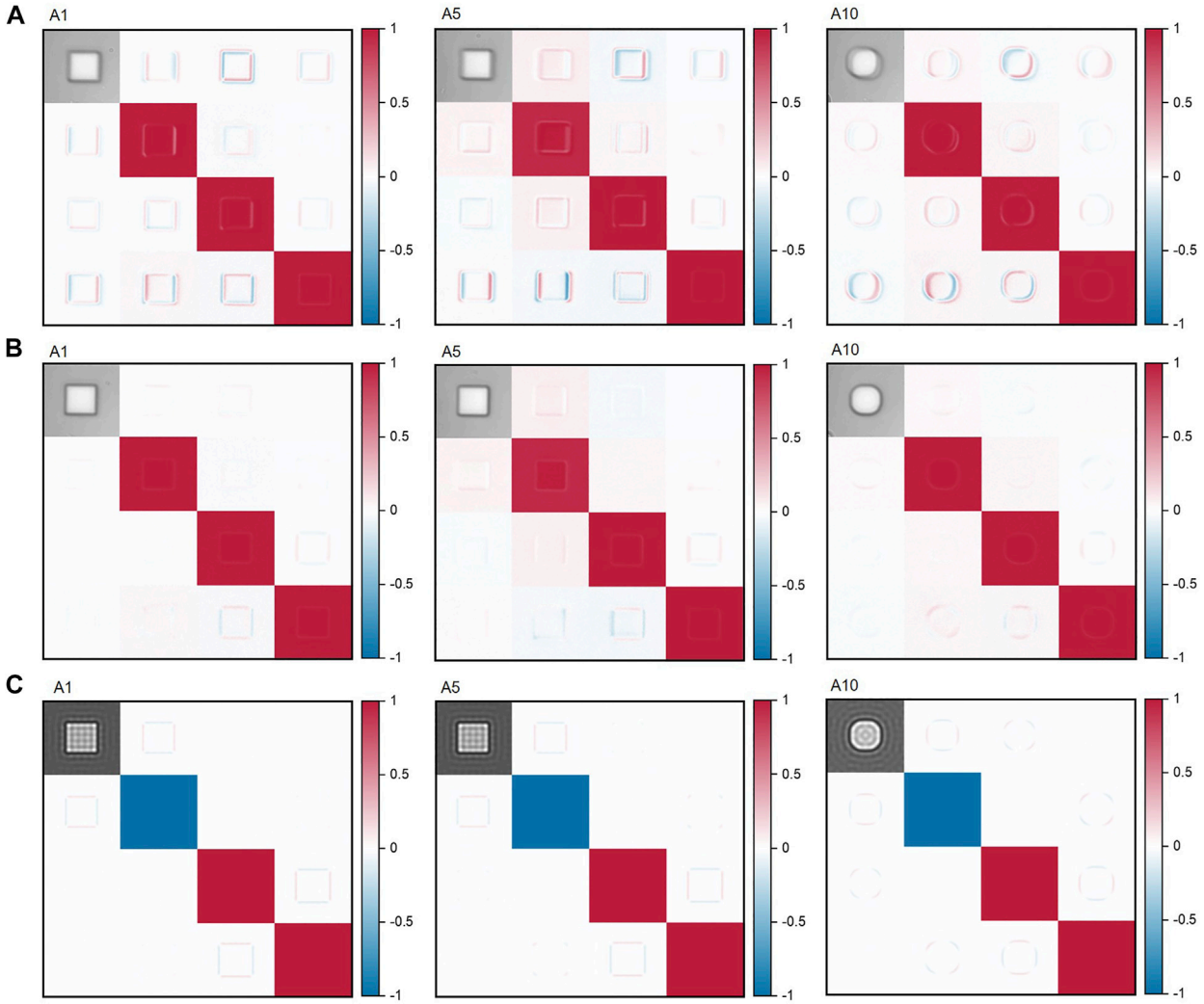


**FIGURE 5 |** Mueller matrix images of structures A1, A5, and A10, **(A)** not corrected for thermal drift, **(B)** corrected for thermal drift, and **(C)** simulated. Target feature sizes: 5 µm width and height, corner radii: 100 nm (A1), 400 nm (A5), 2000 nm (A10).

For comparison, the structures of row A on the sample were also simulated using FEM. The resulting Mueller matrix images for the structures A1, A5, and A10 are presented in **Figure 5C**). Images and results of the remaining structures can be found in the supplement.

The square and circular structures in rows B and C range in size from 50 nm to 2 µm. To test the resolution of our setup, we measured Mueller matrix images of the circular structures in row C. As square structures tend to degenerate into circular ones for very small structure sizes due to the fabrication process, we focused on the evaluation of the circular structures first. **Figure 6** shows the measured Mueller matrix images of the structures C6 and C10 as an example.

## 3.2 AFM Measurements

For comparison with the measurements at our imaging Mueller matrix ellipsometry setup, we performed measurements using a metrological scanning probe microscope (SPM) [31] and a commercial AFM with a high aspect ratio probe that was calibrated using the metrological SPM and a transfer standard. The scan size and resolution were adapted to the feature size, typically using 1,024 by 1,024 pixels per image. The data was processed in the open-source software Gwyddion [32].

For row A, the structures A1, A5, A6, and A10 were measured. Measurements on the structures in row A were evaluated using the Gwyddion function "Fit shape" and using a parametric model for a hole with round corners. Measured images are shown in **Figure 7** and an example of the fitted shape difference from the measured data is shown in **Figure 8**. Measured feature sizes are summarized in **Table 2**. The measurement uncertainty was estimated to be 20 nm. The uncertainty estimations given here are based on the typical uncertainties of the microscopes, repeatability, and estimates of the major uncertainty influences during the measurement (fast axis direction, feedback loop

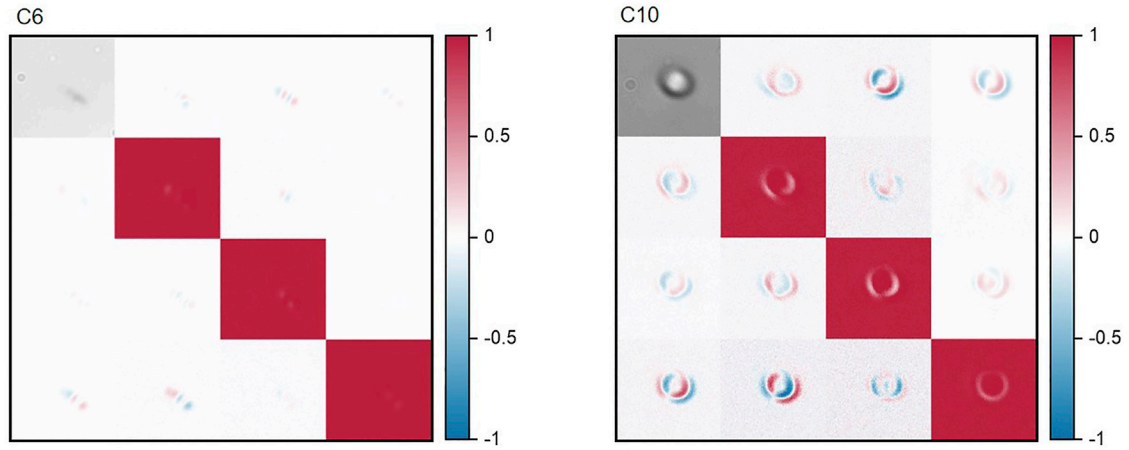


**FIGURE 6 |** Mueller matrix images of structures C6 and C10 not corrected for thermal drift. Target feature sizes: 500 nm width (C6) and 2000 nm width (C10).

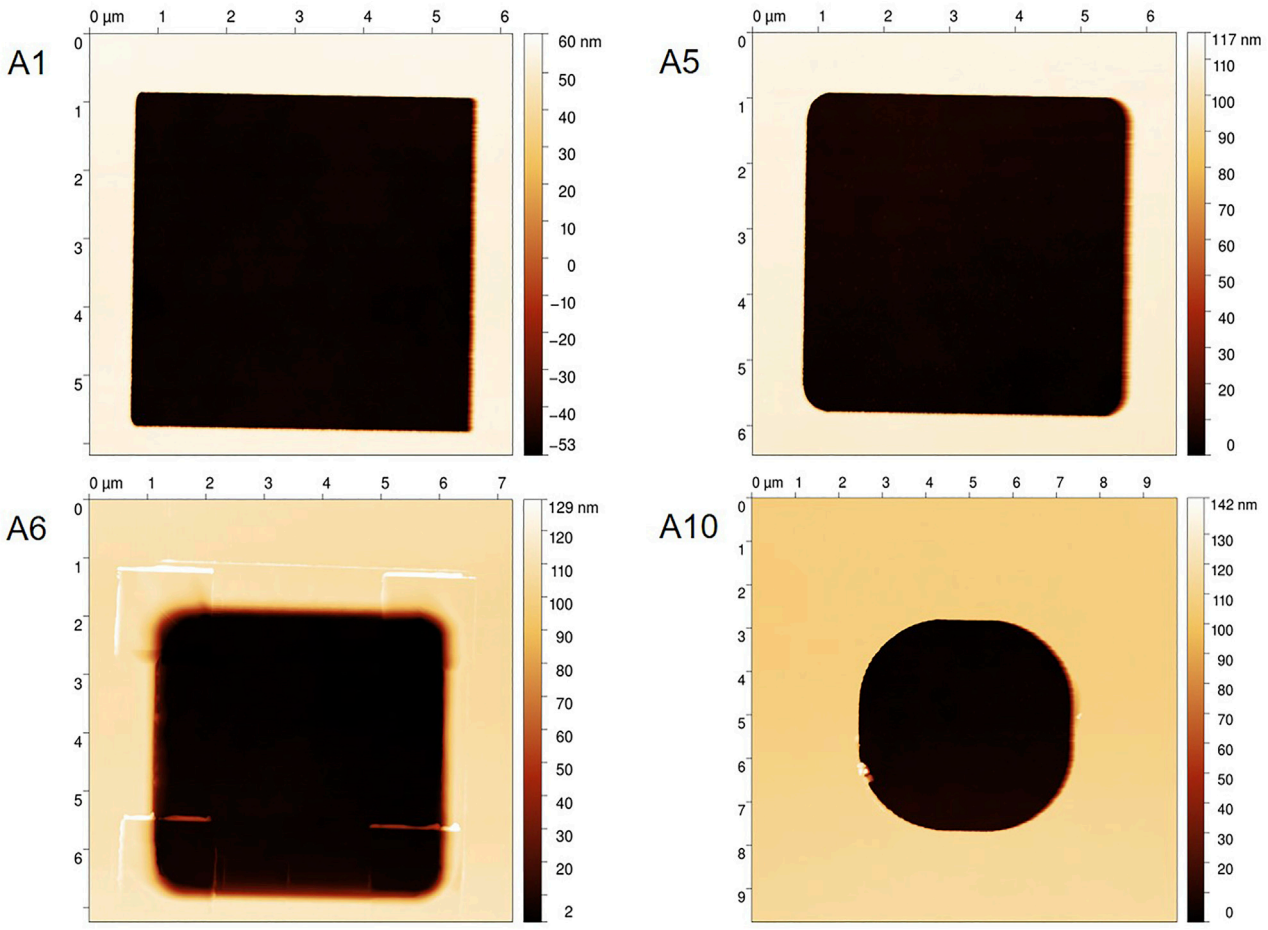


**FIGURE 7 |** AFM measurements of structures in row A.

effects, tip convolution, drift, fit error). The biggest contribution is the tip shape, which affects nearly all the measurements on smaller spots, as can be also seen from the images.

Measurements of the structures B4, B6, C4, C6, D4, and D9 are shown in **Figure 9**. Results for the structures are collected in **Table 3**. The uncertainty is predominantly influenced by the tip

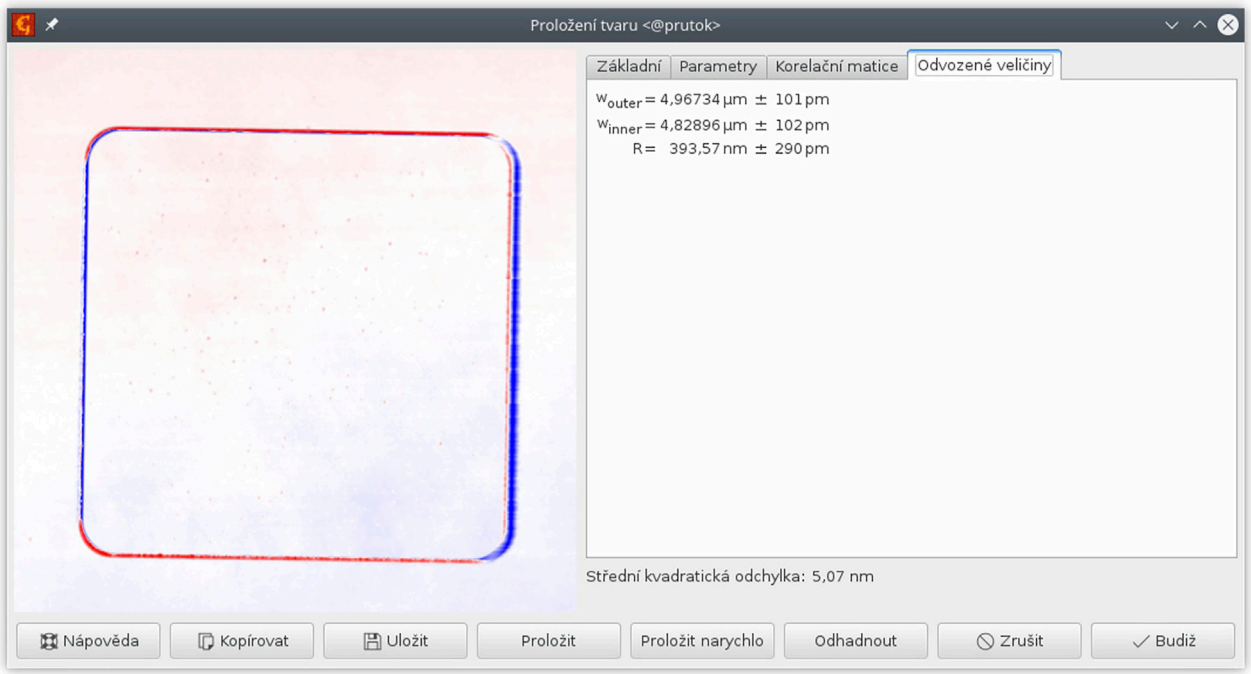


**FIGURE 8 |** Example for fitted shape difference of AFM measurements.

**TABLE 2 |** Feature sizes of structures in row A, measured by AFM.

| Structure | Outer width/µm | Inner width/µm | Radius/nm | Target radius/nm |
|---|---|---|---|---|
| A1 | 5.007 | 4.855 | 111 | 100 |
| A5 | 4.967 | 4.829 | 394 | 400 |
| A6 | 5.210 | 4.697 | 571 | 500 |
| A10 | 4.977 | 4.806 | 2013 | 2000 |

radius. This component was estimated to be 13 nm for width measurements and 30 nm for pitch measurements.

## 4 DISCUSSION

The sizes of the nanoform structures were characterized using traceable AFM. For row A, the structures A1, A5, A6, and A10 were examined. The measured outer widths deviate on average by 1.4% from the fabrication target value of 5 µm. The measured corner radii of these structures deviate from the design by 6.8% on average. Width and corner radius deviation are largely influenced by partial resist damage in structure A6 as visible in **Figure 7**. For the structures in row B and C, the measured feature sizes deviate on average by 8 nm from the design, which is smaller than the estimated measurement uncertainty of 13 nm due to the tip shape. The pitches of the structures measured in row D match the design with a deviation of 14 nm for D4 and 22 nm for D9, which is smaller than the uncertainty estimation for pitch measurements of 30 nm for D4 and 61 nm for D9. The size of the structures varies only by 0.4% nm on average. All in all, the fabricated structures on the sample closely match the design and can be used for further nanoform characterization measurements.

Mueller matrix image measurements on the structures A1, A5, and A10 are depicted in **Figure 5A**). As usual, the Mueller matrix elements are all normalized to the first element $m_{11}$ in the upper left corner, except for this element itself, as it mostly represents the overall measured intensity. The measurements were performed in the perpendicular incidence mode, so the light passed a couple of mirrors on its way to the camera. For this reason, the Mueller matrix images look like transmission measurements, with all main diagonal elements being positive comparable to **Figure 3**, although the light was measured in reflection from the sample. Furthermore, the images were normalized to a reference measurement on the substrate that was taken right after the measurement of the structure to eliminate polarizing effects from the optical elements as well as influences from the substrate itself. The first elements of each Mueller matrix show a certain blur that also reappears in the other matrix elements. This blur is most likely caused by thermal drift of the sample during the measurement. It is accounted for by a drift correction algorithm: In each image of a measurement series, the structure under investigation is detected and the image then recentered to the center of mass of the

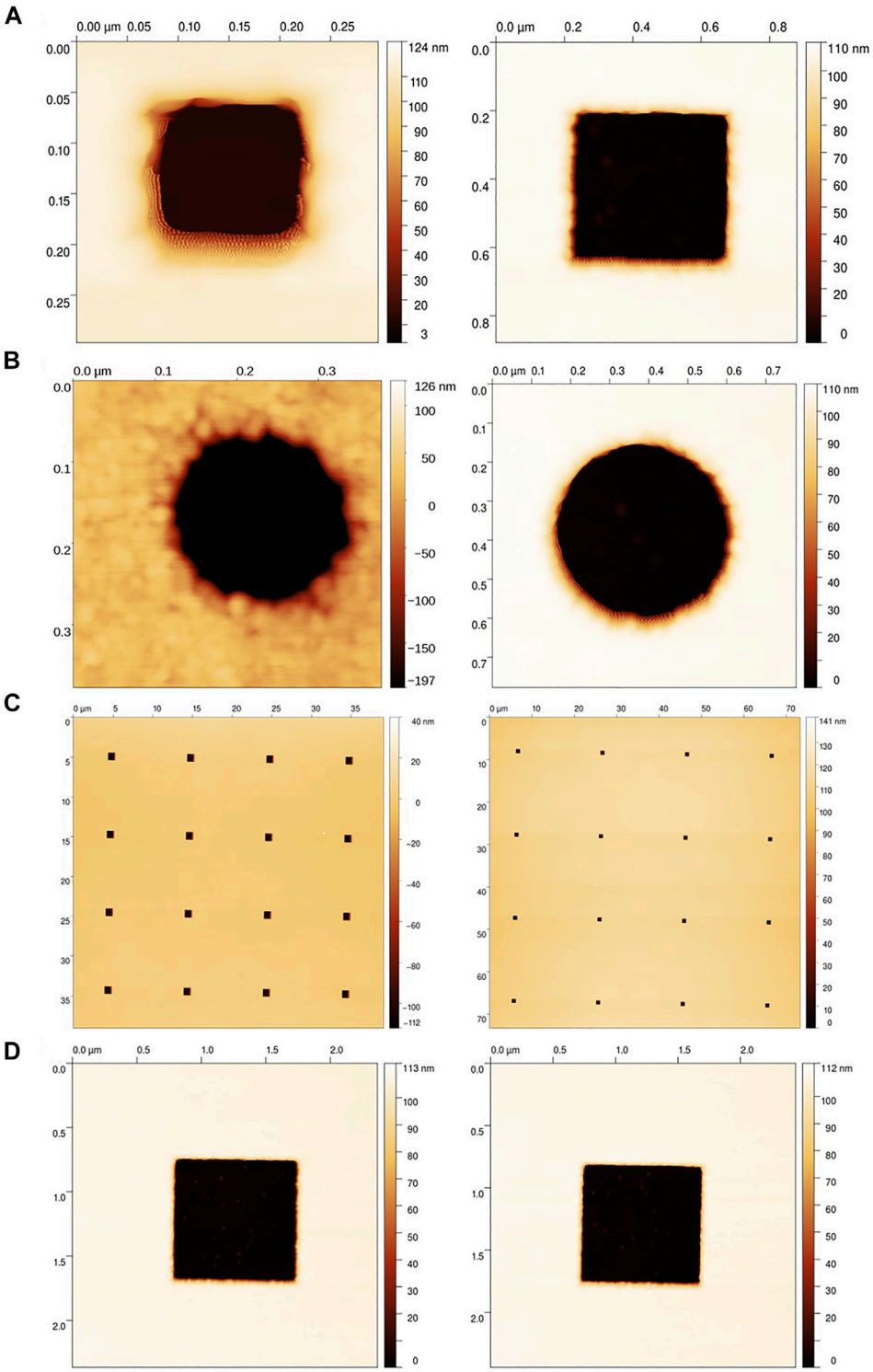


**FIGURE 9 |** AFM measurements of structures **(A)** B4 and B6, **(B)** C4 and C6, and **(C)** D4 and D9 with **(D)** details of single squares.

**TABLE 3 |** Feature sizes of structures in row B, C, and D, measured by AFM.

| Structure | Structure diameter/nm | Target diameter/nm | Pitch/µm | Target pitch/µm |
|---|---|---|---|---|
| B4 | 189 | 200 | – | – |
| B6 | 499 | 500 | – | – |
| C4 | 182 | 200 | – | – |
| C6 | 499 | 500 | – | – |
| D4 | 1,005 | 1,000 | 10.014 | 10 |
| D9 | 1,002 | 1,000 | 20.022 | 20 |

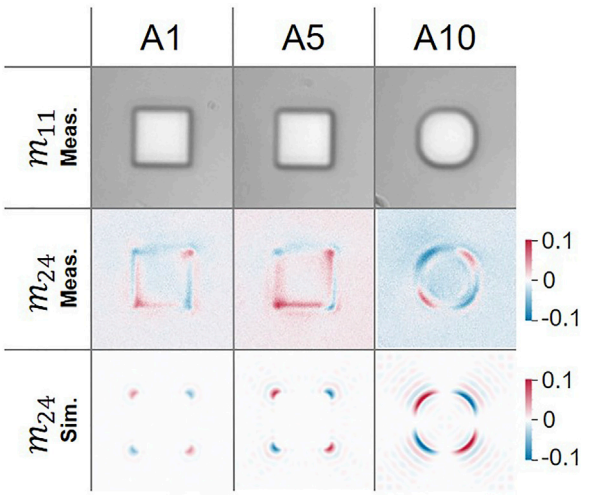


**FIGURE 10 |** Selected Mueller matrix images of structures A1, A5, and A10: Measured $m_{11}$ element and measured and simulated $m_{24}$ elements. Measurement results from drift corrected measurements.

structure. This way, we obtained the drift corrected Mueller matrix images presented in **Figure 5B**) for the structures A1, A5, and A10. A more detailed view of selected images is given in **Figure 10**.

The drift corrected Mueller matrix images show distinct polarization effects at the edges of the structures. These effects would not be measurable in conventional, non-imaging ellipsometry. The effects visible in the uncorrected images are noticeably more pronounced, but are also mostly caused by the thermal drift of the structure. However, the edge effects that are left after the drift correction are inherently local polarization effects caused by the sample. This is confirmed by the simulation results depicted in **Figure 5C**). The simulation results represent idealized measurement results, because for the simulation, the design target values where used and the illumination was assumed to be a perfect plane wave from only one pupil point. During measurements with the setup in perpendicular incidence mode, the light that was reflected from the sample back into the first objective is guided to the analyzing system by several mirrors. In this course, each reflection changes the sign of some of the Mueller matrix elements. Because of this, the measured Mueller matrix looks like a transmission measurement. However, the simulation does not take these mirrors into account. Therefore, some simulated Mueller matrix elements have the opposite sign compared to the measurements, which is most prominent in the $m_{22}$ element. Nevertheless, even without an optimization of the geometrical parameters towards the measured values or using a more elaborate model of the illumination, the local polarization effects visible at the edges and corners of the structures closely resemble the ones observed in the drift corrected measurements, indicating a successful suppression of the drift effect from the correction algorithm.

Concerning their metrological use, the off-diagonal Mueller matrix images deliver additional information channels for structure form characterization exceeding optical microscopy alone. In **Figure 10**, the Mueller matrix elements $m_{11}$ and $m_{24}$ of the measurements as well as $m_{24}$ of the simulations of the structures A1, A5, and A10 are visualized with color bars adjusted to the range of only these elements. Although the $m_{11}$ elements of structures A1 and A5 are visibly indistinguishable, the off-diagonal matrix elements show clear indications on the changing corner rounding from 100 to 400 nm. Especially in element $m_{24}$, the change is evident from the absolute value of the matrix element in the corners changing by 15% in the measurements and 85% in the simulations. The change from A5 to A10 is with about 160% in both measurements and simulations even more pronounced. Other off-diagonal matrix elements, like $m_{42}$, $m_{13}$ and $m_{31}$, also show increasing absolute values in the corners or on the edges of the structures with an increased corner radius. Thus, local geometry features like the orientation of an edge or the curvature of a corner do have significant connections to the sign and value of the local Mueller matrix, even for changes below the wavelength of the illumination, which can be exploited for example by fitting an appropriate three-dimensional model to the structure to solve the inverse problem and retrieving the structural parameters.

The measurements on the smaller structures in rows B and C were also affected by the thermal drift discussed earlier, as can be seen from the example measurements in **Figure 6** on C6 and C10. However, the drift correction algorithm was not able to reliably recognize these structures because of their small size. Therefore, these measurements could not be corrected yet and no meaningful comparison with simulated results would be possible on the uncorrected images. Thus, no clear indications about the resolution limits of our measurement technique could be gained by now. However, the visible difference in off-diagonal matrix elements for structures A1 and A5 with corner radii 100 and 400 nm, respectively, promises a possible distinction of feature sizes well below the wavelength of the system.

## 5 CONCLUSION

In this contribution, we presented our imaging Mueller matrix ellipsometry setup which we constructed and tested on specially designed nanostructures to further investigate in the link between geometrical features and off-diagonal Mueller matrix elements. Our setup has a horizontal positioning of the analyzing ellipsometer arm, enabling us to perform measurements in transmission as well as reflection at arbitrary angle combinations in the visible wavelength regime. Therefore, reflection measurements can be performed between 37.5° and 90° angles of incidence. Additionally, our setup features a microscopy mode that allows for reflection measurements at perpendicular incidence without major reconstructions of the setup. To examine the influence of the form of nanostructures on Mueller matrix elements, we designed and fabricated a collection of structures with simple geometrical shapes and sizes ranging from 50 nm to 5 μm. Traceable AFM measurements showed that the fabricated samples closely match the design, with average size deviations of 2.1% and average corner radius deviations of 6.8%. These deviations can partially be explained by the finite tip shape of the AFM, but are most likely due to fabrication tolerances. The overall small deviation from the design makes the structures suitable for further nanometrological test measurements. We measured structures of the rows A and C using our Mueller matrix microscopy setup. Due to thermal drifts of the sample, the smaller structures in row C could not be evaluated meaningfully. For the larger structures in row A, a drift correction algorithm was successfully implemented and the resulting corrected Mueller matrix images compared to FEM simulations of the design structures. Even without fitting the simulations to the measurements, we could observe a close resemblance of the measurements to the simulations. Furthermore, the measurements as well as the simulations showed a significant influence of a change in the corner radius of the structures from 100 to 400 nm on off-diagonal Mueller matrix elements, most prominently $m_{24}$ and $m_{42}$. This reinforces the potential of imaging Mueller matrix ellipsometry in metrological applications towards the characterization of sub-wavelength sized nanostructures.

## DATA AVAILABILITY STATEMENT

The original contributions presented in the study are included in the article/**Supplementary Material**, further inquiries can be directed to the corresponding author.

## AUTHOR CONTRIBUTIONS

TK: Performing Mueller matrix ellipsometry measurements, code writing, discussing results, writing the paper. JG: Code writing, performing Mueller matrix ellipsometry measurements. TS: Sample fabrication and preparation. PK and MV: Performing AFM measurements and discussing results. SK and BB: Discussing results and writing the paper.

## FUNDING

This work is funded through the project 17FUN01 "BeCOMe" within the Programme EMPIR. The EMPIR initiative is co-founded by the European Union's Horizon 2020 research and innovation program and the EMPIR Participating Countries. This project (20FUN02 "POLight") has received funding from the EMPIR programme co-financed by the Participating States and from the European Union's Horizon 2020 research and innovation programme. SK also acknowledges partial support by the Deutsche Forschungsgemeinschaft (DFG, German Research Foundation) under Germanys Excellence Strategy—EXC-2123 QuantumFrontiers—390 837 967.

## SUPPLEMENTARY MATERIAL

The Supplementary Material for this article can be found online at: https://www.frontiersin.org/articles/10.3389/fphy.2021.814559/full#supplementary-material

## REFERENCES

1. Rothen A The Ellipsometer, an Apparatus to Measure Thicknesses of Thin Surface Films. *Rev Scientific Instr* (1945) 16:26–30. doi:10.1063/1.1770315
2. Vedam K Spectroscopic Ellipsometry: a Historical Overview. *Thin Solid Films* (1998) 313-314:1–9. doi:10.1016/s0040-6090(97)00762-1
3. Losurdo M Applications of Ellipsometry in Nanoscale Science: Needs, Status, Achievements and Future Challenges. *Thin Solid Films* (2011) 519:2575–83. doi:10.1016/j.tsf.2010.11.066
4. M Losurdo, editor. *Ellipsometry at the Nanoscale*. Berlin, Heidelberg: Springer (2013).
5. Chen X, Liu S, Zhang C, Jiang H, Ma Z, Sun T, et al. Accurate Characterization of Nanoimprinted Resist Patterns Using Mueller Matrix Ellipsometry. *Opt Express* (2014) 22:15165–77. doi:10.1364/OE.22.015165
6. Liu S, Chen X, Zhang C Development of a Broadband Mueller Matrix Ellipsometer as a Powerful Tool for Nanostructure Metrology. *Thin Solid Films* (2015) 584:176–85. doi:10.1016/j.tsf.2015.02.006
7. Rossow U A Brief History of Ellipsometry. *Phys Status Solidi B* (2019) 256:1800307. doi:10.1002/pssb.201800307
8. Azzam R. Mueller-matrix Ellipsometry: a Review. *Spie-int Soc Opt Eng* (1997) 3121:396–405. doi:10.1117/12.283870
9. Dixit D, Keller N, Lifshitz Y, Kagalwala T, Elia A, Todi V, et al. Nonconventional Applications of Mueller Matrix-Based Scatterometry for Advanced Technology Nodes. *J Micro/Nanolithography, MEMS, MOEMS* (2018) 17:034001. doi:10.1117/1.jmm.17.3.034001
10. Voloshenko I, Gompf B, Berrier A, Dressel M, Schnoering G, Rommel M, et al. Mueller Matrix Metrology: Depolarization Reveals Size Distribution. *Appl Phys Lett* (2019) 115:063106. doi:10.1063/1.5094409
11. Chipman RA, Pezzaniti JL. Imaging Ellipsometry of Optical Coatings *In Situ*. In: *Optical Thin Films IV: New Developments*, Vol. 2262. Bellingham, Washington, USA: International Society for Optics and Photonics (1994). p. 124–34.
12. Jin G, Jansson R, Arwin H Imaging Ellipsometry Revisited: Developments for Visualization of Thin Transparent Layers on Silicon Substrates. *Rev Scientific Instr* (1996) 67:2930–6. doi:10.1063/1.1147074
13. Kerwien N *Zum Einfluss von Polarisationseffekten in der mikroskopischen Bildentstehung*. Stuttgart, Germany: Universität Stuttgart (2007). doi:10.18419/opus-4130
14. Asinovski L, Beaglehole D, Clarkson MT Imaging Ellipsometry: Quantitative Analysis. *Phys Stat Sol (A)* (2008) 205:764–71. doi:10.1002/pssa.200777855

15. Mujat M, Iftimia N, Ferguson D, Hammer D. Mueller Matrix Microscopy. In: *Biomedical Optics*. Washington, D.C., USA: Optical Society of America (2010). p. BSuD60.
16. Liu S, Du W, Chen X, Jiang H, Zhang C Mueller Matrix Imaging Ellipsometry for Nanostructure Metrology. *Opt Express* (2015) 23:17316–29. doi:10.1364/OE.23.017316
17. Chandel S, Soni J, Ray SK, Das A, Ghosh A, Raj S, et al. Complete Polarization Characterization of Single Plasmonic Nanoparticle Enabled by a Novel Dark-Field Mueller Matrix Spectroscopy System. *Sci Rep* (2016) 6:26466–10. doi:10.1038/srep26466
18. Tan Y, Chen C, Chen X, Du W, Gu H, Liu S Development of a Tomographic Mueller-Matrix Scatterometer for Nanostructure Metrology. *Rev Scientific Instr* (2018) 89:073702. doi:10.1063/1.5034440
19. Duwe M, Quast J-H, Schneider S, Fischer D, Beck U Thin-film Metrology of Tilted and Curved Surfaces by Imaging Mueller-Matrix Ellipsometry. *J Vacuum Sci Technol B* (2019) 37:062908. doi:10.1116/1.5122757
20. Wang C, Chen X, Chen C, Sheng S, Song L, Gu H, et al. Reconstruction of Finite Deep Sub-wavelength Nanostructures by Mueller-Matrix Scattered-Field Microscopy. *Opt Express* (2021) 29:32158–68. doi:10.1364/oe.432611
21. Azzam RMA Photopolarimetric Measurement of the Mueller Matrix by Fourier Analysis of a Single Detected Signal. *Opt Lett* (1978) 2:148–50. doi:10.1364/OL.2.000148
22. Köhler A. Ein neues Beleuchtungsverfahren für mikrophotographische Zwecke. *Z für wissenschaftliche Mikroskopie für Mikroskopische Technik* (1893) 10:433–40.
23. Gross H. *Handbook of Optical Systems, Volume 1, Fundamentals of Technical Optics*. Weinheim, Germany: Wiley VCH (2005).
24. Grundmann J. *Konzeption und Realisierung eines experimentellen Müller-Matrix-Mikroskop-Aufbaus*. Master Thesis. Braunschweig: PTB (2020).
25. Goldstein D. *Polarized Light*. Boca Raton, Florida, USA: CRC Press (2017).
26. Käseberg T, Dickmann J, Siefke T, Wurm M, Kroker S, Bodermann B Mueller Matrix Ellipsometry for Enhanced Optical Form Metrology of Sub-lambda Structures. In: B Bodermann, K Frenner, RM Silver, editors. *Modeling Aspects in Optical Metrology VII. International Society for Optics and Photonics (SPIE)*, Vol. 11057. Bellingham, Washington, USA: SPIE (2019). p. 155–65. doi:10.1117/12.2527419
27. Liu J, Zhang D, Yu D, Ren M, Xu J. Machine Learning Powered Ellipsometry. *Light: Sci Appl* (2021) 10:1–7. doi:10.1038/s41377-021-00482-0
28. Förster S, Gross H, Höller F, Höring L, Extended Depth of Focus as a Process of Pupil Manipulation. *Opt Des Eng* (2005) 5962:596207. doi:10.1117/12.624814
29. Lu X, Gross H Efficient Simulation of Surface Scattering in Symmetry-free Optical Systems. *Opt Express* (2020) 28:39368–86. doi:10.1364/oe.411028
30. JCMsuite. The Simulation Suite for Nano-Optics. (2021). (Accessed 29 October 2021).
31. Lazar J, Klapetek P, Valtr M, Hrabina J, Buchta Z, Cip O, et al. Short-range Six-axis Interferometer Controlled Positioning for Scanning Probe Microscopy. *Sensors* (2014) 14:877–86. doi:10.3390/s140100877
32. Nečas D, Klapetek P Gwyddion: an Open-Source Software for SPM Data Analysis. *Cent Eur J Phys* (2012) 10:181–8. doi:10.2478/s11534-011-0096-2

**Conflict of Interest:** The authors declare that the research was conducted in the absence of any commercial or financial relationships that could be construed as a potential conflict of interest.

**Publisher's Note:** All claims expressed in this article are solely those of the authors and do not necessarily represent those of their affiliated organizations, or those of the publisher, the editors and the reviewers. Any product that may be evaluated in this article, or claim that may be made by its manufacturer, is not guaranteed or endorsed by the publisher.

frontiers in Physics

ORIGINAL RESEARCH
published: 24 January 2022
doi: 10.3389/fphy.2021.814787

# Polarization-Based Histopathology Classification of *Ex Vivo* Colon Samples Supported by Machine Learning

*Deyan Ivanov*[1]*, *Viktor Dremin*[2,3], *Tsanislava Genova*[4], *Alexander Bykov*[5], *Tatiana Novikova*[1,6], *Razvigor Ossikovski*[1] *and Igor Meglinski*[3,5,7,8,9]

[1]LPICM, CNRS, École Polytechnique, Institut Polytechnique de Paris, Palaiseau, France, [2]Research and Development Center of Biomedical Photonics, Orel State University, Orel, Russia, [3]College of Engineering and Physical Sciences, Aston University, Birmingham, United Kingdom, [4]Bulgarian Academy of Sciences, Institute of Electronics, Sofia, Bulgaria, [5]Optoelectronics and Measurement Techniques Unit, University of Oulu, Oulu, Finland, [6]Department of Biomedical Engineering, Florida International University, Miami, FL, United States, [7]Institute of Clinical Medicine N.V. Sklifosovsky, I.M. Sechenov First Moscow State Medical University, Moscow, Russia, [8]Immanuel Kant Baltic Federal University, Kaliningrad, Russia, [9]V.A. Negovsky Scientific Research Institute of General Reanimatology, Federal Research and Clinical Center of Intensive Care Medicine and Rehabilitology, Moscow, Russia

In biophotonics, novel techniques and approaches are being constantly sought to assist medical doctors and to increase both sensitivity and specificity of the existing diagnostic methods. In such context, tissue polarimetry holds promise to become a valuable optical diagnostic technique as it is sensitive to tissue alterations caused by different benign and malignant formations. In our studies, multiple Mueller matrices were recorded for formalin-fixed, human, *ex vivo* colon specimens containing healthy and tumor zones. The available data were pre-processed to filter noise and experimental errors, and then all Mueller matrices were decomposed to derive polarimetric quantities sensitive to malignant formations in tissues. In addition, the Poincaré sphere representation of the experimental results was implemented. We also used the canonical and natural indices of polarimetric purity depolarization spaces for plotting our experimental data. A feature selection was used to perform a statistical analysis and normalization procedure on the available data, in order to create a polarimetric model for colon cancer assessment with strong predictors. Both unsupervised (principal component analysis) and supervised (logistic regression, random forest, and support vector machines) machine learning algorithms were used to extract particular features from the model and for classification purposes. The results from logistic regression allowed to evaluate the best polarimetric quantities for tumor detection, while the use of random forest yielded the highest accuracy values. Attention was paid to the correlation between the predictors in the model as well as both losses and relative risk of misclassification. Apart from the mathematical interpretation of the polarimetric quantities, the presented polarimetric model was able to support the physical interpretation of the results from previous studies and relate the latter to the samples' health condition, respectively.

**Keywords: tissue polarimetry, Mueller matrices, physical realizability, symmetric decomposition, depolarization spaces, *Ex vivo* colon samples, classification, machine learning**

OPEN ACCESS

***Edited by:***
*Haofeng Hu,*
*Tianjin University, China*

***Reviewed by:***
*Honghui He,*
*Tsinghua University, China*
*Chao He,*
*University of Oxford, United Kingdom*

***Correspondence:**
*Deyan Ivanov*
*deyan.ivanov@polytechnique.edu*

***Specialty section:***
*This article was submitted to Optics and Photonics, a section of the journal Frontiers in Physics*

***Received:*** *14 November 2021*
***Accepted:*** *10 December 2021*
***Published:*** *24 January 2022*

***Citation:***
*Ivanov D, Dremin V, Genova T, Bykov A, Novikova T, Ossikovski R and Meglinski I (2022) Polarization-Based Histopathology Classification of Ex Vivo Colon Samples Supported by Machine Learning. Front. Phys. 9:814787. doi: 10.3389/fphy.2021.814787*

## 1 INTRODUCTION

Ellipsometry and polarimetry have established their duly and justified realm for material characterization [1–6]. Yet, in the purview of biomedical optics, tissue polarimetry strives toward a novel domain for non-invasive, supplementary assistance in histopathology [7–13]. Unlike skin cancer, whose origins could be detected at an earlier stage of development due to its presence predominantly in the areas of the human body available for direct visual inspection, colon cancer is localized and diagnosed out of straight sight of notice often at a later stage of development [14]. Such an inevitable obstacle could be overcome by adopting various multimodal optical techniques for providing adequate support to clinicians [15–19]. It was shown earlier that tissue polarimetry techniques could be effectively combined to juxtapose polarization and depolarization parameters from different health conditions after scanning, embrace the Poincaré sphere visualization for qualitative differentiation, and construct various depolarization spaces [20–28]. Ample diagnostic information related to the morphology of the tissue specimens under study is encoded in their Mueller matrices [26, 29–32]. Nevertheless, the intertwined relation between the samples' polarization and depolarization properties and their matrix elements is accessible only after the application of pertinent decomposition algorithms [33–38]. For instance, Cloude's physical realizability is able to filter out experimental errors and/or data noise [39, 40], while logarithmic [37, 41, 42], Lu–Chipman [35, 43–45], or symmetric [36, 46] decompositions were found capable of extracting the embedded diagnostic information for the samples under study. With the increasing size and amount of the experimental data, apt post-processing algorithms are required, alongside the inclusion of statistical analyses and implementation of the artificial intelligence (AI) framework. The latter could be utilized to mimic human-like intellect when handling large and complex datasets, images, etc. Being part of AI, the vastly expanding field of machine learning (ML) covers a wide spectrum of applications for solving multiple scientific problems [47–53] as well as for cancer classification [54–62]. Since conventional programming processes an input data by means of particular syntax and semantics to produce a desired output, such a method is prone to multiple errors repetition. To overcome this issue, ML uses both the input and output data to train an algorithm for an *a priori* defined purpose. Depending on the purpose desired, ML algorithms can be grouped into three distinct classes [63, 64], namely, supervised, unsupervised, and reinforcement. The scope of the current study is focused on an application with both supervised and unsupervised ML algorithms for colon cancer assessment. In this study, the data used were obtained from tissue polarimetric experiments with various formalin-fixed, human *ex vivo* colon samples, containing healthy and malignant zones. For all specimens and health conditions a spatial *x-y* scan was conducted, where for each of the measured locations a Mueller matrix (MM) was obtained. Every MM was filtered for data noise and measurements errors before applying a decomposition algorithm and depolarization metrics calculus. Afterward, a selection of a subset from all polarimetric quantities was carried out, in order to form tissue polarimetric model with predictors, which non-redundantly summarizes all polarization and depolarization properties of both colon's healthy and cancerous tissue zones. In order to avoid multicollinearity and overfitting, the main model was split into two submodels, and consequently, all unsupervised and supervised ML algorithms were applied for both submodels independently. Finally, the performance of each ML algorithm with each of the submodels was evaluated by means of computing the corresponding confusion matrix, areas under the curves (AUC), and loss and relative risk calculations related to misclassifications.

## 2 THEORY

When dealing with light propagation in a turbid medium, it is feasible to adopt the Stokes–Mueller calculus and operate with real and measurable quantities. Hence, the full Stokes vector $\mathbf{S} = (S_0,S_1,S_2,S_3)^T$ is able to provide description for all polarization states even if time dependence $\mathbf{S(t)}$ is on avail. Knowledge of both the total degree of light polarization $\rho \in [0, 1]$ and light intensity $I$ facilitate the adoption of more explicit definitive convention [33, 39]as follows:

$$\begin{aligned} &\mathbf{S} = I\left(1, \mathbf{p}\right)^T, \qquad \mathbf{p} = \rho\mathbf{u}, \\ &\mathbf{u} = \left[cos\left(2\theta\right)cos\left(2\epsilon\right),\ sin\left(2\theta\right)cos\left(2\epsilon\right),\ sin\left(2\epsilon\right)\right]^T, \end{aligned} \tag{1}$$

where $\mathbf{p}$ and $\mathbf{u}$ are the polarization and Poincaré vectors, respectively. The latter translates the conversion from Cartesian to spherical coordinate system, thus making possible to visualize and utilize the Poincaré sphere representation with the available polarimetric data, where $\theta \in [-\pi/2, \pi/2]$ and $\epsilon \in [-\pi/4, \pi/4]$ are the azimuth and the angle of ellipticity, respectively. The individual polarization fingerprint of a turbid medium under study is encoded in its Mueller matrix ($\mathbf{M}$) from which one could read all polarization and depolarization properties related to both the surface and structural sample properties/characteristics. Every output Stokes vector ($\mathbf{S^o}$) is linearly dependent on the input one ($\mathbf{S^i}$) and also on $\mathbf{M}$, obeying the relation $\mathbf{S^o} = \mathbf{M}_{ij}\cdot\mathbf{S^i}$. A minimum of four input and four output polarization co-variations are required to obtain a full Mueller matrix by solving a system of four linear equations for each $i$ [65]:

$$\begin{aligned} \mathbf{S^o_{Q/-Q}} &= \mathbf{M_{i1}} \pm \mathbf{M_{i\prime/2}} \\ \mathbf{S^o_{U/V}} &= \mathbf{M_{i1}} + \mathbf{M_{i\prime/4}}, \end{aligned} \tag{2}$$

where Q/-Q denote horizontal/vertical and U/V denote +45°/ right circular polarization states, while $i,j = \in [1, 4]$. Physically realizable, depolarizing $\mathbf{M}$ must be represented as weighted averages of non-depolarizing $\mathbf{M}$. By this way each Mueller matrix is to preserve the value of $\rho$ parameter for totally polarized input light beam. Imprecise calibration, data noise, and experimental errors may lead to the violation of the Cloude's condition for physical realizability [34, 66], and a filtration procedure is required. In such a case, one needs to solve the eigenvalue-eigenvector problem for the Hermitian covariance matrix $\mathbf{H}$ [33]:

$$\mathbf{H} = \frac{1}{4}\sum_{i,j=1}^{4} \mathbf{M}_{ij}(\sigma \boldsymbol{i} \otimes \sigma \boldsymbol{j}), \tag{3}$$

where $\sigma_{\mathbf{i}}$ are the four Pauli spin matrices and the symbol ⊗ denotes the Kronecker product. If all eigenvalues ($\lambda_i$) of **H** are positive, then the corresponding **M** is in compliance to the Cloude's condition. On the contrary, if the aforementioned condition is not met, then all negative $\lambda_i$ are assigned to zero, and the filtered covariance ($\mathbf{H}^{\boldsymbol{f}}$) and Mueller $\mathbf{M}^{\boldsymbol{f}}$ matrices are obtained likewise [33]:

$$\mathrm{H}^{f} = \mathbf{V}\boldsymbol{\Lambda}\mathbf{V}^{-1}, \qquad m_{ij}^{f} = \mathrm{tr}\left[(\sigma \boldsymbol{i} \otimes \sigma \boldsymbol{j})\mathbf{H}_{ij}^{f}\right]. \tag{4}$$

Here, the matrix **V** is constructed from the eigenvectors of **H**, while $\Lambda$ = diag ($\lambda_{\mathrm{i}}$) and contains only positive eigenvalues, while small $m_{ij}^{f}$ indicates an element of the filtered Mueller matrix. If one is interested only in the polarimetric properties, by setting tr ($\mathbf{H}^{\boldsymbol{f}}$) = 1 or simply normalizing the eigenvalues sum to unit, both processes of transmissivity and reflectivity can be disregarded. Next, additional depolarization information can be extracted from $\mathbf{H}^{\boldsymbol{f}}$, which will be correspondingly related to the depolarization properties of the underlying medium and $\mathbf{M}^{\boldsymbol{f}}$, respectively. Three depolarization indicators could be plainly derived from $\lambda_{\mathrm{i}}$ ($\mathbf{H}^{\boldsymbol{f}}$), whereas the following set of equations is valid when tr ($\mathbf{H}^{\boldsymbol{f}}$) = 1 and $\lambda_1 \geq \lambda_2 \geq \lambda_3 \geq \lambda_4$ [33]:

$$P_1 = \lambda_1 - \lambda_2, \qquad P_2 = \lambda_1 + \lambda_2 - 2\lambda_3, \qquad P_3 = \lambda_1 + \lambda_2 + \lambda_3 - 3\lambda_4. \tag{5}$$

The overall depolarization ability $\mathrm{P}_{\Delta}$ and polarization purity PI could be summarized explicitly as [33]:

$$P_{\Delta} = \sqrt{\frac{1}{3}\left(2P_1^2 + \frac{2}{3}P_2^2 + \frac{1}{3}P_3^2\right)}, \quad PI = \sqrt{\frac{1}{3}\left(P_1^2 + P_2^2 + P_3^2\right)}. \tag{6}$$

From **Eq. 5** and **Eq. 6**, two limiting cases could be identified: pure non-depolarizing media, when $P_i = P_{\Delta} = PI = 1$, and pure depolarizing media, when $P_i = P_{\Delta} = PI = 0$. In some cases it may become useful to form and visualize three-dimensional depolarization space(s) as natural $\Sigma_{\lambda_i}$ and indices of polarimetric purity $\Sigma_{IPP}$, in order to evaluate the (de) polarization properties of an arbitrary Mueller matrix, instead of using the scalar quantities in **Eq. 6**. Yet, even more information is encoded in $\mathbf{H}^{\boldsymbol{f}}$ *via* the Cloude's entropy *S*, which is related to the spatial heterogeneity of a given sample of interest [33]:

$$S = -\sum_{i=1}^{4} \lambda_i \, log_4(\lambda_i). \tag{7}$$

Unlike $P_i$, $P_{\Delta}$, and *PI*, *S* = 1 would lead to an assumption of heterogeneous inner structure, responsible for a complete randomization of the input light polarization state(s). On the contrary, *S* = 0 would presume homogeneous inner structure, indicative for a complete preservation of $\rho$ for fully polarized light.

Currently, the concepts for physical modeling and physical interpretation of a measured Mueller matrix are of growing importance for both theoreticians and experimentalists. However, such tasks are out of the triviality scope, especially for highly anisotropic and heterogeneous structures such as bio-tissues. Once $\mathbf{M}^{\boldsymbol{f}}$ is obtained, on a straightforward manner, it could be useful and even computationally efficient for large number of measurements to acquire another two polarimetric quantities such as the net diattenuation *D* and net polarizance *P* [39]:

$$D = \frac{1}{m_{11}}\sqrt{\sum_{j} m_{1j}^2}, \qquad P = \frac{1}{m_{11}}\sqrt{\sum_{i} m_{i1}^2}, \qquad i, j = 2, 3, 4, \qquad 0 \leq D, P \leq 1. \tag{8}$$

From a phenomenological point of view, each $\mathbf{M}^{\boldsymbol{f}}$ can undergo certain decomposition algorithm(s), in order to extract particular polarimetric characteristics. The interpretation of depolarizing systems and samples has been extensively studied either with Lu–Chipman [35, 43] or logarithmic decompositions [37, 41]. The former may exhibit forward and reverse forms, thus yielding two asymmetric depolarizers containing either polarizance or diattenuation. On the other hand, the latter assumes a transversally homogeneous and longitudinally inhomogeneous anisotropic medium with continuous distribution of all optical features throughout the sample volume. Such a condition might not be met due to macroscopic variations of the refractive index and, additionally, the high anisotropic structure of bio-tissues. Furthermore, a variety of samples require implementation of angular-resolved measurements and also assumption for pure depolarizer with non-polarizance and diattenuation. Hence, an arbitrary $\mathbf{M}^{\boldsymbol{f}}$ can be decomposed into the so called symmetric factorization in such a way so that the canonical depolarizer is placed between pairs of diattenuators and retarders [36, 46]:

$$\mathbf{M}^{f} = \mathbf{M}_{\mathbf{D}_2}\mathbf{M}_{\mathbf{R}_2}\mathbf{M}_{\Delta}\mathbf{M}_{\mathbf{R}_1}^{\mathbf{T}}\mathbf{M}_{\mathbf{D}_1}. \tag{9}$$

For better clarity, it is convenient to adopt a partitioned form for all product matrices in **Eq. 9**, that is, their general form reads as follows:

$$\mathbf{M}_{\mathbf{D}} = \begin{bmatrix} 1 & \vec{\mathbf{D}}^{\mathbf{T}} \\ \vec{\mathbf{D}} & \mathbf{m}_{\mathbf{D}} \end{bmatrix}, \qquad \mathbf{M}_{\mathbf{R}=}\begin{bmatrix} 1 & \vec{\mathbf{0}}^{\mathbf{T}} \\ \vec{\mathbf{0}} & \mathbf{m}_{\mathbf{R}} \end{bmatrix}, \qquad \mathbf{M}_{\Delta=} diag\,(1, d_1, d_2, d_3), \tag{10}$$

where the 3 × 3 sub-matrices $\mathbf{m}_{\mathbf{D}}$ and $\mathbf{m}_{\mathbf{R}}$ are constructed from the diattenuation vector $\vec{\mathbf{D}}$ and the retardance value $\boldsymbol{\varphi}$, respectively. All $d_i$ are termed as the principal depolarization factors and could be utilized to form another three-dimensional depolarization space—the canonical one $\Sigma_{\Delta}$. By this way, additional polarimetric information can be extracted from $\mathbf{M}^{\boldsymbol{f}}$ after finding each product matrices from **Eq. 9** (*from here on, the* $\mathbf{M}^{\boldsymbol{f}}$ *entering the symmetric decomposition will be used interchangeably with* $\mathbf{M}_{\boldsymbol{f}}$). To achieve this, first, one needs to find the diattenuation matrices by solving the eigenvector–eigenvalue problem of [36]:

$$\left(\mathbf{M}_f^{\mathbf{T}}\mathbf{G}\mathbf{M}_f\mathbf{G}\right)\boldsymbol{\xi}_{\mathbf{1}} = \beta^2\boldsymbol{\xi}_{\mathbf{1}}, \qquad \left(\mathbf{M}_f\mathbf{G}\mathbf{M}_f^{\mathbf{T}}\mathbf{G}\right)\boldsymbol{\xi}_{\mathbf{2}} = \beta^2\boldsymbol{\xi}_{\mathbf{2}}, \tag{11}$$

where **G** = *diag* (1,-1,-1,-1) is the Minkowski metric tensor and $\beta^2$ is a common eigenvalue. When the eigenvectors $\xi_{\mathbf{1,2}} = (1, \vec{\mathbf{D}}_{\mathbf{1,2}})^{\mathbf{T}}$ are found, then the diattenuation vectors can be used to obtain $\mathbf{m}_{\mathbf{Di}}$ and $\mathbf{M}_{\mathbf{Di}}$:

$$\mathbf{m_D} = \sqrt{1-\mathbf{D}^2}\mathbf{I} + \left(1-\sqrt{1-\mathbf{D}^2}\right)\hat{\mathbf{D}}\hat{\mathbf{D}}^{\mathrm{T}}, \tag{12}$$

where $\mathbf{I}$ is $3 \times 3$ identity matrix and $\hat{\mathbf{D}}$ is the unit vector along $\vec{\mathbf{D}}$. Once the diattenuation matrices are determined, one can put and calculate:

$$\mathbf{M}_{\mathbf{D}_2}^{-1}\mathbf{M}^f\mathbf{M}_{\mathbf{D}_1}^{-1} = \mathbf{M}_{\mathbf{R}_2}\mathbf{M}_{\mathbf{\Delta}}\mathbf{M}_{\mathbf{R}_1}^{\mathrm{T}} = \mathbf{M}' = \begin{bmatrix} \beta & \vec{\mathbf{0}}^{\mathrm{T}} \\ \vec{\mathbf{0}} & \mathbf{m}' \end{bmatrix}. \tag{13}$$

Since $\mathbf{M}'$ and $\mathbf{M}_{\mathbf{\Delta}}$ contain no diattenuation and polarizance, by virtue of SVD the $3 \times 3$ sub-matrix $\mathbf{m}'$ can be reckoned, which will be sufficient to construct the retarder matrices $\mathbf{M}_{\mathbf{R1,2}}$ and the canonical depolarizer matrix $\mathbf{M}_{\mathbf{\Delta}}$, thus completing the symmetric decomposition algorithm. After this step, it becomes possible to calculate the retardance and the net depolarization values from the following:

$$\begin{aligned} \varphi &= \cos^{-1}\left[\frac{tr\left(\mathbf{m}_{\mathbf{R}}\right)-1}{2}\right], \\ \Delta &= 1 - \frac{|d_1|+|d_2|+|d_3|}{3}, \qquad 0 \le \Delta \le 1. \end{aligned} \tag{14}$$

# 3 MATERIALS AND METHODS

## 3.1 *Ex vivo* Colon Samples

A cooperation framework for optical examination of cancerous tissues (approval #286/2012 of the local Ethical Committee) between the Institute of Electronics—Bulgarian Academy of Sciences and the Surgical Department of University Hospital "Tsaritsa Yoanna—ISUL," Sofia was initially formed. As a result, multiple tissue samples for optical measurements were provided, initially diagnosed by the physicians. The tissue samples included in this study were excised during standard surgical procedure for tumor removal. Part of the excised tumors underwent standard pathology evaluation and the other part of the tumors with the adjacent healthy tissue sections were transported to the optical laboratory. No additional contrast agents were used. The samples' safe-keeping was done *via* modified Kreb's solution under isothermal conditions. First, at the Biophotonics Laboratory, Institute of Electronics, their fluorescence spectra were evaluated with different modalities [67–69]. Although the fluorescence measurements and inelastic scattering are not the subject of this study, we planned to apply the ML approach to the obtained fluorescence spectra for future studies. Afterward, a fixation in 10% formaline solution of the tissue samples was done. For this study in elastic scattering mode, in total five samples were selected for polarimetric measurements in the optoelectronics laboratory, Oulu University. The investigated samples include colon and gastric adenocarcinoma, G2: moderately differentiated (intermediate grade) and G3: poorly differentiated (high grade). The thickness range for both healthy and tumor tissue zones is of several millimeters and, therefore, the polarimetric measurements were performed in reflection geometry with angular configuration of the experimental setup shown in side view for better clarity in **Figure 1**.

## 3.2 Polarimetric Set-Up

For the current study, the angles of incidence and detection were fixed at 55° and 30°, respectively. Schematically, the optical system is shown in **Figure 1**, where the presented optical configuration allowed us to measure a full Mueller matrix of an arbitrary sample with Stokes polarimeter by performing only four sequential measurements.

For each of the input polarization states (H,V,P,R), a continuous modulation was performed with commercially available polarimetric device (Thorlabs Ltd., United States), utilizing a rotating quarter-wave plate and a fixed linear polarizer. The polarimetric device has been initially calibrated by the manufacturer, while the whole optical system was tested in reflection geometry to measure a mirror Mueller matrix, whose theoretical form is diag (1,1,1,1). As a results, for each matrix element a RMSE value of 0.02 was calculated (i.e., see [26]). Tube systems were used to protect all measurements of undesired stray light, while for reproducibility, a motorized *x-y* translation stage was employed. All samples and their corresponding healthy and cancerous zones were scanned two-dimensionally with each of the abovementioned input polarization states. The whole region of interest was selected to be 1 $mm^2$, while the step size in both *x-y* directions—0.2 mm, respectively. The combination of a supercontinuum fiber laser—SC (Leukos Ltd., France) and an acousto-optic tunable filter—AOTF (Leukos Ltd., France) was used to produce a probing wavelength of 635 nm (FWHM 8 nm) and output power—2 mW. The beam was collimated with the help of two sequentially placed irises. To rotate the azimuth of the linearly polarized laser beam, a half-wave plate was used. For acquisition of input circularly polarized light, an electrically-driven liquid crystal variable quarter-wave plate was employed. Objective lenses (10×), lens $L_2$, 100 $\mu$m pinhole, and lens $L_3$ were adopted to collect the scattered light and factor out any out-of-focus photons. Finally, the 90–10 beam splitter and the CMOS camera provided more precise focus adjustments. All Mueller matrix elements were obtained following the approach presented in [26]. In total, 330 healthy and 340 tumor Mueller matrices were measured and filtered with Cloude's physical realizability method. Afterward, the filtered matrices were decomposed using the symmetric decomposition and the depolarization metric calculus, as described in **Section 2**.

# 4 RESULTS AND DISCUSSION

## 4.1 Polarimetry

As can be seen from **Figure 2**, upon inclusion of all experimental data from various colon samples with tumors at different stages of development, a superimposing for the majority of the data points from both health conditions could be observed. Hence, the inter-patient variability restricts us to evaluate two separate clusters corresponding to the measurements of healthy and cancerous zones of colon specimens or to find specific trends within either Poincaré sphere or the three depolarization spaces. As a result, supplementary techniques and algorithms for data processing must be included all of which will be addressed in the following subsections.

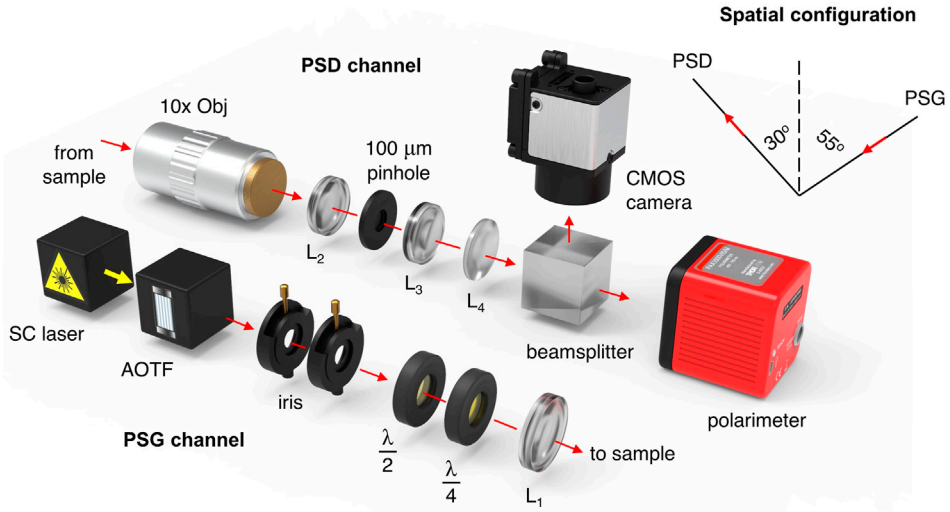


**FIGURE 1 |** Schematic representation of the experimental setup. Reprinted with permission from [26]© The Optical Society (Optica Publishing Group).

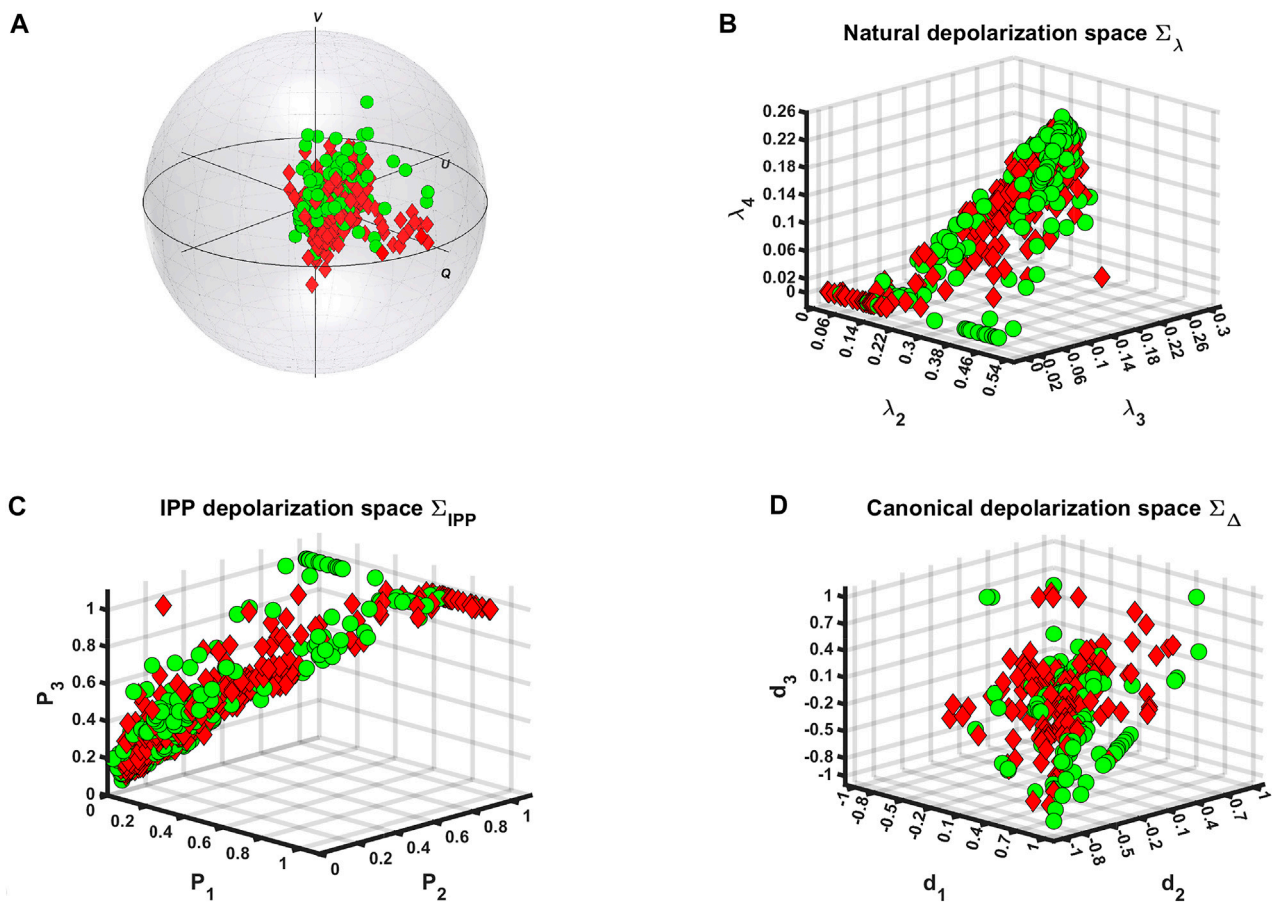


**FIGURE 2 |** Visualization of polarimetric data at all spatial locations for both colon tissue zones measurements ◦—healthy and ◇—tumor *via*: **(A)** Poincaré sphere for probing (or incident) circular polarization, **(B)** natural, **(C)** IPP, and **(D)** canonical depolarization spaces.

## 4.2 Data Post-processing

After inspection of the initial data processing sequence from **Eq. 1** through **Eq. 14**, it became possible to extract 20 polarimetric quantities that describe unambiguously the polarimetric response of the tissue samples and are to be used as predictors, namely, $\lambda_{1,2,3,4}$, $P_{1,2,3}$, $P_{\Delta}$, $PI$, $S$, $D$, $P$, $D_{1,2}$, $d_{1,2,3}$, $\Delta$, and $\varphi_{1,2}$. Initially, the mean values and their standard deviations were calculated, where for both health conditions the second statistical moment of the mean for $\varphi_2$ was found to be approximately three times higher than the second statistical moment of the mean for $\varphi_1$, thus considering $\varphi_2$ as an unreliable predictor and, consequently, it was omitted. Second, the Shapiro–Wilk normality test [70, 71] was computed on a significance level $\alpha = 0.05$, where test's results indicated non-Gaussian distribution for all polarimetric quantities. Thus, further on non-parametric statistical tests and machine learning algorithms (MLAs), which do not require data from normal distribution were used. Next, for each of the polarimetric parameters pairs grouped as healthy vs tumor, the Mann–Whitney test [70, 72] was computed for the same $\alpha$, in order to find out whether the polarimetric pairs were drawn from different or similar distributions. Only for $\lambda_{1,2}$, $P_1$, $D$, $P$, and $D_{1,2}$, the test indicated that these parameters were drawn from different distributions (*all tests were considered as statistically significant if the computed p-value* $< \alpha$). Afterward, the dataset was reorganized with each column $j$ being a polarimetric quantity, where the measurements from both health conditions were concatenated by rows. Then a factor/categorical variable was added to indicate the health condition as either 0–healthy or 1–tumor. Finally, with the exception of the categorical variable, all other quantities were normalized with the following function $\mathcal{F}_{\mathrm{n}} = (x(j) - x_{min}(j)) \cdot (x_{max}(j) - x_{min}(j))^{-1}$, in order to restrict them as dimensionless variables that vary within the closed interval [0,1]. Additional feature selection is necessary, in order to avoid the use of highly correlated predictors and multicollinearity, respectively. For instance, $\Delta$, $S$, $P_{\Delta}$, and $PI$ were removed from the main model since they are derived from $d_i$, $\lambda_i$, and $P_i$, and according to the Mann–Whitney test, their data for both health conditions are drawn from the same distribution. Moreover, *a priori* high correlation is also expected for $\lambda_i$ and $P_i$ after inspection of **Eq. 5**, therefore two submodels were formed: one omitting all $P_i$—shortly denoted as—*"eigenvalue model"* and one omitting all $\lambda_i$ referred as—*"IPP model."* The remaining predictors: $D$, $P$, $D_{1,2}$, $d_{1,2,3}$, and $\varphi_1$ were included in both submodels.

## 4.3 Machine Learning

### 4.3.1 Unsupervised Machine Learning and Principal Component Analysis (PCA)

For $n$ number of predictors, there are $n(n\text{-}1)/2$ scatter plots to summarize and graphically represent the available data. For large number of $n$, such approach would be computationally and analytically ineffective as most of the plots may be redundant, for instance 55 plots to be analyzed for each of the submodels. Therefore, we started the ML approach with the principal component analysis. For each of the submodels PCA was applied to summarize the available data, as shown in **Figure 3**, where from **Figure 3A** it was calculated that 7 principal components (PCs) retain more than 95% of the total variance for the eigenvalue model and 6 PCs—for the IPP model. By this way, PCA can be combined with classification MLAs, in order to use the non-redundant features only from both submodels, and any other collinear or highly correlated features could be avoided (i.e., all collinear features will result in a single PCA component). To project the experimental data onto the principal component space, one can compute the principal component scores (PCS). As a result, there is no correlation between all PCS of both submodels, as shown in **Figures 3B,C**, whereas 95% of the total variance is sustained. Such an approach would facilitate in increasing the final classification accuracy.

### 4.3.2 Supervised Machine Learning

First, the datasets for both submodels without the PCs were randomly split to obtain two data subsets for training and testing as follows: 570 samples (85% of the total data) for training and 100 samples (15% of the total data) for testing. To evaluate the best predictors for tumor detection (see **Figure 4**), logistic regression (LR) was trained independently with both submodels but without using their PCS. By this way, it was found out that the inclusion of $\lambda_1$ is deteriorating for the model performance, and this parameter was consequently removed from the analysis. In **Figure 4** the top and bottom axes include 1D distribution of the predictors' normalized data, for both health conditions (0–Healthy, 1–Tumor), respectively. It could be well observed that $d_1$, $R_1$, and $\lambda_2$ show excellent detection performance for malignant formations, where the uncertainty intervals (in grey) remain close to the probability values (all blue lines). Although the probabilities for $P$, $D_2$, and $P_1$ parameters are lower and have higher uncertainties compared to the former triplet of polarimetric parameters, each one of the latter triplet could also be identified with sufficient probability values. Typically, malignant tumor formations cause morphological alterations in tissues and alter the collagen extracellular matrix as well as the cellular organelles by modifying their sizes and shapes. This leads to changes in tissue heterogeneity, followed by reduced number of scattering events as $R_1$ may indicate. Also, Rayleigh–Mie transition of light scattering regime occurs that in turn affects light (de) polarization [10, 11, 46]. Whereas the depolarization parameter $d_1$ can be considered as a weight coefficient for the Stokes component $S_1$, higher polarimetric purity would indicate less depolarizing media. Such a conclusion is consistent with previously reported results for colon tumor tissues [26, 45]. Additionally, both polarizance and diattenuation (especially $D_2$ from the symmetric decomposition) were also found with higher values for the tumor tissue zones of colon in [26]. By this way, this polarimetric doublet may be considered as noteworthy tumor markers for the angular-resolved measurements with wide angle acceptance or any angles of incidence and detection different from normal.

Next, solely for the classification purpose LR, random forest (RF), and support vector machines (SVM) algorithms were again trained with the corresponding PCS data subsets for both submodels, split again randomly with the same proportions. All MLAs models underwent initial tuning to pick up the best possible hyperparameters. In the case of RF, a randomly selected

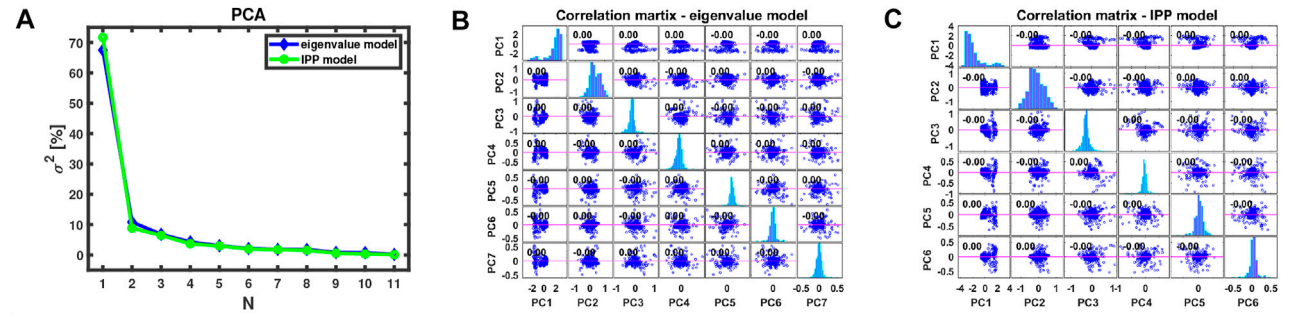


**FIGURE 3 | (A)** PCA for N number of components, explaining the corresponding percentage of variance $\sigma^2$ for both submodels. Correlation matrices for **(B)** 7 PCs and their scores—eigenvalue model and **(C)** 6 PCs and their scores—IPP model.

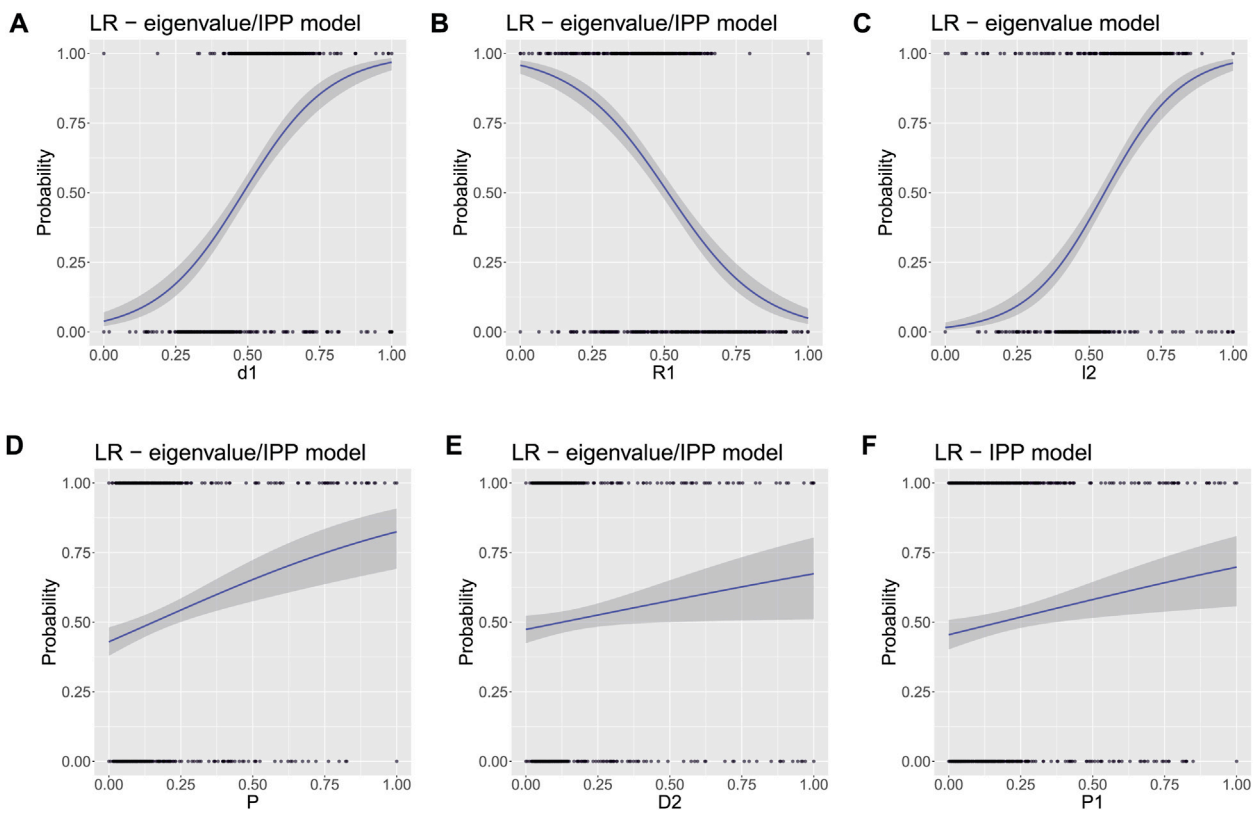


**FIGURE 4 |** Probability for tumor detection, calculated from LR: **(A)** $d_1$, **(B)** $R_1$, **(C)** $\lambda_2$, **(D)** $P$, **(E)** $D_2$, and **(F)** $\boldsymbol{D_2}$. For subfigures **A, B, D,** and **E** the results are comparable for both submodels, while subfigures **C** and **F** were computed from the eigenvalue and the IPP model, respectively ($\varphi_1 \equiv R_1$ and $\lambda_1 \equiv I_1$).

fraction of $k = N^{1/2}$ from all predictors was drawn without replications to create an ensemble of decision trees. For both submodels, having three predictors per split was found to be the most optimal choice. By setting the number of trees to 30, we reached the same classification accuracy as with 500 trees, while the training time was reduced by an order of magnitude. Without replications, there are 35 possible predictor combinations (3 randomly selected PCs and their scores from total 7) for the eigenvalue model and 20 possible predictor combinations (3 randomly selected PCs and their scores from 6) for the IPP model, calculated from $C_N^k = N!{\cdot}(k!(N\text{-}k)!)^{-1}$. For all decision trees in the ensemble (including replications), the possible number of predictor combinations for training is 4,960 for both submodels, calculated from $K_N^k = (N + k\text{-}1)!{\cdot}(k!(N\text{-}1)!)^{-1}$. By this way, RF algorithm could be considered as more reliable MLA for tumor classification, even if the dataset size is small and/or there is a presence of correlated predictors. The out-of-bag (OOB) error was found ≈5% for the eigenvalue model and ≈11% for the IPP model. In the case of SVM algorithm, after

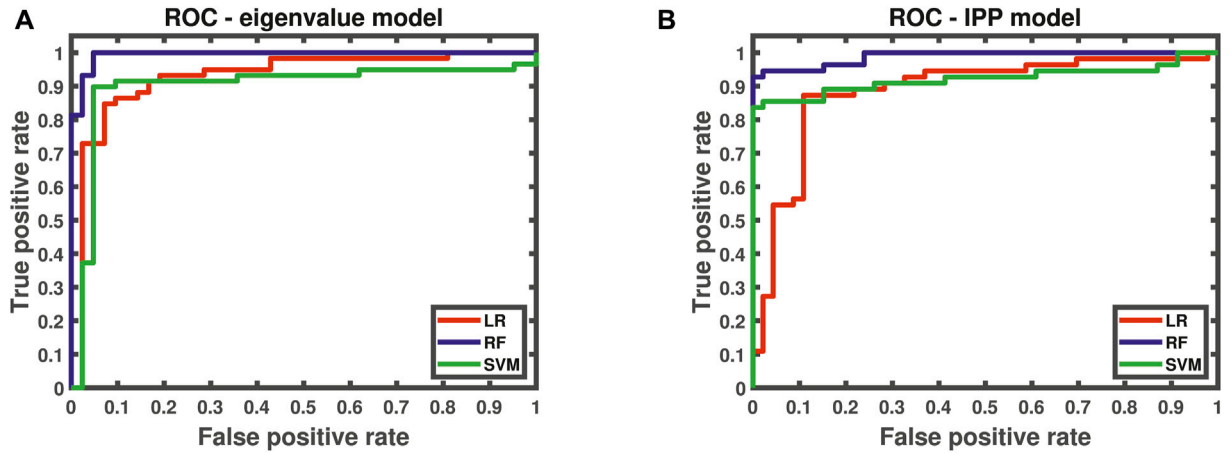


**FIGURE 5 |** ROC curves for **(A)** eigenvalue model (trained with 7 PCs and their scores) and **(B)** IPP model (trained with 6 PCs and their scores).

cross-validation a polynomial kernel of third degree was found to provide the best classification accuracy with both submodels. Additional regularization $C$ [63, 64] was necessary to add a penalty for each misclassified data point. Usually, small values of $C$ result in smaller margin, low bias, and high variance in the model and vice versa for large $C$ values [63, 64]. After the cross-validation cycle, the optimal values of $C$ were found to be 1 for both submodels.

After the application of the aforementioned MLAs for classification, various other metrics were used to evaluate the classifiers' performances. For instance, their accuracy, sensitivity, specificity, relative risk of misclassification ($R_r$), receiver operating characteristic (ROC) curve, and the corresponding area under curve (AUC). While the sensitivity represents the portion of the correctly predicted true positive (TP) values (or in this study—the tumor class), the specificity is related to the amount of the correctly predicted true negative (TN) values (analogously—the healthy class). For the ideal classifier, the accuracy (sum of all true predicted classes normalized to the sum of all true and all false predicted classes), sensitivity, and specificity should be 100%. However, due to the presence of wrongly predicted class values such as false positive (FP—healthy tissue but detected as tumor class) and false negative (FN—tumor tissue but detected as healthy class), the models' detection performance deteriorate. In this regard, the relative risk of misclassifications can be calculated as follows:

$$R_r = \frac{FP}{FP + TN} \cdot \left[\frac{TP}{TP + FN}\right]^{-1}. \tag{15}$$

Ideally, lesser misclassified values will lead to closer proximity of the ROC curve to a stepwise profile. As there is no perfect model, losses introduced from wrongly predicted class values will always be a considerable factor, which can be simply calculated as 1-AUC. The results from all classification MLAs are presented in **Figure 5** and in **Table 1**.

From the graphical representation of the figures above and the values in **Table 1**, it becomes possible to outline both submodels performances for tumor tissue classification. To sum up, all MLAs trained with the corresponding PCS provide reliable accuracy and AUC values close to 1. The eignevalue submodel seems to perform better than the IPP model with lower OOB error and higher diagnostic quantities. Whereas the LR algorithm is better suited to evaluate the predictor's probability for tumor detection and has higher specificity values than SVM, the latter MLA has higher sensitivity values than LR and is better suited to predict the healthy class. On the other hand, the RF algorithm yielded the best results for classification with negligible losses and misclassification risk. However, a parallel should be drawn between RF and SVM. The former can be computed with only two hyperparameters—the number of variables/predictors per each random split and the number of trees. On the other hand, the latter is dependent and highly sensitive to the kernel choice and degree, regularization parameter(s), and choices for support vectors and margins all of which influence the variance-bias trade-off. Additionally, the posterior probabilities for both classes were found to differ at most for RF, whereas for SVM, the difference between these values was very small, thus reducing the reliability of SVM for classification for the current study.

**TABLE 1 |** Supplementary table associated with all classification MLAs performances, where all numerical values are in %. All MLAs were trained with 7 PCs and their scores for the eigenvalue model and 6 PCs and their scores for the IPP model.

| | Accuracy | Sensitivity | Specificity | AUC | Loss | $R_i$ |
|---|---|---|---|---|---|---|
| LR—($\lambda_i$) | 87 | 85 | 91 | 93 | 7 | 11 |
| LR—($P_i$) | 84 | 80 | 89 | 87 | 13 | 14 |
| RF—($\lambda_i$) | 97 | 100 | 93 | 99 | 1 | 7 |
| RF—($P_i$) | 95 | 93 | 98 | 98 | 2 | 3 |
| SVM—($\lambda_i$) | 88 | 92 | 83 | 90 | 10 | 18 |
| SVM—($P_i$) | 77 | 93 | 59 | 92 | 8 | 45 |

## 5 CONCLUSION

In this study, multiple formalin-fixed, *ex vivo*, human colon samples, containing healthy and malignant formations, were

measured with custom-built polarimetric setup in reflection geometry. Analogously to [25, 26, 46], where a single, human colon specimen and tumor grade were considered for binary classification of all measured sites, in the current study the same experimental approach was extended for multiple colon samples and tumor grades, respectively. All experimental Mueller matrices were filtered for data noise and/or experimental errors using Cloude's physical realizability method. Both symmetric decomposition and the depolarization metric calculus were used in order to extract the (de)polarization fingerprint of the samples under examination. By this way, the symmetric decomposition could be regarded as very well suited decomposition algorithm for angular-resolved measurements by providing a pure, canonical depolarizer Mueller matrix and matrices for the corresponding counterparts of $D_1 - D_2$ and $R_1 - R_2$. Also, the polarimetric purity calculus enriched the polarimetric dataset and provided more predictors to be used for ML. Due to the inter-patient variability and the different tumor stages, a superimposing between the dataset points was observed. With the help of statistical analysis, the most prominent polarimetric quantities were selected for inclusion in two tissue polarimetric models. Additionally, normalization and feature selection were performed in order to deal with dimensionless quantities and to avoid highly correlated predictors. Due to the small dataset size, random split of dataset with proportions 50: 25:25 [%] for training:validating:testing was not feasible. Instead, a random split as 85:15 [%] for training:testing was used, thus providing more training data to feed the MLAs. Trained by this way, LR provided the predictors' probability for tumor detection, where $d_1$, $R_1$, $\lambda_2$, $P$, $D_2$, and $P_1$ were found most prominent diagnostic markers. Additionally, the data of these polarimetric quantities for both health conditions, with the exception of $d_1$ and $R_1$, were found to be drawn from different distributions, according to the Mann–Whitney test on a significance level $\alpha = 0.05$. The combination of training parameters was optimized after computing PCA and training all classification MLAs with the PCs and their scores describing 95% of the total variance. By this way, any collinear and/or the redundant features were eliminated from both polarimetric models, hence reducing the computational time for training. Similar approaches and methods have been applied with success very recently to other kinds of biological samples [73]. Additional hyperparameters' optimizations and cross validation were carried out to improve the classification accuracy. To conclude, the classification with the eigenvalue model is more accurate than the classification with the IPP model, whereas RF provided the best results for that purpose. For a single sample and colon cancer grade tissue polarimetry could be utilized as a supplementary diagnostic to support the golden standard histology analysis by a pathologist as previously reported in the studies mentioned in references [25, 26, 46]. However, when more samples are used with different grades of colon cancer, the experimental data may suffer from the inter-patient variability issue and as presented in **Section 4.1**, **Figure 2** to produce superimposing results. In combination, both unsupervised and supervised MLAs may provide an adequate solution to overcome this obstacle. The results from the current study were also found to be consistent to the previously reported results in the studies mentioned in references [25, 26, 46]. The scope of the current pilot study involved small number of samples and measurements; therefore, only a qualitative approach was adopted for the two-class classification problems: either healthy or tumor. With more samples and measurements at avail, the methods proposed in the current study could be extended for multi-class classification, that is, the prediction of the tumor grade. This will require a transition to handle and process larger data frames, use additional boosting algorithms [63, 64] to increase the classification accuracy, and delve into reinforcement and deep learning, as well as to adopt parallel computing to reduce the computational time. By this way artificial intelligence has a great potential to come into force in supporting both physicists and physicians for classification and differentiation between healthy versus tumor colon tissues or for cancer diagnostics in general.

## DATA AVAILABILITY STATEMENT

The datasets presented in this article are not readily available because of both ethical and confidentiality reasons, restricting the data for further redistribution. Requests to access the datasets should be directed to DI, deyan.ivanov@polytechnique.edu.

## ETHICS STATEMENT

The studies involving human participants were reviewed and approved by TG, ts.genova@gmail.com. The patients/participants provided their written informed consent to participate in this study.

## AUTHOR CONTRIBUTIONS

All authors listed have made a substantial, direct, and intellectual contribution to the work and approved it for publication.

## FUNDING

The experimental investigations were supported by the Bulgarian National Science Fund under grant #KP06-N38/13/2019. The current research was supported by the Academy of Finland (Grants 314639 and 325097) and INFOTECH strategic funding. Prof. Igor Meglinski also acknowledges the support from the Ministry of Science and Higher Education of the Russian Federation within the framework of state support for the creation and development of world-class research centres "Digital Biodesign and Personalized Healthcare" No. 075-15-2020-926. VD kindly acknowledges for personal support from the European Union's Horizon 2020 research and innovation programme under the Marie Sklodowska-Curie grant, agreement No. 839888.

## ACKNOWLEDGMENTS

All authors acknowledge the anonymous patients who volunteered for this study. The current article is also intended to pay special tribute in memory of Assoc. Prof. Ekaterina Borisova, PhD. DI acknowledges the PhD fellowship funding by the Doctoral School of Institut Polytechnique de Paris. Last but not least, special acknowledgements to Milen Minev for all his valuable data science advice.

## REFERENCES

1. Azzam RMA, Bashra NM. *Ellipsometry and Polarized Light*. Amsterdam: North-Holland (1977).
2. Bertrand N, Drévillon B, Bulkin P. *In Situ* infrared Ellipsometry Study of the Growth of Plasma Deposited Silica Thin Films. *J Vacuum Sci Technol A: Vacuum, Surf Films* (1998) 16(1):63–71. doi:10.1116/1.581012
3. Fallet C, Novikova T, Foldyna M, Manhas S, Ibrahim BH, De Martino A, et al. Overlay Measurements by Mueller Polarimetry in Back Focal Plane. *J Micro/nanolith MEMS MOEMS* (2011) 10:033017. doi:10.1117/1.3626852
4. Novikova T, Bulkin P, Popov V, Haj Ibrahim B, De Martino A. Mueller Polarimetry as a Tool for Detecting Asymmetry in Diffraction Grating Profiles. *J Vacuum Sci Technol B, Nanotechnology Microelectronics: Mater Process Meas Phenomena* (2011) 29:051804. doi:10.1116/1.3633693
5. Gottlieb D, Arteaga O. Mueller Matrix Imaging with a Polarization Camera: Application to Microscopy. *Opt Express* (2021) 29(21):34723–34. doi:10.1364/oe.439529
6. Manhas S, Swami MK, Buddhiwant P, Ghosh N, Gupta PK, Singh J. Mueller Matrix Approach for Determination of Optical Rotation in Chiral Turbid media in Backscattering Geometry. *Opt Express* (2006) 14:190–202. doi:10.1364/opex.14.000190
7. Meglinski I, Trifonyk L, Bachinsky V, Vanchulyak O, Bodnar B, Sidor M, et al. *Shedding the Polarized Light on Biological Tissues*. Singapore: Spinger Briefs in Applied Science and Technology (2021).
8. Ghosh N, Vitkin I. Tissue Polarimetry: Concepts, Challenges, Applications, and Outlook. *J Biomed Opt* (2011) 16:110801. doi:10.1117/1.3652896
9. Mazumder N, Xiang L, Qiu J, Fu-Jen K. In Pixel Analysis of Molecular Structure with Stokes Vector Resolved Second Harmonic Generation Microscopy. *Proc SPIE* (2014) 8948:894822. doi:10.1117/12.2036651
10. Borovkova M, Peyvasteh M, Dubolazov O, Ushenko Y, Ushenko V, Bykov A, et al. Complementary Analysis of Mueller-Matrix Images of Optically Anisotropic Highly Scattering Biological Tissues. *J Eur Opt Soc.-Rapid Publ* (2018) 14:20. doi:10.1186/s41476-018-0085-9
11. Borovkova M, Bykov A, Popov A, Pierangelo A, Novikova T, Pahnke J, et al. Evaluating β-amyloidosis Progression in Alzheimer's Disease with Mueller Polarimetry. *Biomed Opt Express* (2020) 11:4509–19. doi:10.1364/boe.396294
12. Li P, Lee HR, Chandel S, Lotz C, Groeber-Becker FK, Dembski S, et al. Analysis of Tissue Microstructure with Mueller Microscopy: Logarithmic Decomposition and Monte Carlo Modeling. *J Biomed Opt* (2020) 25(1): 1–11. doi:10.1117/1.JBO.25.1.015002
13. He C, He H, Chang J, Chen B, Ma H, J Booth M. Polarisation Optics for Biomedical and Clinical Applications: a Review. *Nat Light: Sci Appl* (1942) 10:1–20.
14. Sobin L, Gospodarowicz M, Wittekind C. *TNM Classification of Malignant Tumors*. 7th ed. New York: John Wiley & Sons (2009). International Union Against Cancer (UICC).
15. Wang TD, Van Dam J. Optical Biopsy: A New Frontier in Endoscopic Detection and Diagnosis. *Clin Gastroenterol Hepatol* (2004) 2:744–53. doi:10.1016/s1542-3565(04)00345-3
16. Croce AC, Ferrigno A, Bottiroli G, Vairetti M. Autofluorescence-based Optical Biopsy: An Effective Diagnostic Tool in Hepatology. *Liver Int* (2018) 38: 1160–74. doi:10.1111/liv.13753
17. Georgakoudi I, Feld MS. The Combined Use of Fluorescence, Reflectance, and Light-Scattering Spectroscopy for Evaluating Dysplasia in Barrett's Esophagus. *Gastrointest Endosc Clin North America* (2004) 14:519–37. doi:10.1016/j.giec.2004.03.008
18. He K, Zhao L, Chen Y, Huang X, Ding Y, Hua H, et al. Label-free Multiphoton Microscopic Imaging as a Novel Real-time Approach for Discriminating Colorectal Lesions: A Preliminary Study. *J Gastroenterol Hepatol* (2019) 34: 2144–51. doi:10.1111/jgh.14772
19. Khristoforova YA, Bratchenko IA, Myakinin OO, Artemyev DN, Moryatov AA, Orlov AE, et al. Portable Spectroscopic System for *In Vivo* Skin Neoplasms Diagnostics by Raman and Autofluorescence Analysis. *J Biophotonics* (2019) 12:e201800400. doi:10.1002/jbio.201800400
20. Kupinski M, Boffety M, Goudail F, Ossikovski R, Pierangelo A, Rehbinder J, et al. Polarimetric Measurement Utility for Pre-cancer Detection from Uterine Cervix Specimens. *Biomed Opt Express* (2018) 9(11):5691–702. doi:10.1364/boe.9.005691
21. Kupinski M, Rehbinder J, Haddad H, Deby S, Vizét J, Teig B, et al. Tasked-based Quantification of Measurement Utility for *Ex Vivo* Multi-Spectral Mueller Polarimetry of the Uterine Cervix. In: SPIE Proceedings (Optical Society of America, 2017); June 2017; Munich, Germany. paper 104110N–1.
22. Ushenko VA, Hogan BT, Dubolazov A, Grechina AV, Boronikhina TV, Gorsky M, et al. Embossed Topographic Depolarisation Maps of Biological Tissues with Different Morphological Structures. *Sci Rep* (2021) 11:3871. doi:10.1038/s41598-021-83017-2
23. Hogan BT, Ushenko VA, Syvokorovskaya A-V, Dubolazov AV, Vanchulyak OY, Ushenko AG, et al. 3D Mueller Matrix Reconstruction of the Optical Anisotropy Parameters of Myocardial Histopathology Tissue Samples. *Front Phys* (2021) 9:737866. doi:10.3389/fphy.2021.737866
24. Ushenko VA, Hogan BT, Dubolazov A, Piavchenko G, Kuznetsov SL, Ushenko AG, et al. 3D Mueller Matrix Mapping of Layered Distributions of Depolarisation Degree for Analysis of Prostate Adenoma and Carcinoma Diffuse Tissues. *Sci Rep* (2021) 11:5162. doi:10.1038/s41598-021-83986-4
25. Ivanov D, Dremin V, Bykov A, Borisova E, Genova T, Popov A, et al. Colon Cancer Detection by Using Poincaré Sphere and 2D Polarimetric Mapping of *Ex Vivo* colon Samples. *J Biophotonics* (2020) 13:e202000082. doi:10.1002/jbio.202000082
26. Ivanov D, Dremin V, Borisova E, Bykov A, Novikova T, Meglinski I, et al. Polarization and Depolarization Metrics as Optical Markers in Support to Histopathology of *Ex Vivo* colon Tissue. *Biomed Opt Express* (2021) 12: 4560–72. doi:10.1364/BOE.426713
27. Dremin V, Sieryi O, Borovkova M, Näpänkangas J, Meglinski I, Bykov A. Histological Imaging of Unstained Cancer Tissue Samples by Circularly Polarized Light. In: European Conferences on Biomedical Optics 2021 (ECBO); June 2021; Munich, Germany. EM3A.3.
28. Dremin V, Anin D, Sieryi O, Borovkova M, Näpänkangas J, Meglinski I, et al. Imaging of Early Stage Breast Cancer with Circularly Polarized Light. *Proc SPIE* (2020) 11363:1136304. doi:10.1117/12.2554166
29. Rodríguez-Núñez O, Schucht P, Hewer E, Novikova T, Pierangelo A. Polarimetric Visualization of Healthy Brain Fiber Tracts under Adverse Conditions: *Ex Vivo* Studies. *Biomed Opt Express* (2021) 12(10):6674–85. doi:10.1364/boe.439754
30. Lee HR, Saytashev I, Du Le VN, Mahendroo M, Ramella-Roman J, Novikova T. Mueller Matrix Imaging for Collagen Scoring in Mice Model of Pregnancy. *Sci Rep* (2021) 11(1):15621. doi:10.1038/s41598-021-95020-8
31. Schucht P, Lee HR, Mezouar HM, Hewer E, Raabe A, Murek M, et al. Visualization of white Matter Fiber Tracts of Brain Tissue Sections with Wide-Field Imaging Mueller Polarimetry. *IEEE Trans Med Imaging* (2020) 39(12):4376–82. doi:10.1109/tmi.2020.3018439
32. Novikova T, Rehbinder J, Haddad H, Deby S, Teig B, Nazac A, et al. Multi-spectral Mueller Matrix Imaging Polarimetry for Studies of Human Tissue. Clinical and Translational Biophotonics 10.1364/TRANSLATIONAL.2016.TTh3B.2. Fort Lauderdale, Florida United States: OSA Biophotonics Congress (2016). paper TTh3B.
33. Gil-Perez GJ, Ossikovski R. *Polarized Light and the Mueller Matrix Approach*. Boca Raton, Florida: Taylor and Francis: CRC Press (2016).

34. Cloude S. Conditions for the Physical Realizability of Matrix Operators in Polarimetry. *Proc SPIE* (1989) 1166:177–85.
35. Lu S-Y, Chipman RA. Interpretation of Mueller Matrices Based on Polar Decomposition. *J Opt Soc Am A* (1996) 13:1106–13. doi:10.1364/josaa.13.001106
36. Ossikovski R. Analysis of Depolarizing Mueller Matrices through a Symmetric Decomposition. *J Opt Soc Am A* (2009) 26:1109–18. doi:10.1364/josaa.26.001109
37. Ossikovski R. Differential Matrix Formalism for Depolarizing Anisotropic media. *Opt Lett* (2011) 36:2330–2. doi:10.1364/ol.36.002330
38. Gonzalez M, Ossikovski R, Novikova T, Ramella-Roman JC. Introduction of a 3 X 4 Mueller Matrix Decomposition Method. *J Phys D: Appl Phys* (2021) 54(42):424005, 2021 . (1–9). doi:10.1088/1361-6463/ac1622
39. Goldstein DH. *Polarized Light*. 3rd ed. Boca Raton, Florida: Taylor and Francis: CRC Press (2010).
40. Cloude S. Conditions for the Physical Realisability of Matrix Operators in Polarimetry. *Proc SPIE* (1989) 1166:177–85.
41. Lee HR, Li P, Yoo TSH, Lotz C, Groeber-Becker FK, Dembski S, et al. Digital Histology with Mueller Microscopy: How to Mitigate an Impact of Tissue Cut Thickness Fluctuations. *J Biomed Opt* (2019) 24:1–9. doi:10.1117/1.JBO.24.7.076004
42. Trifonyuk L, Sdobnov A, Baranowski W, Ushenko V, Olar O, Dubolazov A, et al. Differential Mueller Matrix Imaging of Partially Depolarizing Optically Anisotropic Biological Tissues. *Lasers Med Sci* (2020) 35(4):877–91. doi:10.1007/s10103-019-02878-2
43. Ahmad I, Ahmad M, Khan K, Ashraf S, Ahmad S, Ikram M. Ex Vivocharacterization of normal and Adenocarcinoma colon Samples by Mueller Matrix Polarimetry. *J Biomed Opt* (2015) 20:056012. doi:10.1117/1.jbo.20.5.056012
44. Rehbinder J, Haddad H, Deby S, Teig B, Nazac A, Novikova T, et al. Ex vivoMueller Polarimetric Imaging of the Uterine Cervix: a First Statistical Evaluation. *J Biomed Opt* (2016) 21(7):071113. doi:10.1117/1.jbo.21.7.071113
45. Pierangelo A, Manhas S, Benali A, Antonelli MR, Novikova T, Validire P, et al. Use of Mueller Polarimetric Imaging for the Staging of Human colon Cancer. *Proc SPIE* (2011) 7895:78950E. doi:10.1117/12.878248
46. Ivanov D, Dremin V, Borisova E, Bykov A, Meglinski I, Novikova T, et al. Symmetric Decomposition of Mueller Matrices Reveals a New Parametric Space for Polarimetric Assistance in colon Cancer Histopathology. *Proc SPIE* (2021) 11646:1164614. doi:10.1117/12.2578090
47. Dremin V, Marcinkevics Z, Zherebtsov E, Popov A, Grabovskis A, Kronberga H, et al. Skin Complications of Diabetes Mellitus Revealed by Polarized Hyperspectral Imaging and Machine Learning. *IEEE Trans Med Imaging* (2021) 40:1207–16. doi:10.1109/tmi.2021.3049591
48. Rodríguez C, Van Eeckhout A, Ferrer L, Garcia-Caurel E, González-Arnay E, Campos J, et al. Polarimetric Data-Based Model for Tissue Recognition. *Biomed Opt Express* (2021) 12:4852–72. doi:10.1364/BOE.426387
49. Zhu Y, Dong Y, Yao Y, Si L, Liu Y, He H, et al. Probing Layered Structures by Multi-Color Backscattering Polarimetry and Machine Learning. *Biomed Opt Express* (2021) 12:4324–39. doi:10.1364/BOE.425614
50. Yousaf MS, Ahmad I, Khurshid A, Ikram M. Machine Assisted Classification of Chicken, Beef and Mutton Tissues Using Optical Polarimetry and Bagging Model. *Photodiagnosis Photodynamic Ther* (2020) 31:101779. doi:10.1016/j.pdpdt.2020.101779
51. Queau Y, Leporcq F, Lechervy A, Alfalou A. Learning to Classify Materials Using Mueller Imaging Polarimetry. *Proc SPIE* (2019) 11172:111720Z. doi:10.1117/12.2516351
52. Vaughn I, Hoover B, Tyo S. Classification Using Active Polarimetry. *Proc SPIE* (2012) 8364:83640S. doi:10.1117/12.922623
53. Zhu Y, Dong Y, Yao Y, Si L, Liu Y, He H, et al. Probing Layered Structures by Multi-Color Backscattering Polarimetry and Machine Learning. *Biomed Opt Express* (2021) 12(7):4324–39. doi:10.1364/BOE.425614
54. Panigrahi S, Swarnkar T. Machine Learning Techniques Used for the Histopathological Image Analysis of Oral Cancer-A Review. *Tobioij* (2020) 13:106–18. doi:10.2174/1875036202013010106
55. Luu N, Le TH, Phan QH, Pham TTH. Characterization of Mueller Matrix Elements for Classifying Human Skin Cancer Utilizing Random forest Algorithm. *J Biomed Opt* (2021) 26:075001. doi:10.1117/1.jbo.26.7.075001
56. Ahmad I, Ahmad M, Khan K, Ikram M. Polarimetry Based Partial Least Square Classification of *Ex Vivo* Healthy and Basal Cell Carcinoma Human Skin Tissues. *Photodiagnosis Photodynamic Ther* (2016) 14:134–41. doi:10.1016/j.pdpdt.2016.04.004
57. Zhou X, Ma L, Brown W, Little J, Chen A, Myers L, et al. Automatic Detection of Head and Neck Squamous Cell Carcinoma on Pathologic Slides Using Polarized Hyperspectral Imaging and Machine Learning. *Proc SPIE* (2021) 11603:16030Q. doi:10.1117/12.2582330
58. Mukhopadhyay S, Kurmi I, Dey R, Das N, Pradhan S, Pradhan A, et al. Optical Diagnosis of colon and Cervical Cancer by Support Vector Machine. *Proc SPIE* (2016) 9887:98870U. doi:10.1117/12.2227316
59. Dremin V, Potapova E, Zherebtsov E, Kandurova K, Shupletsov V, Alekseyev A, et al. Optical Percutaneous Needle Biopsy of the Liver: a Pilot Animal and Clinical Study. *Sci Rep* (2020) 10:14200. doi:10.1038/s41598-020-71089-5
60. Zherebtsov E, Zajnulina M, Kandurova K, Potapova E, Dremin V, Mamoshin A, et al. Machine Learning Aided Photonic Diagnostic System for Minimally Invasive Optically Guided Surgery in the Hepatoduodenal Area. *Diagnostics* (2020) 10:873. doi:10.3390/diagnostics10110873
61. Wang G, Sun Y, Jiang S, Wu G, Liao W, Chen Y, et al. Machine Learning-Based Rapid Diagnosis of Human Borderline Ovarian Cancer on Second-Harmonic Generation Images. *Biomed Opt Express* (2021) 12(9):5658–69. doi:10.1364/boe.429918
62. Dang Y, Wan J, Si L, Meng Y, Dong Y, Liu S, et al. Deriving Polarimetry Feature Parameters to Characterize Microstructural Features in Histological Sections of Breast Tissues. *IEEE T Bio-med Ing* (2021) 68(3):881–92. doi:10.1109/TBME.2020.3019755
63. James G, Witten D, Hastie T, Tibshirani R. *An Introduction to Statistical Learning: With Applications in R*. New York: Springer (2013).
64. Hastie T, Tibshirani R, Friedman J. *The Elements of Statistical Learning: Data Mining, Inference, and Prediction*. 2nd ed. New York: Springer (2009).
65. Wang LV, Hsin W. *Biomedical Optics, Principles and Imaging*. New Jersey: Wiley and Sons (2007).
66. Cloude S. Group Theory and Polarisation Algebra. *Optik* (1986) 75:26–36.
67. Genova T, Borisova E, Penkov N, Vladimirov B, Zhelyazkova A, Avramov L. Excitation-emission Matrices and Synchronous Fluorescence Spectroscopy for the Diagnosis of Gastrointestinal Cancers. *Quan Electron.* (2016) 46:510–4. doi:10.1070/qel16112
68. Genova T, Borisova E, Zhelyazkova A, Penkov N, Vladimirov B, Terziev I, et al. Colorectal Cancer Stage Evaluation Using Synchronous Fluorescence Spectroscopy Technique. *Opt Quant Electron* (2016) 48:378. doi:10.1007/s11082-016-0634-7
69. Genova T, Borisova E, Penkov N, Vladimirov B, Avramov L. Synchronous Fluorescence Spectroscopy with and without Polarization Sensitivity for Colorectal Cancer Differentiation. *Proc SPIE* (2018) 10685:106852L. doi:10.1117/12.2306877
70. Mould RF. *Introductory Medical Statistics*. 3rd ed. Boca Raton: CRC Press (1998).
71. Motulsky H, Christopoulos A. *Fitting Models to Biological Data Using Linear and Nonlinear Regression: A Practical Guide to Curve Fitting*. New York: Oxford University Press (2004).
72. Motulsky H. *Intuitive Biostatistics*. New York: Oxford University Press (1995).
73. Rodríguez C, Van Eeckhout A, Ferrer L, Garcia-Caurel E, González-Arnay E, Campos J, et al. Polarimetric Data-Based Model for Tissue Recognition. *Biomed Opt Express* (2021) 12(8):4852–72. doi:10.1364/boe.426387


**Conflict of Interest:** The authors declare that the research was conducted in the absence of any commercial or financial relationships that could be construed as a potential conflict of interest.

frontiers in Physics

ORIGINAL RESEARCH
published: 14 February 2022
doi: 10.3389/fphy.2021.820637

# Mueller Matrix Ellipsometric Characterization of Nanoscale Subsurface Damage of 4H-SiC Wafers: From Grinding to CMP

*Huihui Li*[1,2], *Changcai Cui*[1,2]*, *Jing Lu*[1,2], *Zhongwei Hu*[1,2], *Wuqing Lin*[1,2,3], *Subiao Bian*[1,2] *and Xipeng Xu*[1,2]

[1]National & Local Joint Engineering Research Center for Intelligent Manufacturing Technology of Brittle Material Products, Huaqiao University, Xiamen, China, [2]Institute of Manufacturing Engineering, Huaqiao University, Xiamen, China, [3]Fujian Norstel Material Technologies Co., Ltd., Quanzhou, China

Subsurface damage of 4H-silicon carbide (SiC) wafers, which is detrimental to the performance and lifetime of SiC-based photoelectric devices, is easily induced during surface machining process due to their particular mechanical and physical properties. A nondestructive and effective characterization technique is essential for high quality products in the wafer manufacturing process. A method based on the Mueller Matrix Spectroscopic Ellipsometry (MMSE) is proposed to detect the nanoscale subsurface damage of 4H-SiC wafers induced by grinding and polishing. The Mueller matrix elements which are sensitive to the damage information have been identified through both simulation and experiment. The damage layer and its roughness are considered in optical modeling at different processing stages. The results show that both the surface texture and the damage layer contribute to the Mueller matrix values. The fitting thickness of the damage layer is consistent with the value from transmission electron microscope (TEM); the refractive index of the damage layer matches the surface elements analysis result from X-ray photoelectron spectroscopy (XPS). The results suggest that the MMSE-based method could offer a promising nondestructive method to detect global wafer subsurface damage and its evolution during grinding and polishing, which eventually could benefit process optimization in the whole wafer manufacturing process.

**Keywords: Mueller matrix spectroscopic ellipsometry, subsurface damage, silicon carbide (SiC), nondestructive characterization, grinding, chemical mechanical polishing (CMP)**

OPEN ACCESS

***Edited by:***
*Hao Jiang,*
*Huazhong University of Science and Technology, China*

***Reviewed by:***
*Honggang Gu,*
*Huazhong University of Science and Technology, China*
*Shuang Xu,*
*Wuhan University of Science and Technology, China*
*Yidong Tan,*
*Tsinghua University, China*

****Correspondence:***
*Changcai Cui*
*cuichc@hqu.edu.cn*

***Specialty section:***
*This article was submitted to Optics and Photonics, a section of the journal Frontiers in Physics*

***Received:*** *23 November 2021*
***Accepted:*** *20 December 2021*
***Published:*** *14 February 2022*

***Citation:***
*Li H, Cui C, Lu J, Hu Z, Lin W, Bian S and Xu X (2022) Mueller Matrix Ellipsometric Characterization of Nanoscale Subsurface Damage of 4H-SiC Wafers: From Grinding to CMP. Front. Phys. 9:820637. doi: 10.3389/fphy.2021.820637*

## 1 INTRODUCTION

4H-silicon carbide (SiC) is considered as one of the most promising third-generation semiconductor materials with applications in many cutting-edge fields, such as semiconductor electronics, optics, and graphene growth [1, 2]. The state-of-the-art SiC device structures are currently grown on the 4H-SiC off-axis cut wafers, which can stop the propagation of threading defects in epilayers [3]. Comparing to C-face, Si-face is more useful for epitaxial film growth [4]. Conductive SiC (*n*-type doped) substrates are used for homoepitaxial device structures such as Schottky diodes [2] and MOSFETS [5]. The premise of those applications is the availability of affordable, high quality, large diameter SiC substrates. However, SiC is a typical difficult-to-machine material due to its high hardness and strong chemical inertness. The subsurface damage (SSD) is easily caused during

substrate processing [6], which will impair the mechanical, electronic, and optical properties of materials [7]. For this reason, the characterization of subsurface damage is conducive to advanced applications.

The processing flow of SiC substrate mainly includes rough grinding, fine grinding, and chemical mechanical polishing (CMP) [7, 8]. Usually, rough grinding will leave large surface texture and a mass of subsurface damage. Although those damages can be gradually removed by subsequent fine grinding and CMP, it is time-consuming. Therefore, monitoring the depth of damage will provide a useful index for the quality control of SiC wafer production chain and the processing technology optimization, especially for wafers with large diameters, which is a trend with the development of material growth. A nondestructive and precise method for measuring the thickness of the SSD layer is indispensable.

Several destructive and nondestructive methods have been used to detect the SSD [9–11]. The destructive methods, for example, cross-sectional microscopy, taper polishing, chemical etching, magnetorheological finishing (MRF) polishing, the inductivity coupled plasma method [12], and TEM microscopy can measure different damage depths from slicing to CMP. These destructive methods are time-consuming and reduce production efficiency and increase cost. The nondestructive methods include micro-Raman spectroscopy, optical coherent tomography, photoluminescence, and laser scattering method. However, their detection accuracy or efficiency is limited, or inappropriate for accurately measuring the thickness of the very thin damage layer.

As a nondestructive strategy, the Mueller Matrix Spectroscopic Ellipsometry (MMSE) is commonly used to measure the thickness and refractive index of thin films and crystal with excellent accuracy [13, 14]. Previously reported refractive ellipsometric characterizations in SiC wafers have been done [17] but were limited in single-sided polished wafer without backside reflection [15] or treated the damage layer as an $SiO_2$ film [16]. Our group [17] took double-sided polished *n*-type 6H-SiC wafer with backside reflection and the damage layer into account based on partial-wave coherence theory. However, effectively assessing the damage layer in the rough stage of grinding or polishing was excluded. Meanwhile, the fitting process was complex and time-consuming. Yao et al. [18] proposed a quasi-Brewster angle technology to quickly evaluate the polishing quality covering rough- and fine-polishing stages using a variable angle ellipsometer, but the thickness of the damage layer was not obtainable. Therefore, quantitative and accurate measurement of the damage layer is essential in different processing stages (rough grinding, fine grinding, and CMP). There are three key issues that need to be addressed. First, the optical constants of SiC must be known well [19]. Second, the sensitivity of the Mueller matrix to the damage layer and surface texture needs to be investigated. Third, the ability of MMSE to characterize the damage layer during the process of rough grinding, fine grinding, and CMP needs to be verified.

In this paper, the damage layers induced by rough grinding, fine grinding, and CMP 4H-SiC off-axis cut wafers are characterized by MMSE. The subsurface quality in the wafer processing is visualized. The paper is arranged as follows: In **Section 1**, the background is introduced. In **Section 2**, the samples and experimental instruments are presented. In **Section 3.1**, a method to extract optical constants of uniaxial 4H-SiC crystal is given. In **Section 3.2**, optical stack models are established according to the damage characteristics. In **Section 3.3**, the Mueller matrix sensitivity for the damage layer is simulated and verified by experiment. In addition, Mueller matrix sensitivity for the direction of surface texture is investigated. In **Section 4**, the accurate optical constants of 4H-SiC crystal are illustrated. The thicknesses and refractive indices of damage layers are analyzed and compared with those given by TEM and XPS.

## 2 SAMPLES AND EXPERIMENTAL INSTRUMENTS

4H-SiC single crystal wafers (*n*-type doped, off-axis cut toward <1120>, 4 inch) after double-sided rough grinding, double-sided fine grinding, and double-sided CMP were selected for research. The Mueller matrix of wafers was measured in transmission and reflection modes with a dual-rotation compensator Muller matrix ellipsometer (DRMME, Wuhan Eoptics Technology Co., China) [20, 21]. Measurements were done in the spectral range of 250 nm (4.96 eV) to 1400 nm (0.89 eV). The short axis diameter of the incident beam spot is 3 mm.

The Si-face surface morphology of 4H-SiC wafers was measured by Atomic Force Microscope (AFM) (Alpha300 RA, WITec, Germany) and 3D optical surface profiler (Newview 7300, ZYGO, United States). The surface roughness of rough grinding, fine grinding, and CMP 4H-SiC wafers were obtained by 3D optical surface profiler, and they were 13.26 nm, 0.78 nm, and 0.32 nm, respectively.

The measurements of optical Absorbance (A), Transmittance (T), and specular Reflectance (R) were done with a UV-Vis-NIR spectrophotometer (Perkin Elmer, lambda-1050). Absorbance spectra were used to obtain the bandgap of 4H-SiC. Transmittance and reflectance spectra were used to calculate the ordinary extinction coefficient of wafers.

The XPS analysis has been performed using the spectrometer (Thermo Fisher Scientific, K-alpha+) with Al$K\,\alpha$ X-ray radiation ($h\nu$ = 1,486.68 eV) to detect the composition on the Si-face of 4H-SiC wafers. All XPS binding energies were calibrated to the C 1s peak at 284.8 eV. The wafers were first cleaned by liquid cleaner and deionized water, and then dried off by air spray gun for measurements. All the above measurements were performed at room temperature.

## 3 ELLIPSOMETRIC CHARACTERIZATION THEORY

### 3.1 Optical Constants of 4H-SiC

Complex optical constants ($\tilde{n} = n + i \cdot k$) of *n*-type doped 4H-SiC substrate are the basis for establishing the optical stack model.

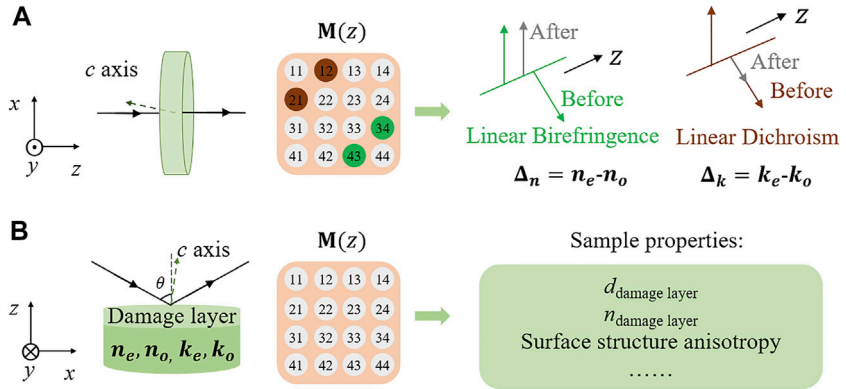


**FIGURE 1 | (A)** The transmission Mueller matrix measurement of off-axis cut uniaxial 4H-SiC wafer. The linear birefringence and linear dichroism can be analyzed. **(B)** The reflective Mueller matrix measurement of processed 4H-SiC wafer with the damage layer. The refractive index and thickness of the damage layer and the surface structure anisotropy of the rough grinding wafers can be analyzed.

Nitrogen impurity introduces weak absorption below the bandgap of 4H-SiC crystal, where anisotropy absorption is observed [22]. Thus, the 4H-SiC uniaxial crystal has two linear horizontal anisotropy, namely linear birefringence ($\Delta_n = n_e - n_o$) and linear dichroism ($\Delta_k = k_e - k_o$) [13].

The optical anisotropy of uniaxial 4H-SiC wafer is obtained by analyzing the transmission Mueller matrix (MM), as shown in **Figure 1A**. The 4 × 4 Mueller matrix (**M**) can be inverted to obtain physical parameters (**L**) in an optical system by using the differential matrix decomposition (**Eq. 1**) [23]. As the considered uniaxial SiC crystal, only two polarization properties were non-vanishing, namely, LB, which describes the phase retardation between $x$ and $y$ polarizations and related to M43 element (M34 = -M43), and LD, which describes the diattenuation between $x$ and $y$ polarizations and related to M12 element (M12 = M21).

$$\mathbf{L} = In(\mathbf{M}) \tag{1}$$

Based on the measured complex retardance ($\delta^{'} = LB + iLD$), a closed-form expression for determination of the linear birefringence and linear dichroism of uniaxial crystal was derived in our previous work (**Eq. 2**) [14].

$$\Delta = \frac{2\delta n_o - n_o sin^2\theta_1 (n_o + 2\delta) + (n_o + \delta) sin\theta_1 \sqrt{n_o^2 sin^2\theta_1 - 2\delta n_o sin\theta_1 cos^2\theta_1}}{(n_o + 2\delta) sin^2\theta_1 - 2\delta} \tag{2}$$

$\delta$ is the redefined complex retardance,

$$\delta = \frac{\lambda}{2\pi d}\delta' \tag{3}$$

In general, the equation gives the algebraic relation between complex optical anisotropy ($\Delta = \Delta_n + i\Delta_k$) and measured complex retardance ($\delta^{'}$). $\theta_1$ is the off-axis cut angle, $n_o$ is the refractive index for the polarization component perpendicular to the incidence plane, and $d$ is the thickness of the wafer.

Moreover, the ordinary extinction coefficient $k_o(\lambda)$ of 4H-SiC crystal is calculated from R and T spectra by using the following equation:

$$k_o(\lambda) = \frac{\alpha(\lambda)}{4\pi}\lambda \tag{4}$$

$$\alpha(\lambda) = -\frac{1}{d}\ln\left[\frac{\sqrt{(1-R)^4 + 4T^2R^2} - (1-R)^2}{2TR^2}\right] \tag{5}$$

where $d$ is the thickness of the wafer along the direction of light propagation. The thickness of the CMP wafer is obtained by digital micrometer with a value of 356.51 ± 0.44 μm. The extraordinary extinction coefficient ($k_e$) is calculated by the known ordinary extinction coefficient ($k_o$) and linear dichroism ($k_e - k_o$). In addition, the extraordinary refractive index ($n_e$) is calculated by using the ordinary refractive index $n_o$ from [24].

Theoretically, each dielectric tensor is rotated from its standard setting to the measurement coordinate system to obtain the objective results. The laboratory coordinate system is defined in **Figure 1**, and an orthogonal transformation is given by:

$$\varepsilon = \mathrm{A}(\alpha,\beta,\gamma)\begin{pmatrix}\varepsilon_{11} & 0 & 0\\ 0 & \varepsilon_{11} & 0\\ 0 & 0 & \varepsilon_{33}\end{pmatrix}\mathrm{A}^{\mathrm{T}}(\alpha,\beta,\gamma) \tag{6}$$

where $A(\alpha,\beta,\gamma)$ is Euler transformation matrix. $\alpha$ has no effect on the uniaxial crystal, $\beta$ is the angle between the $z$-axis and the optic axis of the crystal, corresponding to the off-axis cut angle; $\gamma$ is the angle between the $y$ axis and the projection of the optic axis in $x$-$y$ plane, and the value is 90° when the optical axis is parallel to the incident plane. $\varepsilon_{11}$ and $\varepsilon_{33}$ are dielectric functions for light polarized perpendicular and parallel to the optic axis, respectively.

It is hard to ensure the optic axis is completely parallel to the incident plane in the DRMME experiment. Therefore, it is necessary to evaluate the error of the Mueller matrix caused by Euler angles. The formula is defined by:

$$Error(i) = \sum_{m,n=1}^{4}\sum_{\lambda=380}^{1400}\left[MM_{mn,\lambda}(i) - MM_{mn,\lambda}(i+\delta_i)\right]^2 \tag{7}$$

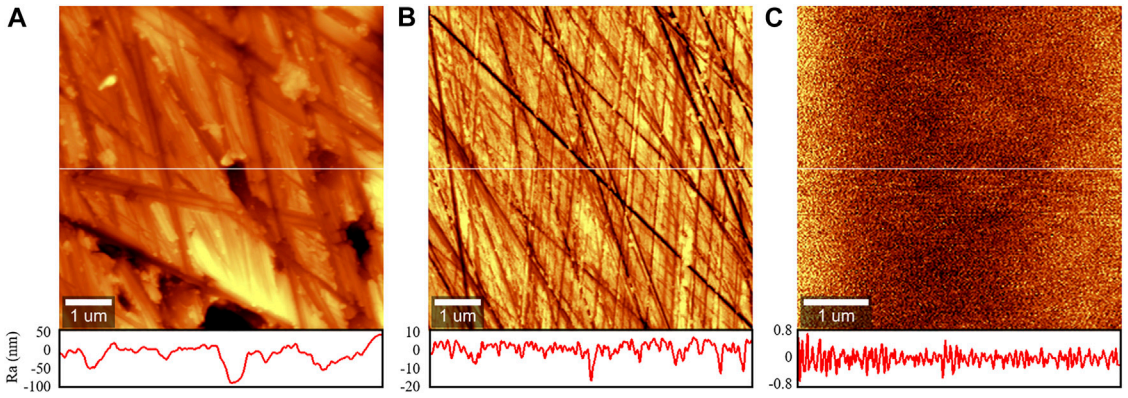


**FIGURE 2 |** The AFM images of **(A)** rough grinding, **(B)** fine grinding, and **(C)** CMP 4H-SiC wafers.

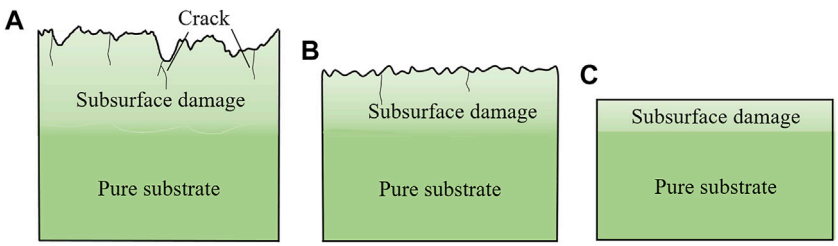


**FIGURE 3 |** Schematic diagrams of **(A)** rough grinding, **(B)** fine grinding, and **(C)** CMP surface/subsurface cross-section of 4H-SiC wafers.

where $i$ represents the Euler angle $\beta$ or $\gamma$. In $MM_{mn,\lambda}$, the subscript $\lambda$ indicates wavelength point, $m$ and $n$ are the indices of the Mueller matrix (MM) elements. When $\delta_\gamma$ is set as 1°, the $Error\,(\gamma)$ is 0.93 mainly reflected in the off-diagonal MM elements, and the effect on M12/M21 and M34/M43 can be ignored. However, the $Error\,(\beta)$ is 2.05 when $\delta_\beta$ is 0.1°. It means the off-axis cut angle greatly affects the calculation error. In this study, the $\beta$ = 3.95° is measured by X-ray crystal orientation instrument with accuracy better than 0.001° for CMP wafer. Therefore, even if there is a shift of $\gamma$, the measurement is considered reliable.

## 3.2 Optical Stack Model

In MMSE reflection measurement, an appropriate optical stack model is acquired to obtain the accurate parameters of thin layers. The refractive index, thickness of the damage layer and surface structure anisotropy of the wafers can be analyzed, as shown in **Figure 1B**.

According to the processing mechanism of brittle materials [25], the surface and subsurface damage of SiC wafers corresponding to rough grinding, fine grinding, and CMP are different. **Figure 2** shows the AFM images that visible scratches and pits damage left on the rough grinding wafer (**Figure 2A**), scratches left on the fine grinding wafer (**Figure 2B**), and those are absent from the CMP wafer (**Figure 2C**).

Besides that, invisible subsurface damage (SSD) is formed above the pure substrate [26], as shown in **Figure 3**. The SSD caused by grinding most contains cracks, phase transformation, an amorphous layer, residual stress, and other types of damage. After CMP, the SSD mostly only contains an amorphous layer. We simplified the model because the SSD on the backside of the wafer is basically the same as that on the surface.

From **Figure 3A**, rough surface, amorphous layer, nonideality boundary (between the damaged zone and pure substrate), and roughed backside are characteristics of the rough grinding wafer surface from top to bottom. These peculiarities are considered for ellipsometric analysis using roughness layer, damage layer, interface layer, and semi-infinite SiC substrate. For fine grinding wafers (**Figure 3B**), there are surface scratches and nonideality damage layer, which are modeled as three layers: roughness layer/damage layer/SiC substrate. CMP wafer with the sub-nanometer roughness is regarded as a specular surface judged by Rayleigh criterion [27]. Therefore, the roughness is omitted and the CMP wafer (**Figure 3C**) is modeled as two layers: damage layer/SiC substrate.

For each optical stack model, the optical constants of 4H-SiC are set as known from the calculation in **Section 4.1**. The interface layer is modeled by the Bruggeman Effective Medium Approximation (B-EMA), which consists of 50% pure substrate and 50% damage layer. The Cauchy dispersion relation is used to model the damage layer given by:

$$n^2_{damage}(\lambda) = A + \frac{B}{\lambda^2} \tag{8}$$

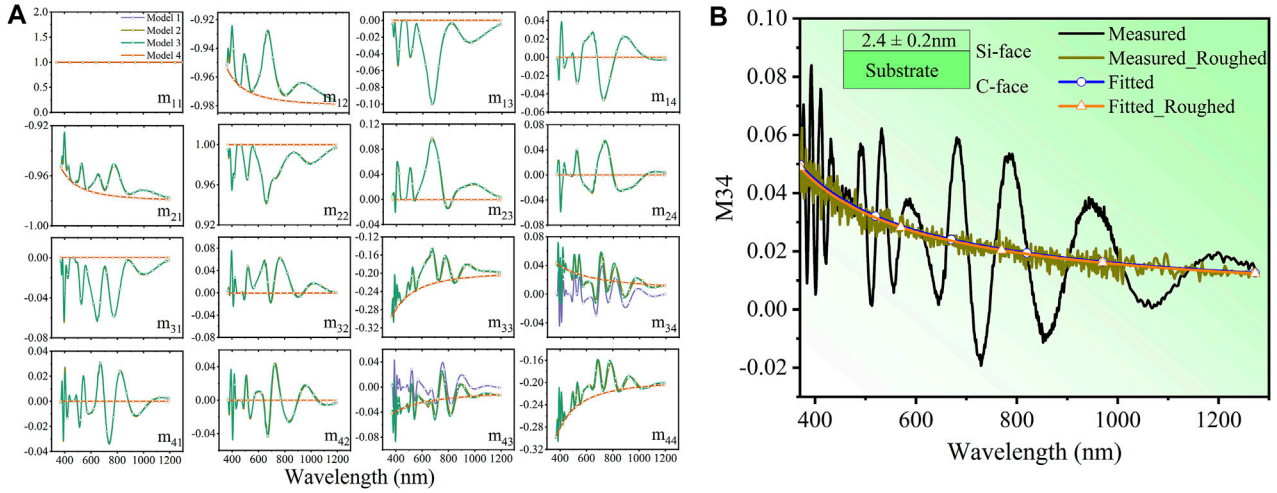


**FIGURE 4 |** The simulation of the Mueller matrix. **(A)** Model 1, 350 μm 4H-SiC thick layer with backside reflection. Model 2, 2 nm $SiO_2$ layer on the Si-face of the 4H-SiC thick layer with backside reflection. Model 3, 2 and 5 nm $SiO_2$ layers on the Si-face and the C-face of the 4H-SiC thick layer with backside reflection. Model 4, 2 nm $SiO_2$ layers on the Si-face of the 4H-SiC semi-infinite substrate without backside reflection. The angle of incidence is 65° and the Euler angle γ is 45°, $\beta$ is 4°. **(B)** Measured and fitted M34 elements of the backside polished and roughed wafer by using the same semi-infinite substrate model.

where $A$ and $B$ are fitting Cauchy parameters and $\lambda$ is the wavelength in micrometers. The roughness layer is modeled by a B-EMA layer formed by 50% bulk material and 50% air.

## 3.3 The Sensitivity of the Mueller Matrix

Different from the traditional thin film analysis, the sensitivity of ultra-thin damage layer needs to be considered in optical modeling for fine grinding and CMP samples with backside reflection. Besides that, the effect of surface texture caused by rough grinding on the Mueller matrix needs to be considered.

First, to figure out the role of surface (Si-face), back (C-face) damage layer, and the backside reflection in the Mueller matrix, the following simulation is executed in **Figure 4A**. Using partial coherence wave [28] and fully coherence wave theory, four models are used to explore the response of the Mueller matrix elements to the ultra-thin layer on the Si-face and the C-face of the 4H-SiC substrate. A known $SiO_2$ layer is used as the material of ultra-thin film. Model 1, 350 μm 4H-SiC thick layer with backside reflection. Model 2, 2 nm $SiO_2$ layer on Si-face of 4H-SiC thick layer with backside reflection. Model 3, 2 and 5 nm $SiO_2$ layers on Si-face and C-face of the 4H-SiC thick layer with backside reflection. Model 4, 2 nm $SiO_2$ layers on the Si-face of the 4H-SiC semi-infinite substrate without backside reflection. The angle of incidence is 65° and the Euler angle $\beta$ is 4°, $\gamma$ is 45°.

From the simulation results, the diagonal element M34 has the highest sensitivity to small changes of the ultra-thin layer compared to other elements. The difference between Model 1 and Model 2 indicates that M34 is only sensitive to the thin layer. The difference between Model 2 and Model 3 indicates that the thin layer on the C-face of the substrate has almost no effect on the values of the Muller matrix. The difference between Model 2 and Model 4 indicates that the fluctuation of MM spectra is related to the backside reflection of substrate. Moreover, the "position balance" of M34 spectra of substrate with backside reflection is the same with that of substrate without backside reflection. Therefore, we can omit the backside reflection when only considering the fitting result of the M34 element.

Furthermore, the backside of the CMP wafer is roughed for experimental comparison. We simplify the optical model to fit the thickness of the damage layer by applying the fully coherence theory to CMP SiC wafer with and without backside reflection. **Figure 4B** shows the measured and fitted M34 element of backside polished and roughed wafer. The oscillation in the experimental data of polished ones comes from the backside reflection. Fitting the polished sample using the fully coherence theory is equivalent to using a semi-infinite substrate model and ignoring the effect of the backside reflection. The thickness results of damage layers obtained by fitting the MM data from the same point before and after roughening are 2.4 ± 0.2 nm and 2.5 ± 0.2 nm, respectively. In addition, we obtained the same fitting M34 curve at the same point before and after roughening (**Figure 4B**). The fitting results further confirm that the backside reflection of the substrate can be ignored when only the thickness of the damage layer is fitted.

Next, to appropriately describe the influence of the surface texture of rough grinding 4H-SiC wafers on the MM spectra, the MM elements are plotted in polar coordinates with wavelength and rotation angle as radial and angular coordinate, respectively. The reflection MM data is measured at 17 Euler rotation angles ($\gamma$ from 0° to 360° in steps of 22.5°) with the incident angle of $\theta$ = 65°.

For demonstration, one point of rough grinding wafer is selected. **Figure 5A** shows the surface morphology measured by a 3D optical surface profiler and its initial texture direction is parallel to the plane of incidence. **Figure 5B** shows the schematic diagram of reflection ellipsometry measurement. The measured 4 × 4 Mueller matrix is shown in the **Supplementary Material**. Theoretically, the anisotropy of the sample is reflected in the non-

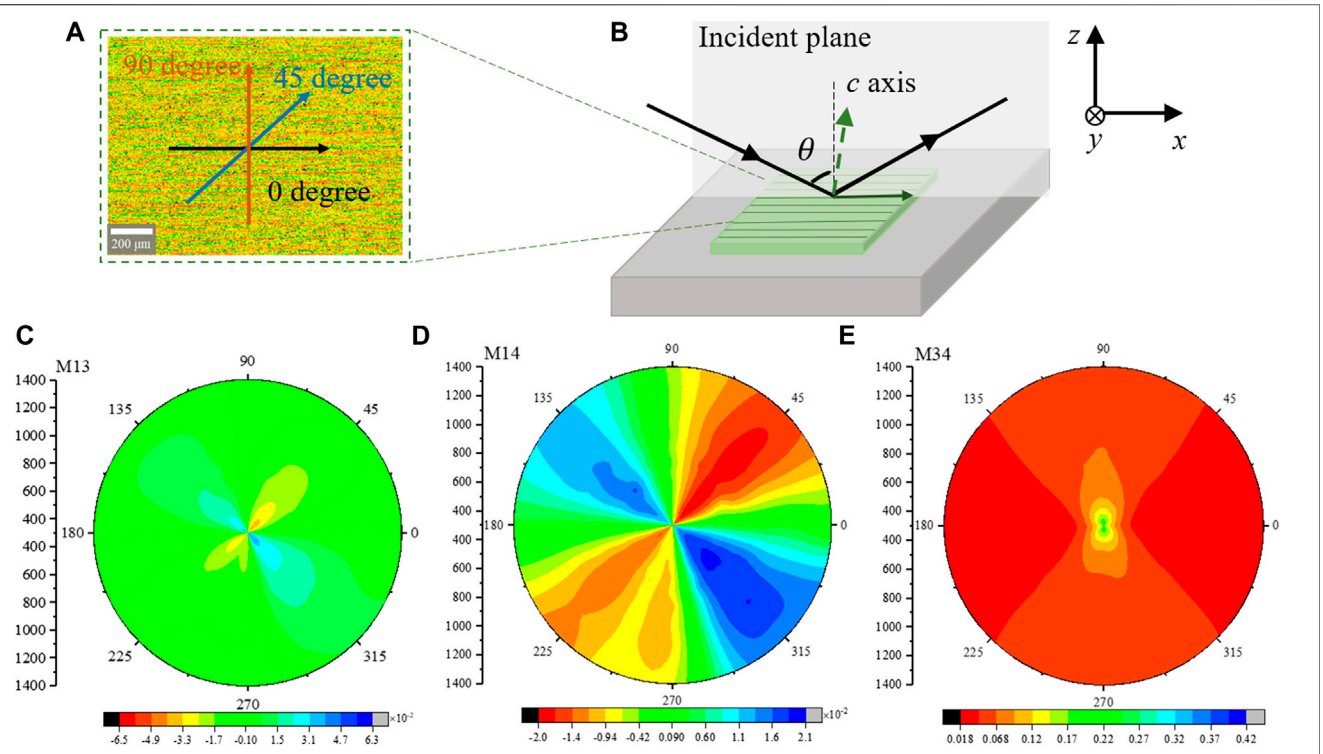


**FIGURE 5 | (A)** The surface morphology of the rough grinding wafer and its initial texture direction parallel to the plane of incidence where the direction of rotation angle is anticlockwise. **(B)** The schematic diagram of reflection ellipsometry measurement. **(C–E)** are the experimental MMSE data of individual M13, M14, and M34 elements from 0 to 360° rotation angles in 65° incident angle, respectively. MM intensities are plotted in polar coordinates with wavelength and rotation angle as radial and angular coordinate.

diagonal elements of the Muller matrix. The difference is that for a rough grinding wafer with surface texture, the 2 × 2 diagonal elements of the Muller matrix at the bottom right corner also have directionality. Specifically, two off-diagonal matrix block elements have the following relationship: M13 = −M31, M23 = −M32, M14 = M41, M24 = M42. Moreover, M13 and M23 are symmetrical about the line formed by 90° and 270° or the line formed by 0° and 180°. The M14 and M24 elements have the same relationship. For diagonal elements we mainly focus on M34/M43 (M34 = −M43). Therefore, we only show the nonzero off-diagonal elements M13, M14 and diagonal element M34 in **Figures 5C–E**, which can reflect the surface structure anisotropy of rough grinding 4H-SiC wafer.

The measurement data indicate that the off-diagonal elements depend on rotation angles and the Mueller matrix has a high sensitivity to structure anisotropy. It can be observed that the off-diagonal elements are zero at 0°, 90°, 180°, and 270° rotation angles. The maximum and minimum values of M13 and M14 spectra are located at 135°, 315° and 45°, 225° rotation angles, respectively. Therefore, off-diagonal Mueller matrix elements can be set as an indicator to judge the direction of the surface rough texture [29]. The result of diagonal element M34 shows that the maximum and minimum values are located at rotation angles of 90° and 0°, respectively. It indicates that when the texture direction of roughness is perpendicular to the incident plane, there are more prominent responses from the Mueller matrix. In this view, the roughness does not appear as an intrinsic characteristic of the surface, which depends on the wavelength and on the direction of propagation of the incident wave.

# 4 RESULTS AND ANALYSIS

## 4.1 Transmission Spectra Analysis

The bandgap of 4H-SiC calculated by Tauc-plot is about 3.3 eV, as shown in **Figure 6A**. **Figure 6B** shows the R and T spectra of 4H-SiC CMP wafer in wavelength range from 220 to 2000 nm. Ordinary extinction coefficient ($k_o$) is first calculated using **Equation 5**, as shown in **Figure 6F**. Then, combined with Mueller matrix differential calculus, the linear birefringence ($n_e - n_o$) and dichroism ($k_e - k_o$) of 4H-SiC are extracted as shown in **Figures 6C,D**. At last, the refractive index ($n_o$ and $n_e$) and extinction coefficients ($k_o$ and $k_e$) of 4H-SiC are completely solved as shown in **Figures 6E,F**.

## 4.2 Reflection Mueller Matrix Analysis

**Figures 7A–C** show the schematic diagrams of multilayer optical models corresponding to the cross-section characteristics of 4H-SiC wafers after three machining stages. From the simulation results in **Section 3.3**, the fully coherence wave theory can be used on wafers with and without back reflection, and the value of M34 element can be used as an indicator of the damage layer.

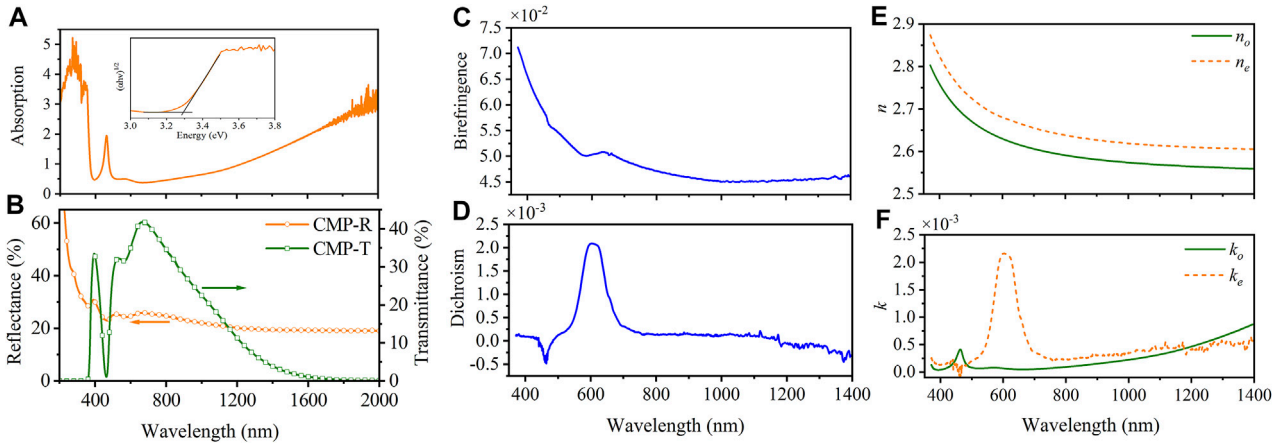


**FIGURE 6 |** Transmission measurement of CMP 4H-SiC wafer with off-axis cut angle. **(A)** Absorption spectra and Tauc-plot, the bandgap 3.3 eV is calculated. **(B)** Reflectance and transmittance spectra. **(C)** Birefringence. **(D)** Dichroism. **(E)** Refractive indices ($n_o$ and $n_e$) and **(F)** extinction coefficients ($k_o$ and $k_e$) of 4H-SiC crystal.

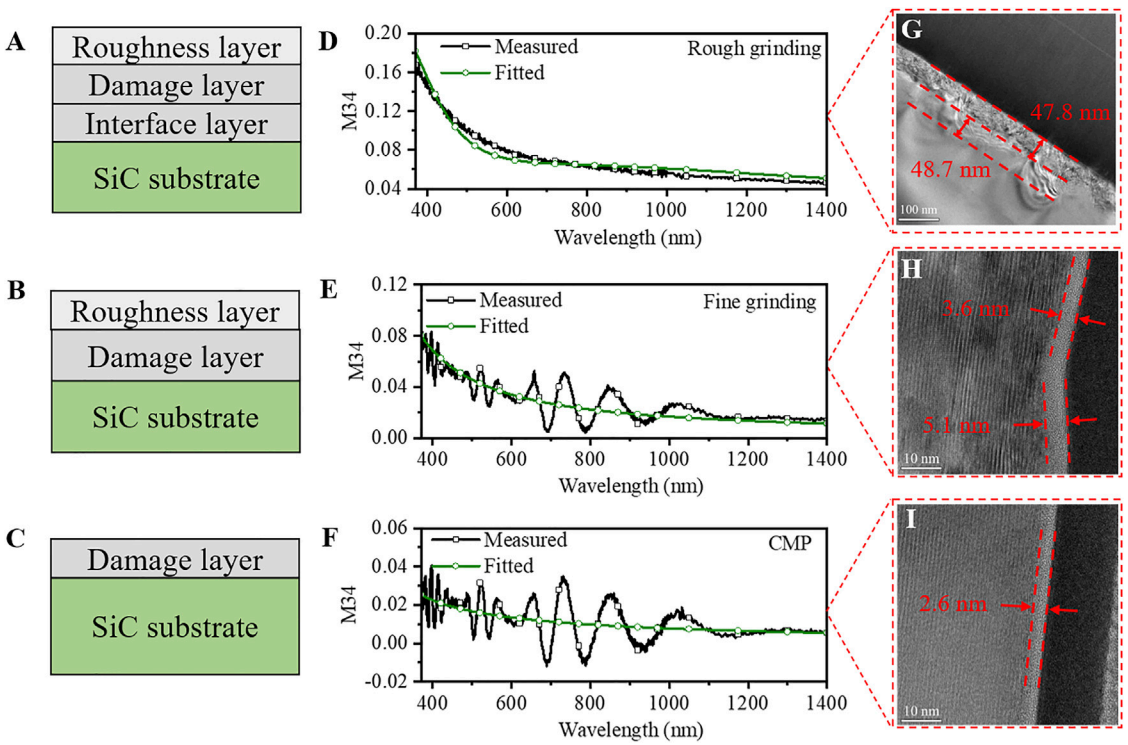


**FIGURE 7 | (A–C)** are the schematic diagrams of optical stack models. **(D–F)** are fitting results of M34. **(G–I)** are the typical TEM images of rough grinding, fine grinding, and CMP 4H-SiC wafers.

Therefore, only the fitted M34 elements are compared with the experimental data of three processed wafers, as shown in **Figures 7D–F**. The smooth curve of measured M34 in **Figure 7D** indicates backside reflection is absent from the rough grinding wafer. The fluctuating curves of measured M34 in **Figures 7E,F** are affected by backside reflection, and their amplitude is related to the absorption of samples. The fluctuations decrease in three higher extinction coefficient ranges, corresponding to 430–480 nm ($k_e$), 520–650 nm ($k_e$), and 1100 nm–1400 nm ($k_o$ and $k_e$) (**Figure 6F**).

The thicknesses of the roughness layer of rough grinding and fine grinding wafers are initialed by 3D optical surface profiler

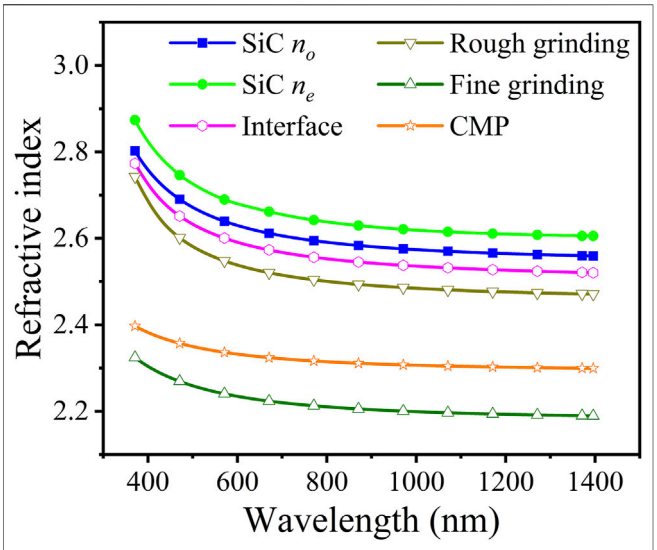


**FIGURE 8 |** The refractive index of the damage layer of three processed wafers compared with that of 4H-SiC crystal.

results, while no roughness layer is set for the CMP wafer. Based on the prior knowledge [17], the Cauchy parameters of the damage layer are initialed as follows: A is 2, B is 0.05 μm$^2$, and the initial thicknesses of damage layers are set to 50 nm, 4 and 2 nm for rough grinding, fine grinding, and CMP wafers according to their processing techniques, respectively.

By fitting the MMSE data, the damage layer thicknesses of rough grinding, fine grinding, and CMP wafers are obtained as 53.7 ± 0.9 nm, 4.6 ± 0.6 nm, and 2.4 ± 0.2 nm, respectively. Besides that, the interface layer under the damage layer of the rough grinding wafer is obtained as 49.2 ± 0.6 nm, which reflects the nonideality of the damage-substrate boundary, residual stress, and other damage types. To verify the reflection Muller matrix analysis method, TEM experiments are carried out. The damage layers are 47.8, 4.35 nm (average of 3.6 and 5.1 nm), and 2.6 nm thick for rough grinding, fine grinding, and CMP 4H-SiC wafers, as shown in **Figures 7G–I**. They have a close agreement with those values obtained by MMSE. Because of the inhomogeneity of the surface, the results of different positions on wafers show some difference, especially for the rough grinding wafer. Three

**TABLE 1 |** The atomic ratio of Si, C, and O elements at the surface of rough grinding, fine grinding, and CMP 4H-SiC wafer.

| Element | Rough grinding (%) | Fine grinding (%) | CMP (%) |
|---|---|---|---|
| Si | 32.14 | 35.16 | 36.68 |
| C | 48.13 | 44.30 | 51.25 |
| O | 19.73 | 20.54 | 12.07 |

positions of each sample are measured by TEM for comparison. Their average thickness value and standard deviation of damage layers are 47.7 ± 8.9 nm, 4.5 ± 0.7 nm, and 2.6 ± 0.1 nm, respectively. It can be seen that the rough surface shows larger damage inhomogeneity than the other two.

The rough grinding also left an interface inhomogeneity (about 48.7 nm thick in one position) under the damage layer, as shown in **Figure 7G**. The average thickness is about 53.7 ± 7.5 nm of three positions, which is also close to that result of MMSE. In this view, although these damages are very inhomogeneously distributed in different areas, the interface layer analyzed by MMSE can reflect them to a certain extent. The experiment shows that MMSE can analyze the damage layers of grinding and polishing wafers in a nondestructive way.

Moreover, the refractive indices of the damage layers after three machining stages are compared with that of 4H-SiC crystal, as shown in **Figure 8**. The refractive indices of all damage layers are smaller than those of the SiC crystal, which means the destruction of the silicon carbide structure and the introduction of other atoms, such as oxygen. The higher refractive index of the rough grinding wafer than those of the fine grinding and CMP wafers can be explained by incomplete amorphization of the damaged zone (**Figure 7**). The higher refractive index of the CMP wafer than that of the fine grinding wafer can be explained by different atomic ratios of elements in XPS analysis (**Section 4.3**).

In general, with further processing, the thickness of the damage layer gradually decreases and the quality of the wafer after CMP has been significantly improved. It should be noted that the thickness of the damage layer determined from the MMSE analysis represents an averaged value across the probed area with 3 mm diameter.

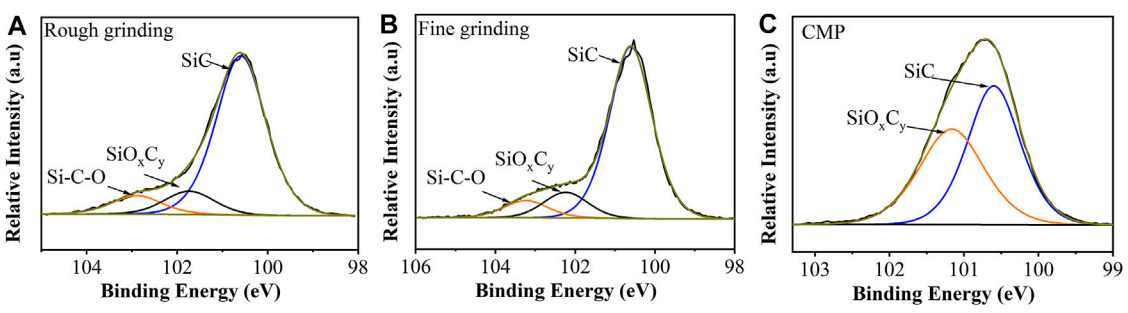


**FIGURE 9 |** Si 2p XPS spectra of **(A)** rough grinding, **(B)** fine grinding, and **(C)** CMP 4H-SiC wafers.

### 4.3 XPS Analysis of Processed Surfaces

The Si-face surface of three processed SiC wafers is shown by XPS full spectra, which mainly is composed of silicon (Si), carbon (C), and oxygen (O). The atomic ratios of Si, C, and O elements on the surface of rough grinding, fine grinding, and CMP 4H-SiC wafer are listed in **Table 1**. It can be clearly seen that the content of the C atom in the CMP wafer is greater than that of grinding wafers, while the content of the O atom is less than that of grinding wafers. This is maybe the reason why the refractive index of the damage layer of the CMP wafer is greater than that of the fine grinding wafer.

By using Avantage software, the Shirley model is selected as the background type and Gauss–Lorentz mixture function is used to fit each XPS spectra. **Figure 9** illustrates the fitting spectra of the narrow Si 2p band of SiC wafers. **Figures 9A,B** show there are three main peaks due to the Si-C peak, and two silicon oxycarbides on the surface of rough grinding and fine grinding wafers. **Figure 9C** illustrates only the Si-C peak and one silicon oxycarbide component on the surface of the CMP wafer.

XPS results indicate that silicon oxycarbide is formed on the processed Si-face surface instead of $SiO_2$. It reveals that the refractive index of the damage layer is between that of SiC and $SiO_2$, which is consistent with the result of ellipsometric analysis (**Figure 8**). The results of rough grinding and fine grinding wafer show different processing parameters and under the same process produce similar surface compositions. It should be noted that the measurement depth of XPS is less than 10 nm. Therefore, it is difficult for XPS analysis to reflect the entire damage depth of the rough grinding wafer.

## 5 CONCLUSION

In this study, a nondestructive detection method based on Mueller matrix spectroscopic ellipsometry is proposed to evaluate the subsurface damage of 4H-SiC wafers in rough grinding, fine grinding, and CMP stages. The elements of the Muller matrix are sensitive indictors of the damage layer and the surface texture. Especially, the change of M34 is significantly induced by the damage layer. When the surface texture direction is perpendicular to the incident plane, the Mueller matrix can obtain maximum response from the damage and interface. According to simulation and experiment, the optical model even can be simplified to ignore the backside reflection.

There is a great agreement between SE experimental and fitting data of the processed SiC wafers. The fitting thickness and refractive index of the damage layer are verified by TEM and XPS. This provides a possible method to achieve rapid quality assessment of SiC wafer in the entire production line. It is critically important for the processing optimization of large-size SiC wafers and the improvement of subsequent epitaxial quality. As a conclusion, this study provides a guide to the engineering applications of ellipsometry in the damage layer evaluation. The influence of incident angle and the light reflection characteristics at different wavelengths can be studied in the future.

## DATA AVAILABILITY STATEMENT

The original contributions presented in the study are included in the article/**Supplementary Material**, further inquiries can be directed to the corresponding author.

## AUTHOR CONTRIBUTIONS

All authors discussed the experiment design and contents of the manuscript. Under the supervision of CC, HL oversaw the MMSE experiment and analysis. ZH and WL provided the wafers. The paper was mainly written by HL and SB, with assistance from CC and JL for advice and proofreading. XX provided suggestions to the material selection. The experimental results were primarily evaluated and discussed by all authors. All authors have read and agreed to the published version of the manuscript.

## FUNDING

This study was supported by the National Natural Science Foundation of China (Grant No. 51835004).

## ACKNOWLEDGMENTS

The authors would like to thank the Instrumental Analysis Center of Huaqiao University. The authors would also like to thank Dr. Hui Cao of the School of Computing and Engineering of Huddersfield University for English language editing.

## SUPPLEMENTARY MATERIAL

The Supplementary Material for this article can be found online at: https://www.frontiersin.org/articles/10.3389/fphy.2021.820637/full#supplementary-material

## REFERENCES

1. Blevins JD. Development of a World Class Silicon Carbide Substrate Manufacturing Capability. *IEEE Trans Semicond Manufact* (2020) 33: 539–545. doi:10.1109/TSM.2020.3028036
2. Naftaly M, Molloy JF, Magnusson B, Andreev YM, Lanskii GV. Silicon Carbide-A High-Transparency Nonlinear Material for THz Applications. *Opt Express* (2016) 24:2590. doi:10.1364/oe.24.002590
3. Kakanakova-Georgieva A, Persson POÅ, Kasic A, Hultman L, Janzén E. Superior Material Properties of AlN on Vicinal 4H-SiC. *J Appl Phys* (2006) 100:036105. doi:10.1063/1.2219380
4. Zhou Y, Pan G, Shi X, Xu L, Zou C, Gong H, et al. XPS, UV-Vis Spectroscopy and AFM Studies on Removal Mechanisms of Si-Face SiC Wafer Chemical Mechanical Polishing (CMP). *Appl Surf Sci* (2014) 316:643–648. doi:10.1016/j.apsusc.2014.08.011
5. McPherson JA, Hitchcock CW, Paul Chow T, Ji W, Woodworth AA. Ion-Induced Mesoplasma Formation and Thermal Destruction in 4H-SiC Power

MOSFET Devices. *IEEE Trans Nucl Sci* (2021) 68:651–658. doi:10.1109/TNS.2021.3068196
6. Lu J, Luo Q, Xu X, Huang H, Jiang F. Removal Mechanism of 4H- and 6H-SiC Substrates (0001 and 0001) in Mechanical Planarization Machining. *Proc Inst Mech Eng B: J Eng Manufacture* (2019) 233:69–76. doi:10.1177/0954405417718595
7. Yan J, Tan T-H. Sintered diamond as a Hybrid EDM and Grinding Tool for the Micromachining of Single-crystal SiC. *CIRP Ann* (2015) 64:221–224. doi:10.1016/j.cirp.2015.04.069
8. Yang X, Yang X, Kawai K, Arima K, Yamamura K. Highly Efficient Planarization of Sliced 4H-SiC (0001) Wafer by Slurryless Electrochemical Mechanical Polishing. *Int J Machine Tools Manufacture* (2019) 144:103431. doi:10.1016/j.ijmachtools.2019.103431
9. Yin J-f., Bai Q, Zhang B. Methods for Detection of Subsurface Damage: A Review. *Chin J Mech Eng* (2018) 31:31. doi:10.1186/s10033-018-0229-2
10. Xu Z, He Z, Song Y, Fu X, Rommel M, Luo X, et al. Topic Review: Application of Raman Spectroscopy Characterization in Micro/nano-Machining. *Micromachines* (2018) 9:361. doi:10.3390/mi9070361
11. Wang N. Review on Brittle Material Subsurface Damage Detection Technology. *Jme* (2017) 53:170. doi:10.3901/jme.2017.09.170
12. Zhang Y, Zhang L, Chen K, Liu D, Lu D, Deng H. Rapid Subsurface Damage Detection of SiC Using Inductivity Coupled Plasma. *Int J Extrem Manuf* (2021) 3:035202. doi:10.1088/2631-7990/abff34
13. Arteaga O, Garcia-Caurel E, Ossikovski R. Anisotropy Coefficients of a Mueller Matrix. *J Opt Soc Am A* (2011) 28:548. doi:10.1364/josaa.28.000548
14. Li H, Cui C, Bian S, Lu J, Xu X, Arteaga O. Model-free Determination of the Birefringence and Dichroism in *c*-Cut Crystals from Transmission Ellipsometry Measurements. *Appl Opt* (2020) 59:2192. doi:10.1364/ao.386583
15. Zollner S, Chen JG, Duda E, Wetteroth T, Wilson SR, Hilfiker JN. Dielectric Functions of Bulk 4H and 6H SiC and Spectroscopic Ellipsometry Studies of Thin SiC Films on Si. *J Appl Phys* (1999) 85:8353–8361. doi:10.1063/1.370682
16. Ossikovski R, Kildemo M, Stchakovsky M, Mooney M. Anisotropic Incoherent Reflection Model for Spectroscopic Ellipsometry of a Thick Semitransparent Anisotropic Substrate. *Appl Opt* (2000) 39:2071. doi:10.1364/ao.39.002071
17. Li H, Cui C, Bian S, Lu J, Xu X, Arteaga O. Double-sided and Single-Sided Polished 6H-SiC Wafers with Subsurface Damage Layer Studied by Mueller Matrix Ellipsometry. *J Appl Phys* (2020) 128:235304. doi:10.1063/5.0026124
18. Yao C, Huo S, Shen W, Sun Z, Hu X, Hu X, et al. Assessing the Quality of Polished Brittle Optical crystal Using Quasi-Brewster Angle Technique. *Precision Eng* (2021) 72:184–191. doi:10.1016/j.precisioneng.2021.04.019
19. Yin J, Chen D, Yang H, Liu Y, Talwar DN, He T, et al. Comparative Spectroscopic Studies of MOCVD Grown AlN Films on $Al_2O_3$ and 6H-SiC. *J Alloys Comp* (2021) 857:157487. doi:10.1016/j.jallcom.2020.157487
20. Gu H, Chen X, Jiang H, Zhang C, Liu S. Optimal Broadband Mueller Matrix Ellipsometer Using Multi-Waveplates with Flexibly Oriented Axes. *J Opt* (2016) 18:025702. doi:10.1088/2040-8978/18/2/025702
21. Liu S, Chen X, Zhang C. Development of a Broadband Mueller Matrix Ellipsometer as a Powerful Tool for Nanostructure Metrology. *Thin Solid Films* (2015) 584:176–185. doi:10.1016/j.tsf.2015.02.006
22. Ellis B, Moss TS. Anisotropy of Absorption Due to Free Electrons in 6H Silicon Carbide. *Solid State Commun* (1985) 3:109–111.
23. Arteaga O, Canillas A. Analytic Inversion of the Mueller-Jones Polarization Matrices for Homogeneous media: Erratum. *Opt Lett* (2010) 35:3525. doi:10.1364/ol.35.003525
24. Wang S, Zhan M, Wang G, Xuan H, Zhang W, Liu C, et al. 4H-SiC: A New Nonlinear Material for Midinfrared Lasers. *Laser Photon Rev* (2013) 7:831–838. doi:10.1002/lpor.201300068
25. Chen J, Fang Q, Li P. Effect of Grinding Wheel Spindle Vibration on Surface Roughness and Subsurface Damage in Brittle Material Grinding. *Int J Machine Tools Manufacture* (2015) 91:12–23. doi:10.1016/j.ijmachtools.2015.01.003
26. Maksoud TMA, Mokbel AA, Morgan JE. Evaluation of Surface and Subsurface Cracks of Ground Ceramic. *J Mater Process Tech* (1999) 88:222–243. doi:10.1016/S0924-0136(98)00403-8
27. Sylvain M. Diffuse Reflection by Rough Surfaces: An Introduction. *Comptes Rendus Physique* (2005) 6:663–674. doi:10.1016/j.crhy.2005.06.014
28. Nichols SM. *Coherence in Polarimetry* (2018). Matlab code available from: https://github.com/shane-nichols/smn-thesis.
29. Dixit D, O'Mullane S, Sunkoju S, Gottipati A, Hosler ER, Kamineni V, et al. Sensitivity Analysis and Line Edge Roughness Determination of 28-nm Pitch Silicon Fins Using Mueller Matrix Spectroscopic Ellipsometry-Based Optical Critical Dimension Metrology. *J Micro/nanolith MEMS MOEMS* (2015) 14:031208. doi:10.1117/1.jmm.14.3.031208

**Conflict of Interest:** Author WL is employed by Fujian Norstel Material Technologies Co., Ltd.

The remaining authors declare that the research was conducted in the absence of any commercial or financial relationships that could be construed as a potential conflict of interest.

**Publisher's Note:** All claims expressed in this article are solely those of the authors and do not necessarily represent those of their affiliated organizations, or those of the publisher, the editors and the reviewers. Any product that may be evaluated in this article, or claim that may be made by its manufacturer, is not guaranteed or endorsed by the publisher.

frontiers in Physics

ORIGINAL RESEARCH
published: 04 March 2022
doi: 10.3389/fphy.2022.815539

# Angular-Based Mueller Matrix Polarimetry Parameters for Subwavelength Pore Size Differentiation

*Jiachen Wan*[1], *Chuhui Wang*[2], *Chunnan Wang*[1], *Shuqing Sun*[1] *and Hui Ma*[1,2,3]*

[1]Shenzhen International Graduate School, Tsinghua University, Shenzhen, China, [2]Center for Precision Medicine and Healthcare, Tsinghua-Berkeley Shenzhen Institute, Shenzhen, China, [3]Department of Physics, Tsinghua University, Beijing, China

Mueller matrix polarimetry is exploited to find a potential polarization feature sensitive to subwavelength pore size variation in porous alumina samples. After careful analysis using standard machine learning methods, it is observed that existing Mueller matrix decomposition methods and parameters are insufficient to distinguish areas with different pore sizes. Thus, a new angular-based Mueller matrix polarimetry parameter capable of linearly separating areas with varying pore sizes is proposed. Such an angular-based parameter is novel because it is based on angular parameters, it utilizes multi-angle measurements, and it extracts physical information independent of existing decomposition methods or parameters. Hopefully this work should inspire future research on the angular parameters in Mueller matrix polarimetry and their relationships to microstructure information.

**Keywords: Mueller matrix polarimetry, polarization, stokes vector, angular parameter, Mueller matrix imaging**

OPEN ACCESS

***Edited by:***
*Ji Qi,*
*Imperial College London, United Kingdom*

***Reviewed by:***
*Igor Meglinski,*
*Aston University, United Kingdom*
*Xiuguo Chen,*
*Huazhong University of Science and Technology, China*
*Daqian Wang,*
*Hefei University of Technology, China*

***Correspondence:**
*Hui Ma*
*mahui@tsinghua.edu.cn*

***Specialty section:***
*This article was submitted to Optics and Photonics, a section of the journal Frontiers in Physics*

***Received:*** *15 November 2021*
***Accepted:*** *03 February 2022*
***Published:*** *04 March 2022*

***Citation:***
*Wan J, Wang C, Wang C, Sun S and Ma H (2022) Angular-Based Mueller Matrix Polarimetry Parameters for Subwavelength Pore Size Differentiation. Front. Phys. 10:815539. doi: 10.3389/fphy.2022.815539*

## INTRODUCTION

Mueller matrix (MM) microscopy is a promising tool for scientific research and clinical application because it reveals the intrinsic optical property of objects [2–4]. When light interacts with samples, the polarization state of light may change due to scattering, absorption, refraction, and other optical phenomena; such changes in the polarization state before and after light interaction can be comprehensively described using the Mueller matrix. Scholars have exploited Mueller matrix polarimetry to analyze various materials and biological samples because the Mueller matrix encodes rich microstructure information [5–8]. Existing studies prove that Mueller matrix polarimetry can differentiate cancerous tissues [6, 7], liver fibrosis [9], selected species of algae [10], and aerosol particles [11].

The Mueller matrix encodes microstructure information, but it would still be obscure to us if the information is unextractable. Specifically, Mueller matrix polarimetry can be exploited to classify different materials, but it is often challenging to find an analytical form of such discriminating parameters. Scholars commonly start by analyzing the Mueller matrix parameters such as the Mueller matrix polar decomposition (MMPD) and Mueller matrix transformation (MMT), which are interpretable physical parameters in extremely simplified models [4, 12, 13]. This approach can be effective but not sufficient because in almost all cases, the samples are too complex to be differentiated using these simple parameters. An alternative way of extracting discriminating parameters from the Mueller matrix is using the PBP-PFP approach. Polarization basis parameters (PBPs) refer to the MMPD and MMT parameters, which are interpretable but

oversimplified. PBPs are then linearly combined to create polarization feature parameters (PFPs), which are much more microstructure-specific. This approach is proven useful in pathological samples [4–6]. To differentiate more complex samples, nonlinear models in machine learning could be utilized, but such models are often uninterpretable, and the results are not generalizable.

Machine learning is a powerful tool for extracting microstructure information from polarimetric data. Given the sample data, machine learning algorithms build a model to make classification predictions or clustering decisions. Studies have shown that by utilizing machine learning, Mueller polarimetry can classify *ex vivo* colon cancer, hematoxylin and eosin (H&E)-stained and unstained breast cancer, H&E-stained cervical cancer, and skin cancer [5, 6, 31, 32]. Using deeper models and convolution layers that specialize on processing imagery data, the models trained using polarimetric data are capable of transforming between polarimetric imaging and brightfield imaging, synthesizing polarization-sensitive optical coherence tomography images from OCT images and classifying objects in degraded environments [33–35]. In this study, the machine learning algorithm, linear discriminant analysis, is applied to classify regions with different pore sizes using rotation-invariant parameters [29].

One of the limitations with the current microstructure feature parameter extraction methods is that they are mainly based on the rotation-invariant parameters. The orientation of the sample should not affect its microstructure information, so consequently, the microstructure feature parameters should not vary as the sample rotates. Therefore, it may seem logical to use rotation-invariant parameters as the basis parameters since their combination will also be rotation-invariant. However, polarization is sensitive to anisotropy, and such information is often contained in azimuthal parameters rather than in rotation-invariant parameters. To fully utilize Mueller matrix optics, the use of angular parameters is essential.

In this work, the idea of angular parameter-based microstructure feature parameters is explored and experimented. Using the porous anodic alumina (PAA) Mueller matrix polarimetry measurement data from the published work of Chuhui Wang [1], it is discovered that while the rotation-invariant parameters could not differentiate the pore size, the proposed parameter can not only differentiate areas with different pore sizes but also do so with a simple explicit analytical form. Through this study, we emphasized the importance of angular parameters in Mueller matrix polarimetry, demonstrated their potential for differentiating different microstructures, and hopefully inspired future research in this area.

# MATERIALS AND METHODS

## Porous Anodic Alumina Fabrication

Porous anodic alumina (PAA) is a nanomaterial with a controllable porous aspect ratio and radius [14–17]. An electrochemically anodized alumina sheet under specific conditions will form an ordered porous alumina film on top of the thin barrier layer alumina (BLA)-covered aluminum substrate [19–24]. Its uniform pore sizes and dense distribution of pores makes PAA an idea membrane. Studies have shown that PAA can also be used as a photonic crystal [18].

Using the secondary anodization method, a PAA sample with two different pore diameters was fabricated and studied. The setup is shown in **Figure 1**. The fabricated sample is imaged under a scanning electron microscope, and **Figure 2** shows the top and side view of the PAA sample. For the detailed fabrication process, please refer to [1].

## Mueller Matrix Polarimetry

The dual-rotating retarder Mueller matrix measurement method is used in this study [1, 26]. An LED light source with a center wavelength of 633 nm is used. The system is calibrated using air as the standard sample, with a maximum error of 2%. Detailed information regarding the Mueller matrix imaging system can be found in [1].

The Mueller matrix images of the samples are measured at two angles: normal incidence and 32° tilting angle. At normal incidence, the pores are colinear with the light ray, so the interaction between the pores and light is relatively weak. At a tilting angle, the interaction starts becoming obvious. By comparing the Mueller matrices from two distinct tilting angles, it is possible to isolate the optical effect due to the pores. The tilting angle of 32° is selected for experimental convenience.

## Analysis of Angular Parameters

The fabricated PAA sample is measured twice. With a random sample orientation, the PAA sample is first measured at normal incidence and then measured again at 32° tilting angle. At 0° tilting angle, the MMT parameter $\alpha_r$ is measured using the following formula:

$$\boldsymbol{\alpha}_{\mathbf{r}}^{(0)} = \frac{1}{2}\mathbf{tan}^{-1}\left(-\mathbf{M}_{24}^{(0)}\big/\mathbf{M}_{34}^{(0)}\right).$$

The superscript $^{(0)}$ indicates that the values from the 0-degree incidence angle measurement are used for calculation. For a pure phase retarder, the MMT parameter $\boldsymbol{\alpha}_{\mathbf{r}}$ is the anisotropic azimuth angle of the retarder [1, 4]. Because this parameter is measured at 0 tilting degree, it should not be sensitive to porous information since the pores and the light ray are colinear. Moreover, at 32° tilting angle, the MMT parameter $\boldsymbol{\delta}$ is calculated using the following formula:

$$\boldsymbol{\delta}^{(32)} = \mathbf{cos}^{-1}\mathbf{M}_{44}^{(32)}.$$

The superscript $^{(32)}$ indicates that the values from the 32-degree incidence angle measurement are used for the calculation. For a pure phase retarder, the MMT parameter δ is the phase of linear retardance [1, 4]. This parameter is sensitive to both the retardance due to the material and the pores. It is assumed that

$$\boldsymbol{\alpha}_{\mathbf{r}}^{(0)} \propto \boldsymbol{\delta}^{(32)},$$

which is experimentally observed to be valid. All the naturally formed blocks and their corresponding $\boldsymbol{\alpha}_{\mathbf{r}}^{(0)}$ and $\boldsymbol{\delta}^{(32)}$ values are

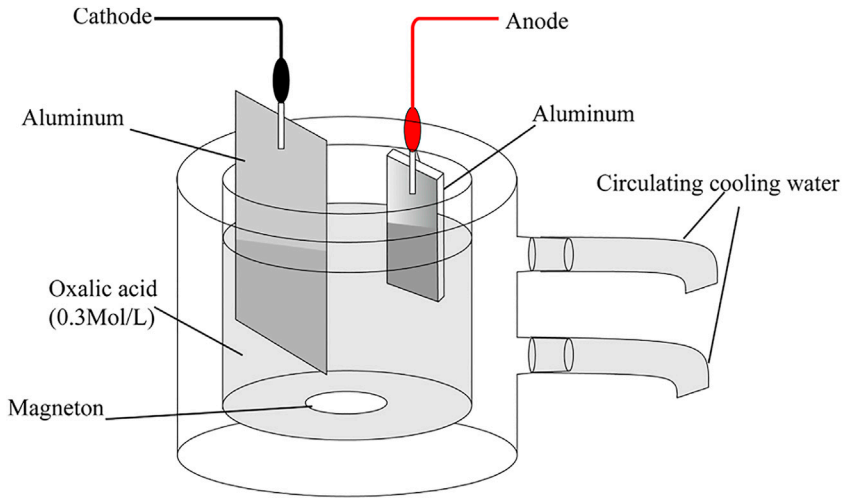


**FIGURE 1 |** Diagram of the secondary anodization method [1]. Reprinted with permission from [1] © The Optical Society.

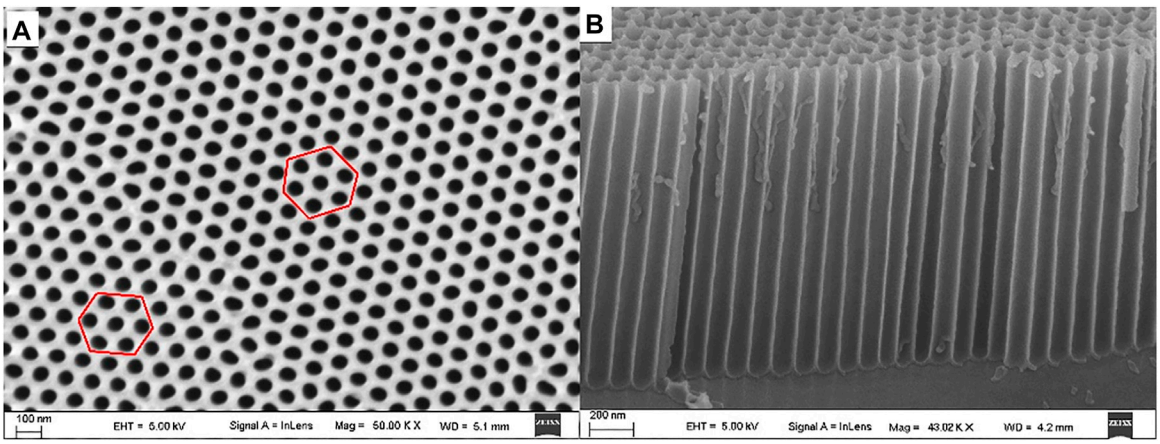


**FIGURE 2 |** SEM images of the PAA sample, from the top view **(A)** and the side view **(B)**. The hexagonal pore structure is clearly observed [1]. Reprinted with permission from [1] © The Optical Society.

measured and recorded. One can then try determining the slope and y-intercept of the scatter plot using the least square linear regression algorithm, by essentially fitting a line to the observed data [28]. It is observed that the y-intercept of the lines encodes pore size information.

## RESULTS

**Figure 3** shows the measured Mueller matrix of the PAA sample. A clear vertical line separates the regions with different pore sizes. It is noted that the M12, M13, M21, and M31 elements are nearly zero, indicating the PAA exhibits a strong birefringence property. Natural formation of blocks is observed, and each block has its distinct azimuthal orientation, as indicated by the MMT parameter $\boldsymbol{\alpha}_{\mathbf{r}}^{(0)}$. As the tilting angle increases, the birefringence signal becomes stronger as well, as reflected in the decrease of the M44 element after inclination. It is noted that the image is distorted when the sample is tilted, so to register the data measured from different incidence angles, we have used control point methods to estimate the geometric transformation matrix.

Now, to proceed with the analysis, we have manually selected several blocks from two regions with different pore sizes. **Figure 4** shows all the blocks that we have chosen.

The PBP-PFP approach is first tested for reference. The rotation-invariant parameters from MMT are used as basis features, in order to linearly combine into a polarization feature parameter that can differentiate the blocks from the two regions with different pore sizes. Linear discriminant analysis is an algorithm that finds the hyperplane that separates different

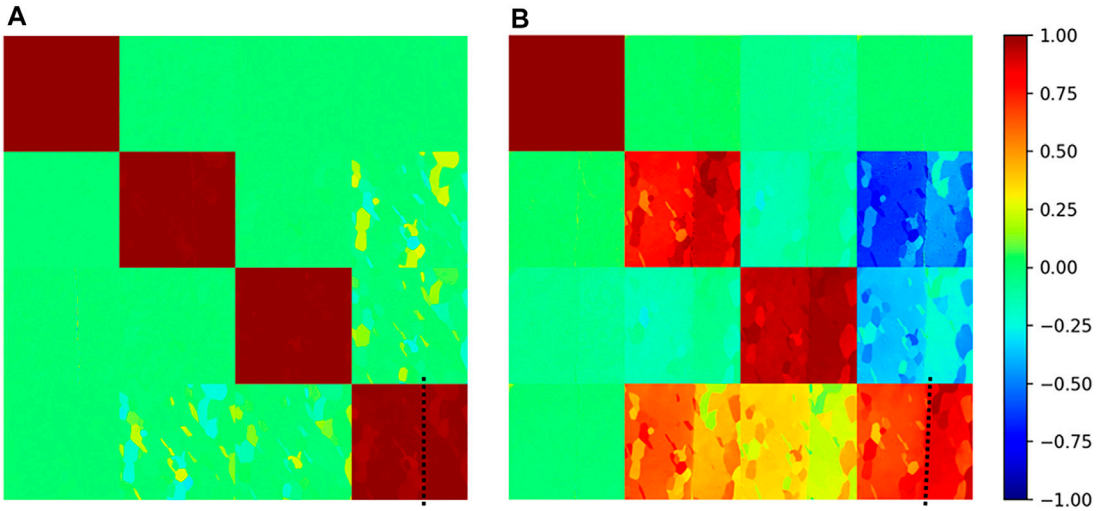


**FIGURE 3 |** Experimentally measured Mueller matrix of the PAA sample with normal incidence **(A)** and 32° tilting angle **(B)**. The black dotted line separates the regions with different pore sizes.

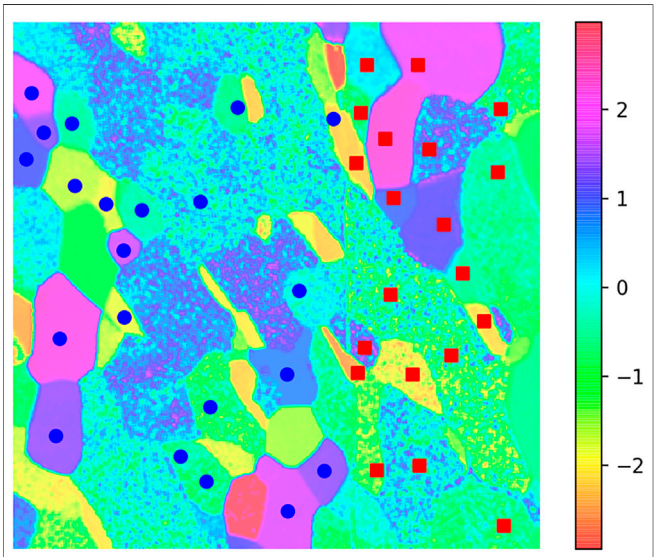


**FIGURE 4 |** Locations of the manually selected block. The blocks from the two regions with different (query) are marked with different markers: one with blue dots and the other with red squares.

groups of data, given the group labels [29]. In this study, it is used to find the optimal linear combination of polarization parameters that discriminate the sets. An 8-fold cross validation method is used to determine the generalizability of the obtained PFP. The data points are partitioned into eight subgroups, and the model is evaluated eight times, each time selecting a subgroup as the testing set and the rest as the training set [30]. Using the 0-degree tilting data, the mean accuracy is 58.8%; with the 32-degree tilting data, the mean accuracy is 92.5%; the mean accuracy using data from both tilting angles is 80.4%. Such results imply that the interaction between the pores and photons is much stronger when the sample is tilted, and the rotation-invariant parameters cannot differentiate areas with different pore sizes.

An alternative approach based on angular parameters is proposed. Assuming a linear relationship between $\boldsymbol{\alpha}_r^{(0)}$ and $\boldsymbol{\delta}^{(32)}$ with no phase delay, the two variables are plotted against each other, where $\boldsymbol{\alpha}_r^{(0)}$ is on the $x$-axis and $\boldsymbol{\delta}^{(32)}$ is on the $y$-axis. We can clearly observe a linear relationship between them, as shown in **Figure 5A**. The points from regions with differing pore sizes clearly lie on two distinct lines, and they are easily differentiable. Due to the observed phenomenon, it is speculated that the y-intercept might correlate with the pore size.

However, the zero-phase-delay assumption is unlikely to be true most of the time, depending on sample orientation. In other words, a perfect straight line is unlikely to be observed. So instead of representing the relationship between two periodic variables in the Euclidian fashion, the proper way of representing the linear relationship between $\boldsymbol{\alpha}_r^{(0)}$ and $\boldsymbol{\delta}^{(32)}$ is by using the polar coordinate. In **Figure 5B**, the scatter points are determined by using $2\boldsymbol{\alpha}_r^{(0)}$ as the angle and $\boldsymbol{\delta}^{(32)}$ as the radius. Two non-overlapping spirals are observed, each representing data from a different pore size.

## DISCUSSION

To summarize, a pore size discriminative parameter is proposed based on the Mueller matrix angular parameter with multi-angle measurement. The parameter proposed in this study is important for three main reasons: first, it contains subwavelength pore size information; second, it extracts microstructure information outside of the existing MM parameters' span; and finally, it proves that multi-angle measurement is necessary for decoding pore size information. All these points will be further addressed in the following paragraphs.

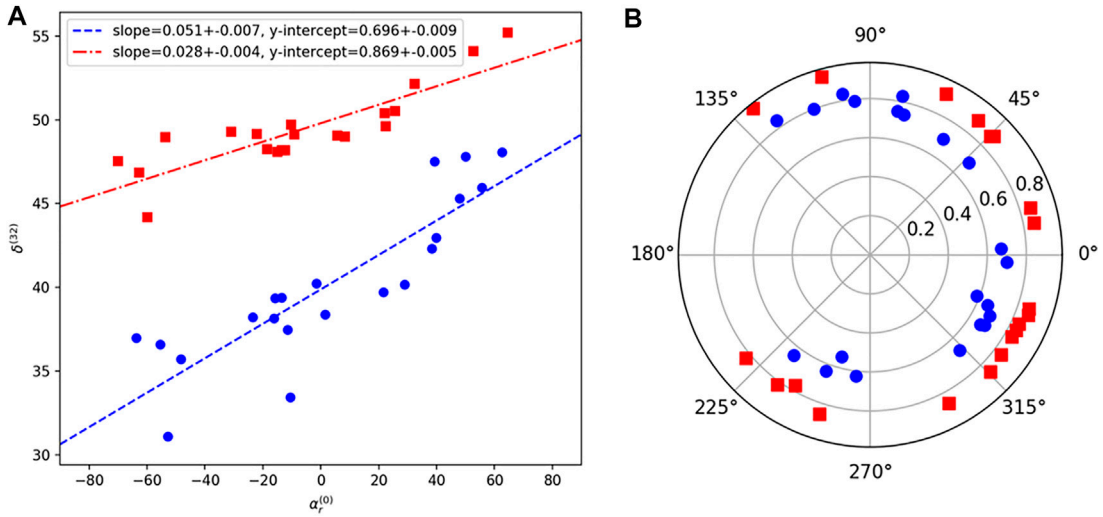


**FIGURE 5 |** Scatter plot of $\alpha_r^{(0)}$ and $\delta^{(32)}$ , drawn in Euclidean **(A)** and polar **(B)** coordinates. For **(B)**, the angle of the scatter plot is $2\alpha_r^{(0)}$ and the radius is $\delta^{(32)}$.

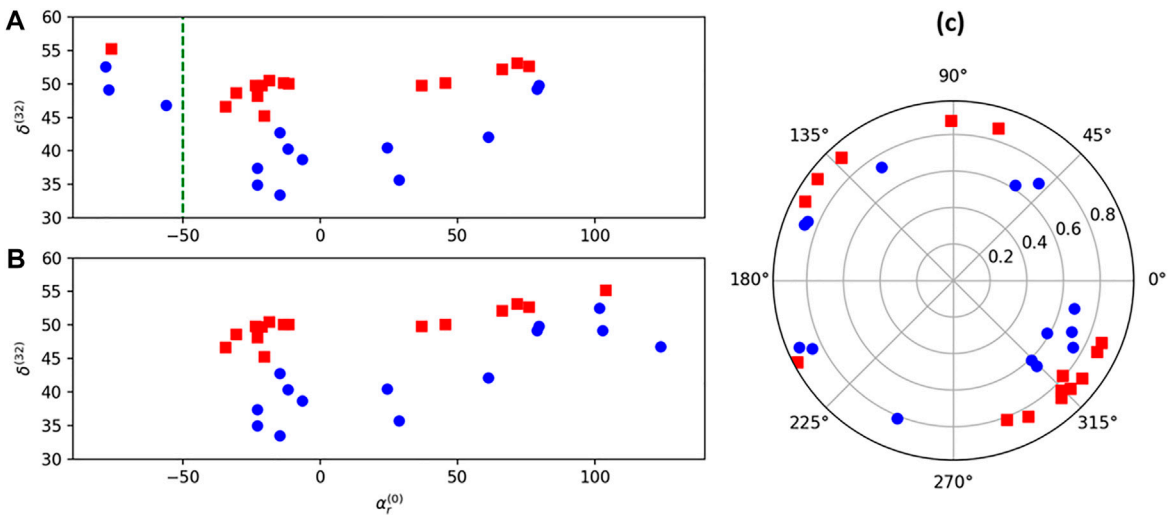


**FIGURE 6 |** Scatter plot of $\alpha_r^{(0)}$ and $\delta^{(32)}$ at a different orientation angle. **(A)** shows the original scatter plot without unwrapping, **(B)** shows the scatter plot after unwrapping, essentially shifting the points on the left of the dotted line by one period, and **(C)** shows the same plot in polar coordinates, where the angle of the scatter plot is $2\alpha_r^{(0)}$ and the radius is $\delta^{(32)}$.

First, the proposed parameter can differentiate PAA regions with different sizes of nanoscale pores. The pore diameter in PAA ranges from 50 to 420 nm [21], depending on the modulating condition. Successfully discriminating regions with varying interpore diameters proves that Mueller matrix polarimetry is capable of resolving the nanostructure beyond the optical resolution limit.

Second, the proposed parameter expands outside the span of known rotation-invariant polarization parameters. Using MMT parameters as basis features, the performance of the linear model is unsatisfactory for the task of discriminating regions with different pore sizes, as shown in the last section. On the other hand, the proposed parameter can fully separate points from different pore size regions with a linear function. It implies that the polarimetric angular parameter encodes microstructure information that is not contained in rotation-invariant parameters.

Finally, the pore size information can only be extracted through multi-angle measurement. Clearly, the MMT parameters cannot fully describe pore size information through single-angle measurement since the best accuracy achieved was 92.5%. Even the newly proposed parameter needs measurement from two distinct

incline angles. Therefore, it is possible that multi-angle measurement is compulsory for pore diameter extraction.

For context, there are two fields of polarimetry for the analysis of periodic nanomaterial: ellipsometry and Mueller matrix imaging. In the field of ellipsometry, experimental data are matched with theoretical simulation to obtain the physical parameters of the observed samples, such as porosity and pore size [27]. This is the idealistic approach for nanomaterial analysis since it has unrealistic assumptions for the sample, such as perfect uniformity. While on the other hand, in the field of Mueller matrix polarimetry, the decomposition/parametric approach is taken, and a non-idealistic sample is assumed. In this context, this study attempts to bridge the two fields, using the parametric approach to decode microstructural information, and attempted to obtain a feature parameter for pore size discrimination without making any unrealistic assumptions for the sample.

It is worth noticing that the linear relationship between $\boldsymbol{\alpha}_{\mathbf{r}}^{(0)}$ and $\boldsymbol{\delta}^{(32)}$ is essentially a form of invariance. In other words, no matter how the PAA sample is rotated, the resulting point will always stay on the line (with proper unwrapping). Invariance indicates conserved quantities, and conserved quantities usually have physical meanings. In the case of the proposed parameter, it is reasonable to hypothesize that the parameter correlates with the porous structure of the sample. In the photonic crystal language, the proposed parameter could encode information in the momentum space. For further studies, a detailed relationship between the proposed parameter and the pore size should be studied, to see if any correlation exists.

Despite the microstructure information it contains, the use of angular parameters for feature parameters has its limitations. The largest problem with angular parameters is unwrapping. As the sample rotates, the $\boldsymbol{\alpha}_{\mathbf{r}}^{(0)}$ parameter changes as well, but it is constrained in its range. The sample orientation displayed in the result section was carefully selected to avoid the unwrapping problem, while in fact, if the sample is rotated at a different angle, the linear relationship between $\boldsymbol{\alpha}_{\mathbf{r}}^{(0)}$ and $\boldsymbol{\delta}^{(32)}$ is a lot less obvious, as shown in 6a. However, if we shift the points on the left of the green-dashed line by one period, the linear relationship between the two variables is restored, as seen in **Figure 6B**. This demonstrates the essence of the unwrapping problem; the fact that one can freely add or subtract any integer amount of period from the angular parameters makes it difficult to determine the real angular value. Here, it is assumed that the true value of $\boldsymbol{\alpha}_{\mathbf{r}}^{(0)}$ is the one that restores the linear relationship. The unwrapping problem could be somewhat avoided if we use the polar coordinate, as shown in **Figure 6C**. Now, instead of lines we can observe spirals, and it solves the unwrapping problem since the angle is now represented in two-dimension instead of one. However, it poses new challenges on the quantification of feature parameters in polar coordinates.

In total, the angular parameter encodes nanoscale structural information regarding the PAA pore diameter. It is proven experimentally that $\boldsymbol{\alpha}_{\mathbf{r}}^{(0)}$ and $\boldsymbol{\delta}^{(32)}$ parameters can linearly discriminate PAA regions with different pore sizes. It can potentially become a method to quantify photonic crystal's microstructure information to reduce the undesired scattering effect. To mass produce, photonic crystals need a high-throughput monitoring method with subwavelength resolution, which Mueller matrix polarimetry is capable of. The use of angular parameters as basis features can be challenging due to the unwrapping problem, but it contains information that rotation-invariant parameters do not. This study provides a new perspective in the analysis of angular parameters, but to further study them, the unwrapping problem must be solved by either unwrapping or devising distribution-based rotation-invariant parameters in future studies.

## DATA AVAILABILITY STATEMENT

The original contributions presented in the study are included in the article/Supplementary Material, further inquiries can be directed to the corresponding author.

## AUTHOR CONTRIBUTIONS

JW analyzed the experimental data and typed the manuscript. CW (2nd author) performed the Mueller matrix experiment. CW (3rd author) fabricated the PAA sample. SS edited the manuscript and organized the PAA fabrication experiment. HM supervised the entire study.

## REFERENCES


1. Wang C, Qin P, Lv D, Wan J, Sun S, Ma H. Characterization of Anisotropy of the Porous Anodic Alumina by the Mueller Matrix Imaging Method. *Opt Express* (2020) 28:6740–54. doi:10.1364/oe.380070
2. He H, Sun M, Zeng N, Du E, Liu S, Guo Y, et al. Mapping Local Orientation of Aligned Fibrous Scatterers for Cancerous Tissues Using Backscattering Mueller Matrix Imaging. *J Biomed Opt* (2014) 19(10):106007. doi:10.1117/1.JBO.19.10.106007
3. Alali S, Vitkin A. Polarized Light Imaging in Biomedicine: Emerging Mueller Matrix Methodologies for Bulk Tissue Assessment. *J Biomed Opt* (2015) 20(6):061104. doi:10.1117/1.JBO.20.6.061104
4. Li P, Dong Y, Wan J, He H, Aziz T, Ma H. Polaromics: Deriving Polarization Parameters from a Mueller Matrix for Quantitative Characterization of Biomedical Specimen. *J Phys D: Appl Phys* (2022) 55:034002. in press. doi:10.1088/1361-6463/ac292f
5. Dong Y, Wan J, Si L, Meng Y, Dong Y, Liu S, et al. Deriving Polarimetry Feature Parameters to Characterize Microstructural Features in Histological Sections of Breast Tissues. *IEEE Trans Biomed Eng* (2021) 68(3):881–92. doi:10.1109/TBME.2020.3019755
6. Dong Y, Wan J, Wang X, Xue J-H, Zou J, He H, et al. A Polarization-Imaging-Based Machine Learning Framework for Quantitative Pathological Diagnosis of Cervical Precancerous Lesions. *IEEE Trans Med Imaging* (2021) 40:3728–38. doi:10.1109/TMI.2021.3097200
7. Du E, He H, Zeng N, Sun M, Guo Y, Wu J, et al. Mueller Matrix Polarimetry for Differentiating Characteristic Features of Cancerous Tissues. *J Biomed Opt* (20142014) 19(7):076013. doi:10.1117/1.JBO.19.7.076013
8. Antonelli M-R, Pierangelo A, Novikova T, Validire P, Benali A, Gayet B, et al. Mueller Matrix Imaging of Human colon Tissue for Cancer Diagnostics: How Monte Carlo Modeling Can Help in the Interpretation of Experimental Data. *Opt Express* (2010) 18:10200–8. doi:10.1364/oe.18.010200

9. Dubreuil M, Babilotte P, Martin L, Sevrain D, Rivet S, Le Grand Y, et al. Mueller Matrix Polarimetry for Improved Liver Fibrosis Diagnosis. *Opt Lett* (2012) 37:1061–3. doi:10.1364/ol.37.001061
10. Svensen Ø, Stamnes JJ, Kildemo M, Aas LMS, Erga SR, Frette Ø. Mueller Matrix Measurements of Algae with Different Shape and Size Distributions. *Appl Opt* (2011) 50:5149–57. doi:10.1364/ao.50.005149
11. Chen Y, Zeng N, Chen S, Zhan D, He Y, Ma H. Study on Morphological Analysis of Suspended Particles Using Single Angle Polarization Scattering Measurements. *J Quantitative Spectrosc Radiative Transfer* (2019) 224:556–65. doi:10.1016/j.jqsrt.2018.12.006
12. Lu S-Y, Chipman RA. Interpretation of Mueller Matrices Based on Polar Decomposition. *J Opt Soc Am A* (1996) 13:1106–13. doi:10.1364/josaa.13.001106
13. He H, Zeng N, Du E, Guo Y, Li D, Liao R, et al. A possible quantitative Mueller matrix transformation technique for anisotropic scattering media/Eine mögliche quantitative Müller-Matrix-Transformations-Technik für anisotrope streuende Medien. *Photon Lasers Med* (2013) 2(2):129–37. doi:10.1515/plm-2012-0052
14. Evans PR, Kullock R, Hendren WR, Atkinson R, Pollard RJ, Eng LM. Optical Transmission Properties and Electric Field Distribution of Interacting 2D Silver Nanorod Arrays. *Adv Funct Mater* (2008) 18(7):1075–9. doi:10.1002/adfm.200701289
15. Gerein NJ, Haber JA. Effect of Ac Electrodeposition Conditions on the Growth of High Aspect Ratio Copper Nanowires in Porous Aluminum Oxide Templates. *J Phys Chem B* (2005) 109(37):17372–85. doi:10.1021/jp051320d
16. Itoh N, Tomura N, Tsuji T, Hongo M. Strengthened Porous Alumina Membrane Tube Prepared by Means of Internal Anodic Oxidation. *Microporous Mesoporous Mater* (1998) 20(4-6):333–7. doi:10.1016/s1387-1811(97)00043-7
17. Musselman KP, Mulholland GJ, Robinson AP, Schmidt-Mende L, MacManus-Driscoll JL. Low-Temperature Synthesis of Large-Area, Free-Standing Nanorod Arrays on ITO/Glass and Other Conducting Substrates. *Adv Mater* (2008) 20(23):4470–5. doi:10.1002/adma.200801253
18. Masuda H, Yamada M, Matsumoto F, Yokoyama S, Mashiko S, Nakao M, et al. Lasing from Two-Dimensional Photonic Crystals Using Anodic Porous Alumina. *Adv Mater* (2006) 18:213–6. doi:10.1002/adma.200401940
19. Jessensky O, Gösele F, Gosele U. Self-Organized Formation of Hexagonal Pore Arrays in Anodic Alumina. *Appl Phys Lett* (1998) 72:1173–5. doi:10.1063/1.121004
20. Li F, Zhang L, Metzger RM. On the Growth of Highly Ordered Pores in Anodized Aluminum Oxide. *Chem Mater* (1998) 10:2470–80. doi:10.1021/cm980163a
21. Li AP, Müller F, Birner A, Nielsch K, Gösele U. Hexagonal Pore Arrays with a 50-420 Nm Interpore Distance Formed by Self-Organization in Anodic Alumina. *J Appl Phys* (1998) 84:6023–6. abs/. doi:10.1063/1.368911
22. Chen W, Wu J-S, Yuan J-H, Xia X-H, Lin X-H. An Environment-Friendly Electrochemical Detachment Method for Porous Anodic Alumina. *J Electroanalytical Chem* (2007) 600:257–64. doi:10.1016/j.jelechem.2006.10.022
23. Chen W, Wu J-S, Xia X-H. Porous Anodic Alumina with Continuously Manipulated Pore/Cell Size. *ACS Nano* (2008) 2:959–65. doi:10.1021/nn700389j
24. Gâlcă AC, Kooij ES, Wormeester H, Salm C, Leca V, Rector JH, et al. Structural and Optical Characterization of Porous Anodic Aluminum Oxide. *J Appl Phys* (2003) 94(7):4296–305. doi:10.1063/1.1604951
25. Wang G, Wang C, Shao R, Sun S. Fabrication of Orderly Porous Anodic Alumina Optical Waveguide Sensor via Interface Hydrophilic Treatment for the Detection of Small and Large Molecules. *Adv Mater Inter* (2020) 7(15):2000622–7350. doi:10.1002/admi.202000622
26. Goldstein DH. Mueller Matrix Dual-Rotating Retarder Polarimeter. *Appl Opt* (1992) 31(31):6676–83. doi:10.1364/AO.31.006676
27. Ngo D, Liu H, Sheth N, Lopez-Hallman R, Podraza NJ, Collin M, et al. Spectroscopic Ellipsometry Study of Thickness and Porosity of the Alteration Layer Formed on International Simple Glass Surface in Aqueous Corrosion Conditions. *Npj Mater Degrad* (2018) 2:20. doi:10.1038/s41529-018-0040-7
28. Lai TL, Robbins H, Wei CZ. Strong Consistency of Least Squares Estimates in Multiple Regression. *Proc Natl Acad Sci* (1978) 75(7):3034–6. doi:10.1073/pnas.75.7.3034
29. Suresh B, Ganapathiraju A. Linear Discriminant Analysis-A Brief Tutorial. *Inst Signal Inf Process* (1998) 18:1–8.
30. Fushiki T. Estimation of Prediction Error by Using K-fold Cross-Validation. *Stat Comput* (2011) 21:137–46. doi:10.1007/s11222-009-9153-8
31. Ivanov D, Dremin V, Genova T, Bykov A, Novikova T, Ossikovski R, et al. Polarization-based Histopathology Classification of *Ex Vivo* colon Samples Supported by Machine Learning. *Front Phys* (2022). doi:10.3389/fphy.2021.814787in press
32. Dremin V, Sieryi O, Borovkova M, Näpänkangas J, Meglinski I, Alexander B. Histological Imaging of Unstained Cancer Tissue Samples by Circularly Polarized Light. *ECBO, OSA Tech Dig* (2021). doi:10.1117/12.2614468paper EM3A.3
33. Lu S, Li N, Huang T, Du S, Yang D, Yao Y, et al. Computational Image Translation from Mueller Matrix Polarimetry to Bright-Field Microscopy. *J Biphotonics* (2021). doi:10.1002/jbio.202100242in press
34. Sun Y, Wang J, Shi J, Boppart SA. Synthetic Polarization-Sensitive Optical Coherence Tomography by Deep Learning. *Npj Digit Med* (2021) 4:105. doi:10.1038/s41746-021-00475-8
35. Usmani K, Krishnan G, O'Connor T, Javidi B. Deep Learning Polarimetric Three-Dimensional Integral Imaging Object Recognition in Adverse Environmental Conditions. *Opt Express* (2021) 29:12215–28. doi:10.1364/OE.421287


**Conflict of Interest:** The authors declare that the research was conducted in the absence of any commercial or financial relationships that could be construed as a potential conflict of interest.

The handling editor declared a past co-authorship with one of the authors HM.

frontiers in Physics

REVIEW
published: 18 March 2022
doi: 10.3389/fphy.2022.815296

# Polarimetric Imaging Through Scattering Media: A Review

*Xiaobo Li*[1,2], *Yilin Han*[3], *Hongyuan Wang*[3], *Tiegen Liu*[3], *Shih-Chi Chen*[2]* and *Haofeng Hu*[1,3]*

[1]School of Marine Science and Technology, Tianjin University, Tianjin, China, [2]Department of Mechanical and Automation Engineering, The Chinese University of Hong Kong, Hong Kong, China, [3]Key Laboratory of Opto-electronics Information Technology, School of Precision Instrument and Opto-electronics Engineering, Ministry of Education, Tianjin University, Tianjin, China

Imaging in scattering media has been a challenging and important subject in optical science. In scattering media, the image quality is often severely degraded by the scattering and absorption effects owing to the small particles and the resulting nonuniform distribution of the intensity or polarization properties. This study reviews the recent development in polarimetric imaging techniques that address these challenges. Specifically, based on the polarization properties of the backscattering light, polarimetric methods can estimate the intensity level of the backscattering and the transmittance of the media. They can also separate the target signal from the undesired ones to achieve high-quality imaging. In addition, the different designs of the polarimetric imaging systems offer additional metrics, for example, the degree/angle of polarization, to recover images with high fidelity. We first introduce the physical degradation models in scattering media. Secondly, we apply the models in different polarimetric imaging systems, such as polarization difference, Stokes vector, Mueller matrix, and deep learning-based systems. Lastly, we provide a model selection guideline and future research directions in polarimetric imaging.

**Keywords: polarization, polarimetric imaging, scattering media, imaging recovery, physical imaging**

OPEN ACCESS

***Edited by:***
*Venugopal Rao Soma, University of Hyderabad, India*

***Reviewed by:***
*Nirmal Mazumder, Manipal Academy of Higher Education, India*
*Paramasivam Senthilkumaran, Indian Institute of Technology Delhi, India*
*Antti Penttilä, University of Helsinki, Finland*

***Correspondence:**
*Shih-Chi Chen*
*scchen@mae.cuhk.edu.hk*
*Haofeng Hu*
*haofeng_hu@tju.edu.cn*

***Specialty section:***
*This article was submitted to Optics and Photonics, a section of the journal Frontiers in Physics*

***Received:*** *15 November 2021*
***Accepted:*** *14 February 2022*
***Published:*** *18 March 2022*

***Citation:***
*Li X, Han Y, Wang H, Liu T, Chen S-C and Hu H (2022) Polarimetric Imaging Through Scattering Media: A Review. Front. Phys. 10:815296. doi: 10.3389/fphy.2022.815296*

## 1 INTRODUCTION

Optical imaging through scattering media, including turbid water [1, 2], haze [3, 4], fog [5], and biological tissue [6–8], enjoys a wide range of applications in areas such as underwater rescue [9], automatic driving [10], underwater archaeology [11], and biomedical imaging [12]. Therefore, the realization of clear visions in scattering media is of great interest and significance. However, the visibility and identifiability of the target scene are usually compromised as the radiance observed from a scene is scattered and absorbed by aerosols and particles existing in the environment [13]. The optical performance is thus limited in many practical applications [14]. In other words, the image quality captured by a camera deteriorates significantly, resulting in low image contrast [15], distorted color [16], and poor visibility [17].

Various dehazing or de-scattering techniques that have been developed to restore the image quality can be classified into two categories, non-physical and physical model-based methods, as shown in **Figure 1**. The non-physical methods, based on the image enhancement method, aim to highlight the target of interest and improve the contrast. The simplest non-physical method is the histogram equalization (HE) method, which enhances the overall image contrast by increasing the dynamic range of the gray value. Depending on the difference in the computing region of an image, HE can be divided into global HE (GHE) and local HE (LHE). The advantage of GHE lies in its higher

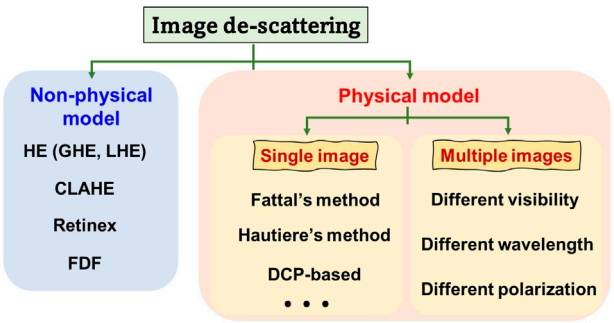


**FIGURE 1 |** Classification of dehazing/de-scattering methods.

efficiency and lower computation requirement, which is particularly suitable for enhancing excessively dark or bright images. This method does not fit images with high local brightness values, which often cause the "halo" effect. Such an issue can be addressed by applying the LHE method, for example, contrast limited adaptive histogram equalization (CLAHE) [18]. However, the "blocking effect" accompanied by increased computation complexity [19] cannot be avoided. Besides, HE methods may amplify noises during dehazing. Retinex-based algorithms [20, 21] are models based on the color perception of human eyes, with the main concept of obtaining an object's reflection property to model the color invariance. Thus, the Retinex-based algorithms have been widely applied in the field of image enhancement to remove haze and scattered light. In addition, this method helps increase an image's contrast and brightness and regulate the dynamic range of its gray level. Nevertheless, the Retinex-based algorithms do not preserve edges well, which may lead to the halo phenomena in sharp boundary regions [21, 22]. Finally, with regard to the dehazing technique, the frequency domain filtering (FDF) method proves to be another popular solution for image enhancement. More details can be found in the previous works [23–25].

The physical model-based dehazing and de-scattering methods are based on the knowledge related to the scene's physical features. To successfully restore an image, one of the key factors is to acquire an accurate depth of the scene [26], that is, the physical distance between the camera and target scene. However, the depth map is always unattainable for practical applications [27]. Therefore, a fundamental challenge in optical de-scattering techniques is to accurately estimate the depth map, that is, the transmission of scattering media [28]. Various methods have been proposed to overcome the challenge. For example, Fattal et al. [27] proposed a method that inferred the medium transmission map by estimating the albedo of the scene. However, such a method assumes that the transmission and surface shading are locally uncorrected and thus may fail when handling dense haze. Hautiere et al. [29] estimated the depth by determining the relationship between the road visibility and the contrast in the foggy image. Based on the analysis of the side geographical information obtained *via* an onboard optical sensor system, a 3D geographical model was established to remove the fog. Upon observing the property of haze-free outdoor images, He et al. [3] proposed the dark channel prior (DCP), based on the premise that "dark pixels" had a very low intensity in at least one-color channel except in the sky region. His method included three steps: air-light/scattered light estimation, transmission map estimation and refinement, and the final image reconstruction. Thanks to its effectiveness in dehazing, DCP has been adopted by most of the recent physical model-based techniques.

Almost all methods above are implemented based on the input of a single image, where certain assumptions or prior knowledge are necessary. The other physical model-based methods are based on multiple images corresponding to the same scene, that is, the images obtained under different visibility [30], images obtained with visible and near-infrared cameras [31], and images acquired with different polarization angles [15, 32, 33]. While images under different visibilities render the estimation of the depth map and scene structures to significantly enhance the image contrast, it remains challenging to handle real-time scenes [34]. Thanks to the excellent "long-distance transmission capacity" of the near-infrared light, the visible and near-infrared fusion methods improve the image quality by combining the rich color information of the visible image and the high visibility of the near-infrared image. However, the major obstacle is to acquire the visible and near-infrared images simultaneously, where expensive equipment and accurate optical alignment are both required. As opposed to the above methods, polarimetric imaging [35–37] is more effective because the scattered light is partially polarized [35] and the polarization information of the object and the turbid medium is different. Therefore, in principle, obtaining the polarization information of the scene and then processing them can effectively suppress the scattered light and extract the light coming from the object light [15, 32, 38]. A series of studies have shown that polarization-based imaging is a physical, low-cost, and applicable way to enhance the image quality, especially in highly scattering environments [2, 39, 40].

The typical polarimetric imaging systems include the polarization difference (PD) imaging [1, 41, 42], Stokes-based polarimetric (SP) imaging [43], and Mueller matrix (MM) imaging [44, 45]. The PD imaging is based on two orthometric polarized sub-images to estimate the transmittance by analyzing the degree of linear polarization. The SP imaging, especially the full-SP imaging, leverages the robustness of the polarization angle [38] or the "memory effect" of circular polarization to achieve the backscatter removal [39, 46, 47]. The MM imaging benefits from its complete polarization characterization. These three basic models are built upon different optical systems that offer flexible options subject to different application requirements. Besides, the polarization-based methods can be further improved by integrating with computer-vision-based and learning-based methods [2, 15, 48]. In other words, by introducing the polarization information into the traditional vision or learning-based method, greater application possibilities can be explored due to enhanced performance in image quality [2, 49–52].

This study first introduces the basic principles of the common polarimetric imaging models in scattering media and provides a comprehensive and up-to-date review for both traditional and

advanced works. We explore topics that include the progress in model optimization and parameter estimation and the analysis of different methods from the perspectives of their limitations and potential solutions, with application-based recommendations for readers in optics and engineering communities. **Section 2** introduces the imaging model through the scattering media and the related optical imaging systems. **Section 3** demonstrates the polarimetric methods for imaging through turbid media based on different imaging systems. **Section 4** provides a conclusion and an overlook for future development.

# 2 IMAGING MODEL IN SCATTERING MEDIA

## 2.1 Physical Imaging Model in Scattering Media

The particles existing in the scattering media, such as in the atmosphere during hazy or foggy weather and under turbid water or sea, generally absorb and scatter light, resulting in the decay of image contrast, saturation attenuation, and color-shifting in the detected images [39, 46]. Therefore, image dehazing or de-scattering plays an important role in various practical applications, such as traffic surveillance systems, security systems, object recognition, medical imaging, and remote sensing. Studies related to the image degradation mechanism, imaging systems, and recovery algorithms are receiving much attention.

Koschmieder et al. [53] proposed the first atmospheric scattering model, which was further modified by Narasiman and Nayar [54, 55]. Based on their model, the image signal received by the camera is composed of two components: 1) direct transmission $D(x, y)$, which represents the effect of scattering of light and the eventual decay of light before it reaches the camera, and 2) backscattered light $A(x, y)$, which denotes the undesired backscattered lights from the particles in the object line of sight (LOS) [1, 32]:

$$I(x, y) = D(x, y) + A(x, y). \tag{1}$$

As the light from the target progresses towards the camera, its energy is lost due to scattering and absorption. The fraction that does reach the camera is the direct transmission given by

$$D(x, y) = L_{object}(x, y)e^{-\beta z(x,y)}, \tag{2}$$

where $z(x, y)$ is the distance between the object and the camera and depends on the pixel coordinates $x$ and $y$; $\beta$ is the attenuation coefficient; and $L_{object}(x, y)$ is the object radiance not scattered and absorbed along the LOS [1, 35]. The attenuation coefficient is given by $\beta$, and the term $e^{-\beta z(x,y)}$ is also called the transmittance of light $t(x, y)$.

$A(x, y)$ denotes the undesired lights received by the camera mainly due to scattering by particles. It does not originate from the object on the LOS but varies with the horizontal distance by

$$A(x, y) = A_{\infty}(x, y)[1 - t(x, y)], \tag{3}$$

where $A_{\infty}$ refers to the intensity value of backscattered light from infinity in the turbid medium. In most works, it is assumed to be a global constant independent of the location $(x, y)$. **Figure 2A** shows the image formation and visual illumination components through the scattering medium. According to **Eq. 2** and **Eq. 3**, we can observe that $L_{object}(x, y)$ and, thus, the recovered image could be obtained as far as the transmittance and backscattering are estimated accurately and the attenuation of the object light is compensated. Combining **Eq. 1** and **Eq. 2**, one can recover $L_{object}(x, y)$ as follows:

$$L_{object}(x, y) = \frac{I(x, y) - A(x, y)}{1 - A(x, y)/A_{\infty}}. \tag{4}$$

The currently reported polarimetric imaging-based dehazing methods are based on the above physical model and the scattered light's polarization property. The published results in various works show the high information restoration capacity and computational efficiency [56]. For the recovered image in **Eq. 4**, many quantitative criteria are used to characterize the quality of results, including the visibility range or distance [56, 57], Michelson contrast (MC) [43], peak-to-correlation energy (PCE) [58], mean gradient [51], measure of enhancement (EME) [2, 17, 48], blind-reference-less image spatial quality evaluator (BRISQUE) [2], natural image quality evaluator (NIQE) [17], entropy [2], and peak signal-to-noise ratio (PSNR) [19, 27, 54]. Among the above criteria, PCE and PSNR describe the similarity between the restoration and clear image, EME and entropy describe the image contrast, and BRISQUE and NIQE quantify the distortion indicator of quality.

The superiority of the polarimetric methods also embodies the robustness of polarization parameters in various complex scattering conditions. Many works study the propagating light's physical characteristics and polarization properties in scattering media [59–61]. For example, with the aid of the Monte Carlo simulations, Xu et al. [62] demonstrated that the intensity of the polarized light after being transmitted underwater sharply decreases as the transmission distance increases, but the degree of polarization (DoP) of the transmitted lights remains above 0.75. It means that compared with the traditional imaging encoded with intensity information (in which the intensity will be significantly lost), the polarization encoding by DoP has overpowering advantages. Besides, Shen et al. [61] demonstrated that the depolarization behavior of light is sensitive to the mixing ratio or the distribution state of particles. Tao et al. [60] also found that the polarization properties provide additional information for the imaging, and the contrast of the polarization image can be significantly enhanced compared to the simplex intensity image in the turbid media. Moreover, the circular polarization images offer better contrast and higher visibility than linear ones under the same circumstance. All these reported results make the polarimetric methods and polarization control more promising for imaging in scattering media.

To date, whether it is on the basis of two images [15, 32], three or four images [38, 46], and nine or 16 images [44, 45], various polarization recovery methods have been developed by modifying the basic model in **Eq. 1**. These methods are related to different polarization information, such as the PD, Stokes vector, DoP,

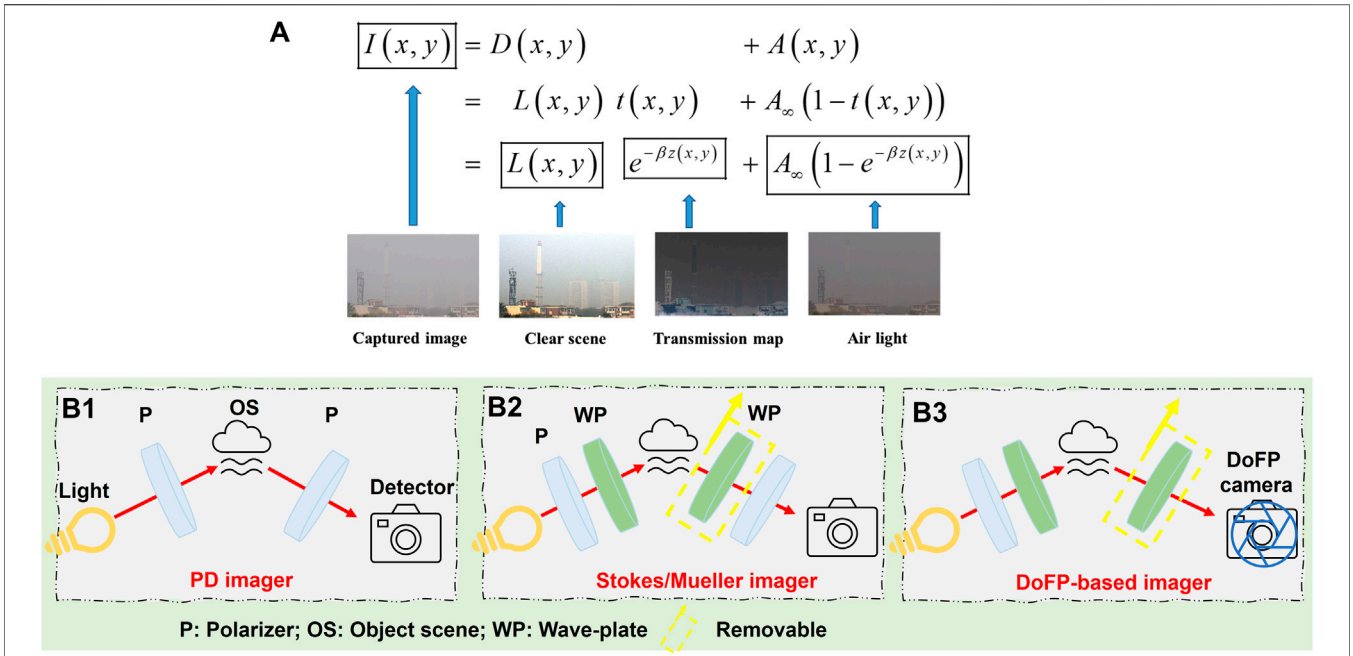


**FIGURE 2 | (A)** Image formation and visual example of illumination components through the turbid media (reprinted from Springer Nature: Scientific Reports [2], copyright 2018). **(B)** Different polarimetric imaging systems: **(B1)** PD imager, **(B2)** Stokes/Mueller imager, and **(B3)** DoFP camera-based imager.

angle of polarization (AoP), and MM. The following section introduces the related imaging systems and configurations.

## 2.2 Polarimetric Imaging Systems

Based on different polarization information, various polarimetric imaging systems have been developed. Early works in polarimetric imaging applications mainly focused on cases with linearly polarized light. This cross-polarization imagery, also called the PD imagery, was commonly used to enhance image contrast and minimize the blurring light in media with relatively low concentrations. The main element of this system is shown in **Figure 2B1**. In the setup, a light source, such as a light-emitting diode or a laser, is expanded with a beam expander. The light is polarized with a linear polarizer and hits on the target scene. A camera is positioned normal to the target scene to avoid most of the glare created by the interface. Finally, a rotating analyzer, always a linear polarizer, is placed in front of the camera to filter the back-reflected polarized light. By this configuration, two images $(I_\parallel, I_\perp)$ with orthogonal polarization states are acquired, from which one can calculate the degree of linear polarization (DoLP) as

$$P = \frac{I_\parallel - I_\perp}{I_\parallel + I_\perp}. \tag{5}$$

Stokes parameters have played a prominent part in the optical literature on polarized light [63, 64]. As early as 1947, Chandrasekhar [65] used the Stokes vector to formulate the radiative transfer equations for scattering partially polarized light. Furthermore, the Stokes parameters give a complete description of any polarization state of light:

$$\mathbf{S} = [S_0,\ S_1,\ S_2,\ S_3]^{\mathrm{T}}, \tag{6}$$

where the first three parameters are linear components of the Stokes, while the last one is the circular component [49, 63]. From this formalism, other parameters can be deduced, such as the DoP ($P$), the DoLP ($P_l$), the degree of circular polarization (DoCP), that is, $P_c$, and the AoP ($\alpha$). They are defined as follows:

$$P = \frac{\sqrt{S_1^2 + S_2^2 + S_3^2}}{S_0},\ P_l = \frac{\sqrt{S_1^2 + S_2^2}}{S_0},\ P_c = \frac{S_3}{S_0},\ \text{and}\ \alpha = \frac{1}{2}\tan^{-1}\left[\frac{S_2}{S_1}\right]. \tag{7}$$

A more detailed description of Stokes vector can be found in the books about polarized light [63].

Unlike the PD imagery for linear polarized light, the Stokes vector contains the ellipticity of the beam. Hence, the complete imaging system for the Stokes vector requires an extension of the instrumentation. Optical retarders or wave plates (WP) are usually introduced into the system to generate or measure elliptical or circular states. Four intensity measurements are needed to calculate the complete Stokes vector parameters. **Figure 2B2** shows a typical Stokes vector imagery, consisting of two sections: the polarization state generation (PSG) and the polarization analysis (PSA). In PSG, a WP and a linear polarizer are used to generate polarized illumination with an arbitrary state. The reflected intensity from the target scene is measured by adjusting the WP and/or polarizer's states in PSA. Based on these captured intensities, one can estimate the Stokes vector of the reflected light. In practice, the measurement of $S_0$, $S_1$, and $S_2$ is conducted by removing the WP in PSA. Only the last term, $S_3$, requires this element to measure an elliptical/circular state.

Moreover, with the development of nano-structures fabrication, a snapshot imaging solution has recently gained much attention using a division of focal plane (DoFP) polarization camera [66, 67]. It can simultaneously capture four polarization angles from each video frame without image mismatch [68]. Besides, by adding a rotated WP, one can measure the full Stokes with only two shots [69]. The polarization camera makes real-time polarimetric imaging a reality and its applications possible.

The MM, proposed by Hans Mueller in the early 1940s [63, 70], is another common parameter in addition to the Stokes vector in polarization imaging technology. The Stokes vector is a parameter describing the characteristics of the incident and the outgoing light when interacting with the materials, while the Mueller matrix is a "bridge" between the light and the material and describes the modulation of the incident light by the material [71, 72]. The Stokes vector's description of a light beam requires four parameters. The modulation relationship between the incident and outgoing light can be fully described using a 4 × 4 matrix [73]. This matrix is called the MM. When a beam of light is incident on objects, the polarization properties of the reflected or transmitted light generally change [74, 75]. Assuming that the Stokes vector of the incident light is S, the Stokes vector of the outgoing light after interaction with the medium is $S^{'}$, and the MM can express their relationship as follows:

$$\begin{pmatrix} S_0^{'} \\ S_1^{'} \\ S_2^{'} \\ S_3^{'} \end{pmatrix} = \begin{pmatrix} m_{00} & m_{01} & m_{02} & m_{03} \\ m_{10} & m_{11} & m_{12} & m_{13} \\ m_{20} & m_{21} & m_{22} & m_{23} \\ m_{30} & m_{31} & m_{32} & m_{33} \end{pmatrix} \begin{pmatrix} S_0 \\ S_1 \\ S_2 \\ S_3 \end{pmatrix}. \tag{8}$$

That is,

$$\mathbf{S}' = \mathrm{M} \cdot \mathbf{S}. \tag{9}$$

In practice, the MM can be obtained using some possible PSG and PSA combinations in **Figure 2B2**. A straightforward implementation includes setting the light source at three linear states and the right circular state. Finally, 16 intensity measurements are needed to calculate the full 4 × 4 MM. By removing the WPs in PSG and PSA, the configuration becomes the same as that of the Stokes imager (**Figure 2B2**). Then, by respectively rotating the directions of the two polarizers three times and obtaining a total of nine intensities, one can calculate a linear or incomplete MM with a size of 3 × 3.

In addition, according to the light sources' properties or the selected optical elements, the configurations can be categorized into different types as follows:

(1) Depending on the existence of light sources, it can be categorized into "active illumination type" (with additional source) and "passive illumination type" (with nature light).
(2) Depending on PSG's composition, it can be categorized into "unpolarized illumination type" and "polarized illumination type." In particular, the "polarized illumination type" can be further divided into "linearly polarized illumination" and "circularly polarized illumination."
(3) To match the type of illumination, the PSA will contain a polarizer with "linearly polarized illumination" or a polarizer together with a retarder if it is "circularly polarized illumination."

Choosing the configuration types depends not only on the polarization parameters being used but also on the environment in reality. For example, in the atmospheric environment, "passive illumination type" with sunlight is recommended, while in underwater, undersea, or low-light surroundings, the "polarized active illumination type" is preferred. In addition, for different target scenes, one needs to switch between linear and circular polarized illuminations. In the following section, we introduce well-established polarimetric methods in accordance with the above-mentioned configurations for imaging in scattering media.

# 3 MODELS OF POLARIMETRIC IMAGING IN SCATTERING MEDIA

## 3.1 Polarization Difference Imaging

### 3.1.1 Basic Model and Configuration

Inspired by the polarization-sensitive vision of some animals, PD imaging systems are proposed and developed to improve the visibility of objects in scattering media. This model is served as a common-mode rejection amplifier that can reduce the effects of background scattering and amplify the signal from targets where the PD magnitude is distinct from the background [41, 76]. Based on the images captured for the same scene at two orthogonal linear polarization states ($I_{\parallel}(x, y)$ and $I_{\perp}(x, y)$), the traditional PD system, proposed by Tyo et al. in 1995 [76], generates the PD and polarization-sum (PS) images as

$$I_{PD} = I_{\parallel}(x, y) - I_{\perp}(x, y), \; I_{PS} = I_{\parallel}(x, y) + I_{\perp}(x, y) \; , \tag{10}$$

where the PS image is equivalent to a polarization blind image obtained by a conventional imaging system. The PD image clearly depends on the choice of polarization axes, whereas the PS image does not. Such a relationship with the choice of axes can be used to minimize the effects of a partially polarized background in a PD image [42]. Notably, the scattered light is partially polarized and has the orthogonal and the same polarization components to the incident light at the same time. The performance of the PD method depends on the ratio of different components, which may be determined by the properties of scattering media, the incident polarization, the incident and observed angles, and so on.

Unlike Tyo's PD model, which is based on the theory of common-mode rejection, Schechner et al. [32, 35] proposed a novel de-scattering method based on the atmospheric scattering model in **Eq. 1**, as shown in **Figure 3**. Similarly, this method captures two orthogonal polarized images composed of two unknown components (the scene radiance in the absence of haze and air-light). Because the air-light is usually partially polarized, these two images can be described by

$$I_i(x, y) = \frac{D(x, y)}{2} + A_i(x, y), \; i \in [\parallel, \perp] \, . \tag{11}$$

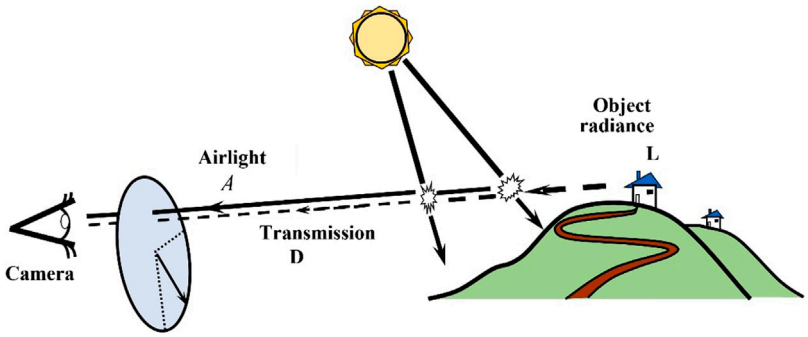


**FIGURE 3 |** Polarization-based atmospheric scattering model (reprint from OSA: Applied Optics [32], copyright 2003).

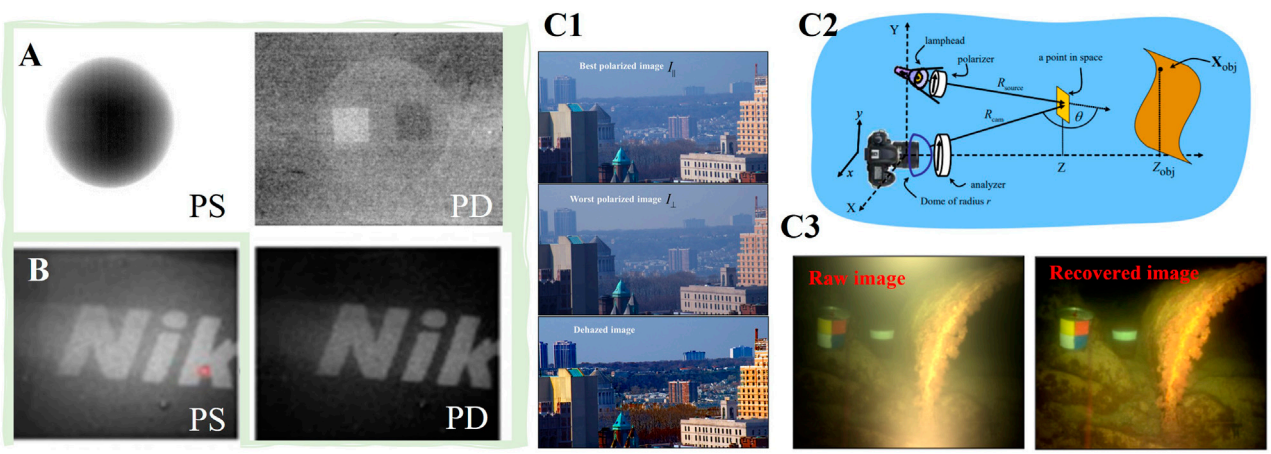


**FIGURE 4 |** The comparison results by **(A)** Tyo's imaging method (reprint from OSA: Applied Optics [41], copyright 1996) and **(B)** Guan's methods (reprint from OSA: Optics Express [42], copyright 2013). **(C1)** Imaging recovery example in air-environment (reprint from OSA: Applied Optics [32], copyright 2003), **(C2)** and **(C3)** underwater based on Schechner's model (reprint from IEEE: Transactions on Pattern Analysis and Machine Intelligence [35], copyright 2008).

This model considers the natural polarization effects in imaging through the haze and builds the relationship of atmospheric properties, polarization properties, and imaging formalism. It does not require modeling the scattering particles' size or the precise scattering mechanisms. In general, such methods based on Schechner's model need to estimate two critical global parameters: air-light at infinity $A_\infty$ and DoP $p$. Then, the air-light and the transmittance can be calculated by

$$\hat{A}(x,y) = \frac{I_{\parallel}(x,y) - I_{\perp}(x,y)}{p}, \quad \hat{t}(x,y) = 1 - \frac{\hat{A}(x,y)}{A_\infty}, \tag{12}$$

respectively. Here, $A_\infty$ and $p$ rely on the choice of background or sky region $\Omega$ and are usually calculated by

$$p = \frac{I_\Omega^{\parallel} - I_\Omega^{\perp}}{A}, \quad A_\infty = I_\Omega^{\parallel} + I_\Omega^{\perp}. \tag{13}$$

Finally, all these parameters are involved in the polarimetric model to obtain the recovered image as

$$L(x,y) = \frac{I(x,y) - A(x,y)}{1 - A(x,y)/A_\infty} = \frac{I^{\parallel}(x,y) + I^{\perp}(x,y) - A(x,y)}{1 - A(x,y)/A_\infty}. \tag{14}$$

The PD-based methods share the same configuration shown in **Figure 2B1**. The polarizer in front of the camera or other intensity detectors is a must to capture two orthogonal polarized images. In contrast, the polarizer behind the light illumination source is optional and depends on the actual scene, active or passive illumination.

### 3.1.2 Representative Methods

As the first attempt, Tyo et al. [41, 76] designed a special sample, an aluminum target containing two abraded patches with orthogonal directions, to verify the effectiveness of PD imaging systems. This sample is placed in a tank with inside dimensions of $30 \times 30 \times 15$ cm$^3$. This tank is filled with water and milk to simulate the scattering environments. PS and PD images after being transformed for optimal display are shown in

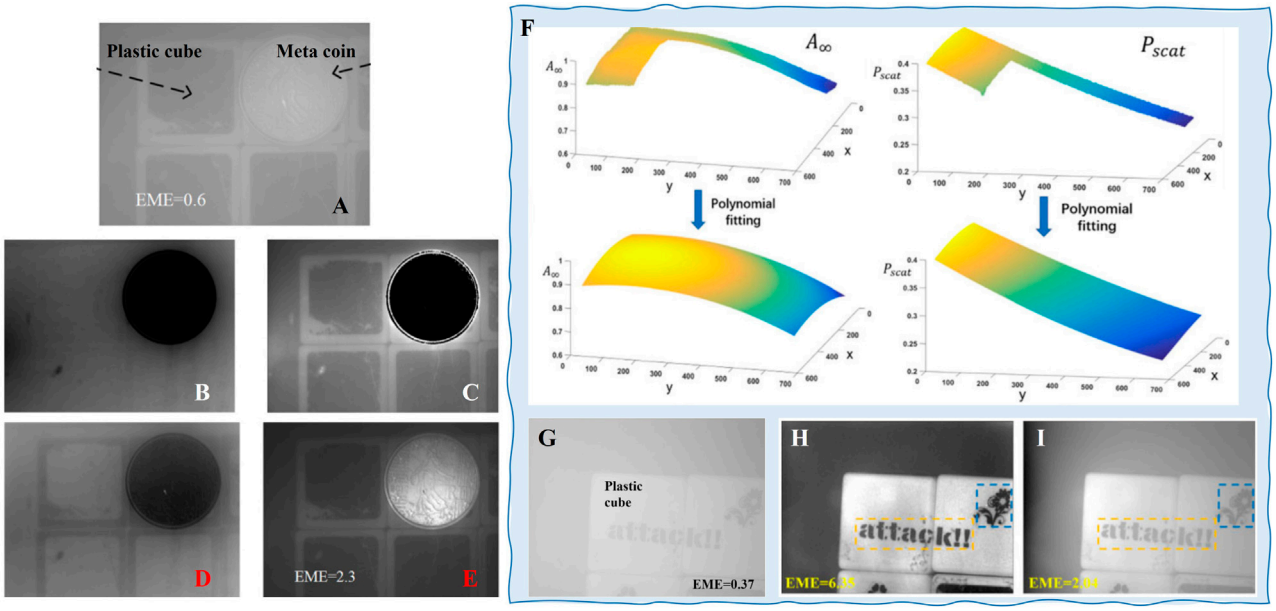


**FIGURE 5 | (A)** Raw image. The deduced **(B)** transmittance and the recovered **(C)** radiance of the objects when the light emanating from objects in the scene is unpolarized. The retrieved **(D)** transmittance and **(E)** radiance of the objects by Huang's method (reprint from OSA: Optics Express [59], copyright 2016). **(F)** The fitting spatial distribution of $A_\infty$ and $p$. **(G)** Raw intensity image of the scene. **(H)** Recovered image by Hu's and **(I)** Schechner's methods [32] (reprint from IEEE: Photonics Journal [79], copyright 2018).

**Figure 4A**. We can see that the abraded patches are clearly visible in the transformed PD image but practically invisible in the transformed PS image. The key factor contributing to the enhanced visibility of the two patches in the PD image is the common-mode rejection feature intrinsic to PD. Based on a series of validation, Tyo et al. [76] found that the PD imaging model is quite sensitive to intrinsically small signals and possesses valuable qualities of being passive, simple, and potentially fast.

This method does not employ polarized illumination, which makes it constantly suffer from a reduced signal-to-noise ratio (SNR) because light reflected from the target and diffusive light backscattered from the turbid medium are superposed. Guan et al. [42] developed the traditional model and added a linear polarizer behind the light source to generate a polarized illumination. By measuring the co-polarization (parallel to the incident light's polarization state) and cross-polarization (perpendicular to the incident light's polarization state) images, they obtain an improved PD image, expressed as $I_{PDI} = I_{\parallel} - I_{\perp}$. **Figure 4B** presents the comparison between PS and PD images. The result shows that the proposed method significantly suppresses the background noise, and the image contrast is improved approximately 1.7 times [42].

However, the biggest challenge of the common-mode rejection-based method is that it cannot process scenes with complex conditions and objects because it does not consider the degradation mechanism in the scattering media. To solve this problem, Schechner et al. [32, 35, 77, 78] combined both polarized optics and the typical atmospheric scattering model and showed how the polarization tool boosts the vision clarity in scattering media. An example in the air environment is shown in **Figure 4C1**. The dehazed image has much better contrast and color, especially in the distant regions of the scene noted as the green forest and the red roofs [32]. Unlike such applications in the air environment, which rely on natural sun illumination, active illumination is necessary for underwater applications. In 2004, Schechner et al. [57] developed their original model for the de-scattering in turbid water by introducing a polarized illumination, as shown in **Figure 4C2**. The corresponding results are shown in **Figure 4C3**. From the results, we may observe that the objects (i.e., the iron box) are well restored in both contrast and color. However, we must point out that their model is based on three assumptions:

(1) Only the backscattering light/air-light is polarized, while the objects are unpolarized.
(2) The total attenuation for objects at infinity also equals inhomogeneous haze; that is, $t_\infty = 0$.
(3) The multiple scattering (which affects the angular scattering distribution) is dominated by single scattering.

The first assumption does not apply to all practical cases because the object radiance could also contribute to polarization. When the depolarization degree of target objects is low, the light scattered or reflected by objects could contribute considerably to polarization. As a result, the previous methods may cause significant estimation errors. Huang et al. [59] found that the estimation produces negative values of $t$ (as shown in **Figures 5A–D**) at the pixels corresponding to the low-depolarizing material if one assumes that the light emanated from objects in the scene is unpolarized. To solve this problem, they modified

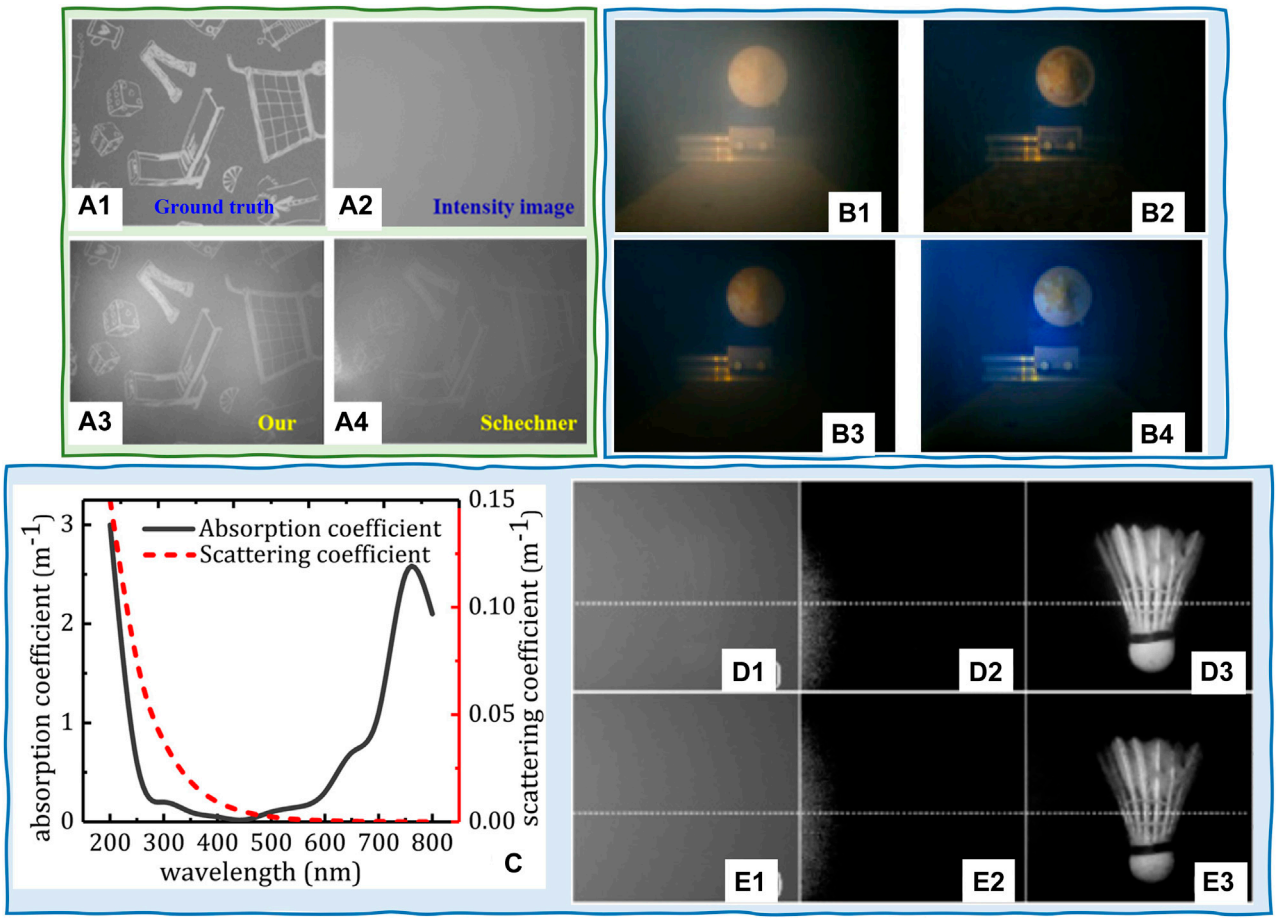


**FIGURE 6 | (A) (A1)** Ground truth and **(A2)** the raw intensity image under water. Comparison of recovered scenes by using **(A3)** Li's [2] (labeled as "Our") and **(A4)** Schechner's [32] methods (reprinted from Springer Nature: Scientific Reports [2], copyright 2018). Comparison of the recovered images when the raw image is **(B1)**: using **(B2)** DCP, **(B3)** DCP with transmission map by soft matting, and **(B4)** Brosseau's method (reprint from OSA: Optics Express [80], copyright 2019). **(C)** Measured absorption and scattering coefficients of pure seawater (reprint from OSA: Optics Letters [82], copyright 2018). **(D1)** and **(E1)** Directly captured images in 41 NTU and 70 NTU turbid water; **(D2)** and **(E2)** results from traditional polarization imaging method; **(D3)** and **(E3)** finally detected images by the Liu's method (reprint from OSA: Optics Letters [82], copyright 2018).

the traditional model by estimating the PD image of the target signal with feasible region fitting. **Figure 5E** shows that the recovered results reveal the details, which are not visible in the intensity images, regardless of the area corresponding to the objects having a high depolarization degree (plastic cube) or a low depolarization degree (metal coin).

To overcome the limitation caused by the second assumption and improve the recovery performance in complex conditions, such as that in the non-uniform optical field, Hu et al. [79] proposed a method of retrieving the radiance of the object based on estimating the spatial distributions of the DoP and the intensity of backscatter light by extrapolation fitting. For example, the progress of fitting spatial distribution is shown in **Figure 5F**, and the corresponding results are also shown for comparison. It shows that this method reveals the details of the scene (in orange and blue rectangles) that decay significantly in the intensity image, and it has better quality than the image recovered by Schechner's method because, under the non-uniform optical field, the DoP of backscatter $A_\infty$, represented by $p$, on the right side of the background region is considerably higher than that on the left side. Suppose we recover the image with Schechner's method, which considered the backscatter and its DoP to be constants; the transmittance can be considerably overestimated because of the improper estimations of $A_\infty$ and $p$. In that case, it will lead to incomplete haze removal, thus a less clear recovered image [79].

The third assumption makes the traditional methods perform poorly in the case of dense haze [2, 39]. To overcome this issue, Li et al. [2] proposed to combine the polarization-based model and the computational processing method, such as histogram stretching (HS). Their main idea is to reduce the density of haze computationally. Specifically, this method stretches the histograms of the orthogonal polarization images while maintaining the polarization relation in between. Based on the processed orthogonal polarization images, the recovered image with higher quality can be obtained by the traditional

polarimetric recovery method. **Figure 6A** presents an example in the dense turbid medium. The results show that the method significantly removes the scattered light and restores more details than Schechner's method. This method opens a door and verifies the feasibility and effectiveness of combining computer vision and polarimetric methods for image recovery in scattering media. Although the HS method and Schechner's polarimetric recovery method involved in this work are both old methods, the core idea of this combination has many perspectives. For example, Brosseau et al. [80] combined the low-pass polarization filter and DCP method and demonstrated the ability to significantly improve visibility and reduce runtime by a factor of about 50 for a 4K image. **Figure 6B** shows the natural imaging experiments at sea.

It is worth noting that the wavelength of the active illumination also affects the imaging performance because the scattered light caused by both water and particles is wavelength-dependent. Smith and Baker [81] measured the absorption coefficients and scattering coefficients of pure seawater on the wavelength ranging from 200 to 800 nm and validated the dependence of scattering on wavelength. Liu et al. [82] plotted the measured absorption and scattering coefficients of pure seawater in the visible-light range, as shown in **Figure 6C**. Results show that scattering decreases with wavelength increase. Based on this wavelength-dependent fact, they proposed a wavelength-selection-based polarization imaging method to image through highly turbid water with red light illumination. This method makes a good balance between range and vision and can turn targets from "undetectable" into "detectable," as shown in **Figures 6D,E**.

In fact, as one of the earliest polarimetric imaging techniques, the PD-based methods have received a great deal of attention for image dehazing/de-scattering in scattering media. This makes them enjoy fast development in terms of scientific research and engineering applications. However, the PD-based methods only contain two polarized images, which means that the freedom degree of information is limited to two. A complete polarization characterization of the scattered light and objects is helpful in further enhancing the recovery performance. Naturally, possible solutions include capturing more images and obtaining polarization parameters with high information freedom degrees, such as Stokes vector and MM [64, 83].

## 3.2 Stokes-Based Polarimetric Imaging

### 3.2.1 Basic Model and Configuration

As the information dimension (number of polarization sub-images) in Stokes vector configurations is higher (i.e., three for linear Stokes and four for complete Stokes) than two in the PD imaging system, the Stokes vector is more suited for characterizing polarization properties of scattered light. In contrast, as the two important parameters (AoP and DoP), which are highly relevant to the scattered lights' properties [66, 84], can be directly deduced from the Stokes parameters, introducing Stokes analysis into the scattering removal is promising.

According to the fundamental model in **Eq. 1**, we know that the estimation of transmittance $t(x, y)$ depends on the scattering section $A(x, y)$, where the polarization property can be characterized by the Stokes vector $\mathrm{S}^A(x, y)$. Here, $S_0^A$ is the captured intensity corresponding to $A(x, y)$. In this way, **Eq. 1** can be rewritten as

$$\mathbf{S}(x, y) = \mathbf{S}^D(x, y) + \mathbf{S}^A(x, y), \tag{15}$$

where $\mathrm{S}^D(x, y)$ denotes the Stokes vector related to the direct transmission $D(x, y)$. If the target objects are assumed unpolarized, $\mathrm{S}^D(x, y)$ equals $[D(x, y), 0, 0, 0]^T$; conversely, $\mathrm{S}^D(x, y) = [D(x, y), S_1^D(x, y), S_1^D(x, y), S_1^D(x, y)]^T$, and the last three polarization parameters cannot be ignored. Based on the intensity measurements in different polarization states, we can estimate $\mathrm{S}^A$. Accordingly, we can obtain the $A_\infty$ and $t(x, y)$. In other words, the Stokes-based methods remove the veiling light by building the model between Stokes vectors (or the related polarization parameters) and $(A_\infty, t(x, y))$; that is,

$$\left(A_\infty, t(x, y)\right) = f(P, P_l, P_c, \alpha), \tag{16}$$

where the parameters in **Eq. 16** (i.e., $P$, $P_l$, $P_c$, and $\alpha$) are defined in **Eq. 7**. The basic configuration of the Stokes-based methods can refer to that in **Figure 2B2**, and the specific choice depends on the used algorithm and realistic environments. According to the number of the used Stokes parameters, the methods can be classified as the linear-Stokes (LS) and the circular-Stokes (CS) based methods. In particular, for the LS-based methods, the PSA contains a fixed linear polarizer to generate polarized illumination, while the PSG contains a rotating linear polarizer. By adjusting the polarizer in PSG at least three times, we can obtain polarization sub-images. Based on these images, we can obtain a $1 \times 3$ linear Stokes vector. In contrast, in the CS-based methods, both PSG and PSA contain a linear polarizer and a retarder (e.g., QWP or liquid crystal variable retarders). By adjusting PSG's states at least four times and obtaining the related intensity images, we can get a $1 \times 4$ complete Stokes vector. The difference between the two systems is whether the circular component of the Stokes vector (i.e., $S_3$) is considered.

However, the CS-based methods do not depend on the scattering angle and can survive more multi-scattering events than linearly polarized light [47, 85, 86]. **Figures 7A,B** present the DoP as a function of optical depth in water with different diameter particles, from which we can observe that the CP light maintains better polarization characteristics than linear polarization (LP) [47]. This property, the so-called circular polarization (CP) memory effect, can be explained by the Mie scattering phase functions of LP and CP. The phase function in the circular case possesses a marked forward lobule that permits the photons to propagate around the beam axis with a higher probability than in the linear case [87, 88]. **Figure 1B** presents the effects of size on the DoP. Results show that when the size parameter is large, the DOP for CP is greater than that for LP [85]. The characteristics in **Figure 7B** attest to the superiority of CS-based methods in dense turbid water or underwater environments with large-sized particles. Besides, Sara et al. [89] quantitively demonstrated the superiority of circularly polarized light in foggy environments. The experiments are carried out at CEREMA's 30 m fog chamber under controlled fog density conditions. **Figure 7C** compares the ratio of CO channels (probe the prevalence of the input polarized light

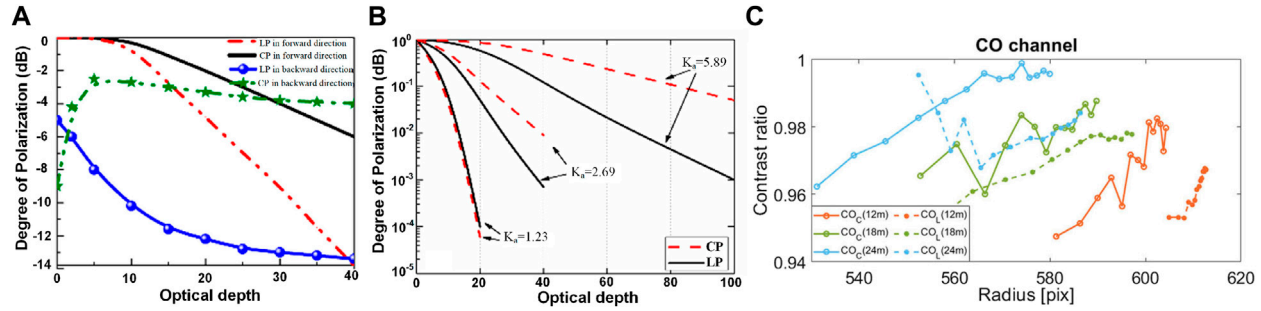


**FIGURE 7 |** DoP as a function of optical depth in water with different diameter particles; **(A)** 2 μm particle; **(B)** the size parameter (ka) varies (reprint from Elsevier: Applied Sciences [47], copyright 2021). **(C)** Comparison of the ratio of Co channel with respect to the intensity signal as a function of the radius of the intensity profile of the source image for circular (solid lines) and linear (dashed lines) polarizations at three visibilities: 12, 18, and 24 m (reprint from OSA: Optics Letters [89], copyright 2022).

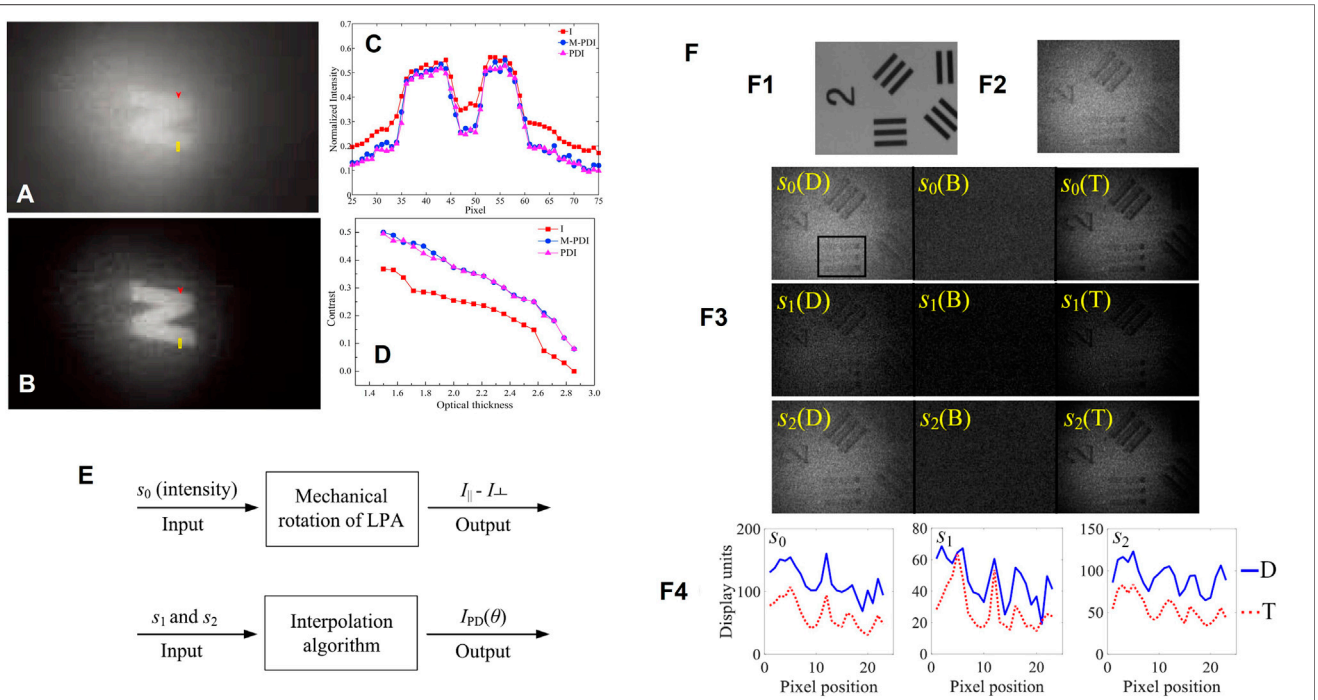


**FIGURE 8 | (A)** Raw intensity. **(B)** Imaging results by M-PDI. **(C)** Intensity profiles by raw intensity, traditional PI, and M-PDI. **(D)** Contrast distributions of the object obtained by raw intensity, traditional PI, and M-PDI versus optical thickness (reprint from Elsevier: Optics and Laser Technology [90], copyright 2018). **(E)** Comparison of traditional and interpolation method-based PDI systems. **(F)** Images corresponding to target in **(F1)** clear water and **(F2)** turbid conditions. **(F3)** Stokes vector elements for the direct measurement **(D)**, separated scatter **(B)**, and target (T). **(F4)** Generation of numerical plots for the direct measurement and separated target (reprint from IOP: Journal of Physics D: Applied Physics [91], copyright 2018).

through the fog) with respect to the intensity signal as a function of the radius of the intensity profile of the source image for circular (solid lines) and linear (dashed lines) polarizations at three visibilities. The results imply that circular polarization has a larger signal-to-noise ratio in transmission at deeper layers, whereas the signal from the linearly polarized light carries some noise due to its higher depolarization ratio when propagating in scattering media.

### 3.2.2 Representative Methods

To enhance the contrast, the two orthogonal polarized images in the traditional PD imaging model must be strictly selected to make the projections of the veiling light onto the two orthogonal axis directions equal [41]. However, this selection is time-consuming and inconvenient by rotating the polarizer mechanically, which is unsuitable for rapid imaging applications. Tian et al. optimized the traditional PD model to deal with this

limitation. They proposed a modified PD imaging method (M-PDI) based on the Stokes vector analysis of the veiling light [90]. The output image after removing the veiling light is expressed by

$$I_{M-PDI} = S_1 \sin 2\alpha - S_2 \cos 2\alpha, \tag{17}$$

where $\alpha$ is the polarization orientation angle of the veiling light. The optimal value of $\alpha$ corresponds to the highest image contrast. A linear Stokes vector is calculated by capturing three images in polarizer's directions of 0, 45, and 90° and searching the optimal $\alpha$. The significant advantage of this method is that the recovery performance can be updated automatically by the computation program when obtaining the Stokes parameters, which makes the implementation of PD imaging ideal for rapid imaging. **Figures 8A–D** show the recovery results of this method. The result shows the background noise is significantly suppressed, and the contrast of the target "Z" is significantly improved.

In 2018, Guan et al. [91] modified the above method and proposed another M-PDI method *via* the Stokes vector-based interpolation method. **Figure 8E** compares the traditional and the modified polarization filtering methods in PD imaging. The principle of this method is shown in **Figure 8F** [91]. From the image results, the object's contrast is significantly enhanced, and the background noise is significantly decreased. More details of this method and the comparison with the traditional PD method can be found in [91].

Although the M-PDI method has partially addressed certain inherent drawbacks of the traditional model based on Stokes analysis, the determination of crucial parameters, based on the computational searching, makes the model performance unstable and sensitive to noise [38]. To overcome this issue, Liang et al. [38] further explored the relationship between the Stokes vector and veiling light and estimated the backscattering/air-light using the AoP analysis. Based on the three captured images on different polarizer directions (i.e., 0, 45, and 90°), the Stokes vector is calculated by the expressions in [38]

$$\begin{aligned} S_0 &= I(0) + I(90) \\ S_1 &= I(0) - I(90) \\ S_2 &= 2I(45) - S_0 \end{aligned}, \tag{18}$$

where $I(i)$ denotes the captured image when the direction of the polarizer is set to $i$ degree. Then, we can calculate the intensity level of air-light as

$$A_p = \frac{2I(0)}{\cos^2\theta} - S_0, \tag{19}$$

where $\theta = 1/2 actan(S_2/S_1)$ denotes the AoP of air-light. Then, the output with a clear vision can be obtained by the typical physical model in **Eq. 14**. In this method, the noise in the sky area can be eliminated without any imaging-processing algorithm, which makes this method much more convenient and reliable in practical applications. Based on the technique, Liang et al. developed a series of algorithms to further enhance the recovery performance. For example, in 2015, they optimized the estimation of critical parameters (e.g., AoP and the intensity level of the air-light) to accommodate dense haze and achieved a 74% enhancement in the range of visibility (ROV) [43]. In 2016, as the infrared radiance has a better capacity for traveling through the haze, they modified the model by merging visible and infrared images. The ROV was thus improved by 100% [43]. In 2021, they introduced low-pass filtering into the AoP-based polarimetric imaging model and overcame the drawback of "noise sensitivity" in estimating the AoP value. The final imaging performance of these methods is shown in **Figure 9**. We can observe from the results that the faint information in hazy images is well preserved, and the contrast of the recovered image is increased significantly [92].

Such works based on AoP analysis accelerate the development of polarimetric imaging in specific scattering media. However, all these methods are based on the linear Stokes vector, which only includes three parameters and merely reflects the interaction of target objects with the linearly polarized light without considering the response to circularly polarized light. In particular, in some special scattering media requiring active illumination, the circularly polarized light tends to maintain its original polarization property better than the linearly polarized light, namely, the "circular polarization memory" effect [93, 94]. Therefore, using circularly polarized light can improve the recovery performance in dense turbid media more than linearly polarized light. Therefore, Hu et al. [46] proposed a new polarimetric image recovery method in dense turbid media with the illumination light featuring circular polarization. In this method, the active illumination is modulated by a polarizer and an additional retarder to generate circularly polarized light. The estimated Stokes vector is decomposed into linear polarization, circular polarization, and un-polarization parts as follows:

$$\mathbf{S} = \mathbf{S}_{l-\text{polarized}} + \mathbf{S}_{c-\text{polarized}} + \mathbf{S}_{\text{unpolarized}}, \tag{20}$$

where the subscripts of $l$ and $c$ indicate the linearly and circularly polarized light, respectively. According to this decomposition, the linear and circular components of the veiling light are removed by solving the DoLP and DoCP of the backscattering. **Figure 10A** shows the difference between these two degrees of polarization, while the circular one is always missed in most methods. This is the first polarimetric imaging system and algorithm considering circularly polarized lighting. The recovered result and its comparison with the linear one are as shown in **Figure 10B** and further evidenced by experimental results for the scenes with different polarization properties, for example, a rough wooden board with patterns and words on its surface and the non-flat plastic toy.

With the improvement in the theoretical model, the trend of Stokes-based polarimetric imaging in scattering media continues to optimize the estimation of key parameters and render more accurate values, such as the polarization information of object and scattering signals. For example, Jin et al. [52] proposed a scattering removal method from the perspective of global estimation of polarization information to realize polarimetric calculation of global pixels for automatically estimating the

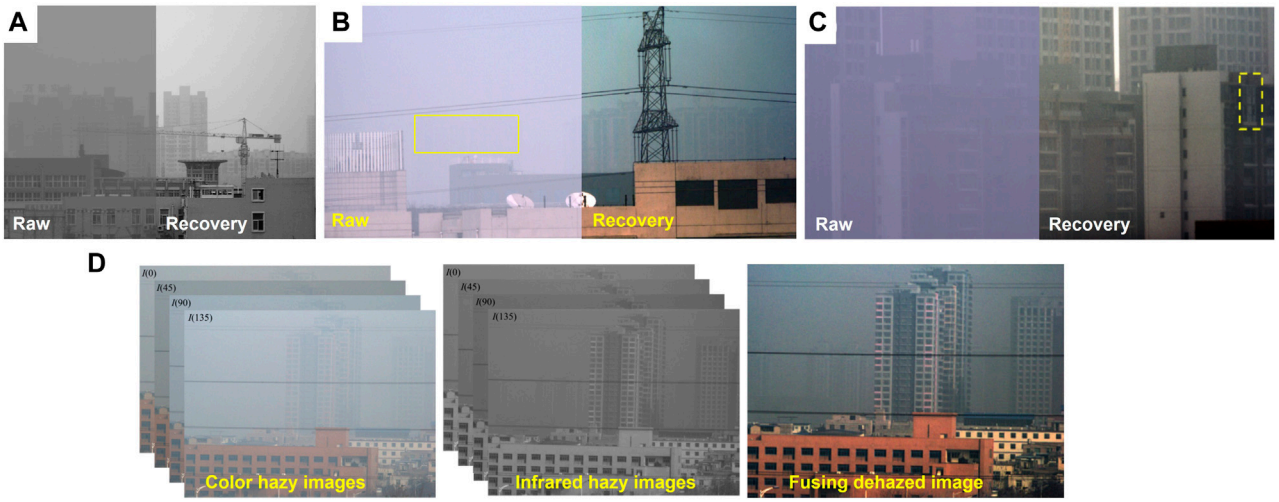


**FIGURE 9 |** Recovery performance for Liang's methods in Refs. **(A)** Ref1 (reprint from Chinese Laser Press: Photonics Research [38], copyright 2014). **(B)** Ref2 (reprint from OSA: Optics Express [43], copyright 2015). **(C)** Ref3 (reprint from OSA: Optics Express [40], copyright 2021). **(D)** Ref4 (reprint from OSA: Applied Optics [56], copyright 2016).

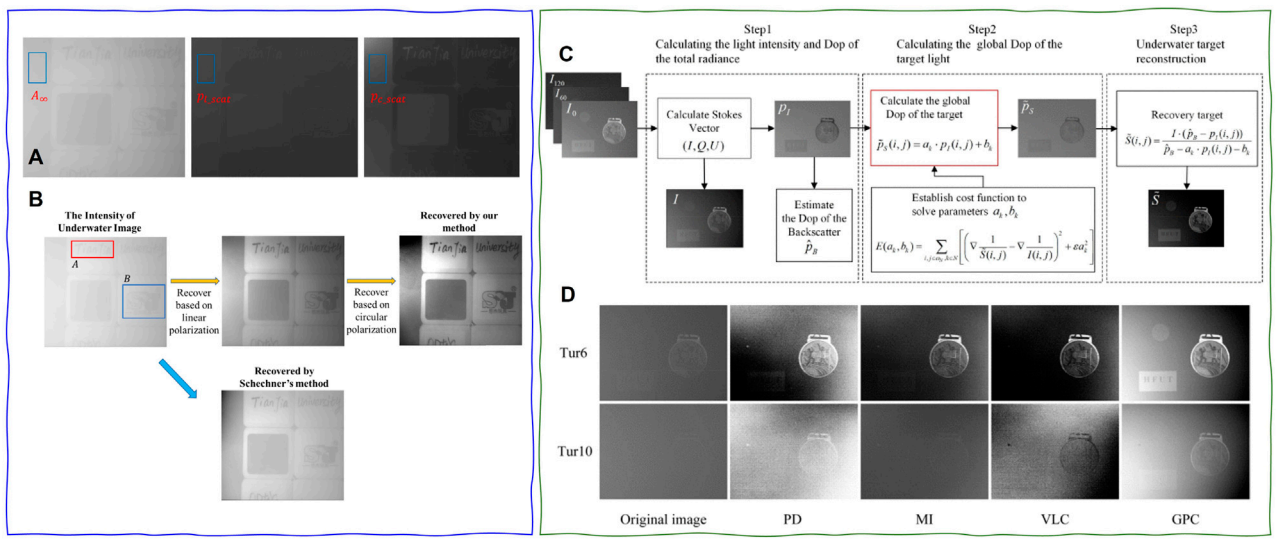


**FIGURE 10 | (A)** Intensity image of the scene, DoLP, and DoCP. **(B)** Recovery comparison for methods in [46] and [32] (reprint from OSA: Optics Express [46], copyright 2018). **(C)** Flowchart of underwater polarization reconstruction utilizing polarimetric calculation method of the global pixel. **(D)** Comparison results of three classical restoration methods (PD: polarization difference [41], ML: Schechner's method [35], VLC: Vanderlugt correlator) and this method in different turbidity (reprint from IEEE: Photonics Journal [52], copyright 2021).

DoP. This global pixel calculation is accomplished by utilizing the gradient prior information of the total intensity image. **Figure 10C** shows the flowchart of this method, and (**Figure 10D**) shows the comparison results of three classical recovery methods and this method in different turbidity [32, 41, 82]. Apparently, as opposed to methods with the assumption of constant DoP of target light, this method can retrieve the DoP of the target light of each pixel in the image. As a result, it has a better performance of recovering the scene's details even though the water is turbid [52].

In short, the Stokes-based methods outperform the PD-based methods because the Stokes vector renders more useful polarization information, such as DoP and AoP, which are closely related to the backscattering/veiling light caused by the existing particles. Improving the information dimension and estimating key parameters are two effective ways to boost

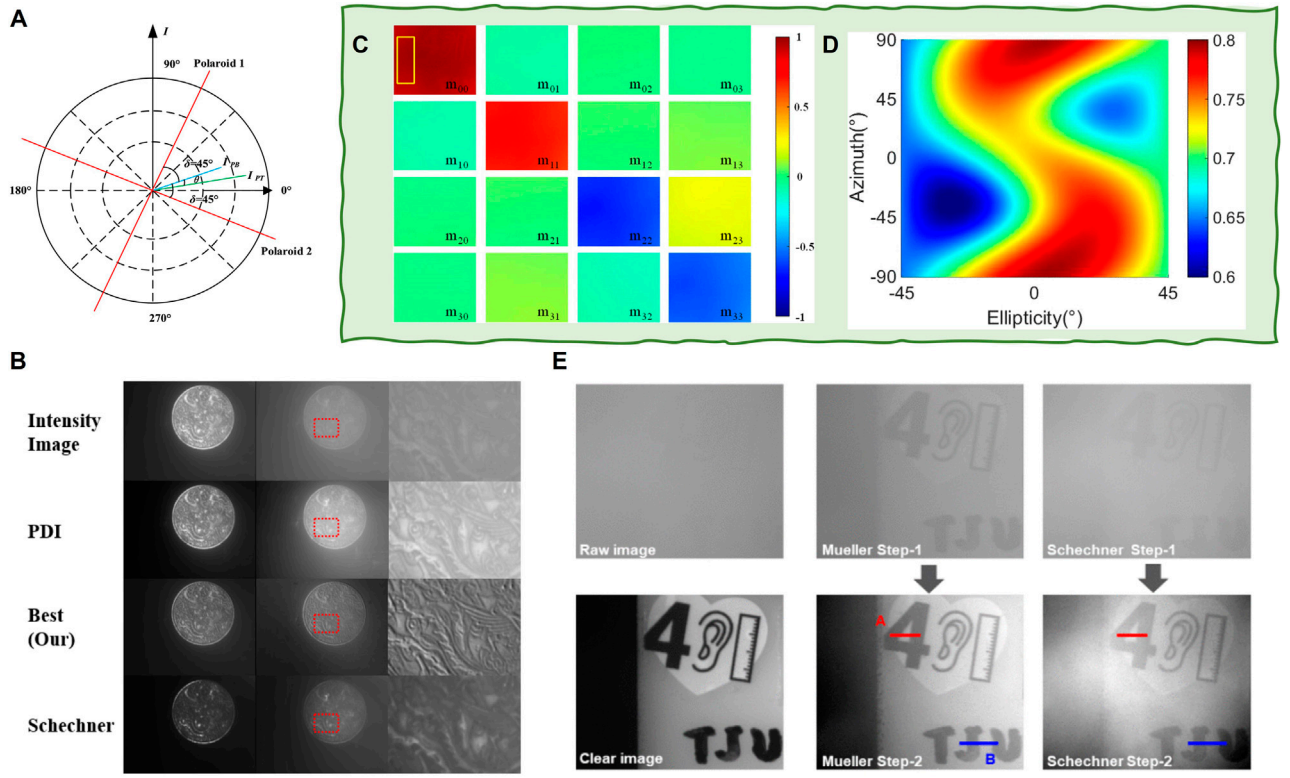


**FIGURE 11 | (A)** Principal diagram of polarization difference method based on MM. **(B)** Comparison results of scattering suppression by different methods and different scattering medium concentration, where Wang's method is labeled by "Best (Our)" (reprint from Elsevier: Optics Communications [103], copyright 2021). **(C)** MM image of the scene in turbid water. **(D)** Variation of DoP with the azimuth and the ellipticity of PSG. **(E)** Underwater image restoration results and the histograms in different turbidities of water (reprint from IEEE: Photonics Journal [45], copyright 2021).

imaging performance. However, we must remember that, unlike MM, the Stokes vector is not a complete polarization characterization [63, 95]. Therefore, the trial based on the MM has become the preferred approach to improve the information dimension, an exciting solution to enhance imaging performance in scattering media further.

## 3.3 MM-Based Polarimetric Imaging in Scattering Medium

### 3.3.1 Basic Model and Configuration

Unlike the Stokes vector, which is usually used to characterize the polarization properties of the light beam, the MM contains all the polarization information of the target materials. Therefore, the MM is always applied to distinguish different materials [8, 96–98] and 3D physical imaging [99–101]. According to the basic model in **Section 2**, the received signal or images can be classified into the target and scattered signals. The Stokes-based methods build the relationship between the Stokes vector and the scattered light. However, they fail to distinguish objects with different polarization properties. These methods are unsuitable for objects whose reflected light has a similar Stokes vector with the backscattering light.

With the information provided by MM, the operational space for polarization image processing is greatly improved, making it possible to distinguish objects in a high degree of freedom for the polarization information [102]. In addition, the MM-based configuration opens the door to modulate the incident illumination with a significant polarization space. In other words, the MM-based scattering suppression imaging technology modulates the illumination and analysis parts simultaneously. The basic configuration of MM-based methods is as shown in **Figure 2B2**, and one can remove the WPs in accordance with the type of MM (incomplete or complete) that is desired.

### 3.3.2 Representative Methods

The MM-based polarimetric suppression method for the imaging in scattering media is mainly based on modulating the polarization state of the active illumination. The earliest attempts focused on imaging linear MM and required nine intensity images [44, 45, 103]. In the related configurations, the WPs in PSG and PSA in **Figure 2B2** are removed, and the polarizers in PSG and PSA are rotated to three different positions to capture nine images, respectively.

In 2019, Guan et al. [44] found that the illumination polarization angle and the MM difference between the

medium and the object could affect the SNR of recovered results obtained by the rotation orthogonal polarization imaging method. They designed a linear MM-based polarimetric method to precisely control the illumination polarization angle and achieve a rapid imaging process. In 2021, Wang et al. [45] plotted backscattered light and target reflected light in the point cloud diagram in **Figure 11A** by establishing a differential imaging model. According to **Figure 11A**, on the premise that the angle between the polarizer's direction and the backscattering light's polarization direction is 45°, the backscattering light can be removed by the PD method to achieve scattering suppression. By analyzing the principle of polarization difference, the output result under ideal conditions is given by

$$\begin{aligned} I_{out}(x,y) &= \left(I_{PB_\parallel}(x,y) - I_{PB_\perp}(x,y)\right) + \left(I_{PT_\parallel}(x,y) - I_{PT_\perp}(x,y)\right) \\ &= \left|I_{PT}(x,y)\right| \cdot \sin(2\theta), \end{aligned} \tag{21}$$

where $I_{PB\parallel}(x,y)$, $I_{PB\perp}(x,y)$, $I_{PT\parallel}(x,y)$, and $I_{PT\perp}(x,y)$ represent the horizontal and vertical projection of the polarized part of the backscattering and target light, respectively. It can be seen from the above formula that the output result of the differential image will be affected by the polarization angle between the target and backscattered light. Therefore, by modulating the incident light and changing $\theta$, the performance of the traditional PD method can be improved. **Figure 11B** presents the comparison results of this method with the traditional PD method and other classical methods. We see that the modulation of incident light has a significant influence on polarization differential scattering suppression.

In other work, the authors disregard the traditional PD method and instead directly process the image according to the MM[45]. By modulating the polarization state of the incident active illumination light, the DoP of the backscattered light is directly maximized, thus achieving the best suppression of the backscattered light. Based on the configuration in **Figure 2B2**, one can obtain any specific polarized incident light by adjusting the PSG. The Stokes vector of the incident light $S^{in}$ can be expressed by its DoP value $P$, azimuth $\alpha$, and ellipticity $\varepsilon$ as follows:

$$\mathbf{S}^{in} = \mathbf{S}_0^{in}\begin{bmatrix} 1 & P\mathrm{S}^{\mathrm{T}} \end{bmatrix}^{\mathrm{T}} = S_0^{in}\begin{bmatrix} 1 \\ P\cos 2\alpha\cos 2\varepsilon \\ P\sin 2\alpha\cos 2\varepsilon \\ P\sin 2\varepsilon \end{bmatrix}, \tag{22}$$

where $S_0^{in}$ denotes the intensity of the illustration light and $\mathrm{S} = [S_1^{in}, S_2^{in}, S_3^{in}]$ is the normalized Stokes vector. When the DoP of backscattered light $P_{back}$ is higher, more backscattered light can be blocked by the PSA. Therefore, to suppress the backscattered light optimally, one must maximize the DoP of the backscattered light by choosing an optimal set of azimuths and ellipticities $(\alpha_{opt}, \varepsilon_{opt})$. This optimization problem can be expressed by

$$\left(\alpha_{opt}, \varepsilon_{opt}\right) = \underset{(\alpha_{opt},\varepsilon_{opt})}{\arg} \max\{P_{back}(M,\alpha,\varepsilon)\}, \tag{23}$$

where

$$P_{back}(M,\alpha,\varepsilon) = \frac{1}{\sum_{j=0}^{3} M_{0j} s_j^{in}(\alpha,\varepsilon)} \left\{ \sum_{i=1}^{3}\sum_{j=0}^{3} \left[M_{ij} s_j^{in}(\alpha,\varepsilon)\right]^2 \right\}^{\frac{1}{2}}. \tag{24}$$

**Figure 11C** presents the MM image of the target scene, and the corresponding optimal set of azimuths and ellipticities can be found by a global search shown in **Figure 11D**. The imaging results and the comparison with the traditional PD method are shown in **Figure 11E**. The results demonstrate that this method is stable and can be implemented with any digital image processing to achieve a more scattering suppression performance.

In 2022, Liu et al. [104] developed an MM-based de-scattering method and introduced the depolarization (Dep) index into the de-scattering algorithm. Dep is derived from the MM and is defined by

$$Dep_M(x,y) = \frac{\sqrt{\mathrm{tr}(M^T M) - m_{00}^2(x,y)}}{\sqrt{3m_{00}^2(x,y)}}. \tag{25}$$

By studying the backscattering distribution in different NTU turbidities, it is found that the background intensity correlates linearly with Dep in a remarkable way, as shown in **Figures 12A–B**. Therefore, Dep is used to characterize scattering media. By quantifying the light attenuation with the transmittance map, a clear vision of targets can be recovered using the information of scattering media. An example of recovery performance is shown in **Figures 12C1,C2**. The results demonstrate that the image contrast is significantly improved after recovery. In particular, the paper stripe and metal ruler are both clearly visible. From the zoomed-in view in **Figures 12C3,C4**, the ruler in the intensity image blurs, especially the tick mark and edges. In contrast, the edges of the ruler are visible after recovery, even with distinguishable tick marks.

The MM-based methods have many advantages. For example, they provide more helpful information by increasing the degree of freedom for polarization and making a clear differentiation among objects with similar intensity appearance but different polarization properties. However, it should be noted that a very scarce amount of works, less than five to the best of our knowledge, has placed the focus on MM-based de-scattering. Indeed, making full use of the MM decomposition and other MM-related parameters is promising and needs more attention.

## 3.4 Learning-Based Polarimetric Imaging

As discussed in **Section 2**, one of the dehazing methods is based on a physical model where prior knowledge is applied to extract physical parameters related to the scattering media and then recover the targeted signal. In this case, the estimation accuracy of these key parameters determines the final performance. Therefore, almost every developed method strives to optimize the accuracy of parameter estimation to make it as close as possible to the physical values in the scene. However, the optimizations come at the cost of increased computation complexity and reduced universality. In contrast, the methods not directly based on a physical model aim to improve the image

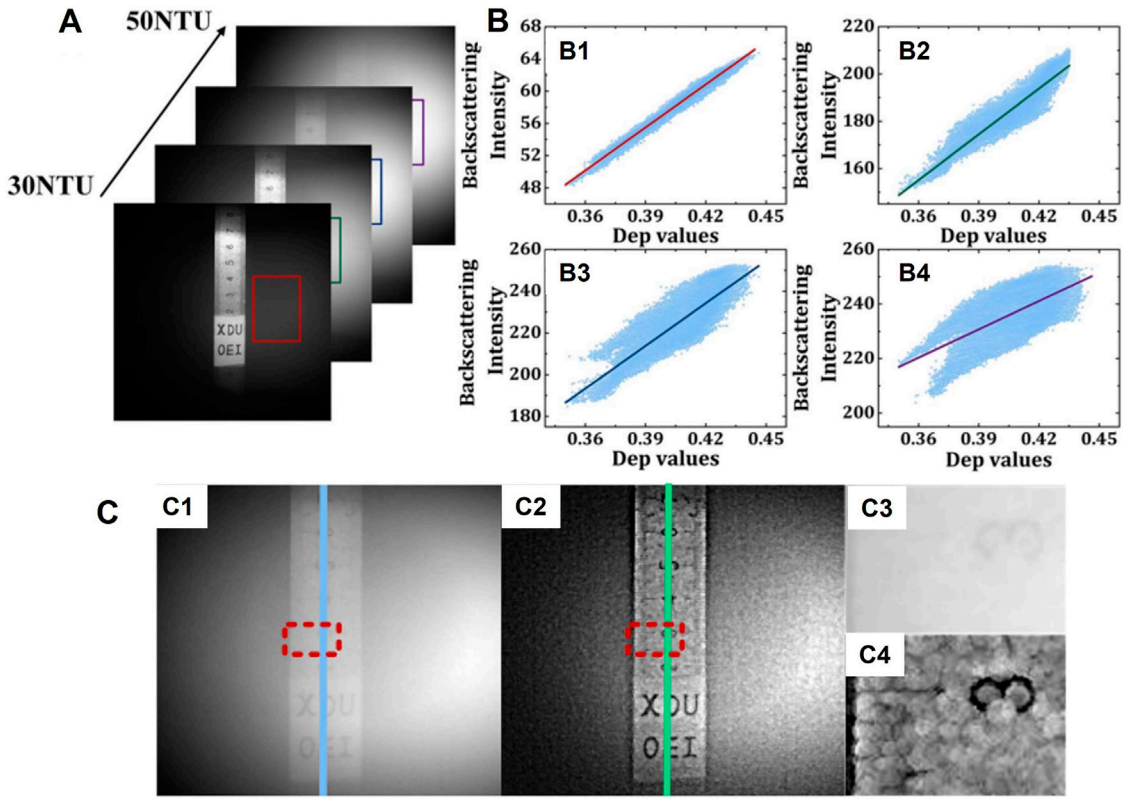


**FIGURE 12 | (A)** Four measured intensity images at different values of NTU. **(B1–B4)** Fitting results of backscattering intensity as a function of Dep values. **(C1)** Intensity image; **(C2)** recovered image with the proposed de-scattering method; **(C3)** and **(C4)** the zoomed-in view of the region of interest in **(C1)** and **(C2)** marked out with red rectangle (reprint from Chinese Laser Press: Chinese Optics Letters [104], copyright 2022).

quality by enhancing the image contrast and the difference between different image structures. This kind of method handles different scenarios indiscriminately but can perform poorly, especially with complex conditions.

The deep learning- (DL-) based method is data-driven and thus capable of extracting the hidden relationship and physical properties between/in the raw and target data. This makes it a promising choice for de-scattering. In some ways, the traditional "end-to-end" network corresponds to methods that are not based on the physical model, while the "physical embodiment" network is based on physical models. The following section introduces learning-based polarimetric imaging in scattering media from the basic concepts to well-established applications.

### 3.4.1 Basic Concepts of the DL and Neural Network

In 1943, psychologist Warren McCulloch and mathematical logician Walter Pitts proposed the concept of the artificial neural network and the mathematical model of the artificial neuron, thus prompting the era of artificial neural network research [105]. They abstracted the entire working process of neurons into the model shown in **Figure 13A**. In the model, input data $x_i$ are given to the network processed with weights and bias parameters. Then, a nonlinear activation function $\varphi(*)$ is applied to obtain the final output $Y$. The whole process is called forward propagation. The weights $w_i$ and bias $b$ are the parameters to be learned, which can be seen as the memory of the neural network. The final output is the prediction result obtained by the network according to the input data, which may be different from the ground truth. Therefore, it is necessary to calculate the deviation between the predicted result and the ground truth, or the network loss, to update network parameters. The process of updating weights is usually *via* some variant of a gradient descent algorithm. The training process of the network repeats the forward propagation and backpropagation process until the loss is minimal so that when we put in input data, we obtain an output nearly the same as the ground truth [106].

To boost the network performance and suitability for various tasks, different advanced network structures have been developed, such as LeNet [107], AlexNet [108], GoogleNet [109], ResNet [110], and DenseNet [111]. In the field of computer vision, learning-based solutions have become the hottest topic. Particularly, various learning-based works focus on improving imaging quality in scattering media. For example, Chen et al. [112] proposed an "end-to-end" dehazing network. In their review, a generative adversarial network (GAN) is used to realize end-to-end image dehazing. The work focuses on solving

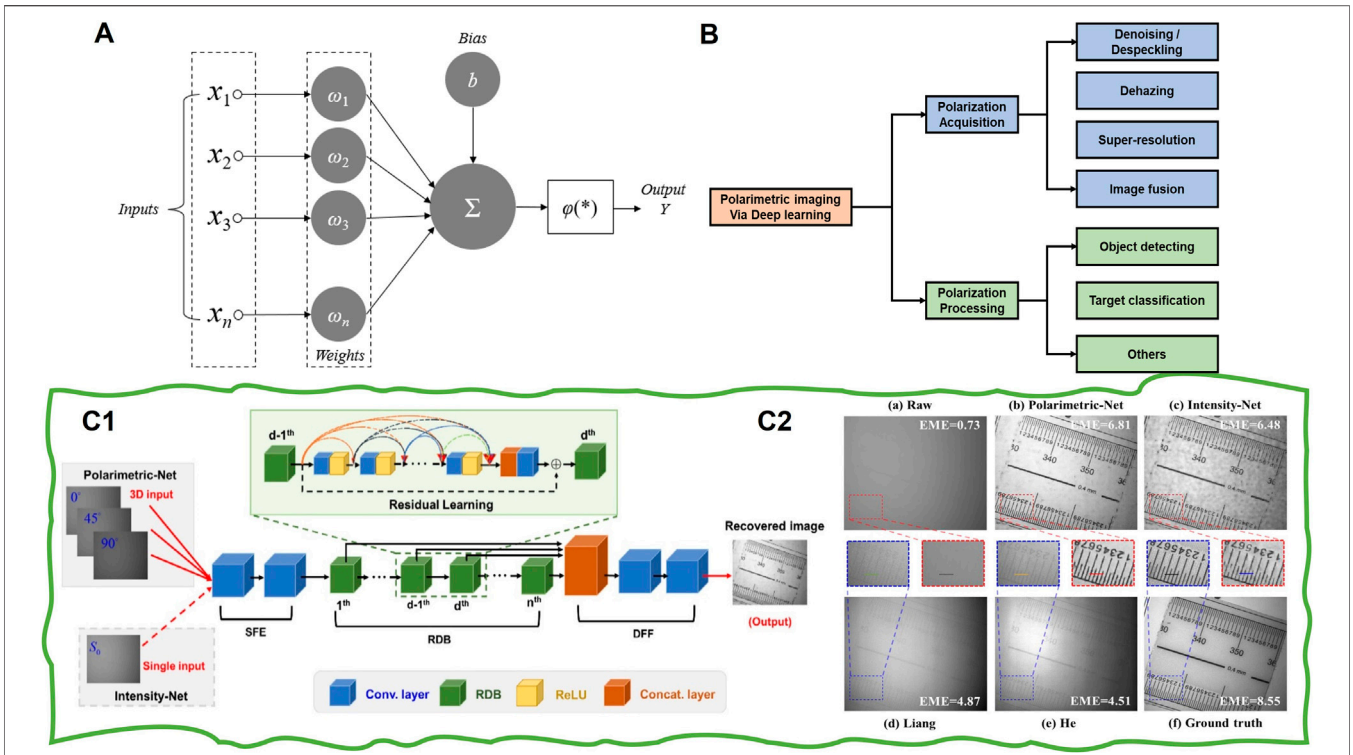


**FIGURE 13 | (A)** Schematic diagram of neural network structure. **(B)** Classification of polarimetric imaging *via* DL. **(C1)** The architecture of polarimetric dense network (PDN) and **(C2)** recovered image (reprint from Elsevier: Optics and Lasers in Engineering [50], copyright 2020).

the problem of grid artifacts and has greatly improved the indexes of peak signal-to-noise ratio (PSNR) and Structural Similarity Index Measure (SSIM). In 2019, Pan [113] proposed a physics-based feature dehazing network for image dehazing network. In contrast to most existing end-to-end trainable network-based dehazing methods, they explicitly considered the physical model of the hazing process in the network design and removed haze in a deep feature space. However, all these de-scattering methods are based on a single intensity image. In recent years, DL has been successfully applied to polarimetric imaging [49, 66, 114]. Such works develop mainly from two parts: polarization acquisition and polarization processing. The related applications include denoising, dehazing, image fusion, targets detection and classification, and super-resolution (a brief classification is shown in **Figure 13B**). In the following, we focus on the learning-based de-scattering works.

### 3.4.2 Representative Methods

The currently popular neural network ResNet was first proposed by He et al. [110] in 2015 and is widely used in many scenarios of DL. This structure can solve the problem of gradient disappearance when the network is deep. Huang et al. [111] proposed DenseNet in 2017, which can alleviate gradient disappearance, strengthen feature propagation, encourage feature reuse, and significantly reduce the number of parameters through the dense connections between layers. Based on these two networks, Hu et al. [50] first proposed a polarimetric dense network (PDN) and applied it to underwater polarization image restoration. The network structure of PDN is shown in **Figure 13C1**. This network includes three main components (shallow feature extraction, residual dense block, and dense feature fusion) to deeply extract shallow features of polarization information from three polarization images and then fuse them. The loss function used is defined as

$$l(\Theta) = \frac{1}{2N}\sum_{i=1}^{N}\left\|I_i^{pred}(x,y;\Theta) - I_i^{gt}(x,y)_F^2\right\|, \qquad (26)$$

where $I_i^{pred}(x,y)$ and $I_i^{gt}(x,y)$ refer to predicted and ground truth images, respectively, with their polarization information. Because the polarization is considered, the recovered image in **Figure 13C2** has more detailed features than the intensity image used alone. Besides, there are more artifacts in the recovered result by "intensity-Net" than "Polarimetric-Net." These results demonstrate that embedding polarization information and constraints into the network helps improve performance.

In 2021, Zhang et al. [115] studied how to optimize the network structure and loss function to improve the suitable model performance. They found that, by adding polarized information along with the light intensity information to the model at the very front of the model structure, a better-recovered image can be obtained. The model structure proposed can be used for image recovery in turbid water or

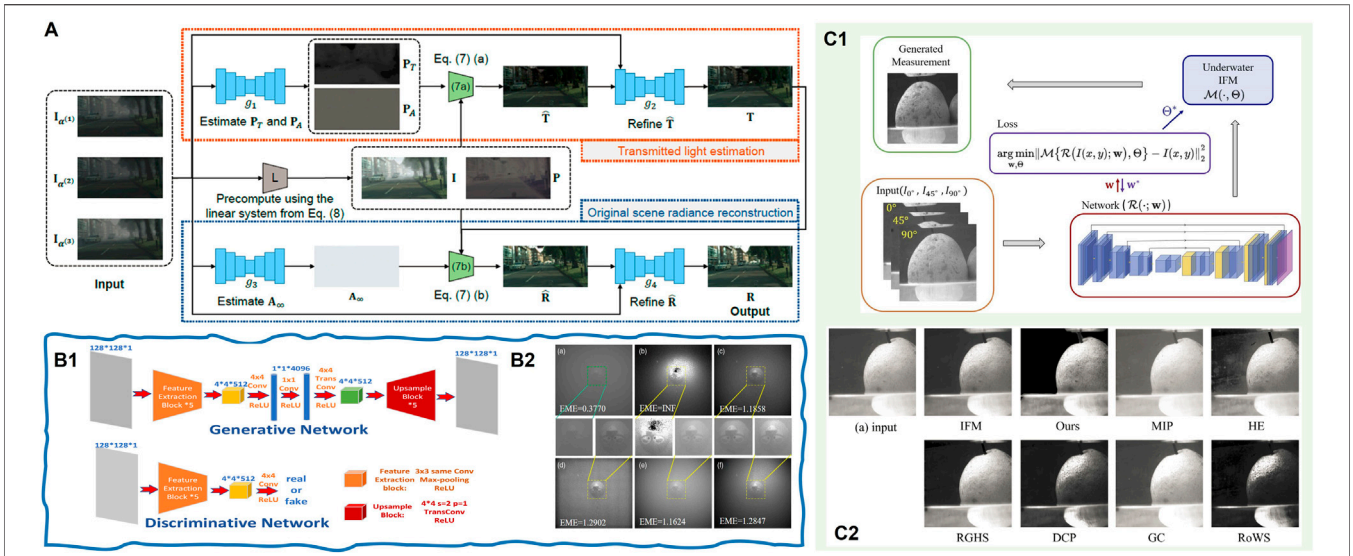


**FIGURE 14 | (A)** Schematic diagram of neural network structure proposed by Zhou et al. (reprint from MIT Press: Advances in Neural Information Processing Systems [117], copyright 2021). **(B1)** The architecture of the GAN-based polarization network and **(B2)** the recovered images (reprint from OSA: Applied Optics [118], copyright 2021). **(C1)** The architecture of untrained network in [119] and **(C2)** visual comparison among different de-scattering methods: our method, i.e., Zhu's method [119], IFM, MIP [120], HE [121], RGHS [122], DCP [3], GC [123], and RoWS [124] (reprint from OSA: Optics Express [119], copyright 2021).

other scattering environments. It should be noted that both the above methods are "end-to-end" and depend on paired training data. Although the application of neural networks has significantly improved image de-scattering performance compared with traditional methods, its disadvantages are also easily recognizable. DL networks, especially end-to-end networks, have poor interpretability as the neural networks are more like a black box. It is difficult to explain and understand the inner operation process. To solve this problem, Ren et al. [116] integrated the polarimetric imaging model with the DL-based method and proposed a lightweight network structure, which can restore underwater images with different turbidity. This method makes the image restoration through neural networks more in line with the physical principle and achieves good results.

To complete the physical meaning in the network and reduce the degree of freedom of the model, Zhou et al. [117] proposed a generalized physical formation model of hazy images and a robust polarization-based dehazing pipeline without the assumptions in traditional polarimetric methods. The designed network includes sub-networks to estimate different parameters, as shown in **Figure 14A**. The network divides the whole image de-scattering process into two steps. At the end of each step, semantic and contextual information is used to refine the output of the corresponding sub-network. This method provides a new perspective for the fusion of physical models and neural networks. However, the generalization ability on the real dataset is still limited for utilizing computer-synthesized datasets. In order to get rid of the paired data's dependence and make the learning-based methods applicable in practice, the unsupervised model-based and untrained model-based solutions are proposed. For example, Yang et al. [118] designed an end-to-end unsupervised generative network to remove the backscattering light, as shown in **Figure 14B1**. This method produces an adversarial loss with the discriminative network to improve the performance. In addition to using GAN to remove the backscattering light, they also modified the underwater imaging model based on several physical priors. The DoP of backscatter is the same as that of background light. This new model can be applied in a variety of non-uniform optical fields. **Figure 14B2** shows its recovered results by different methods. Besides, they also verified that this unsupervised solution could adapt to the non-uniform optical field with different incident angles. In 2021, Zhu et al. [119] proposed a non-GAN unsupervised method by combining the polarization physics model and DL technology. **Figure 14C1** presents the network's architecture. Rather than using atmospheric scattering model directly, they input the polarimetric hazy images into U-Net to obtain the corresponding de-scattered images, added haze to the output of the network through the model proposed by Liang et al. [43], and finally calculated the loss between the generated hazy images and corresponding captured images. **Figure 14C2** presents a visual comparison among different de-scattering methods. From the results, we may observe that the background area with the homogeneous scattering effects is removed using this method, but the object information is preserved. In short, the unsupervised image de-scattering through U-Net does not need paired datasets or even haze-free images.

All the above works can be considered strong evidence that learning-based, especially the physics-embedded learning-based method, can resolve the limitations of traditional methods and provide an irreplaceable solution for imaging tasks in scattering media. It should be noted that the reported

**TABLE 1 |** Summary of polarimetric de-scattering methods.

| Method | Principle | Captures num. | Pros & cons | Ref |
|---|---|---|---|---|
| PDI | • Common-mode rejection amplifier<br>• Physical degradation model | 2 | Pros<br>• Easy to operate<br>• Low computational complexity<br>• Low system complexity<br>Cons<br>• Poor performance under complex conditions<br>• Prior knowledge-dependent<br>• Inability to distinguish objects of different polarization properties | 1,15,16<br>32,33,35<br>38,40,41<br>47,50,78<br>79,82 |
| Stokes-based | • Stokes polarimetry<br>• Physical degradation model | 3 or 4 | Pros<br>• Adjustable incident illumination<br>• Low computational complexity<br>Cons<br>• Higher system complexity<br>• Ability to partially distinguish objects of different polarization properties | 34,38-40<br>43,46,47<br>56,92 |
| MM-based | Mueller polarimetry | 9 or 16 | Pros<br>• Adjustable incident illumination<br>• Ability to fully distinguish objects of different polarization properties<br>Cons<br>• More captured images required<br>• Highest system complexity<br>• Fails in real-time applications | 44,45<br>103,104 |
| DL-based | DL techniques and polarization model | ≥2 | Pros<br>• Excellent performance<br>• Fast processing speed (after finishing the training)<br>Cons<br>• Data-dependent | 50<br>116-119 |

DL models and research largely depend on a particular dataset, and it is hard to guarantee similar performance from other datasets. This is where this method falls short if compared with other common traditional models. Nevertheless, we firmly believe that DL techniques hold a crucial place in this field.

## 3.5 Polarimetric Imaging Through Scattering Tissues

In the above sections, we have reviewed the polarimetric imaging through such scattering media as fog, haze, and turbid water. Meanwhile, biological tissues as another important scattering media and the related polarimetric imaging techniques have gained great attention in the biomedical field. To be more specific, the biological tissues contain fiber-like macromolecules (e.g., the collagen fibers in the skin and tendons, muscle fibers, and myofibrils in skeletal muscles), which exhibit a certain degree of structural anisotropy and anisotropy in dielectric response. These properties manifest themselves *via* birefringence [125, 126], which can be observed using polarization measurement or polarimetric imaging [127]. For example, many works have shown that the depolarization, retardance, and diattenuation induced by the birefringent tissues can be considered indicators to assess macromolecules' microstructure, thus being conducive to diagnosis and the study of pathological alterations [128, 129]. However, the scattering (especially the multiple scattering) in thick tissues often results in the depolarization of light, which makes detection of the remaining information-carrying polarization signals challenging. Therefore, various polarimetry or polarimetric imaging techniques have been developed to maximize measurement sensitivity to assist in analyzing useful tissue information [97, 127, 130, 131].

In fact, the polarimetric imaging through the biological tissues often shares the same basic polarization configurations as mentioned in **Section 2**: polarization difference, Stokes vector, and Mueller matrix polarimeters. However, the focus and methods of the related research are significantly different from those in **Section 3**. Here, the main focus is to study the properties of scattering media, namely, the tissues themselves. For example, the emphasis will be placed on modeling the polarized light transport and the depolarization of multiply scattered light in tissues by both Monte Carlo simulation and the real experiments [132–135] or the study of the mechanism of depolarization and its dependence on the different tissue or media parameters (e.g., the density, size, distribution, shape, and refractive index) [131, 136–140]. On the contrary, for the reviewed physical degradation mode-based polarimetric recovery methods in **Section 3**, the properties of scattering media do not directly impact the recovery performance. This is because these techniques aim to remove the scattered light (i.e., $A(x, y)$ in **Eq. 1**) and recover the direct transmission (i.e., $D(x, y)$ in **Eq. 1**). The critical step is to calculate media transmittance (i.e., $t(x, y)$) and the intensity level of scattered light (i.e., $A_\infty$) by estimating polarization properties (i.e., DoP and AoP). In short, the recovery performance mainly relies on the accuracy of the estimation polarization properties. More details can be found in the related works in Refs. [130, 141].

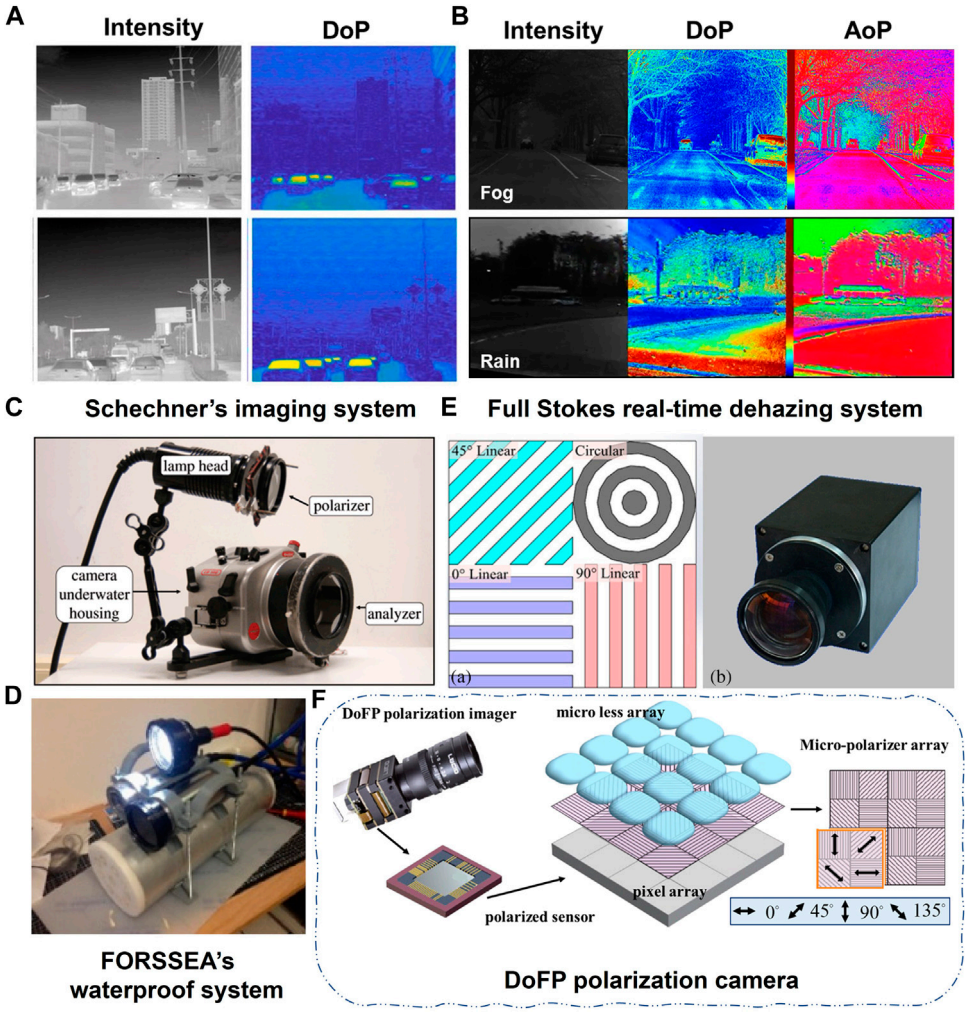


**FIGURE 15 | (A)** Images by LWI-DoFP camera (reprint from Elsevier: ISPRS Journal of Photogrammetry and Remote Sensing [146], copyright 2021). **(B)** Polarimetric imaging in the field of self-driving [153]. Different systems of polarimetric underwater imaging were developed for realistic applications. **(C)** Schechner's imaging system (reprint from IEEE: Transactions on Pattern Analysis and Machine Intelligence [35], copyright 2008). **(D)** FOREEEA's waterproof system (reprint from OSA: Optics Express [80], copyright 2019). **(E)** Full Stokes real-time dehazing system (reprint from OSA: Applied Optics [34], copyright 2017). **(F)** DoFP polarization camera (reprint from OSA: Optics Express [49], copyright 2020).

## 4 CONCLUSION AND OUTLOOKS

In this review, we have presented an overview of the polarimetric imaging methods through scattering media from the perspectives of the basic model, imaging system, and representative works. **Table 1** provides a brief summary and comparison across these methods.

Thanks to the property of polarized light propagated in scattering media, polarimetric methods outperform traditional intensity-based methods, particularly under complex conditions such as high-density turbid media, non-ideal illumination environments, and scenes with multi-material objects. We have demonstrated that the increase in polarization information dimension can constantly improve the imaging performance and the polarimetric methods. However, the complexity in both the imaging systems and computations is inevitably increased. It is worth noting that to achieve the balance between performance and complexity, advanced optical equipment and innovation in imaging systems must come into play. In addition, the demand for practical applications will certainly drive the development of polarimetric imaging methods. As such, we propose several topics of interest for future studies:

### 4.1 Multispectral-Polarization Systems and Fusion Algorithms

The combination of multi-spectral and polarization is often applied in the field of remote sensing [142, 143]. They found that more complex and accurate indices and models can be developed to reveal more information when the polarization

information is supplemented [144, 145]. Therefore, combining multi-spectral and polarization into an integrated imaging system and fusing multi-parameters are two possible directions to enhance the image quality in complex scattering media.

As mentioned in **Section 3**, the long-wave light is more robust for transmitting through the haze than visible light. Another powerful example is using a long-wave infrared DoFP polarization in road detection, as shown in **Figure 15A** [146]. The fusion of short and long wavelengths effectively increases the visual range at the cost of decreased resolution. Therefore, an optimal tradeoff is helpful for this solution [147, 148]. Besides, in the realistic underwater scene, seawater appears in different colors because the scattering and absorption depend on both the wavelength and the physical properties of the particles. It seems that a tunable wavelength source will make the imaging system have a wide range of application scenarios. On the contrary, the existing polarimetric methods mainly focus on recovering information only related to the intensity, that is, "to see it." However, the most significant advantage of polarization is that it can see what human eyes cannot (in the intensity condition), such as information related to DoP [149], AoP [150], or the index of polarization pure (IPP) [151, 152]. These parameters help distinguish different materials and different optical responses. For example, the DoP and AoP have been successfully applied in self-driving. They can provide additional information in complicated meteorological environments (fog and rain), as shown in **Figure 15B** [153].

Fusing multiple polarization parameters and intensity into a frame, further increasing the information dimension, may open a new door for the imaging in scattering media and take a transform from "could be seen" to "see far" and from "see clearly" to "see more."

## 4.2 Real-Time, Real-Scenario, and Robust (3R) Solution for Polarimetric Imaging

Most reported polarimetric imaging methods for scattering media have been demonstrated under laboratory conditions. Although some were implemented in real-life scenarios, the imaging process was static, and the analysis was completed afterward. To achieve real-time, real-scenario, and robust (3R) solutions for polarimetric methods, advanced algorithms for optical information processing need to be developed and an improved collaborative imaging system is also required.

Schechner et al. first developed an underwater polarimetric imaging system, as shown in **Figure 15C**. This system is designed based on their basic PD imaging model and performs better in real-life scenarios by combining necessary post-processes [35]. In 2019, Khadidja et al. used the waterproof imaging system designed by FORSSEA Robotics Company, as shown in **Figure 15D**, to carry out the experiments under more realistic conditions [80]. Compared with the preceding imaging system, their setup is improved and can be integrated into underwater detectors, such as the underwater robot and autonomous underwater vehicles. However, these two systems are based on linear polarized light, and there are only two images with orthogonal polarization states. Zhang et al. designed an aperture-division polarimetric camera, as shown in **Figure 15E**, to capture four polarization images in the atmosphere *via* methods based on the full Stokes vector. It successfully achieves real-time image haze removal with an output rate of 25 fps [34]. However, the dehazing performance can be significantly affected by the registration accuracy. With the development of the DoFP polarization camera, as shown in **Figure 15F**, real-time processing is made possible without registration error. Our team has integrated this DoFP camera with a watertight device and an adjustable polarized illumination to create the underwater polarimetric imaging system (UPIS). The corresponding configuration is shown in **Figure 2B3** to perform de-scattering (in air and undersea) tasks in real-life scenarios. Using custom dehazing algorithms, the visual range is increased by about 8.5 times, and the processing speed reaches 15–25 fps for images with a resolution of approximately 1000 × 1000 [154]. In other words, this custom-made system has fulfilled the "3R-criterion" to a much greater extent. However, compared with traditional solutions with a single image and advanced computer-vision-based algorithms, there remains room for further improvement in the 3R-polarimetric imaging system.

A possible approach going forward is to further exploit integrated polarimetric imaging systems based on the DoFP polarization camera and automatic rotating devices in PSG and PSA [155–159]. As such, the polarization modulations in both illumination and detector can be controlled simultaneously to handle multifunctional applications.

In the review, we have covered some, if not all, of the established works in the fields of polarimetric imaging in scattering media, and we are keen to see more studies in the area as further understanding in polarimetric imaging will undoubtedly benefit both the academic and industrial communities in a significant way.

## AUTHOR CONTRIBUTIONS

XL, YH, and HW prepared the references and data. XL wrote the manuscript with input from all authors. TL reviewed and improved the writing. S-CC and HH supervised the project.

## FUNDING

National Natural Science Foundation of China (62075161, 61775163); HKSAR Research Grants Council, General Research Fund (14206517); Innovation and Technology Commission, Innovation Technology Fund (ITS/428/17FP); and Guangxi Innovation-Driven Development Project (GuikeAA21077008).

## REFERENCES


1. Schechner YY, Karpel N. Recovery of Underwater Visibility and Structure by Polarization Analysis. *IEEE J Oceanic Eng* (2005) 30:570–87. doi:10.1109/joe.2005.850871
2. Li X, Hu H, Zhao L, Wang H, Yu Y, Wu L, et al. Polarimetric Image Recovery Method Combining Histogram Stretching for Underwater Imaging. *Sci Rep* (2018) 8:12430–10. doi:10.1038/s41598-018-30566-8
3. He K, Sun J, Tang X. Single Image Haze Removal Using Dark Channel Prior. *IEEE Trans Pattern Anal Mach Intell* (2011) 33:2341–53. doi:10.1109/TPAMI.2010.168
4. Tarel J-P, Hautiere N. Fast Visibility Restoration from a Single Color or gray Level Image. In: in 2009 IEEE 12th international conference on computer vision. 2201-2208. IEEE (2009).
5. Davis GB, Carley KM. Clearing the FOG: Fuzzy, Overlapping Groups for Social Networks. *Social Networks* (2008) 30:201–12. doi:10.1016/j.socnet.2008.03.001
6. Chenault DB, Pezzaniti JL. *In Polarization Analysis, Measurement, and Remote Sensing III*. International Society for Optics and Photonics (2018). p. 124–33.
7. Dang X, Bardhan NM, Qi J, Gu L, Eze NA, Lin CW, et al. Deep-tissue Optical Imaging of Near Cellular-Sized Features. *Sci Rep* (2019) 9:3873–12. doi:10.1038/s41598-019-39502-w
8. Ghosh N, Wood MF, Vitkin IA. Mueller Matrix Decomposition for Extraction of Individual Polarization Parameters from Complex Turbid media Exhibiting Multiple Scattering, Optical Activity, and Linear Birefringence. *J Biomed Opt* (2008) 13:044036. doi:10.1117/1.2960934
9. Piazza P, Cummings V, Guzzi A, Hawes I, Lohrer A, Marini S, et al. Underwater Photogrammetry in Antarctica: Long-Term Observations in Benthic Ecosystems and Legacy Data rescue. *Polar Biol* (2019) 42:1061–79. doi:10.1007/s00300-019-02480-w
10. Nowosielski A, Małecki K, Forczmański P, Smoliński A. Spoofing 2D Face Recognition Systems with 3D Masks. In: International Conference on Computer Recognition Systems. Springer (2013). p. 174–83.
11. Drap P, Papini O, Sourisseau J-C, Gambin T. Mining the Semantic Web. In: European semantic web conference. Springer (2012). 3–6.
12. Sheng W. *Photonics. 34*. Multidisciplinary Digital Publishing Institute (2022).
13. Singh D, Kumar V. A Comprehensive Review of Computational Dehazing Techniques. *Arch Computat Methods Eng* (2019) 26:1395–413. doi:10.1007/s11831-018-9294-z
14. Tyo JS, Goldstein DL, Chenault DB, Shaw JA. Review of Passive Imaging Polarimetry for Remote Sensing Applications. *Appl Opt* (2006) 45:5453–69. doi:10.1364/ao.45.005453
15. Li X, Hu H, Zhao L, Wang H, Han Q, Cheng Z, et al. Pseudo-polarimetric Method for Dense Haze Removal. *IEEE Photon J.* (2019) 11:1–11. doi:10.1109/jphot.2018.2890771
16. Liu T, Guan Z, Li X, Cheng Z, Han Y, Yang J, et al. Polarimetric Underwater Image Recovery for Color Image with Crosstalk Compensation. *Opt Lasers Eng* (2020) 124:105833. doi:10.1016/j.optlaseng.2019.105833
17. Hu H, Qi P, Li X, Cheng Z, Liu T. Underwater Imaging Enhancement Based on a Polarization Filter and Histogram Attenuation Prior. *J Phys D: Appl Phys* (2021) 54:175102. doi:10.1088/1361-6463/abdc93
18. Reza AM. Realization of the Contrast Limited Adaptive Histogram Equalization (CLAHE) for Real-Time Image Enhancement. *J VLSI Signal Processing-Systems Signal, Image, Video Tech* (2004) 38:35–44. doi:10.1023/b:vlsi.0000028532.53893.82
19. Wang W, Yuan X. Recent Advances in Image Dehazing. *Ieee/caa J Autom Sinica* (2017) 4:410–36. doi:10.1109/jas.2017.7510532
20. Land EH. The Retinex Theory of Color Vision. *Sci Am* (1977) 237:108–28. doi:10.1038/scientificamerican1277-108
21. Land EH, McCann JJ. Lightness and Retinex Theory. *J Opt Soc Am* (1971) 61:1–11. doi:10.1364/josa.61.000001
22. Zhongli M, Jie W. Single-scale Retinex Sea Fog Removal Algorithm Fused the Edge Information. *J Computer-Aided Des Comp Graphics* (2015) 27:217–25.
23. Seow M-J, Asari VK. Ratio Rule and Homomorphic Filter for Enhancement of Digital Colour Image. *Neurocomputing* (2006) 69:954–8. doi:10.1016/j.neucom.2005.07.003
24. Yong Du Y, Guindon B, Cihlar J. Haze Detection and Removal in High Resolution Satellite Image with Wavelet Analysis. *IEEE Trans Geosci Remote Sensing* (2002) 40:210–7. doi:10.1109/36.981363
25. Starck J-L, Murtagh F, Candès EJ, Donoho DL. Gray and Color Image Contrast Enhancement by the Curvelet Transform. *IEEE Trans Image Process* (2003) 12:706–17. doi:10.1109/tip.2003.813140
26. Guan L. Model-based Neural Evaluation and Iterative Gradient Optimization in Image Restoration and Statistical Filtering. *J Electron Imaging* (1995) 4:407–12. doi:10.1117/12.217268
27. Fattal R. Single Image Dehazing. *ACM Trans Graph* (2008) 27:1–9. doi:10.1145/1360612.1360671
28. Lu H, Li Y, Nakashima S, Serikawa S. Single Image Dehazing through Improved Atmospheric Light Estimation. *Multimed Tools Appl* (2016) 75:17081–96. doi:10.1007/s11042-015-2977-7
29. Hautiére N, Tarel J-P, Lavenant J, Aubert D. Automatic Fog Detection and Estimation of Visibility Distance through Use of an Onboard Camera. *Machine Vis Appl* (2006) 17:8–20. doi:10.1007/s00138-005-0011-1
30. Narasimhan SG, Nayar SK. Proceedings of the 2001 IEEE Computer Society Conference on Computer Vision and Pattern Recognition. CVPR 2001. In: Proceedings of the 2001 IEEE Computer Society Conference on Computer Vision and Pattern Recognition. CVPR 2001. II-II. IEEE (2001).
31. Feng C, Zhuo S, Zhang X, Shen L, Süsstrunk S. ICDAR 2013 Document Image Binarization Contest (DIBCO 2013). In: 2013 IEEE International Conference on Image Processing. IEEE (2013). 2363–7.
32. Schechner YY, Narasimhan SG, Nayar SK. Polarization-based Vision through Haze. *Appl Opt* (2003) 42:511–25. doi:10.1364/ao.42.000511
33. Fade J, Panigrahi S, Carré A, Frein L, Hamel C, Bretenaker F, et al. Long-range Polarimetric Imaging through Fog. *Appl Opt* (2014) 53:3854–65. doi:10.1364/ao.53.003854
34. Zhang W, Liang J, Ren L, Ju H, Qu E, Bai Z, et al. Real-time Image Haze Removal Using an Aperture-Division Polarimetric Camera. *Appl Opt* (2017) 56:942–7. doi:10.1364/ao.56.000942
35. Treibitz T, Schechner YY. Active Polarization Descattering. *IEEE Trans Pattern Anal Mach Intell* (2008) 31:385–99. doi:10.1109/TPAMI.2008.85
36. Seow KLC, Török P, Foreman MR. Single Pixel Polarimetric Imaging through Scattering media. *Opt Lett* (2020) 45:5740–3. doi:10.1364/ol.399554
37. El Ketara M, Breugnot S. *Polarization: Measurement, Analysis, and Remote Sensing XIII. 106550N*. International Society for Optics and Photonics (2018).
38. Liang J, Ren L, Qu E, Hu B, Wang Y. Method for Enhancing Visibility of Hazy Images Based on Polarimetric Imaging. *Photon Res* (2014) 2:38–44. doi:10.1364/prj.2.000038
39. Li X, Wang H, Hu H, Liu T. AOPC 2019. In: *Optical Sensing and Imaging Technology. 113382O*. International Society for Optics and Photonics (2019).
40. Liang J, Ren L, Liang R. Low-pass Filtering Based Polarimetric Dehazing Method for Dense Haze Removal. *Opt Express* (2021) 29:28178–89. doi:10.1364/oe.427629
41. Tyo JS, Rowe MP, Pugh EN, Engheta N. Target Detection in Optically Scattering media by Polarization-Difference Imaging. *Appl Opt* (1996) 35:1855–70. doi:10.1364/ao.35.001855
42. Guan J, Zhu J. Target Detection in Turbid Medium Using Polarization-Based Range-Gated Technology. *Opt Express* (2013) 21:14152–8. doi:10.1364/oe.21.014152
43. Liang J, Ren L, Ju H, Zhang W, Qu E. Polarimetric Dehazing Method for Dense Haze Removal Based on Distribution Analysis of Angle of Polarization. *Opt Express* (2015) 23:26146–57. doi:10.1364/oe.23.026146
44. Guan J, Ma M, Sun P. Optimization of Rotating Orthogonal Polarization Imaging in Turbid media via the Mueller Matrix. *Opt Lasers Eng* (2019) 121:104–11. doi:10.1016/j.optlaseng.2019.04.001
45. Wang H, Li J, Hu H, Jiang J, Li X, Zhao K, et al. Underwater Imaging by Suppressing the Backscattered Light Based on Mueller Matrix. *IEEE Photon J.* (2021) 13:1–6. doi:10.1109/jphot.2021.3094359
46. Hu H, Zhao L, Li X, Wang H, Yang J, Li K, et al. Polarimetric Image Recovery in Turbid media Employing Circularly Polarized Light. *Opt Express* (2018) 26:25047–59. doi:10.1364/oe.26.025047
47. Liu F, Li X, Han P, Shao X. Advanced Visualization Polarimetric Imaging: Removal of Water Spray Effect Utilizing Circular Polarization. *Appl Sci* (2021) 11:2996. doi:10.3390/app11072996

48. Hu H, Zhao L, Huang B, Li X, Wang H, Liu T. Enhancing Visibility of Polarimetric Underwater Image by Transmittance Correction. *IEEE Photon J.* (2017) 9:1–10. doi:10.1109/jphot.2017.2698000
49. Li X, Li H, Lin Y, Guo J, Yang J, Yue H, et al. Learning-based Denoising for Polarimetric Images. *Opt Express* (2020) 28:16309–21. doi:10.1364/oe.391017
50. Hu H, Zhang Y, Li X, Lin Y, Cheng Z, Liu T. Polarimetric Underwater Image Recovery via Deep Learning. *Opt Lasers Eng* (2020) 133:106152. doi:10.1016/j.optlaseng.2020.106152
51. Liu F, Cao L, Shao X, Han P, Bin X. Polarimetric Dehazing Utilizing Spatial Frequency Segregation of Images. *Appl Opt* (2015) 54:8116–22. doi:10.1364/ao.54.008116
52. Jin H, Qian L, Gao J, Fan Z, Chen J. Polarimetric Calculation Method of Global Pixel for Underwater Image Restoration. *IEEE Photon J* (2020) 13:1–15.
53. Koschmieder H. Theorie der horizontalen Sichtweite. *Beitrage zur Physik der freien Atmosphare* (1924) 33-53.
54. Koranga P, Kumawat S. Face Mask Detection Classifier and Model Pruning with Keras-Surgeon. In: 2020 5th IEEE International Conference on Recent Advances and Innovations in Engineering (ICRAIE). IEEE (2020). 1–6.
55. Narasimhan SG, Nayar SK. Vision and the Atmosphere. *Int J Comp Vis* (2002) 48:233–54. doi:10.1023/a:1016328200723
56. Liang J, Zhang W, Ren L, Ju H, Qu E. Polarimetric Dehazing Method for Visibility Improvement Based on Visible and Infrared Image Fusion. *Appl Opt* (2016) 55:8221–6. doi:10.1364/ao.55.008221
57. Schechner YY, Karpel N. Component-Based Face Recognition with 3D Morphable Models. In: Proceedings of the 2004 IEEE Computer Society Conference on Computer Vision and Pattern Recognition. CVPR 2004. I-IIEEE (2004).
58. Han P, Liu F, Wei Y, Shao X. Optical Correlation Assists to Enhance Underwater Polarization Imaging Performance. *Opt Lasers Eng* (2020) 134:106256. doi:10.1016/j.optlaseng.2020.106256
59. Huang B, Liu T, Hu H, Han J, Yu M. Underwater Image Recovery Considering Polarization Effects of Objects. *Opt Express* (2016) 24: 9826–38. doi:10.1364/oe.24.009826
60. Tao Q, Sun Y, Shen F, Xu Q, Gao J, Guo Z. Active Imaging with the Aids of Polarization Retrieve in Turbid media System. *Opt Commun* (2016) 359: 405–10. doi:10.1016/j.optcom.2015.09.109
61. Shen F, Zhang B, Guo K, Yin Z, Guo Z. The Depolarization Performances of the Polarized Light in Different Scattering media Systems. *IEEE Photon J* (2017) 10:1–12.
62. Xu Q, Guo Z, Tao Q, Jiao W, Wang X, Qu S, et al. Transmitting Characteristics of Polarization Information under Seawater. *Appl Opt* (2015) 54:6584–8. doi:10.1364/ao.54.006584
63. Goldstein DH. *Polarized Light*. CRC Press (2017).
64. Li X, Liu T, Huang B, Song Z, Hu H. Optimal Distribution of Integration Time for Intensity Measurements in Stokes Polarimetry. *Opt Express* (2015) 23:27690–9. doi:10.1364/oe.23.027690
65. Chandrasekhar S. *Radiative Transfer*. Courier Corporation (2013).
66. Hu H, Lin Y, Li X, Qi P, Liu T. IPLNet: a Neural Network for Intensity-Polarization Imaging in Low Light. *Opt Lett* (2020) 45:6162–5. doi:10.1364/ol.409673
67. Shibata S, Hagen N, Otani Y. Robust Full Stokes Imaging Polarimeter with Dynamic Calibration. *Opt Lett* (2019) 44:891–4. doi:10.1364/ol.44.000891
68. Qiu S, Fu Q, Wang C, Heidrich W. Polarization Demosaicking for Monochrome and Color Polarization Focal Plane Arrays. In: International Symposium on Vision, Modeling and Visualization. The Eurographics Association (2019).
69. Li X, Hu H, Boffety M, Roussel S, Liu T, Goudail F. Optimal Tradeoff between Precision and Sampling Rate in DoFP Imaging Polarimeters. *Opt Lett* (2019) 44:5900–3. doi:10.1364/ol.44.005900
70. Mueller H. On the Theory of Scattering of Light. Proceedings of the Royal Society of London. Series A. *Math Phys Sci* (1938) 166:425–49.
71. Gil JJ. Polarimetric Characterization of Light and media. *Eur Phys J Appl Phys* (2007) 40:1–47. doi:10.1051/epjap:2007153
72. Ghosh N, Wood MFG, Li S-h., Weisel RD, Wilson BC, Li R-K, et al. Mueller Matrix Decomposition for Polarized Light Assessment of Biological Tissues. *J Biophoton* (2009) 2:145–56. doi:10.1002/jbio.200810040
73. Spandana K, Sindhoora K, Mahato K, Banik S, Mazumder N. Frontiers in Optics. In: *FTu8B. 3*. Optical Society of America (2022).
74. Sindhoora K. Journal of Physics. In: Conference Series. 012045. IOP Publishing (2022).
75. Spandana K, Mahato K, Mazumder N. Polarization-resolved Stokes-Mueller Imaging: a Review of Technology and Applications. *Lasers Med Sci* (2019) 34: 1283–93.
76. Rowe MP, Tyo JS, Engheta N, Pugh EN. Polarization-difference Imaging: a Biologically Inspired Technique for Observation through Scattering media. *Opt Lett* (1995) 20:608–10. doi:10.1364/ol.20.000608
77. Horvath H. On the Applicability of the Koschmieder Visibility Formula. *Atmos Environ* (1967) 5(1971):177–84.
78. Schechner YY, Narasimhan SG, Nayar SK. In: Proceedings of the 2001 IEEE Computer Society Conference on Computer Vision and Pattern Recognition. CVPR 2001. I-I. IEEE (2001).
79. Hu H, Zhao L, Li X, Wang H, Liu T. Underwater Image Recovery under the Nonuniform Optical Field Based on Polarimetric Imaging. *IEEE Photon J.* (2018) 10:1–9. doi:10.1109/jphot.2018.2791517
80. Amer KO, Elbouz M, Alfalou A, Brosseau C, Hajjami J. Enhancing Underwater Optical Imaging by Using a Low-Pass Polarization Filter. *Opt Express* (2019) 27:621–43. doi:10.1364/oe.27.000621
81. Smith RC, Baker KS. Optical Properties of the Clearest Natural Waters (200-800 Nm). *Appl Opt* (1981) 20:177–84. doi:10.1364/ao.20.000177
82. Liu F, Han P, Wei Y, Yang K, Huang S, Li X, et al. Deeply Seeing through Highly Turbid Water by Active Polarization Imaging. *Opt Lett* (2018) 43: 4903–6. doi:10.1364/ol.43.004903
83. Li X, Hu H, Wu L, Liu T. Optimization of Instrument Matrix for Mueller Matrix Ellipsometry Based on Partial Elements Analysis of the Mueller Matrix. *Opt Express* (2017) 25:18872–84. doi:10.1364/oe.25.018872
84. Li X, Hu H, Wu L, Yu Y, Liu T. Impact of Intensity Integration Time Distribution on the Measurement Precision of Mueller Polarimetry. *J Quantitative Spectrosc Radiative Transfer* (2019) 231:22–7. doi:10.1016/j.jqsrt.2019.04.021
85. Ishimaru A, Jaruwatanadilok S, Kuga Y. Polarized Pulse Waves in Random Discrete Scatterers. *Appl Opt* (2001) 40:5495–502. doi:10.1364/ao.40.005495
86. Singh MD, Vitkin IA. Discriminating Turbid media by Scatterer Size and Scattering Coefficient Using Backscattered Linearly and Circularly Polarized Light. *Biomed Opt Express* (2021) 12:6831–43. doi:10.1364/boe.438631
87. Ramella-Roman JC, Prahl SA, Jacques SL. Three Monte Carlo Programs of Polarized Light Transport into Scattering media: Part I. *Opt Express* (2005) 13:4420–38. doi:10.1364/opex.13.004420
88. Ramella-Roman JC, Prahl SA, Jacques SL. Three Monte Carlo Programs of Polarized Light Transport into Scattering media: Part II: Part II. *Opt Express* (2005) 13:10392–405. doi:10.1364/opex.13.010392
89. Peña-Gutiérrez S, Ballesta-Garcia M, García-Gómez P, Royo S. Quantitative Demonstration of the Superiority of Circularly Polarized Light in Fog Environments. *Opt Lett* (2022) 47:242–5. doi:10.1364/ol.445339
90. Tian H, Zhu J, Tan S, Zhang Y, Zhang Y, Li Y, et al. Rapid Underwater Target Enhancement Method Based on Polarimetric Imaging. *Opt Laser Tech* (2018) 108:515–20. doi:10.1016/j.optlastec.2018.07.057
91. Guan J, Ren W, Cheng Y. Stokes Vector Based Interpolation Method to Improve the Efficiency of Bio-Inspired Polarization-Difference Imaging in Turbid media. *J Phys D: Appl Phys* (2018) 51:145402. doi:10.1088/1361-6463/aab28f
92. Wei Y, Han P, Liu F, Shao X. Enhancement of Underwater Vision by Fully Exploiting the Polarization Information from the Stokes Vector. *Opt Express* (2021) 29:22275–87. doi:10.1364/oe.433072
93. MacKintosh FC, Zhu JX, Pine DJ, Weitz DA. Polarization Memory of Multiply Scattered Light. *Phys Rev B* (1989) 40:9342–5. doi:10.1103/physrevb.40.9342
94. Ni X, Alfano RR. Time-resolved Backscattering of Circularly and Linearly Polarized Light in a Turbid Medium. *Opt Lett* (2004) 29:2773–5. doi:10.1364/ol.29.002773
95. Pérez JJG, Ossikovski R. *Polarized Light and the Mueller Matrix Approach*. CRC Press (2017).
96. Sun M, He H, Zeng N, Du E, Guo Y, Liu S, et al. Characterizing the Microstructures of Biological Tissues Using Mueller Matrix and

Transformed Polarization Parameters. *Biomed Opt Express* (2014) 5:4223–34. doi:10.1364/boe.5.004223
97. Du E, He H, Zeng N, Sun M, Guo Y, Wu J, et al. Mueller Matrix Polarimetry for Differentiating Characteristic Features of Cancerous Tissues. *J Biomed Opt* (2014) 19:76013. doi:10.1117/1.JBO.19.7.076013
98. Kudenov MW, Escuti MJ, Hagen N, Dereniak EL, Oka K. Snapshot Imaging Mueller Matrix Polarimeter Using Polarization Gratings. *Opt Lett* (2012) 37: 1367–9. doi:10.1364/ol.37.001367
99. Carnicer A, Bosch S, Javidi B. Mueller Matrix Polarimetry with 3D Integral Imaging. *Opt Express* (2019) 27:11525–36. doi:10.1364/oe.27.011525
100. Kobata T, Nomura T. Digital Holographic Three-Dimensional Mueller Matrix Imaging. *Appl Opt* (2015) 54:5591–6. doi:10.1364/ao.54.005591
101. Ellingsen PG, Aas LM, Hagen VS, Kumar R, Lilledahl MB, Kildemo M. Mueller Matrix Three-Dimensional Directional Imaging of Collagen Fibers. *J Biomed Opt* (2014) 19:026002. doi:10.1117/1.JBO.19.2.026002
102. Gil JJ, Ossikovski R. *Polarized Light and the Mueller Matrix Approach*. CRC Press (2017).
103. Wang H, Hu H, Jiang J, Li J, Li X, Zhang W, et al. Polarization Differential Imaging in Turbid Water via Mueller Matrix and Illumination Modulation. *Opt Commun* (2021) 499:127274. doi:10.1016/j.optcom.2021.127274
104. Liu F. Depolarization index from Mueller Matrix Descatters Imaging in Turbid Water. *Chin Opt Lett*. 20 (2022) 022601.
105. McCulloch WS, Pitts W. A Logical Calculus of the Ideas Immanent in Nervous Activity. *Bull Math Biophys* (1943) 5:115–33. doi:10.1007/bf02478259
106. Bishop CM. *Neural Networks for Pattern Recognition. (Oxford University Press,*(1995).
107. LeCun Y, Bottou L, Bengio Y, Haffner P. Gradient-based Learning Applied to Document Recognition. *Proc IEEE* (1998) 86:2278–324. doi:10.1109/5.726791
108. Krizhevsky A, Sutskever I, Hinton GE. Imagenet Classification with Deep Convolutional Neural Networks. *Adv Neural Inf Process Syst* (2012) 25: 1097–105.
109. Szegedy C. In: Proceedings of the IEEE Conference on Computer Vision and Pattern Recognition. (2016). 1–9.
110. He K, Zhang X, Ren S, Sun J. In: Proceedings of the IEEE Conference on Computer Vision and Pattern Recognition. (2021). 770–8.
111. Huang G, Liu Z, Van Der Maaten L, Weinberger KQ. In: Proceedings of the IEEE Conference on Computer Vision and Pattern Recognition. (2016). 4700–8.
112. Chen D. In: 2019 IEEE Winter Conference on Applications of Computer Vision (WACV). IEEE (2019). 1375–83.
113. Pan J. Physics-based Generative Adversarial Models for Image Restoration and beyond. *IEEE Trans Pattern Anal Machine Intelligence* (2020) 43: 2449–62.
114. Zhang J, Shao J, Chen J, Yang D, Liang B, Liang R. PFNet: an Unsupervised Deep Network for Polarization Image Fusion. *Opt Lett* (2020) 45:1507–10. doi:10.1364/ol.384189
115. Zhang R, Gui X, Cheng H, Chu J. Underwater Image Recovery Utilizing Polarimetric Imaging Based on Neural Networks. *Appl Opt* (2021) 60: 8419–25. doi:10.1364/ao.431299
116. Ren Q, Xiang Y, Wang G, Gao J, Wu Y, Chen R-P. The Underwater Polarization Dehazing Imaging with a Lightweight Convolutional Neural Network. *Optik* (2022) 251:168381. doi:10.1016/j.ijleo.2021.168381
117. Zhou C, Teng M, Han Y, Xu C, Shi B. Learning to Dehaze with Polarization. *Adv Neural Inf Process Syst* (2021) 34.
118. Yang S, Qu B, Liu G, Deng D, Liu S, Chen X. Unsupervised Learning Polarimetric Underwater Image Recovery under Nonuniform Optical fields. *Appl Opt* (2021) 60:8198–205. doi:10.1364/ao.432994
119. Zhu Y, Zeng T, Liu K, Ren Z, Lam EY. Full Scene Underwater Imaging with Polarization and an Untrained Network. *Opt Express* (2021) 29:41865–81. doi:10.1364/oe.444755
120. Carlevaris-Bianco N, Mohan A, Eustice RM. *In Oceans 2010 Mts/IEEE Seattle*. IEEE (2010). 1–8.
121. Hummel R. *Image Enhancement by Histogram Transformation* (1975). Unknown.
122. Huang D, Wang Y, Song W, Sequeira J, Mavromatis S. In: International Conference on Multimedia Modeling. Springer (2022). p. 453–65.
123. Huang SC, Cheng FC, Chiu YS. Efficient Contrast Enhancement Using Adaptive Gamma Correction with Weighting Distribution. *IEEE Trans Image Process* (2012) 22:1032–41. doi:10.1109/TIP.2012.2226047
124. Chao L, Wang M. In: 2010 2nd international conference on computer engineering and technology. V2-35-V32-39. IEEE (2010).
125. Courtney T, Sacks MS, Stankus J, Guan J, Wagner WR. Design and Analysis of Tissue Engineering Scaffolds that Mimic Soft Tissue Mechanical Anisotropy. *Biomaterials* (2006) 27:3631–8. doi:10.1016/j.biomaterials.2006.02.024
126. Jain A, Maurya AK, Ulrich L, Jaeger M, Rossi RM, Neels A, et al. Polarimetric Imaging in Backscattering for the Structural Characterization of Strongly Scattering Birefringent Fibrous media. *Opt Express* (2020) 28:16673–95. doi:10.1364/oe.390303
127. Tuchin VV. Polarized Light Interaction with Tissues. *J Biomed Opt* (2016) 21: 71114. doi:10.1117/1.JBO.21.7.071114
128. Yakovlev DD, Shvachkina ME, Sherman MM, Spivak AV, Pravdin AB, Yakovlev DA. Quantitative Mapping of Collagen Fiber Alignment in Thick Tissue Samples Using Transmission Polarized-Light Microscopy. *J Biomed Opt* (2016) 21:71111. doi:10.1117/1.JBO.21.7.071111
129. He H, Zeng N, Li D, Liao R, Ma H. Quantitative Mueller Matrix Polarimetry Techniques for Biological Tissues. *J Innov Opt Health Sci* (2012) 05:1250017. doi:10.1142/s1793545812500174
130. Ghosh N, Vitkin AI. Tissue Polarimetry: Concepts, Challenges, Applications, and Outlook. *J Biomed Opt* (2011) 16:110801. doi:10.1117/1.3652896
131. Sankaran V, Walsh JT, Jr, Maitland DJ. Comparative Study of Polarized Light Propagation in Biologic Tissues. *J Biomed Opt* (2002) 7:300–6. doi:10.1117/1.1483318
132. Wang X, Wang LV. Propagation of Polarized Light in Birefringent Turbid media: a Monte Carlo Study. *J Biomed Opt* (2002) 7:279–90. doi:10.1117/1.1483315
133. Nishizawa N, Hamada A, Takahashi K, Kuchimaru T, Munekata H. Monte Carlo Simulation of Scattered Circularly Polarized Light in Biological Tissues for Detection Technique of Abnormal Tissues Using Spin-Polarized Light Emitting Diodes. *Jpn J Appl Phys* (2020) 59:SEEG03. doi:10.35848/1347-4065/ab69db
134. Yun T, Zeng N, Li W, Li D, Jiang X, Ma H. Monte Carlo Simulation of Polarized Photon Scattering in Anisotropic media. *Opt Express* (2009) 17: 16590–602. doi:10.1364/oe.17.016590
135. Wang X, Wang LV, Sun C-W, Yang C-C. Polarized Light Propagation through Scattering media: Time-Resolved Monte Carlo Simulations and Experiments. *J Biomed Opt* (2003) 8:608–17. doi:10.1117/1.1606462
136. Sankaran V, Schönenberger K, Walsh JT, Maitland DJ. Polarization Discrimination of Coherently Propagating Light in Turbid media. *Appl Opt* (1999) 38:4252–61. doi:10.1364/ao.38.004252
137. Shukla P, Sumathi R, Gupta S, Pradhan A. Influence of Size Parameter and Refractive index of the Scatterer on Polarization-Gated Optical Imaging through Turbid media. *J Opt Soc Am A* (2007) 24:1704–13. doi:10.1364/josaa.24.001704
138. Schilders SP, Gan XS, Gu M. Resolution Improvement in Microscopic Imaging through Turbid media Based on Differential Polarization Gating. *Appl Opt* (1998) 37:4300–2. doi:10.1364/ao.37.004300
139. Morgan SP, Khong MP, Somekh MG. Effects of Polarization State and Scatterer Concentration on Optical Imaging through Scattering media. *Appl Opt* (1997) 36:1560–5. doi:10.1364/ao.36.001560
140. Rodríguez C. *Polarized Light and Optical Angular Momentum for Biomedical Diagnostics*. *116460P*. International Society for Optics and Photonics (2021).
141. Ghosh N, Pradhan A, Gupta PK, Gupta S, Jaiswal V, Singh RP. Depolarization of Light in a Multiply Scattering Medium: Effect of the Refractive index of a Scatterer. *Phys Rev E Stat Nonlin Soft Matter Phys* (2004) 70:066607. doi:10.1103/PhysRevE.70.066607
142. Li S, Jiao J, Wang C. Research on Polarized Multi-Spectral System and Fusion Algorithm for Remote Sensing of Vegetation Status at Night. *Remote Sensing* (2021) 13:3510. doi:10.3390/rs13173510
143. Chowdhary J, Cairns B, Waquet F, Knobelspiesse K, Ottaviani M, Redemann J, et al. Sensitivity of Multiangle, Multispectral Polarimetric Remote Sensing over Open Oceans to Water-Leaving Radiance: Analyses of RSP Data

Acquired during the MILAGRO Campaign. *Remote Sensing Environ* (2012) 118:284–308. doi:10.1016/j.rse.2011.11.003
144. Dubovik O, Li Z, Mishchenko MI, Tanré D, Karol Y, Bojkov B, et al. Polarimetric Remote Sensing of Atmospheric Aerosols: Instruments, Methodologies, Results, and Perspectives. *J Quantitative Spectrosc Radiative Transfer* (2019) 224:474–511. doi:10.1016/j.jqsrt.2018.11.024
145. Yan L, Li Y, Chandrasekar V, Mortimer H, Peltoniemi J, Lin Y. General Review of Optical Polarization Remote Sensing. *Int J Remote Sensing* (2020) 41:4853–64. doi:10.1080/01431161.2020.1724350
146. Li N, Zhao Y, Pan Q, Kong SG, Chan JC-W. Illumination-invariant Road Detection and Tracking Using LWIR Polarization Characteristics. *ISPRS J Photogrammetry Remote Sensing* (2021) 180:357–69. doi:10.1016/j.isprsjprs.2021.08.022
147. Bu Y. Hyperspectral and Multispectral Image Fusion via Graph Laplacian-Guided Coupled Tensor Decomposition. *IEEE Trans Geosci Remote Sensing* (2020) 59:648–62.
148. Xue J, Zhao Y-Q, Bu Y, Liao W, Chan JC-W, Philips W. Spatial-spectral Structured Sparse Low-Rank Representation for Hyperspectral Image Super-resolution. *IEEE Trans Image Process* (2021) 30:3084–97. doi:10.1109/tip.2021.3058590
149. Wang Hui 王. 辉., Wang Jin 王. 进., Li Xiaobo 李., Hu Haofeng 胡., Liu Tiegen 刘. Optimization for a Polarimetic Dehazing Method Based on the Circularly Polarized Light. 红外与激光工程 (2019) 48:1126001. doi:10.3788/irla201948.1126001
150. Wang H, Hu H, Li X, Guan Z, Zhu W, Jiang J, et al. An Angle of Polarization (AoP) Visualization Method for DoFP Polarization Image Sensors Based on Three Dimensional HSI Color Space. *Sensors* (2019) 19:1713. doi:10.3390/s19071713
151. Van Eeckhout A, Lizana A, Garcia-Caurel E, Gil JJ, Ossikovski R, Campos J. Synthesis and Characterization of Depolarizing Samples Based on the Indices of Polarimetric Purity. *Opt Lett* (2017) 42:4155–8. doi:10.1364/ol.42.004155
152. Sheppard CJ, Bendandi A, Gratiet AL, Diaspro A. *Photonics. 88*. Multidisciplinary Digital Publishing Institute (2022).
153. Biosensors Lab. Bioinspired Camera Could Help Self-Driving Cars See Better (2022). <https://biosensors.web.engr.illinois.edu/events-view/bioinspired-camera-could-help-self-driving-cars-see-better/>.
154. Li J. Research of Underwater Image Recovery Based on Mueller Matrix and Stokes Vector. *Master Thesis*. Tianjin University (2020).
155. Li X, Goudail F, Qi P, Liu T, Hu H. Integration Time Optimization and Starting Angle Autocalibration of Full Stokes Imagers Based on a Rotating Retarder. *Opt Express* (2021) 29:9494–512. doi:10.1364/oe.418399
156. Gottlieb D, Arteaga O. Mueller Matrix Imaging with a Polarization Camera: Application to Microscopy. *Opt Express* (2021) 29:34723–34. doi:10.1364/oe.439529
157. Goudail F, Li X, Boffety M, Roussel S, Liu T, Hu H. Precision of Retardance Autocalibration in Full-Stokes Division-Of-Focal-Plane Imaging Polarimeters. *Opt Lett* (2019) 44:5410–3. doi:10.1364/ol.44.005410
158. Huang T, Meng R, Qi J, Liu Y, Wang X, Chen Y, et al. Fast Mueller Matrix Microscope Based on Dual DoFP Polarimeters. *Opt Lett* (2021) 46:1676–9. doi:10.1364/ol.421394
159. Li X, Le Teurnier B, Boffety M, Liu T, Hu H, Goudail F. Theory of Autocalibration Feasibility and Precision in Full Stokes Polarization Imagers. *Opt Express* (2020) 28:15268–83. doi:10.1364/oe.390882

**Conflict of Interest:** The authors declare that the research was conducted in the absence of any commercial or financial relationships that could be construed as a potential conflict of interest.

frontiers in Physics

ORIGINAL RESEARCH
published: 31 March 2022
doi: 10.3389/fphy.2022.836523

# Multi-Angle Polarization Index System for Pollen Type Bioaerosol Recognition

*Qizhi Xu*[1,2], *Nan Zeng*[1]*, *Wei Guo*[1,2], *Jun Guo*[1], *Yonghong He*[1] *and Hui Ma*[1,3]*

[1]*Shenzhen Key Laboratory for Minimal Invasive Medical Technologies, Guangdong Research Center of Polarization Imaging and Measurement Engineering Technology, Graduate School at Shenzhen, Tsinghua University, Shenzhen, China,* [2]*Department of Biomedical Engineering, Tsinghua University, Beijing, China,* [3]*Center for Precision Medicine and Healthcare, Tsinghua-Berkeley Shenzhen Institute, Shenzhen, China*

In this work, we propose a high-throughput online identification method of bioaerosols based on multi-angle polarization index system (MAPIS). In the study, four categories and 10 subclasses of aerosol samples from biological and non-biological sources are detected under three incident polarization mode. Then their measured MAPIS shows that bioaerosols like pollen can be easily distinguished from other types of aerosols. Not only that, experimental results also indicate the feasibility of fine identification between different kinds of bioaerosols based on MAPIS in P and R modes. To further extract simple and optimized polarization characterization parameters suitable for bioaerosols, we analyze the multidimensional data of MAPIS by PCA then validate the aerosol recognition accuracy using the first two principal components by multiple groups of randomly mixed aerosol datasets. The comparison with PCA components based on only scattering intensity demonstrate that MAPIS can be not only applied in the specific identification of bioaerosols but also suitable for the distinction between different kinds of bioaerosols.

**Keywords: polarization scattering, bioaerosol, stokes vector, PCA, pollen**

OPEN ACCESS

***Edited by:***
*Ji Qi,*
*Imperial College London, United Kingdom*

***Reviewed by:***
*Jean-Baptiste Renard, Laboratoire de Physique et Chimie de l'Environnement et de l'Espace (LPC2E), France*
*Jiawei Song, Zhejiang Lab, China*

***Correspondence:**
*Nan Zeng*
*zengnan@sz.tsinghua.edu.cn*
*Hui Ma*
*mahui@tsinghua.edu.cn*

***Specialty section:***
*This article was submitted to Optics and Photonics, a section of the journal Frontiers in Physics*

***Received:*** *15 December 2021*
***Accepted:*** *17 February 2022*
***Published:*** *31 March 2022*

***Citation:***
*Xu Q, Zeng N, Guo W, Guo J, He Y and Ma H (2022) Multi-Angle Polarization Index System for Pollen Type Bioaerosol Recognition. Front. Phys. 10:836523. doi: 10.3389/fphy.2022.836523*

## 1 INTRODUCTION

Bioaerosols are highly associated with a wide range of health effects with major public health impact [1]. It is important to develop some monitoring system that could offer the capability of real-time monitoring of biological aerosols [2]. Pollen is a major fraction of bioaerosols and is receiving increasing attention due to its high allergenic potential and the associated impacts on personal life quality and economy [3]. Pollens have various effects on human health and the environment. Plant pollens are similarly IgE binding allergens that may cause allergic reactions [4]. Airborne pollens are often considered major agents of allergy-related diseases [5] such as asthma, rhinitis, and atopic eczema [6, 7]. The allergenicity of some pollen is further enhanced by particulate pollution in the atmosphere [8]. Due to the effects of climate change on biota, the negative effects of airborne pollen on humans are increasing [9–11]. The number of people suffering from allergies due to pollen inhalation is increasing every year [12]. Also, for environment, pollen can also act as an environmental pollutant by acting as a nucleus for cloud droplets and ice crystals, affecting the solar radiation reaching earth and the optical properties of clouds, thereby reducing visibility [13].

In the area of public health and allergies, the monitoring and predicting of pollens is challenging, partly due to the lack of standardized and widely applicable offline laboratory analysis or online

continuous monitoring methods [14]. Traditional pollen monitoring employs fluorescence microscopy, such as extractive staining fluorescence microscopy [15] and direct staining fluorescence microscopy [16]. Moreover, various imaging techniques have been used for pollen detection, such as scanning electron microscopy (SEM) [17], transmission electron microscopy (TEM) [18], x-ray imaging [19], etc. These techniques allow for single particle analysis but provide data at a relatively low time resolution due to time-consuming preparation steps or complicated setups [20–23].

Also, some other methods have been developed based on light scattering, ultraviolet laser-induced fluorescence, and holography combined with deep learning [24]. Wu developed a label-free bioaerosol sensor based on holographic microscopy and deep-learning, which is designed to get rid of transferring to laboratory and manual inspection [25]. Mitsumoto proposed a novel flow particle analyzer based on the design of flow cytometer [26]. The device classifies pollen species by simultaneously detecting both scattered light and the characteristic fluorescence excited by ultraviolet light in the flow cell. Kawashima developed a device which measures the sideward and forward scattering intensities of laser light from each particle to quantify a specific pollen type (Japanese cedar) in Japan [27].

Currently, there are very few related literatures on the polarization characteristics of pollens in ambient air, and the corresponding polarization measurement is only limited to the depolarization rate of pollens [28]. The optical properties of pollen particles can be described by the depolarization rate obtained in the lidar detection [22, 29]. Here non-spherical pollens can produce a strong depolarization rate, which can be distinguished from the background backscattering of other aerosols [22]. In addition, according to the depolarization rate [30–33], many studies have shown the potential to distinguish different kinds of pollens in the atmosphere. There is research work on the Muller matrix of ragweed pollen in the visible spectral range [28], which provides a feasible way to identify pollens by using precise polarimetric fingerprints.

Our previous studies have shown that multi-angle polarization index system (MAPIS) could be used for characterizing non-biologically derived aerosols such as dust [34], soot [35] or irregular particle samples [36]. In this study, focusing on bioaerosols, we detect the multi-angle polarization scattering signals of individual biological aerosols and then show their characteristic MAPIS different from other abiotic aerosol particles under different incident polarization states. The measured data of various types of aerosol samples are given and compared in this paper, including two dust type samples, two water-soluble type samples, two carbonaceous aerosol samples, and several kinds of bioaerosols (including three kinds of pollens and pearl powder). Each sub-category is measured independently. By principal component analysis (PCA), an unsupervised learning method, we extract some specific indicators based on MAPIS. The results show that, even without the assistance of fluorescence, only by MAPIS, we can accurately distinguish bioaerosols such as pollens from non-biologically derived particles and can also subdivide the subclasses of pollens. The technology used in this study has the advantages of non-invasive, online real-time and high-throughput analysis. These preliminary studies confirm the potential of MAPIS applied in a fine identification and characterization of bioaerosols.

# 2 EXPERIMENTS AND SAMPLES

## 2.1 Experimental Setup

**Figure 1** shows the schematic diagram of our experimental setup, which has been presented in [37]. The light source is a solid laser (532 nm, 100 mW, MSL-III-532, Changchun New Industries Optoelectronics Technology Co., Ltd.). The incident light can be modulated into three polarization states (horizontal linear, 45° linear and right-handed circular polarization) by PSG (polarization state generator). We define these three measurement modes as H mode, P mode, and R mode. The polarized light is then focused at the center of the air flow by a cylindrical lens. The width and height of the laser spot is 1 and 0.04 mm. In the actual measurement, in order to judge whether any suspended particle is passing through the detection area, we use the intensity at 10° scattering angle as the trigger basis of polarization signal acquisition. When the forward 10° scattering signal exceeds the preset discrimination threshold, the scattered signals at four angles (30°, 60°, 85°, 115°) are then synchronously recorded. For each angle, a spatial filter module composed of a lens and an aperture at fixed location is used to eliminate the influence of stray light. Also, there is an optical trap at the end of laser beam to eliminate the forward stray light.

A four-quadrant polarization state analyzer (0°, 90°, 45°, 135° linear polarizer) is applied at each angle. We also test every four-quadrant polarization module using polarimeter to ensure the orientation deviation of polarizers no more than 2°. The scattered light is spatially divided into four parts and transmitted respectively to four SiPMT detectors via an optical fiber bundle. The light intensity is converted and recorded by data acquisition device (FCFR-USB2068, Fcctec Technology, China) at a sampling rate of 1 MHz. The Stokes parameter elements $S_0$, $S_1$, and $S_2$ could be easily calculated as described in **Eq. 1**. Currently we only use linear polarizing films due to the restrictions of the manufacture process, so this study does not involve the circular polarization items. Even so, $S_1$ and $S_2$ of Stokes vector at multi-angles already shows ability to characterize bioaerosols such as pollen.

$$S = \begin{bmatrix} S_0 \\ S_1 \\ S_2 \\ S_3 \end{bmatrix} = \begin{bmatrix} I_0 + I_{90} \\ I_0 - I_{90} \\ I_{45} - I_{135} \\ I_R - I_L \end{bmatrix} \tag{1}$$

An optimally designed sheath nozzle is used to make sure particles passing through the center of detection area one by one. Sample flow carries sample particles passing through the laser beam within the protection of sheath flow. The effectiveness of the instrument is verified by experiments of standard PSL particles, which has been mentioned in our previous work [38]. The agreement between the measured results and Mie

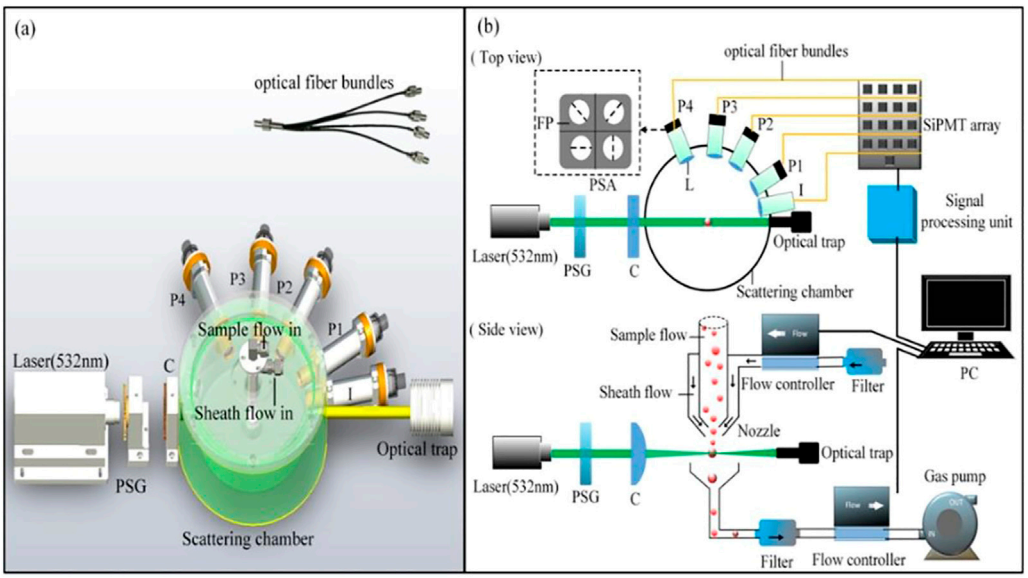


**FIGURE 1 | (A)** Overview of structure of measuring instrument; **(B)** schematic diagram of experiment setup. PSG, polarization state generator (composed of a polarizing prism with a quarter wave plate for R mode and a half wave plate for H and P mode); C, cylindrical lens; L, spatial filter module (composed of a lens and an aperture); P1-P4, scattered light polarization signal channel at four angles (30°, 60°, 85°, 115°); I, scattered light intensity signal channel at 10°; PSA, polarization state analyzer; FP, film polarizer; PC, personal computer.

theoretical calculation results based on a single scattering assumption can further confirm that the multiple scattering is hardly involved in our measurements. The velocity of air flow is controlled by two-flow controller and a gas pump. A particle flies through the detection area within 50 μs and we sample one point of signal every 1 μs. Thus, our current instrument can obtain signals of up to around 20,000 particles in about 1 s.

## 2.2 Sample Preparation

We choose four types of typical aerosol samples with different properties: dust, water-soluble salts, carbon, and biologically derived particles. Arizona dust and fly ash are measured as representation of dust. Sodium sulfate and sodium chloride are measured as representation of water-soluble salts. Disordered mesoporous carbon and hollow carbon spheres are measured as representation of carbon aerosols. Chamomile pollen, rose pollen, Osmanthus pollen, and pearl powder are measured as representation of biologically derived aerosols. Each subclass above is measured independently. The Stokes vector elements $S_0$, $S_1$, and $S_2$ are measured at four angles for each measurement mode. Pollen is a common and easily accessible class of biological aerosols. It should be noted that these pollen samples were provided by the drug supplier (Yiqi Herbs), and the pollen went through the grinding process which caused their size to be smaller, but its composition unchanged. According to Ref. [39–42], the untreated pollen size will be larger than 10 um. For example, the diameter of Chamomile Pollen is around 16.6 um [39]. As for pearl powder, it is a mixture of protein ($\beta$-chitin, silk-like proteins, and acidic glycoproteins) and calcium carbonate [43, 44], which can also belong to biomass source in composition.

Before measurements, aerosol particles from dust type, carbon type and biological type are screened through a 500-mesh sieve to ensure a relatively uniform particle size and then generated and diffused into uniformly dispersed suspended particles by the TSI-3400A aerosol generator. Salt aerosols of water-soluble type are atomized by a Met One 255 atomizer and then pass through a drying tube. All the detailed morphology information of samples can be found in **Table 1**. The particle size after screening in our experiments is less than 10 microns and was monitored synchronously by an optical particle sizer. In our experiments, we used optical particle sizer (OPS-3330, TSI) for particle size measurement. The measurement process and the accuracy of the OPS can be referenced in [45].

# 3 RESULTS

## 3.1 Differentiation Between Bioaerosols and Non-Biological Particles

The Stokes parameters $S_1$ and $S_2$ at four angles in each measurement mode for different types of aerosol samples are shown in **Figure 2**. In **Figure 2**, non-biological samples are represented by dots of different colors, while pollen samples are represented by green series cross-symbols. For each sub-category sample, we randomly select 10,000 measured data points to display for convenience. Apparently, compared with the differences within sub-categories of non-biological particles, the difference between non-biological origin samples and bioaerosol samples are significantly larger intuitively in terms of multi-angle polarization index system (MAPIS) regardless of the measurement mode.

**TABLE 1 |** Morphology of samples.

| Major type | Sub class | Morphology | Diameter | Refractive index |
|---|---|---|---|---|
| Dust | Arizona Dust | Irregular, diverse shapes from spheres to polygon symmetries [47–49] | 1.75 um | 1.56–0.026i ((1.56 ~1.65)–i (0.002 ~0.03) [56]) |
| | Fly Ash | Irregular shapes with flaky precipitates or approximately spherical shapes [50, 51] | 1.55 um | 1.60–0.018i ((1.48 ~1.57)–i (0 ~0.01) [57]) |
| Water Soluble Salts | Sodium Sulfate | Monoclinic, orthorhombic or hexagonal crystal system | 0.85 um | 1.47–0.002i (1.48–0.001i [58]) |
| | Sodium Chloride | Face-centered cubic | 0.57 um | 1.50–0.01i (1.54–0.001i [59]) |
| Carbon | Disordered Mesoporous Carbon | Mesoporous material with a disordered structure [52] | 0.79 um | 1.71–0.212i |
| | Hollow Carbon Spheres | Hollowed spheres [53, 54] | 0.71 um | 1.65–0.324i |
| Biologically Derived Particles | Chamomile Pollen | Prolate-spheroidal, radial symmetry, echinate [39] | 1.48 um | 1.350–0.012i |
| | Rose Pollen | Prolate or sub-prolate spheroidal, 3 germ furrows, prominent grooves on the exine surface [40] | 1.69 um | 1.410–0.020i |
| | Osmanthus Pollen | Approximately spherical, 3 germ furrows, mesh pattern on the exine surface, slightly wrinkled [41, 55] | 1.51 um | 1.490–0.022i |
| | Pearl Powder | Irregular polygonal plate-like structure [42, 44] | 2.01 um | 1.690–0.046i |

PCA is defined as an orthogonal linear transformation that transforms the data to a new coordinate system such that the greatest variance by some scalar projection of the data comes to lie on the first coordinate (called the first principal component), the second greatest variance on the second coordinate, and so on [46]. The first principal component can be considered as a projection direction that can best explain the data difference. Then, the ability of the second and third principal components to explain the data difference decreases in turn. Therefore, when we distinguish between biological and non-biological aerosols, the first principal component from the measured data of all kinds of aerosols provides a possible optimal expression for the distinction between these two categories. Similarly, when we further want to accurately identify different subclasses under the category of biological aerosols, the first principal component from the measured data of only various bioaerosols can used as a classification parameter to identify which kind of biological aerosol is detected.

Here we define $X$ as a measured multidimensional data matrix, and $w$ as a weight coefficient matrix of each principal component. Then the weight coefficient vector of the first principal component, $w_1$, can be obtained by optimizing Rayleigh quote.

$$\mathrm{w}_1 = \arg\max\left\{\frac{\mathrm{w}^{\mathrm{T}}\mathrm{X}^{\mathrm{T}}\mathrm{X}\mathrm{w}}{\mathrm{w}^{\mathrm{T}}\mathrm{w}}\right\} \tag{2}$$

To further extract some specific indicator to distinguish between bioaerosols and abiotic particles, we employ the PCA (Principal Component Analysis) method to analyze the measured MAPIS. The PCA results under different measurement modes are shown in **Figures 3A–C**. PCA is an unsupervised learning method, which means that the input data of PCA does not contain the type information of each particle point. Based on the data distribution along the horizontal axis direction of **Figures 3A–C**, the first principal component extracted by PCA, that is, the direction that shows the overall maximum variance of data, can perfectly separate pollen samples and non-biological samples. Next, the intra-class differences of pollen samples and non-biological samples are roughly along the vertical axis direction of **Figures 3A–C**, implying that the second principal component probably is suitable for the subdivision of different bioaerosols. The PCA coefficients and interpretation coefficients of the first two principal components for different measurement modes are shown in **Table 2**. Regardless of the measurement mode, the contribution by the extracted first principal component is significantly greater than the contribution of the second principal component.

As a reference, we also use $S_0$ at four scattering angles in three measurement modes as input for PCA operation. The results are shown in **Figures 3D–F**, which is similar with the sideward and forward scattering intensities measured in [27]. The PCA results using only multi-angle scattering intensity are quite similar under different incident polarization modes. There is not much difference in the relative positions of different samples, and the difference is likely due to the rotation of the coordinate system. So, the intensity of scattered light from multiple angles alone is not enough to distinguish bioaerosols and non-biological origin particles. However, with the help of MAPIS based on linear polarization vector analysis of the detected light, the high discrimination and specific recognition of bioaerosols can be easily realized. By PCA, we can further extract the first principal components as a good indicator specifically for bioaerosols like pollen.

Concretely, for MAPIS under H mode, we can set the position where the first principal component is equal to −0.5 as the discrimination line, and then determine that the measured data whose value range is on the left of this line comes from biological particles. Similarly, for P mode, the discrimination line can be set at the position of the first principal component equal to 0.4, and for R mode, the line can be set at the position of the first principal component equal to 0.25.

The above discrimination basis can be evaluated on 15 measured datasets which is randomly generated. Each dataset contains measured MAPIS data of bioaerosols and non-biological particles mixed with a certain proportion, and the predicted proportions using the above judgment and the comparison with the preset proportion can be shown in **Figure 4**. We preset five particle number contents of biological aerosols in

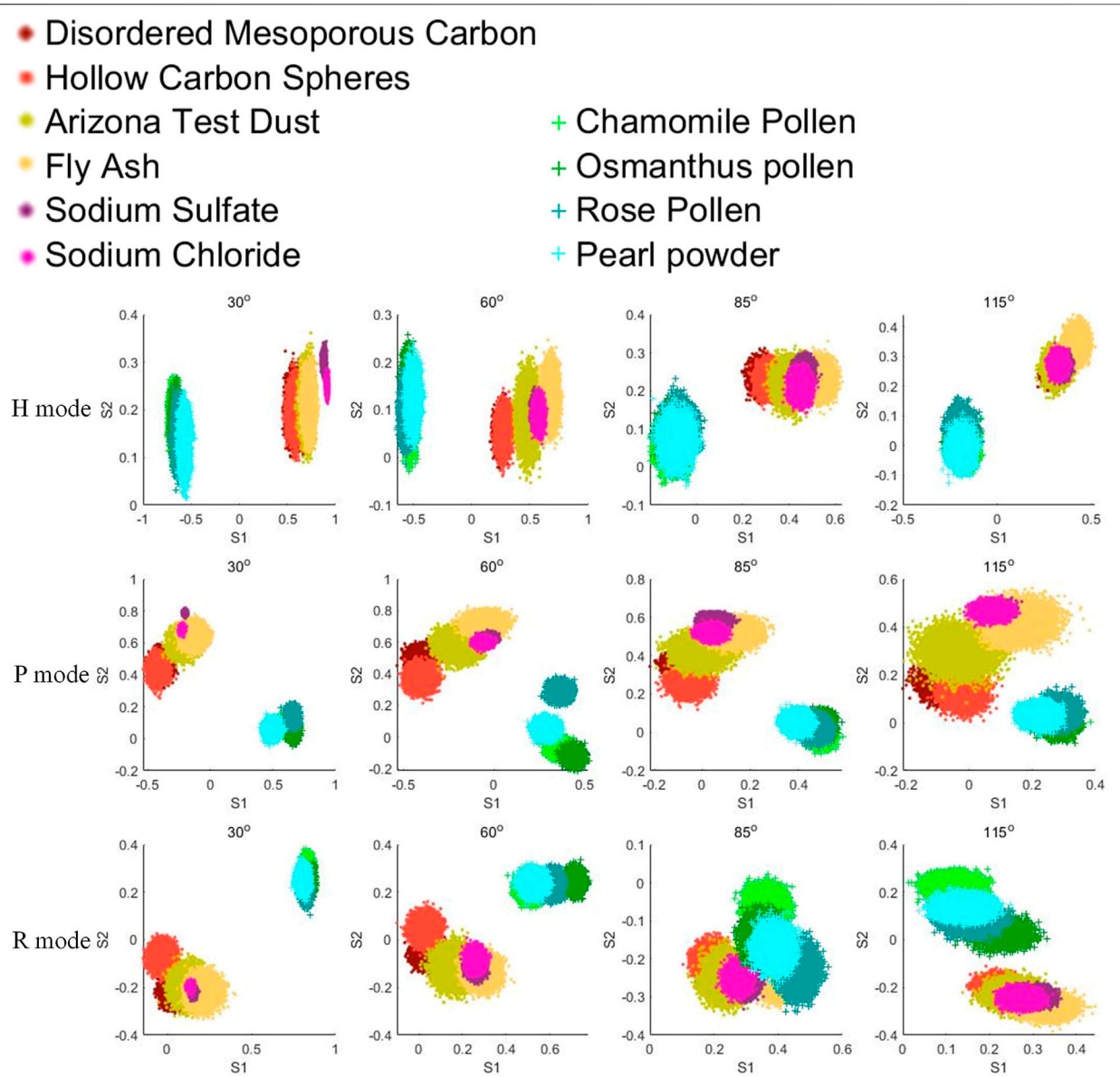


**FIGURE 2 |** Pollen and non-biological samples under the multi-angle polarization index system (MAPIS), 10,000 samples for each type.

the mixed dataset, and then randomly extract data three times for each specified proportion to establish total 15 verification datasets.

For all the 15 datasets, **Figure 4** indicates minor deviations less than 1% between the predicted and true proportion, which further confirms the feasibility of our method to specifically distinguish between bioaerosols and non-biological particles. By an auxiliary observation using a particle size analyzer, there is little difference in the particle size distribution interval of the measured samples. SEM photos of bioaerosols reveal more complex and regular microstructures compared to non-biological particles. So, the polarization optical difference between non-biological particles and bioaerosols may be due to the microstructures combined with the complex refractive index factor. The relevant detailed microphysical interpretation needs to be further studied.

## 3.2 Fine Subclass Recognition of Bioaerosols

Next, the measured MAPIS of the sub-categories of bioaerosols are shown in **Figure 5**. Compared with **Figure 2**, various Stokes elements at different angles and for different incident polarization states have different recognition abilities. Specifically, the polarization indexes in H mode show a weaker discrimination than those in P mode and R mode. Both the forward (30° and 60°) polarized scattering signals in P mode and the backward (85° and 115°) polarized scattering signals in R mode seem to be suitable

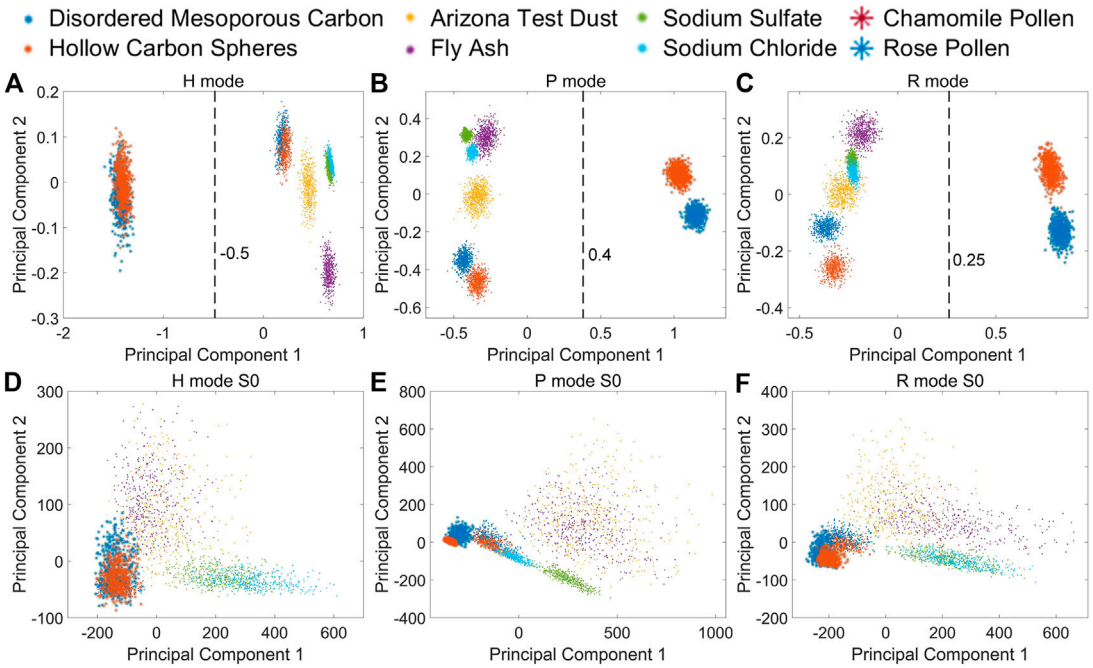


**FIGURE 3 |** Pollen and non-biological samples on PCA first and second principal component. **(A)** MAPIS under H mode; **(B)** MAPIS under P mode; **(C)** MAPIS under R mode. **(D)** $S_0$ at four angles under H mode; **(E)** $S_0$ at four angles under P mode; **(F)** $S_0$ at four angles under R mode.

**TABLE 2 |** Principal component coefficients and interpretation coefficients under different mode for pollen and non-biological samples MAPIS data.

| Mode | PC[a] | 30° $S_1$ | 30° $S_2$ | 60° $S_1$ | 60° $S_2$ | 85° $S_1$ | 85° $S_2$ | 115° $S_1$ | 115° $S_2$ | IC[b] (%) |
|---|---|---|---|---|---|---|---|---|---|---|
| H Mode | PC1 | 0.728 | 0.037 | 0.267 | 0.073 | 0.549 | 0.004 | 0.268 | 0.132 | 97 |
| | PC2 | 0.638 | 0.063 | −0.404 | 0.093 | −0.571 | −0.230 | −0.115 | −0.151 | 1 |
| P Mode | PC1 | 0.612 | −0.337 | 0.306 | −0.306 | 0.377 | −0.330 | 0.362 | −0.206 | 81 |
| | PC2 | 0.306 | 0.383 | 0.187 | 0.347 | 0.465 | 0.402 | 0.209 | 0.424 | 15 |
| R Mode | PC1 | 0.678 | 0.408 | 0.136 | 0.082 | 0.370 | 0.267 | −0.118 | 0.353 | 87 |
| | PC2 | 0.249 | −0.386 | 0.371 | −0.192 | 0.543 | −0.377 | 0.256 | −0.329 | 9 |

[a]*PC, principal component.*
[b]*IC, interpretation coefficients.*

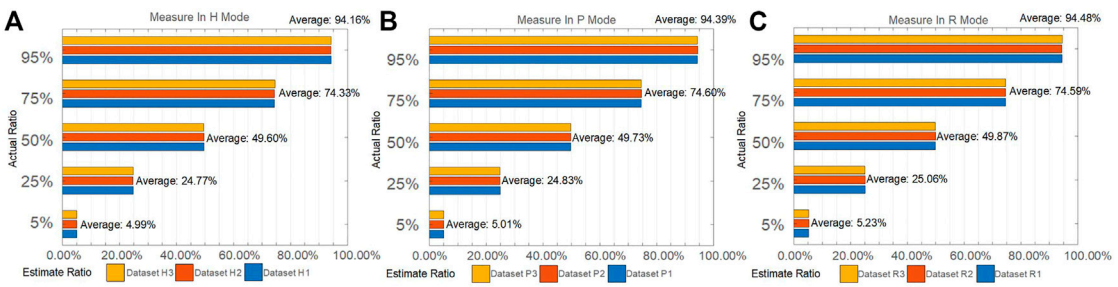


**FIGURE 4 |** True and predicted proportion of pollen using PC1 from MAPIS. **(A)** Measurement conducted in H mode; **(B)** Measurement conducted in P mode; **(C)** Measurement conducted in R mode.

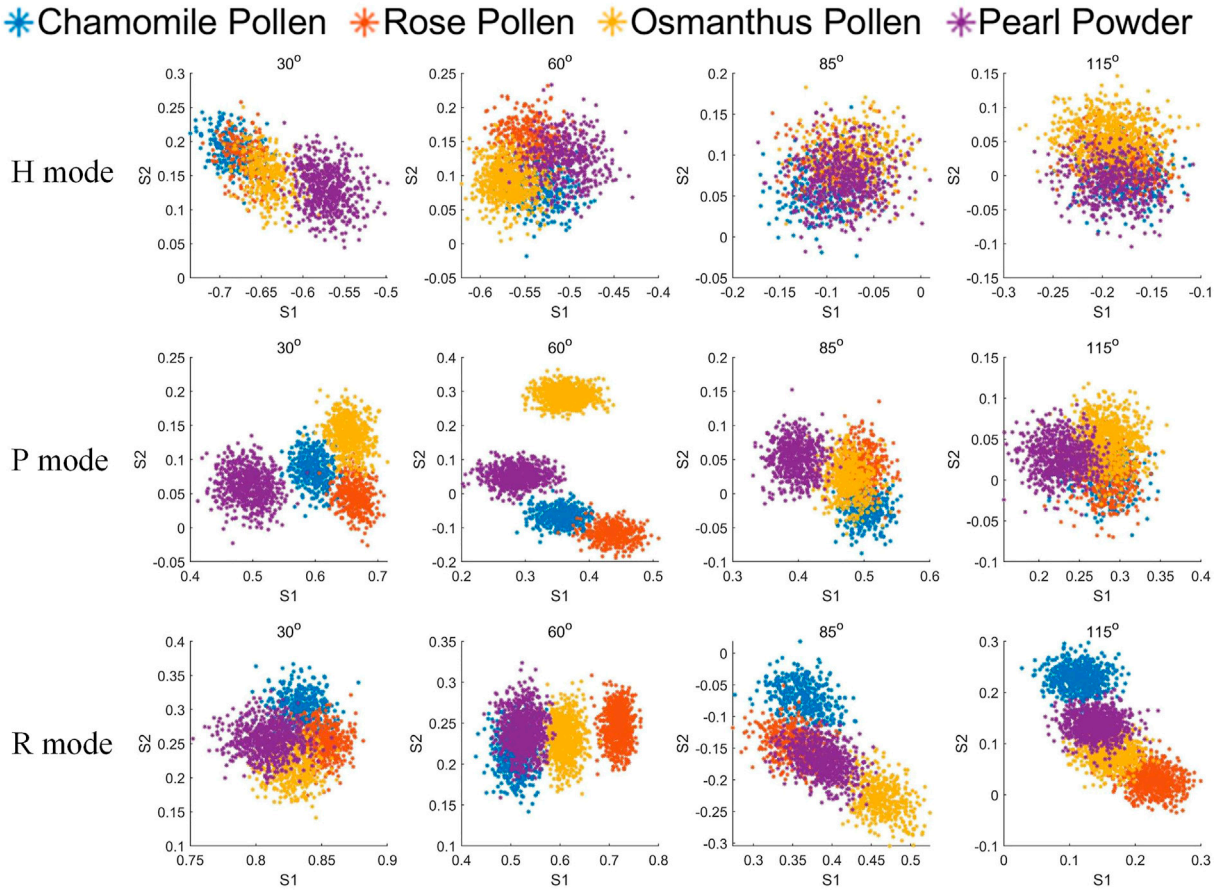


**FIGURE 5 |** Biological samples under the multi-angle polarization index system (MAPIS).

**TABLE 3 |** Principal component coefficients and interpretation coefficients under different mode for biological samples MAPIS data

| Mode | PC[a] | 30° $S_1$ | 30° $S_2$ | 60° $S_1$ | 60° $S_2$ | 85° $S_1$ | 85° $S_2$ | 115° $S_1$ | 115° $S_2$ | IC[b] (%) |
|---|---|---|---|---|---|---|---|---|---|---|
| H Mode | PC1 | 0.526 | −0.409 | 0.049 | −0.177 | 0.572 | 0.127 | 0.034 | −0.420 | 25 |
| | PC2 | −0.345 | 0.532 | −0.281 | −0.307 | 0.286 | −0.154 | 0.289 | −0.484 | 18 |
| P Mode | PC1 | 0.019 | 0.185 | 0.004 | 0.007 | −0.112 | 0.969 | 0.009 | 0.112 | 64 |
| | PC2 | 0.682 | 0.103 | 0.454 | −0.090 | 0.487 | 0.022 | 0.265 | −0.025 | 24 |
| R Mode | PC1 | −0.038 | 0.237 | −0.172 | 0.385 | −0.567 | −0.063 | −0.228 | 0.621 | 60 |
| | PC2 | −0.134 | −0.199 | 0.662 | −0.553 | −0.360 | −0.019 | −0.147 | 0.210 | 24 |

[a]*PC, principal component.*
[b]*IC, interpretation coefficients.*

for the classification and identification of different kinds of biological aerosols.

Similarly, PCA is used to analyze the measured Stokes element $S_1$ and $S_2$ at four angles in each incident polarization mode and extract the optimized polarization characterization expression. The PCA coefficients and interpretation coefficients of the first two principal components in different measurement modes are shown in **Table 3**, and the measured data distribution of different biological particles using the first two principal components is shown in **Figures 6A–C**. It can be seen that four bioaerosols are almost inseparable in H mode but can be clearly distinguished by the principal components in P and R mode. The class separation distances among biological samples using MAPIS in R mode show better discrimination of biological aerosol species than using data in P mode, which implies that particles of biological origin are more sensitive to circularly polarized incident light.

Also, we extract principal components from the scattering intensity $S_0$ at four angles in three measurement modes for comparison, which is shown in **Figures 6D–F**. Similar with the case in **Figures 3D–F**, the PCA results using only multi-

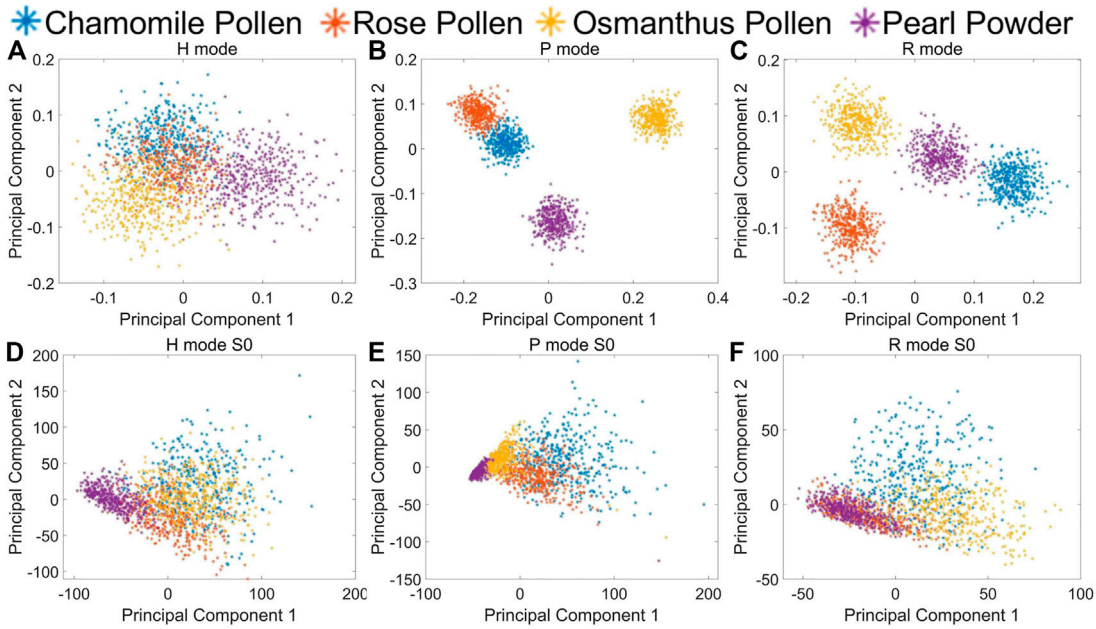


**FIGURE 6 |** Biological samples on PCA first and second principal component. **(A)** MAPIS under H mode; **(B)** MAPIS under P mode; **(C)** MAPIS under R mode. **(D)** $S_0$ at four angles under H mode; **(E)** $S_0$ at four angles under P mode; **(F)** $S_0$ at four angles under R mode.

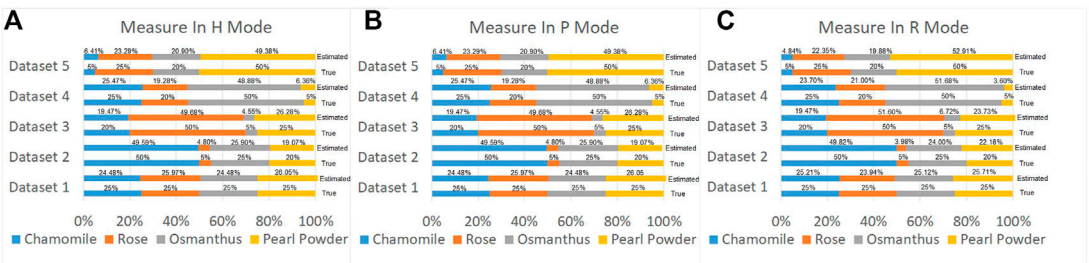


**FIGURE 7 |** True and predicted proportion of biological samples using MAPIS. **(A)** Measurement conducted in H mode; **(B)** Measurement conducted in P mode; **(C)** Measurement conducted in R mode.

angle scattering intensity cannot distinguish different kinds of bioaerosols. There is not much difference in the relative positions of the measured data.

Then, we used a verification method similar to that in **Section 3.1**; we constructed five measured datasets of four biological aerosols mixed with different ratios. Based on the statistical distribution on the first principal component for each incident polarization mode, we can predict the proportion of different kinds of bioaerosols and compare them with the preset ratios. The number of aerosol class measured is $k$; $x_n$ is the probability density curve of the $n$th aerosol sample on the first principal component. $y$ is the measured probability density curve on the first principal component for a mixture of these $k$ kinds of aerosols, where $y$ and $x_n$ are vectors. If $\alpha_n$ is the estimated proportion of the $n$th aerosol class, we multiply and sum the probability density curve for polarization parameters of different kinds of bioaerosols by their proportions, then by fitting the probability density curve based on the estimated mixing ratio of different aerosol class with the real $y$ based on randomly sampled measured datasets. By least square method in **Eq. 1**, the optimal solution of proportions could be found out, as shown in **Figure 7**.

$$arg\ min \left\| y - \sum_{n=1}^{k} (a_n * x_n) \right\|_2 \tag{3}$$

By observing the classification results based on the measured biological aerosol datasets with five different mixture ratios, using MAPIS measured in P and R mode, the identification error of the first principal component is less than 3% for all the datasets. Compared with other abiotic types, the differences of polarization parameters among various bioaerosols are not so big. However, with the help of PCA, different measured Stokes indexes can be combined to form an optimized parameter with a sufficient discrimination suitable for bioaerosol classification.

## 4 CONCLUSION

In this paper, we investigate the characterization ability of the multi-angle polarization index system (MAPIS) for bioaerosols (especially pollen). Stokes vectors S1 and S2 of 10 kinds of aerosol samples are measured at four scattering angles under three incident polarization states. The types of samples can be divided into four major categories, namely, dust, water-soluble salts, carbon, and bioaerosols. Among them, the first three types belong to non-biological particles, and each of them contains two subclass samples. There are four kinds of bioaerosols, mainly pollens.

Experiment results show that, regardless of the polarization state of the incident light, non-biological particles and bioaerosols can be clearly differentiated based on the measured MAPIS. Moreover, when the incident light is 45° linear polarized or circular polarized, we can also subdivide the kind of bioaerosols according to the data distribution of MAPIS. By comparison with the measured data of multi-angle scattering intensity, the scattering signals without polarization analysis are not sufficient to determine whether the particulate matter is of biological origin or distinguish the sub-categories of bioaerosols. To simplify the multidimensional characterization parameters of MAPIS, the first two principal components extracted by a PCA analysis of all 10 kinds of sample data can be used as specific indicators of bioaerosols. Also, another PCA analysis of four kinds of biological sample data can confirm the feasibility of its first principal component to predict the particle proportion of mixed bioaerosol samples.

To fully obtain and understand the polarization scattering response from more types of biological aerosols, we still have a lot of follow-up work to promote. The limitations of biological aerosol samples in this paper will affect the universality of specific indicators of polarization characterization and related errors. However, the research of this paper still shows the potentials of the synchronous polarization analysis at multi scattering angles. Taking pollen as an example, the microphysical differences between real biological aerosols and abiotic aerosols are difficult to be simply attributed to size or composition factors. Based on the measured MAPIS and the information extraction by machine learning, the accurate discrimination and fine classification of biological aerosols like pollen are feasible in on-line high-throughput measurements. The above studies demonstrate the characterization ability of the multi-angle polarization index system (MAPIS) for *in situ* fast identification of bioaerosols from other non-biological particles. Also, we can subdivide different biological particles based on measured MAPIS of various aerosol samples. PCA analysis can help us extract one or two optimized polarization indexes based on the combination of multiple Stokes vector elements, according to different characterization needs for bioaerosols. Using the first principal component respectively from ten kinds of sample data and four kinds of biological sample data, the specific recognition error of biological type aerosols is no more than 1%, and the discrimination error of different bioaerosols is less than 3%. Our preliminary study lays a solid foundation to further apply polarization technology and method to analyze more important aerosols such as bacteria and virus particles.

## DATA AVAILABILITY STATEMENT

The raw data supporting the conclusion of this article will be made available by the authors, without undue reservation.

## AUTHOR CONTRIBUTIONS

NZ and QX conceived the idea of the manuscript. QX and WG prepare the samples and performed the experiments. QX wrote the original manuscript and analyzed the results. NZ, JG, YH, and HM performed the language editing. All authors have given approval to the final version of the manuscript.

## FUNDING

This work is supported by the National Key Program of Science and Technology Supporting Economy of China (2020YFF01014500ZL); Science and Technology Research Program of Shenzhen Grant (JCYJ20200109142820687).

## REFERENCES

1. Douwes J, Thorne P, Pearce N, Heederik D. Bioaerosol Health Effects and Exposure Assessment: Progress and Prospects. *Ann Occup Hyg* (2003) 47(3): 187–200. doi:10.1093/annhyg/meg032
2. Miaomiao T, Fangxia S, Maosheng Y, Tong Z. Development of an Automated Electrostatic Sampler (AES) for Bioaerosol Detection. *Aerosol Sci Tech* (2011) 45(9):1154–60. doi:10.1080/02786826.2011.582193
3. Pöhlker C, Huffman JA, Förster J-D, Pöschl U. Autofluorescence of Atmospheric Bioaerosols: Spectral Fingerprints and Taxonomic Trends of Pollen. *Atmos Meas Tech* (2013) 6:3369–92. doi:10.5194/amt-6-3369-2013
4. King MD, Lacey RE, Pak H, Fearing A, Ramos G, Baig T, et al. Assays and Enumeration of Bioaerosols-Traditional Approaches to Modern Practices. *Aerosol Sci Tech* (2020) 54:611–33. doi:10.1080/02786826.2020.1723789
5. Taketomi EA, Sopelete MC, de Sousa Moreira PF, de Assis Machado Vieira F. Pollen Allergic Disease: Pollens and its Major Allergens. *Braz J Otorhinolaryngol* (2006) 72:562–7. doi:10.1016/S1808-8694(15)31005-3
6. Weber RW, Adkinson N, Jr, Bochner B, Burks A, Busse W, Holgate S, et al. *Middleton's Allergy: Principles and Practice*. Elsevier Health Sciences (2013). p. 430.
7. Bousquet J, Khaltaev N, Cruz AA, Denburg J, Fokkens WJ, Togias A, et al. Allergic Rhinitis and its Impact on Asthma (ARIA) 2008 Update (In Collaboration with the World Health Organization, GA(2)LEN and AllerGen). *Allergy* (2008) 63:8–160. doi:10.1111/j.1398-9995.2007.01620.x
8. Behrendt H, Becker W-M. Localization, Release and Bioavailability of Pollen Allergens: the Influence of Environmental Factors. *Curr Opin Immunol* (2001) 13:709–15. doi:10.1016/S0952-7915(01)00283-7
9. Beggs PJ. Impacts of Climate Change on Aeroallergens: Past and Future. *Clin Exp Allergy* (2004) 34:1507–13. doi:10.1111/j.1365-2222.2004.02061.x

10. D'amato G, Cecchi L. Effects of Climate Change on Environmental Factors in Respiratory Allergic Diseases. *Clin Exp Allergy* (2008) 38:1264–74. doi:10.1111/j.1365-2222.2008.03033.x
11. Shea KM, Truckner RT, Weber RW, Peden DB. Climate Change and Allergic Disease. *J Allergy Clin Immunol* (2008) 122:443–53. doi:10.1016/j.jaci.2008.06.032
12. Schmidt CW. Pollen Overload: Seasonal Allergies in a Changing Climate. *Environ Health Perspect* (2016) 124:A70–5. doi:10.1289/ehp.124-A70
13. Steiner AL, Brooks SD, Deng C, Thornton DCO, Pendleton MW, Bryant V. Pollen as Atmospheric Cloud Condensation Nuclei. *Geophys Res Lett* (2015) 42:3596–602. doi:10.1002/2015GL064060
14. Walser SM, Gerstner DG, Brenner B, Bünger J, Eikmann T, Janssen B, et al. Evaluation of Exposure-Response Relationships for Health Effects of Microbial Bioaerosols - A Systematic Review. *Int J Hyg Environ Health* (2015) 218:577–89. doi:10.1016/j.ijheh.2015.07.004
15. Dong L, Qi J, Shao C, Zhong X, Gao D, Cao W, et al. Concentration and Size Distribution of Total Airborne Microbes in Hazy and Foggy Weather. *Sci Total Environ* (2016) 541:1011–8. doi:10.1016/j.scitotenv.2015.10.001
16. Perrino C, Marcovecchio F. A New Method for Assessing the Contribution of Primary Biological Atmospheric Particles to the Mass Concentration of the Atmospheric Aerosol. *Environ Int* (2016) 87:108–15. doi:10.1016/j.envint.2015.11.015
17. Schrank E. Scanning Electron and Light Microscopic Investigations of Angiosperm Pollen from the Lower Cretaceous of Egypt. *Pollen et Spores* (1983) 25:213–42.
18. Behnke H-D. Transmission Electron Microscopy and Systematics of Flowering Plants. In: *Flowering Plants. Springer* (1977). p. 155–78. doi:10.1007/978-3-7091-7076-2_11
19. Wang S, Wang D, Wu Q, Gao K, Wang Z, Wu Z. 3D Imaging of a rice Pollen Grain Using Transmission X-ray Microscopy. *J Synchrotron Radiat* (2015) 22:1091–5. doi:10.1107/S1600577515009716
20. Chen L-WA, Zhang M, Liu T, Fortier K, Chow JC, Alonzo F, et al. Evaluation of Epifluorescence Methods for Quantifying Bioaerosols in fine and Coarse Particulate Air Pollution. *Atmos Environ* (2019) 213:620–8. doi:10.1016/j.atmosenv.2019.05.051
21. Park C, Lee S, Kim G, Lee S, Lee J, Heo T, et al. Three-dimensional Refractive-index Distributions of Individual Angiosperm Pollen Grains. *Curr Opt Photon* (2018) 2:460–7. doi:10.3807/COPP.2018.2.5.460
22. Shang X, Giannakaki E, Bohlmann S, Filioglou M, Saarto A, Ruuskanen A, et al. Optical Characterization of Pure Pollen Types Using a Multi-Wavelength Raman Polarization Lidar. *Atmos Chem Phys* (2020) 20:15323–39. doi:10.5194/acp-20-15323-2020
23. Swanson BE, Huffman JA. Pollen Clustering Strategies Using a Newly Developed Single-Particle Fluorescence Spectrometer. *Aerosol Sci Tech* (2020) 54:426–45. doi:10.1080/02786826.2019.1711357
24. Huffman JA, Perring AE, Savage NJ, Clot B, Crouzy B, Tummon F, et al. Real-time Sensing of Bioaerosols: Review and Current Perspectives. *Aerosol Sci Tech* (2020) 54:465–95. doi:10.1080/02786826.2019.1664724
25. Wu Y, Calis A, Luo Y, Chen C, Lutton M, Rivenson Y, et al. Label-free Bioaerosol Sensing Using mobile Microscopy and Deep Learning. *ACS Photon* (2018) 5:4617–27. doi:10.1021/acsphotonics.8b01109
26. Mitsumoto K, Yabusaki K, Kobayashi K, Aoyagi H. Development of a Novel Real-Time Pollen-Sorting Counter Using Species-specific Pollen Autofluorescence. *Aerobiologia* (2010) 26:99–111. doi:10.1007/s10453-009-9147-1
27. Kawashima S, Thibaudon M, Matsuda S, Fujita T, Lemonis N, Clot B, et al. Automated Pollen Monitoring System Using Laser Optics for Observing Seasonal Changes in the Concentration of Total Airborne Pollen. *Aerobiologia* (2017) 33:351–62. doi:10.1007/s10453-017-9474-6
28. Cholleton D, Bialic E, Dumas A, Kaluzny P, Rairoux P, Miffre A. Laboratory Evaluation of the (VIS, IR) Scattering Matrix of Complex-Shaped Ragweed Pollen Particles. *J Quant Spectrosc Radiat Transf* (2020) 254:107223–9. doi:10.1016/j.jqsrt.2020.107223
29. Noh YM, Müller D, Lee H, Choi TJ. Influence of Biogenic Pollen on Optical Properties of Atmospheric Aerosols Observed by Lidar over Gwangju, South Korea. *Atmos Environ* (2013) 69:139–47. doi:10.1016/j.atmosenv.2012.12.018
30. Cao X, Roy GA, Bernier R. Lidar Polarization Discrimination of Bioaerosols. *Opt Eng* (2010) 49:116201. doi:10.1117/1.350587710.1117/12.849649
31. Noh YM, Müller D, Lee H, Choi TJ. Influence of Biogenic Pollen on Optical Properties of Atmospheric Aerosols Observed by Lidar over Gwangju, South Korea. *Atmos Environ* (2013) 69:139–47. doi:10.1016/j.atmosenv.2012.12.018
32. Sassen K. Boreal Tree Pollen Sensed by Polarization Lidar: Depolarizing Biogenic Chaff. *Geophys Res Lett* (2008) 35:1–4. doi:10.1029/2008GL035085
33. Sicard M, Izquierdo R, Alarcón M, Belmonte J, Comerón A, Baldasano JM. Near-surface and Columnar Measurements with a Micro Pulse Lidar of Atmospheric Pollen in Barcelona, Spain. *Atmos Chem Phys* (2016) 16:6805–21. doi:10.5194/acp-16-6805-2016
34. Li D, Chen F, Zeng N, Qiu Z, He H, He Y, et al. Study on Polarization Scattering Applied in Aerosol Recognition in the Air. *Opt Express* (2019) 27:A581–A595. doi:10.1364/OE.27.00A581
35. Li D, Zeng N, Zhan D, Chen Y, Zeng M, Ma H. Differentiation of Soot Particulates in Air Using Polarized Light Scattering Method. *Appl Opt* (2017) 56:4123–9. doi:10.1364/AO.56.004123
36. Chen Y, Zeng N, Chen S, Zhan D, He Y, Ma H. Study on Morphological Analysis of Suspended Particles Using Single Angle Polarization Scattering Measurements. *J Quantitative Spectrosc Radiative Transfer* (2019) 224:556–65. doi:10.1016/j.jqsrt.2018.12.006
37. Liao R, Zeng N, Zeng M, He Y, Ma H. Estimation and Extraction of the Aerosol Complex Refractive index Based on Stokes Vector Measurements. *Opt Lett* (2019) 44:4877–80. doi:10.1364/OL.44.004877
38. Liao R, Guo W, Zeng N, Guo J, He Y, Di H, et al. Polarization Measurements and Evaluation Based on Multidimensional Polarization Indices Applied in Analyzing Atmospheric Particulates. *Appl Sci* (2021) 11:5992. doi:10.3390/app11135992
39. Stanski C, Moro RSS, Nogueira MKF, Kuniyoshi YS, da Luz CFP. Palynology of Species of Anthemideae, Eupatorieae, Inuleae, Mutiseae and Senecianeae Tribes Occurring in the Region of Campos Gerais, Paraná State, Brazil. *Iheringia Ser Bot* (2018) 73:353–62. doi:10.21826/2446-8231201873312
40. Singh K, Sharma YP, Sharma PR, Gairola S. Pollen Morphology and Variability of the Rosa L. Species of Western Himalaya in India. *Genet Resour Crop Evol* (2020) 67:2129–48. doi:10.1007/s10722-020-00967-8
41. Duan Y, Li W, Zheng S, Sylvester SP, Li Y, Cai F, et al. Functional Androdioecy in the Ornamental Shrub Osmanthus Delavayi (Oleaceae). *Plos One* (2019) 14:e0221898. doi:10.1371/journal.pone.0221898
42. Yu ZR, Wang XD, Su BM, Zhang Y. First Evidence of the Use of Freshwater Pearls as a Cosmetic in Ancient China: Analysis of white Makeup Powder from a Northern Song Dynasty Lv Tomb (Lantian, Shaanxi Province, China). *Archaeometry* (2017) 59:762–74. doi:10.1111/arcm.12268
43. Chen X, Peng L-H, Chee S-S, Shan Y-H, Liang W-Q, Gao J-Q. Nanoscaled Pearl Powder Accelerates Wound Repair and Regeneration *In Vitro* and *In Vivo*. *Drug Dev Ind Pharm* (2019) 45:1009–16. doi:10.1080/03639045.2019.1593436
44. Dai J, Yang S, Jin J, Li G. Electrospinning of PLA/pearl Powder Nanofibrous Scaffold for Bone Tissue Engineering. *RSC Adv* (2016) 6:106798–805. doi:10.1039/C6RA21796F
45. Guo W, Zeng N, Liao R, Xu Q, Guo J, He Y, et al. Simultaneous Retrieval of Aerosol Size and Composition by Multi-Angle Polarization Scattering Measurements. *Opt Lasers Eng* (2022) 149:106799. doi:10.1016/j.optlaseng.2021.106799
46. Wold S, Esbensen K, Geladi P. Principal Component Analysis. *Chemometrics Intell Lab Syst* (1987) 2:37–52. doi:10.1016/0169-7439(87)80084-9
47. Fletcher R, Bright D. Shape Factors of ISO 12103-A3 (Medium Test Dust). *Filtration + Sep* (2000) 37:48–56. doi:10.1016/S0015-1882(00)80200-1
48. Groundwater H, Twardowski MS, Dierssen HM, Sciandra A, Freeman SA. Determining Size Distributions and Composition of Particles Suspended in Water: A New SEM-EDS Protocol with Validation and Comparison to Other Methods. *J Atmos Oceanic Tech* (2012) 29:433–49. doi:10.1175/JTECH-D-11-00026.1
49. Keskinen H, Kortelainen A-M, Jaatinen A, Yli-Pirilä P, Joutsensaari J, Romakkaniemi S, et al. Increased Hygroscopicity of Arizona Test Dust Seeds by Secondary Organic Aerosol Coating from α-pinene Ozonolysis. *Boreal Environ Res* (2014) 19:182–90.
50. Chen H, Laskin A, Baltrusaitis J, Gorski CA, Scherer MM, Grassian VH. Coal Fly Ash as a Source of Iron in Atmospheric Dust. *Environ Sci Technol* (2012) 46:2112–20. doi:10.1021/es204102f

51. Wang S, Baxter L, Fonseca F. Biomass Fly Ash in concrete: SEM, EDX and ESEM Analysis. *Fuel* (2008) 87:372–9. doi:10.1016/j.fuel.2007.05.024
52. Chuan Z, Ji-Tong W, Xu L, Dong-Hui L, Wen-Ming Q, Li-Cheng L. Facile Preparation, Structural Control and Spheroidization of Mesoporous Carbons Using Hydrolyzed Water Glass as a Template. *J Inorg Mater* (2015) 30:848–54. doi:10.15541/jim20150036
53. Li S, Pasc A, Fierro V, Celzard A. Hollow Carbon Spheres, Synthesis and Applications - a Review. *J Mater Chem A* (2016) 4:12686–713. doi:10.1039/C6TA03802F
54. Yuan C, Liu X, Jia M, Luo Z, Yao J. Facile Preparation of N- and O-Doped Hollow Carbon Spheres Derived from Poly(o-Phenylenediamine) for Supercapacitors. *J Mater Chem A* (2015) 3:3409–15. doi:10.1039/C4TA06411A
55. Yang Q. Pollen Morphology of Osmanthus Decorus and O.× Burkwoodii. *J Hubei Univ Nationalities-Natural Sci Edition* (2010) 28:286–8.
56. Kandler K, Benker N, Bundke U, Cuevas E, Ebert M, Knippertz P, et al. Chemical Composition and Complex Refractive index of Saharan Mineral Dust at Izaña, Tenerife (Spain) Derived by Electron Microscopy. *Atmos Environ* (2007) 41:8058–74. doi:10.1016/j.atmosenv.2007.06.047
57. Wyatt PJ. Some Chemical, Physical, and Optical Properties of Fly Ash Particles. *Appl Opt* (1980) 19:975–83. doi:10.1364/AO.19.000975
58. Tang IN. Chemical and Size Effects of Hygroscopic Aerosols on Light Scattering Coefficients. *J Geophys Res* (1996) 101:19245–50. doi:10.1029/96JD03003
59. Li HH. Refractive index of Alkali Halides and its Wavelength and Temperature Derivatives. *J Phys Chem reference Data* (1976) 5:329–528. doi:10.1063/1.555536

**Conflict of Interest:** The authors declare that the research was conducted in the absence of any commercial or financial relationships that could be construed as a potential conflict of interest.

The handling editor declared a past co-authorship with one of the authors HM.

**Publisher's Note:** All claims expressed in this article are solely those of the authors and do not necessarily represent those of their affiliated organizations, or those of the publisher, the editors, and the reviewers. Any product that may be evaluated in this article, or claim that may be made by its manufacturer, is not guaranteed or endorsed by the publisher.

frontiers in Physics

ORIGINAL RESEARCH
published: 31 March 2022
doi: 10.3389/fphy.2022.813634

# Polarization Reconstruction Algorithm of Target Based on the Analysis of Noise in Complex Underwater Environment

*Qiang Song*[1,2,3], *Xiao Liu*[1,3,4], *Honglian Huang*[1,3,4], *Rufang Ti*[1,3] *and Xiaobing Sun*[1,3,4]*

[1]Anhui Institute of Optics and Fine Mechanics, Hefei Institutes of Physical Science, Chinese Academy of Sciences, Anhui Hefei, China, [2]University of Science and Technology of China, Anhui Hefei, China, [3]Key Laboratory of Optical Calibration and Characterization, Chinese Academy of Sciences, Anhui Hefei, China, [4]Hefei Chief Expert Studio of Agricultural Industry, Anhui Hefei, China

How to effectively eliminate interference such as scattering, absorption, and attenuation is a hot topic of underwater photoelectric detection at present. Around the hot issues, this paper carries out studying the method of polarization-imaging recovery in a dynamic complex underwater environment from the theory of underwater radiation transfer, and numerical simulation of imaging interference characteristics to the simulation of underwater environment experiment. First, by conducting the analysis and simulation of scattering characteristics of underwater suspension particles and bubble by using the theory of radiation transfer, and taking advantage of quantitative description on changing tendency of radiation intensity and polarization properties of light waves in turbid water under the condition of scattering interference. Second, by constructing an underwater target polarization reconstruction model on the basis of the Mueller matrix analysis, and taking target polarization characteristic into reconstruction model on the basis of classical Schechner's model, automatically estimating polarization information of target by the method of covariance. Finally, by building a polarization imaging system in the simulated complex underwater environment that contains bubble and suspended particles, obtaining reconstructed results with different underwater environments and different materials of target. According to experiment results, and compared with other traditional methods, using the proposed method in this paper can get higher resolution and higher contrast of target in the reconstructed result.

**Keywords: underwater transmission rate, polarization filtering, target polarization information, image reconstruction, imaging waveband**

OPEN ACCESS

***Edited by:***
*Haofeng Hu,*
*Tianjin University, China*

***Reviewed by:***
*Xiaobo LI,*
*Tianjin University, China*
*Zhongyi Guo,*
*Hefei University of Technology, China*

***Correspondence:**
*Xiaobing Sun*
*xbsun@aiofm.ac.cn*

***Specialty section:***
*This article was submitted to "Optics and Photonics", a section of the journal Frontiers in Physics*

***Received:*** *12 November 2021*
***Accepted:*** *25 January 2022*
***Published:*** *31 March 2022*

***Citation:***
*Song Q, Liu X, Huang H, Ti R and Sun X (2022) Polarization Reconstruction Algorithm of Target Based on the Analysis of Noise in Complex Underwater Environment. Front. Phys. 10:813634. doi: 10.3389/fphy.2022.813634*

## INTRODUCTION

Underwater optical imaging plays a very important application value and scientific research significance in the field of marine engineering, including marine biological monitoring, ecosystem assessment, marine rescue, navigation, etc. Compared with atmospheric optical imaging, due to water environment being relatively complex, all kinds of suspension medium in water to light scattering effect will seriously affect the imaging quality, the forward scattering noise can reduce imaging resolution, and the backward scattering noise leads to decrease of imaging

contrast [1] The research of underwater imaging technology will focus on taking efforts to reduce influence of optical transmission energy absorption and attenuation on underwater communications and target detection, and prevent the strong scattering effect produced by water. Because target features characterized by polarization information are less affected by water attenuation in the process of underwater transmission, and the polarization characteristics of underwater targets and the surrounding environment have differences, obtaining two orthogonal intensity images in same scenario and using polarization difference imaging method can enhance contrast and resolution of image and weaken the influence of scattering light on target imaging [2]. At present, polarization imaging technology has been widely used in underwater target imaging [2–4] and biomedical imaging [5]. Schechner [6] has proposed a polarization difference reconstruction method where the algorithm has several advantages such as a simple reconstruction model and low computational complexity, providing important reference value on exploration of underwater polarization-imaging. Tali Treibitz [7] has used formulas to take the separation of target information and background information, then polarization information of the target is added into the reconstruction model, he then takes a brief analysis on the forward scattering effect of water body, and the reconstructed results are ideal. Huang [8] has considered target and background light polarization information at the same time in the process of model derivation, and taken correction on three parameters in the model step by step in order to get optimal parameters and achieve the best results of image restoration. Feng [9] has put forward a kind of polarization reconstruction algorithm that estimates degree of polarization (DOP) of global backward scattering light, according to Schechner's model and definition of DOP, the DOP of reflected light of target have been considered in the model, and have realized clear imaging of underwater target with high DOP. Liu [10] has achieved good results through underwater experiments by using large aperture imaging system for obtaining light-field information with a wide angle and accurately estimating the parameter values that reflect characteristics of a global scene through integration of scene depth information. Tian [11] has combined synthetic aperture imaging with polarimetric imaging and proposed a method for retrieving the radiation of an object based on the degree of polarization and intensity of backward scattering at the multi-view image. AMER [12] has used a polarimetric imaging optical system to reduce the effect of diffusion on the image acquisition and has received a great deal of attention for image dehazing based on an optimized version of the dark channel prior (DCP) method.

Through theoretical analysis and formula derivation, this paper has used expressions to represent reflected light information of target and scattering light information of background respectively, estimated intensity of scattering light and the transmission coefficient, optimized expression of underwater transmission rate, and used a step by step searching method for optimal estimation of polarization information to underwater target, achieved the purpose that the suppressing effect of scattering light on imaging and improved the quality of images. In part 2, this paper takes the mathematical deduction and numerical analysis on backward scattering noise and forward scattering noise and in part 3, describes the basic theory of underwater imaging and the establishment process of a reconstruction model that considers polarization information of underwater target on the analysis of Mueller matrix, and estimates reconstruction parameters. Part 4, builds experiment platform of target polarization-imaging in a complex underwater environment. Part 5, explores the feasibility and validity of the proposed method in this paper by using actively imaging experiments with linear polarized light, which provides theoretical verification for future practical methods of application.

# QUANTITATIVE ANALYSIS OF SCATTERING NOISE AFFECTING TARGET IMAGING IN UNDERWATER ENVIRONMENT

## Scattering Noise in Underwater Environment and Classification

In a real environment, water is a very complex mixed medium, which contains water molecules, suspended particles, microorganisms, and its physical properties are related to geography, climate and environment. The inhomogeneity of water lets light waves be affected by absorption and scattering in the transmission, and the attenuation has serious influence on the transmission distance and signal-to-noise ratio. In order to simplify the research situation, the media in the water body can be divided into two kinds of situations: suspended medium and rising air bubble, as shown in **Figure 1**. Water scattering is the phenomenon of taking migration of motion path of photons due to particle collision, and the scattering effect can make the decrease of strength of the signal at the receiving end, and can cause intersymbol interference. The suspended medium in the water and bubble are often the important factor in the production of scattering phenomenon. These two kinds of influence factors of scattering will be shown in the detailed analysis below.

## The Quantitative Simulation Analysis on Scattering Noise Caused by Suspension Medium

In the process of target imaging using active light in an underwater environment, assuming that there exists a small scattering volume element $dv$ in imaging system field, the distance to target of light source and imaging system are $l$ and $l^{'}$ respectively, and the distance of light source and imaging system is $r$, and $l >> r$, $l \approx l^{'}$, and output power of light source is set to $P_0$. In order to quantitatively evaluate the noise of an underwater environment, this article will use the method of distance-gate to take mathematical derivation and simulation analysis on backward scattering noise and forward scattering noise respectively, in an underwater environment. In the procession map of underwater target imaging in a backward

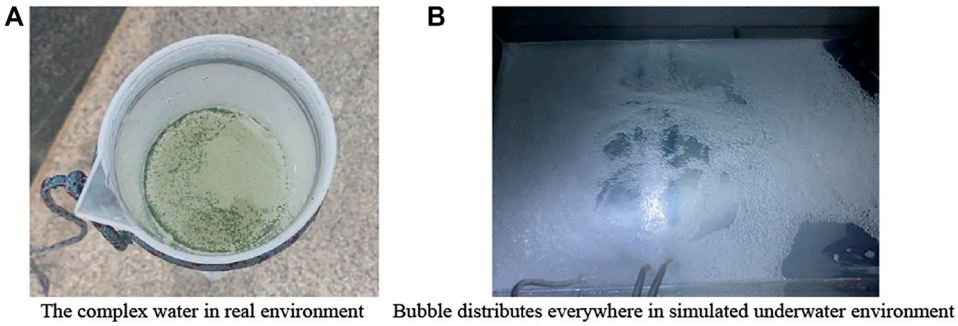


**FIGURE 1 |** Coexistence of suspended medium and rising air bubbles in underwater environment. **(A)** The complex water in real environment **(B)** Bubble distributes everywhere in simulated underwater environment.

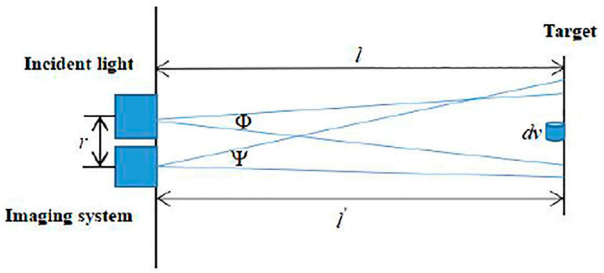


**FIGURE 2 |** The schematic diagram of backward scattering to underwater particles.

scattering environment as shown in **Figure 2**, $\Phi$ represents emission angles of light source, and $\Psi$ represents receiving angle of imaging receiver. Assuming that light shows uniform distribution in emission angle $\Phi$, irradiance $E(l)$ of scattering volume element $dv$[13] is expressed as:

$$E(l) = \frac{\delta_l}{\pi(l\tan\Phi)^2}P_0 \qquad (2-1)$$

with $\delta_l = e^{-kl}$ represents photon loss of one-way transmission in water, $k$ is overall attenuation coefficient, l represents transmission distance of photon.

The radiation intensity of the incident light source at site of scattering volume element $dv$ and direction of divergence angle $\Theta$ can be expressed as:

$$dI = E(l)\beta(\Theta)dv = \frac{\delta_l\beta(\Theta)}{\pi(l\tan\Phi)^2}P_0 dv \qquad (2-2)$$

The volume scattering function is expressed as $\beta(\Theta)$, setting approximation $\Theta = \pi$ under condition of backward scattering. Definition of efficiency of imaging optical system is $T_{oe}$, objective aperture of imaging system is $D$, solid angle surrounded by objective with scattering volume element is $\pi D^2/4l^2$. Under the condition of no gating, surrounded space of original location to transmission distance $l$ that incident light transmits in water are represented as integral area $V_1$, thus setting backward scattering power obtained by imaging system is [14] $P_b = T_{oe}\int\frac{\pi D^2}{4l^2}\delta_l dI = T_{oe}\int_0^l\frac{\pi\delta_l^2 D^2\beta(\pi)}{4l^2}P_0 f_b dv$, with $f_b$ represents backward scattering interception factor, when field $\Psi$ of imaging system is greater than divergence angle $\Phi$ of incident light beam, setting $f_b = 1$. Under the condition of gating, surrounded space from transmission distance $l$ to transmission distance $l + uT$ of incident light are represented as integral area $V_2$. When gating time $T$ is very small, and integral area $V_2$ is a small cylinder contained inside beam divergence angle, expression of $P_b$ can be changed into follow formula [14]:

$$P_b = T_{oe}\int_l^{l+uT}\frac{\pi\delta_l^2 D^2\beta(\pi)}{4l^2}P_0 f_b dv \approx \frac{\pi T_{oe}\delta_l^2 D^2\beta(\pi)}{4l^2}uTf_b P_0 \qquad (2-3)$$

Setting $P_r$ as power of reflected light to target received by underwater imaging system [13], and is expressed as $P_r = \rho_m T_{oe}\delta_l^2 H_o(\Phi,\Psi,A_P)D^2P_0/4l^2$, with $\rho_m$ represents reflectivity of underwater target, $H_o(\Phi,\Psi,A_p)$ is expressed as intercept factor of receiving power of imaging system that is codetermined by viewing angle $\Psi$, divergence angle $\Phi$ and projection area $A_p$ of underwater target with imaging system, and is simplified as $H_o$. In order to qualitatively study influence of backward scattering on underwater target imaging, effect coefficient of backward scattering of underwater imaging is defined as power ratio $\eta_b = P_r/P_b$. Effect coefficient of backward scattering can be defined as follows:

$$\eta_b = \frac{\rho_m}{\pi uT\beta(\pi)f_b}H_o \qquad (2-4)$$

The mathematical analysis and simulation calculation on power of backward scattering $P_b$ and effect coefficient of backward scattering $\eta_b$ can analyze the scope of influence of noise to backward scattering on target imaging in an underwater environment [13]. Taking related parameters of model in process of simulation according to actual situations, underwater transmission distance of light are separately set for $l$ = 1.0 m, $l$ = 1.5 m, $l$ = 2.0 m, $l$ = 3.0 m and setting $P_0$ = 1 MW as initial incident power. Depending on **Equations (2-3)** and **Equation (2-4)** can obtain the change trend about power of backward scattering and effect coefficient of backward scattering

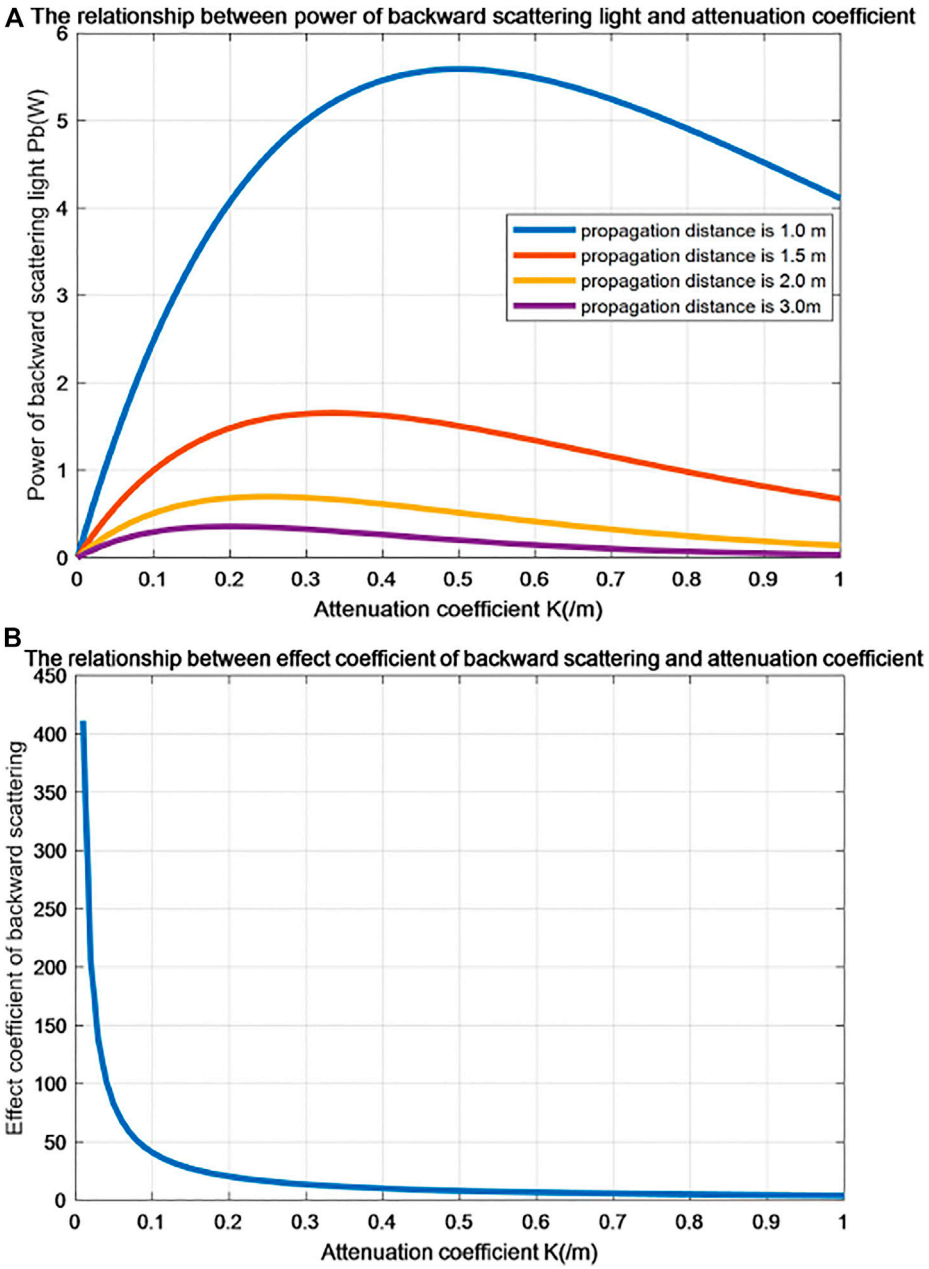


**FIGURE 3 |** The relationship between backward scattering and attenuation coefficient. **(A)** The relationship between power of forward scattering light and attenuation coefficient. **(B)** The relationship between effect coefficient of forward scarttering and attenuation coefficient.

along with different attenuation coefficient. Results are shown in **Figure 3A,B**.

In **Figure 3A**, we can see that power $P_b$ of backward scattering noise is affected by propagation distance and attenuation coefficient. In the meantime, performance tendency of power $P_b$ of backward scattering are increasing at original time and gradually decreasing with different values of attenuation coefficient $K$. When propagation distance of incident light in the underwater environment is relatively short, and $l$ is less than 2 m, water quality effects on target imaging from backward scattering noise has always appeared. Under the condition of same attenuation coefficient and same quality of water environment, with the increase of propagation distance, backward scattering is appears to rapidly decline and slowly reducing afterward. **Figure 3B** shows that effect coefficient $\eta_b$ of backward scattering gradually decreases with increase of $K$, and illustrates that the influence of noise to backward scattering on quality of target image gradually increases with the increase of attenuation coefficient. When water is too cloudy, noise of underwater backward scattering will cover up reflected target

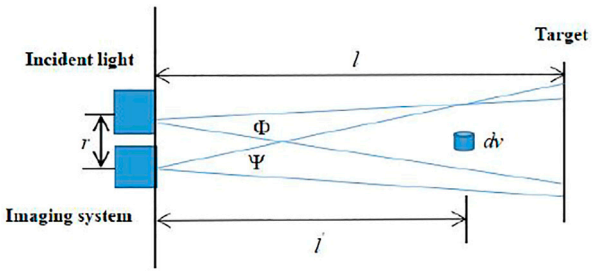


**FIGURE 4 |** The schematic diagram of forward scattering to underwater particles.

light, and we cannot identify target by underwater imaging equipment. Because of reflected light of underwater target occurring phenomenon of forward scattering with particles in the process of transmission, forward scattering light is produced which can make internal details of the target become blurred. Forward scattering light belongs to background stray light affecting target imaging that appear in synchronous transmission with incident light. The existing time lag between reflected target light and backward scattering light in the process of underwater transmission, and the effect of using imaging technology of gate-distance to filter backward scattering light is obvious, but the inhibitory effect of forward scattering light is not obvious. In the following paper, we will use the theoretical derivation process for analyzing effects of noise to forward scattering on the process of underwater target imaging. Simulating the process of forward scattering as shown in **Figure 4**, $l$ is defined as relative distance of light emitter and underwater target, $dv$ represents a small scattering volume element that has a certain distance $l^{'}$ with underwater imaging system.

Defining expression of reflected intensity from underwater target as [11]:

$$I(l) = \frac{\rho_m E(l) A_p}{\pi} = \frac{\rho_m \delta_l}{\pi} P_0 f_f \qquad (2-5)$$

with $E(l)$ represents irradiance that has distance $l$ with light emitter, $A_p$ represents projection area of underwater target, $\rho_m$ represents reflectivity to underwater target. $f_f$ represents interception factor of forward scattering that associated with projection area $A_p$ and divergence angle $\Phi$. Irradiance expression of reflected target light that has distance $l^{'}$ with underwater imaging system is defined as: $E(l^{'}) = \frac{\delta_{l-l^{'}} I(l)}{(l-l^{'})^2} = \frac{\rho_m \delta_l \delta_{l-l^{'}} f_f}{\pi (l-l^{'})^2} P_0$, with $\delta_{l-l^{'}} = e^{-k(l-l^{'})}$ represents energy loss as a result of original reflected light from target surface taking transmission to scattering volume element. Defining expression of radiation intensity that reflected target light sited at location of scattering volume element $dv$ and direction of $\theta$ is: $dI = \beta(\theta) E(l^{'}) dv = \frac{\rho_m \delta_l \delta_{l-l^{'}} f_f \beta(\theta)}{\pi (l-l^{'})^2} P_0 dv$. For transmission process of forward scattering, we can take approximation $\theta = 0$. Similar to derivation process of received power of backward scattering, power of forward scattering received imaging system can be expressed as [15]: $P_f = T_{oe} \int \frac{\pi D^2}{4l^2} \delta_{l^{'}} dI = T_{oe} \int \frac{D^2 \rho_m \delta_l \delta_{l-l^{'}} \delta_{l^{'}} f_f \beta(0)}{4l^2 (l-l^{'})^2} P_0 dv$, with $\delta_{l^{'}} = e^{-k(l^{'}-h)}$ represents energy loss as a result of reflected target light that sited at scattering volume element taking transmission to underwater imaging system, with $h = l - l^{'}$, and $\delta_l \delta_{l-l^{'}} \delta_{l^{'}} = \delta_l^2$. Defining integral area to power of forward scattering $P_f$ is volume of vertebral body surrounded by object lens of imaging system and underwater target, and can be expressed as $dv = \pi [(l - l^{'}) D/2l]^2 dl^{'}$, that is:

$$P_f \approx T_{oe} \int_0^l \frac{\pi \delta_l^2 D^2 \rho_m P_0 f_f \beta(0)}{4l^{'2} (l-l^{'})^2} \left[ \left(l - l^{'}\right) \frac{D}{2l} \right]^2 dl^{'}$$
$$= \frac{\pi T_{oe} \delta_l^2 D^4 \rho_m f_f \beta(0)}{16 l^3} P_0 \qquad (2-6)$$

Similar to definition of effect coefficient of backward scattering in field of underwater imaging, similarly defining power ratio $\eta_f = P_r / P_f$ as effect coefficient of forward scattering in field of underwater imaging. $P_r$ represents reflected power of underwater target received by imaging system [15], and is expressed as: $P_r = \rho_m T_{oe} \delta_l^2 H_o D^2 P_0 / 4l^2$. The available expression of effect coefficient of forward scattering $\eta_f$ in field of underwater imaging is expressed as:

$$\eta_f = \frac{4l}{\pi D^2 f_f \beta(0)} H_o \qquad (2-7)$$

Taking mathematical simulation and calculation analysis on power of forward scattering $P_f$ and effect coefficient of forward scattering $\eta_f$ can qualitatively obtain the influence degree of forward scattering on underwater target imaging. The simulation results are shown in **Figure 5**, the change trend of power $P_f$ of forward scattering along with change of attenuation coefficient $K$ has some similarities to the results of backward scattering, power of forward scattering are influenced by light propagation distance and attenuation coefficient of water at the same time. Under the condition of the same propagation distance, effect coefficient of forward scattering $\eta_f$ appear to decrease with the increase of attenuation coefficient $K$. Under the condition of same attenuation coefficient $\eta_f$, with increase of propagation distance, effect coefficient of forward scattering also increases gradually. The simulation results illustrate that the more turbid of water quality, the shorter of transmission distance, the more influence of noise to forward scattering on imaging quality of underwater target. It can be found in **Figure 3A** and **Figure 5A** that power of backward scattering has been larger than the power of forward scattering in the field of longitudinal axis at the conditions of same propagation distance and same attenuation coefficient, and it shows that influence degree of backward scattering is greater than forward scattering in turbid underwater target imaging.

## Effects of Existence of Bubble on the Target Imaging

Light transmits from a dense medium to a hydrophobic medium of bubbles in water. The incident light in the bubble that runs along the

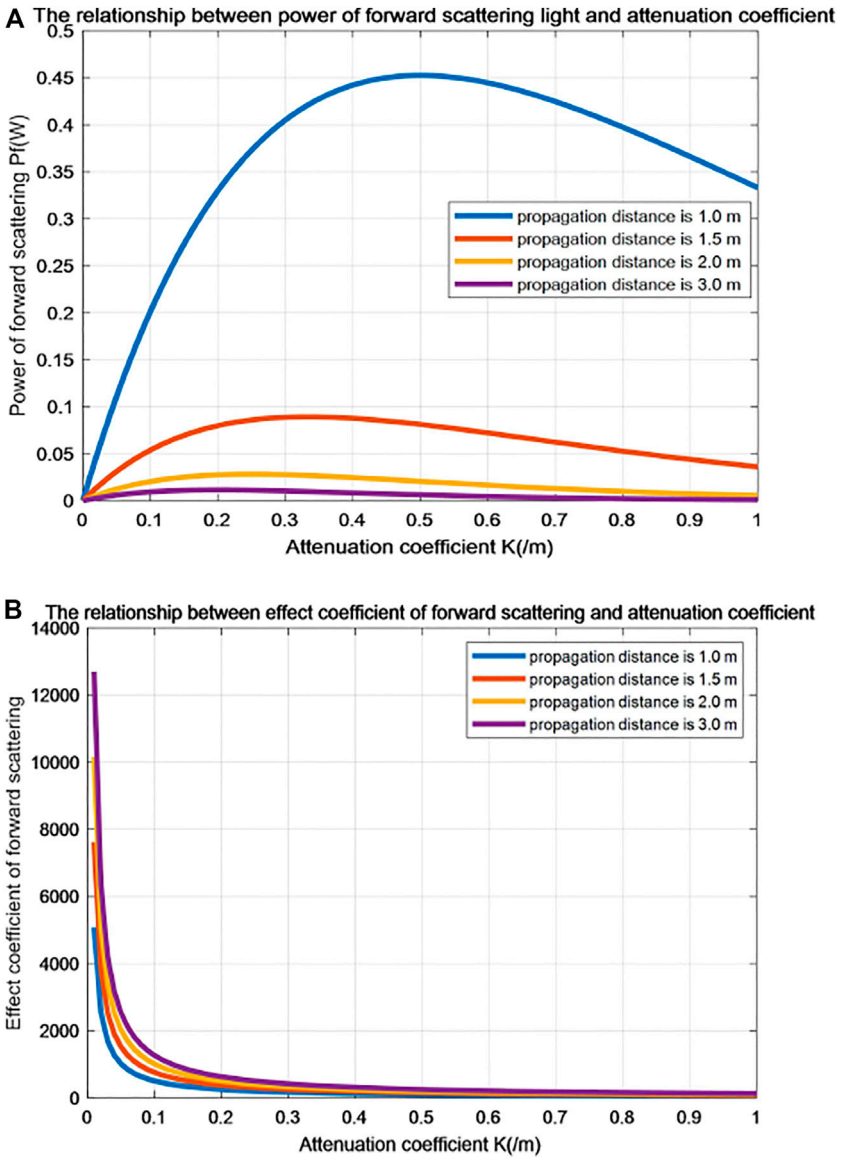


**FIGURE 5 |** The relationship between forward scattering and attenuation coefficient. **(A)** The relationship between power of forward scattering light and attenuation coefficient. **(B)** The relationship between effect coefficient of forward scarttering and attenuation coefficient.

diameter of the bubble remains the same, and the rest of the light completely deviates from the original path and does not reach the detector. As the surface area of the bubble increases, increasingly more light is refracted, the light that reaches the probe decreases, and the light intensity detected decreases. Because diffraction is more complex, this paper simplifies light transmission formation in the bubble geometrical optics. Fresnel law indicates that the reflectivity and transmissivity are connected with the polarization and incident angle of incident light and the refractive index of the medium. Any polarization of light can be decomposed into a pair of mutually perpendicular components, a vibrating direction perpendicular to the plane of incidence, expressed as S, and another vibrating direction parallel to the plane of incidence, expressed as P. According to [17] the Fresnel formula, we can obtain the reflection coefficient and the refraction coefficient expression of the polarized component expressed by P . Similarly, we can obtain the reflection coefficient and refraction coefficient expression of the polarized component expressed by S. The theoretical calculation shows that the light intensity on the bubble interface decreases continuously with increasing transmission time, and for the fourth reflection and refraction cycle, the intensity of refracted light of bubble tends to zero [16]. The value of DOP increases with increasing transmission frequency, and at the interface in the fourth transmission cycle, DOP of refraction and reflection light is the largest, being converted to almost completely polarized light [17].

Regarding the influence of distance between bubble group and imaging system on acquisition of underwater image, the related schematic diagram is shown in **Figure 6A**. Setting same

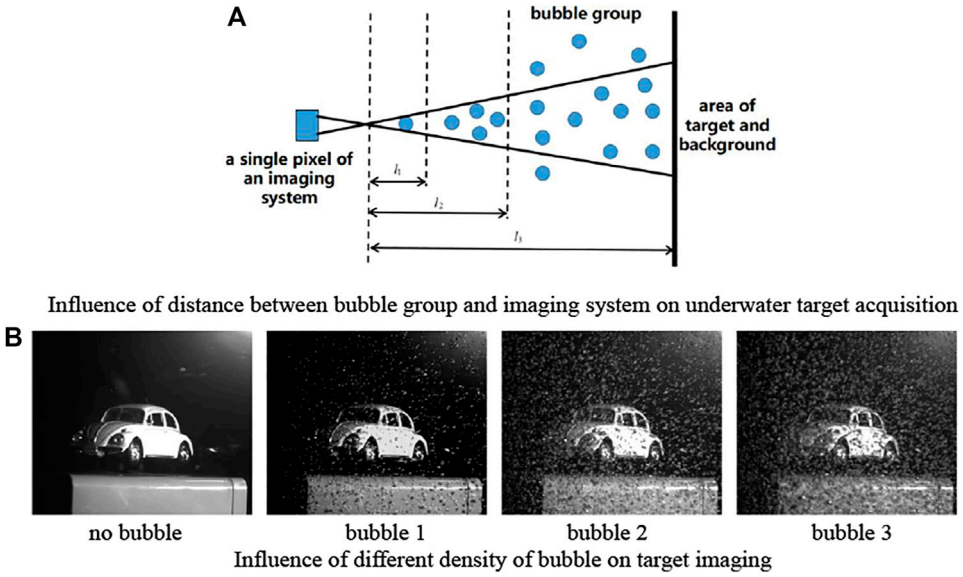


**FIGURE 6 |** Exploration of influence of bubble group on underwater target acquisition. **(A)** Influence of distance between bubble group and imaging system on underwater target acquisition **(B)** Influence of different density of bubble on target imaging.

integration time when distance is long, bubble are alike to suspended particles and cover target information. When distance is shorter, bubbles are equivalent to a layer of lens and the amount of light does not decline, but increase [16]. Form and expression of bubble in image are different when the camera is set in different integration time. When integration time is small, bubbles are alike to a white dot in an image, the intensity value has no relation to intensity of background and is only related with its bubble brightness. When integration time is bigger, bubbles are alike to a blocking strip, and affect brightness of the target area, and its intensity and intensity of the background has a certain linear relationship [16], the related schematic diagram is shown in **Figure 6B**.

The relative difference of the polarization information of the target and background region will be different with the change of incident angle of light source under the condition of bubbles. Under the condition of the same bubble thickness, target polarization information of different material are different. When the thickness of the bubble is higher, intensity and polarization imaging techniques are difficult to identify the underwater target, as can be seen in **Figure 6B**. According to the scattering theory, the suspending medium and bubble will produce certain polarization characteristics in the process of light transmission, it also does some bedding for the subsequent content of target polarization imaging.

## ESTABLISHMENT OF POLARIZATION RECONSTRUCTION MODEL OF UNDERWATER TARGET AND PARAMETER ESTIMATION

As shown in **Figure 7**, from the microscopic perspective in underwater target imaging, incident light takes transmission into the surface of the target, and energy redistribution and reflection occurs on the surface of the target, then reflected light of the target enters into CCD detector of the imaging system with attenuation, because reflected light of this road carrying information of target and are different with other locations of stray light and polarization information, therefore we can make use of the method of polarization imaging to suppress stray light, highlight information of target, so as to realize clear imaging of target under complex underwater environment.

### Underwater Polarization Imaging Measurement Theory

The polarization expression of incident light is $S = \begin{pmatrix} I \\ Q \\ U \\ V \end{pmatrix}$, when the incident light has passed through one medium (Mueller matrix is $M$), the Stokes vector $S$ of incident light will be changed to $S'$[1, 12]:$S' = M \cdot S \Leftrightarrow$

$$\begin{pmatrix} I' \\ Q' \\ U' \\ V' \end{pmatrix} = \begin{pmatrix} m_{11} & m_{12} & m_{13} & m_{14} \\ m_{21} & m_{22} & m_{23} & m_{24} \\ m_{31} & m_{32} & m_{33} & m_{34} \\ m_{41} & m_{42} & m_{43} & m_{44} \end{pmatrix} \cdot \begin{pmatrix} I \\ Q \\ U \\ V \end{pmatrix} \quad (3-1)$$

The Mueller matrix can fully describe the relationship of the change of polarization with wavelength, scattering angle, scattering particle size, shape and concentration and other parameters in the single scattering. The diagram of underwater target polarization detection is shown in **Figure 8A**, where Pol1 represents the polarization generator, Si represents Stokes vector i.

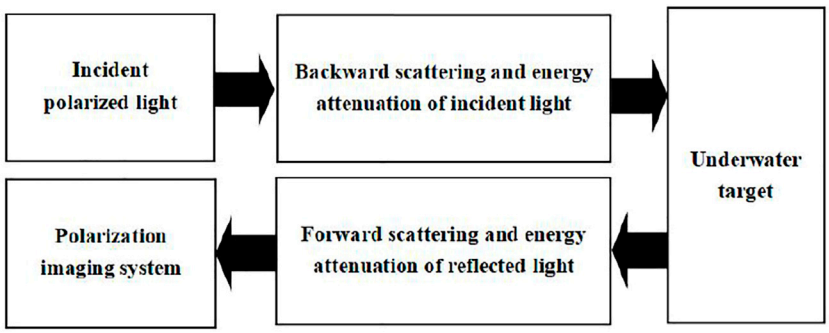


**FIGURE 7 |** The flow chart of light propagation in underwater environment.

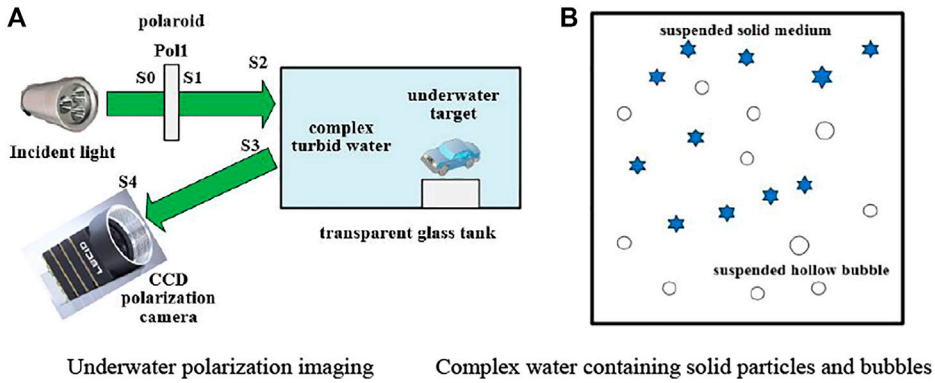


**FIGURE 8 |** The schematic diagram of underwater polarization imaging. **(A)** Underwater polarization imaging. **(B)** Complex water containing solid particles and bubbles.

The linear combination of three kinds of light and construction of underwater light transmission model are shown in as:

$$I^{total} = T + F + B \tag{3-2}$$

with $I^{\text{total}}$ represents original intensity images collected by imaging system, $T$ represents target intensity that arriving to imaging system after attenuation, $F$ represents the forward scattering intensity, $B$ represents the backward scattering intensity. **Figure 8** shows a diagram of target imaging under condition of complex underwater environment containing suspended particles and bubbles through active imaging with polarized light. Assumes that the incident light of Stokes vector as follows:

$$S_0 = \begin{pmatrix} I_0 \\ Q_0 \\ U_0 \\ V_0 \end{pmatrix} \tag{3-3}$$

When incident light has passed through the partial device Polar1, the Mueller matrix is defined as $M_{\text{polar1}}$, then the Stokes vector $S_0$ of the incident light will be changed to $S_1$:

$$S_1 = M_{polar1} S_0 \tag{3-4}$$

The process of transmission of incident light to the target, the Mueller matrix of water is defined as $M_{\text{w1}}$, the Stokes vector of incident light will be changed to $S_2$:

$$S_2 = M_{\text{w1}} S_1 \tag{3-5}$$

Supposing the Mueller matrix of the target is $M_{\text{target}}$, and the Stokes vector of the incident light will become $S_3$:

$$S_3 = M_{target} S_2 \tag{3-6}$$

In the process of reflection and transmission of light source from the target surface to the CCD imaging system, setting the Mueller matrix of water is $M_{\text{w2}}$, the Stokes vector of incident light will become into $S_4$:

$$S_4 = M_{\text{w2}} S_3 \tag{3-7}$$

Arrived at the CCD imaging system, the definition of Mueller matrix of partial detector Polar2 in CCD imaging system is $M_{\text{polar2}}$, finally the Stokes vector of incident light will be changed into $S_5$:

$$S_5 = M_{polar2} S_4 \tag{3-8}$$

According to **Figure 8**, the underwater target polarization imaging using the Mueller matrix to take concrete analysis on the

light transmission process steps are as follows: Step 1) setting the incident light is natural light, and setting its polarization is $S_0 = (S_{00}, 0, 0, 0)^T$; Step 2) the Mueller matrix expressions of the analyzer are as follows [18]:

$$M_{polar1} = \frac{1}{2} \times \begin{pmatrix} 1 & \cos(2\phi) & \sin(2\phi) & 0 \\ \cos(2\phi) & \cos^2(2\phi) & \cos(2\phi)\sin(2\phi) & 0 \\ \sin(2\phi) & \cos(2\phi)\sin(2\phi) & \sin^2(2\phi) & 0 \\ 0 & 0 & 0 & 0 \end{pmatrix} \quad (3-9)$$

Step 3) the aquatic environment shows different physical properties with the change of attenuation coefficient, the Mueller matrix expression of water is as follows:

$$M_w = \begin{pmatrix} M_{11}(\theta) & M_{12}(\theta) & M_{13}(\theta) & M_{14}(\theta) \\ M_{21}(\theta) & M_{22}(\theta) & M_{23}(\theta) & M_{24}(\theta) \\ M_{31}(\theta) & M_{32}(\theta) & M_{33}(\theta) & M_{34}(\theta) \\ M_{41}(\theta) & M_{42}(\theta) & M_{43}(\theta) & M_{44}(\theta) \end{pmatrix} \quad (3-10)$$

When medium is uniform distribution in water and only the Rayleigh scattering occurs, in order to simplify the analysis process, the Mueller matrix expression will be changed to [1]:

$$M_w = \begin{pmatrix} 1 & M_{12}(\theta) & 0 & 0 \\ M_{12}(\theta) & 1 & 0 & 0 \\ 0 & 0 & M_{33}(\theta) & 0 \\ 0 & 0 & 0 & M_{33}(\theta) \end{pmatrix} \quad (3-11)$$

with $M_{11} = M_{22} = 1$, $M_{12}(\theta) = M_{21}(\theta) = \frac{-1+\cos^2(\theta)}{1+\cos^2(\theta)}$, $M_{33}(\theta) = M_{44}(\theta) = \frac{2\cos(\theta)}{1+\cos^2(\theta)}$. When the backward scattering angle $\theta = 180°$, Mueller matrix expressions of water scattering medium is simplified to:

$$M_{w1} = M_{w2} = \begin{pmatrix} 1 & 0 & 0 & 0 \\ 0 & 1 & 0 & 0 \\ 0 & 0 & -1 & 0 \\ 0 & 0 & 0 & -1 \end{pmatrix} \quad (3-12)$$

Due to suspension medium in water belongs to the dynamic change, different concentration of suspension medium will show different polarization characteristics, and also can have different Mueller matrix, and its expression is more complicated. It can make use of the Monte Carlo method to simulate its polarization characteristics under the condition of different medium concentration of water (different attenuation coefficient). In order to analyze the relationship of underwater radiation transmission characteristics of polarized light with wavelength of incident light and thickness of scattering medium, this paper uses Monte Carlo method to simulate the change trend of intensity and DOP of backward scattering, and related parameter settings in simulation process are as follows: wavelength of incident light are set to 450, 550, 650 nm, respectively. Radius of suspended particle in water is 2 microns, medium layer are same kind of suspended particles, refraction coefficient of particle is set to 1.15, weight threshold is 0. When incident light is horizontal linear polarized light, taking calculation on average value of intensity and DOP of received photon, thus the corresponding mean curve of scattering intensity and DOP with change of thickness to scattering

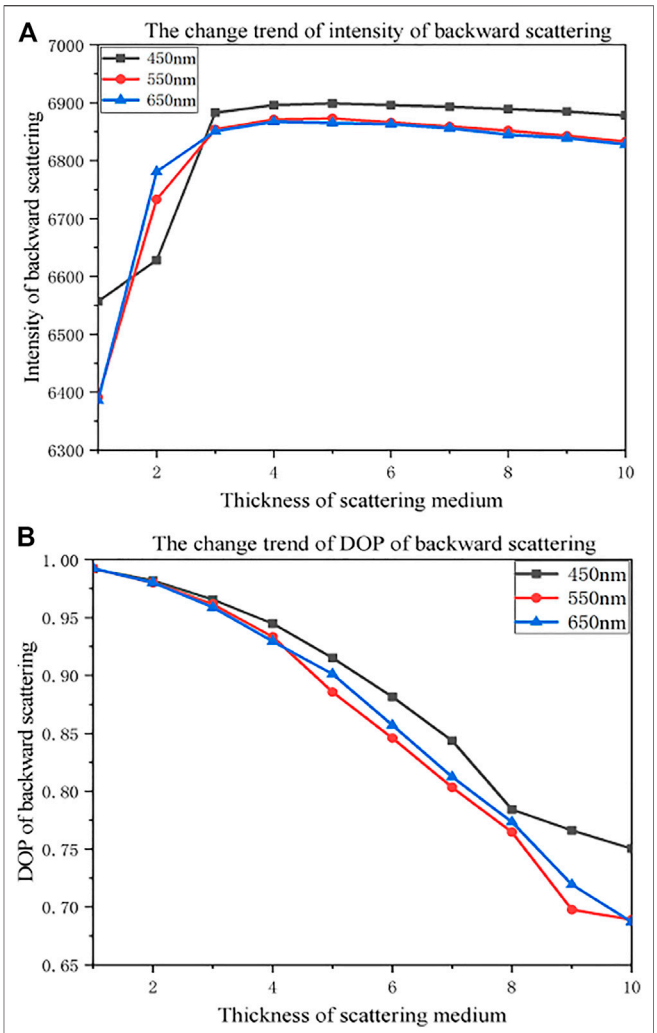


**FIGURE 9 |** The change trend of intensity and DOP of backward scattering light in underwater environment. **(A)** The changes trend of intensity of backward scattering. **(B)** The change trend of Dop of backward scattering.

medium are shown in **Figure 9**, the longitudinal axis represents average value of intensity and DOP to all photons received by receiving surface, and the horizontal axis represents thickness coefficient of scattering medium.

Due to scattering phenomenon of suspended particles in water, polarized light will become partly polarized light, appearing as the phenomenon of depolarization, with increasing of medium thickness (transmission distance), and incident light taking transmission among particles, the probability of photons absorbed and the number of scattering are constantly improving, leading to variation of original polarization state to polarized light, and becoming another kind of state of polarized light, with the degree of depolarization shows monotone decreasing. When medium thickness is greater, the medium layer is equivalent to a reflection plane [19], so scattering intensity shows a rapid increasing trend firstly, and then decreasing slowly. As for incident light source with different wavelengths appearing at

different attenuation degrees when transmitting in water, intensity and polarization information of backward scattering also shows different values with the change of transmission distance. Step 4) is the polarization characteristics of the target, and its Mueller matrix expression can be defined as follows:

$$M_{target} = \begin{pmatrix} m_{11}^T & m_{12}^T & m_{13}^T & m_{14}^T \\ m_{21}^T & m_{22}^T & m_{23}^T & m_{24}^T \\ m_{31}^T & m_{32}^T & m_{33}^T & m_{34}^T \\ m_{41}^T & m_{42}^T & m_{43}^T & m_{44}^T \end{pmatrix} \quad (3-13)$$

The photoelectric field vector of incident light, reflected light, and refracted light can be decomposed into the component P parallel to the incident plane and the component S perpendicular to the incident surface, based on the Fresnel's law, reflectance and transmittance of amplitude are $r_{\mathrm{p}} = \frac{\tan(\theta_{\mathrm{i}}-\theta_{\mathrm{t}})}{\tan(\theta_{\mathrm{i}}+\theta_{\mathrm{t}})}$, $r_{\mathrm{s}} = \frac{-\sin(\theta_{\mathrm{i}}-\theta_{\mathrm{t}})}{\sin(\theta_{\mathrm{i}}+\theta_{\mathrm{t}})}$ and $t_{\mathrm{p}} = \frac{2\sin\theta_{\mathrm{t}}\cos\theta_{\mathrm{i}}}{\sin(\theta_{\mathrm{i}}+\theta_{\mathrm{t}})\cos(\theta_{\mathrm{i}}-\theta_{\mathrm{t}})}$, $\mathrm{t_s} = \frac{2\sin\theta_{\mathrm{t}}\cos\theta_{\mathrm{i}}}{\sin(\theta_{\mathrm{i}}+\theta_{\mathrm{t}})}$ respectively. Using the type to deduce the Mueller matrix of target interface reflection as follows [20]:

$$M_{\mathrm{target}} = \begin{pmatrix} \cos^2\alpha+\cos^2\beta & \cos^2\alpha-\cos^2\beta & 0 & 0 \\ \cos^2\alpha-\cos^2\beta & \cos^2\alpha+\cos^2\beta & 0 & 0 \\ 0 & 0 & -2\cos\alpha\cos\beta & 0 \\ 0 & 0 & 0 & -2\cos\alpha\cos\beta \end{pmatrix} \quad (3-14)$$

with $\theta_{\mathrm{i}}$ represents the incident angle, $\theta_t$ represents the refraction angle of incident light, in the interface, $n_{\mathrm{i}}\sin\theta_i = n_t\sin\theta_t$, and formulas are $\alpha = \theta_{\mathrm{i}} - \theta_t$, $\beta = \theta_{\mathrm{i}} + \theta_t$. Different targets with different polarization properties, have different Mueller matrix expression. Step 5) polarization CCD imaging system has obtained the Stokes vector of target reflection light after transmission and attenuation in water.

## Underwater Polarization Imaging Reconstruction Method of Removing Scattering

The directly transmitted light of underwater target $T$ (that is the transmitted intensity information having passed through attenuation) is defined as shown in:

$$T = L_{object}e^{-kl} \quad (3-15)$$

with $L_{\mathrm{object}}$ represents intensity information of target, $t = e^{-kl}$ represents the transmission rate of underwater transmitted light, $k$ is expressed as the total attenuation coefficient of water (coefficient is affected by absorption and scattering), $l$ is expressed as distance between the target and imaging system. In this paper, $k$ is simplified and defined as constants in the underwater environment.

After Mueller matrix calculation of target area in turbid environment, the Stokes vector expression of target is obtained by CCD imaging system as follows:

$$S_{target} = M_{\mathrm{w2}}M_{target}M_{\mathrm{w1}}M_{polar1}S_0 \quad (3-16)$$

Supposing internal partial detector of polarization CCD imaging system is Polar2, when the partial detector Polar1 and the partial detector Polar2 are parallel, ideally $\phi_{pol1} = \phi_{pol2} = 90°$, getting parallel light intensity of the target area is $I_{target}^{//}$ (represented by $T^{\max}$). When the partial detector Polar1 and the partial detector Polar2 are vertical, and in the ideal case, $\phi_{pol1} = 0°$ and $\phi_{pol2} = 90°$, getting vertical light intensity of the target area is $I_{target}^{\perp}$ (represented by $T^{\min}$).

The backward scattering light $B$ can be defined [4] as follows:

$$B = \int_{\Theta} B(\Theta)d\Theta = B_{\infty}(1-t) \quad (3-17)$$

with $B(\Theta)$ represents volume element function of backward scattering, $\Theta$ is defined as a set of scattering angle to a small volume element, $B_{\infty} = \int_{\Theta} B_{\infty}(\Theta)d\Theta$ represents for infinite intensity value of underwater background light.

In water environment, using Mueller matrix to calculate the area of backward scattering light, CCD imaging system can get the Stokes vector expression of backward scattering light which is:

$$S_{backsca} = M_{\mathrm{w2}}M_{\mathrm{w1}}M_{polar1}S_0 \quad (3-18)$$

when the partial detector Polar1and the partial detector Polar2 are parallel, ideally $\phi_{pol1} = \phi_{pol2} = 90°$, getting parallel light intensity of the backward scattering area is $I_{backsca}^{//}$ (represented by $B^{\max}$). When the partial detector Polar1 and the partial detector Polar2 are vertical, and in the ideal case, $\phi_{pol1} = 0°$ and $\phi_{pol2} = 90°$, getting vertical light intensity of the backward scattering area is $I_{\mathrm{backsca}}^{\perp}$ (represented by $B^{\min}$).

We use the focal plane polarization camera to take data acquisition, the camera can obtain four intensity images at different polarization direction at one-time, I0, I45, I90, I135 respectively, and can obtain Stokes vector of target reflection and backward scattering light after passing through water at the same time. This paper uses method of curve fitting to obtain the best image of orthogonal polarization, taking Stokes vector and fitting out the curve of relationship between $I(\theta)$ and $\theta$, using **Equation (3-19)** to compute the corresponding figure of maximum intensity $I^{\max}$ with angle is $\theta^{\max}$ and figure of minimum intensity $I^{\min}$ with angle is $\theta^{\min}$.

$$\begin{cases} I^{max} = \frac{1}{2}(I + Q\cos 2\theta^{\max} + U\sin 2\theta^{\max}) \\ I^{\min} = \frac{1}{2}\left(I + Q\cos 2\theta^{\min} + U\sin 2\theta^{\min}\right) \end{cases} \quad (3-19)$$

In an underwater environment, because the forward scattering mechanism are more complicated, the influence extent of backward scattering is greater than the forward scattering this article does not take the forward scattering factor into subsequent process of modeling, and specific content can refer to **Section 2**. According to **Equation (3-2)**, the maximum intensity expression and minimum intensity expression are shown in **Equation (3-20)**:

$$\begin{cases} I^{max} = T^{\max} + B^{\max} \\ I^{\min} = T^{\min} + B^{\min} \end{cases} \quad (3-20)$$

Using **Equation (3-20)** can get intensity expression of underwater scene as shown in **Equation (3-21)**:

$$I = I^{\max} + I^{\min} \tag{3-21}$$

According to calculation formula of DOP, the DOP of underwater scene light $P_I$, the DOP of background light $P_B$ and the DOP of reflected light of underwater target $P_S$ can be expressed as follows:

$$\begin{cases} P_I = \dfrac{I^{\max} - I^{\min}}{I} \\ P_B = \dfrac{B^{\max} - B^{\min}}{B} \\ P_T = \dfrac{T^{\max} - T^{\min}}{T} \end{cases} \tag{3-22}$$

Uniting **Equation (3-20)** to **Equation (3-22)** can obtain expressions on synthesis intensity and differential intensity of underwater scene light expressed as follows:

$$\begin{cases} I^{\max} + I^{\min} = T + B \\ I^{\max} - I^{\min} = \Delta I = P_T T + P_B B \end{cases} \tag{3-23}$$

**Equation (3-24)** can be derived by **Equation (3-23)**:

$$\begin{aligned} \Delta I &= \left(L_{object}^{\max} - L_{object}^{\min}\right)t + \left(B_{\infty}^{\max} - B_{\infty}^{\min}\right)(1-t) \\ &= P_T L_{object} t + P_B B_{\infty}(1-t) \\ &= P_T (I - B_{\infty}(1-t)) + P_B B_{\infty}(1-t) \end{aligned} \tag{3-24}$$

Using **Equation (3-24)** can further conclude new rate transmission expression $t$ is defined as:

$$t = 1 - \frac{\Delta I - P_T I}{B_{\infty}(P_B - P_T)} \tag{3-25}$$

Uniting **Equation (3-22)** to **Equation (3-24)** can obtain intensity information of underwater target $S$ and intensity information of underwater background $B$:

$$T = \frac{1}{P_B - P_T}\left[I^{\min}(1+P_B) - I^{max}(1-P_B)\right] \tag{3-26}$$

$$B = \frac{1}{P_B - P_T}\left[I^{\max}(1-P_T) - I^{\min}(1+P_T)\right] \tag{3-27}$$

As you can see, in the polarization reconstruction model of underwater target of **Equation (3-26)**, we have considered the reflected radiation of underwater target containing polarization information. Compared with traditional underwater light transmission map [4], the new expression of transmission rate $t$ is not only related to underwater infinite background light intensity value $B_{\infty}$, but also has relation to underwater scene light intensity $I$, DOP of background light $P_B$, DOP of reflected light to underwater target $P_S$ and other relevant parameters, the stand or fall of calculation results of the underwater transmission rate are also important factors to affect target recovery. Finally, uniting **Equation (3-24)** and **Equation (3-26)** can get radiation information expression of target in an underwater environment:

$$L_{object} = \left[\frac{I^{\min}(1+P_B) - I^{\max}(1-P_B)}{P_B - P_T}\right] \Big/ \left(1 - \frac{\Delta I - P_T I}{B_{\infty}(P_B - P_T)}\right) \tag{3-28}$$

with the effective intensity information of reflected target light is defined as $L_{object}$ (the intensity information that has passed through underwater transmission).

The degree of polarization of backward scattering light is automatically estimated for the non-target region, as shown in the following equation:

$$P_{\mathrm{B}} = \frac{\sum_{\Omega^T} B^{//}(x,y) \Big/ N - \sum_{\Omega^T} B^{\perp}(x,y)/N}{\sum_{\Omega^T} B^{//}(x,y) \Big/ N + \sum_{\Omega^T} B^{\perp}(x,y)/N} \tag{3-29}$$

with $\Omega^T$ representing local region of background in image. According to the principle of the dark channel prior, scattering light of background region can use the maximum value of the dark channel in scattering image (not the maximum light intensity of the original image, but the maximum light intensity in dark channel) to estimate. As the experiment data acquisition is grayscale image, the principle of the bright color method to estimate infinite intensity value in underwater background is used [21], and its expression is defined as:

$$L^{bright} = \max_{z \in \Omega}(L(z)) \tag{3-30}$$

with $L(z)$ represents input image $L$, $\Omega$ represents center block of one point in image. Using **Equation (3-31)** can automatically estimate image block of optimal neighborhood $\Omega$.

$$\Omega = \alpha^{'} \times normalize\left(-1 \Big/ \ln\left(1 - B^{'} \Big/ L^{bright}\right)\right) + C \tag{3-31}$$

with $B^{'}$ represents intensity values of background light, $\alpha^{'}$ represents scale parameter, $C$ represents minimum window size, normalize is normalization function. Bringing best neighborhood image block $\Omega$ to **Equation (3-30)**, and can finally obtain optimally infinite intensity estimation of underwater background light $B_{\infty}$, and $B_{\infty} = L^{bright}$.

As can be seen from the above estimation process of polarization parameter, estimation of underwater target polarization information $P_T$ is irrelevant with polarization information of underwater backward scattering light $P_B$. As can be seen from **Equation (3-26)** and **Equation (3-27)**, intensity information of underwater target $T$ and intensity information of backward scattering light $B$ can be expressed as function of DOP to target at same time, thus, when correlation between $T$ and $B$ is minimum, the corresponding DOP value of target $P_T$ is requested. In order to show this correlation, the covariance of $T$ and $B$ is used to measure the size of independence of these two parameters. Using mathematical expression to express $P_T$ is as follows:

$$P_T(x,y) = \underset{P_S(x,y) \in [0,1]}{\arg\min} \left| Cov\left(B(x,y), T(x,y)\right)\right| \tag{3-32}$$

The covariance can be expressed as:

$$\begin{aligned} &\mathrm{Cov}\left(B(x,y), T(x,y)\right) = \\ &\underset{x_{obj} \in \Omega}{Cov}\left(\frac{P_B(x,y)I(x,y) - \Delta I(x,y)}{P_B(x,y) - P_T(x,y)}, \frac{\Delta I(x,y) - P_T(x,y)I(x,y)}{P_B(x,y) - P_T(x,y)}\right) \end{aligned} \tag{3-33}$$

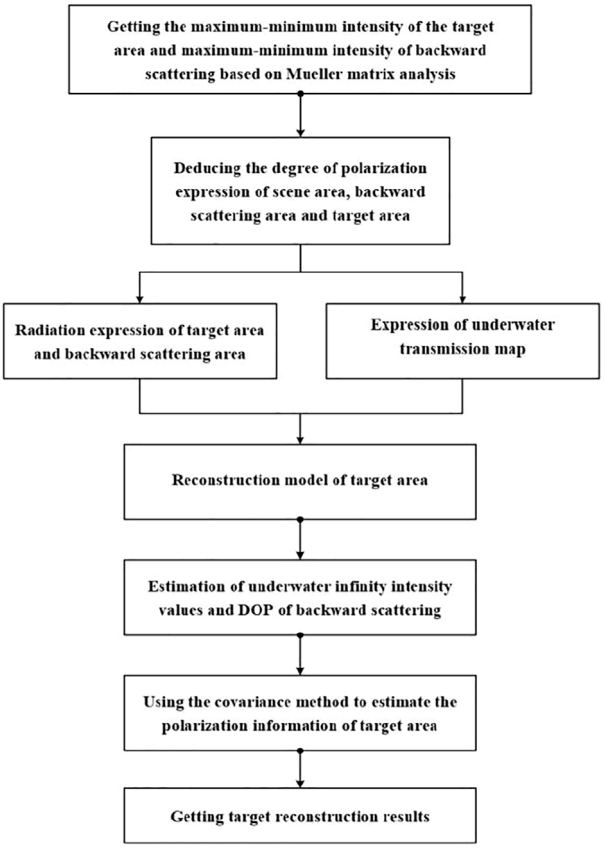


**FIGURE 10 |** The structure diagram of proposed method.

Covariance is function expression of DOP to target $P_S$, and $P_S(x, y) \in [0, 1]$, therefore, proposing an iterative method to obtain the optimal solution of DOP to the target. Within the interval of [0,1], getting about 200 points and the step length being 0.05, obtaining absolute value of covariance by iterative calculation, getting array constituted by absolute value of covariance with corresponding DOP of different targets, we can obtain optimal solutions of corresponding DOP value to target when taking the minimum value of array.

The structure of underwater polarization imaging reconstruction algorithm is shown in **Figure 10**.

# COMPLEX UNDERWATER ENVIRONMENT POLARIZATION IMAGING EXPERIMENT AND QUANTITATIVE ANALYSIS OF RESULT

## Setting up Polarization Imaging Experiments in Dynamic Complex Underwater Environment

In order to verify the validity of the polarization reconstruction method, we have carried out polarization imaging experiments of an underwater target. A transparent glass tank was used in the underwater imaging experiment, according to the principle of actively optical underwater transmission in **Section 2** and requirements in actual scene, using an LED lamp with high power that has been installed one polaroid in front of experiment for lighting target, it is shown in **Figure 8A**. Emission light first passed through line-polaroid and is transformed into polarized light and arrives to targets, then reflected light from the target surface enters into the imaging system, where the imaging system will collect polarization images that are taken into the terminal equipment for eventual data processing. Relevant data show that the average concentration of suspended medium is 0.8–2.5 mg/L in seawater, and milk can simulate the scattering characteristics of seawater [22]. The relative refractive index of tap-water at room temperature is 1.333, volume attenuation coefficient is about 0.15 $m^{-1}$. Real underwater experiment scene is shown in **Figure 11A** and **Figure 11B**. A LUCID focal plane polarization camera was used in the experiment, as shown in **Figure 11C**. The polarization filter is added to the front location of pixel in this camera, each 2*2 pixel array have four different directions of polarization filter (0°, 45°, 90° and 135°), and the camera takes output intensity and polarization information of each image pixel [23]. Specific parameters of the LUCID polarization camera are referred to in **Table 1**. According to the experiment scene, camera exposure time is set in 5,000 microseconds and kept unchanged. The calculation formula of Stokes vector are shown in Equation (4-1):

$$\begin{cases} I = I0 + I90 \\ Q = I0 + I90 \\ U = I45 + I135 \end{cases} \quad (4-1)$$

In the experiment, using the process of dropping milk into a transparent glass tank containing water, step by step, for quantitatively controlling the quality of water in order to simulate suspended particles in water, and installing bubble generator in the front of target to simulate real environment of underwater exploration, the experiment scene of complex underwater environment is shown in **Figure 11**. In the experiment, bubble density is defined as bubble 1, bubble 2 and bubble 3, respectively, with different numbers of bubble generators: one bubble generator represents bubble 1, two bubble generators represent bubble 2, three bubble generators represent bubble 3, and suspended medium density are defined as density 1, density 2 and density 3, respectively, with different concentrations of milk Adding 1 ml of milk represents density 1, adding 2 ml of milk represents density 2, adding 3 ml of milk represents density 3. Target area contains a small-sized gun.

## The Result of Experiment and Analysis of Processed Images

Experimental data collection are divided into three kinds of circumstances. The first kind of circumstance is to explore image recovery results under the condition of different bubble density, without adding milk into the water. The second is to


**FIGURE 11 |** Diagram of dynamic turbid underwater complex environment and experimental scene. **(A)** Intensity map with bubble **(B)** Intensity map with bubble and suspended medium **(C)** LUCID camera.

**TABLE 1 |** Specific parameters of LUCID polarization camera.

| Camera Indicators | Parameters |
|---|---|
| Sensor | Sony IMX250MZR CMOS (mono), adds four different orientation polarization filter (0°, 45°, 90° and 135°) |
| Target Surface Size | 11.1 mm (Type 2/3") |
| Resolution | 2448 * 2048 pix |
| Size of Pixel | 3.45 μm (H) * 3.45 μm (V) |
| Frame Rate | 24 FPS |
| Data Format | Mono8/10/12/16 |
| ADC | 12 bit |
| Gain Range | 0–48 dB analog and digital |
| Exposure Time Range | 30 μs to 10 s |

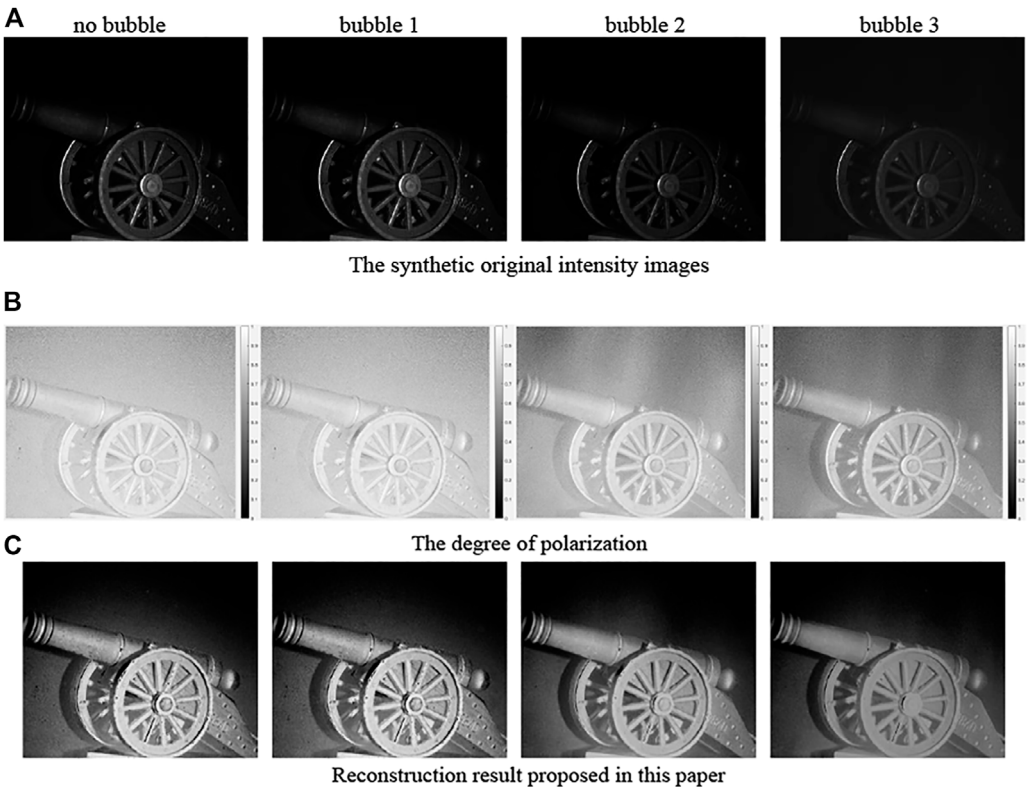


**FIGURE 12 |** Effects of different density of bubble on target polarization imaging. **(A)** The synthetic original intensity images. **(B)** The degree of polarization. **(C)** Reconstruction result proposed in this paper.

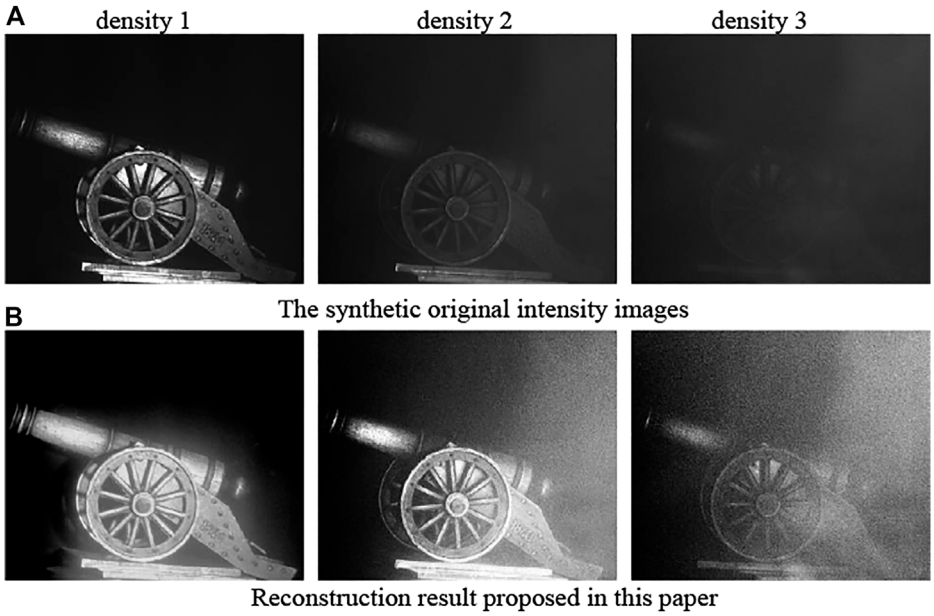


**FIGURE 13 |** Figure processing under the condition of different density of medium without bubble. **(A)** The synthetic original intensity images. **(B)** Reconstruction result proposed in this paper.

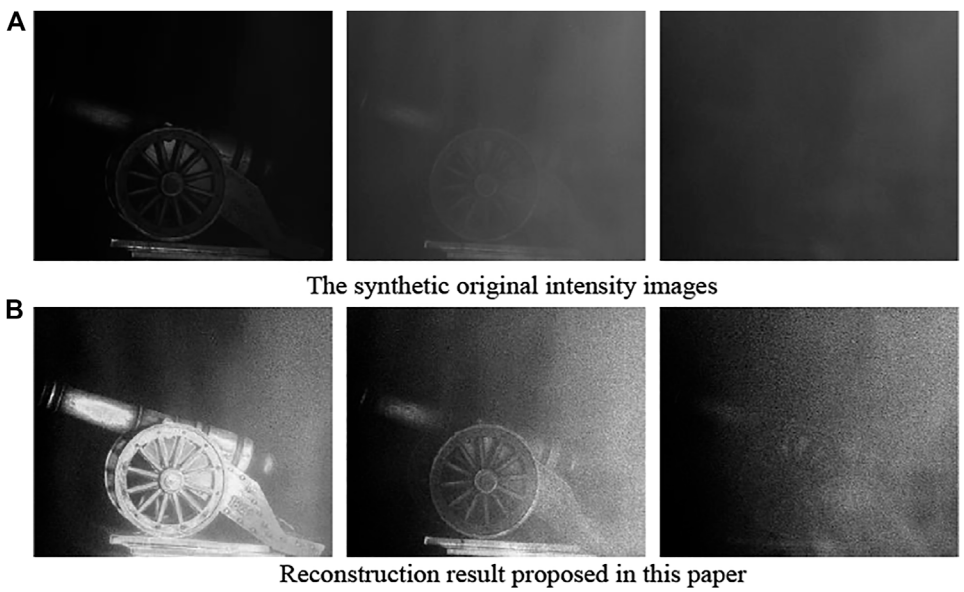


**FIGURE 14 |** Figure processing under the condition of different density of medium with bubble density is bubble 3. **(A)** The synthetic original intensity images. **(B)** Reconstruction result proposed in this paper.

explore image recovery results under the condition of different concentrations of suspended medium, without adding bubble into the water. The third is to explore image recovery results under the condition of the coexistence of suspended medium with bubble (bubble density belongs to high density, named bubble 3, and concentration of suspended medium is different).

1) Exploring the influence of different bubble density on target imaging

In this experimental scenario, a small-sized gun is placed in a dynamic underwater complex environment. Collecting original images in all-pass channel under four different polarization directions by polarization-imaging system, synthetic original

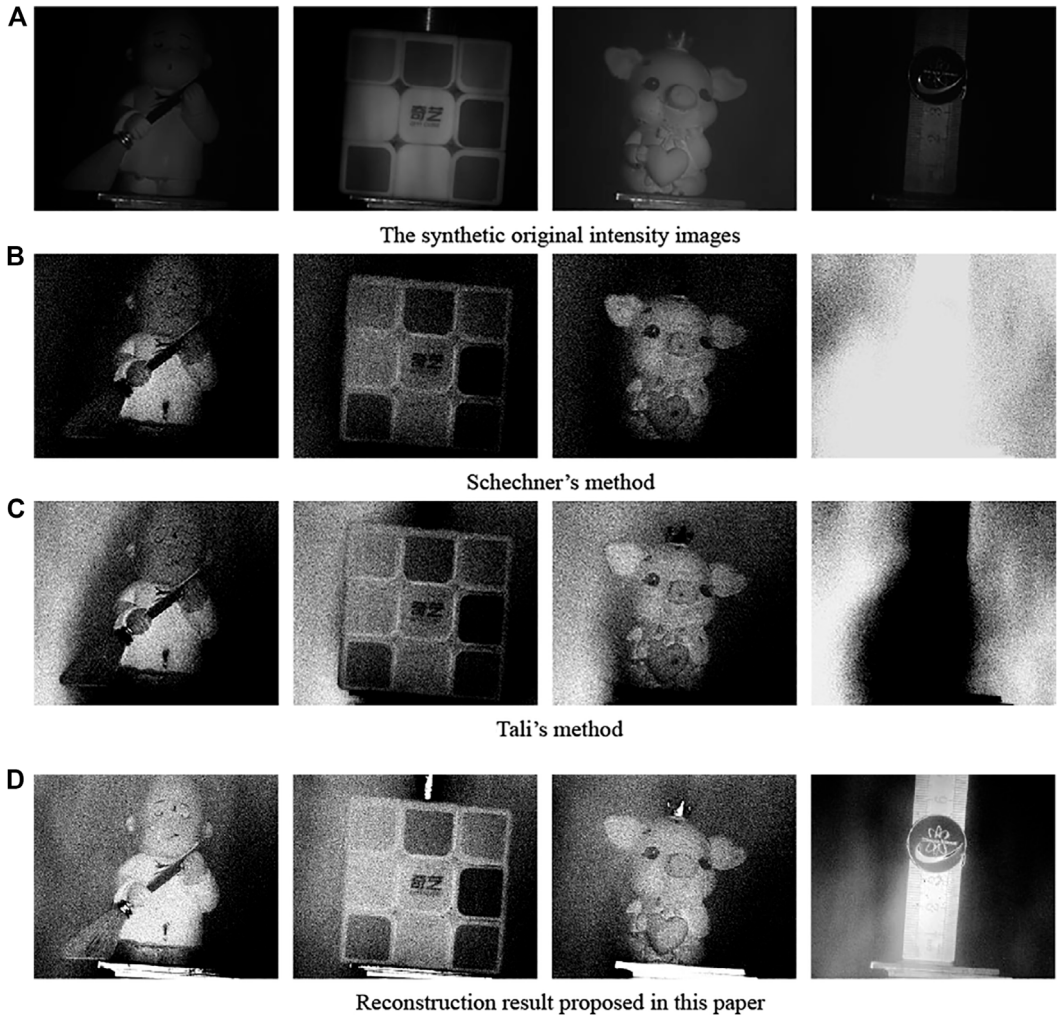


**FIGURE 15 |** The processing results of other material target under the condition of bubble concentration is bubble 3 and medium concentration is density 1. **(A)** The synthetic original intensity images. **(B)** Schechner's method. **(C)** Tali's method. **(D)** Reconstruction result proposed in this paper.

intensity images under the condition of different bubble density are shown respectively, in **Figure 12A**. It can be seen that the existence of bubble has affected the common optical imaging of target to a certain extent, intensity value decreases with the increase of bubble density. The degree of polarization under the condition of different bubble density are shown, respectively, in **Figure 12B**. After calculation, with the increase of bubble density and the degree of polarization of target region and background region gradually decrease, but compared with ordinary optical imaging, the polarization imaging has obvious advantages such as suppressing noise interference on imaging. **Figure 12C** are reconstructed images proposed by this paper, and compared with original intensity figures, reconstructed images overall have better quality and better vision.

2) Exploring the influence of different media concentration on target imaging

The second case is shown in **Figure 13**. The proposed method in this paper has proved that clear imaging method of underwater target can effectively suppress backward scattering that reduces contrast of image, and the proposed method still has a certain effectiveness when concentration of suspended medium is high.

3) Coexistence of bubble and suspending medium

The third case will explore the influence of different media concentration on target imaging in condition of bubble concentration is bubble 3, as shown in **Figure 14**. The proposed method in this paper has also proved that clear imaging method of underwater target can effectively suppress backward scattering and noise that reducing clearity of image, the proposed method have a certain effectiveness under the condition of a dynamic complex underwater environment.

According to results in **Figure 12**, **Figure 13** and **Figure 14**, it can be concluded that the reconstruction method proposed in

this paper can get clear recovery results of underwater target when waveband is all-pass [24]. In order to prove the applicability of the algorithm, we took polarization imaging experiments of four target groups made of different material under the conditions of all-pass waveband in complex underwater environment. **Figure 15A** shows synthetic original intensity images, **Figure 15B** shows the processed results of Schechner's method, **Figure 15C** shows the processed results of Tali's method, **Figure 15D** shows the processed results of proposed method in this paper. It also can be seen that the proposed method can restrain effects of underwater particle scattering and bubbles on the imaging of the target, and the recovery images have greatly been improved in resolution and texture detail, and processed detail edge is better.

### Comparative Analysis of Classic Methods

Existing underwater polarization recovery method generally has the following challenges: 1) Obtaining orthogonal polarization images by using method of artificially spinning polarization analyzer or ways of directly taking operation on camera device that have not been calibrated, the selection of the best and worst polarization direction will affect recovery result are good or bad. 2) When constructing a polarization reconstruction model of an underwater target by directly borrowing formula of atmospheric scattering model, there will be a certain treatment effect, but the underwater environment and the atmospheric environment have some differences, such as types of media and the degree of light attenuation, so there is a need for further optimization of the polarization reconstruction model. 3) The manual way to estimate parameters and processed time of algorithm is long, so these proposed methods are difficult to meet the demand of practical applications on underwater target imaging. It is found in experimental process that Schechner's method [6] and Tali's method [7] use artificial selection of background region to estimate parameters and substitute constant value to calibrate polarization reconstruction parameters, these method increases the complexity of the recovery algorithm, and can't solve disadvantages of recovery effect are not well that only estimating parameters in one background area. Using the way of actively calculating polarization parameters to get reconstructed parameters and using the way of bright color principle to automatically estimate optimal intensity values of underwater infinite background, can reasonably solve the above problems in this article. When using the maximum and minimum intensity algorithm to calculate the intensity the polaroid does not need to be manually turned. The target polarization information in the model was taken into account and the covariance method to automatically estimate the parameters of underwater target polarization information was used. Compared to the original intensity image and recovery results of other methods, processed results by using the proposed method can enhance the definition of results, and targets can be well distinguished.

## CONCLUSION

This paper has carried out imaging studies of targets in an underwater environment from theoretical derivation, numerical simulation of environmental noise, underwater polarization-imaging experiments, and restored processing of images. Taking theoretical derivation and simulation on noise analysis of backward scattering field and forward scattering field in underwater environment, it is concluded that power of backward scattering light and forward scattering light show a change trend of firstly increasing and then decreasing with increasing of attenuation coefficient, effect coefficient of backward scattering and forward scattering decreases with increasing of attenuation coefficient, power of backward scattering light is greater than power of forward scattering light, the degree of influence of backward scattering is greater than forward scattering in underwater imaging. Polarization information of the target has been considered in the polarization imaging model of underwater target, and the way of estimating the underwater transmission rate has improved, obtaining good recovery effect through adaptive estimation method of optimal polarization information parameters. Designing polarization imaging experiments of underwater targets with different concentrations of suspension medium and bubble and different materials under complex environment. The coexistence of the suspension medium and bubble in the complex water at the same time, and combine **Section 2** to the scattering noise analysis, explores the result of the underwater target polarization imaging and recovery under different materials and water environment. According to experiments of underwater polarization-imaging and contrast results of processed images, we can see that targets restored by the proposed method have high resolution, and verify the validity of proposed method. Finding the best observation condition in a complex underwater environment for clear target imaging will be our research priorities in the future.

## DATA AVAILABILITY STATEMENT

The raw data supporting the conclusions of this article will be made available by the authors, without undue reservation.

## AUTHOR CONTRIBUTIONS

All authors listed have made a substantial, direct and intellectual contribution to the work, and approved it for publication.

## FUNDING

We received financial support by the National Key R&D Program of China (Grant No. 2016YFE0201400) and the Key Project of Hefei Research Institute of Chinese Academy of Sciences (Grant No. Y73H9P1801).

## REFERENCES


1. Amer KO, Elbouz M, Alfalou A, Brosseau C, Hajjami J. Enhancing Underwater Optical Imaging by Using a Low-Pass Polarization Filter. *Opt Express* (2019) 27:621–43. doi:10.1364/OE.27.000621
2. Han P, Liu F, Wei Y, Shao X. Optical Correlation Assists to Enhance Underwater Polarization Imaging Performance. *Opt Lasers Eng* (2020) 134: 106256. doi:10.1016/j.optlaseng.2020.106256
3. Li X, Hu H, Zhao L, Wang H, Yu Y, Wu L, et al. Polarimetric Image Recovery Method Combining Histogram Stretching for Underwater Imaging. *Sci Rep* (2018) 8:12430. doi:10.1038/s41598-018-30566-8
4. Fade J, Panigrahi S, Carré A, Frein L, Hamel C, Bretenaker F, et al. Long-range Polarimetric Imaging through Fog. *Appl Opt* (2014) 53:3854–65. doi:10.1364/AO.53.003854
5. Pierangelo A, Manhas S, Benali A, Fallet C, Totobenazara J-L, Antonelli M-R, et al. Multispectral Mueller Polarimetric Imaging Detecting Residual Cancer and Cancer Regression after Neoadjuvant Treatment for Colorectal Carcinomas. *J Biomed Opt* (2013) 18:046014. doi:10.1117/1.jbo.18.4.046014
6. Schechner YY, Karpel N. Recovery of Underwater Visibility and Structure by Polarization Analysis. *IEEE J Oceanic Eng* (2005) 30:570–87. doi:10.1109/JOE.2005.850871
7. Treibitz T, Schechner YY. Active Polarization Descattering. *IEEE Trans Pattern Anal Mach Intell* (2009) 31:385–99. doi:10.1109/TPAMI.2008.85
8. Huang B, Liu T, Hu H, Han J, Yu M. Underwater Image Recovery Considering Polarization Effects of Objects. *Opt Express* (2016) 24:9826–38. doi:10.1364/OE.24.009826
9. Feng F, Wu GJ, Wu YF, Miao YH, Liu B. Algorithm for Underwater Polarization Imaging Based on Global Estimation. *Acta Opt. Sin.* (2020) 40: 2111002. doi:10.3788/AOS202040.2111002
10. Liu B, Zhao P-X, Zhao X, Luo Y, Zhang L-C. Multiple Aperture Underwater Imaging Algorithm Based on Polarization Information Fusion. *Acta Phys Sin* (2020) 69:184202. doi:10.7498/aps.69.20200471
11. Tian Y, Liu B, Su X, Wang L, Li K. Underwater Imaging Based on LF and Polarization. *IEEE Photon J.* (2019) 11:1–9. doi:10.1109/JPHOT.2018.2890286
12. Wei Y, Han P, Liu F, Shao X. Enhancement of Underwater Vision by Fully Exploiting the Polarization Information from Stokes Vector. *Opt Express* (2021) 29:22275–87. doi:10.1364/OE.433072
13. Qian WX, Bai LF, Chen Q, Gu GH. Theoretical Study on Back-Scattering Model of Laser's Transmission Underwater Based on Frequency Domain. *Infrared Laser Eng* (2006) 35:441–4. doi:10.3969/j.issn.1007-2276.2006.04.015
14. Ge WL, Hua LH, Zhang XH, Han HW. Calculation of Water Backscattering Light Energy Distribution in Range-Gated Underwater Laser Imaging System. *J Naval Univ Eng* (2013) 25:53–6. doi:10.7495/j.issn.1009-3486.2013.02.010
15. Zhong SC, Li ZR, Wang RB. Forward-scattering Effect on Underwater Laser Imaging. *High Power Laser and Particle Beams* (2012) 24:61–4. doi:10.3788/HPLPB20122401.0061
16. Tang YH, Xie GY, Liu HC, Shao JB, Ma Q, Liu HP, et al. Study of the Interface Optical Property of Bubbles in Water Based on PIV. *Acta Phys Sin* (2006) 55: 2257–62. doi:10.7498/aps.55.2257
17. Liang SY, Wang JA, Zong SG, Wu RH, Ma ZG, Wang XY, et al. Laser Detection Method of Ship Wake Bubbles Based on Multiple Scattering Intensity and Polarization Characteristics. *Acta Phys Sin* (2013) 62: 62060704. doi:10.7498/aps.62.060704
18. Garg K, Nayar SK. Vision and Rain. *Int J Comput Vis* (2007) 75:3–27. doi:10.1007/s11263-006-0028-6
19. Cariou J, Le Jeune B, Lotrian J, Guern Y. Polarization Effects of Seawater and Underwater Targets. *Appl Opt* (1990) 29:1689. doi:10.1364/AO.29.001689
20. Cao Nian-Wen NW, Liu Wen-Qing WQ, Zhang Yu-Jun YJ. Measuring the Depolarization for Scattering Light at Several Kinds of Media. *Acta Phys Sin* (2000) 49:647–53. doi:10.7498/aps.49.647
21. Rahman Z, Yi-Fei P, Aamir M, Wali S, Guan Y. Efficient Image Enhancement Model for Correcting Uneven Illumination Images. *IEEE Access* (2020) 8: 109038–53. doi:10.1109/access.2020.3001206
22. Agaian SS, Panetta K, Grigoryan AM. Transform-based Image Enhancement Algorithms with Performance Measure. *IEEE Trans Image Process* (2001) 10: 367–82. doi:10.1109/83.908502
23. Li HY, Li CY, Li XB, Wang H, Hu HF, Liu TG. Optimization of Polarization-Camera-Based Full Stokes Polarimeter. *Acta Opt. Sin.* (2020) 40(3):0326001. doi:10.3788/AOS202040.0326001
24. Hu H, Zhao L, Li X, Wang H, Liu T. Underwater Image Recovery under the Nonuniform Optical Field Based on Polarimetric Imaging. *IEEE Photon J.* (2018) 10:1–9. doi:10.1109/jphot.2018.2791517


**Conflict of Interest:** The authors declare that the research was conducted in the absence of any commercial or financial relationships that could be construed as a potential conflict of interest.

# Advantages of publishing in Frontiers

**OPEN ACCESS**
Articles are free to read for greatest visibility and readership

**FAST PUBLICATION**
Around 90 days from submission to decision

**HIGH QUALITY PEER-REVIEW**
Rigorous, collaborative, and constructive peer-review

**TRANSPARENT PEER-REVIEW**
Editors and reviewers acknowledged by name on published articles

**Frontiers**
Avenue du Tribunal-Fédéral 34
1005 Lausanne | Switzerland

**Visit us:** www.frontiersin.org
**Contact us:** frontiersin.org/about/contact

**REPRODUCIBILITY OF RESEARCH**
Support open data and methods to enhance research reproducibility

**DIGITAL PUBLISHING**
Articles designed for optimal readership across devices

**FOLLOW US**
@frontiersin

**IMPACT METRICS**
Advanced article metrics track visibility across digital media

**EXTENSIVE PROMOTION**
Marketing and promotion of impactful research

**LOOP RESEARCH NETWORK**
Our network increases your article's readership